Peptide-Directed Supramolecular Self-Assembly of *N*-Substituted Perylene Imides

by

Galen L. Eakins

A thesis
submitted to Victoria University of Wellington
in fulfillment of the requirements for the degree of
Doctor of Philosophy

Victoria University of Wellington
2015

Abstract

Synthetic peptides offer enormous potential to encode the assembly of molecular electronic components, provided that the complex range of interactions is distilled into simple design rules. Herein is reported a spectroscopic investigation of aggregation in an extensive series of peptide-perylene imide conjugates designed to interrogate the effect of structural variations. Throughout the course of this study, the self-assembly and photophysical properties of the compounds are explored to better understand the behavior and application of these materials. Three principal avenues of inquiry are applied: (1) the evaluation of structure-property relationships from a thermodynamic perspective, (2) the examination of peptide chiral effects upon properties and self-assembly, and (3) an application of the understanding gained from rationally designed systems to effectively utilize naturally optimized peptides in bio-organic electronics.

By fitting different contributions to temperature-dependent optical absorption spectra, this study quantifies both the thermodynamics and the nature of aggregation for peptides with incrementally varying hydrophobicity, charge density, length, amphiphilic substitution with a hexyl chain, and stereocenter inversion. Coarse effects like hydrophobicity and hexyl substitution are seen to have the greatest impact on binding thermodynamics, which are evaluated separately as enthalpic and entropic contributions. Moreover, significant peptide packing effects are resolved via stereocenter inversion studies, particularly when examining the nature of aggregates formed and the coupling between π-electronic orbitals.

Peptide chirality overall is seen to influence the self-assembly of the perylene imide cores into chiral nanofibers, and peptide stereogenic positions, stereochemical configurations, amphiphilic substitution, and perylene core modification are evaluated with respect to chiral assembly. Stereocenters in peptide residue positions proximal to the perylene core (1-5 units) are seen to impart helical chirality to the

perylene core, while stereocenters in more distal residue positions do not exert a chiral influence. Diastereomers involving stereocenter inversions within the proximal residues consequently manifest spectroscopically as pseudo-enantiomers. Increased side-chain steric demand in the proximal positions gives a similar chiral influence but exhibits diminished Cotton Effect intensity with additional longer wavelength features attributed to interchain excimers. Amphiphilic substitution of a peptide with an alkyl chain disrupts chiral self-assembly, while an amphiphilic structure achieved through the modification of the perylene imide core with a bisester moiety prompts strongly exciton-coupled, chiral, solvent-responsive self-assembly into long nanofilaments.

Informed by rationally designed sequences, and capitalizing upon the optimization seen in many natural systems, specific peptide sequences designed by inspection of protein-protein interfaces have been identified and used as tectons in hybrid functional materials. An 8-mer peptide derived from an interface of the peroxiredoxin family of self-assembling proteins is exploited to encode the assembly of perylene imide-based organic semiconductor building blocks. By augmenting the peptide with additional functionality to trigger aggregation and manipulate the directionality of peptide-semiconductor coupling, a series of hybrid materials based on the natural peptide interface is presented. Using spectroscopic probes, the mode of self-assembly and the electronic coupling between neighboring perylene units is shown to be strongly affected by the number of peptides attached, and by their backbone directionality. The disubstituted material with peptides extending in the N-C direction away from the perylene core exhibits strong coupling and long-range order, which are both attractive properties for electronic device applications. A bio-organic field-effect transistor is fabricated using this material, highlighting the possibilities of exploiting natural peptide tectons to encode self-assembly in other functional materials and devices.

These results advance the development of a quantitative framework for establishing structure-function relationships that will underpin the design of self-assembling peptide electronic materials. The results further advance a model for adapting natural peptide sequences resident in β-continuous interfaces as tectons for bio-organic electronics.

Publications

The following publications were produced during the course of this research project and were generated from the results presented in this thesis. The key findings in the articles listed below are discussed, respectively, in chapters 3, 4, and 5.

"Thermodynamic Factors Impacting the Peptide-Driven Self-Assembly of Perylene Diimide Nanofibers"

G. L. Eakins; J. K. Gallaher; R. A. Keyzers; A. Falber; J. E. A. Webb; A. Laos; Y. Tidhar; H. Weissman; B. Rybtchinski; P. Thordarson; J. M. Hodgkiss

Journal of Physical Chemistry B, **2014**, *118*, 8642−8651.

"Chiral Effects in Peptide-Substituted Perylene Diimide Nanofibers"

G. L. Eakins, J. P. Wojciechowski, A. Martin, J. E. A. Webb, P. Thordarson, J. M. Hodgkiss

Supramolecular Chemistry, accepted June **2015**, *in press*

doi: 10.1080/10610278.2015.1066011

"Functional Organic Semiconductors Assembled via Natural Aggregating Peptides"

G. L. Eakins, R. Pandey, J. P. Wojciechowski, H. Y. Zheng, J. E. A. Webb, C. Valéry, P. Thordarson, N. O. V. Plank, J. A. Gerrard, J. M. Hodgkiss

Advanced Functional Materials, **2015**, *25*, 5640–5649.

Collaborations

Microscopy imaging, peptide assays, ultraviolet circular dichroism spectroscopy, nonsymmetrical perylene precursor synthesis, and organic semiconductor device fabrication were performed in collaboration with the following research groups:

Yaron Tidhar, Haim Weissman, Elisha Krieg, and Boris Rybtchinski

Rybtchinski Research Group
Department of Organic Chemistry
Weizmann Institute of Science • Rehovot, Israel

Alistair Laos, James Webb, Jonathan Wojciechowski, Adam Martin, Alexander Falber, and Pall Thordarson

Thordarson Research Group
School of Chemistry and the Australian Centre for Nanomedicine
The University of New South Wales • Sydney, Australia

Rishi Pandey, Céline Valéry, and Juliet Gerrard

Gerrard Research Group
Biomolecular Interaction Centre
University of Canterbury • Christchurch, New Zealand

Han Yue Zheng, Cameron Wood, and Natalie Planck

Plank Research Group
School of Chemical and Physical Sciences
Victoria University of Wellington • Wellington, New Zealand

Specified Contributions

The following contributions to the work presented in this thesis were made by collaborators as summarized here:

1. Perylene intermediates **Q1**, **Q2**, **Q3**, and **Q4** - Synthesized by the Thordarson Group at the University of New South Wales
2. AFM images (Chapter 3) - Collected jointly by Alistair Laos and G. L. Eakins
3. AFM image (Figure 4.6c) - Collected by Adam Martin
4. AFM images (Chapter 5) - Collected by Jonathan Wojciechowski
5. TEM images (Chapter 3) - Collected by the Rybtchinski Group
6. TEM images (Chapter 5) - Collected by Rishi Pandey
7. ThT and turbidity assays (Chapter 5) - Collected by R. Pandey and G. Eakins
8. UV circular dichroism spectra (Chapter 5) - Collected by Rishi Pandey
9. OFET fabrication and analysis (Chapter 5) - Conducted jointly by G. L. Eakins and the Planck Group

All other data presented in this thesis was collected exclusively by G. L. Eakins.

Except those figures adapted for review from literature (mostly cited in Chapter 1), all figures contained in this thesis were originated by G. L. Eakins from the raw data or raw microscopy images collected.

All chapters in this thesis were fully written by G. L. Eakins with experimental details for items 1-9 (above) included in Chapter 8 as given by collaborators. The manuscripts of the publications listed on page IV were written by G. L. Eakins, and accordingly, these articles serve (with adaptations) as the content of Chapters 3-5.

Acknowledgements

No effort such as this reaches its best potential without the generosity, insight, and support of others. This project has found such in good measure, as many people have aided the success of this work and have helped to foster its achievements.

Grateful acknowledgement is extended to:

Dr. Jeff Tallon and the Robinson Research Institute (Victoria University) for the use of their CD spectrometer.

Ian Vorster (Victoria University) for instrumental technical assistance with mass spectrometry and NMR spectroscopy.

Shyamal Prasad of the Hodgkiss Research Group (Victoria University) for technical assistance with the FT-IR spectral smoothing.

Special thanks are further extended to:

Justin Hodgkiss for excellent supervision, profitable and experienced advice, fruitful ideas, insightful guidance in problem solving and data analysis, and for promoting an openness and availability which allowed the reception of these qualities to thrive.

Rob Keyzers for excellent guidance as secondary supervisor, for valuable ideas to address synthetic and analytical challenges, for expert direction in experimental methodologies, and for enabling the exploration of ideas.

Joe Gallaher for indispensable, experienced advice in the synthesis and characterization of peptide-substituted perylene imides, and for many helpful consultations throughout the development and investigations of this project.

Victoria University and the School of Chemical and Physical Sciences for financial and instructional support throughout the duration of this project.

Co-workers who have been helpful personally and professionally along the way.

New friends far from home who have been welcoming, supportive, and helpful during many challenges along the way.

Old friends who have been encouraging and supportive throughout new opportunities and difficulties when success was uncertain.

Family, who have always been ready to encourage and to help across the distance.

Thank you.

Each of you shares a part in the success of this work.

Table of Contents

List of Figures

List of Schemes

List of Tables

List of Abbreviations

Ac	acetyl
AFM	atomic force microscopy
Ala	alanine (alphabet symbol designation: A)
Arg	arginine (alphabet symbol designation: R)
Asn	asparagine (alphabet symbol designation: N)
Asp	aspartic acid (alphabet symbol designation: D)
β-CD	β-cyclodextrin
biOFET	bio-organic field-effect transistor
Boc	tert-butoxycarbonyl
CD	circular dichroism
DFT	density functional theory
DIPEA	*N*,*N*′-diisopropylethylamine
DMF	*N*,*N*′-dimethylformamide
DMSO	dimethyl sulfoxide
dodecane@2β-CD	host-guest inclusion of dodecane by two β-cyclodextrin units
Et	ethyl
Fmoc	9-fluorenylmethoxycarbonyl
FT-IR	Fourier transform infrared
FTO	fluorine-doped tin oxide

Glu	glutamic acid (alphabet symbol designation: E)
Gly	glycine (alphabet symbol designation: G)
HBTU	*O*-benzotriazole-*N*,*N*,*N*,*N*′-tetramethyluronium hexafluorophosphate
hexyl-PDI	*N*-hexyl-perylene diimide
HFIP	1,1,1,3,3,3-hexafluoroisopropanol
His	histidine (alphabet symbol designation: H)
HOMO	highest occupied molecular orbital
HRMS	high-resolution mass spectrometry
Ile	isoleucine (alphabet symbol designation: I)
Leu	leucine (alphabet symbol designation: L)
LUMO	lowest unoccupied molecular orbital
Lys	lysine (alphabet symbol designation: K)
MALDI	matrix-assisted laser desorption ionization
MCH	methylcyclohexane
NDI	naphthalene diimide
NIR	near infrared
NMP	*N*-methyl-2-pyrrolidone
NMR	nuclear magnetic resonance
OAll	allyloxy
OFET	organic field-effect transistor
OPV	oligo-*p*-phenylenevinylene
OtBu	*tert*-butyl ester
P3HT	poly(3-hexylthiophene)
PDI	perylene diimide

PDMS	polydimethylsiloxane
PEDOT	poly(3,4-ethylenedioxythiophene)
peptide-PDI	peptide-substituted perylene diimide
Phe	phenylalanine (alphabet symbol designation: F)
PIBE	perylene imide bis(*n*-butyl)ester
Prx	peroxiredoxin
Prx3	peroxiredoxin III protein
PSS	poly(styrene sulfonate)
PTCDA	perylene tetracarboxylic acid dianhydride
SEM	scanning electron microscopy
Ser	serine (alphabet symbol designation: S)
SPPS	solid-phase peptide synthesis
TEM	transmission electron microscopy
TFA	trifluoroacetic acid
THF	tetrahydrofuran
ThT	thioflavin-T
TOF	time of flight
Tyr	tyrosine (alphabet symbol designation: Y)
UV-vis	ultraviolet-visible
Val	valine (alphabet symbol designation: V)

Peptide sequence abbreviations (alphabet symbol notation):

Ac-IKHLSVN-NH_2	Ac-Ile-Lys-His-Leu-Ser-Val-Asn-NH_2 *Ac-Ile: acetylated amino terminus (capped)* *Asn-NH_2: amidated carboxyl terminus (capped)*
Ac-IK(-yl)HLSVN-NH_2	Ac-Ile-Lys(-yl)-His-Leu-Ser-Val-Asn-NH_2 *Lys(-yl): peptide fragment bound via Lys side-chain*
Ac-EEEIRHLSVN-Et-NH_2	Ac-$(Glu)_3$-Ile-Arg-His-Leu-Ser-Val-Asn-CH_2CH_2-NH_2
Ac-EEEIRHLSVN-Et−	Ac-$(Glu)_3$-Ile-Arg-His-Leu-Ser-Val-Asn-CH_2CH_2− *(peptide fragment bound via ethyl terminal chain)*
Ac-IRHLSVN	Ac-Ile-Arg-His-Leu-Ser-Val-Asn
GIRHLSVN	Gly-Ile-Arg-His-Leu-Ser-Val-Asn
GIRHLSVNEEE	Gly-Ile-Arg-His-Leu-Ser-Val-Asn-Glu-Glu-Glu
−GIRHLSVNEEE	−Gly-Ile-Arg-His-Leu-Ser-Val-Asn-Glu-Glu-Glu *(peptide fragment bound via Gly amino terminus)*
−GD	−Gly-Asp
−GY	−Gly-Tyr

Chapter 1

Introduction

1.1 Building from a Molecular Foundation

In distinction to molecular synthesis which is employed to alter the covalently bonded atomic architecture of molecular structures, molecular self-assembly involves the spontaneous, unaided self-organization of molecules themselves into larger, ordered supramolecular architectures that are formed and cohere via noncovalent interactions.[1] Because the innate features of a molecular structure determine the nature of any ensembles resulting from molecular self-assembly, molecular synthesis can, therefore, be used to produce molecular structures with particular features designed to encode specific assembly interactions toward desired supramolecular self-assembly goals. Successful self-assembly by a molecular system is determined by five principal system characteristics:[1] (1) structural components, (2) system interactions, (3) interactive adjustability, (4) the assembly environment, and (5) mass transport. For self-assembly, the structural components are simply the homo- or heteromolecular units (or macromolecular segments) interacting during the process. During the process, the system interactions are just the balancing of repulsive and attractive noncovalent forces driving self-assembly. As self-assembly occurs, the nature of the interactions must be sufficiently reversible (not permanently affixed) to allow molecular units to have adjustable positioning within the supramolecular architecture while self-assembly proceeds. Irreversible processes leading to rigid bonding states would not accommodate the development of an evolving assembly as it forms. The molecular environment must then also be

supportive of the self-assembly process by permitting sufficient motion and mass transport of the self-assembling units (such as in solution or at an interface). If molecular structural units possessing complementary forms and mutually supportive noncovalent interactions are placed in an appropriately conducive environment, elaborate self-assembly can be achieved from relatively simple molecular building blocks as illustrated in Figure 1.1.

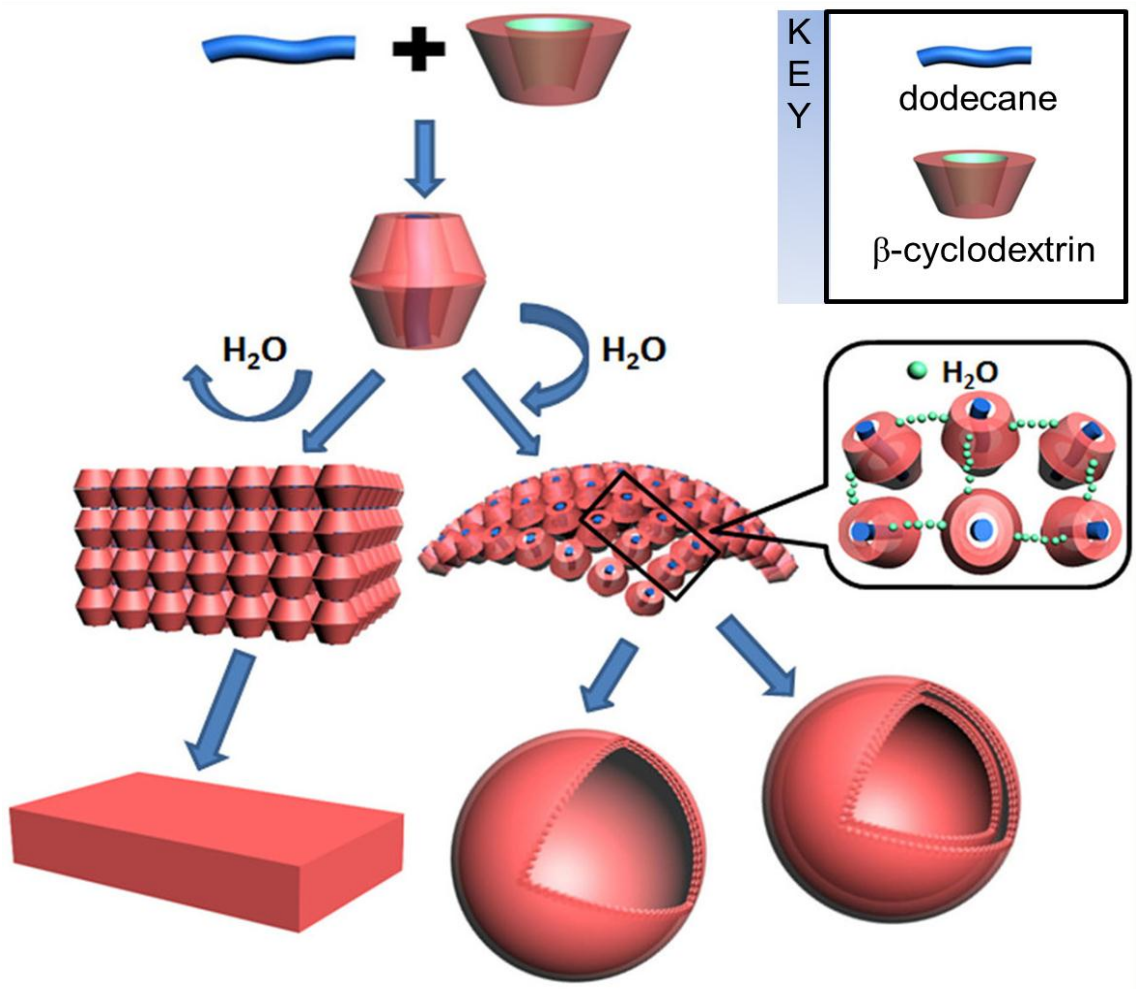

Figure 1.1 Schematic illustration for the self-assembling behavior of the dimers of β-cyclodextrin (β-CD) threaded by one dodecane molecule via a host-guest inclusion. The dimer is a supramolecular building block of dodecane@2β-CD. (Figure adapted for review from Zhou et al.[2] with permission of NPG.)

For the system shown in Figure 1.1, each of the previously discussed aspects underpinning self-assembly are seen to be present. Structurally, the doughnut ring-like form of the β-cyclodextrin molecule and the thread-like structure of the

dodecane molecule mutually facilitated a host-guest interaction. Interactively, the structures are driven together by noncovalent hydrophobic/hydrophilic influences wherein the mutual attraction of the hydrophobic dodecane molecule to the hydrophobic cavity of the β-cyclodextrin prompts self-assembly of dodecane within the interior of two β-cyclodextrin units such that the hydrophobic aspects of all molecules involved are shielded by a shell of the β-cyclodextrin hydrophilic exterior. This dynamic also is derived from the innate molecular structural features of the respective molecules. Environmentally, the aqueous solution provided a medium to make the assembly favored and facilitated the motion and mass transport of the molecular units. Through such scenarios molecular self-assembly is easily achieved.

Informed by these principles of self-assembly, the focus of the work described in the subsequent chapters of this study is that of the self-assembly of organic semiconductors — in particular, perylene imide semiconductors. Extending from this focus, the goal of this study is to use the diverse, adaptable structures of peptides to encode the self-assembly of the semiconductor moieties to ultimately create macroscopically conductive devices.

1.2 Why Self-Assembly?

Electronic delocalization, which is an intrinsic characteristic in organic molecules containing conjugated π-orbital systems, can facilitate the movement of charge carriers as electrons or electron vacancies (holes) through a conjugated network.[3,4] This property, together with an accessible material band-gap, permits many π-functional organic molecules, oligomers, and polymers to exhibit semiconducting properties.[3] Developing such compounds into organic semiconducting materials has received considerable interest since organic semiconductors may potentially provide several advantages over traditional inorganic materials.

Organic semiconducting materials have desirable mechanical properties (flexibility and durability) and can be processed at lower temperatures (using less energy) by industrial methods such as vacuum evaporation, solution casting, inkjet printing, stamping, etc., which are already in use for semiconductor fabrication.[3]

Additionally, organic synthesis, which is governed by functional group interactions, provides an added dimension of molecular-scale structural control not always present with inorganic materials, and this additional control becomes an increasingly important advantage as cost-effective improvements to silicon-based device performance reaches a limit.[3] The molecular-scale control provided by organic synthesis may allow the production of electronically-tuned organic semiconductors that facilitate the construction of high density, extremely miniaturized, inexpensive, low power electronic components and devices.[5] To realize the potential of these organic semiconductors, however, a further level of structural control is needed — supramolecular control. An example of this molecule-up approach to self-assembly is shown in a timed molecular assembly progression in Figure 1.2.

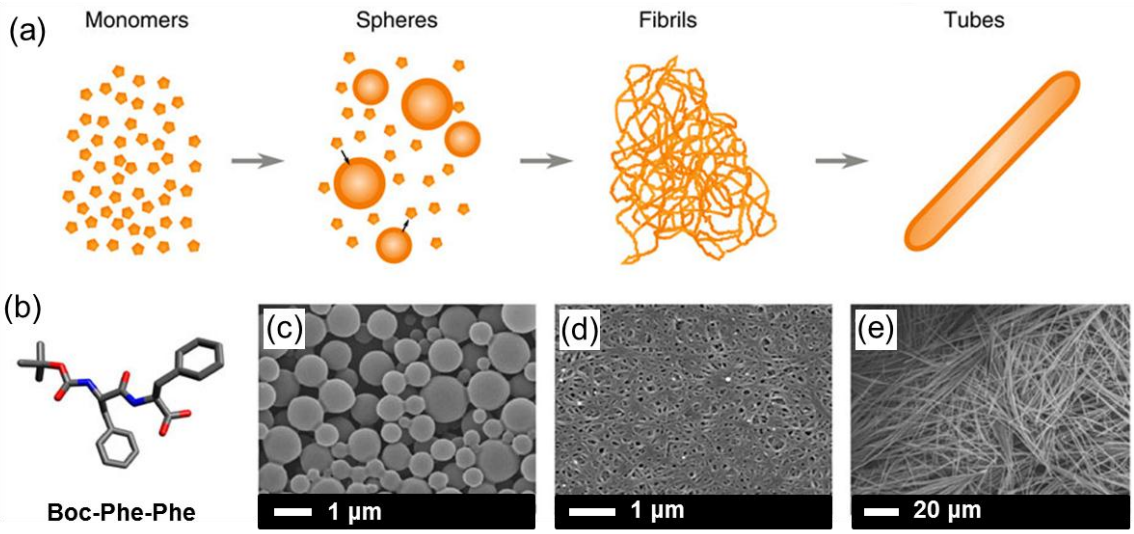

Figure 1.2 (a) Schematic depiction of the phase transition observed in the Boc-Phe-Phe system over time. (b) Schematic molecular structure of Boc-Phe-Phe. (c-e) Microscopy images of aliquots of Boc-Phe-Phe in 10% ethanol/water solution were collected and left to dry on glass slides at 2, 40 and 60 min. from initial mixing. (Figure adapted for review from Levin et al.[6] with permission from NPG.)

For organic semiconductors, self-assembly into nanostructures like those shown in Figure 1.2 can greatly improve the material properties needed for electronic applications. Since organic π-functional materials are primarily two-dimensional

semiconductors, interchain electronic coupling highly impacts the performance of devices employing them.[7] This is because conduction within such materials requires that the two-dimensionally semiconducting π-functional units electronically interact three-dimensionally. To enhance the interchain electronic coupling and charge transfer needed for this, the formation of crystalline-like mono-domains is desirable; however, this can be difficult to achieve beyond that of a few hundred nanometers in size.[7] When making the transition from molecular properties to macroscopic, bulk material properties, a combination of chemical synthesis and process controls can be employed to alter material morphology and optimize material performance. Beyond this, however, applying supramolecular self-assembly design affords a means to directly facilitate the formation of fundamental nano-architectural arrays within the material across larger length-scales to promote order and enhance bulk material performance.[7]

1.3 How to Assess Self-Assembly?

Given the goal of using self-assembly to enhance interchain electronic coupling, charge transfer, and conduction in organic semiconductors for improved material function, a simple means to assess the effectiveness of a self-assembly strategy toward material performance is desirable. For π-functional materials, this is easily achieved since changes in the conductive properties are reflected in the photophysical properties of the materials. The conjugated π-bond networks of π-functional molecules give them characteristically strong absorption features. Moreover, π-stacking becomes important, wherein noncovalent aromatic-aromatic electrostatic attractions between the *p*-orbitals of two separate aromatic rings produce a stacked *p*-orbital alignment of electrostatic potential between the two rings. Due to π-stacking by the molecules, the individual chromophores exhibit sensitivity to the local electronic environment induced by their mutual orientations. This sensitivity, in turn, is manifest spectroscopically by the chromophores. Because self-assembly changes the orientation of π-functional molecules, prompting a change in the local electronic environments of the chromophores that is expressed photophysically, spectroscopy may be used as a convenient tool for assessment. Spectroscopic evaluations in solution offer a simple means of evaluating a self-

assembly strategy (and any refinements to it) before progressing to more involved solid-state examinations of nano-architectures.

Following from the spectroscopic assessments, once indications of the successful formation of the desired nano-architectures are obtained in solution, solid-state microscopy methods such as transmission electron microscopy (TEM), scanning electron microscopy (SEM), and atomic force microscopy (AFM) can be used to image the actual nanostructures formed (as previously exemplified in Figure 1.2). In addition to providing verification of the presence of the nanostructures indicated by spectroscopy, microscopy can show and easily distinguish the exact morphologies of the nanostructures obtained. Moreover, microscopy has value in showing the topographical detail and material distribution of nanostructures applied to surfaces, which can be helpful during material device fabrication.

As a final means of assessing self-assembly (from an applied perspective) once the microscopy imaging reveals favorable morphologies, the construction of devices from the material can be undertaken to measure the actual solid-state semiconducting characteristics of the nanostructures.

1.4 How to Self-Assemble?

Self-assembly of molecular units into ordered supramolecular groups of molecules, in general, is achieved using weak noncovalent interactions such as Coulombic, ion-dipole, or dipole-dipole attractions, amphiphilic associations, hydrogen bonding, and π-π interactions.[7] Hydrogen bonding and π-π interactions (π-stacking) are particularly important and are often used to prompt self-assembly of small molecular units and some oligomers, whereas supramolecular ordering of polymers is often achieved through more complex block copolymer-solvent methodologies.[7] Often, more than one type of noncovalent interaction is employed simultaneously within a system to effect self-assembly. The structures employed as substituents (or scaffolds) to prompt self-assembly are diverse. While some are the result of clever, rational design, others are inspired by (or adapted from) natural systems. Bio-inspired structures used for self-assembly include small molecules (Watson-Crick

base pairs), nucleic acids, peptides, proteins, and even viruses.[8] Yet despite the structural diversity of the moieties used as agents of self-assembly, in general, the same simple, noncovalent interactions can be seen to underpin the architectures formed. Figures 1.3-1.5 provide three examples of self-assembled systems reported in the literature which illustrate common noncovalent self-assembly methodologies.

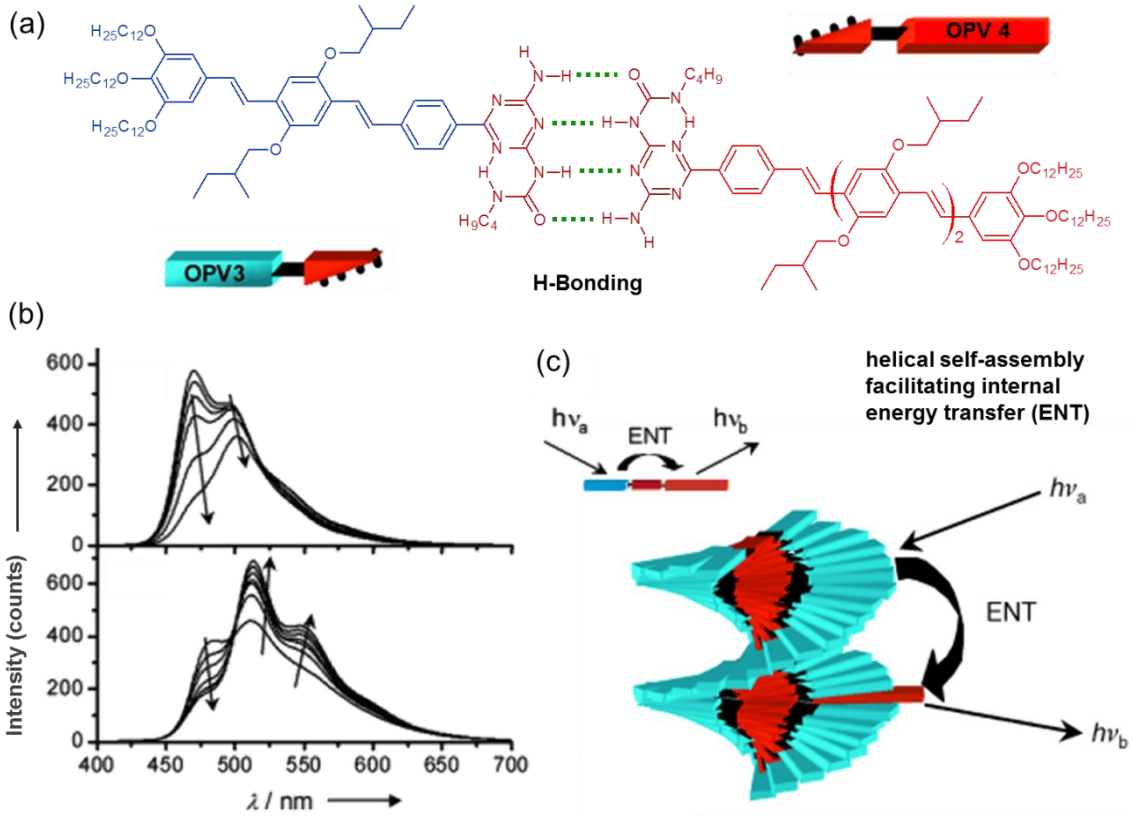

Figure 1.3 (a) A self-complementary hydrogen-bonding strategy for self-assembly of an organic semiconductor, enabling the formation of mixed dimers and mixed aggregates. (b) Photoluminescence spectra for mixtures in dodecane solution: (top panel) 0-30 mol % **OPV 4** at 80 °C, (lower panel) 0-1.2 mol % **OPV 4** at 10 °C. (c) Inside the mixed stacks efficient energy transfer is observed from **OPV 3** to **OPV 4**. (Figure adapted for review from Hoeben et al.[9] with permission from Wiley.)

In addition to providing an example of the use of hydrogen-bonding to effect self-assembly, the system shown in Figure 1.3 also demonstrates how self-assembly can achieve advantageous supramolecular architectures that enhance the primary molecular structural features of the individual units forming it. Other systems,

however, need not use hydrogen-bonding due to the presence of significant π-π interactions, as shown in Figures 1.4-1.5. The system shown in Figure 1.4 also demonstrates that hydrophobic-hydrophilic interactions are often an important factor in supramolecular self-assembly. The π-stacking interactions of this system are shepherded by hydrophobic-hydrophilic interactions, wherein the hydrophilic oligo(ethyleneoxide) dendrons preferentially associate while the hydrophobic phenylene faces undergo π-stacking. While the π-stacking assures that the hydrophobic association is not disordered, it does not provide a definite orientation for molecules within the aggregate, meaning both parallel and radial π-stacking arrangements (or a mixture) might be possible. The amphiphilicity and molecular packing efficiency, therefore, drive the shape of the self-assembly. Beyond shepherding self-assembly behavior, strong hydrophobic-hydrophilic interactions can also improve the robustness of supramolecular architectures, which can be fragile due to the weak nature of the forces driving their assembly.[10]

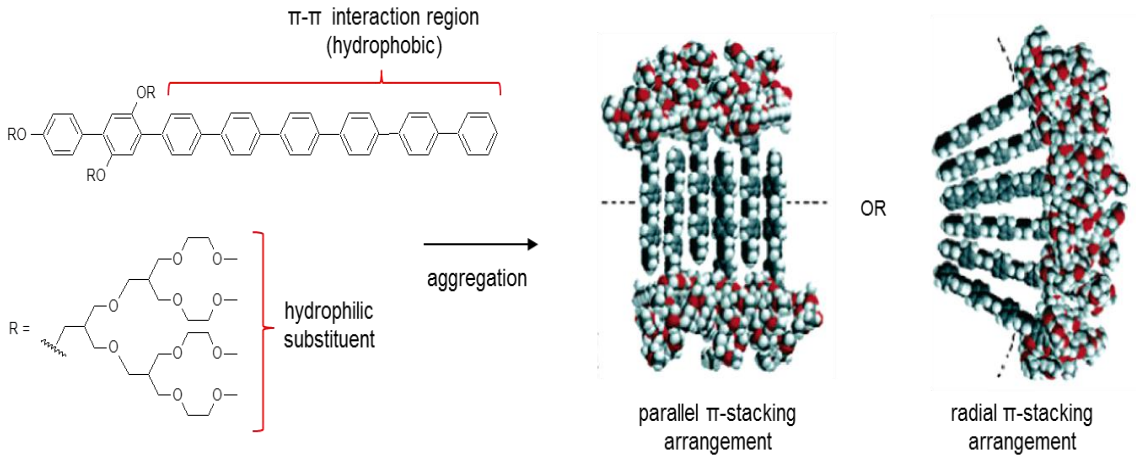

Figure 1.4 An example of a π-π interactions and amphiphilic influences in supramolecular self-assembly. (Figure adapted for review from Yoo et al.[11] with permission from ACS.)

For the system depicted in Figure 1.5, additional influences from both structural design and from electrostatic interactions are seen to guide the π-stacking associations. Variable length helical spine segments act as modular spacers for the π-stacking aromatic layers. Self-assembly occurs at the connecting points on the helix branches via amine salt formation between the substituents of the two

components of the block co-polymer. The helical spine segments and the aromatic plates are held together both by electrostatic attraction from the amine salt moieties as well as by the π-stacking interactions of the aromatic layers.

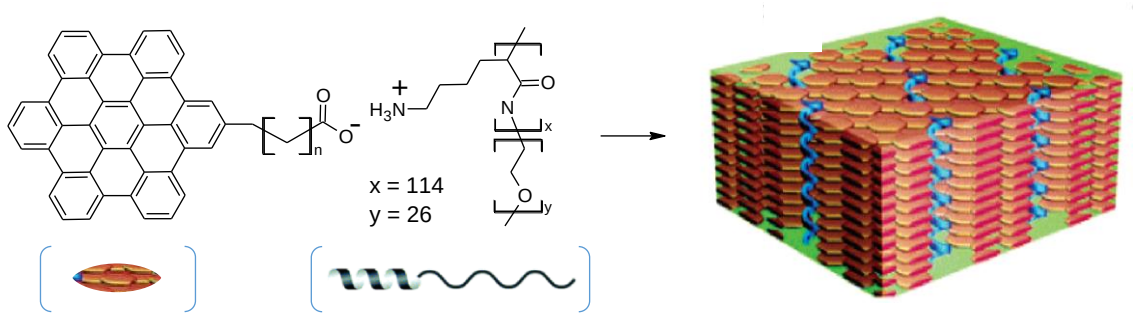

Figure 1.5 An example of supramolecular self-assembly in a block co-polymer. (Figure adapted for review from Thünemann et al.[12] with permission from ACS.)

1.5 Why Peptides?

Among the many possible moieties which may be employed to impart the noncovalent interactions which drive self-assembly, peptides hold great potential and versatility. Peptides are known to innately exhibit self-assembly into secondary structures such as β-sheets (parallel or anti-parallel), β-turns, helical forms,[13,14] supramolecular gels,[15] nanosheets,[16] and nanofibres.[17] Moreover, peptide interfaces are known to underpin and drive protein homodimer assembly.[18] Incorporating peptides with their demonstrated innate propensity toward self-assembly within larger molecular structures offers a tunable means of guiding the self-assembly of other attached moieties. The self-assembly of the peptide sequences can be influenced (enhanced or disrupted) by many factors such as electrostatic effects,[19] hydrogen-bonding influences,[20] side-chain hydrophobicity,[20–22] pH,[23] π-π interactions of attached moieties,[15,24] and solvent effects. These extrinsic and intrinsic characteristics and behaviors resulting from the structure of the peptide sequence all influence which type of supramolecular structure may result. Since the properties of a peptide are sequence-dependent, a wealth of possible amino acid permutations is possible, which may be used to tune the overall self-assembly of an

appended moiety of interest. Accordingly, several studies applying peptide sequences for material development have been undertaken.

Even peptides of relatively short length can often provide remarkable results in self-assembly endeavors. For example, native phenylalanine dipeptide (Phe-Phe) strands have been shown to form extensive nanotubes,[25] highlighting that peptide length is simply one more useful variation within peptide diversity. In fact, the formation of conjugated hydrogels has been achieved with a simple dipeptide. One such reported hydrogel was constituted using an Fmoc-dipeptide appended to a naphthalene diimide semiconductor as shown in Figure 1.6).[15]

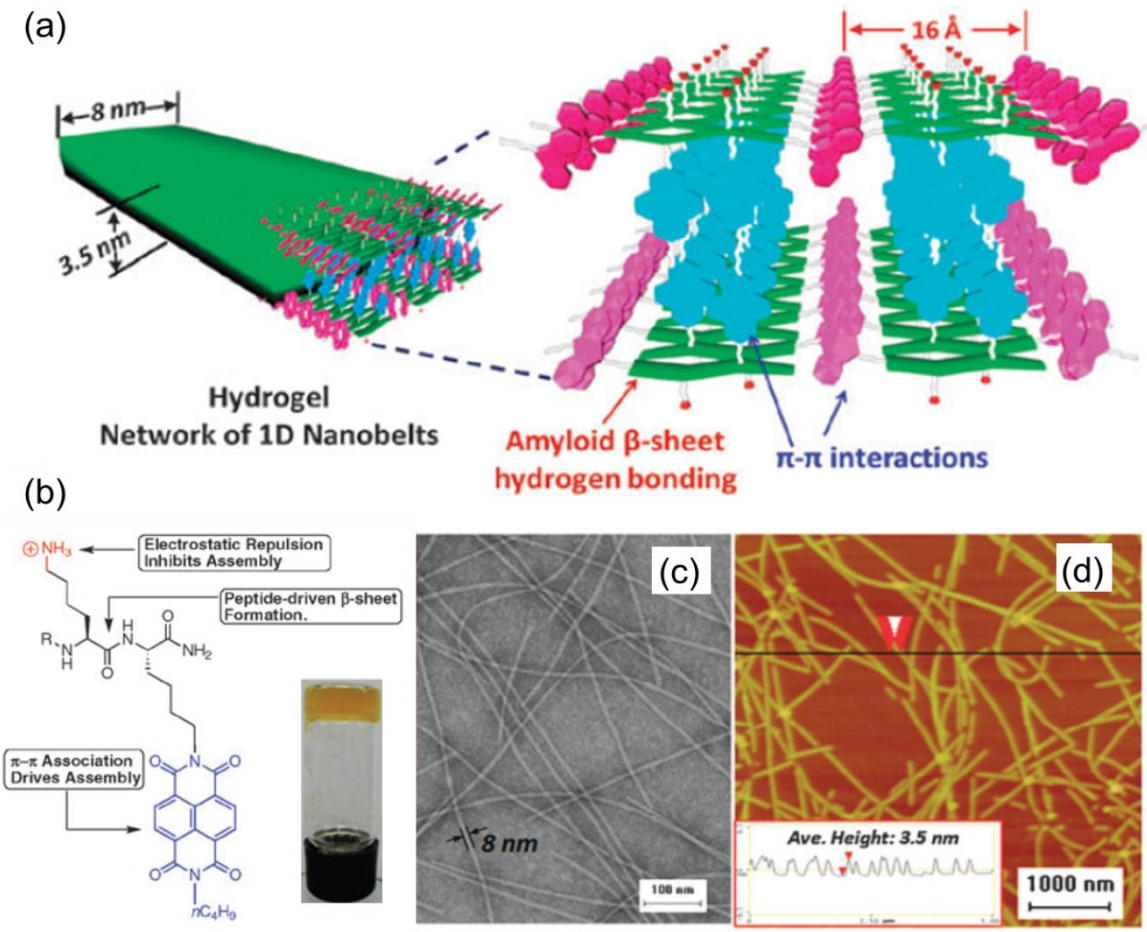

Figure 1.6 Self-assembly of an Fmoc-Lys-Lys dipeptide naphthalene diimide semiconductor: (a) Self-assembly in water produces a hydrogel from a network of nanobelts; (b) Key molecular structural aspects, (inset: photo of hydrogel formed at 1.5 wt%); (c) TEM image (negatively stained) of hydrogel fibers (scale bar = 100 nm); (d) AFM image (tapping mode), showing segments with regular height. (Figure adapted for review from Shao et al.[15] with permission from RSC.)

The hydrogel in Figure 1.6 was found to be composed of uniform micrometer-sized nanobelts (Figure 1.6c,d). The model proposed for the nanobelts based on the data collected (Figure 1.6a) suggested an interior structure with a significant extent of π-π interactions. Notably, these results were achieved simply by the inclusion of a dipeptide as a moiety within the rational design for the material (Figure 1.6b).

Longer peptides may also be used effectively to prompt chromophore self-assembly, resulting in additional chromophore interactions that impact the expressed photophysics. The use of peptide self-assembly to modify fluorophore photophysics has been demonstrated by a peptide (amino acid residues 105-115 from the protein transthyretin) functionalized with a fluorene moiety (Figure 1.7a),[24] wherein peptide β–sheet formation was found to coordinate the fluorene moieties into an ordered π-stacking arrangement (Figure 1.7b) which altered the photophysical response of the fluorene fluorophores.

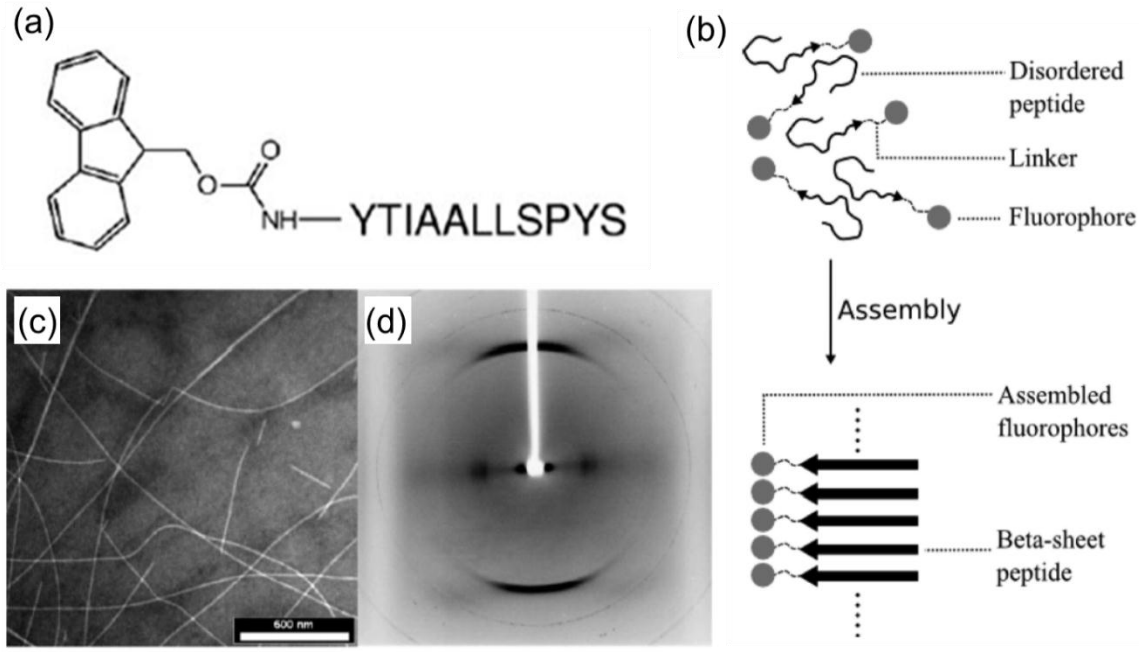

Figure 1.7 Self-assembly of a peptide-fluorophore conjugate: (a) Peptide sequence with appended fluorophore; (b) Peptide self-assembly into stacked β–sheets orients the attached fluorene fluorophore into an ordered π-stacking arrangement; (c) TEM image of fibrils resulting from self-assembly (scale bar = 500 nm); (d) Wide-angle X-ray fiber diffraction pattern of a partially aligned, dried stalk produced from the compound gel. (Figure adapted for review from Channon et al.[24] with permission from ACS.)

Transmission electron microscopy (TEM) imaging of the gel found it to contain an array of self-assembled fibrils throughout (Figure 1.7c), and a dried stalk produced from the gel was also found to produce an X-ray diffraction pattern (Figure 1.7d). Beyond the self-assembly demonstrated by this system, the study also highlights the opportunity to use self-assembly as a means to tune the photophysical response from a moiety of interest.

In a similar scheme, but using an alternating glycine-alanine peptide sequence inspired by silk (such as in spider silk[26]), an oligo(*p*-phenylenevinylene)-peptide (OPV-peptide) conjugate was produced for a self-assembly study (shown in Figure 1.8).[27] The alternating GAGAG motif of the peptide sequence used (which is common in silk) has been shown to be important in β-sheet formation, and was found to behave in a similar fashion in the self-assembly of the OPV-peptide conjugate material.

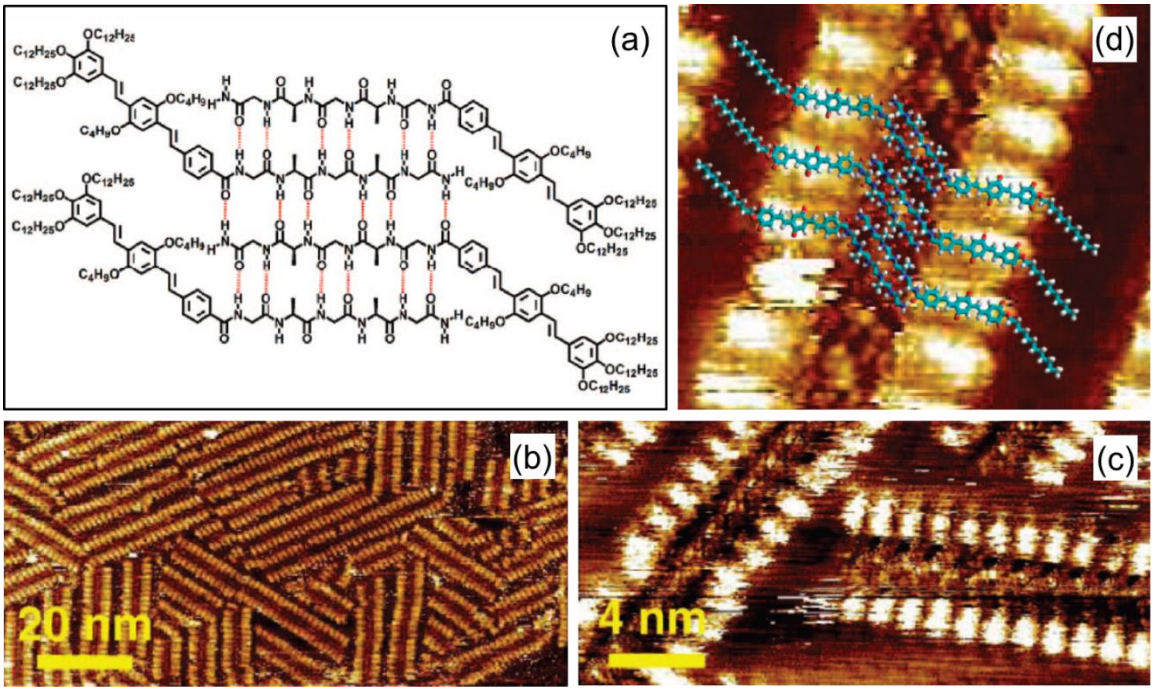

Figure 1.8 (a) Illustration of the hydrogen-bonding anti-parallel peptide β-sheet formation leading to the self-assembly of a peptide-substituted π-functional moiety. (b, c) STM images of the self-assembled architectures of the compound shown in panel (a). (d) Magnified view of image from panel (c) with a superimposed molecular model. (Figure adapted for review from Matmour et al.[27] with permission from ACS)

The β-sheets formed by the extensive hydrogen-bonding of the peptide (depicted in Figure 1.8a) provided an organizing influence leading to ordered assemblies of OPV-peptide stacks and lamellar-like domains within the material as shown in the scanning tunneling microscopy (STM) image in Figure 1.8b,c. The order achieved in the material (as evidenced by the STM images) was of sufficient quality to propose a model for the self-assembled, stacked arrays as shown in Figure 1.8d.

The structural design of the OPV-peptides shown in Figure 1.8 immediately signals the potential for a modular, analogous approach of applying a similar design using various other chromophores which might be targeted for self-assembly. Moreover, these reported OPV-peptide structures also underscore the underexplored potential of other peptide sequences. In fact, the silk peptide motif applied in the OPV-peptide study is only one of many potential natural motifs which may be advantageously applied in self-assembly.

Yet peptides can offer more than simply enhancing self-assembly. Peptide-driven hierarchical self-assembly can also impact other material aspects such as thermomechanical properties. A study conducted by Croisier et al. reported a mixture of oligopeptide-terminated polymers of different lengths, in which the oligopeptide-polymer strands selectively self-assembled into small aggregates and nanofibrils in a length-dependent, self-sorting manner, resulting in a self-assembled bulk material with intermingled, distinctive nanostructural domains together yielding elastomeric character.[28] Moreover, the thermomechanical properties of the bulk material were observed to vary with the oligopeptide-polymer structures and blend ratios. Accordingly, adjusting the oligopeptide-polymer structure and blend to alter the relative numbers of cross-linking, hydrogen-bonding aggregates, single β-sheet tapes, and stacked β-sheet nanofibrils formed during self-assembly, yielded elastomers which could be tailored to express a broad range of thermomechanical properties. Illustrations for this material approach are shown in Figure 1.9. The material structural dynamic in these elastomers is reminiscent or natural systems such as silk, wherein the mechanical traits of various types of silk arise from the combined contributions of three types of nanostructural domains:[28] (1) well-ordered β-sheet nanofibrils (for reinforcement),[29,30] (2) short β-sheet tapes (aiding energy dissipation during stretching),[29,31–33] and (3) amorphous regions (for elasticity).[30,34]

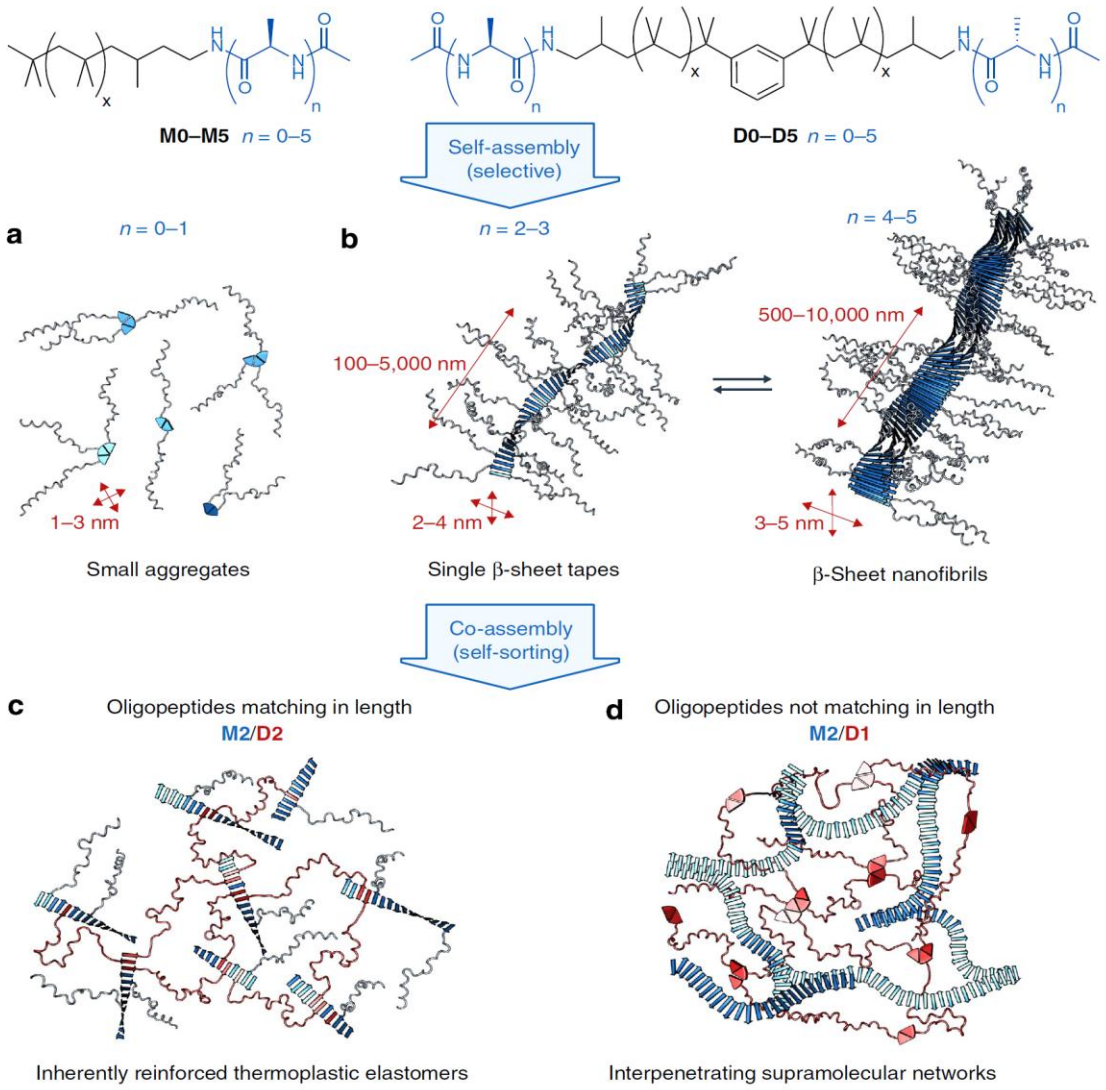

Figure 1.9 Schematic illustration of the selective self-assembly and self-sorting co-assembly processes for oligopeptide-polymer strands. Depending on the oligopeptide length, compounds **M0**–**M5** (n=0–5; x≈20) and the corresponding derivatives **D0**–**D5** (n=0–5; x≈20) self-organize into (a) small H-bonded aggregates or (b) stacked β-sheet fibrils, accompanied by single β-sheet tapes. Coexistence of these nanostructures in blends of molecules with different oligopeptide termini results in (c) inherently reinforced thermoplastic elastomers, or (d) interpenetrating supramolecular networks. (Figure adapted for review from Croisier et al.[28] with permission from NPG.)

The selected examples discussed in this section (and the references noted) underscore the versatility and diverse potential of peptides for application in supramolecular self-assembly. Peptides themselves are highly prone to self-

assembly and may be appended to other moieties to drive or guide the formation of nano-architectures of those moieties. Peptides offer an array of variations which can be used to tune material responses as expressed in both the Nano architectural form assembled and, by extension, in the optical properties observed. Yet whether alone or appended to a chromophore, peptides themselves remain highly responsive to the solvent environment experienced. Accordingly, this quality may be invoked through solution media changes to trigger nanostructure formation or to prompt nanostructural rearrangements, adding yet another layer to the use of peptides as agents of self-assembly. The selected examples discussed in this section (and the references noted) underscore the versatility and diverse potential of peptides for application in supramolecular self-assembly. Peptides themselves are highly prone to self-assembly and may be appended to other moieties to drive or guide the formation of nano-architectures of those moieties. Peptides offer an array of variations which can be used to tune material responses as expressed in both the Nano architectural form assembled and, by extension, in the optical properties observed. Yet whether alone or appended to a chromophore, peptides themselves remain highly responsive to the solvent environment experienced. Accordingly, this quality may be invoked through solution media changes to trigger nanostructure formation or to prompt nanostructural rearrangements, adding yet another layer to the use of peptides as agents of self-assembly.

1.6 Why Perylene Imides?

Perylene imides have attracted considerable attention as organic semiconducting materials since these compounds exhibit good n-type properties when functionalized as diimides or dianhydrides.[35] The high electron affinity of perylene diimides makes these molecules among the best n-type organic semiconductors known.[36–38] Perylene diimides also have a high fluorescence quantum yield and photostability,[39] making them some of the best fluorophores for single molecule spectroscopy with a quantum yield often near unity.[40,41] The stability and unique properties of perylene imides and perylene derivatives have led to the exploration of perylene imides in numerous applications including pigments (paint, automotive coatings, etc.), organic field effect transistors, xerographic photoreceptors and

photovoltaics, fluorescent dyes, laser dyes, fluorescent light collectors, and light-induced energy and electron transfer processes.[3,39]

Extending from the interest in capitalizing on the properties of perylene imides, a multitude of studies have been reported related to the self-assembly and application of perylene imide nanostructures. The extensive, reported variety of self-assembled perylene imide nano-architectures include: conductive nanofibers,[42,43] photofunctional supramolecular fibers,[44] long polymer fibers built upon polyisocyanide scaffolds,[45] semiconducting columnar assemblies,[46,47] light-harvesting crystalline nanosheets,[48] chiral helical assemblies,[49] chiral lactose-functionalized, multivalent glycoclusters,[50] fluorescent, thermotropic columnar mesophases,[51] hairpin linkers or end-capping groups for DNA duplexes used in DNA photonics,[52] and DNA-based oligomeric stacks.[53,54] In order to give an appropriate research context and to provide illustrations, selected examples of reported perylene diimides (PDIs) and their applications will be highlighted here with an emphasis toward organic electronic aspects.

Due to the highly fluorescent nature of the PDI chromophore, PDIs are often used as emitters for spectroscopy. The fluorescence spectra of PDIs often resemble a mirror image of the vibronically-structured absorbance band of an isolated, monomeric chromophore which exhibits three distinct vibronic peaks within the band; however, concentration effects can impact the observed spectral profiles (as seen in Figure 1.10). This effect is caused by a strong tendency of the PDI units to aggregate (co-facially π-stack) in solution, which is intensified as concentration increases. Upon aggregation, the distinctive vibronic peaks of the absorption band redistribute in position and intensity (Figure 1.10a), and the corresponding fluorescence emission spectral profiles lose vibronic structure and shift position to longer wavelengths (as seen in Figure 1.10b).

It is important to note here that this tendency of PDIs toward self-aggregation and the subsequent changes observed in the spectral profiles can together be exploited to invoke, detect, and monitor PDI self-assembly. The shift in the fluorescence band with increasing concentration also highlights the potential value of this for tuning PDI material properties through self-assembly. More immediately, the prospect of

tuning fluorescent emission via concentration is also evident; however, for many PDI compounds, the strongly aggregating tendency of PDIs leads to poor solubility which prevents achieving the range of concentration required to observe concentration-dependent effects like those exemplified in Figure 1.10.

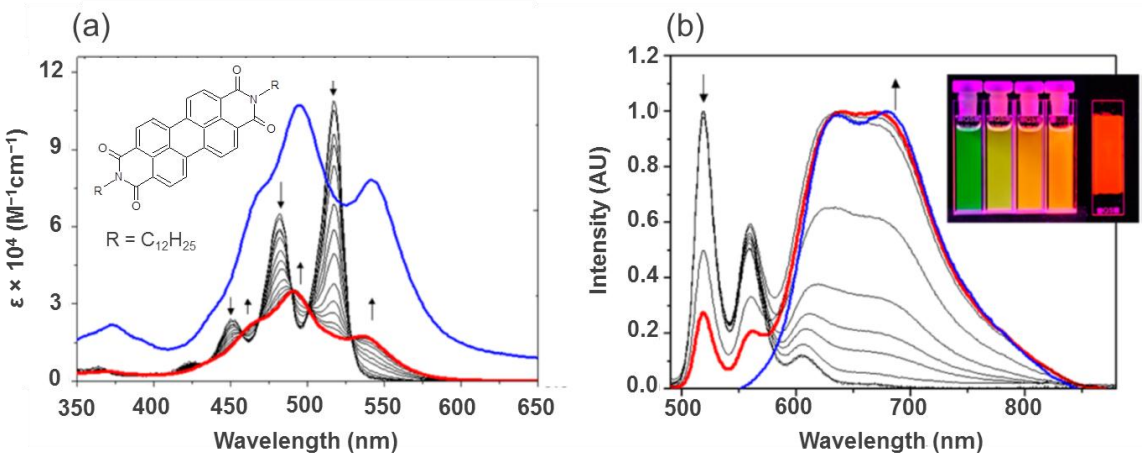

Figure 1.10 (a) Concentration-dependent UV-vis absorption spectra of a dialkyl PDI (2.0×10^{-7} to 1.0×10^{-3} M) in methylcyclohexane (MCH). Arrows indicate spectral changes upon increasing concentration. Blue line: UV-vis spectrum of a spin-coated film of the PDI after annealing at 150 °C for 3 h. (b) Normalized concentration-dependent fluorescence spectra (excitation at 469 nm) of the PDI (2.1×10^{-7} to 2.1×10^{-4} M) in MCH solution and of a spin-coated thin film (blue line). Inset: Color photographs of MCH solutions of the PDI with increasing concentration (left to right) and a thin film. Red lines indicate spectra for a concentrated 1.0×10^{-3} M solution. (Figure adapted for review from Chen et al.[55] with permission of Wiley-VCH.)

One such example which utilized self-assembly of a PDI material to achieve desirable fluorescent properties potentially suitable for application in a solid-state red light emitter was reported by Refiker and Icil (Figure 1.11).[56] Chiral imide substituents (selected to impart tunable chiral amphiphilicity to the overall molecule) achieved controlled PDI self-assembly through intermolecular hydrogen-bonding. This hydrogen-bonding was found to impact the fluorescent properties of the material, causing the excited state of the chiral dye to decay in the solid-state exclusively by fluorescing red light.[56] Accordingly, the material has been proposed for use in solid-state lighting technologies and solid-state dye-sensitized solar cells.[56]

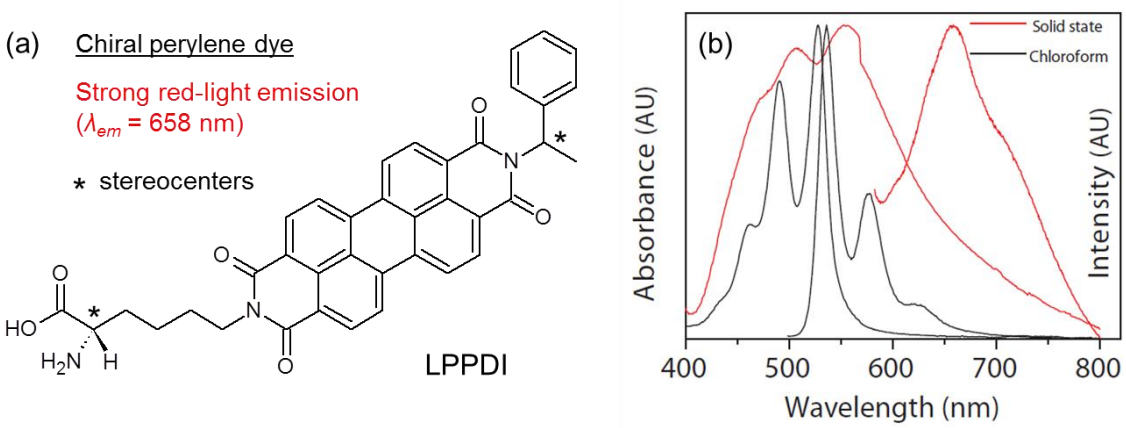

Figure 1.11 Chiral amphiphilic LPPDI dye with potential for solid-state lighting technologies: (a) Chemical structure of the dye; (b) Absorption and emission spectra of LPPDI in solid-state and chloroform (excitation wavelength = 485 nm). (Figure adapted for review from Refiker and Icil.[56] with permission from Tübitak.)

Changes in PDI fluorescence can also be used in fluorescence sensing, as shown in the example in Figure 1.12.[57] For this system, a PDI sensing agent was synthesized with imide substituents capable of forming complexes with metal ions (Figure 1.12a). Upon complexation, photoinduced electron transfer could occur, prompting enhanced fluorescent emission with particularly distinctive responses observed for Cu^{+2} and Fe^{+3} (Figure 1.12b), highlighting a responsive selectivity for those ions.

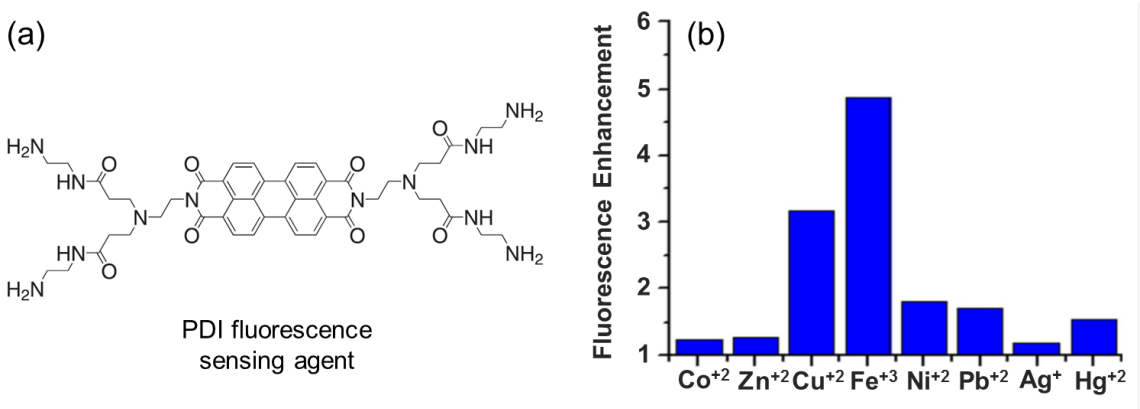

Figure 1.12 Fluorescence sensing based on photoinduced electron transfer using a novel perylene diimide sensing agent: (a) PDI fluorescence sensing compound structure; (b) Effect of the metal cations (2 μM concentrations) on the fluorescence of PDI sensing agent (1 μM concentration) in DMF solution. (Figure adapted for review from Giorgiev et al.[57] with permission from Elsevier.)

A more qualitative example of fluorescence sensing reported for the detection of organic compounds is seen in Figure 1.13.[58] Here, a PDI cyclophane (Figure 1.13a) is employed as the fluorescence sensing agent by utilizing host-guest interactions with other smaller aromatic molecules to be detected. In this scheme, the smaller organic molecules are drawn to π-stack as guests within the PDI cyclophane host cavity.

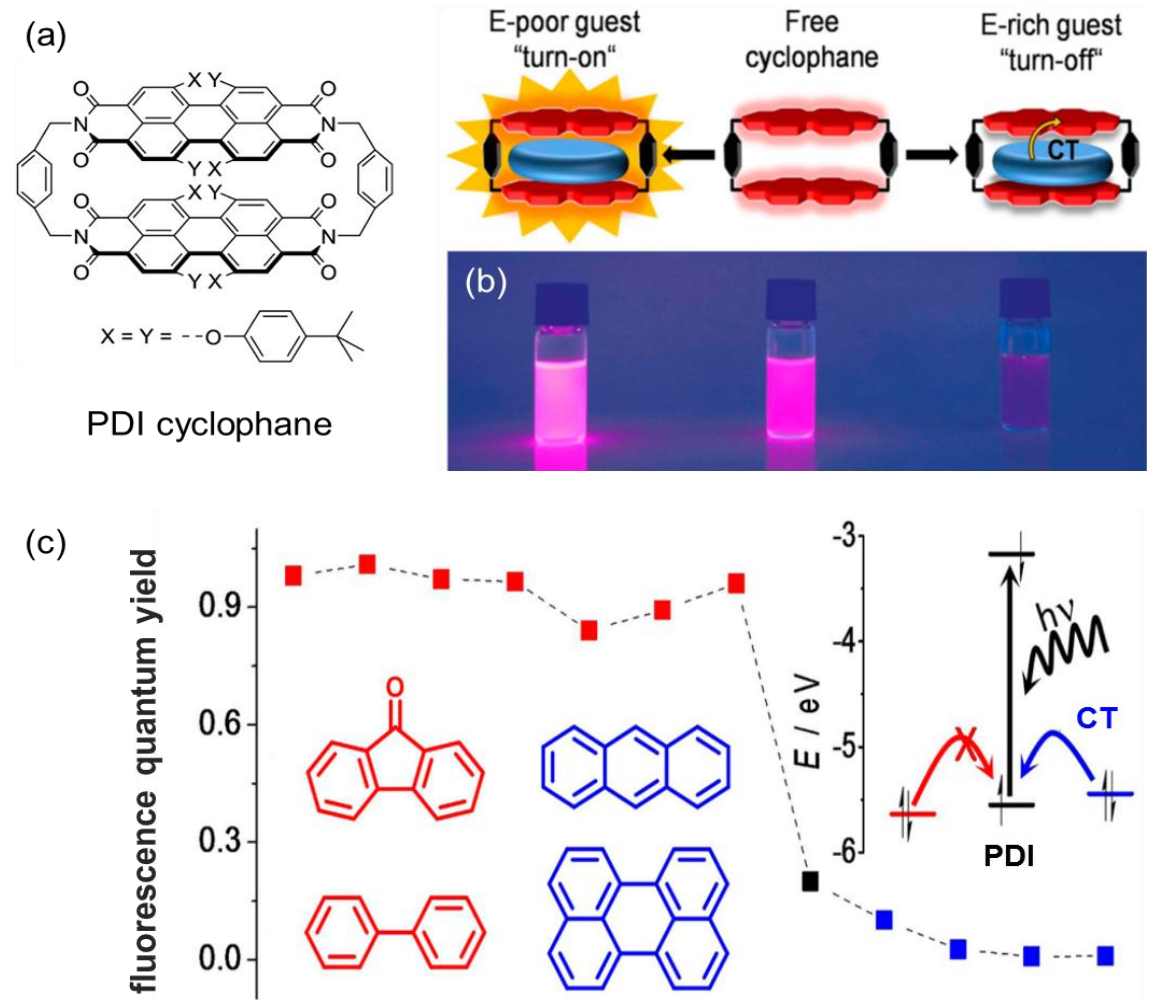

Figure 1.13 PDI Cyclophane host-guest interactions: (a) PDI cyclophane chemical structure; (b) Schematic illustration of the fluorescence "turn-on" and "turn-off" process of PDI cyclophane upon complexation with electron-poor and electron-rich aromatic guests (top) with the respective photographs; (c) A plot of the fluorescence quantum yields of the host-guest complexes. (Inset) A schematic illustration for the fluorescence quenching mechanism via charge transfer (CT) from electron-rich guests. Structures of selected electron-poor (red) and electron-rich (blue) guest molecules are shown. (Figure adapted for review from Spenst and Würthner.[58] with permission from Wiley-VCH.)

Formation of the host-guest complex with an electron-poor aromatic molecule results in a high increase in fluorescence and "turns on" the PDI cyclophane; whereas formation of the host-guest complex with an electron-rich aromatic molecule quenches fluorescence and "turns off" the PDI cyclophane (Figure 1.13b,c). This on/off response by the PDI cyclophane which permits distinguishing between electron-poor and electron-rich aromatic guest molecules can be explained by charge transfer. The electron-withdrawing imide substituents on the perylene cores of the PDI units produce an electron-deficient character. If guest molecules with a similar electron-deficient character reside in the host-guest complex, the electron deficient nature of the PDI core is enhanced and promotes fluorescence. Conversely, electron-rich guest molecules can provide charge transfer to the electron-deficient PDI core which quenches the fluorescence (Figure 1.13c).

Beyond fluorescence characteristics, the hydrogen-bonding and π-stacking aggregation behaviors noted for the fluorescent dye in Figure 1.11 have been exploited to form self-assembled fibers and gels comprised of PDI stacks as illustrated in Figure 1.14. Here, hydrogen-bonding orientationally directs the inherent π-stacking behavior of the perylene cores within each PDI monomer unit, thus producing a helical stacked assembly propagated in one dimension.

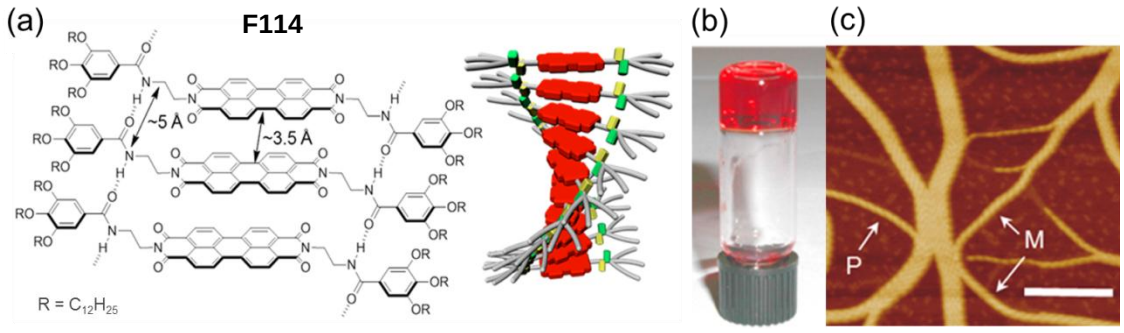

Figure 1.14 (a) Concept for self-assembly of PDI **F114** supported by side-chain amide-amide hydrogen-bonding interactions. The dodecyl groups are simplified as R. Right part depicts a schematic representation of face-to-face stacks of rotationally displaced PDI cores. (b) Toluene organogel of **F114** formed at 1.5 mM. (c) AFM height image of an aggregate sample spin-coated from diluted gel solution of **F114** in toluene onto mica; scale bar = 200 nm. (Figure adapted for review from Li et al.[59] with permission from RSC.)

Alternatively, helical π-stacked PDI assemblies have been formed using polymer scaffolds such as polyisocyanide (as shown in Figure 1.15). Using this approach, the structural order of the underlying scaffold directs the assembly of the individual PDI units. For the example in Figure 1.15, the ordered, helical structure of the polyisocyanide is functionalized with amino acid linkers (Figure 1.15b) which serve as hydrogen-bonding tethers for the PDI units (Figure 1.15a) and prompt PDI assembly into a four-strand, helical array (Figure 1.15c). Using this material as an organic semiconductor blended with polymers such as poly(3-hexylthiophene) (P3HT), organic photovoltaic devices[60–63] were successfully fabricated, displaying photocurrent and voltage bias output such as that shown in the plot in Figure 1.15d.

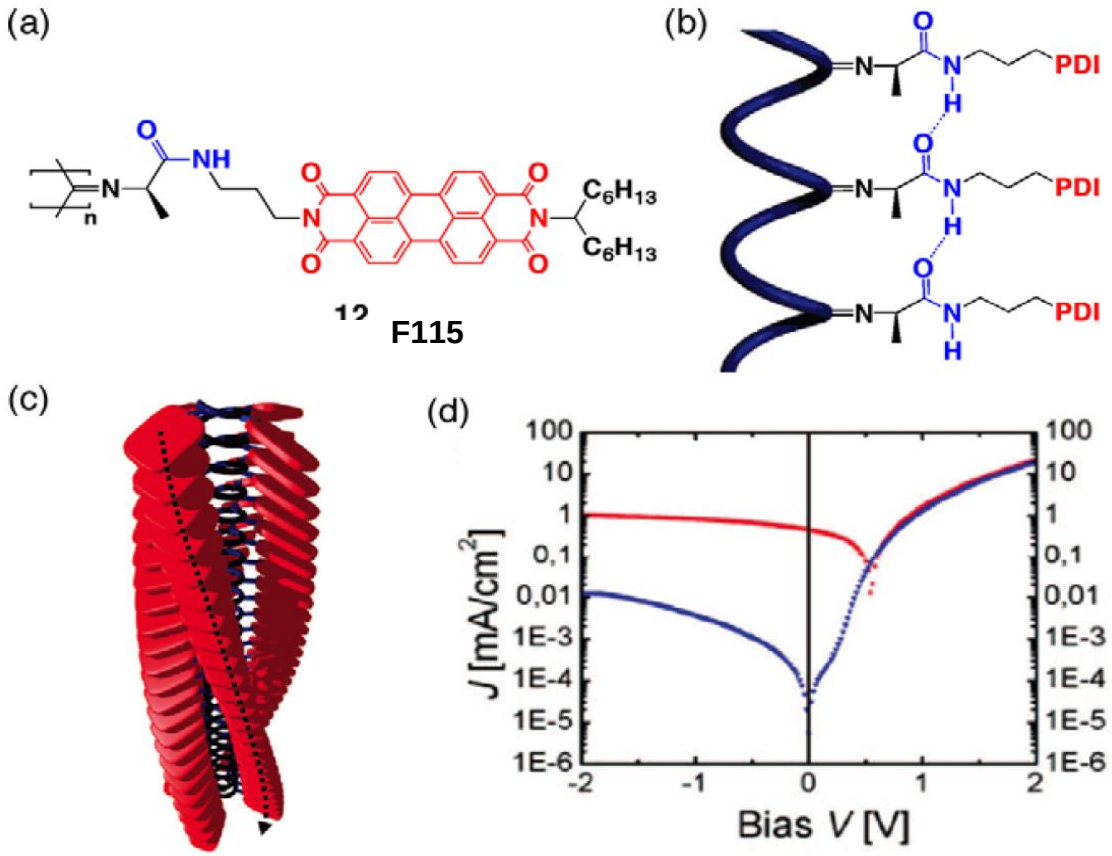

Figure 1.15 (a) Molecular structure of PDI-substituted polyisocyanide **F115**. (b) Illustration of the hydrogen-bonding between the n^{th} and $(n + 4)^{th}$ monomeric units within the polymer. (c) Cartoon showing the complete helical structure. The dashed arrow indicates a stack of PDI units running along the central polyisocyanide backbone. (d) Semi-logarithmic J–V plots in darkness (blue) and under illumination (red) for a 1:1 P3HT/**F115** photovoltaic cell. (Figure adapted for review from Palermo et al.[63] with permission from ACS.)

Other PDI photovoltaic devices have been reported which do not use the scaffold approach of Figure 1.15. Instead, a PDI organogelator which forms nanowires during gelation (such as **F116** in Figure 1.16a) can be blended with a suitable conducting polymer (such as pvDMTPD) and used to fabricate a photovoltaic device (as illustrated in Figure 1.16b) with output shown in Figure 1.16c.

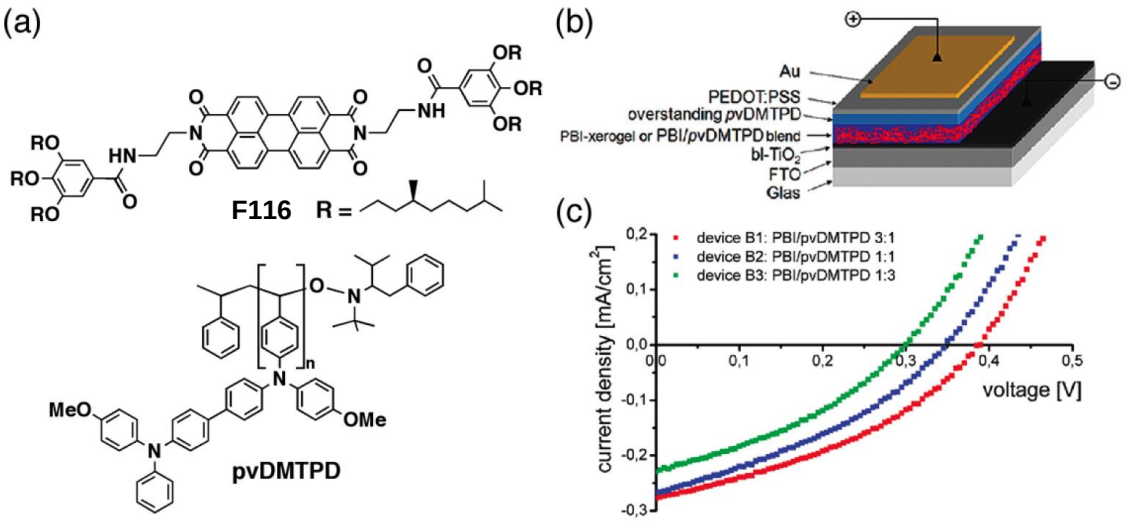

Figure 1.16 (a) Molecular structures of PDI **F116** and pvDMTPD. (b) Device architecture with inverted cell configuration. FTO=fluorine-doped tin oxide, PEDOT=poly(3,4-ethylenedioxythiophene), PSS=poly(styrene sulfonate). (c) J–V plots under illumination with white light (AM 1.5 spectral conditions, 100 mW cm^{-2}) for photovoltaic devices constructed from a PDI xerogel/pvDMTPD blend with an additional pvDMTPD layer. The compositions for the devices B1, B2, and B3 are 3:1, 1:1 and 1:3 (PDI:pvDMTPD wt%), respectively. (Figure adapted for review from Wicklein et al.[64] with permission from ACS.)

PDIs which self-assemble (but are not organogelators) have also been used to fabricate devices. One such example is shown in Figure 1.16 which shows the fabrication of an organic inverter device consisting of two organic field-effect transistors made from self-assembled nanowires. For this device, nanowires of *N*,*N*′-dioctyl perylene diimide (**F117**) were grown by carefully layering a volume of methanol onto an aliquot of a chloroform solution of **F117** (monomers) without mixing the layers. Over the course of 25-30 minutes, mixing of the methanol and

chloroform layers by diffusion induced self-assembly of the monomers into nanowires (Figure 1.17a). The resulting nanowires were then applied across pre-fabricated gold electrode junctions (Figure 1.17b) arrayed in an interdigitated fashion on top of a doped silicon wafer with silicon dioxide dielectric layer (Figure 1.17c). For the device, PDI **F117** served as an n-type material (electrons generated as charge carriers), while hexathiapentacene (applied in similar fashion to **F117**) served as a p-type material (electron vacancies generated as charge carriers). Together the joint n-type and p-type transistors formed the inverter device (Figure 1.17c) with output characteristics as shown in Figure 1.17d.

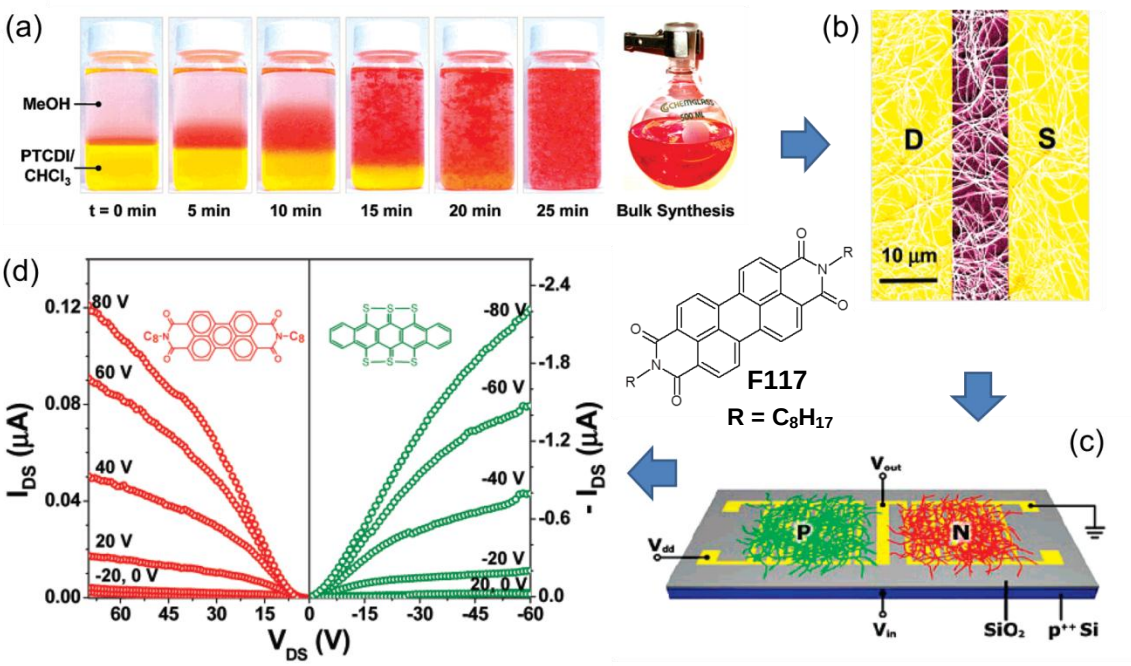

Figure 1.17 (a) A series of optical photographs detailing the interfacial self-assembly of PDI **F117** nanostructures. The top layer of the vial is methanol, and bottom layer is **F117** dissolved in chloroform (~1.5 mg/mL). The last picture frame illustrates a 500 mL flask containing a large quantity of PDI **F117** nanowires that were also synthesized in ~25 min. (b) A colorized SEM image of a network of PDI **F117** nanowires drop-cast across the gold electrodes from a methanol suspension. (c) Schematic of an inverter with p- and n-type nanowire networks covering interdigitated source-drain electrodes. (d) Output characteristics of field-effect transistors fabricated from nanowires of n-type PDI **F117** (red) and p-type hexathiapentacene (green). (Figure adapted for review from Briseno et al.[65] with permission from ACS.)

For each of the examples highlighted in this section, self-assembly and/or morphology play a crucial role in the PDI material application. Often, manipulation of the solvent environment for a PDI solution is used to invoke solvophobic/solvophilic interactions to trigger and drive self-assembly. For many perylene imides, low solubility is a common feature, which introduces solution concentration limitations and may complicate material processing, but these potential limitations can be mediated through the selection of appended substituents. Moreover, the strong aggregation and solvophobic characteristics associated with the low solubility of many PDI compounds, can, in fact, provide an enhanced robustness to self-assembled perylene imide nanostructures.[10] The interplay between solvophobic and solvophilic interactions modulated appropriately by suitable perylene imide substituents can yield compounds such as stimuli-responsive perylene imide gels that are responsive to changes in ionic charging, solvent environment, and temperature.[66] Consequently, the innately low solubility of many perylene imides joined in tandem with appropriate substituents can become an advantageously solvent-responsive trait impacting self-assembly and its associated morphology.[67,68]

With regard to the possibility of achieving tunable, responsive self-assembly and morphology from perylene imide compounds by balancing the influences from the perylene core and its substituents, a highly illustrative example was reported from a study by Zhang and co-workers.[68] In the study, a detailed evaluation of morphological controls was examined based on fine-tuning the secondary forces acting upon an amphiphilic perylene imide compound (Figure 1.18a). The sensitive and nuanced response to the solvent environment by the compound yielded a variety of distinctive morphological outcomes (Figure 1.18b,c) and permitted the construction of phase diagrams for the compound in the solvent systems examined (Figure 1.18b,c and Figure 1.19). As seen from Figure 1.18, both the acidic and the acid-free solvent environments induce a morphological response in the perylene imide dye. In the acid-free solvent series, solvophobic/solvophilic influences are primarily driving the changes observed in the morphology. In the acidic solvent series, however, acid-base ionization interactions are at work in addition to the solvophobic/solvophilic influences.

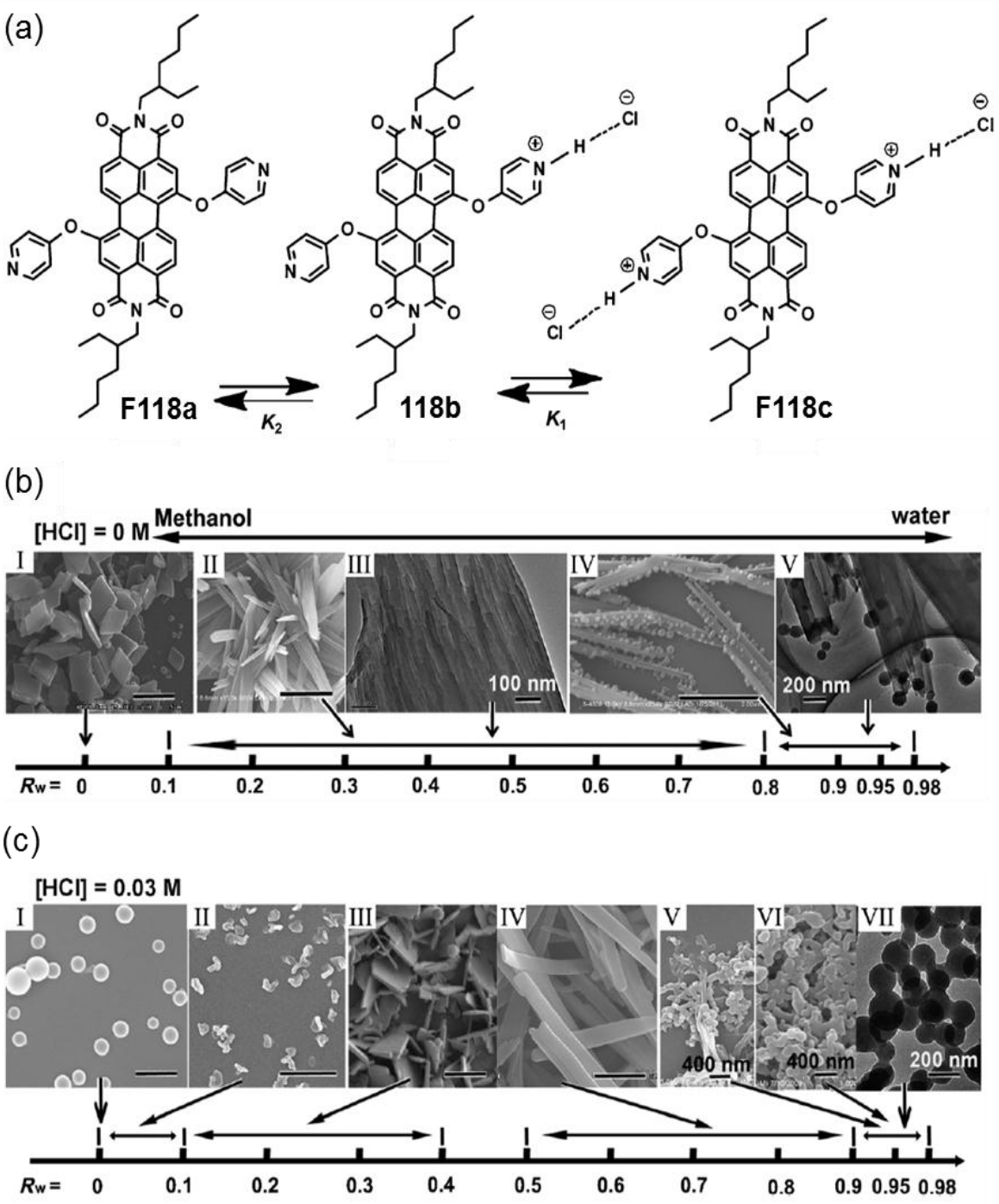

Figure 1.18 SEM/TEM images showing changes in self-assembled nanostructure morphology of a perylene diimide dye: (a) Dynamic protonation among dyes **F118a**, **F118b**, and **F118c**; (b,c) The 1D phase diagram shows morphologies formed either from (b) proton-free dye **F118a** or (c) from doubly protonated dye **F118c** equilibrating with mono-protonated dye **F118b** and **F118a** at [HCl] = 0.03 M controlled by the volume fraction of water (R_w), where $R_w = V_{water}/(V_{water}+V_{methanol})$. For all samples, [dye] = 1×10^{-3} M. Unlabeled scale bars = 2 μm. (Figure adapted for review from Zhang et al.[68] with permission from Wiley-VCH.)

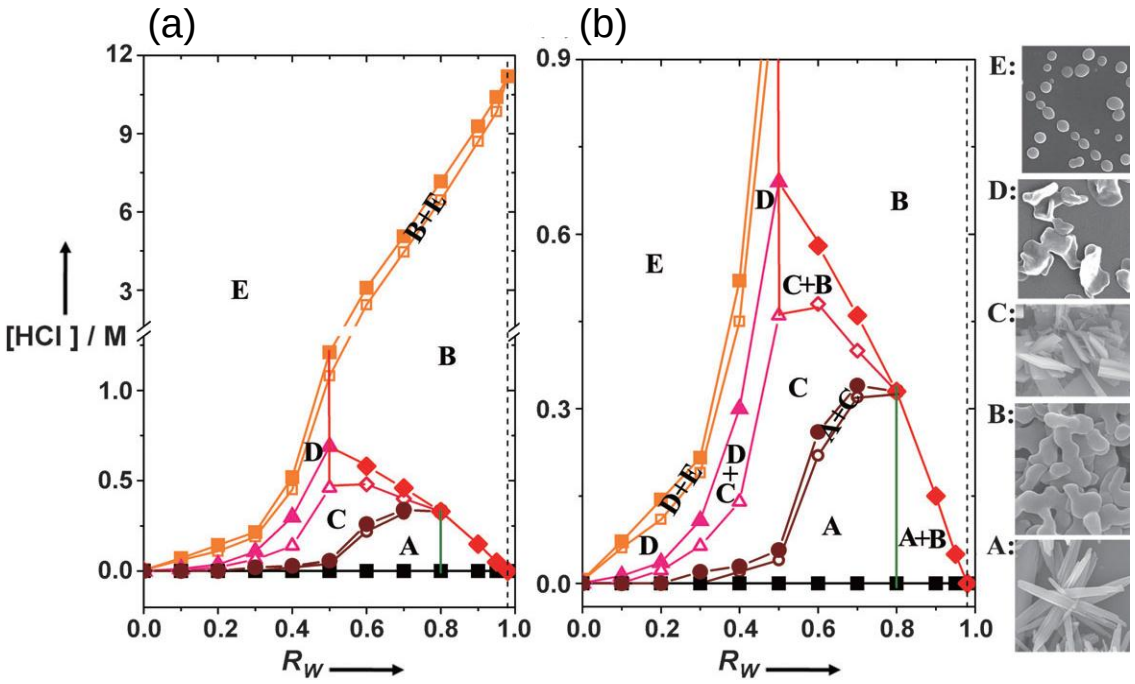

Figure 1.19 The 2D phase diagram showing the various self-assembled nanostructures formed by the interplay of dyes **F118a**, **F118b**, and/or **F118c** (from Figure 1.18), where the volume fraction of water (R_w) and [HCl] both control the morphological transitions. Open plot shapes represent the starting concentration of hydrochloric acid and the transformation from one morphology to the binary mesophases. The filled plot shapes represent the final acid concentration and the transition from the binary phases to the single phase again. Panel (b) is an enlarged view of panel (a) for [HCl] = 0 to 0.9 M. (Figure adapted for review from Zhang et al.[68] with permission from Wiley-VCH.)

As seen from Figure 1.18 and Figure 1.19, multiple influences in the solvent environment can impact the self-assembly and morphology of perylene imide compounds. When it is possible to independently adjust these various influences, they may be advantageously tailored as a part of the morphological tuning. Thus, perylene imide compounds are attractive candidates for supramolecular material design for three principal reasons. First, they have desirable electronic properties. Second, their strong solvophobic/solvophilic responses to the solvent environment may be utilized to enhance the robustness of the nanostructures formed. Third, the morphology of their self-assembly can be tuned through substituent and solvent environment selections. Accordingly, appropriate selection of the substituent moieties employed for these interactions is underscored here.

1.7 Why Peptides and Perylene Imides Together?

Peptides and perylene imides each demonstrate respective innate tendencies to self-assemble. By the simple means of hydrogen-bonding, peptides exhibit a diversity of self-assembly outcomes, which display strong, innate, versatile, sequence-dependent, and functional behavior (as discussed in Section 1.5). Likewise, by simply π-stacking, perylene imides form a variety of self-assembled morphologies which yield a diverse expression of the desirable optoelectronic properties which these compounds possess (as discussed in Section 1.6). For both peptides and perylene imides, the orientational aspects of the self-assembled architectures impact the properties expressed. Accordingly, joining the perylene imide and peptide moieties together into a single molecular unit holds promise of a synthesis of self-assembly characteristics toward advantageous nano-architectures.

Since peptides are comprised of amino acids, an initial examination of amino acids as *N*-substituents for perylene imides provides an appropriate beginning in the consideration of peptides as *N*-substituents. A recent review of amino acid derivatized arylenediimides, which covered both naphthalene diimides (NDIs) and perylene diimides, has highlighted numerous arylenediimides with amino acid *N*-substituents.[69] Although NDIs have important differences to PDIs, the two groups do share some similarities; therefore, amino acid derivatized NDIs may be instructive to PDIs. Many NDIs with amino acid *N*-substituents expressing fascinating self-assembling outcomes have been studied.[69] Among the reported nano-architectures are: nanospheres, particles, nanobelts, fibers, and fractals assembled from tryptophan-appended NDIs architectures,[70] highly crystalline nanosheets with large lateral dimensions assembled from enantiomers of phenylalanine methyl ester appended NDIs,[71] cylindrical microstructures assembled from bolaamphiphiles constructed with a hydrophobic core of NDI and hydrophilic ends of glycine or β-alanine,[72] and encapsulation of single-walled carbon nanotubes (via surface functionalization) by self-assembled stacks of (*L*-4-iodophenylalanine) derivatized NDI.[73] Likewise, PDIs with amino acid *N*-substituents have also shown good self-assembly behavior and a few examples are worth noting. As shown in Figure 1.20, a tetrachloroperylene diimide with carboxybenzyl-protected *L*-lysine *N*-substituents (Figure 1.20a) has been reported which exhibited concentration-

dependent self-assembly outcomes.[74] As the concentration was increased prior to self-assembly, the resulting nanostructures transitioned from nanowires (Figure 1.20c), to nanobelts (Figure 1.20d), to nanosheets (Figure 1.20e), and then to nanotubes (Figure 1.20f), leading to the proposal of the self-assembly pathway shown in Figure 1.20b.

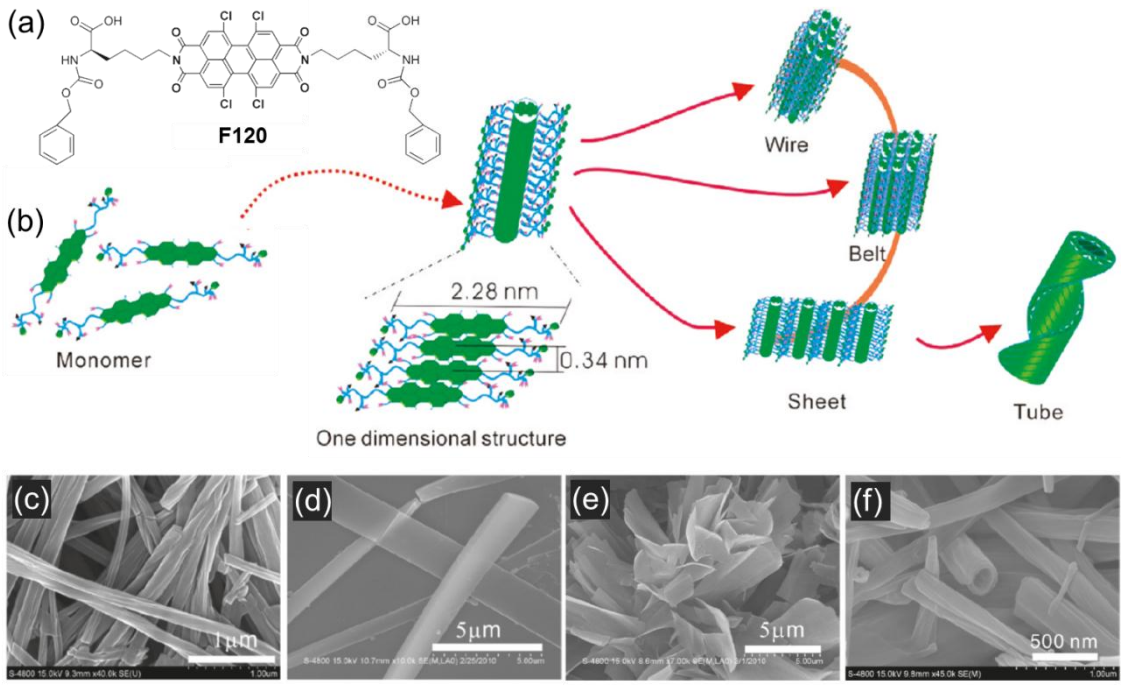

Figure 1.20 (a) Chemical structure of tetrachloroperylene diimide **F120** with carboxybenzyl-protected *L*-lysine *N*-substituents. (b) Proposed self-assembly pathway for PDI **F120** toward different nanostructures. (c-f) SEM images of nanostructures assembled from PDI **F120** in 45% H_2O/acetone mixture at different concentration: (c) 100 μM, (d) 300 μM, (e) 800 μM, and (f) 1 mM. (Figure adapted for review from Sun et al.[74] with permission from ACS.)

Resulting from fibrous nanostructural formations, other PDIs with amino acid *N*-substituents have been found to be organogelators, including PDIs with *N*-substituents of alanine, histidine, phenylalanine, and valine.[75] Gels have also been demonstrated using tryptophan.[76] Of particular interest among the PDIs gels are those which show photoconductivity. One notable example of this is the alanine PDI derivative **F121**, which is shown in Figure 1.21, wherein a gel of **F121** (Figure 1.21a) is formed from a solution of **F121**. The gel and the solution were deposited

(Figure 1.21e,f) and were both found to be air-stable and photoconductive films. This was further supported by indications following irradiation of the deposited samples with 365 nm light. Upon irradiation, the samples changed color and then

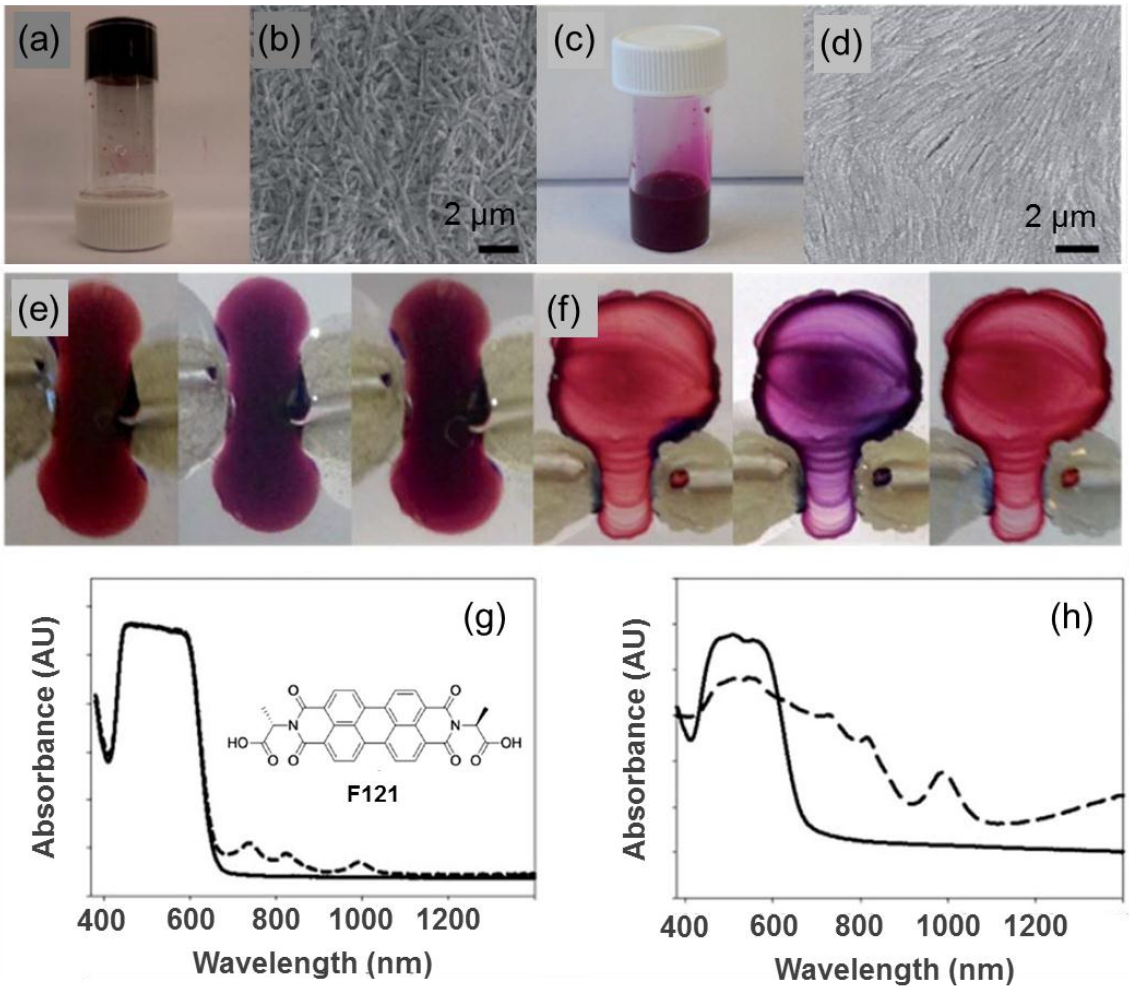

Figure 1.21 (a) Photograph of a gel formed on acidification of a solution of *N,N'*-dialaninyl PDI **F121** (5 mg/mL). (b) SEM image of structures formed on drying the gel. (c) Photograph of a solution of PDI **F121** (5 mg/mL) at pH 10. (d) SEM image of structures formed on drying the solution. (e) On irradiation with 365 nm light, a xerogel of PDI **F121** (left) changes color (middle). After the light is turned off, the original color slowly returns (right), photograph after 18 hours. (f) A similar effect is observed for the dried solution. (g) UV-Vis-NIR spectra for a xerogel of PDI **F121** (—), and for the same film 1 minute after irradiation with 365 nm light (- - -). (h) UV-Vis-NIR spectra for a dried solution of PDI **F121** (—), and for the same film 1 minute after irradiation with 365 nm light (- - -). (Figures adapted for review from Draper et al.[75] with permission from RSC.)

slowly returned to the original color over several hours (Figure 1.21e,f). Spectroscopic investigations of color this transition indicated spectral features consistent with the formation of the radical anion and the dianion PDI species within the samples upon irradiation with the 365 nm light (Figure 1.21g,h).[75]

Another gel formed by a *N*-substituted PDI coupled with tryptophan (via the primary amino end) was also found to be photoconductive (as shown in Figure 1.22).[76] For this compound, current on the microamp scale was observed upon irradiation with both visible and white light (Figure 1.22a). Clear evidence of photo-switching can be seen in the current over time as the light source is turned on and off (Figure 1.22b). Similar results with photo-switching behavior were seen for a gel made from a bolaamphiphile amino acid comprised of a tyrosine moiety tethered to the PDI core by a hydrophobic 11-carbon alkyl linker.[77]

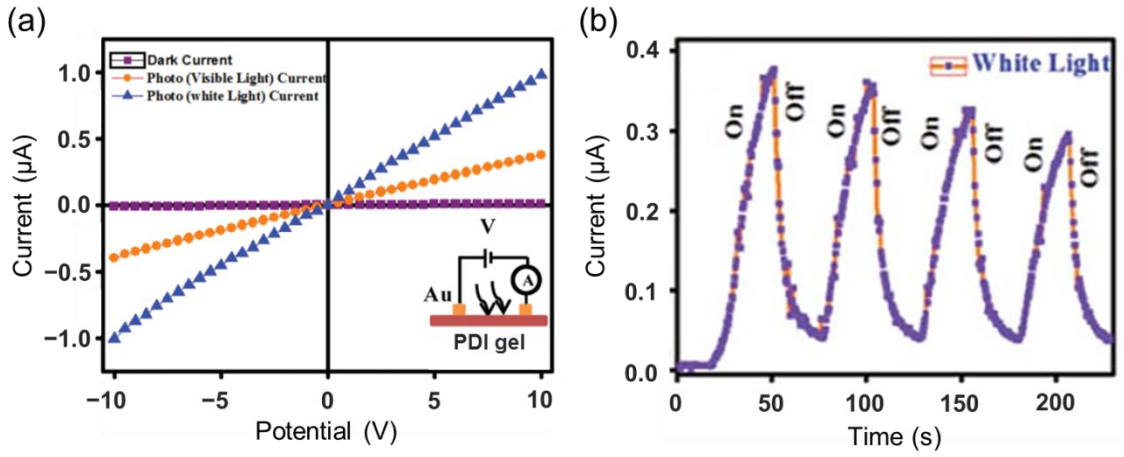

Figure 1.22 (a) Plots of *I–V* curves of a simple conductor device made of *N,N′*-dityrosinyl PDI xerogel in darkness (purple line), visible light (orange line), and white light (blue line). Inset: A schematic representation of the layout of the circuit diagram for *I–V* measurements. (b) Transient photo-response by turning on/off white light illumination of a representative conductor device made of the *N,N′*-dityrosinyl PDI xerogel. (Figures adapted for review from Roy et al.[76] with permission from RSC.)

Following from the examples of good self-assembly and gel formation observed for PDI compounds employing single amino acids as imide substituents, an examination of longer peptide segments is of interest. Accordingly, since peptides

with two amino acid residues are the next step in size from single amino acids, the peptide-PDIs in Figure 1.23 merit consideration. For these compounds, the peptides form a glycine link to the perylene core which then connects to either a tyrosine or an aspartic acid residue. Both compounds were found to be gelators, but

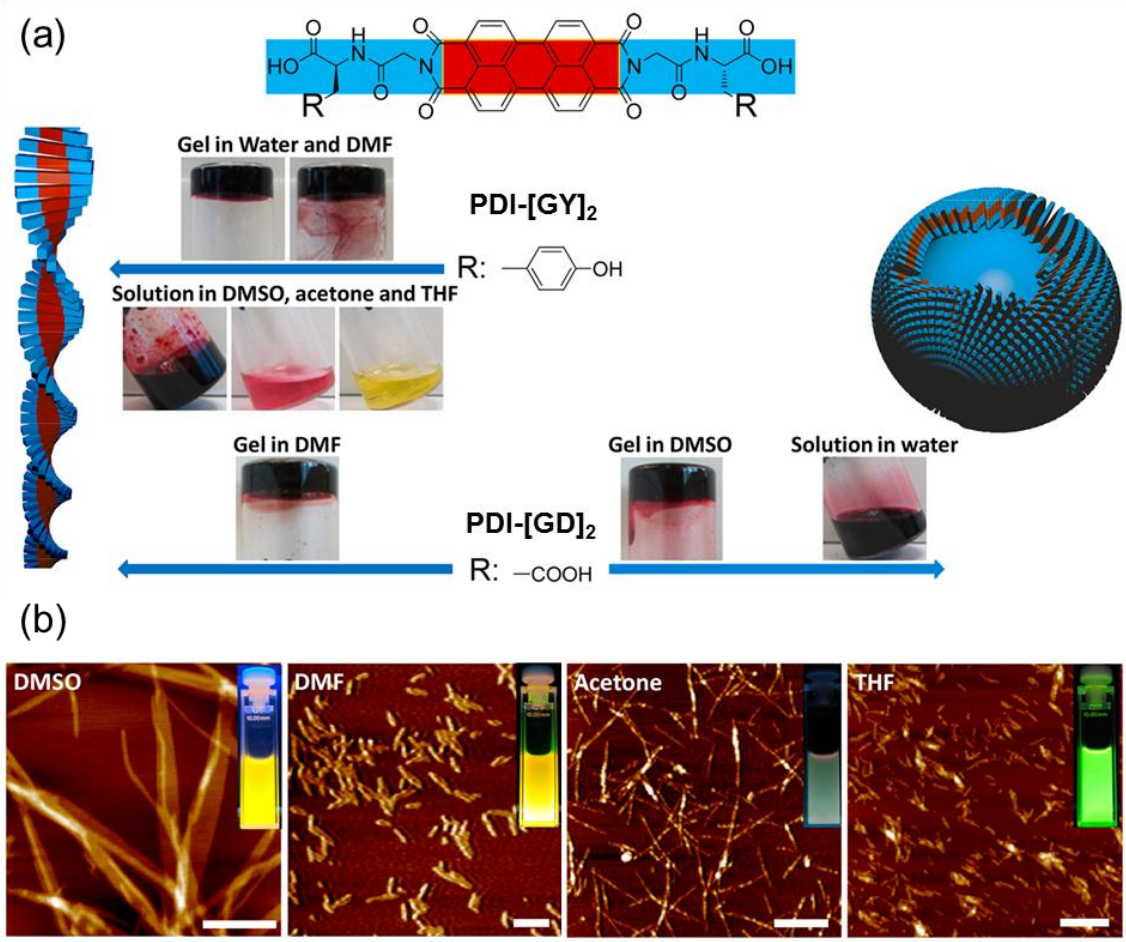

Figure 1.23 (a) Self-assembly of PDI-$[GY]_2$ and PDI-$[GD]_2$ to chiral fibrous and spherical structures in different polar solvents: PDI-$[GY]_2$ forms fibers in buffer solution (pH 10.8), DMSO, DMF, THF, and acetone. PDI-$[GD]_2$ forms fibers in DMF and spheres in water and DMSO. Inset photographs are PDI-$[GY]_2$ gels in buffer solution (pH 10.8) and DMF, solutions in DMSO, acetone, and THF. PDI-$[GD]_2$ gels in DMF and DMSO, and solution in buffer solution (pH 10.8). (b) AFM images of structures of PDI-$[GY]_2$ assembled in DMSO, DMF, THF, and acetone at a concentration of 1×10^{-4} M. All scale bars = 500 nm. Insets are optical photographs showing the different fluorescence emissions of PDI-$[GY]_2$ in DMSO, DMF, THF, and acetone under a UV lamp (365 nm) at the same concentration. (Figures adapted for review from Bai et al.[78] with permission from ACS.)

both compounds were also seen to be highly sensitive to the solvent environment. This sensitivity was seen to prompt different modes of self-assembly in different solvents which was evidenced both by the different nanostructures obtained from the solutions (Figure 1.23b) as well as by the corresponding change in the fluorescence emission observed (at the same concentration) from the solutions.

Given the solvent-responsiveness invoked by the short peptide substituents used for the compounds in Figure 1.23, peptide of even greater length may hold further possibilities for tuning self-assembly. Longer peptide segments provide an extended hydrogen-bonding interface via the accompanying longer polyamide backbone. The added residue positions also increase the capacity for additional combined structural functionalities. Moreover, longer peptides allow for the formation of interface-type segments (like those found in proteins) in which factors such as the segment size, the charge, and the overall interface shape, etc., can be relevant in ways not applicable to shorter peptides or to single amino acids.

Given the need for appropriately balanced substituent influences to modulate perylene imide morphology (as demonstrated in Figures 1.18, 1.23), highly tunable substituents (such as longer peptides) may hold added value for modulating the supramolecular self-assembly of perylene imide compounds. As an example of this, research published by Gallaher, et al.[79] has described the development of peptide-substituted perylene diimides (peptide-PDIs) using longer peptides and has reported many characteristics of these compounds and their aggregates. The published spectroscopy from the study demonstrated that the peptide-PDIs form aggregates as a result of competing hydrophobic/hydrophilic interactions between the peptide substituents and the perylene core (Figure 1.24a), making the peptide-PDIs very sensitive to the solvent environment and readily influenced by solvent composition (Figure 1.24b). The peptide substituents employed (which were comprised of 5-7 amino acid residues containing a glycine linking unit, three central hydrophobic alanine or leucine residues, and 1-3 terminal hydrophilic glutamic acid residues) elucidated several properties which could be exploited to tune the PDIs. Firstly, the ionizable glutamic acid residues in the peptide sequences were seen to provide sensitivity to pH, allowing pH-triggered aggregation and the exploitation of electrostatic interactions to adjust the orientation of PDI monomers in aggregation

(Figure 1.24c,d). Secondly, the charged glutamic acid residues were seen to act as ligands toward metal cations, providing modulation of the orientation of PDI monomers in aggregation via cation binding or charge screening (Figure 1.24c,d).

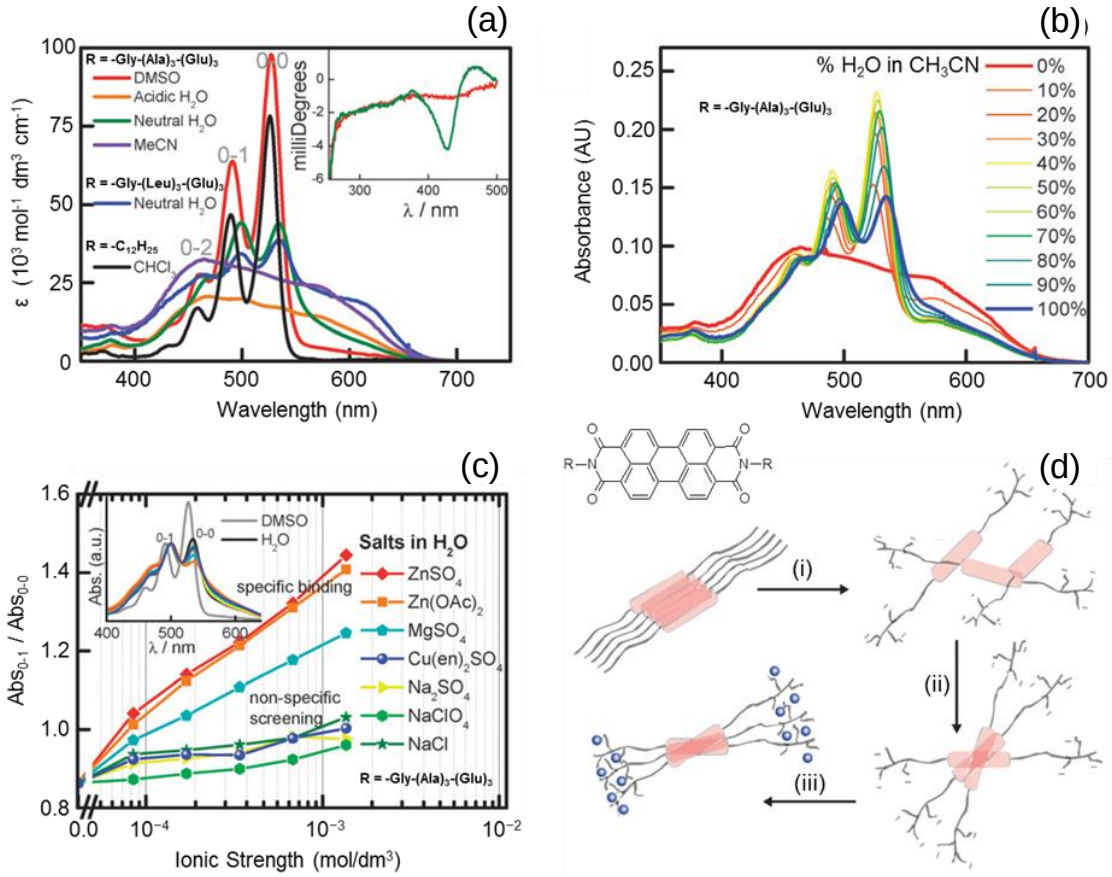

Figure 1.24 A composite of selected results for peptide-PDIs: (a) UV-vis spectra of a monomeric reference dialkyl-PDI and two peptide-PDIs in selected solvents with the vibronic peaks labeled. The inset shows the CD spectrum of the *N*,*N*′-di[-Gly-(Ala)$_3$-(Glu)$_3$]PDI. (b) UV-vis spectra of the *N*,*N*′-di[-Gly-(Ala)$_3$-(Glu)$_3$]PDI in varying water/acetonitrile solvent compositions. (c) A plot of the 0-1/0-0 vibronic absorption peak ratio versus ionic strength of various salts in aqueous solutions for the *N*,*N*′-di[-Gly-(Ala)$_3$-(Glu)$_3$]PDI. The inset shows spectra of the same solutions (salt ionic strength = 6.8×10^{-4} M), as well as the spectra of the *N*,*N*′-di[-Gly-(Ala)$_3$-(Glu)$_3$]PDI in water and in DMSO (without salt) for comparison. (d) Models showing transitions in the relative orientations of the *N*,*N*′-di[-Gly-(Ala)$_3$-(Glu)$_3$]PDI monomers in an aggregate upon (i) moving from CH_3CN to a CH_3CN/H_2O mix, (ii) changing solvent composition to a high water content, and (iii) adding cross-linking dications. (Figure adapted for review from Gallaher et al.[79] with permission from RSC.)

Thirdly, the three central hydrophobic amino acid residues were found to impart chirality to the supramolecular structure of the aggregates formed (suggesting helix formation) as indicated by circular dichroism (CD) spectroscopy (inset Figure 1.24a). These results spectroscopically demonstrate the use of longer peptides to easily modulate the self-assembly of PDIs through small changes in the solvent environment. In later research conducted by Marty et al.,[80] a hybrid peptide-PDI system was investigated in which the perylene imide substituent consisted of a -Gly-$(Ala)_4$ peptide with a 19-mer polyisobutylene polymer appended to the peptide's carboxyl terminus (Figure 1.25a). Like the system reported by Gallaher et al., the

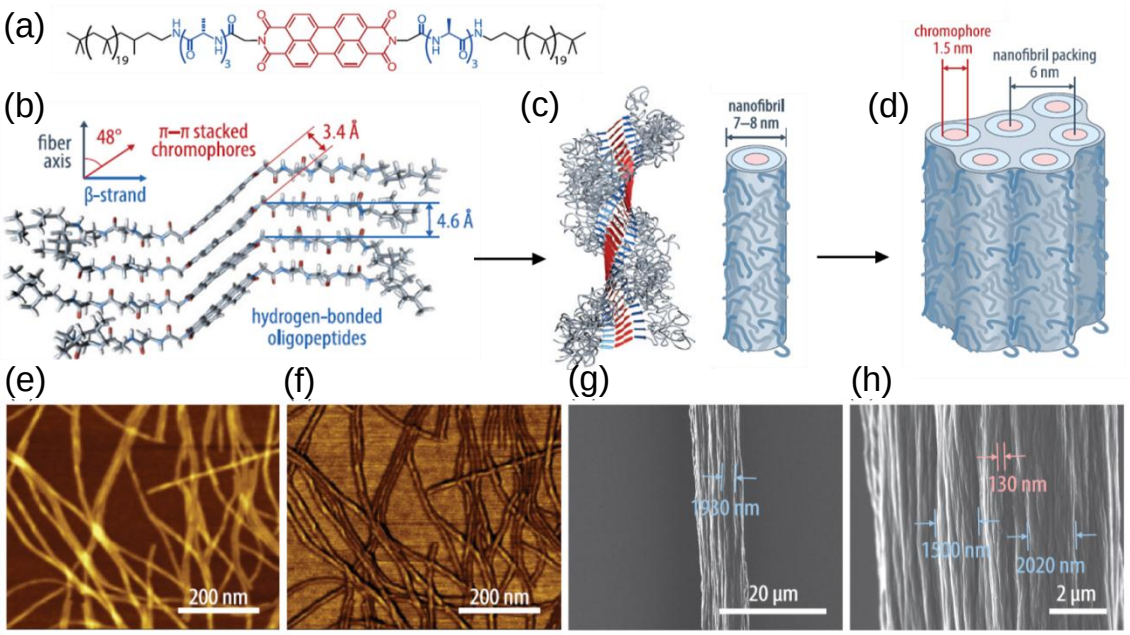

Figure 1.25 Self-assembly of oligo(*L*-alanine)-poly(isobutylene)-substituted PDI: (a) Molecular structure of the compound; (b) Synergistic aggregation enhanced by β-sheet-like hydrogen-bonding (of the oligopeptide segments) and π-π stacking (of the central chromophores); (c) Molecular chirality and polymer attachment suppress lateral aggregation in solution, giving curled (helical) or twisted tapes formed from single stacks of the chromophores; (d) Hierarchically structured microfibers comprised of highly aligned arrays of the randomly close-packed nanofibrils with helical grooves filled by collapsed, appended polymer; (e,f) AFM height and phase images (respectively) showing the formation long single nanofibrils; (g,h) SEM images of microfibers comprised of highly aligned microfibrils constituted of smaller protofibrils. (Figure adapted for review from Marty et al.[80] with permission from ACS.)

hybrid peptide-PDI reported by Marty et al. exhibited spectral profiles consistent with self-assembly induced by the solvent environment. Likewise, the CD spectra also were consistent with that of chiral assemblies. Additionally, the system studied by Marty et al. was verified by microscopy methods to form helical fibers or twisted tapes (Figure 1.25e-h) supporting the expectations for the system studied by Gallaher et al.

1.8 Focus of This Study

Being informed by the numerous aforementioned studies employing amino acids and peptides for self-assembly, and arising from pioneering work with peptide-PDIs reported by Gallaher, et al. and the subsequent work by Marty, et al., this study seeks to further investigate several aspects related to the self-assembly of peptide-PDI systems. These aspects may be broadly grouped into three overarching queries: (1) What is the impact of specific peptide structural changes on the self-assembly of peptide-PDIs? (2) What impact do peptide chiral centers (and their relative positions) within longer peptides have on the self-assembly of peptide-PDIs and their material function? (3) Can peptide-PDI systems — particularly those involving natural peptide sequences — be applied to advantageously assemble organic semiconductors within organic electronic devices?

While peptides have been shown to successfully aid in self-assembly, a limited quantitative understanding of the balance of competing aggregation forces has thwarted efforts to deterministically encode assembly of electronically active units via peptide sequences. This study achieves a systematic investigation of how specific modifications to short (4-7 residue) peptide sequences affect the binding thermodynamics of peptide-PDI molecules toward an understanding of rational design principles.

Peptide stereocenters have been shown to impart a chiral sense to the supramolecular architectures formed by several reported systems, but how does this chiral sense impact material performance? While no difference in material performance would be anticipated between supramolecular assemblies resulting

from enantiomers, what impact (if any) might be seen in supramolecular assemblies resulting from diastereomers generated from selectively inverted peptide stereocenters along a short (4-7 residues) peptide chain? This study investigates chiral modes of self-assembly to assess the impact of chiral supramolecular arrangements on material behavior.

Natural peptide interfaces within proteins often exhibit highly refined self-assembly during protein folding, but these interfaces have yet to be exploited in electronic devices. This study capitalizes on the exquisite self-assembly characteristics of a natural peptide and applies it in an organic electronic device.

1.9 Topical Overview

Following from the various aspects which have been discussed in this chapter, and leading on from the areas of further interest highlighted in the last section, the chapters ahead present a detailed study of the peptide-directed self-assembly of *N*-substituted perylene imide compounds using a variety of peptide sequence variations.

In the next chapter, a discussion of the rational design, synthetic approaches, and analytical methods used for the compounds studied will be presented. Particular emphasis will be given to the theoretical spectroscopic framework applied for the interpretation of the data obtained from the analytical methods used throughout this study.

In Chapter 3, an examination of the impact of specific peptide structural changes will be explored from a thermodynamic perspective using temperature-dependent UV-vis spectroscopy and spectral data-fitting to ascertain peptide structure-to-property relationships as they relate to supramolecular self-assembly.

In Chapter 4, an evaluation of the effect of chiral amino residues on the internal architectures of self-assembled nanofibers will be explored via circular dichroism spectroscopy and by spectral data-fitting models.

In Chapter 5, an exploration of the use of natural peptide sequences for the self-assembly of organic semiconductors will be presented, culminating in a proof-of-concept solid-state organic field-effect device.

Chapters 6 and 7 enumerate the conclusions and ideas for future work, respectively, which were prompted out of this work.

Chapter 8 provides full experimental details for reference with additional supporting information given in the appendices.

Chapter 2

Synthesis and Analytical Strategy

2.1 Introduction

The use of peptides as moieties to guide supramolecular self-assembly brings with it a wealth of possible amino acid sequential variations which may be used to tune the structural properties and behavior impacting self-assembly. To effectively use this wealth of sequential possibilities, a consideration of peptide structure is warranted. A peptide varies principally in the type and order of the side-chain groups (represented by R_1, R_2, R_3, and R_i in Figure 2.1) attached at the alpha carbon positions of the amino acid residues and incorporated along the polyamide backbone of the peptide. It is these side-chain groups which not only give the amino

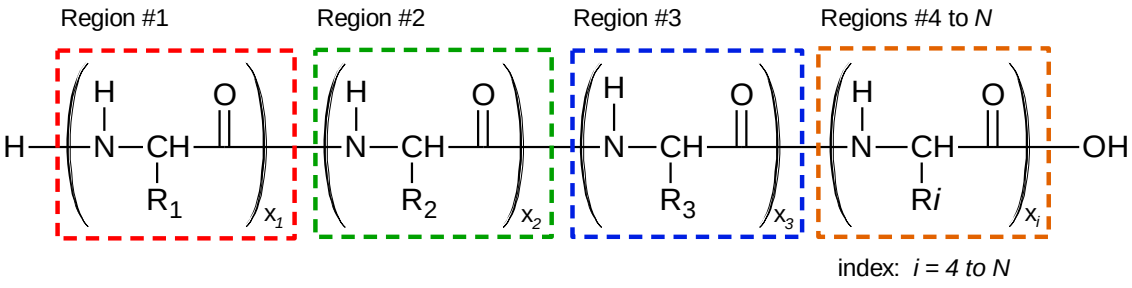

Figure 2.1 A general peptide structure showing the polyamide backbone for a peptide of unspecified length with *N* regions. Variable side-chain groups within each region are noted as R_1, R_2, R_3, and R_i. Regions vary in size by the number of monomers contained in each (unspecified sizes noted as x_1, x_2, x_3, and x_i).

acid building blocks a distinctive identity and distinctive properties, but it is also these groups which, when taken together, largely determine the overall properties of a peptide.

From the twenty-one natural amino acids, these side-chain groups are diverse and classified as hydrophilic, hydrophobic, charged, uncharged, polar, nonpolar, etc. Accordingly, the polyamide strand of a peptide, which is comprised of amino acid monomers, may be divided into regions defined as a block of one or more consecutive amino acid monomers of the same type. Each region will share properties similar to those of its corresponding amino acid, and the size of a region depends upon the number of amino acid residues it contains. Many different regions can be found in a single peptide, and a similar (or identical) region occurring in one position along the peptide chain may recur at another position elsewhere along the peptide chain. In addition to underscoring the high number of sequential permutations possible in such polymeric structures where subunit order is relevant, recognizing that region block placements along the peptide also matter serves to further underscore the importance of the specific amino acid sequence order. This takes on an added dimension when considering peptide units for use as moieties to aid in self-assembly. Upon chemically bonding a peptide sequence with a moiety for self-assembly, the specific regions within the sequence will have a relative position to the bound moiety based upon the point of attachment. For peptide-guided supramolecular self-assembly, sequence variations change the proximity of particular regions in a peptide relative to the appended moiety to be guided in self-assembly. As a result, the specific amino acid sequence, length, regions, and regional properties of a peptide must be taken into account when selecting a peptide sequence to use as a substituent.

Secondary structures formed by peptides add another dimension to sequence and structural considerations. Most basically, for example, intramolecular hydrogen-bonding between adjacent carbonyl and amide-NH groups causes these units to tend toward co-planarity with the side-chain groups projecting from either side of the polyamide plane. Other intramolecular and intermolecular interactions within a specific peptide sequence (with specific sequentially positioned regions) can produce a molecule which becomes structurally more than the sum of its parts,

leading to the formation of secondary structures such as β-sheets (parallel or anti-parallel), β-turns, and α-helices (or other helical forms). Selecting (or rationally designing) sequences with a propensity toward forming a particular secondary structure can facilitate the inclusion of these secondary structural tendencies into a larger self-assembly scheme. Yet whether rationally designed or naturally occurring sequences are selected, a means to acquire sufficient amounts of the peptide material must be possible. Moreover, once the peptides are synthetically applied for self-assembly by incorporating them with another moiety into a larger structure, a means to assess the self-assembly (and the impact of particular peptide sequence differences on that self-assembly) must be possible. Some avenues applied to address these issues are examined in this chapter.

2.2 Solid-Phase Peptide Synthesis

To reliably obtain significant quantities of peptides with high sequential and chemical purity without reliance on isolation from natural sources, solid-phase peptide synthesis (SPPS) delivers markedly. Since its initial development by Merrifield,[81] SPPS has now become the preferred method for a majority of peptide syntheses due to several advantages over solution-phase methods.[82] Chief among these advantages is a simplified separation of the desired peptide product from unreacted starting materials and side-products. In SPPS, a solid support (such as cross-linked divinyl benzene resin beads) is employed to which a loading of amino acid moieties are chemically bound (generally through the carboxyl group of the amino acid via a linker). These amino acid moieties on the resin become the reaction sites to start peptide formation, and these moieties are incorporated as the C-terminal residue of the peptide. As such, the selection of the moiety used in the resin loading must be deliberate since the amino acid on the resin becomes the first residue incorporated into the peptide. Over the course of the SPPS processes, the peptide essentially "grows" on the resin support. Because SPPS is performed on a solid support, purification is greatly simplified, in that, the peptide product remains attached to the resin; excess reagents and some side-products are simply removed by washing and filtration without the need to transfer any resin material from the reaction column throughout the various steps. This solid-phase approach also

avoids difficulties related to the changing solubility properties of the peptide with each step as it is produced. A further striking advantage of SPPS is that it can be automated and performed by machines programmed with specific parameters to generate desired peptide sequences according to a pre-designed synthetic strategy.[82] One common SPPS protocol employs the 9-fluorenylmethoxycarbonyl (Fmoc) protecting group with a Wang resin solid support. An overview of a general synthetic scheme is given in Scheme 2.1, which illustrates standard Fmoc-based SPPS protocols.[81]

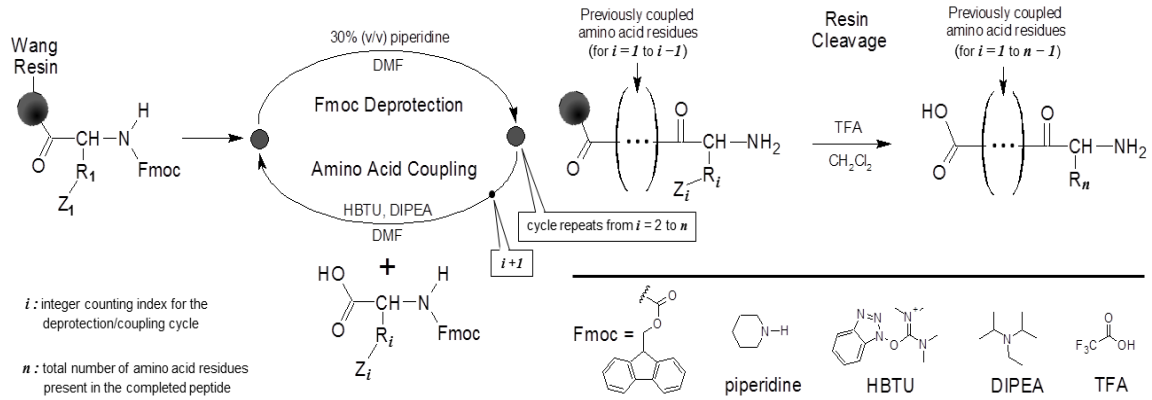

Scheme 2.1 An overview of the solid-phase peptide synthesis procedures. Functionalized resin beads are employed in a repeated Fmoc-deprotection/amino acid coupling cycle until the desired peptide sequence is obtained. Each full cycle introduces one additional Fmoc-protected amino acid link into the peptide chain. The completed peptide is subsequently removed from the resin.

A central feature of the SPPS process is the deprotection/coupling cycle shown in Scheme 2.1. This cycle is repeated for each amino acid residue to be incorporated into the peptide and continues until the end of the peptide sequence. The principal change occurring in the cycle involves the introduction of the different amino acids (in the necessary order) to produce the desired peptide. Each full cycle adds one amino acid link to the peptide chain via the formation of a new amide bond through a reaction between the terminal amino group of the growing peptide and the activated carboxylic acid group of the amino acid introduced. To enhance the formation of the amide linkage, a high excess of the amino acids used during coupling is supplied to drive the coupling reaction to completion, and the

carboxylic acid moiety is activated with agents such as *O*-benzotriazole-*N*,*N*,*N*′,*N*′-tetramethyluronium hexafluorophosphate (HBTU) along with a small amount of the non-nucleophilic base *N*,*N*-diisopropylethylamine (DIPEA). The amino acids used in SPPS processes incorporate protecting groups such as Fmoc to ensure that only the amine functionality on the growing peptide is available to react during the coupling reaction. Additional protecting groups (such as *tert*-butyl groups, noted generally in Scheme 2.1 as Z_i) are used for sensitive functional groups in the amino acid residue side-chains (noted in Scheme 2.1 as R_i). Protecting groups used for the side chains are selected to be stable under the conditions used during the SPPS deprotection/coupling cycle but to be unstable and easily removed under the final conditions applied to cleave the peptide from the resin and conclude the SPPS protocol. This feature of protecting group orthogonal behavior is a key aspect affording the success of the SPPS protocols. In Scheme 2.1, the side-chain protecting groups and resin link are stable under the basic conditions used, but the

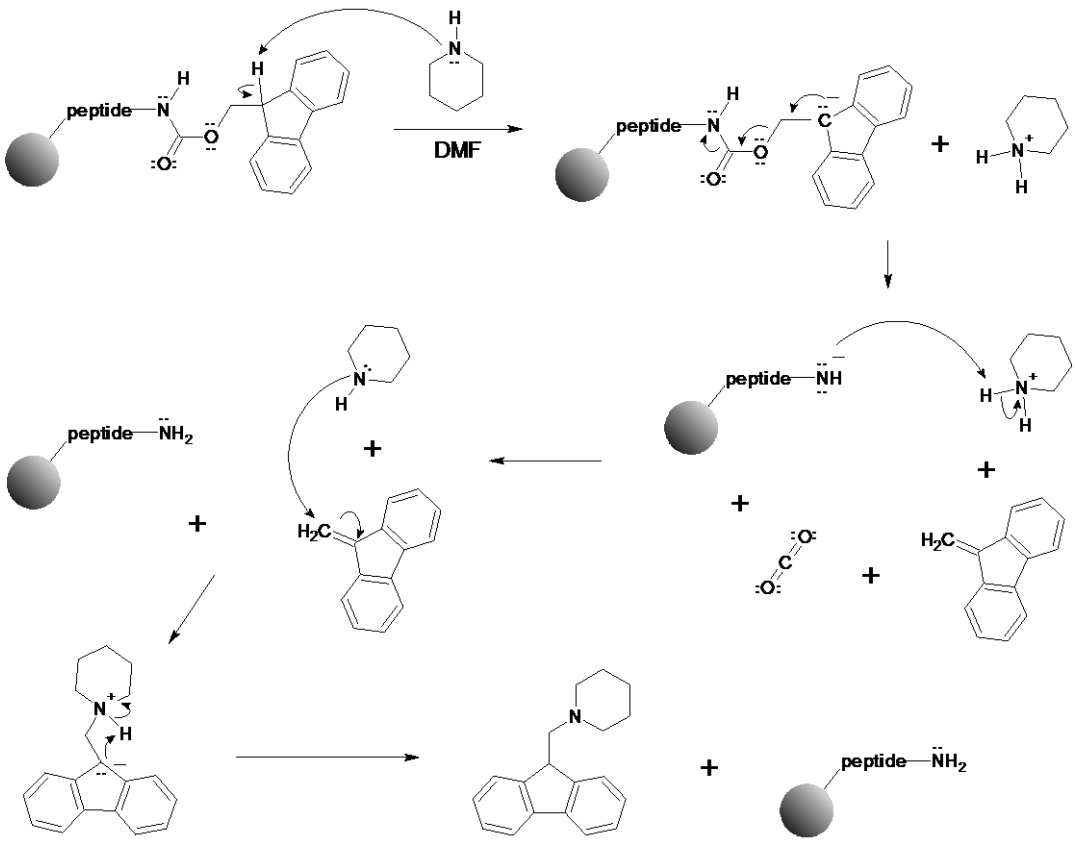

Scheme 2.2 Reaction mechanism for the Fmoc deprotection of the amino terminus of a resin-bound peptide during SPPS.

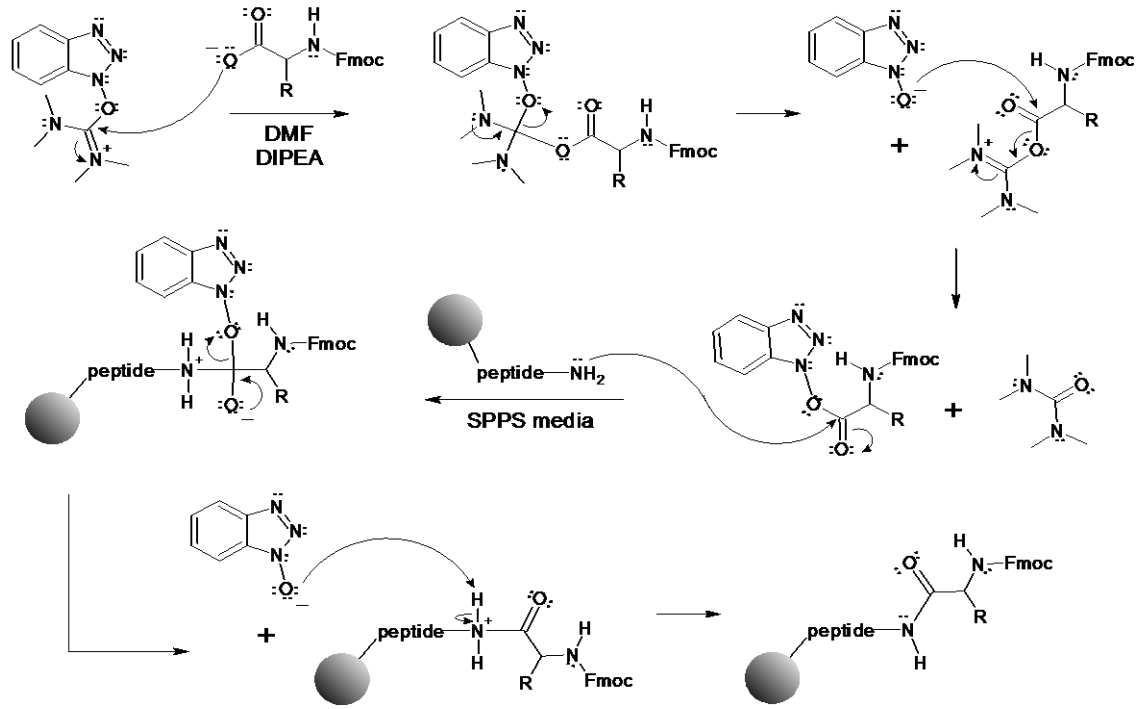

Scheme 2.3 Reaction mechanism for the coupling of an HBTU activated carboxyl group of an Fmoc-protected amino acid with the amino terminus of a resin-bound peptide forming during SPPS.

Fmoc group is cleaved from the growing peptide with an appropriate base. In the final step, the resin link and the side-chain protecting groups are unstable are removed under the acidic conditions applied. Mechanisms for the deprotection and coupling reactions are given in Schemes 2.2 and 2.3, respectively.

2.2.1 Synthesis of Protected Peptide Products

In some cases, it may be desired to retain one or more of the SPPS protecting groups in the final peptide product. For example, retaining specific protecting groups may shield certain side-chain moieties during subsequent reactions between the peptide and another compound during a targeted synthesis. Although the general SPPS protocol previously outlined is designed for the removal of all side-chain protecting groups upon cleavage of the completed peptide from the resin, it can be adapted easily to obtain peptides which have some (or all) of the side-chains protected. In fact, if carefully planned, adaptations can often be made to

simultaneously apply multiple strategies, thus allowing a staged, selective deprotection of certain amino acid residues. Three main types of adaptations are made to the standard protocol to effect selective deprotection during resin cleavage. These are: (1) Change the reaction cleavage solution; (2) Change the type of support resin used; (3) Change the specific protecting groups used on one or more amino acids incorporated into the peptide during SPPS. Often changes of more than one of these parameters may be needed for the desired outcome.

The first approach is to change the reaction cleavage conditions. Some protecting groups are more labile than others. As a result, in some instances, lowering the trifluoroacetic acid (TFA) concentration in the cleavage solution below a certain threshold or switching to a solvent such as 1,1,1,3,3,3-hexafluoroisopropanol (HFIP) can permit the removal of the more acid-labile protecting groups while retaining the less acid-labile protecting groups. This method, however, is often limited by the types of protecting groups (in conjunction with others on the peptide) which are removed by this strategy.

The second approach is to change the type of support resin used. Although Wang resins are standard in the Fmoc SPPS protocol discussed here, other more acid labile resins such as 2-chloro-trityl resins are also used. Perhaps the simplest protected peptide to achieve is one in which all side-chain protecting groups are retained. This is accomplished by changing both the support resin and the cleavage solution of the standard Fmoc protocol. Using a 2-chloro-trityl resin to perform the SPPS, and then cleaving from the resin using HFIP gives a scenario in which the HFIP is acidic enough to cleave the highly acid-labile 2-chloro-trityl resin but too weak to remove the side-chain protecting groups normally removed by TFA.[83] When considering an alternative resin, however, it is important to evaluate the loading of reactive sites in the resin network. Some solid supports not specifically for SPPS may have a loading which is detrimental to the synthesis, since a loading which is too high may introduce steric crowding or promote aggregation between neighboring peptide strands and hinder reaction completion, necessitating more repeated coupling cycles and longer coupling times. For shorter peptides (11 residues or less), a loading of 0.35-0.60 mmol/g is usually desirable, but in general, the longer the sequence, the more the loading may need decreased.

The third approach is to change the protecting groups applied to the amino acid side-chains. Numerous protecting groups have been developed which are removed under specific conditions.[84] Some available protecting groups employ removal conditions very different to the solvent environments encountered in SPPS[84] such as $N_2H_2 \cdot H_2O$ in DMF, Zn in acetic acid, or photolysis. Protecting groups with very specific removal conditions outside of the SPPS regime may thus be selected where required.

2.2.2 Other Specialized Resins

Although most pre-loaded resins are loaded with an amino acid derivative, a small number of resins are available which are loaded with other linker moieties such as ethylenediamine (or other diamine alkyl chains). Alternatively, unloaded resins may be purchased for custom loading with other moieties. In the case of the ethylenediamine-loaded resin, one amino end is tethered to the solid support while the other amino group is free to bond with an amino acid during SPPS. The end result upon resin cleavage is a peptide with an ethylamino group appended to its carboxyl terminus. This outcome demonstrates the potential use of specialized resins to introduce customized linkers during the SPPS, which affords a much more reliable approach with a higher yield than trying to form an amide linkage via a solution protocol after the peptide is synthesized.

In similar fashion, special resins may be applied to "cap" the carboxyl end of the peptide against further reaction upon completion of the synthesis. This is accomplished via resins such as Rink resins which produce an amidated carboxyl terminus upon resin cleavage.

2.2.3 The Kaiser Test

Regardless of the resin employed, during the SPPS protocol, after each new amino acid coupling reaction is done, verification must be obtained that the reaction has gone to completion and that all amino acids at the ends of the peptide chains have

added the new amino acid unit. This is done by testing for free primary or secondary amines via the Kaiser test.[85] The test involves exposing a small amount of the SPPS active resin to a mixture of three drops of ninhydrin solution (5 g in 100 mL ethanol), three drops of phenol solution (80 g in 20 mL ethanol), and three drops of a KCN solution (2 mL 0.001 M aqueous KCN in 98 mL pyridine) and then heating near 95-100 ˚C for about 5 minutes. Overheating should be avoided since deprotection of the amino acids can occur resulting in false-positive test results. If free, unbound primary or secondary amino groups are present (presumed to be those of unreacted amino acids on the ends of the peptide), a color change will result from the reaction of the ninhydrin with the amino functionality as outlined in Scheme 2.4. The Kaiser test is obvious for primary amino groups, releasing a strong, distinctive blue chromophore into the yellow solution. Consequently, a blue color change indicates that an amino acid coupling reaction is

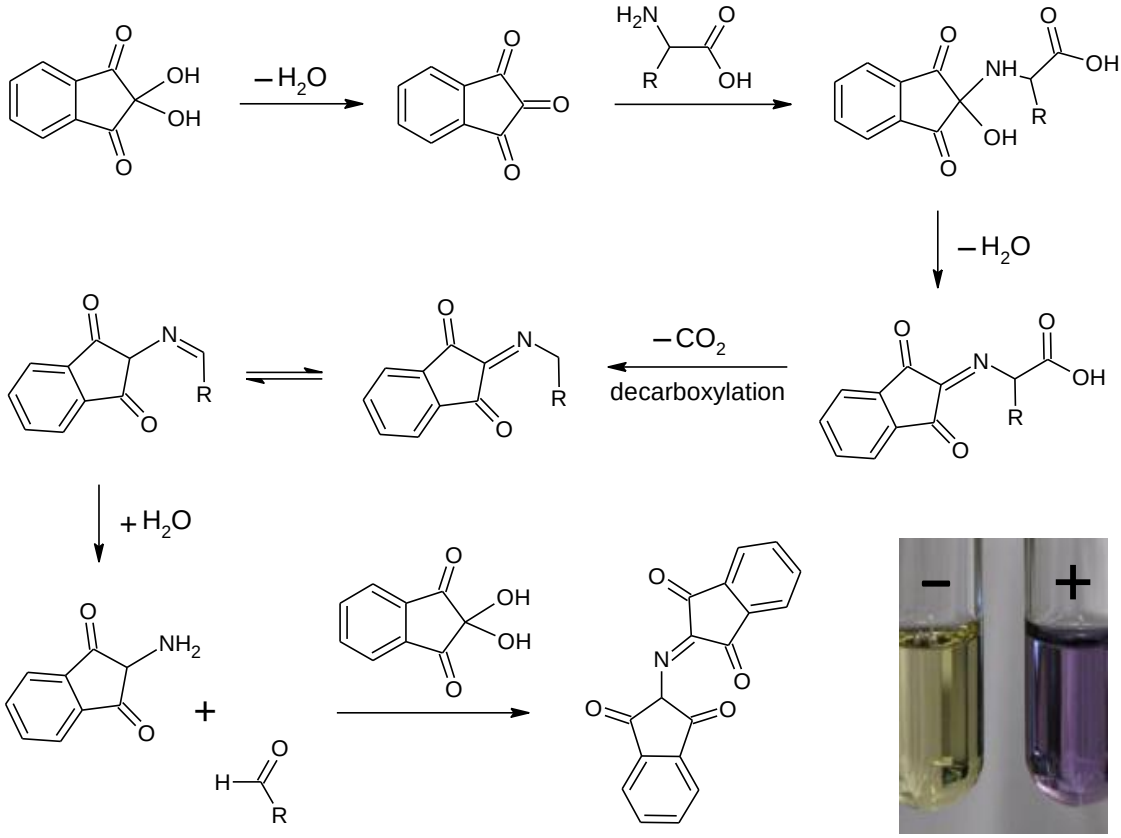

Scheme 2.4 Reaction pathway for the reaction of an amino acid primary amine with ninhydrin, generating a chromophore having a dark blue color indicative of a positive Kaiser test result, which signals an incomplete coupling reaction during SPPS. A photo (inset) shows a positive and negative result.

incomplete and needs repeated. The Kaiser test is less suited to secondary amines (such as methylated amino acids), however, since it produces a weaker brownish-red color which may be difficult to distinguish in the solution.

2.3 Peptide-Perylene Imide Synthesis

Although solid-phase peptide synthesis makes a wealth of peptide sequences accessible in sufficient quantities, the peptide materials obtained still require a synthetic strategy to couple the sequences to a moiety selected for peptide-mediated self-assembly. While reactions with functional groups on the peptide side-chain is possible, for self-assembly this may be undesirable since bonding through the side-chains could disrupt the inter-chain and intra-chain interactions present in peptide self-assembly. Bonding through the peptide termini, therefore, may be more desirable since this leaves the lateral aspects of the chain free to associate as occurs in proteins. The carboxyl terminus, while available to synthetic transformations, holds less intrinsic reactivity and presents the associated challenges of this. In distinction, the amino terminus of a peptide is ideally suited as a resident functionality which can facilitate a variety of synthetic options adaptable to the moiety chosen for self-assembly. A target molecule functionalized to be responsive toward amine chemistry can provide a way to attach a peptide sequence to a target moiety provided that the reaction employed is compatible with the other portions of the structures involved. For self-assembling perylene moieties, the formation of perylene imides is ideal and is easily accomplished via an amine condensation reaction with an anhydride functionalized chromophore.

The methods used to synthesize the *N*-substituted peptide-perylene imides in this study were based on amine condensation with perylene anhydrides using methods previously reported for the synthesis of symmetric perylene diimide derivatives.[86] Using these reactions (or adaptations) as a synthetic framework, several symmetric and non-symmetric perylene imide compounds with significant structural variations were synthesized as outlined in Scheme 2.5. (Synthesis of appropriate perylene anhydride precursors for the general amine condensation reaction drew upon additional synthetic methodologies[87,88] noted in Chapter 8.) While the mechanism

for the amine condensation with perylene anhydride is not fully understood, it is thought to proceed by a radical initiated pathway.[89] The reaction is often performed in molten imidazole as the solvent in part to address solubility limitations of perylene compounds in other solvents; however, DMSO, DMF, or *N*-methyl-2-pyrrolidone (NMP) can alternatively be used in some perylene imide reaction protocols. Using solvents other than molten imidazole may, in fact, be advantageous in some cases. In this study, it was observed that reactions involving the perylene bisester anhydride in imidazole would result in some cleavage of ester groups, reducing the yield of the desired product obtained.

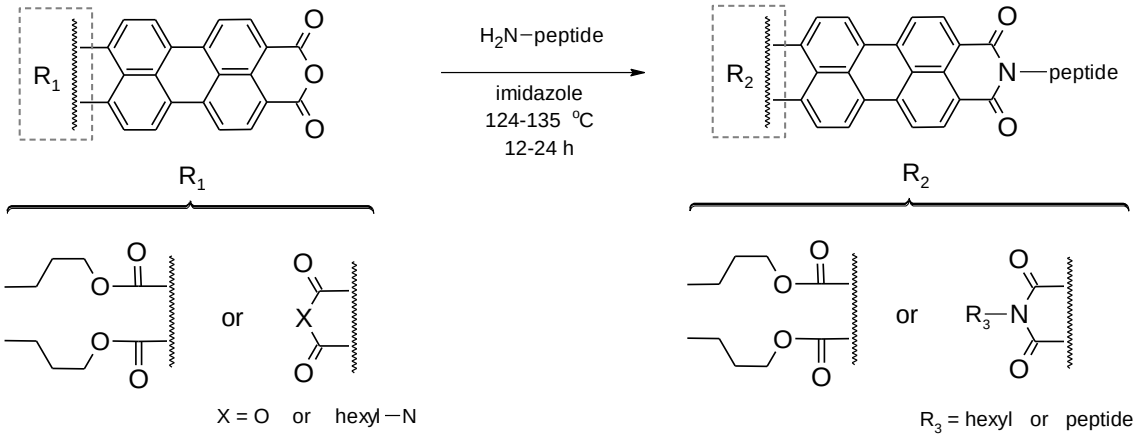

Scheme 2.5 General perylene imide synthesis reaction performed.

2.4 Rational Design of the Peptide-Perylene Imides Synthesized

Having recognized peptides as a promising, versatile substituent for self-assembly, and having identified synthetic pathways to produce desired peptides and subsequently incorporate them into perylene imides, a selection of appropriate peptide sequences must still be made. Here, previously published studies of peptide amphiphiles are instructive. Peptide amphiphiles consist of a long hydrophobic alkyl chain appended to the terminus of a peptide, thus producing molecules with segments having strongly competing hydrophobic and hydrophilic character. These

features prompt peptide amphiphile to self-assemble into highly ordered nanostructures such as rod-like nanofibers. Emerging from pioneering work with peptide amphiphiles by Stupp et al.,[17,23,90–95] it was found that successful self-assembly by peptide amphiphiles into functional nano-architectures requires the inclusion of four essential structural regions, as illustrated in Figure 2.2a. These regions are: (1) a hydrophobic tail to produce hydrophobic interactions and engender amphiphilicity, (2) a peptide sequence capable of intermolecular hydrogen-bonding to aid self-assembly and the impartation of interfacial curvature in the self-assembled structure, (3) charged amino acids (for solubility), and (4) a functional (such as a biologically-active) peptide epitope.[96,97] (Appropriately placed linkers or spacers such glycine or alkyl chains may also be added with these regions.[17]) Upon triggering self-assembly, the hydrophobic tails orient away from the aqueous environment to form a hydrophobic core, while the more hydrophilic peptide segment orient toward the aqueous environment and begin to associate (through hydrogen-bonding) into β-sheets. These interactions produce a radial curvature around a 1D assembly directionality, resulting in a rod-like nanofiber formation (as shown in Figure 2.2b).

Based on the synthetic strategies discussed in Section 2.2 and the peptide amphilphile considerations outlined here, a small library of peptide-perylene imides was synthesized primarily employing peptide sequences with three regions as outlined in Scheme 2.6. The three regions were: (1) a glycine unit to serve as a low steric demand linking unit for condensation with perylene anhydride precursors, (2) a central region (3-7 amino acid residues) to serve as a structural variable and the central assembly interface for investigating steric, chiral, and hydrogen-bonding influences, and (3) a terminal glutamic acid region (1-3 amino acid residues) to influence solubility and to investigate the impact of charged groups. This structural design in Scheme 2.6 shares some similarity with that of the peptide amphiphile in Figure 2.2a (notably regions 2 and 3), but two important differences are also present. First, rather than utilizing a hydrophobic tail like the peptide amphiphile, Scheme 2.6 achieves amphiphilicity by replacing the tail with the hydrophobic, π-stacking perylene imide moiety. This serves both to impart amphiphilicity as well as to achieve π-stacking self-assembly of the perylene core. Additionally, no biologically

active peptide segment is included in Scheme 2.6, since the functional goal of the self-assembly resides with the perylene imide moiety.

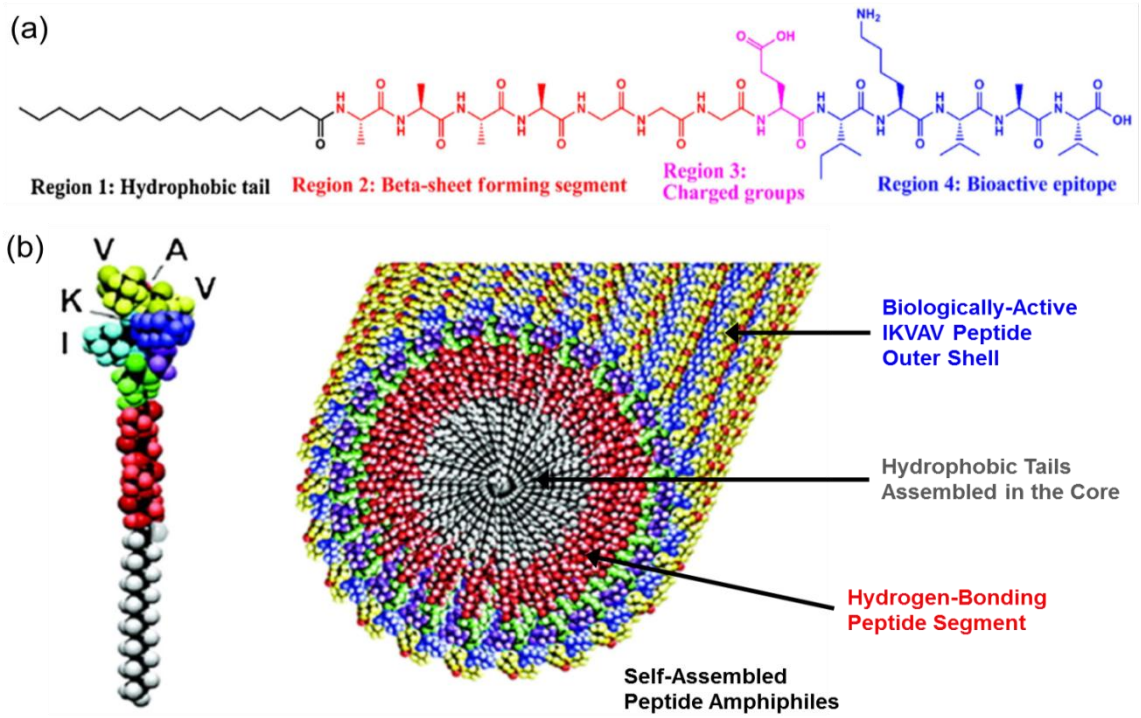

Figure 2.2 An example of peptide amphiphile self-assembly. (a) Four essential structural regions are required for self-assembly into a functional system. Constituents in these regions may be altered to influence nanostructural and self-assembly properties (b) Model of a cylindrical nanofiber formed as a result of the aggregation of individual peptide amphiphile molecules with an IKVAV peptide terminal group. (Figure adapted for review from Hamley et al.[97] with permission from John Wiley & Sons, Ltd.)

Due to the proximity of the central variable region to the perylene core, amino acid residues in this region were expected to impart a much greater impact with regard to steric effects, chiral effects, and hydrogen-bonding during aggregation than the amino acid residues more distal on the peptide chain. As a result, changes in this region were investigated to alter aggregate associations and impact supramolecular assembly. Since the more distal glutamic acid residues on the chain are not held as closely to the perylene core and can diverge more easily during aggregation, these were not expected to impact aggregate trends as strongly and were incorporated into the structure to aid in solubility and to enable pH-triggered aggregation.

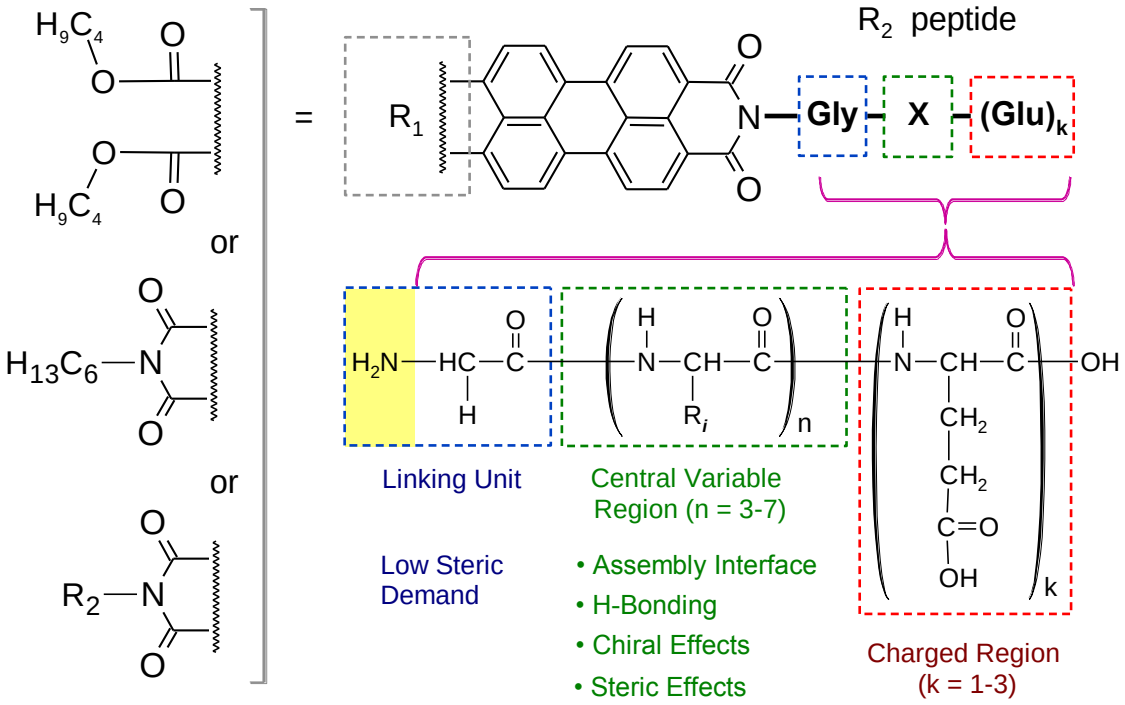

Scheme 2.6 An overview of the structural variations employed in the peptide-PDI synthesis. Three structural regions were modified in the peptide along with three perylene core variations to investigate the influence of specific structural effects.

In addition to the peptide variations explored, both symmetric and non-symmetric peptide-PDIs were investigated by substituting a hexylimide moiety in place of a peptide in some structures. Additionally, two variations of the perylene chromophore were examined by substituting a bisester moiety in place of an imide group in other structures. Two exceptions to the structural design depicted in Scheme 2.6 were also examined. In the first exception, the linking unit was attached to the carboxyl end of the peptide to allow a reversed mode of peptide attachment. In the second exception, Lysine residues were used in place of glutamic acid in the charged region of the peptide. Following from the variations outlined here and those depicted in Scheme 2.6, a summary of the synthesized peptide-perylene imides studied is given in Scheme 2.7.

The compounds summarized in Scheme 2.7 were selectively synthesized to provide structures permitting specific comparisons which evaluate the impact of particular

structural features on self-assembly. Firstly, compounds **1**-**8**, and **1H**-**5H** allow the examination of peptide steric effects, ionizable groups, chiral centers, and hydrophobicity. These comparisons are discussed in Chapter 3 from a thermodynamic perspective. Secondly, diastereomer and enantiomer sets represented by compound sets **3**/**3E**/**4**, **3H**/**3HE**, and **7**/**8** along with glycine-rich **1** and meso **3M** (as control compounds) permit an examination of the effects of chiral centers in close proximity to the perylene imide core. Implications of these chiral effects are discussed in Chapter 4. Thirdly, compounds **9**-**11** provide test structures involving lysine-terminated peptides, to be noted in Chapter 7. Lastly, an assortment

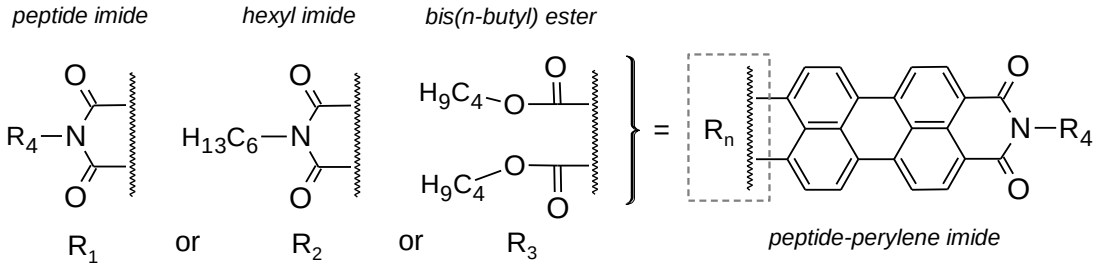

Cpd	R_n	R_4	Cpd	R_n	R_4
1	R_1	-Gly-$(Gly)_3$-$(Glu)_3$	**1H**	R_2	-Gly-$(Gly)_3$-$(Glu)_3$
2	R_1	-Gly-$(Ala)_3$-Glu	**2H**	R_2	-Gly-$(Ala)_3$-Glu
3	R_1	-Gly-$(Ala)_3$-$(Glu)_3$	**3H**	R_2	-Gly-$(Ala)_3$-$(Glu)_3$
3E	R_1	-Gly-(D-Ala)$_3$-(D-Glu)$_3$	**3HE**	R_2	-Gly-(D-Ala)$_3$-(D-Glu)$_3$
3M	R_1	-Gly-(D/L-Ala)$_3$-(D/L-Glu)$_3$			
4	R_1	-Gly-(D-Ala)$_3$-$(Glu)_3$	**4H**	R_2	-Gly-(D-Ala)$_3$-$(Glu)_3$
5	R_1	-Gly-$(Glu)_3$	**5H**	R_2	-Gly-$(Glu)_3$
6	R_1	-Gly-$(Phe)_3$-$(Glu)_3$			
7	R_1	-Gly-$(Leu)_3$-$(Glu)_3$			
8	R_1	-Gly-(D-Leu)$_3$-$(Glu)_3$	**10**	R_2	-Lys(-R_2)-$(Ala)_3$-$(Glu)_3$
9	R_1	-Gly-$(Ala)_3$-$(Lys)_3$	**11**	R_3	-Lys(-R_3)-$(Ala)_3$-$(Glu)_3$
12	R_1	Ac-IK(-yl)HLSVN-NH_2	**12H**	R_2	Ac-IK(-yl)HLSVN-NH_2
13	R_1	-GIRHLSVNEEE	**15**	R_3	-GIRHLSVNEEE
14	R_1	Ac-EEEIRHLSVN-ethyl-	**16**	R_3	Ac-EEEIRHLSVN-ethyl-

Scheme 2.7 Summary of *N*-peptide perylene imides synthesized, arranged by structural similarity.

of compounds incorporating a natural peptide sequence (**12, 12H, 13-16**) enables an examination of the application of natural peptide sequences optimized in nature. This topic is discussed in Chapter 5. To make these comparisons and evaluate crucial differences, informative methods are needed which can probe and discriminate the subtle differences produced by the various structural aspects; these methods will be discussed in the next section.

Before discussing the analytical methods useful for investigating the compounds in Scheme 2.7, it is worth briefly mentioning four compounds which are not included in the list due to unsuccessful (or partially unsuccessful) synthetic attempts to produce them. These syntheses are summarized by Scheme 2.8.

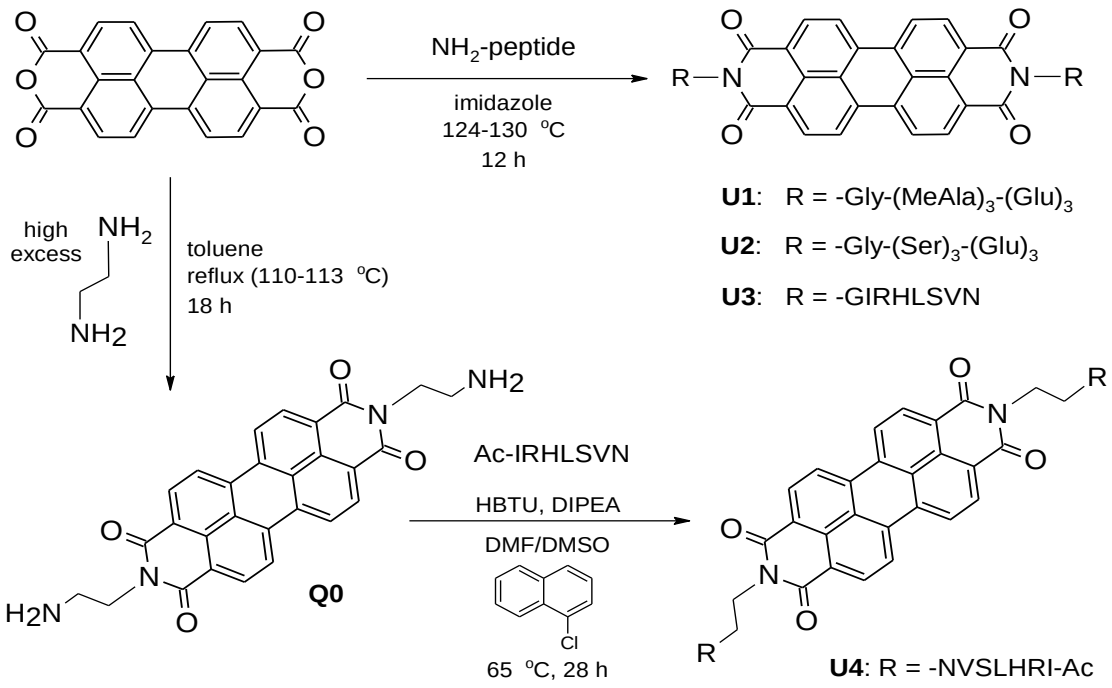

Scheme 2.8 Unsuccessful (or incomplete) synthetic pathways explored.

Syntheses of compounds **U1** and **U2** (Scheme 2.8) were attempted with the intention of generating a set of compounds (**3**, **U1**, and **U2**) for the investigation of H-bonding effects on self-assembly. Comparison of the *N*-methylated alanine (MeAla) derivative **U1** with the non-methylated PDI **3**, was desired to examine the effect of H-bonding originating along the polyamide peptide backbone during PDI self-assembly, while comparison of **3** and serine derivative **U2** was desired to

examine the effect of H-bonding originating from peptide side-chains. Attempts to synthesize the *N*-methylated peptide for **U1** failed to produce a peptide precipitate during SPPS, and no peptide material could be isolated from the solution. It was suspected that the MeAla couplings did not proceed even with two or more attempted coupling attempts lasting 3 hours or longer. Synthesis of the serine peptide for **U2** was successful; however the reaction with perylene dianhydride to form **U2** did not proceed. No traces matching those expected for **U2** could be confirmed. The serine hydroxyl side-chains were suspected to have generated some interfering side-reaction during the attempted PDI formation.

Syntheses of **U3** and **U4** were attempted as part of early investigations using natural peptides in PDIs (to be discussed later in Chapter 5). The respective peptides used as precursors for both **U3** and **U4** were both successfully synthesized. Likewise, the reaction to form **U3** was also accomplished; however, the reaction methodology to form **U4** was not fully effective. Both compounds were difficult to purify due to very poor solubility. During purification on HP20ss resin, the compounds were found to be difficult to elute. This difficulty was compounded for **U4** since the reaction mixture utilized during synthesis was difficult to fully remove. An atypical reaction solvent mixture was employed for **U4** due to the competing solubility characteristics of the reagents. The unusual selection of 1-chloronaphthalene was made to provide an aromatic liquid with the ability to partially solvate some aromatic compounds that have low solubility. The reaction proceeded, but the yield was also very low due to the unfavorable equilibrium toward amide coupling, necessitating a higher molar excess of peptide to shift the equilibrium toward the amide formation. This solution-phase amide coupling was ultimately abandoned in favor of an SPPS methodology which employed a resin-bound linker on which to form the peptide directly. This SPPS method was seen to be superior for joining the peptide and the linker since it did not require excess peptide for a coupling with an ethylenediamino PDI precursor. Accordingly, more of the peptide with the appended linker (made via SPPS) could be carried forward to a reaction to produce the final desired peptide-PDI. Therefore, this SPPS methodology was adopted for the subsequent syntheses of PDI **14** and PIBE **16** (studied in Chapter 5). Since **U3** and **U4** were not fully purified, these and the synthesized diethylendiamino PDI precursor **Q0**[57] are not reported in this thesis.

2.5 Synthetic Characterization Methods

Following the synthesis of the compounds, several techniques were applied to verify that the correct synthetic conversions were achieved in high purity. Although these methods will not be discussed in detail, for context, these techniques are mentioned in this section in relation to the primary indications sought from each analysis. Specific experimental details for these methods are given for reference in the experimental Chapter 8.

2.5.1 Nuclear Magnetic Resonance (NMR) Spectroscopy

Spectra for the ^{1}H and ^{13}C nuclei were of primary interest for the compounds studied. Spectra of both nuclei were collected for the synthesized peptide precursors and were examined in detail to verify sequence production–and to check for the presence of aberrant sequence impurities. Due to the low solubility of the peptide-perylene imide conjugates, however, ^{13}C spectra could only be obtained for the unbound peptide precursors (not for their perylene imide conjugates), making comparison of the ^{1}H spectra of a free peptide with that of its respective perylene imide conjugate useful for verification of the synthesis of the conjugate. In such comparisons, resonance peak groups seen in the peptide spectrum were analogously seen in the conjugate spectrum along with the inclusion of the perylene aryl resonance at highest chemical shift in the spectrum.

2.5.2 High Resolution Mass Spectrometry (HRMS)

Synthesized peptides were screened by HRMS from solution using electrospray ionization (ESI) to verify that the material samples exhibited primary ions having mass-to-charge ratios (m/z) consistent with that theoretically expected for the desired products. The HRMS spectra were further evaluated for possible aberrant species such as deletion sequences. Due to poor solubility in the preferred solvents used for HRMS instrumental analysis from solution, the peptide-perylene imide

conjugates were instead screened in a solid-state matrix via MALDI mass spectrometry.

2.5.3 Matrix-Assisted Laser Desorption Ionization (MALDI) Mass Spectrometry

Synthesized peptide-perylene imide conjugates were screened from solid-state samples via MALDI time-of-flight (TOF) mass spectrometry to verify that the samples displayed spectral features consistent with that theoretically expected for the desired product and to check for indications of starting materials or side-products. Since poor solubility of the perylene imide conjugates did not permit the collection of ^{13}C NMR spectra, MALDI was also applied further to collect ion fragmentation spectra for ion fragment assignment. Assigned ion fragmentation spectra were supplied, when possible, as data verifying the expected molecular carbon frame in place of the unavailable ^{13}C NMR spectra.

2.5.4 Fourier-Transform Infrared (FT-IR) Spectroscopy

Following the synthesis of the peptide-perylene imide conjugates, samples of the compounds were screened via FT-IR spectroscopy to verify the complete conversion of the anhydride functionality to the imide functionality. This conversion manifested as a distinct shift of the associated carbonyl stretch band to lower frequency. Accordingly, mixtures of anhydride and imide functionalities are easily detected, making FT-IR a simple synthetic conversion screening tool.

FT-IR amide band analysis is often performed for peptides and proteins to ascertain secondary structural features and modes of assembly adopted by such compounds.[98–101] Briefly stated, this band analysis method examines the amide absorbance bands as a composite of several contributing bands which are computationally resolved. The evaluated contributing bands are then assigned to specific secondary structural features based on band correlations determined through protein structure studies. Due to interferences from the carbonyl stretches

of the perylene imides such band analyses were not applied in this study for the evaluation of the modes of peptide self-assembly apart from selected cases which will be discussed later in Chapter 5. Due to the limited use of amide band analysis in this study, it will not be discussed in detail.

2.6 Nanostructure Analysis Methods

Although the application of many analytical techniques is limited by the low solubility of the synthesized perylene imide compounds, both microscopy and spectroscopy are well suited for the analysis of nanostructures formed by the compounds in dilute solutions. These two types of techniques also firmly address two essential goals in the analysis of self-assembled nanostructures: (1) To prove that ordered nanostructures have indeed formed (rather than simple disordered aggregates), and (2) To probe the internal architectures of the nanostructures to discriminate differences in self-assembly between compounds for informing structure-property correlations. Microscopy can provide valuable nanoscale imaging of the morphological character of aggregates formed in solution, and supply proof of the type of nanostructures resident. While microscopy can also supply clues about the internal architectures of the nanostructures in some instances, often these clues are limited. Spectroscopy, however, is sensitive toward differences in the local electronic environment between chromophores within supramolecular assemblies and is well suited to discriminate packing differences in the internal architectures of perylene imide nanostructures. Specifically, ultraviolet-visible (UV-vis) and circular dichroism (CD) spectroscopy are particularly useful in evaluating nanostructure architectures. Herein is presented a discussion of the theoretical framework applied from these methods to evaluate the self-assembled nanostructure architectures of the perylene imides from this study.

2.6.1 Microscopy Methods for Nanostructure Analysis

Beyond supplying proof of the formation of ordered nanostructure architectures, microscopy techniques can inform the application of those nanostructures from

solution to solid-state applications such as device fabrication. Identification and characterization of any supramolecular assemblies forming from the compounds synthesized in this study was facilitated primarily by atomic force microscopy (AFM) and cryogenic transmission electron microscopy (cryo-TEM). Microscopy images reported in this study were collected via collaborations with technique specialists at the University of New South Wales (Sydney, Australia) for AFM and the Weizmann Institute of Science (Rehovot, Israel) for cryo-TEM. In this study, cryo-TEM and AFM were used primarily in a supportive role to provide additional evidence of nanostructure formation and were not the main analytical emphasis of this study. Due to its supportive role, analyses and theory associated with these techniques are not discussed at length, but some brief method details and associated examples are included here for context.

2.6.1.1 Atomic Force Microscopy (AFM)

AFM works on the basis of interactions between surface atoms and the atoms of a probe tip which is attached to a cantilever, as illustrated in Figure 2.3a.[102] Attractive or repulsive forces between the surface and the tip cause a deflection of the position

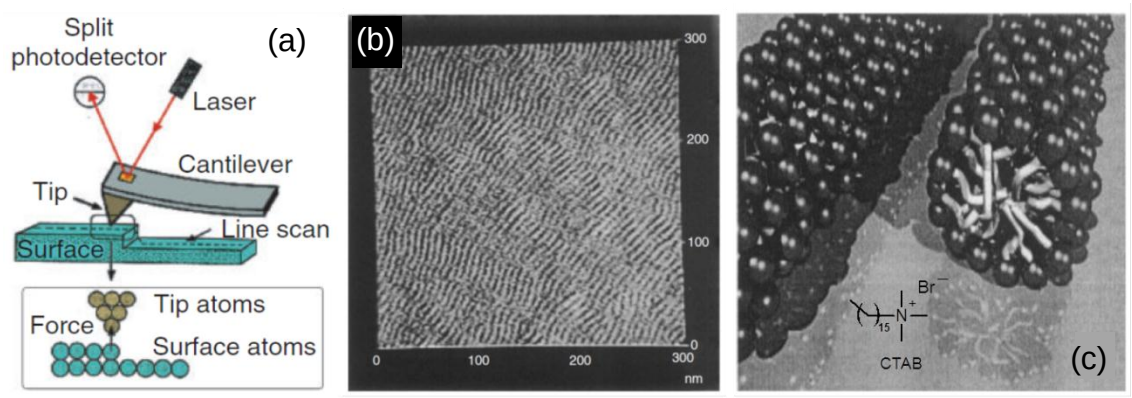

Figure 2.3 (a) AFM instrumental diagram representing the tip and detector setup, (b) AFM image of the adsorption of 1.8 mM cetyl trimethylammonium bromide (CTAB) on mica in the presence of 10 mM KBr showing the formation of cylindrical rows. (c) A model of the cylindrical structure of adsorbed CTAB. A cross-section of the cylinder on the right shows the interior of the cylinder. (Figure adapted for review from Thordarson et al.[102] with permission from CSIRO.)

of the cantilever corresponding to changes in the topography of the surface. The changes in the position of the cantilever are monitored by a laser reflected from a point on the cantilever to a position-sensitive photo detector. Scanning in a raster pattern along the x- and y-directions across the surface allows the monitored changes in the cantilever position to be translated into z-direction contrasts in order to construct an image of the surface scanned. In this way, objects on the surface (such as deposited supramolecular structures) can be imaged. An example AFM image is shown in Figure 2.3b. Such images allow the visualization and measurement of fine structures which facilitates efforts to ascertain or support proposed models of supramolecular assembly (see Figure 2.3b,c).

2.6.1.2 Cryogenic Transmission Electron Microscopy (cryo-TEM)

Cryo-TEM can be superior to other microscopy methods for visualizing fine structures. The true shape and structure of supramolecular aggregates formed in solution may be difficult to observe by dry microscopy methods since fine structures may collect together into indistinguishable masses when drying solution samples onto the microscope substrate. Cryo-TEM overcomes this limitation by flash cooling (avoiding ice crystal formation) to vitrify a solution and capture any dissolved nanostructures it may contain in their native form within the solution. Slow sublimation of the vitrified media gently reveals fine structures which then be visualized by electron microscopy. A general process used in cryo-TEM is as follows:[103] (1) The analyte solution is applied to a support film such as holey carbon affixed to an EM copper grid; (2) The prepared sample is quickly plunged into liquid ethane at the temperature of liquid nitrogen; (3) The sample is then transferred to a cryo holder and placed in the electron microscope; (4) Images of fine structures revealed as the sublimation process occurs are recorded under low dose conditions via a CCD camera. Images collected by cryo-TEM may then be used to measure and model the supramolecular structures observed. Examples of some cryo-TEM images of a self-assembling polyethyleneglycol-PDI (PEG-PDI) monomer along with measurements and proposed models for its self-assembly into nanofibers are shown in Figure 2.4.[10,44]

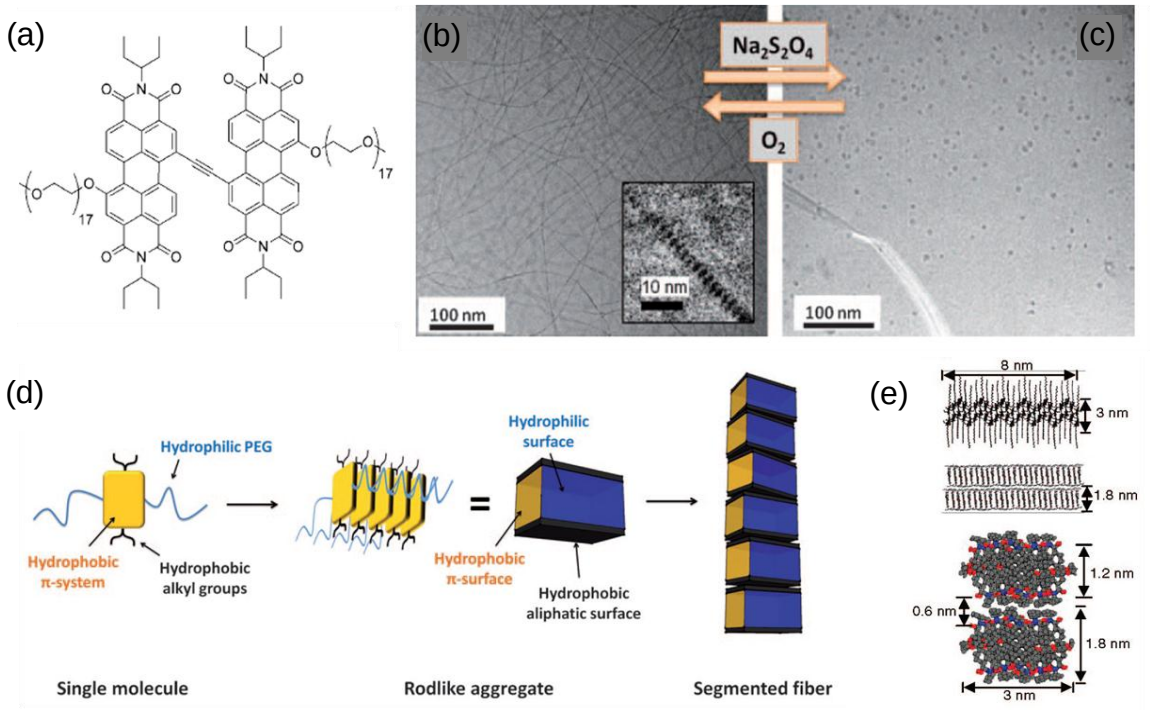

Figure 2.4 (a) Molecular structure of a self-assembling PEG-PDI monomer.[10,44] (b) Cryo-TEM image showing segmented nanofibers formed by the self-assembly of the PEG-PDI monomers in water. (c) Cryo-TEM image showing the disruption of the nanofibers into spherical assemblies following reduction. The nanofibers were seen to reform upon oxidation. (d) Proposed models of the self-assembly and the supramolecular structures observed by cryo-TEM. (e) Measurements for the proposed models taken from the cryo-TEM images. (Figures adapted for review from Krieg et al.[10] and Baram et al.[44] with permission from Wiley and ACS.)

2.6.2 UV-vis Spectroscopy for Aggregate Analysis

In spite of solubility limiting spectroscopic investigations to micromolar concentrations, peptide-perylene imide solutions display UV-vis spectra with rich behavioral detail. This is due to the sensitivity of the perylene chromophore to changes in the local electronic environment associated with perylene π-stacking interactions. The response of the perylene chromophore to these changes can be detected spectroscopically and used to discriminate packing differences in the internal architectures of perylene imide nanostructures.

As a solid-state example of these factors, a comparison of the crystal structures of *N,N'*-disubstituted perylene diimides has shown that the alignment of π-stacking interactions between two neighboring molecules within the crystal unit cell is shifted longitudinally or transversely as the imide substituents are changed.[39,104] As a result, intermolecular charge transfer through π-stacking interactions is impacted solely by crystal packing, leading to crystallochromic changes in these compounds.[39] These effects are illustrated by the crystal structure packing (and the associated color change) in red, maroon, and black perylene diimide-based pigments, as shown in Figure 2.5.[39,105–107]

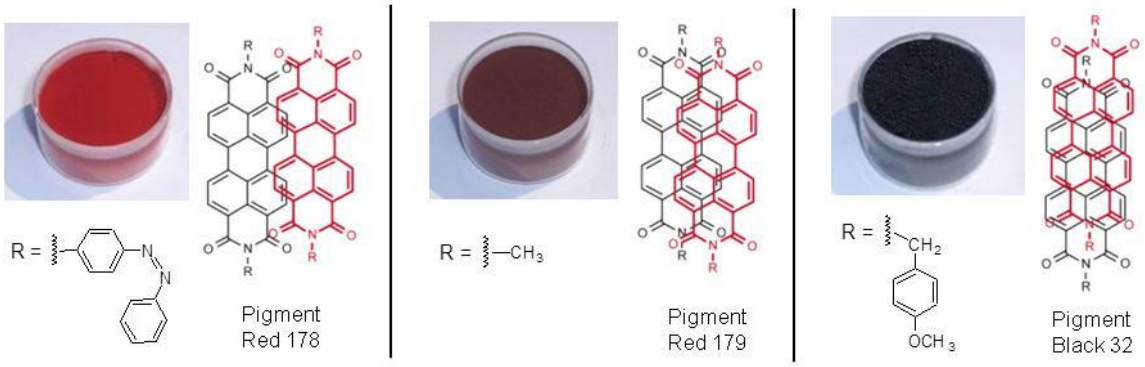

Figure 2.5 Three commonly used perylene diimide-based pigments. The colors of the pigments are seen to result from changes in the perylene core packing arrangement, which is influenced by the imide substituents. (Figure adapted for review from Würthner[39] with pigment images from Liaoning Liangang Pigment and Dyestuff Chemicals Co., Ltd.[107] and permission from RSC.)

The crystallochromic effects observed can be attributed directly to changes in the local electronic environment of intermolecular π-stacking interactions rather than to direct imide substituent electronic interactions because of the presence of a node at each of the imide nitrogen atom positions in the calculated HOMO and LUMO molecular orbitals shown in Figure 2.6.[108] Consequently, the imide nodal position also means that changes observed in the PDI spectral profile in solution can similarly be attributed directly to supramolecular self-assembly interactions and not to any inductive substituent effects produced by the imide peptides acting on the molecular orbital of the perylene core.

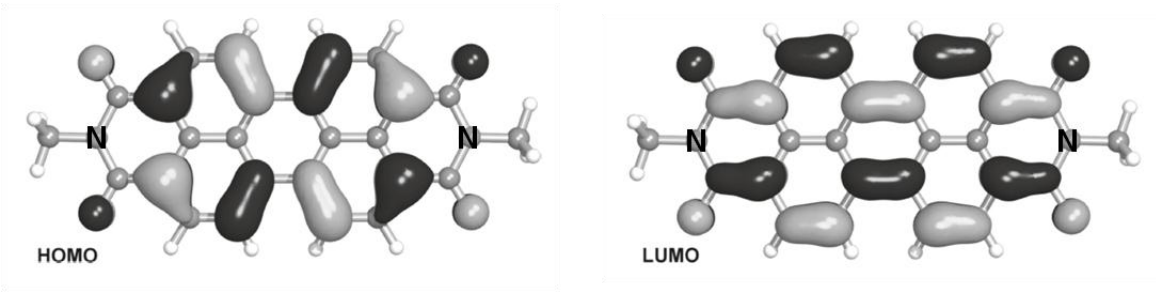

Figure 2.6 DFT calculations of the HOMO and LUMO orbitals of *N,N'*-dimethyl-PDI as a simple model PDI. No HOMO or LUMO density is seen on the marked imide nitrogen atoms. (Figure adapted for review from Huang et al.[108] with permission from ACS.)

Conjugated π-functional molecules give strong π→π* electronic transitions during electronic excitation. Coupling of an electronic excitation to a vibrational mode results in a vibronic progression being displayed in the UV-vis spectrum of the molecule (Figure 2.7a,b). In the case of an isolated PDI chromophore, the vibronic progression shown in Figure 2.7b is seen to result from the coupling of a π→π* electronic transition to the principal PDI vibrational mode (a C=C stretch near

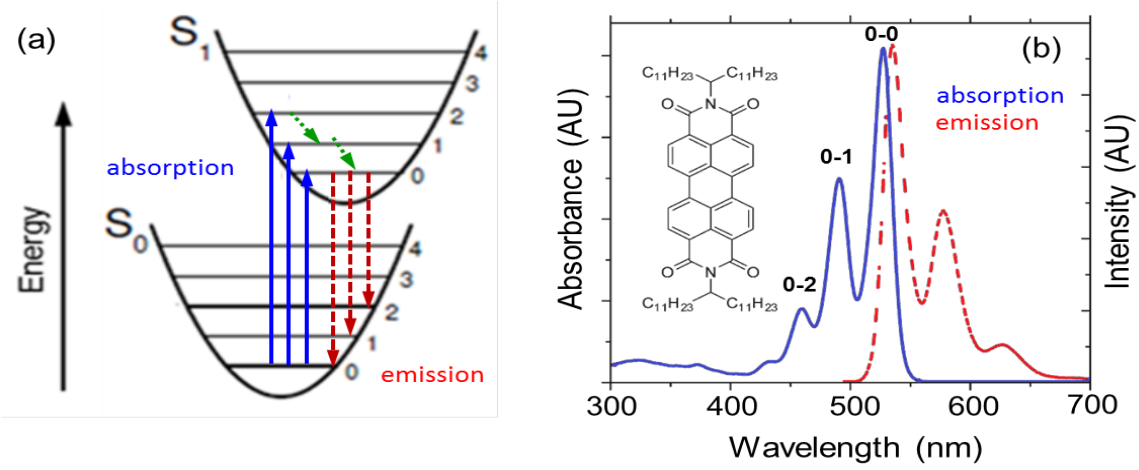

Figure 2.7 Illustrations related to the vibronic progression seen in the UV-vis spectra of organic molecules: (a) Absorption (blue) of a photon gives an electronic transition from the ground state (S_0) to one of the vibrational levels in the excited (S_1) with emission (red) following relaxation (green). (b) The absorption and emission spectra displaying a vibronic progression for an isolated PDI molecules in toluene. (Figures adapted for review from Spano[109] and Huang et al.,[108] respectively, with permission from ACS.)

1400 cm^{-1}). Changes to this vibronic progression may be taken as indications of PDI aggregation (PDIs which are no longer isolated). In the notation used to specify the electronic transitions, the first number gives the vibrational level of the initial state, and the second number gives the vibrational level of the state following the transition. For example, in Figure 2.7a, the 0-2 absorption transition is shown by the longest solid blue line, and the 0-2 emission transition is shown by the shortest dashed red line. The spectral features corresponding to these transitions are labeled in Figure 2.7b.

For molecules which participate in π-stacking, the extent and orientation of the π-stacking between two neighboring molecules is dependent upon the nature of the aggregation. Aggregation changes the electronic and dipolar interactions of neighboring molecules which gives rise to specific spectroscopic signatures from the aggregates which are different to those of an isolated (monomeric) molecule. These distinct spectroscopic traits can be identified and utilized to evaluate the mode of supramolecular assembly. Two important modes of assembly are H-aggregates and J-aggregates. H-aggregates occur when the monomer molecular dipoles are in predominantly "side-by-side" orientations in the aggregates; J-aggregates occur when the monomer molecular dipoles are predominantly in "head-to-tail" orientations in the aggregates.[109] Distinguishing H- and J-aggregates spectroscopically can be accomplished by evaluating changes in the vibronic absorption peaks relative to those of the monomer spectrum. A comparison of the spectroscopic differences between H- and J-aggregates using computational modeling is shown in Figure 2.8.

Broadly stated, in H-aggregates, the main absorption peak tends to blueshift to higher energies and fluorescence is quenched, but for J-aggregates the main absorption peak tends to redshift to lower energies and fluorescent emission may be observed.[109–111] Relative to the monomer absorbance spectrum, in H-aggregates the 0-0 peak of the absorbance spectrum decreases while the 0-2 peak increases relative to the 0-1 peak.[109] The opposite trends are seen for J-aggregates. Although seen to a greater extent in H-aggregates, in both H- and J-aggregates, the vibronic peaks become irregularly spaced as the aggregate bands develop.[109]

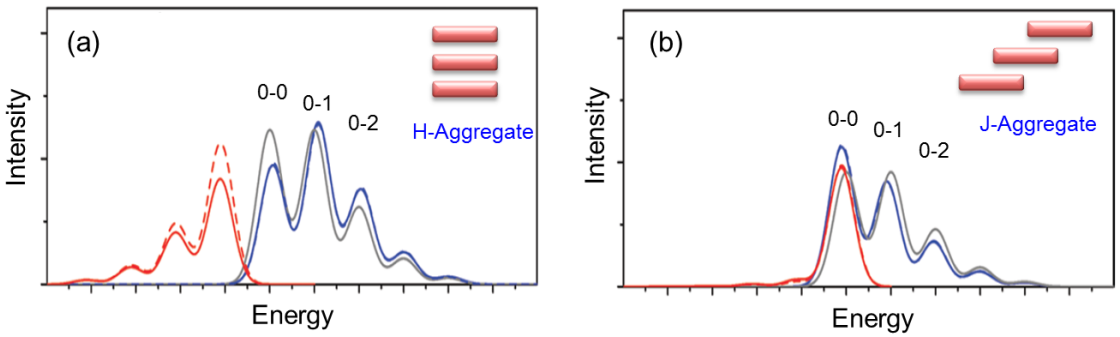

Figure 2.8 Comparisons of calculated spectra for the absorption (blue) and emission (red) of H- and J-aggregates compared to the spectrum of a non-aggregated free molecule (grey) and its associated monomer emission (red dashed). (a) Calculated spectra for an H-aggregate compared to that of a free molecule. (b) Calculated spectra for a J-aggregate compared to that of a free molecule. (Figure adapted for review from Spano[109] with permission from ACS.)

To explain these spectroscopic changes produced by aggregation, an application of some aspects of exciton theory can be made. An exciton, which can be generated during electronic excitation, is an electron-hole pair in a bound state via a mutual electrostatic Coulomb force attraction. Excitation by an incoming photon of sufficient energy can produce electronic transitions between states. These electronic transitions involve interactions with the oscillating displacement of an electron.[112] Because the distribution of electron density between the ground state and the excited state is different, an electronic transition dipole moment (μ) with a specific magnitude (intensity) and orientation (direction of displacement) is produced.[112] Oscillations of μ in a chromophore may be represented by a double-headed arrow which simultaneously depicts both phases of the oscillation along an axis of polarization (generally the long axis of a chromophore).[113] In the case of PDIs, the symmetry seen in the DFT calculations of the HOMO and LUMO orbitals (recall Figure 2.6) means that PDIs are polarized along an axis running between the nitrogen atoms as illustrated in Figure 2.9.

When two or more chromophores are associated closely together (as in aggregation or as with ligands bound to a metal center, etc.), the chromophores may become exciton coupled, wherein an electronic excitation in one chromophore is

delocalized across one or more additional chromophores in the associated group.[112] A consequence of exciton coupling between two degenerate chromophores is the generation of two non-degenerate excited states (S_1 and S_2) arising from the *in-phase* and *out-of-phase* interactions of the electronic transition dipole moments of the chromophores as illustrated in Figure 2.10.

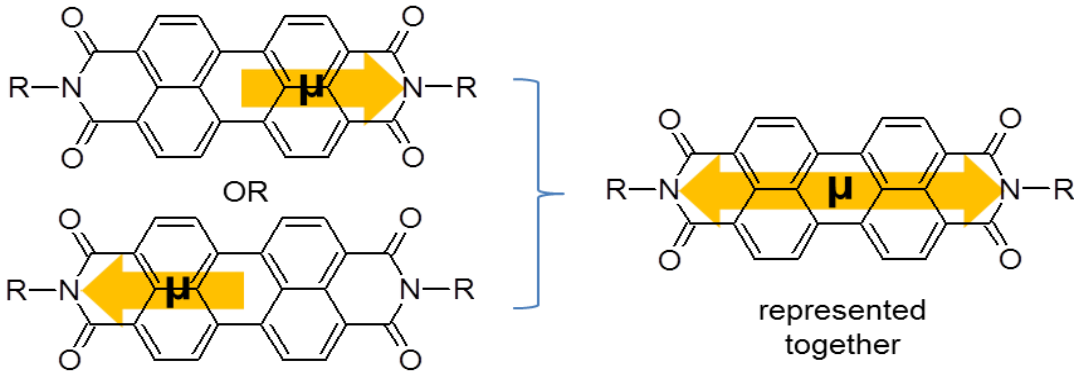

Figure 2.9 An illustration of the oscillations of the electronic transition dipole moment, μ, across the long axis of a PDI molecule.

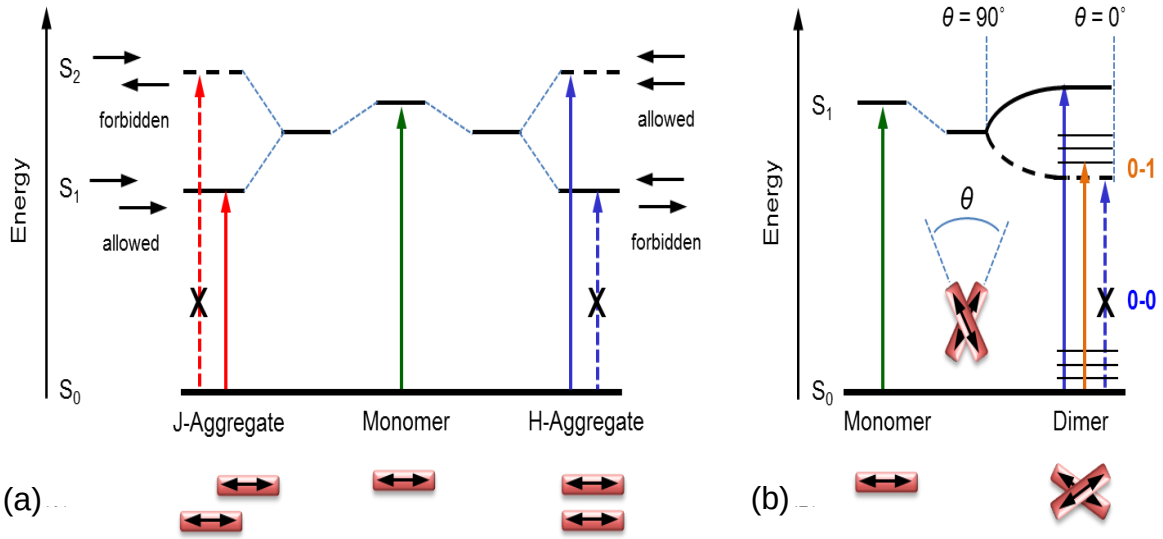

Figure 2.10 Energy diagrams for exciton coupled aggregate dimers comprised of degenerate chromophores: (a) Comparison of J- and H-aggregates, showing the emergence of two non-degenerate excited states (S_1 and S_2); (b) Energy diagram for an H-aggregate with a rotational displacement, showing a forbidden 0-0 transition and a weakly allowed 0-1 transition via coupling to a vibrational mode.

As seen from Figure 2.10a, the *in-phase* and *out-of-phase* interactions of the electronic transition dipole moments of the chromophores gives differences in the allowed and forbidden electronic transitions of each type of aggregate based upon the relative orientations of the dipoles. For a strongly coupled H-aggregate without any rotational displacement between co-facial chromophores, the lower energy transition is forbidden since there is no net dipole for the transition. But in cases of a weakly coupled H-aggregate with some rotational offset between chromophores (Figure 2.10b), the 0-1 transition can become partially allowed through an increase in oscillator strength resulting from coupling to a vibrational mode.[109] Accordingly, in the case of a weakly coupled H-aggregate, a redistribution of oscillator strength to higher energy occurs, resulting in a diminished intensity of the 0-0 vibronic peak and an increased intensity in the 0-1 vibronic peak compared to the vibronic spectrum of monomer (recall Figure 2.8a). The opposite scenario is seen from the energy diagram for a J-aggregate, leading to a vibronic redistribution to lower energy as previously shown in Figure 2.8b. These vibronic changes can be used to indicate aggregate formation, to identify the type of aggregates formed, and to identify changes in the mode of aggregation produced by structural or solvent environment effects.

Although UV-vis spectroscopy serves as a powerful technique to probe aggregate systems, it cannot examine the aspects of chirality which factor strongly in peptide structures. For evaluating the impact of chirality, a second type of spectroscopy is needed which is sensitive to chiral systems.

2.6.3 CD Spectroscopy to Detect Chiral Self-Assembly

Circular dichroism (CD) spectroscopy can be used to detect the presence of chiral supramolecular assemblies formed from the self-assembly of perylene imide monomers. CD spectroscopy is sensitive to the absolute configuration and conformation of a molecule[114] and only gives a signal for chiral, non-racemic molecules which are either intrinsically chiral, or which are achiral but part of a larger chiral supramolecular group.[115] In CD spectroscopy, a solution is exposed to circularly polarized light. The generation of circularly polarized light proceeds by

using prisms and filters to cause the electric field associated with a light wave to oscillate,[14] producing a helical electromagnetic waveform along the axis of propagation. When the helical wave of the circularly polarized light is viewed on end with the direction of propagation, and perpendicular to its central axis, the oscillating wave can be seen as the resultant vector of two component vectors of equal magnitude which each sweep out rotating circles with one moving in a counter-clockwise (left-handed, E_L) direction and the other moving in a clockwise (right-handed, E_R) direction.[14,115] As such, the circularly polarized light consists of two circularly polarized component waves which are of opposite rotation and ninety degrees out of phase.[14,115] Non-symmetric, chiral molecules interact with and absorb the left-handed and right-handed components of circularly polarized light to different extents, causing an unequal change in E_L and E_R which produces an elliptical polarization in the resultant vector.[14,115] Illustrations of circularly polarized light and its interactions with chiral and achiral media are shown in Figure 2.11.

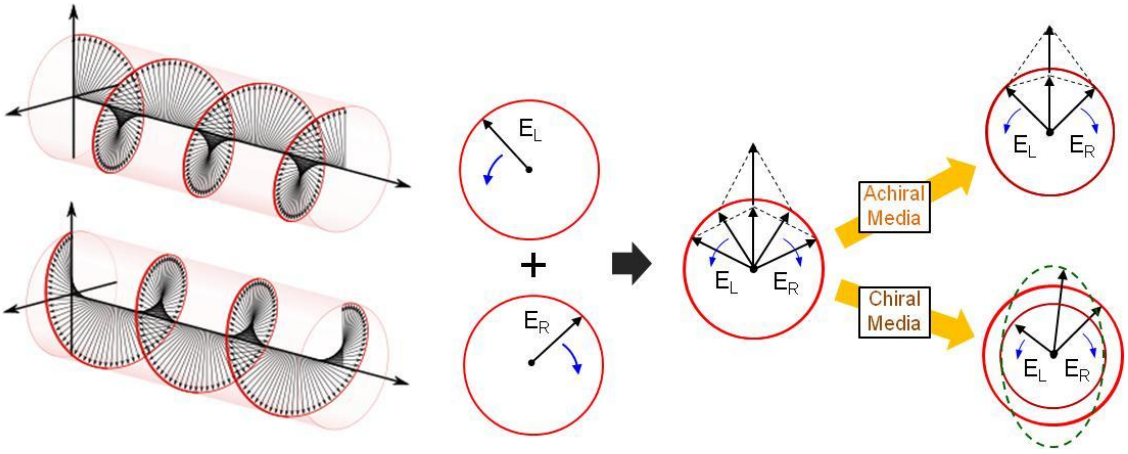

Figure 2.11 Illustration of the left- and right-handed components of circularly polarized light. Interactions of circularly polarized light with chiral media produce a differential absorption between left- and right-handed components causing the light to become elliptically polarized. No differential absorption with achiral media. (Figure partially based on illustrations by Kelly et al.[115])

During electronic excitation of a chiral molecule, the helical waveform produces a helical electron displacement which manifests as a difference in extinction coefficient for left and right circularly polarized light (Equation 2.1).[116] The

measurement of a CD signal by CD spectrometers is typically accomplished by measuring the differential absorbance of the left and right circularly polarized light by the sample (Equation 2.2) using polarization modulation and phase-locked detection techniques for signal enhancement.[116] As a result, the cell path length (b) and molar concentration (c) must be reliably known to determine $\Delta\varepsilon$, according to the Beer-Lambert Law (Equation 2.3),[14,116] or alternatively, to express in as molar ellipticity by Equation 2.4. Examples of a CD spectrum are given in Figure 2.12.

$$\Delta\varepsilon = \varepsilon_L - \varepsilon_R \quad (2.1)$$

$$\Delta A = A_L - A_R \quad (2.2)$$

$$A = \varepsilon bc \quad (2.3)$$

$$[\theta] = 3298.2\Delta\varepsilon \quad (2.4)$$

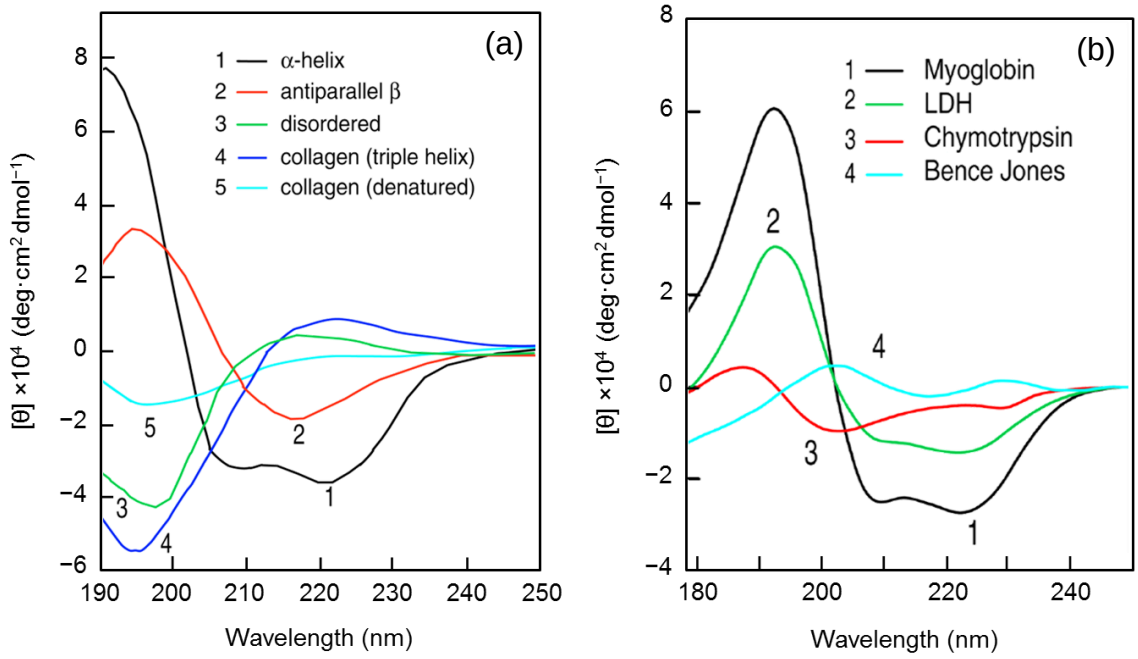

Figure 2.12 Overlaid CD spectra of peptides and proteins with representative secondary structure profiles: (a) CD spectra of poly-L-lysine and collagen under various conditions, and (b) CD spectra of selected proteins. (Figure adapted for review from Greenfield[14] with permission from NIH.)

Because CD spectroscopy is sensitive to the conformation of a molecule, the spectral profiles seen in a CD spectrum can frequently be used to identify some

types of secondary structures which molecules may adopt. This is particularly true for proteins, polypeptides, and some shorter peptides, for which the UV region of the CD spectrum can be used to detect the presence of secondary structures such as helices, β-sheets, β-turns, and random coils.[14,115,117,118] Examples of these common diagnostic CD spectral profiles are shown in Figure 2.12 for some selected polypeptides and proteins.[14]

For molecules containing chromophores, conformational configurations or supramolecular assembly can produce a CD signal in the visible region of the spectrum. The CD response in the visible region arises exclusively from chirally arranged chromophores and does not contain contributions from individual monomeric chromophores. A CD response in the visible can be advantageous in cases where the UV region contains many CD active moieties. Numerous studies using CD spectroscopy for analysis of chiral perylene supramolecular assemblies have been reported. Among these are: the ionic self-assembly of perylene-chiral surfactant complexes,[119] the hydrogen-bond-directed formation of chiral, helically-stacked PDI-melamine assemblies,[120] and the co-self-organization of oligo(p-phenylene vinylene) and PDI dyes.[121] In these examples, the achiral perylene core is incorporated into a chiral arrangement or environment by substituent influences

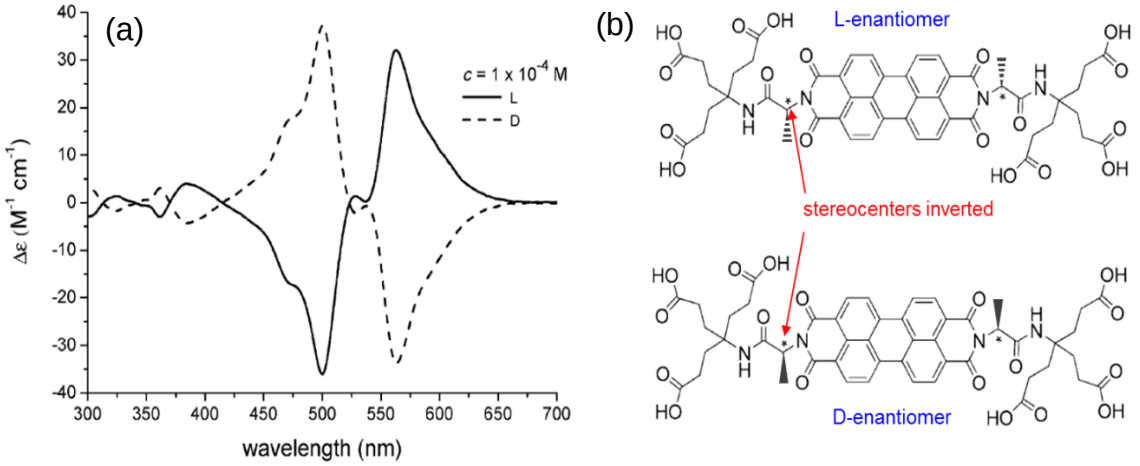

Figure 2.13 (a) Overlaid CD spectra of a chiral enantiomeric perylene diimide pair measured in toluene solution with an inversion of the CD couplet observed between the enantiomers. (b) The PDI structures differ only in the stereocenter (*) configurations adjacent to the perylene core. (Figure adapted for review from Schmidt et al.[122] with permission from Wiley-VCH.)

invoking self-assembly. In a simple case, chiral centers in moieties near the perylene core can impart a chiral sense upon π-stacking as illustrated in Figure 2.13.[122] An inversion of the chiral centers causes the sign of the CD spectrum to switch.

A more in-depth discussion of CD spectroscopy as a diagnostic tool in analyzing chiral chromophore self-assembly will be made in Chapter 4; however, the distinctive, diagnostic CD spectral profiles associated with peptide β-sheets (Figure 2.12) and with chiral chromophore assemblies (Figure 2.13) will feature in various instances throughout this work and are noted here in advance.

2.6.4 Chiral Aggregate Modeling

Calculations based on the exciton (coupled oscillator) model for optical activity may be applicable along with CD spectra to provide non-empirical determinations of structural configurations of both organic and inorganic molecules.[123] CD spectroscopy has been used in relation to exciton coupling to study oligothiophenes,[124] coordination compounds,[112] dissymmetric pseudo-tetragonal metal complexes,[125] and perylene diimides.[126] Using structural and spectroscopic clues to model the supramolecular structures formed, CD spectra potentially can provide additional information, permitting the derivation of geometric models of the ordered, chiral aggregate structures detected. A discussion of these calculations follows from the illustrations given in Figure 2.14.[114]

For the derivation of geometric models using CD spectra, helical supramolecular assemblies yield immediate clues regarding configuration. For such helical assemblies, the presence of a Cotton Effect couplet indicates a left-handed, counter-clockwise (M) helical arrangement or a right-handed, clockwise (P) helical arrangement of the transition dipoles.[119] Upon confirmation of a helical assembly, calculations pertaining to exciton coupling may allow estimates of the torsion angle between two chromophores around the central axis leading to modeling of the helix.[121] Accomplishing such calculations, however, requires either an assessment of the associated parameters or some simplifying assumptions.

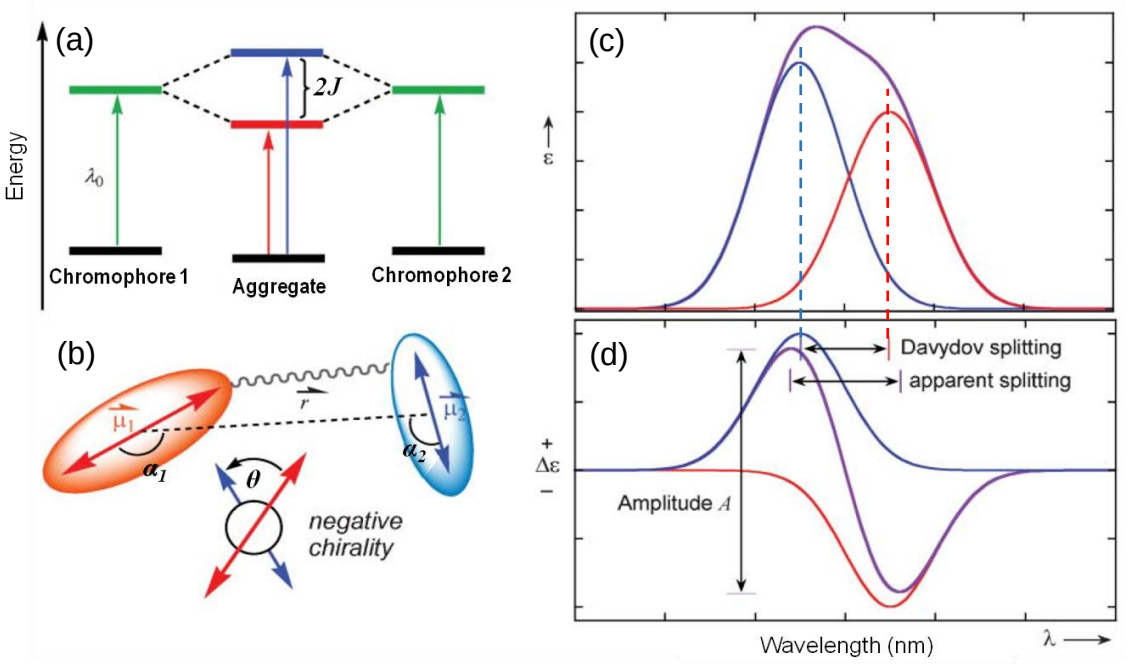

Figure 2.14 Illustrations relating chiral geometry, exciton coupling, and CD spectra: (a) Splitting of the excited states of two degenerate exciton coupled chromophores; (b) Illustration of the geometrical parameters relating two exciton coupled chromophores; (c, d) Theoretical absorbance and CD spectra, respectively, resulting with exciton splitting. Component spectral curves are given in blue/red; resultant spectra are shown in violet. (Figure adapted for review from Berova et al.[114] with permission from RSC.)

As previously discussed, when two or more chromophores are associated closely together, they may become exciton coupled, causing the excited states of the chromophores to split into two levels as shown in Figure 2.14a. The interval between these levels (known as Davydov splitting) has an energy difference equal to twice the exciton splitting energy, J, which is defined from exciton theory by Equation 2.5,[126] where μ_1 and μ_2 are the magnitudes of the electronic transition dipole moments of the two chromophores (in isolation), r is the center-to-center separation distance between the chromophores, θ is the rotational offset, and α_1 and α_2 are the angles between the dipole vectors and the r vector. These parameters are illustrated in Figure 2.14b.

$$J = \frac{\mu_1 \mu_2}{r^3}\left[cos(\theta) - 3\,cos(\alpha_1)\,cos(\alpha_2)\right] \qquad (2.5)$$

The exciton splitting energy depends upon both the magnitudes of the electric transition dipole moments as well as their mutual orientation and proximity. For cases where the chromophores are degenerate, $\mu_1 = \mu_2$ which simplifies these terms in Equation 2.5 to μ^2. Evaluation of μ^2 can be accomplished by integrating the absorption band of the chromophore according to Equation 2.6,[127] where $\varepsilon(\tilde{\nu})$ is the molar extinction coefficient as a function of wavenumbers, c is the speed of light, h is Planck's constant, ε_0 is the permittivity, and N_A is Avogadro's number.

$$\mu^2 = \frac{3hc\varepsilon_0 \ln 10}{2\pi^2 N_A} \int_{\tilde{\nu}_1}^{\tilde{\nu}_2} \frac{\varepsilon(\tilde{\nu})}{\tilde{\nu}} d\tilde{\nu} \tag{2.6}$$

Two parameters associated with an exciton-coupled helix may be immediately assessed via spectroscopy. First, the exciton splitting energy itself may be evaluated from a well-defined positive and negative peak couplet (Cotton effect) within a CD spectrum (purple line in Figure 2.14d), where J is equal to half of the difference in energy associated with the Davydov splitting (Figure 2.14a,d). Second, a value for μ can be evaluated from the integrated absorption spectrum. Proceeding with a model from this point requires more information or simplifying assumptions. One such possibility is to assign a separation distance for r based on known PDI crystal structures. Computational assessments of the chromophore orientation angles θ, α_1 and α_2 might then be possible. During this study, however, such attempts were not successful given the numerous value combinations possible which can result in the same value of exciton splitting, J. Accordingly, simple data fitting was found to be an inappropriate computational approach. Further attempts at such analyses would be expected to be improved through the use of statistical methods such as a Markov Chain Monte Carlo methodology,[128] which might successfully evaluate multiple permutations of interdependent variables across a range of values in a probabilistic manner. Such efforts might arrive to a set of likely variable values which could be applied to the aggregate models.

2.7 Summary

The topics discussed in detail in this chapter enumerate several crucial aspects which enable the development of peptide-substituted perylene imides. Solid-phase

peptide synthesis enables access to a wealth of peptide sequential variations which may be used to enhance, guide, and tune guide supramolecular self-assembly. Peptide termini (particularly the amino terminus), present resident moieties which can facilitate incorporation of the peptide into a molecule of interest for self-assembly, and synthesis of *N*-substituted peptide-perylene imides can be easily achieved via amine condensation reactions, permitting the synthesis of a small library of peptide-perylene imides employing peptide sequences with three key regions relevant to rational self-assembly design.

Both microscopy and spectroscopy are well suited for the analysis of peptide perylene imide nanostructures formed in dilute solutions, and these techniques firmly address two essential goals of proving the formation of ordered nanostructures and probing the internal architectures of any nanostructures formed. Cryo-TEM allows superior visualization of fine nanostructures in solution, while AFM provides evaluation of the nanostructure morphology in solid-state. Even at micromolar concentrations, UV-vis spectroscopy is sensitive to changes in the local electronic environment associated with perylene π-stacking interactions, supplying rich behavioral detail which can be attributed exclusively to chromophore stacking due to the imide nodal positions. Enhancing this rich behavioral detail further, CD spectroscopy can be used in the visible region of the CD spectrum to detect the presence of chiral assemblies formed from the self-assembly of perylene imide monomers, while the UV region of the CD spectrum can be used to detect the presence of secondary structures formed by the peptide.

Taken together, the information gathered from the clues these techniques provide facilitates the evaluation of structural features impacting self-assembly and nanostructure morphology. Consequently, underlying thermodynamic factors as well as chiral influences may be evaluated toward the goal of applying self-assembling peptide-substituted organic semiconductors into organic electronic devices.

Chapter 3

Thermodynamic Factors Impacting the Peptide-Driven Self-Assembly of Perylene Diimide Nanofibers

3.1 Introduction

Nature has a refined, exquisite self-assembly toolbox, which is illustrated in proteins whose precise three dimensional folding and interaction with other elements is encoded by the sequence of amino acids.[129–131] Protein subunits can be bound in specific configurations via relatively short (<10 residue) sequences that have very high affinities driven by a balance of charge interactions, hydrogen bonding, hydrophobicity, and shape.[18,130]

Inspired by self-assembly in natural systems, synthetic peptides have gained significant interest as a powerful new class of molecular self-assembly agents.[17,18,20,24] Peptide amphiphiles, generated via the attachment of a long alkyl chain to a peptide headgroup, have been shown to exhibit sequence dependent self-assembly into well-defined fibers,[132] sheets,[16] vesicles,[133] micelles,[134] and sacs.[135] These self-assembled nanostructures have been explored for use as small molecule encapsulation and

delivery assemblies,[22,136] mineralization templates,[17] magnetic resonance imaging contrast agents,[137] and support networks for regenerative medicine.[96]

π-conjugated molecular semiconductors have also been incorporated into peptide amphiphile type molecules, raising new possibilities in molecular electronics applications.[138] Here, tethered peptides could fulfill the requirement for building blocks to be deposited from an ink and assembled over macroscopic length scales with finely tuned electronic coupling between neighboring molecules. π-conjugated molecules also exhibit optical absorption and emission signatures that are sensitive to their immediate environment and the nature of coupling with their neighbors, providing an incisive probe of their assembly. Several studies have undertaken spectroscopic investigations of short peptides attached to π-conjugated units, including perylene diimides (PDIs),[74,79,122,139,140] naphthalene diimides,[15] oligophenylene vinylenes,[141] 1,4-distyryl benzene,[142] pyrene,[22] fluorene,[24] and naphthalene.[143] PDIs are particularly attractive, owing to their excellent performance as n-type semiconductors in field effect transistors[37,38,65,144,145] and photovoltaic devices,[121,146–148] excellent photostability,[37,39] and their synthetic accessibility. Moreover, the electronic properties of PDIs exhibit strong spectroscopic sensitivity to the orientation of neighboring PDI units.[39] By tethering substituents to the imide position of PDIs, it is possible to alter the type of assembly, while ensuring that spectroscopic perturbation relates only to aggregate structures, since imide substituents are not directly coupled to the frontier molecular orbitals responsible for the visible absorption in the PDI chromophore.[39,108] Non-peptide imide substituents have previously been used to control the formation and morphology of PDI nanofibers and demonstrate their potential for use in nanoscale devices.[43,65,149] However, limited quantitative understanding of the balance of competing aggregation forces has thwarted efforts to deterministically encode assembly of electronically active units via peptide sequences.

Herein is presented a systematic investigation of how incremental changes to short peptide sequences affect the binding thermodynamics of peptide-PDI molecules. By spectroscopically parameterizing the type and degree of aggregation as a function of temperature, it is possible to decouple enthalpic and entropic contributions to aggregation and link them to structural features of the peptides. In this chapter most

of the measurements presented were undertaken in water, which can itself can act as a self-assembly "matrix",[150] and leads to pronounced sensitivity to the peptide hydrophobicity. Other factors whose significance we quantify include; asymmetric substitution with hexyl chains, peptide charge density, steric bulk, and isomeric substitution. Collectively, it was found that coarse parameters like hydrophobicity and hexyl substitution play the biggest role in driving aggregation, however the nature of interactions between neighboring PDI units can be finely tuned via more subtle effects like the peptide's three dimensional shape.

3.2 Results and Discussion

To investigate the effect of peptide sequence on the self-assembly of peptide-PDI conjugates, a set of conjugates with widely varied structural features was synthesized consisting of the following three strategic peptide regions highlighted in Scheme 3.1. i) a glycine unit presents a reactive terminal amine and low steric demand efficiently condensing with perylene anhydride; ii) a central sequence of three amino acids; and iii) a terminal glutamic acid region introduces charge that engenders solubility and hydrophilic character. Coupling peptides via an imide ensures that we can spectroscopically isolate their effect on assembly rather than directly modulating the electronic structure of the chromophore, because PDI does not have frontier orbital density in this position.

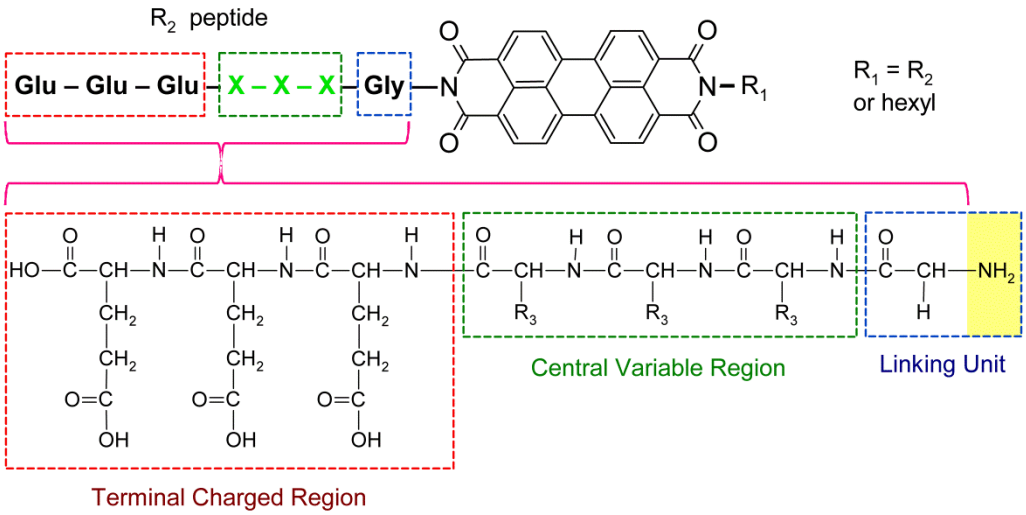

Scheme 3.1 General structure of the peptide-PDIs explored in this study.

Based on this strategy, the specific peptide sequences shown in Scheme 3.2 were synthesized in order to probe the effects of incremental structural variations on the multifaceted interactions that govern peptide-driven PDI assembly. This modular synthetic strategy, detailed in Chapter 2, relies on standard solid-phase peptide synthesis, followed by condensation of cleaved peptides with perylene dianhydride to deliver peptide-PDI conjugates in high yield. In addition to the dipeptide-PDI series **1**-**8**, conjugates **1H**-**5H** featured PDIs with a hydrophobic hexyl chain in place of one of the peptides to engender pronounced amphiphilic character.[96] The effect of different amino acids may be considered relative to glycine rich references PDI **1** (for dipeptide-PDIs **1**-**8**) and PDI **1H** (for hexyl-PDIs **1H**-**5H**). The impact of increasing the peptide hydrophobicity and the steric demand can be evaluated by comparing PDIs **1**-**8**, while the effect of replacing one peptide with a hexyl chain is revealed by comparing dipeptide-PDIs **1**-**5** with their hexyl-PDI counterparts **1H**-**5H**. The effect of charge density can be examined by comparing PDI pairs **2**/**3** and **2H**/**3H**, and the effect of peptide length is probed by comparison of **1** and **5**. Additionally, the diastereomer pairs **3**/**4**, **7**/**8**, and **3H**/**4H** provide an opportunity to examine the role of stereocenters and specific structure within the peptides.

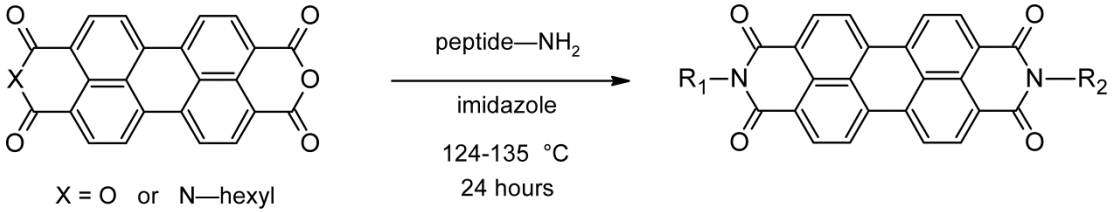

1	$R_1 = R_2$,	R_2 = -Gly-$(Gly)_3$-$(Glu)_3$	**1H**	R_1 = hexyl,	R_2 = -Gly-$(Gly)_3$-$(Glu)_3$
2	$R_1 = R_2$,	R_2 = -Gly-$(Ala)_3$-Glu	**2H**	R_1 = hexyl,	R_2 = -Gly-$(Ala)_3$-Glu
3	$R_1 = R_2$,	R_2 = -Gly-$(Ala)_3$-$(Glu)_3$	**3H**	R_1 = hexyl,	R_2 = -Gly-$(Ala)_3$-$(Glu)_3$
4	$R_1 = R_2$,	R_2 = -Gly-$(D\text{-}Ala)_3$-$(Glu)_3$	**4H**	R_1 = hexyl,	R_2 = -Gly-$(D\text{-}Ala)_3$-$(Glu)_3$
5	$R_1 = R_2$,	R_2 = -Gly-$(Glu)_3$	**5H**	R_1 = hexyl,	R_2 = -Gly-$(Glu)_3$
6	$R_1 = R_2$,	R_2 = -Gly-$(Phe)_3$-$(Glu)_3$			
7	$R_1 = R_2$,	R_2 = -Gly-$(Leu)_3$-$(Glu)_3$			
8	$R_1 = R_2$,	R_2 = -Gly-$(D\text{-}Leu)_3$-$(Glu)_3$			

Scheme 3.2 Synthesis of peptide-substituted perylene diimides.

3.2.1 Solution Preparation

Concentrated stock solutions were prepared by dissolving 1.3-1.8 mg samples of the PDI compounds into 1 mL of water containing a small amount of an added base, thus producing 800 μM stock solutions. This approach utilized the ionizable glutamic acid residues built into the three-region peptide design (Scheme 3.1) to engender aqueous solubility. Although many possible bases are available which might be used for the stock solutions, prolonged exposure to strongly nucleophilic bases such as sodium hydroxide and primary amines was avoided to prevent potentially destabilizing the imide moieties of the compounds. For example, during initial solubility investigations using PDI **6**, high concentrations of primary amines such as 1-hexylamine and ethylenediamine were found spectroscopically to slowly degrade the PDI material over time. Additionally, bases such as sodium hydroxide were avoided to minimize potential charge-screening by introduced ions and salts, which had been shown in previously published studies of peptide-PDIs to impact their aggregation.[79] To minimize potential issues with strongly nucleophilic bases and introduced ions and salts, pyridine was selected as the base for use in the stock solutions used for spectroscopy and was added at a concentration of 200 μL per 10 mL of water. Pyridine was also anticipated to provide some small enhancement to peptide-PDI solubility through π-stacking while also being easily removable as a volatile organic base. It should be noted here, however, that while pyridine was used for the stock solutions diluted for spectroscopy, it was avoided (due to toxicity) in the stock solutions prepared for AFM imaging, since these samples did not require extended exposure to the basic solution during preparation, and since charge-screening was not relevant to the solid-state imaging.

Solutions for the spectroscopic analyses were prepared by diluting (injecting) small volumes (20-40 μL) of the aqueous stock solutions of the PDI materials (described above) into 5 mL of the dilution solvents of interest, thus producing 3-6 μM solutions for spectroscopic analysis. At this stage, the resulting solution could be designed to leave either a slight residual of base or a slight residual of acid. For example, if the stock solution (described above) is injected into distilled water, a solution with some residual base is produced, but if the stock solution is injected into 0.1 M HCl, a solution with some residual acid is obtained instead. Thus, the

final pH of the solvent environment can be adjusted to influence the extent of equilibrium exchange between the self-assembled aggregates and the solution.

For the studies presented in this chapter, solutions having residual base were chosen since these solutions were found to exhibit UV-vis spectra with a greater temperature-dependence than those spectra examined for solutions with residual acid (which displayed minimal temperature-dependence). The negligible temperature-dependence for the spectra of the residual acid solutions suggested strongly aggregated assemblies with little or no self-assembly equilibrium in the solvent, while the greater temperature-dependence for the spectra of the solutions with residual base indicated the presence of some extent of a self-assembly equilibrium which was crucial for the application of the temperature-dependent analyses presented in this chapter.

The use of the aqueous stock solutions described earlier presupposes a dilution solvent which is miscible with water; however, this method may be modified by making the stock solutions in acidic solvents such as TFA or HFIP. These solvents effectively dissolve the peptide-PDI materials due to the disruption of hydrogen-bonding and the protonation of many sites on the molecules. Care must be taken when diluting such stock solutions to ensure dilution solvent compatibility, and the acids must be appropriately neutralized within the dilution solvent (if necessary) to ensure the desired pH in the resulting solution.

3.2.2 Self-Assembly Process

Self-assembly of the peptide-PDI materials was simultaneously achieved with solution preparation. During the solution preparation, the final dilution step of the aqueous stock solution into the solvent of interest also served as the process to induce self-assembly. Accordingly, upon injecting, diluting, and mixing the stock solution aliquot into the solvent of interest, a change in pH and/or a change in solvent environment for the peptide-PDI units occurs. With this change, the ionizable glutamic acid region of the peptide no longer moderates the strong solvophobic/solvophilic interactions, which consequently triggers the peptide-PDI

units to self-assemble during the process. This employed self-assembly process is specified here, since the process employed (not just the particular molecular units undergoing self-assembly) has been shown to be relevant to self-assembly outcomes, such that different processes (for the same molecular units) sometimes produce different self-assembly results.[151] This can arise from the fact that molecular self-assembly units with strong solvophobic/solvophilic influences may assemble by kinetic control in favor of the most direct mode of assembly which alleviates the solvophobic/solvophilic tensions without necessarily arriving to the most thermodynamically favorable self-assembly state. Accordingly, kinetically controlled self-assembly processes may produce assemblies which are effectively trapped states that are energetically above some thermodynamic minimum. As a result, different processes may be either kinetically or thermodynamically controlled and may access different states. In this study, the term "thermodynamic factors" is used to indicate thermodynamic *properties* measured for the nanostructural outcomes (states) achieved by the self-assembly process described here. The term "thermodynamic factors" is *not* used with regard to kinetically versus thermodynamically controlled self-assembly process distinctions which this study does not directly address.

3.2.3 Nanostructure Formation from Peptide-PDIs

To verify that the peptide-PDIs self-assembled into ordered nanostructures, samples were analyzed by atomic force microscopy (AFM), transmission electron microscopy (TEM), and circular dichroism (CD) spectroscopy. AFM imaging of samples dropcast and dried onto mica from solutions with PDI concentrations near saturation were observed to produce particulate formations (Figure 3.1).

AFM imaging of samples dropcast and dried onto mica from solutions with lower PDI concentrations plus some residual base (NaOH) were also observed to produce larger aggregated deposits, but these deposits did not display a particulate morphology. In one instance, morphologies resembling crystalline deposits or aligned fibrous bundles were observed (Figure 3.2a). In most cases, only irregular clusters were seen, but fiber-like strands could be seen to be forming among the

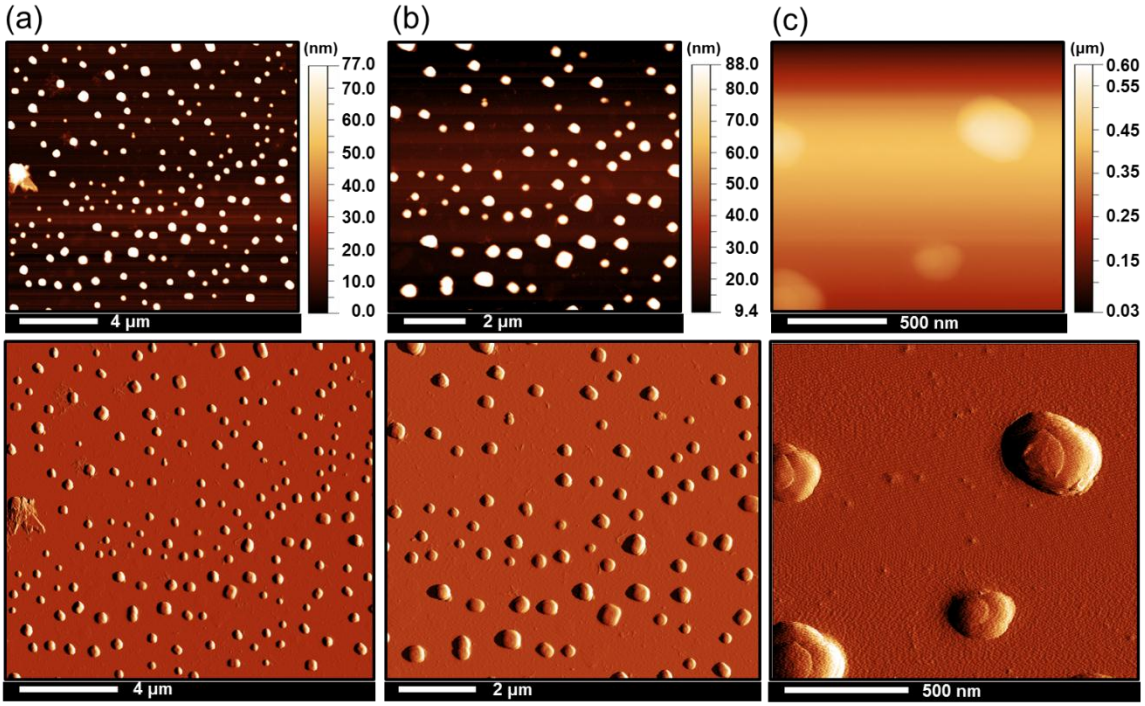

Figure 3.1 AFM images shown in height mode (top row) and deflection mode (bottom row) of deposits of PDI **3** (dropcast from 1000 μM solution in 0.1 M HCl, solution aged 2 minutes), showing particulate formations in three views (a,b,c).

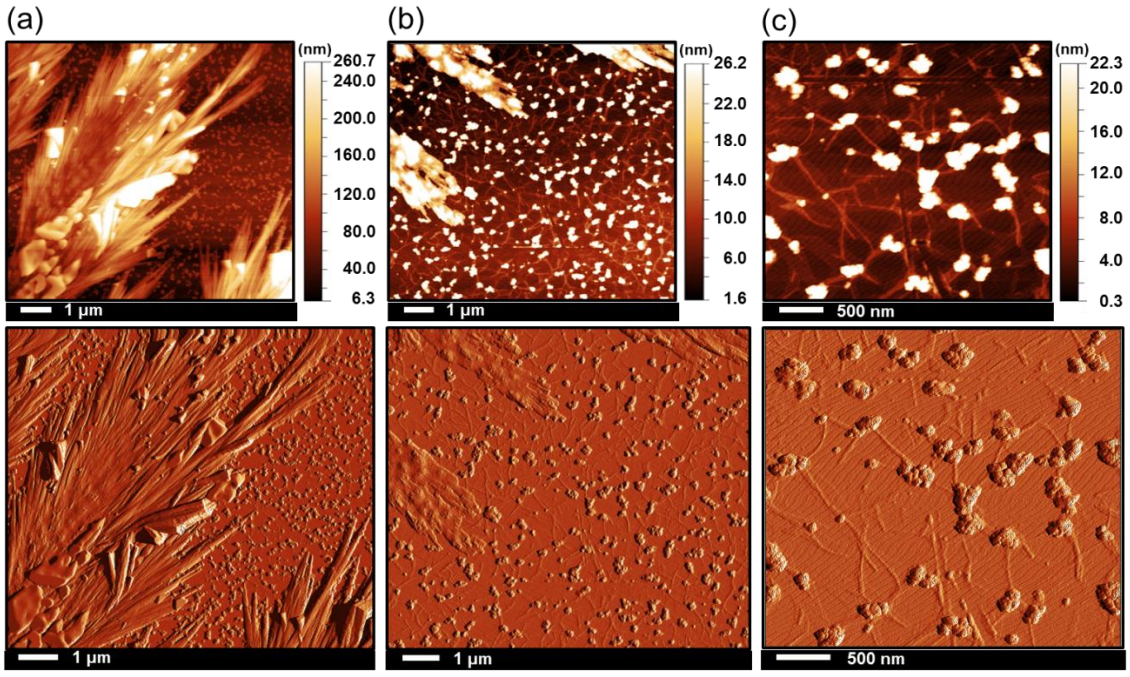

Figure 3.2 AFM images shown in height mode (top row) and deflection mode (bottom row) of deposits of PDI **3** (dropcast from 50 μM aqueous solution with residual base, aged 4 days): (a) Crystalline formations or aligned fibrous bundles; (b,c) Fiber-like strands seen between larger deposits.

clusters (Figure 3.2b,c). However, imaging of samples dropcast from solutions in dilute acid (to fully pH-trigger self-assembly) displayed abundant fibers (Figure 3.3).

Here it is important to make some comments about solution aging. In a few instances, aging the solution prior to dropcasting samples onto the mica substrate initially appeared to impact the quality and number of the fibers, as illustrated when comparing Figure 3.3a,b (fibers from solutions aged 3 days) to Figure 3.3c (fibers from a freshly prepared solution aged 2 minutes). Usually, however, the onset of extensive aggregation and fiber formation was observed to occur rapidly and completely. Further investigation of solution aging (using solutions of the same concentration and solvent environment), however, revealed no conclusive evidence that aging impacted the nature or extent of the self-assembled nanostructures. Instead, the earlier perceived differences were found to be most likely attributed to mass distribution differences on the mica substrate surface. Nevertheless, the solution ages associated with the selected AFM images shown in this chapter are included for completeness along with the other reported experimental conditions.

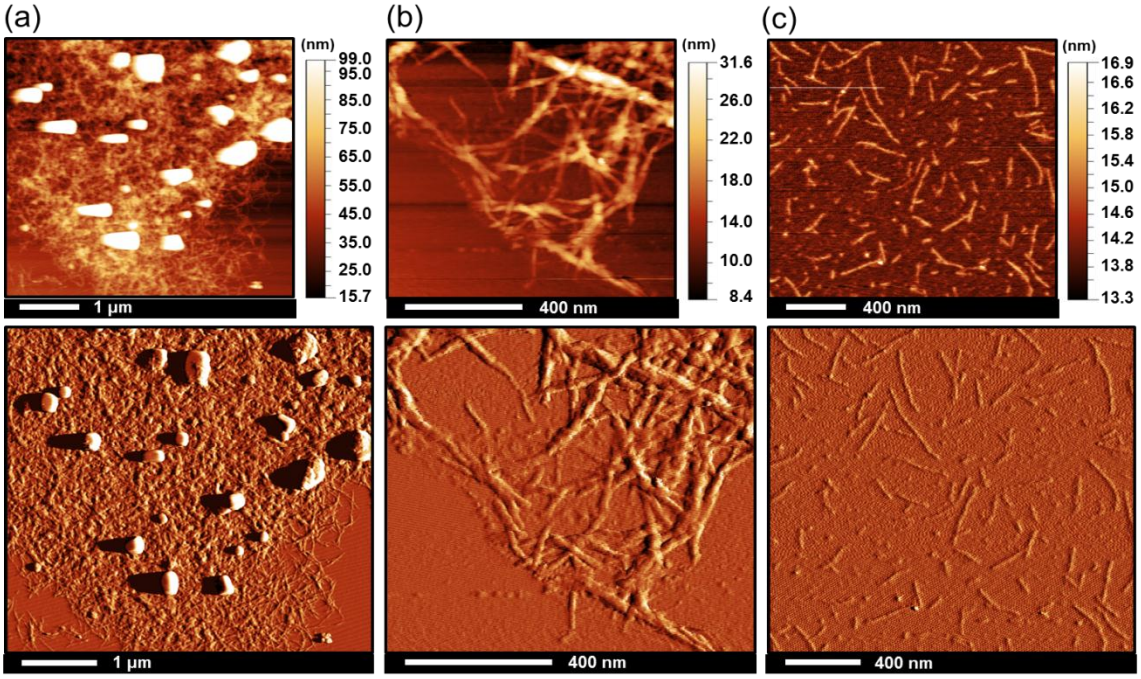

Figure 3.3 AFM images shown in height mode (top row) and deflection mode (bottom row) of deposits of PDI **3** (dropcast from 50 µM solution in 0.1 M HCl): (a) Fibrous formations surrounding larger aggregates (aged 3 days); (b) Magnified view of interlaced fibers (aged 3 days); (c) Isolated fibers (solution aged 2 minutes).

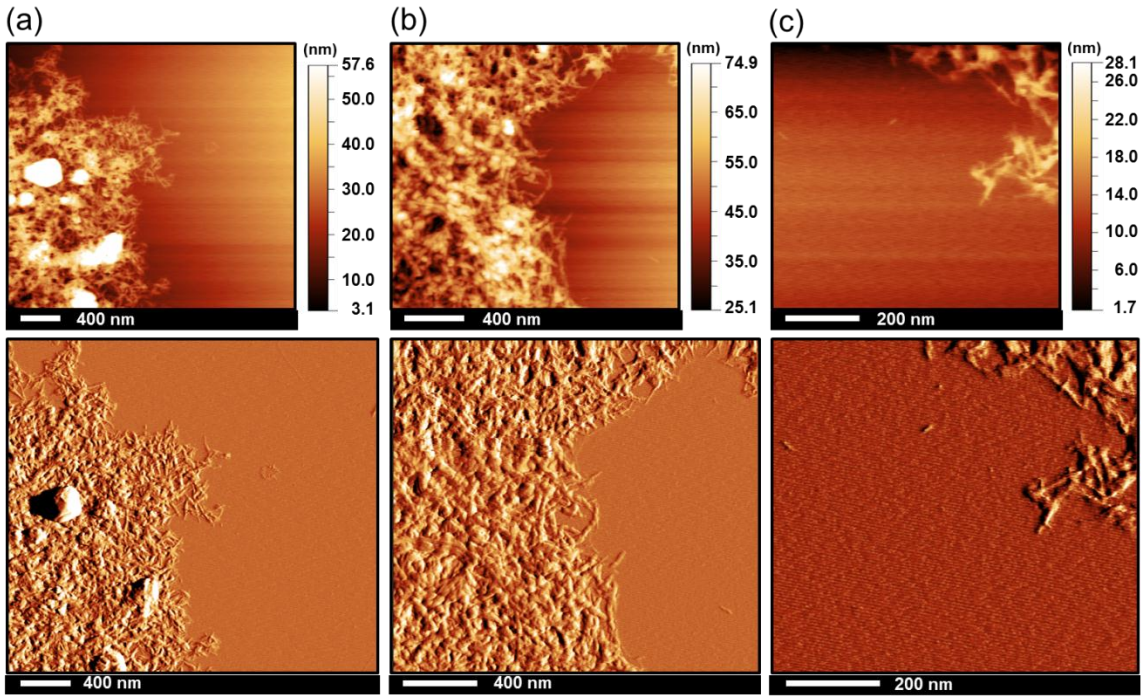

Figure 3.4 AFM images shown in height mode (top row) and deflection mode (bottom row) of deposits of PDI **4** (dropcast from 50 μM solution in 0.1 M HCl, aged 3 days): (a) Fibrous formations surrounding larger aggregates; (b) Magnified view of matted fibers; (c) Magnified view of interlaced fibers.

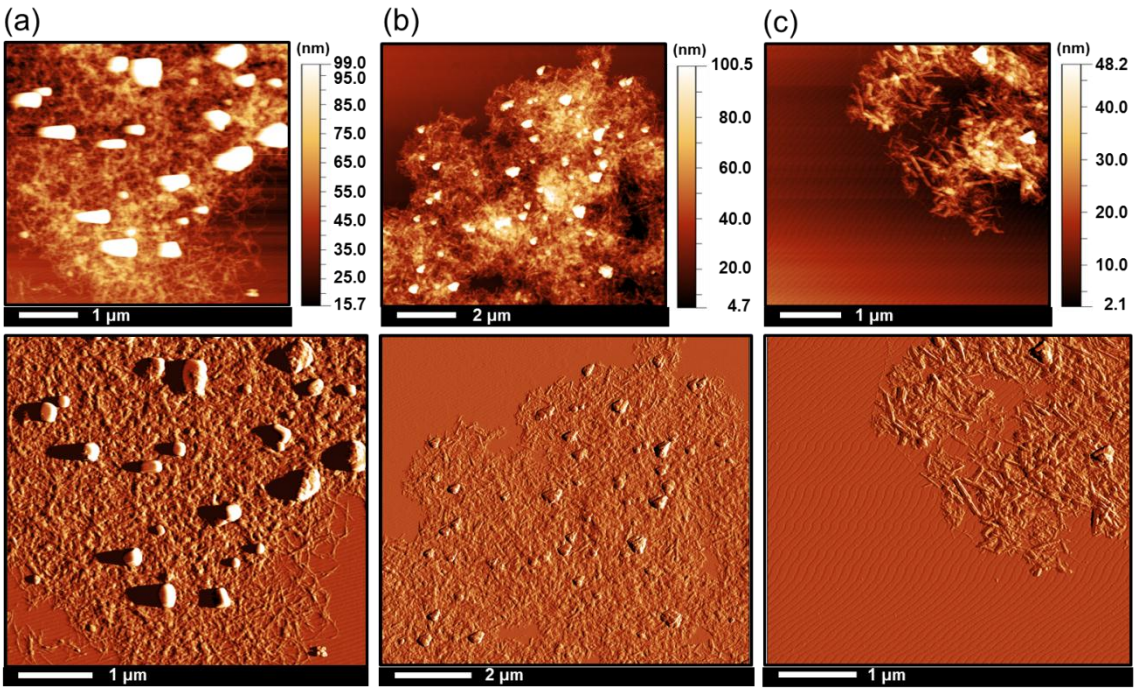

Figure 3.5 AFM images shown in height mode (top row) and deflection mode (bottom row) of deposits (dropcast from 50 μM solution in 0.1 M HCl): (a) PDI **3** (aged 3 days); (b) PDI **3H** (aged 1 day); (c) PDI **3H** (aged 1 day).

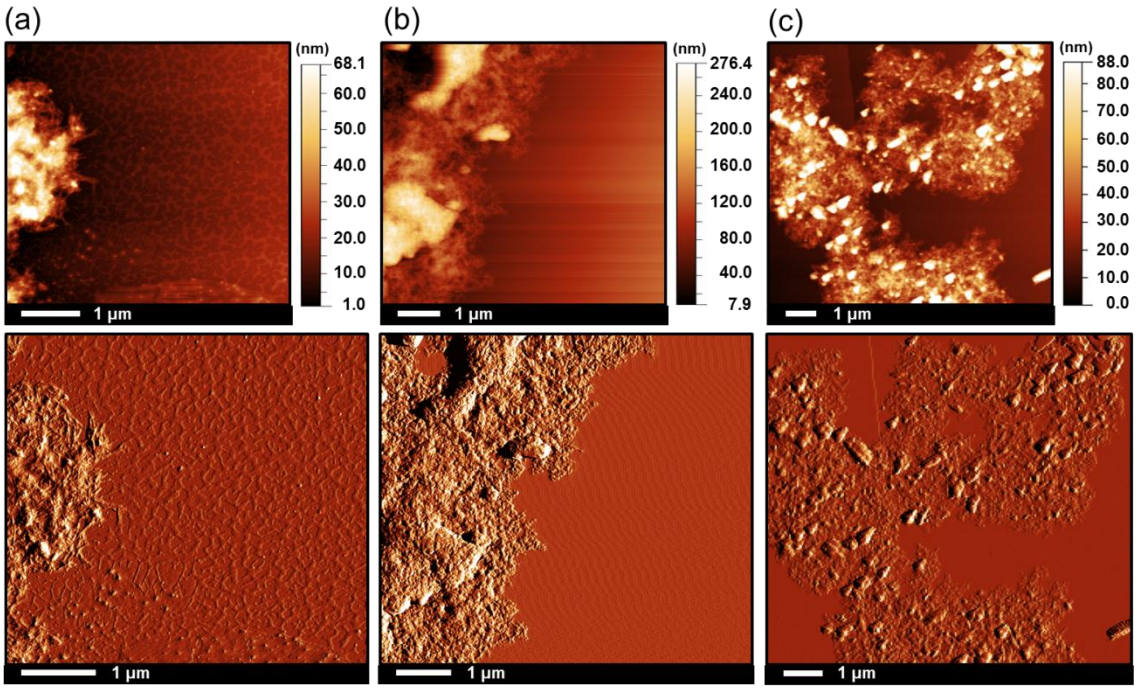

Figure 3.6 AFM images shown in height mode (top row) and deflection mode (bottom row) of deposits (dropcast from 50 µM solution in 0.1 M HCl): (a) PDI **2** (aged 3 days); (b) PDI **5** (aged 4 days); and (c) PDI **5H** (aged 1 day).

Of the samples imaged, PDIs **3** and **4** were both observed to most readily form fibrous nanostructures and both gave similar morphologies; however PDI **4** was found to produce masses of fibers with a denser, matted appearance in all cases observed. The fibrous networks generally appeared less diffusive (Figure 3.4a,b), while individual fibers also appeared shorter (Figure 3.4c).

To further investigate the internal architectures of the nanostructures of PDIs **3** and **4** confirmed by AFM, TEM microscopy and CD spectroscopy analyses were undertaken. As shown in Figure 3.7a,b, well solvated monomers of PDIs **3** and **4** in DMSO lack CD features in the visible region because the solvated chiral amino acids do not affect the PDI chromophore. However, aqueous solutions of PDIs **3** and **4** exhibited a CD couplet in the visible region (as did other aggregated compounds), indicating exciton coupling between ordered PDI chromophores in a chiral supramolecular assembly.[119] These chiral aspects provide significant insight about the internal structure of the fibers and will be addressed in detail (along with relevant comments about dynode voltage data) in Chapter 4. Strong light absorption from the residual pyridine in the solutions obscured the UV range,

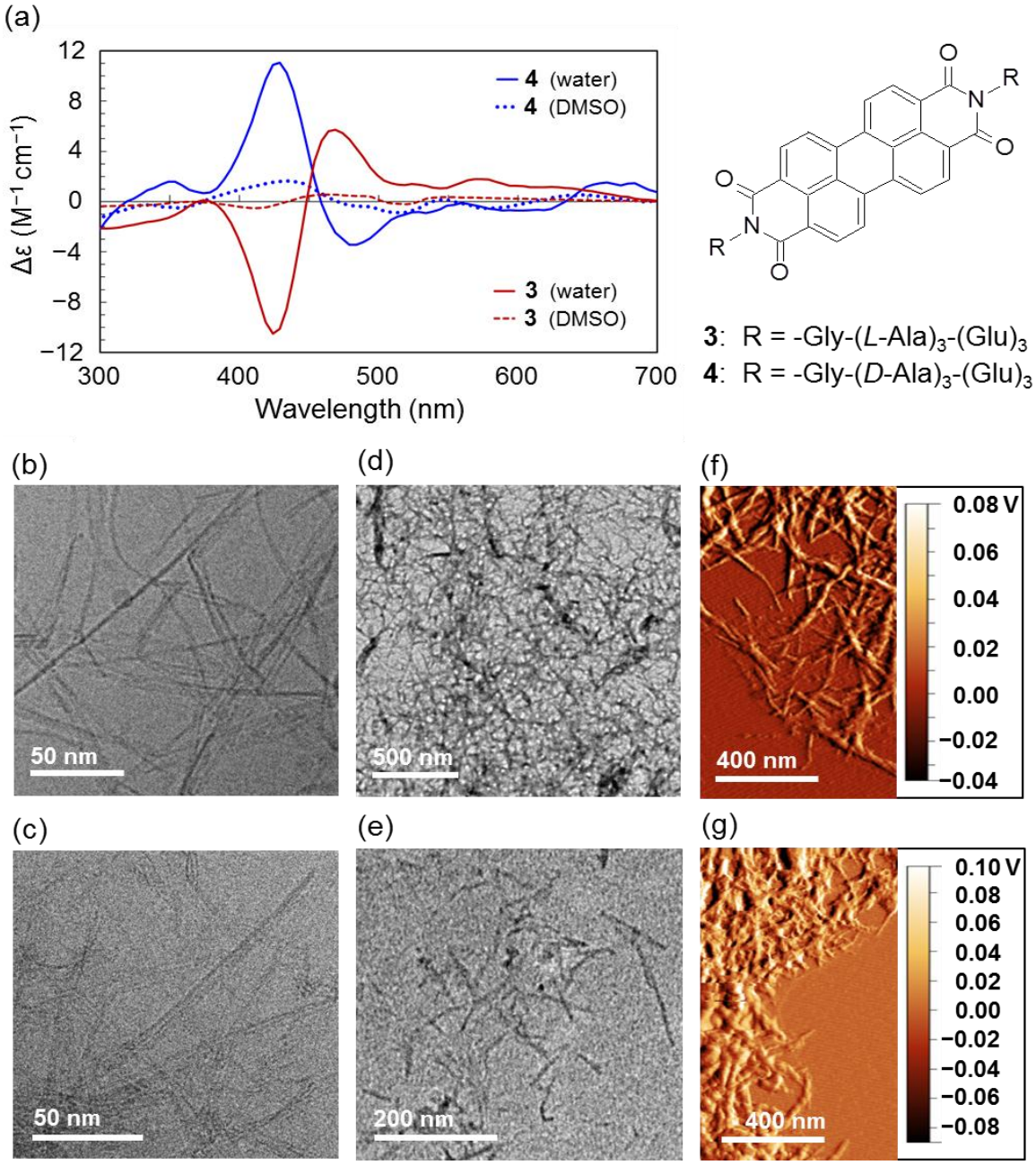

Figure 3.7 Detection of PDI nanostructure self-assembly as exemplified by **3** and **4**: (a) Circular dichroism spectra of **3** and **4** showing chiral supramolecular assembly in aqueous solutions. Reference spectra are shown for DMSO solutions, where molecules exist as monomers (all solutions 3 μM). Cryo-TEM image of nanofibers captured in vitrified aqueous solution of (b) **3** and (c) **4**. TEM image of an air-dried deposit of nanofibers of (d) **3** cast from a 50 μM aqueous solution at pH 5, and (e) **4** cast from a 50 μM solution in 10% DMSO/water at pH 5. AFM deflection (error) mode image of dry 72 h aged nanofibers deposited on mica from a 50 μM solution in aqueous hydrochloric acid (0.1 M) of (f) **3** and (g) **4**. (Figure adapted from Eakins et al.[88] with permission from ACS.)

preventing inspection of any peptide CD response; however, the visible region of the spectrum was of primary interest as proof of chirally assembled achiral chromophores.

Cryogenic TEM images of PDIs **3** and **4** (Figure 3.7c,d) provided further detail on the nature of the supramolecular aggregates captured in vitrified solution, verifying the formation of nanofibers. Closer magnification of PDI **4** (Figure 3.7d) shows a ribbon-like architecture comprised of aligned, interacting fibers, where the dark lines correspond to hydrophobic fiber interiors comprised of π-stacked perylene cores of individual PDI units and the lighter-contrast areas correspond to interfiber regions comprised of the hydrated peptides. Nanofiber deposits of PDI **3** and **4** shown in the dry TEM images (Figure 3.7e,f) exhibited extensive fibers or fiber bundles with an average width of the bundles of PDI **3** being around 13 nm.

By comparison, AFM measurements of the nanofiber deposits from solutions of PDIs **3** and **4** found that the nanofibers formed from PDI **3** (Figure 3.7g) also tended to be present in more diffusive bundles with heights of 15-20 nm (along with some isolated fibers), while the nanofibers formed from PDI **4** (Figure 3.7h) tended to be present in matted bundles with heights of 30-45 nm. These matted fiber bundles were a common feature seen by AFM as previously discussed.

3.2.4 UV-vis Spectroscopy and Data Fitting Analyses

Having confirmed that peptide-PDIs self-assemble into nanofibers in solution, a spectroscopic examination of their assembly was performed. UV-vis spectroscopy is ideally suited to probe the local electronic environment of the PDI core because small differences in the extent, nature, or orientation of coupling between neighboring chromophores result in spectral shifts. The spectra shown in Figure 3.8a illustrate three important representative spectral profiles that dominate all of the spectra we measured: monomer, H-aggregate, and π-aggregate. The absorption spectrum of **3** in DMSO exhibits a well-defined vibronic progression with ~1400 cm^{-1} splitting and diminishing intensity for higher energy transitions, consistent

with isolated (monomeric) PDI units. This was further verified by comparison with an *N*,*N*′-dialkyl PDI reference compound in a dilute chloroform solution. The spectrum of **3** in water, however, exhibits a relatively diminished 0-0 transition, which is a clear signature of a weakly coupled H-aggregate. In a strongly exciton-coupled pure H-aggregate, the 0-0 transition is dipole forbidden and higher transitions are only allowed by coupling to vibrations of the appropriate symmetry. In real cases with weak coupling or rotational offset and disorder between chromophores, the 0-0 transition has a reduced intensity, as we observe here.[109] More extensive changes are seen for **3** in acetonitrile, where the broad spectrum lacking vibronic features is reminiscent of spectra found for ordered liquid crystalline phases of PDI derivatives that exhibit strong coupling between π-orbitals that become delocalized.[152–156] This indicates that the solution of **3** in acetonitrile induces a spectroscopically distinct aggregation mode, for which the term "π-aggregate" is used to refer to electronic interactions that manifest differently from the vibronically structured H-aggregate mode described above. In spite of solubility limiting spectroscopic investigations to micromolar concentrations that are too dilute for NMR spectroscopy, the peptide-PDI solutions display UV-vis spectra with rich and quantifiable behavioral detail.

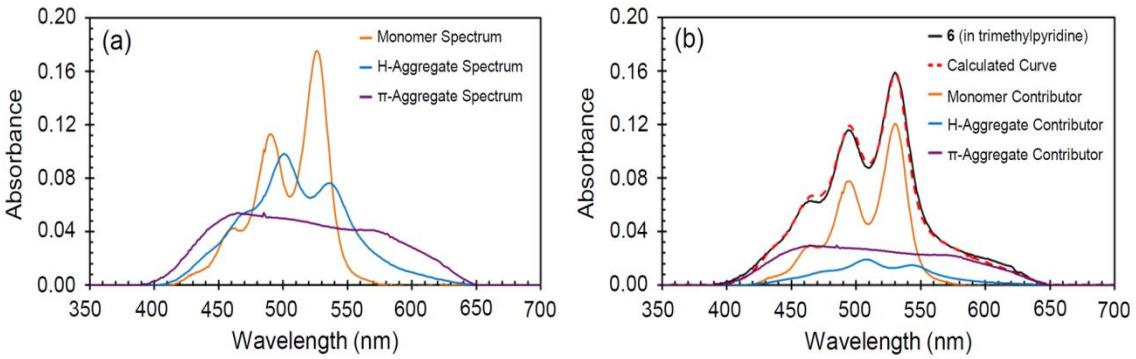

Figure 3.8 Data fitting to determine spectral contributions: (a) Representative spectra (normalized by peak area) of monomers, H-aggregates, and π-aggregates obtained from **3** in DMSO, water, and acetonitrile, respectively. (b) Absorption spectrum of **6** in 2,4,6-trimethylpyridine fit to a sum of the three spectral components (labeled as 'calculated curve'). The evaluated individual spectral contributors (as determined by Equation 3.1) are overlaid for comparison. All solutions 3 μM. (Figure adapted from Eakins et al.[88] with permission from ACS.)

Most absorption spectra appeared to reflect a combination of the three spectral components, as shown in the representative plot in Figure 3.8b (and other spectral data in the supporting information, Appendix D), prompting an approach to fit each spectrum to a sum of the three basis spectra.

For the fitting procedure, all absorption spectra were first baseline corrected to remove effects attributed to scattering from aggregated particles, then normalized by their integrated area (on an energy scale). Each absorption spectrum, $C(\lambda)$, was fit as a linear combination of three representative spectra corresponding to monomer ($M(\lambda)$), H-aggregate ($H(\lambda)$) and π-aggregates ($A(\lambda)$) as given by Equation 3.1. Fits were accomplished by varying their respective coefficients x, y, and z, along with parameters m, h, and a, which compensated for any solvent-dependent spectral shifts. The residual sum of squares was minimized subject to the constraints that all coefficients have positive values and sum to one and spectral shifts for each component could not exceed 15 nm.

$$C(\lambda) = x[M(\lambda - m)] + y[H(\lambda - h)] + z[A(\lambda - a)] \qquad (3.1)$$

This simple model was found to fit the experimental spectra very well and gave a means to quantify the underlying aggregate components under different conditions and thereby develop meaningful structural and thermodynamic correlations. While many spectra were dominated by one or two components, others were only well fit with contributions of all three, as the example in Figure 3.8b shows. Earlier attempts at spectral data-fitting involving a simple subtraction of a scaled multiple of the monomer spectrum were unsuccessful. The rationale to the earlier approach was that if all monomers contributions were subtracted, all remaining contributions would be those of any aggregated species present. Using this approach and minimizing the residual sum of squares for the second derivative (as a measure of spectral trace smoothness) was found to produce unrealistic calculated aggregate spectral profiles which incorrectly evaluated effects from H-aggregate species and overstated monomer species contributions. This prompted the three-component spectral fitting described by Equation 3.1.

3.2.5 Thermodynamic Properties of PDIs in Aqueous Solution

The effect of temperature was investigated in order to extract thermodynamic parameters associated with aggregation. In all cases, the fraction of monomeric species was found to increase with increasing temperature, as expected. For example, Figure 3.9a shows a room-temperature H-aggregate spectrum for an aqueous solution of PDI **3** that gradually becomes monomeric with increasing temperature as aggregates are broken up, at least in the spectroscopic sense of short-range coupling. Clear isosbestic points were observed, suggesting that the transition is well described by these two species, as confirmed by the data fit in Figure 3.9b.

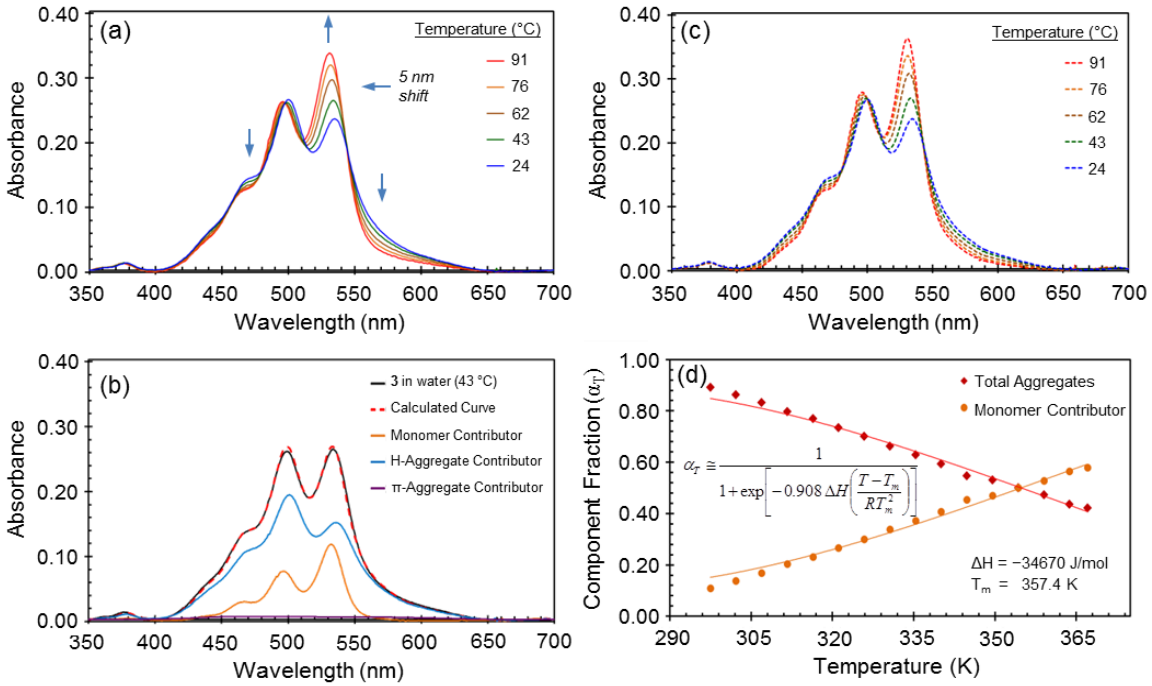

Figure 3.9 (a) Temperature-dependent absorption spectra of an aqueous solution of **3**. (b) Spectral fitting confirming dominance of monomer and H-aggregate contributions, and yielding (c) a calculated spectral-fit series, which was fit in (d) to Equation 3.2 (inset) to obtain ΔH and T_m. All solutions 6 μM. (Figure adapted from Eakins et al.[88] with permission from ACS.)

Spectral data fitting done as shown in Figure 3.9b at each selected temperature produced a calculated spectral series (Figure 3.9c) which closely matched the measured experimental series (Figure 3.9a). The temperature-dependent conversion

of H-aggregates to monomers was plotted in Figure 3.9d, and was also confirmed to be reversible upon cooling (Figure 3.10), justifying the thermodynamic approach. This reversibility is also important from the perspective of the self-assembly process, since different processes (for the same molecular units) have been shown to sometimes produce different self-assembly outcomes.[151] In this context, is it important to underscore that, while a pH-triggered process was used to prompt the initial self-assembly of the nanofibers and a different heat-cycle process was used to disrupt (and reform) the nanofibers during the temperature-dependent analysis, both the pH-triggered and the heat-cycle processes arrived at the same self-assembly outcome (as verified by the spectral the profiles observed).

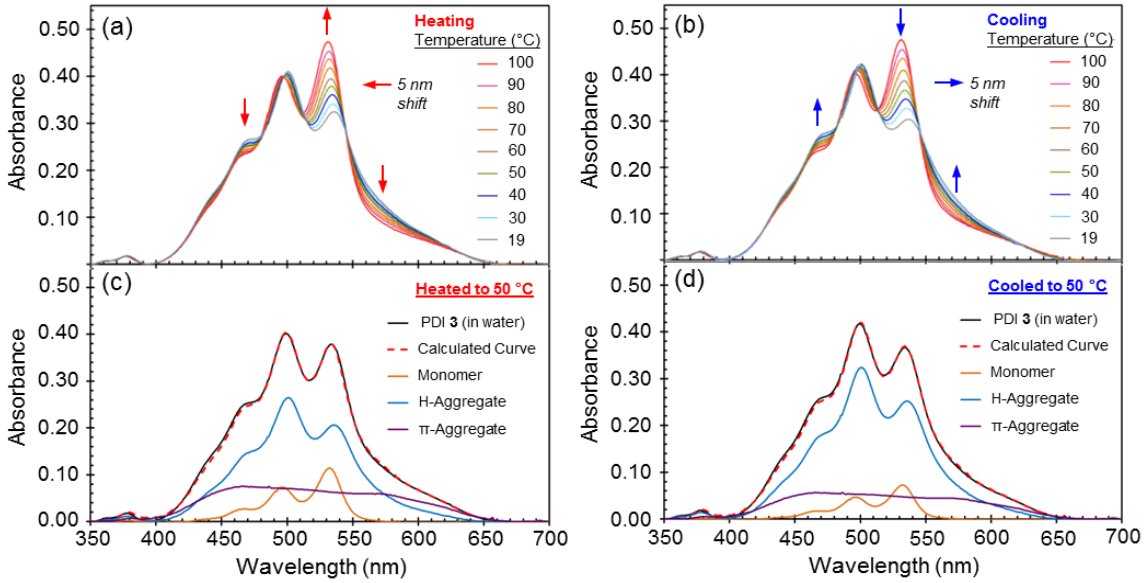

Figure 3.10 Representative spectral data fitting for a solution of PDI **3** during heating and cooling, demonstrating thermodynamic reversibility with temperature. (a) Spectra collected during solution heating. (b) Spectra collected during solution cooling. (c) Spectral data fit at a selected temperature during solution heating and (d) during solution cooling. All solutions 7 μM. (Figure adapted from Eakins et al.[88] with permission from ACS.)

As summarized in Table 3.1, thermodynamic parameters were then evaluated using Equations 3.2-3.4, which are derived from the isodesmic model of aggregation that considers the addition of monomers to an aggregate to be described by a single binding constant, regardless of the aggregate size.[157,158] The temperature-dependent

data (e.g., Figure 3.9d) were fit to Equation 3.2, where α_T is the measured total aggregated fraction, and the fitting parameters, ΔH and T_m are, respectively, the molar enthalpy of aggregation and the aggregate melting temperature (where α_T = 0.5).[158] Using the aggregate fraction values at 298 K, Equation 3.3 afforded values for K_e (aggregation equilibrium constant) and DP_N (average number of monomers in an aggregate stack),[158] permitting the evaluation of the free energy (ΔG) and entropy (ΔS) of aggregation from temperature dependent data.

$$\alpha_T \cong \frac{1}{1+\exp\left[-0.908\Delta H\left(\frac{T-T_m}{RT_m^2}\right)\right]} \tag{3.2}$$

$$DP_N = \frac{1}{\sqrt{1-\alpha(T)}} = \frac{1}{2}+\frac{1}{2}\sqrt{4K_e(T)+1} \tag{3.3}$$

It must be noted here that DP_N measures the size of spectroscopic aggregates, which does not give an accurate measure of the much larger physical aggregates imaged in Figures 3.5-3.7 owing to the short range of optical coupling. Values of K_e and ΔG for nonaqueous PDI solutions at 298 K were determined using Equation 3.4,[157] where c_1 is the molar concentration of monomer species present and c_T is the molar concentration of the total number of molecules in the solution.

$$K_e = c_1^{-1} - (c_1 c_T)^{-0.5} \tag{3.4}$$

Within the thermodynamic data evaluated from the aqueous temperature-dependent measurements summarized in Table 3.1, emerging trends can be seen. The ΔH and ΔS data give valuable insight into the influences that cause the emergence of the observed values of K_e and ΔG. Although many compounds had similar aggregation constants, ΔH and ΔS were found to be much more sensitive to structural changes including hydrophobicity, steric demand, charge, chiral centers, and the addition of an imide hexyl chain. In the next section, each of these effects is evaluated in order of their observed importance on the overall aggregation constant.

Table 3.1. Aggregation Constants and Thermodynamic Parameters of Peptide-PDIs in Water

cpd	$\Phi_{peptide}$ (kJ mol^{-1}) [a]	K_e [b] (M^{-1})	ΔG [b] (kJ mol^{-1})	ΔH (kJ mol^{-1})	ΔS (J mol^{-1}K^{-1})	T_m [c] (K)	DP_N [d]	α_H [b,e]	α_T [b,f]
1	2.9 ± 0.63	4.6×10^6	−38.0	−53.8	−52.9	385.6	5.7	0.76	1.00
2	1.9 ± 0.54	1.8×10^6	−35.7	−44.8	−30.5	373.4	3.9	0.78	1.00
3	1.5 ± 0.63	7.6×10^5	−33.6	−34.7	−3.8	357.4	2.6	0.88	0.89
4	1.5 ± 0.63	2.0×10^6	−35.9	−29.8	20.5	357.3	2.3	0.11	0.80
5	1.5 ± 0.54	6.1×10^5	−33.0	−32.3	2.4	354.6	2.4	0.86	0.86
6	−0.14 ± 0.63	1.5×10^5	−29.6	−14.6	50.3	305.1	1.5	0.10	0.87
7	−0.34 ± 0.63	1.5×10^5	−29.6	−12.8	56.3	312.9	1.5	0.50	0.59
8	−0.34 ± 0.63	3.6×10^5	−31.7	−16.4	51.4	375.2	1.9	0.25	0.71
1H	2.9 ± 0.63	1.5×10^6	−35.3	−34.3	3.2	1055	3.7	0.49	0.93
2H	1.9 ± 0.54	9.6×10^6	−39.9	−55.1	−51.0	447.0	9.5	0.00	0.99
3H	1.5 ± 0.63	5.7×10^6	−38.6	−43.3	−15.7	484.0	6.6	0.00	0.98
4H	1.5 ± 0.63	3.1×10^6	−37.1	−44.2	−23.9	407.8	5.0	0.20	0.97
5H	1.5 ± 0.54	2.1×10^6	−36.1	−34.4	5.6	756.1	4.6	0.49	0.95

[a] Peptide substituent hydrophobicity calculated by summing and averaging the contribution of each residue according to the whole-residue octanol-interface scale reported by White and Wimley.[21] More negative values indicate greater hydrophobicity.

[b] Evaluated at 298 K.

[c] Aggregate melting temperature defined where the aggregated fraction $\alpha_T = 0.50$.

[d] Average stack length, representing the average number of monomers in an aggregate stack.

[e] α_H is the fraction of H-aggregates.

[f] α_T is the total fraction of aggregates (H-aggregates and π-aggregates).

3.2.5.1 Effects from Peptide Hydrophobicity

The peptide hydrophobicity may be tuned either by changing the number of ionizable amino acid residues or by employing amino acid residues with more hydrophobic side-chains (e.g., phenylalanine in **6** and leucine in **7**). Both approaches carry other consequences, since ionizable amino acid residues bring electrostatic interactions and large hydrophobic residues are expected to induce

steric effects. Nevertheless, the effect of overall hydrophobicity can be established by observing whether thermodynamic parameters correlate with values obtained by applying an empirical hydrophobicity scale to the peptides considered in this study. The hydrophobicity values given in Table 3.1 were assessed using published values of the contribution of each amino acid that were derived from whole-residue hydrophobicity measurements at water interfaces.[21] It is worth noting that these values from empirical measurements of amino acids do not quantify the dominant hydrophobic contributions of the perylene core or the hexyl chains (in the case of **1H**-**5H**). These measurements therefore underestimate the overall effect of hydrophobicity, but nevertheless allow a comparison of the relative effect that the peptide hydrophobicity has on tuning the assembly of compounds containing the same hydrophobic core. Comparing dipeptide PDIs **1**-**7** (excluding diastereomers **4** and **8**, which will be discussed later), increased peptide hydrophobicity (reflected by more negative values) is correlated with lower aggregation constants. Figure 3.11a shows how each of the thermodynamic parameters vary with hydrophobicity, with strong correlations observed across a wide range of binding energies. Since the hydrophobicity scale neglects effects like specific sequences, and electrostatic repulsion, the observed correlation suggests that crude hydrophobicity is of primary importance.

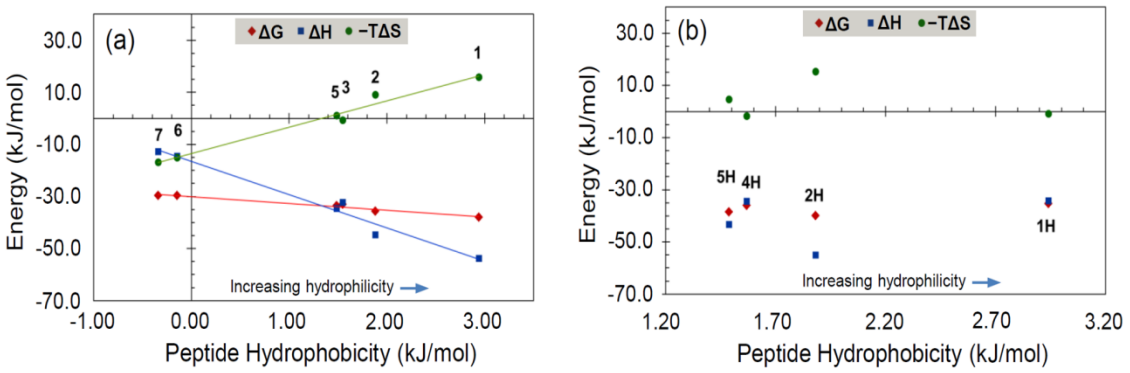

Figure 3.11 Thermodynamic parameters of (a) dipeptide-PDIs and (b) hexyl-PDIs plotted against hydrophobicity (as ranked by the peptide residue average on the octanol-interface scale). (Figure adapted from ref. 88 with permission from ACS.)

Figure 3.11a also shows that the variation in Gibbs free energy is underpinned by much more pronounced, but opposing changes in binding enthalpy and entropy.

The observation that aggregation is strongly entropically favored for hydrophobic peptides is in line with expectations. Aggregation allows hydrophobic residues to be buried away from the water interface to reduce the effect of the entropically disfavored ordered hydration shell. This trend is most clearly seen in PDIs **1**, **3**, **6**, and **7**, where the hydrophobicity in the central region progressively increases via replacing glycine with alanine, phenylalanine, and leucine, respectively. The variation in aggregation entropy across this series exceeds the difference between **2** and **3**, where the central alanine region is retained and lower hydrophobicity in **3** results from the removal of two glutamic acid residues.

The effects on binding enthalpy are more difficult to explain through hydrophobicity alone. Instead, the apparent trend that aggregation becomes more enthalpically disfavored for more hydrophobic peptides may reflect the greater steric demand of the more hydrophobic peptides (e.g., containing phenylalanine and leucine sequences). Large residues can interfere with hydrogen bonding between neighboring peptide backbones, and even disrupt π-stacking interactions between the nearby PDI units. Indeed, we find a steric effect on the spectroscopic nature of aggregation (H- vs. π-aggregate), as we discuss later.

There was no discernible effect of hydrophobicity when comparing hexyl PDIs **1H-5H** in Figure 3.11b. The relative importance of hydrophobicity significantly diminished compared with the dipeptide series since the peptide accounts for a smaller fraction of the hexyl PDI molecules.

3.2.5.2 Effects from an Imide Hexyl Chain

Replacing one peptide substituent in dipeptide-PDIs **1-5** with a hexyl chain in order to produce hexyl-PDIs **1H-5H** gave five PDI pairs to contrast. As illustrated in Figure 3.12a, with the exception of **1/1H**, the five PDI pairs show that the replacement of a peptide substituent with a hexyl chain resulted in a more favorable Gibbs free energy of aggregation. This is largely driven by more attractive aggregation enthalpies for hexyl derivatives (Figure 3.12b), while no clear trend emerged in the widely varying entropic component (Figure 3.12c).

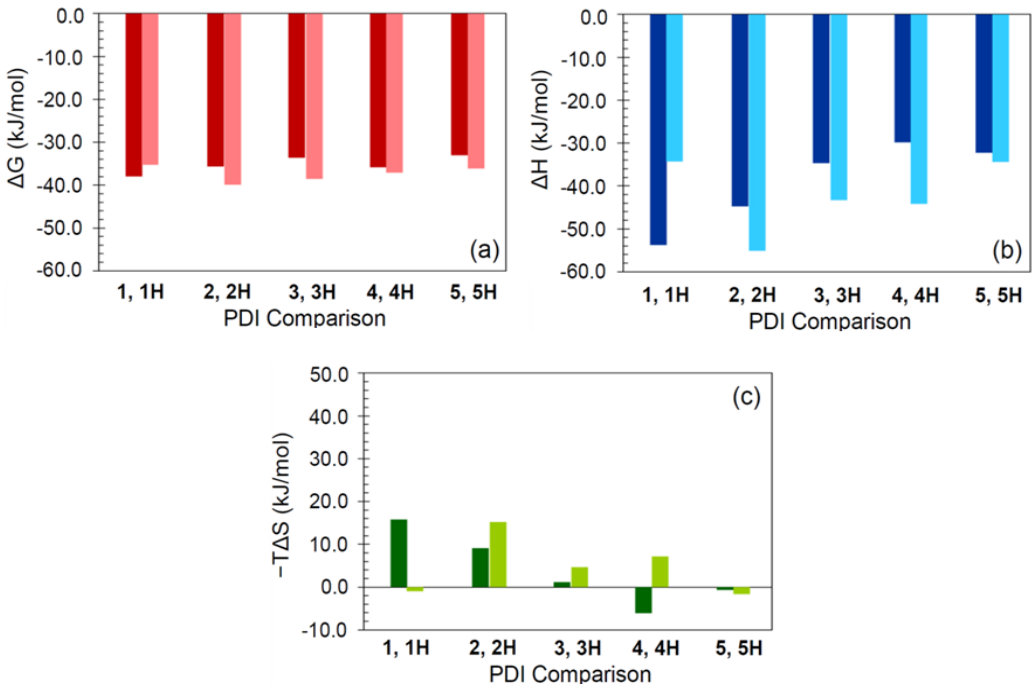

Figure 3.12 Thermodynamic comparisons of dipeptide and hexyl-peptide PDI pairs showing the effect of an imide hexyl substituent on; (a) ΔG; (b) ΔH; (c) –TΔS. (Figure adapted from Eakins et al.[88] with permission from ACS.)

More favorable enthalpies for the hexyl derivatives are likely the result of diminished charge repulsion, which will be specifically discussed later, and in spite of replacing hydrogen bonding peptides with hexyl chains that have a weaker van der Waals interaction. The strong amphiphilicity of the hexyl PDIs also suggests that ordered supramolecular assemblies such as cylindrical, rod-like fibers are likely to form, where the entropic penalty of ordering must be balanced against the entropic penalty associated with solvating hydrophobic chains. The entropic contributions specific to aggregate structures may account for the sequence-dependent aggregation entropies observed.

3.2.5.3 Effects from Ionizable Amino Acids Residues

As previously illustrated in Scheme 3.1, the terminal charged and central uncharged peptide regions were subject to variation. The length of the charged region could be adjusted to impact solubility and to tune sensitivity to solvent composition (salts, pH, etc.). When comparing PDI **2** with **3** or PDI **2H** with **3H**, it was found that

increasing from one to three glutamic acid residues on each peptide leads to weaker aggregate binding. Delineating the enthalpic and entropic contributions, an increased number of charged residues was found to lead to significantly decreased enthalpic attraction, presumably due to the electrostatic repulsion associated with aggregating a more highly charged peptide. The enthalpic effects overwhelm more favorable binding entropy for peptides with more charged groups, where the binding entropy may be associated with changes to the hydration shell around the charged glutamate groups. The overall observation that decreasing the charge density favors aggregation parallels previous work where aggregation in highly charged peptides could be triggered by adding salts to screen charge repulsion.[79]

The removal of three glycine residues from **1** to produce **5** decreased the length of peptide-peptide interface while retaining the same terminal glutamic acid region. This change resulted in weaker binding for **5**, driven largely by a substantially decreased enthalpic attraction compared with **1**. The diminished enthalpic contribution to binding is likely the result of removing the attractive glycine interface, which accommodates strong hydrogen bonding along the peptide backbone.[20] Additionally, the glutamic acid region in **5** is positioned closer to the perylene core than in **1**, where its increased steric demand and electrostatic repulsion could more effectively inhibit aggregation.

3.2.5.4 Effects from Peptide Stereocenters

Given that attractive peptide-peptide interactions are found to influence peptide-PDI self-assembly, the effect of inverting stereocenters was interrogated in order to probe the extent of specific structural effects that go beyond hydrophobicity, size, and charge, none of which are affected by stereocenter inversion. PDIs **3**/**4**, **7**/**8**, and **3H**/**4H** served as three diastereomeric PDI pairs with identical structures except in the stereochemistry of the three central amino acids. The diastereomeric pairs are not enantiomers (in which case thermodynamic parameters would not be affected), because the stereochemistry of the glutamic acid region (*L*-) remained constant. Comparison of these pairs in Table 3.1 shows that the thermodynamic parameters were significantly affected by stereocenter inversion, particularly in **3** vs.

4, however no universal trend was observed across all three pairs. Particularly noteworthy was the stereocenter influence on H-aggregate expression. Evaluating the H-aggregate fraction, α_H, as a percentage of α_T at room temperature (Table 3.1), diastereomeric pairs **3** vs. **4** contrasted, with 99% and 14% H-aggregates, respectively. The contrast was also evident for diastereomeric pairs **7** (85% H-aggregates) vs. **8** (35% H-aggregates), which featured more sterically demanding leucine residues in the central region. While π-aggregates require direct overlap of π-orbitals, H-aggregates arise from dipolar coupling between chromophores that do not need to be electronically coupled. In line with this consideration, it was found that some degree of enforced orientation between PDI units impacts H-aggregation. Thus, molecular packing considerations were seen to play a dominant role in determining the *type* of aggregation, although the effect of a given stereocenter inversion cannot yet be predicted. Measurements in this study did not show that the percentage of H-aggregates correlated well with the other structural parameters interrogated in this study (*vida supra*), with solvent polarity (*vida infra*), or with the thermodynamic parameters of binding.

3.2.5.5 Comparative Summary of Structural Effects

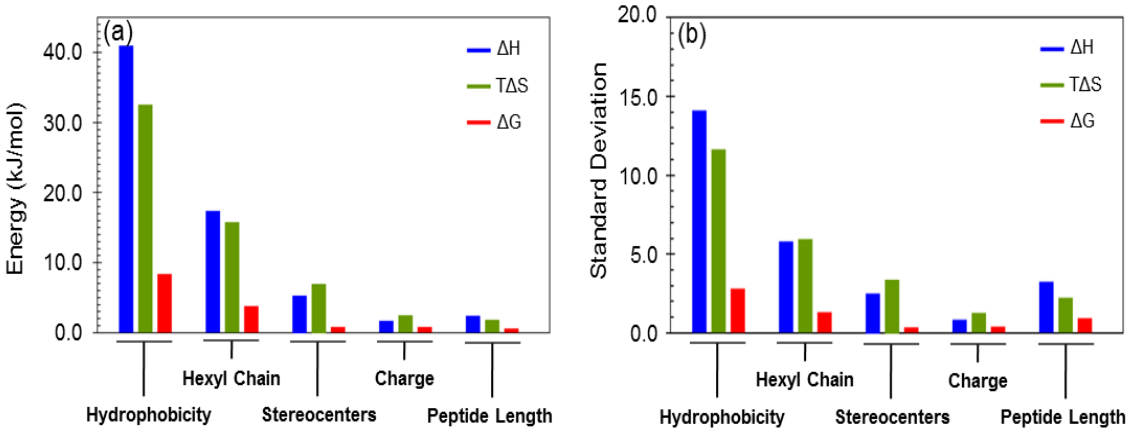

Figure 3.13 A ranking (from greatest to least) of the impact of structural influences affecting the PDI thermodynamic parameters. (a) The bars indicate the magnitude of the range between the lowest value and the highest value observed for each parameter in the relevant PDIs, as well as (b) the standard deviation as a more collective measure of variation. Structural influences of higher impact produced greater variation in the parameters. (Adapted from ref. 88 with permission of ACS.)

Among the structural variations examined, hydrophobicity and the inclusion of an imide hexyl substituent produced the greatest changes in the thermodynamic properties. Comparatively smaller influences were seen from changing stereocenter chirality, varying the number of ionizable amino acid residues or the length of the central peptide sequence. This relative importance of the effects examined through comparison of thermodynamic binding parameters for various sets of compounds is summarized in Figure 3.13.

3.2.6 PDI Binding in Nonaqueous Solutions

The strong inherent amphiphilicity of the peptide-PDI molecules was expected to produce pronounced sensitivity to the solvent environment, which may be exploited to manipulate self-assembly. Spectroscopic data fitting as previously described was applied to probe aggregation at room temperature in selected organic solvents chosen to provide a range of solvent characteristics. Given that solvent-solute interactions influence both solubility and chemical equilibria, Figure 3.14 compares the aggregated fraction compounds **3** and **6** in solution versus empirical solvation parameters for a range of solvents (using the E_T^N solvatochromic scale[159]), which permits indirect inference into aspects such as solvent polarity and hydrogen bonding interactions.[159,160]

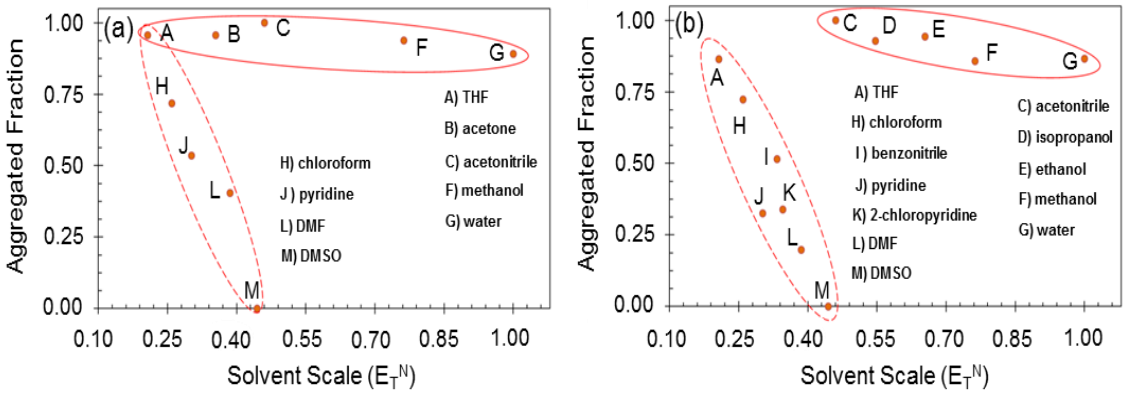

Figure 3.14 Selected plots of the aggregated fraction of (a) **3** and (b) **6** in various solvents across a wide range of solvent character (as described by the E_T^N solvatochromic scale), showing the emergence of two solvent groups. All solutions 3 μM. (Figure adapted from Eakins et al.[88] with permission from ACS.)

Two separate solvent groups clearly emerge, as indicated by the circled regions in Figure 3.14. The first solvent group (solid red oval) covered a very wide range across the E_T^N scale but maintained a consistently high aggregated fraction. Moreover, DMSO and acetonitrile had similar solvation parameters, but DMSO

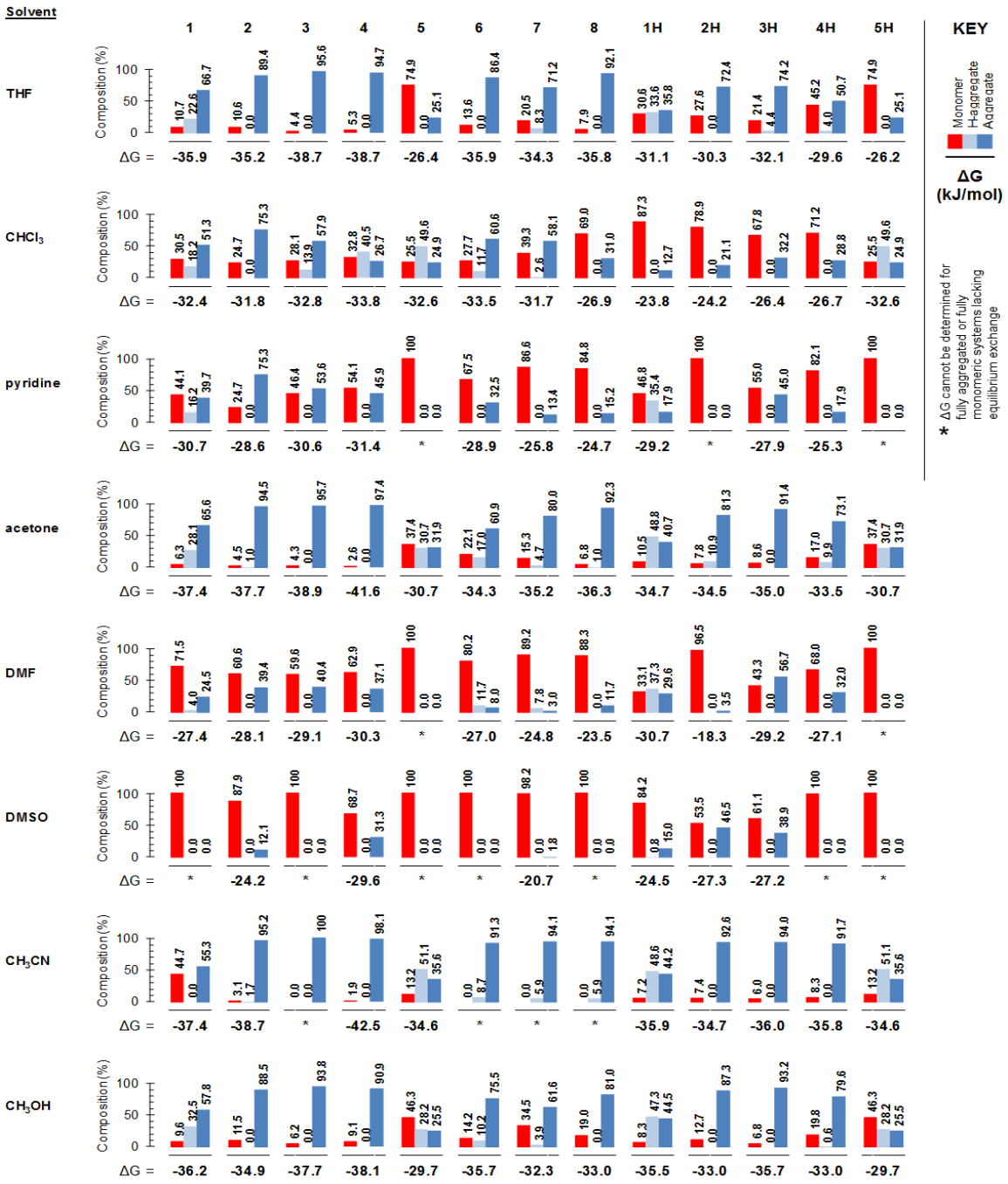

Figure 3.15 Results of spectral data fitting for PDIs in various solvents showing changing species composition and aggregate binding. Compounds are listed in order of increasing hydrophobicity; solvents are listed in order of increasing polarity. (Figure shown from Eakins et al.[88] with permission from ACS.)

produced a monomeric solution, while acetonitrile produced a highly aggregated solution. The second solvent group (dashed red oval), on the other hand, is characterized by widely varying aggregate fractions for solvents with similar solvation parameters. The emergence of these two solvent groups shows that the solvation parameter E_T^N does not determine aggregation, and that other solvent characteristics must be considered. In particular, solvents capable of π-stacking gave noticeably lower aggregate fractions since such solvents can interact favorably with the PDI core. For example, a solution in benzonitrile gave much more monomeric character than did a solution in acetonitrile (Figure 3.14b). Other solvent structural features may provide an additional influence. Pyridine and benzonitrile, for example, are both capable of π-stacking to solvate the PDI core, but the more basic pyridine can interact with the acidic glutamic acid residues and produced a greater proportion of monomers in solution than benzonitrile. Similarly, the ability of DMSO to solvate the peptide-PDIs may reflect its Lewis base properties. A summary of calculated aggregate species fractions of PDIs **1**-**8** and **1H**-**5H** in selected organic solvents is given in Figure 3.15.

3.3 Conclusions

A series of peptide-functionalized PDI molecules were synthesized which were designed to establish design rules for peptide-driven aggregation through incremental variations in peptide hydrophobicity, length, charge density, as well as stereocenter inversion and amphiphilic substitution. Having observed the formation of nanostructures in solution, a spectroscopic investigation of the thermodynamics and nature of aggregation for the series of peptides was implemented. It was found that non-specific effects like peptide hydrophobicity and nonsymmetrical substitution with a hexyl chain had the greatest impact on binding thermodynamics. However, more specific variations like diastereomeric substitution were also shown to have a significant impact, particular on the dominance of H- versus π-aggregates, highlighting how peptide packing modulates coupling between PDI units. Solvent dependent spectroscopy also highlighted the range of peptide- and PDI-based interactions responsible for aggregation in these materials.

Chapter 4

Chiral Effects in Peptide-Substituted Perylene Imide Nanofibers

4.1 Introduction

Molecules capable of supramolecular self-assembly into nanofibers often possess an amphiphilic structure, enabling strong solvophobic/solvophilic associations in solution which drive self-assembly. Accordingly, many moieties capable of non-covalent interactions such as hydrogen-bonding or π-stacking have been utilized to form nanofibers, including amino acid or amide groups,[161–163] sugar units,[164–166] gluconamides,[167,168] urea functionalities,[169,170] and aromatic systems.[171–173] Often these appended moieties also contain chiral centers that can exert significant influence on the nature and stability of the assembled supramolecular architectures.[174] Such influences are strongly exemplified in gelators, the gels of which are comprised of large numbers of fibers, and therefore, highly sensitive to the molecular packing and thermodynamic constraints imposed on fiber growth by stereogenic centres.[174] For example, in one reported case of a monosaccharide with five stereocenters, out of the eleven possible stereoisomer configurations, only five were found to be good gelators.[164,165] Diastereomers, therefore, may behave very differently toward self-assembly and yield differing morphologies, as demonstrated by *n*-alkyl aldonamide-derived lipids, which haves been shown to form helical

ribbons, rolled-up sheets, or multiple helices, depending upon the particular diastereomeric configuration.[167,175]

Even for self-assembling systems involving π-stacking of achiral chromophores, chiral substituents may impart a chiral bias (such as a twist or an orientation offset) to nanofiber architectures. Many examples of this have been reported including twisted ribbons made from stacked cholesteryl saccharidic porphyrins,[171] a hydrogel made from a peptide-substituted naphthalene diimide,[15] and a twisted tape was made of stacked oligoalanine-polyisobutylene-substituted quarterthiophene units.[80]

This imparted chiral twist motif noted in the preceding examples is also commonly observed in self-assembling perylene imide systems with chiral imide substituents. Examples of this include: helical strands of a non-symmetric perylene diimide (PDI) with a phenyl-linked chiral monosaccharide moiety,[176] helical assembly in a symmetric PDI employing the chiral disaccharide *D*-lactose linked to the imide by a two-carbon chain,[50] and enantiomeric helices resulting from enantiomeric amino acid linkers acting as tethers to Newkome-type dendrimers (repetitively branched, tree-like molecules with a 1-to-3 carbon-branching pattern and carboxyl or ester terminal groups).[122] For these perylene imide examples, the linkers adjoining to the perylene core, as well as the extended moieties are all different, but all have one or more chiral centers influencing the π-stacking of the perylene core.

Perylene imide compounds with multiple chiral centers present added complexity. Such is the case for perylene imides with peptide substituents of 4-7 amino acids in length which have been reported to form fibers that possess a helical chirality.[80,88] In these systems, up to seven chiral centers are in place at increasing distances from the perylene core. While chiral centers have been shown to induce a helical arrangement on the fibers formed in these systems,[80,88] the position-specific effects of multiple stereogenic systems on chiral and structural changes have not been investigated. In this chapter, the effects of specific chiral variations are resolved within a series of peptide-functionalized perylene imide molecules that assemble into nanofibers. The impact of peptide stereogenic positions, stereochemical configurations, amino acid steric demand, and amphiphilic substitution along with perylene core modification is examined.

4.2 Results and Discussion

To investigate the influence of peptide chiral centers on the self-assembly of *N*-peptide-substituted perylene imides, a series of compounds was synthesized to provide key chiral and structural differences, as shown in Scheme 4.1.

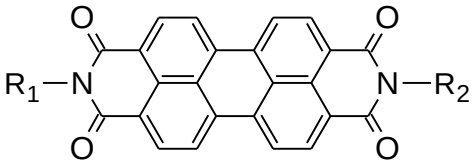

perylene diimide (PDI)

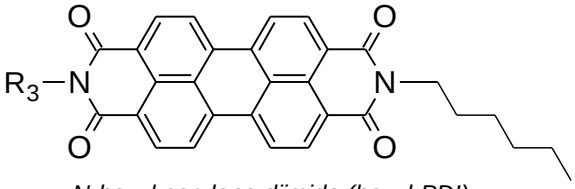

N-hexyl perylene diimide (hexyl-PDI)

1 $R_1 = R_2$ = -Gly-$(Gly)_3$-$(Glu)_3$

3 $R_1 = R_2$ = -Gly-$(Ala)_3$-$(Glu)_3$

3E $R_1 = R_2$ = -Gly-$(D\text{-}Ala)_3$-$(D\text{-}Glu)_3$

3M R_1 = -Gly-$(L\text{-}Ala)_3$-$(L\text{-}Glu)_3$; R_2 = -Gly-$(D\text{-}Ala)_3$-$(D\text{-}Glu)_3$

4 $R_1 = R_2$ = -Gly-$(D\text{-}Ala)_3$-$(Glu)_3$

6 $R_1 = R_2$ = -Gly-$(Phe)_3$-$(Glu)_3$

7 $R_1 = R_2$ = -Gly-$(Leu)_3$-$(Glu)_3$

8 $R_1 = R_2$ = -Gly-$(D\text{-}Leu)_3$-$(Glu)_3$

3H R_3 = -Gly-$(Ala)_3$-$(Glu)_3$

3HE R_3 = -Gly-$(D\text{-}Ala)_3$-$(D\text{-}Glu)_3$

4H R_3 = -Gly-$(D\text{-}Ala)_3$-$(Glu)_3$

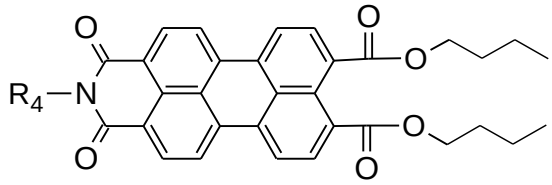

perylene imide bis(n-butyl) ester (PIBE)

Q3 R_4 = -Gly-$(Ala)_3$-$(Glu)_3$

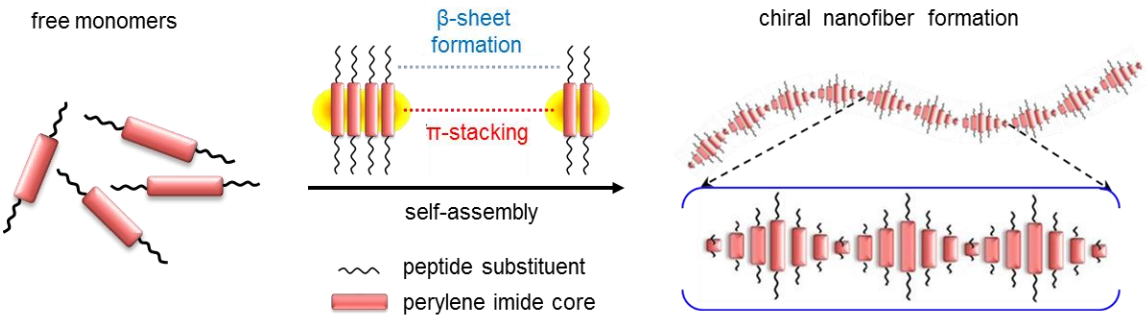

Scheme 4.1 Summary of the *N*-peptide-substituted perylene imides examined for chiral effects, arranged by structural similarity, and an illustration of the self-assembly strategy employed for these compounds. (Scheme adapted from Eakins et al.[177] with permission from Taylor and Francis.)

The compounds in Scheme 4.1 provided enantiomer and diastereomer pairs to be examined in parallel with other structural variables such as peptide side-chain steric demand (**1**, **3**, **6**, **7**), replacement of a peptide substituent with an alkyl chain (**3**/**3H**, **4**/**4H**), and modification of the perylene core (**Q3**). In conjunction with these comparisons, differentiating enantiomer pairs **3**/**3E** and **3H**/**3HE** along with diastereomer pairs **3**/**4** and **7**/**8** enabled the assessment of the impact of chiral center proximity to the perylene core when contrasted with **1** and **3M**, which served as control compounds.

The peptide substituents were designed to incorporate three regions: an achiral glycine linking unit, a central region of three residues to serve as the peptide structural variable, and a terminal region of three ionizable glutamic acid units to assist solubility and pH-triggered aggregation. The self-assembly strategy depicted in Scheme 4.1 capitalized on the innate β-sheet-forming tendency of the peptide moieties in concert with the strong π-stacking behavior intrinsic to perylene imides. Interactions in this manner thus generated self-assembly principally in one dimension, leading to the formation of chiral nanofibers as has been previously demonstrated for these compounds.[88] This study examined influences related to the chiral architecture of these fibers.

4.2.1 Solution Preparation and Self-Assembly Process

Solutions for the CD spectroscopy analyses were prepared using the same methods and self-assembly processes as those described in Chapter 3 for the UV-vis analyses. Briefly, 40 μL aliquots of aqueous stock solutions of the peptide-PDI materials (prepared from 1.3-1.8 mg of each compound dissolved into 1 mL of a pyridine/water mixture) were diluted into 5 mL of the dilution solvents of interest, thus producing 6 μM solutions with residual base for analysis. Solutions for the CD spectroscopy in this chapter were prepared exactly as those presented in Chapter 3 in order to examine chiral aspects under the same conditions as those under which the thermodynamic aspects were explored.

4.2.2 CD Spectroscopy Methodology

CD spectra were collected in the visible range of the spectrum from 350-700 nm. Although it was desirable to also record the UV region of the CD spectra, which could allow identification of any secondary structures formed by the peptides[14] (as noted in Chapter 2) and provide insight about their self-assembly behavior within any peptide-PDI architectures formed, strong light absorption from the residual pyridine present in the solutions prevented inspection of the UV range. The visible region of the CD spectrum, however, was of primary interest since chirally ordered architectures built from the self-assembly of the achiral chromophore cores of the peptide-PDIs would manifest distinctively within the visible region of the spectrum. Accordingly, the results discussed in this chapter focus on the visible range of the CD spectra collected.

During the collection of the CD spectra, the photomultiplier tube detector voltage, which is sometimes called the dynode voltage or the high tension (HT) voltage, provides a useful instrumental detector response indicator which should be monitored during data collection. Appropriate HT voltage ranges during spectral acquisition ensures a suitable signal-to-noise ratio and detector response is maintained for good data quality. The HT data are further useful to assess spectral profiles for potential artifacts. HT data may also be used to assess the extent of scattering produced by aggregates in solution, which manifests in the HT data as a sloping baseline. In general, the HT voltage should be maintained below 600 V for the data to be valid; however, the signal-to-noise ratio declines significantly above 500 V and may produce noisy spectra which must be evaluated cautiously.[14]

For all CD spectra presented in this chapter (and elsewhere), HT voltages were maintained below 600 V with most spectra exhibiting HT profiles near or below 500 V. Some extent of baseline noise was observed but was not sufficient to disqualify the spectral data. Also, some moderate sloping of the HT data baseline (indicative of scattering) was observed at longer wavelengths for some spectra, but the impact of the scattering was determined not to compromise the spectral data acquired. Due to the detected scattering, however, the evaluation of apparent fine spectral features at the longer wavelengths must be made very cautiously.

4.2.3 Chiral Templation

The formation of chiral chromophore architectures was indicated by circular dichroism (CD) spectroscopy in the visible region of the absorption spectrum, where only the perylene chromophore contributes. The chiral environment of the perylene was found to depend upon the proximity of the peptide chiral centers to the perylene core. As shown in Figure 4.1a, compound **1** was CD silent, independent of solvent. Although the glutamic acid residues of perylene diimide (PDI) **1** have chiral centers, these residues are distal to the perylene core. The proximal positions occupied by the glycine residues conversely lack chiral centers. These results indicate that effective templation of a chiral arrangement on the perylene chromophore requires closer proximity of the chiral centers.

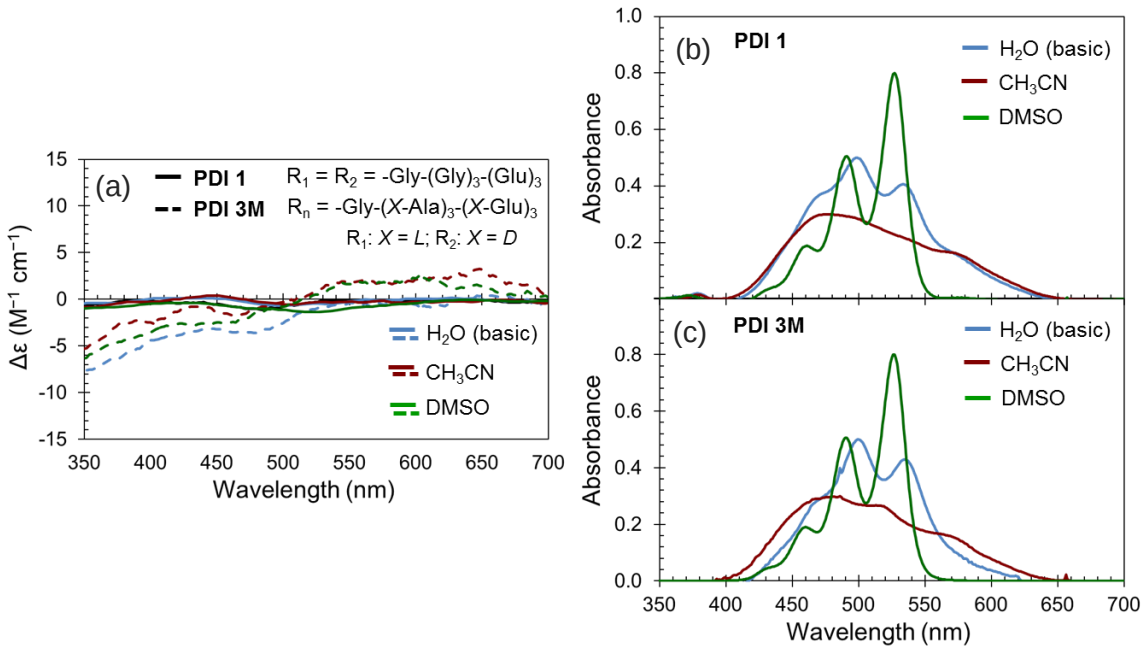

Figure 4.1 CD and UV-vis spectra for the control compounds: (a) CD spectra of compounds **1** and **3M** in three solvents; (b,c) UV-vis spectra of compounds **1** and **3M** (respectively) showing spectral profiles indicative of solvent-dependent changes in the modes aggregation adopted by the compounds. (Figure adapted from Eakins et al.[177] with permission from Taylor and Francis.)

The presence of proximal chiral centers alone, however, is not sufficient to induce an extended chiral architecture with a dominant handedness during self-assembly,

as demonstrated by PDI **3M** in Figure 4.1. Although **3M** has chiral centers close to the perylene core, **3M** is a *meso*-compound, an achiral compound containing chiral centers but having an internal mirror plane. As a result, since **3M** lacks an overall chirality, the chirally opposed proximal peptide stereocenters appear to engender a mixed templation of left- and right-handed chiral orientations to segments of the π-stacking perylene chromophores within the self-assembled fibers. Consequently, no dominant, extended chiral orientation is expressed throughout the fibers to a sufficient extent to produce a strong, well-defined, dominant CD spectral profile as expressed by the weak, but non-zero CD response of **3M** in Figure 4.1a.

In spite of the lack of a strong CD response by PDIs **1** and **3M**, the UV-vis spectra of the compounds (Figure 4.1b,c) gave clear indications of solvent-dependent aggregate assembly behavior.[79,88] In DMSO, the spectral profiles exhibited a well-defined, three-peak vibronic progression indicative of well-solvated, isolated (monomeric) PDI units with electronic transitions coupled to the primary vibrational mode (C=C stretch). In water, however, the spectral profiles indicated an H-aggregated system, having a diminished 0-0 vibronic transition.[109] More dramatic changes were seen for solutions in acetonitrile, in which the spectral profiles of the compounds exhibited a broad, band-like shape similar to spectra reported for ordered liquid crystalline phases of PDI derivatives,[152–156] suggesting a high degree of aggregated π-stacking behavior (termed π-aggregate here in distinction to H-aggregates). Thus, while PDIs **1** and **3M** illustrated solvent responsive self-assembly, the architectures formed were found to be achiral or to lack an extended, dominant orientation.

4.2.4 Chiral Self-Assembly Behavior

In distinction to the cases of PDIs **1** and **3M**, for PDIs **3**, **3E**, and **4** which possess peptide chiral centers positioned proximal to the perylene core, an extended, dominant chiral sense was found to be imparted onto the self-assembling perylene units resulting in a bisignate couplet (Cotton Effect) in the CD spectra (Figure 4.2a,c) indicative of exciton-coupled chromophores in a helical arrangement.[120,121] The positive sign of the couplet for PDI **3** (for which the couplet lobes switch from

negative Δε to positive Δε with increasing wavelength) indicates a right-handed, P-helix, wherein the helix twists clockwise around the helical axis viewed with the direction of helical propagation.[119] For **3E** (the enantiomer of **3**) in which all stereocenters are inverted relative to **3**, a mirror image CD spectrum was produced, corresponding to the opposite case with a negative sign of the CD couplet and a left-handed, counter-clockwise M-helix. Interestingly, when comparing diastereomers **3**/**4**, a similar spectral scenario (Figure 4.2c) was seen to that of the enantiomers **3**/**3E** (Figure 4.2a).

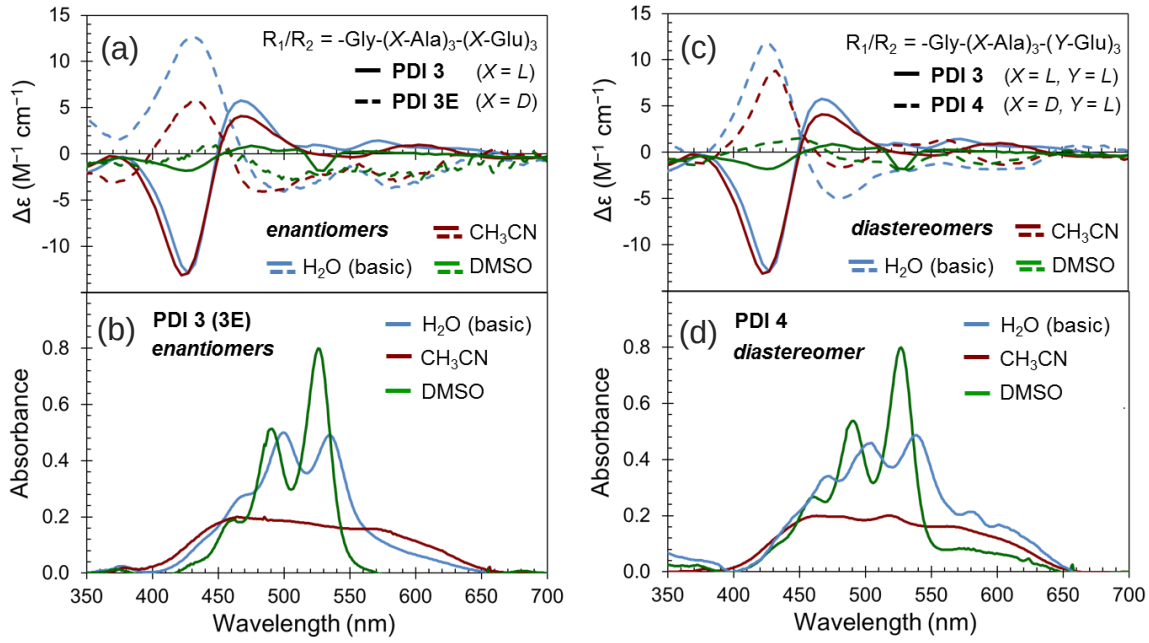

Figure 4.2 CD and UV-vis spectra of enantiomers **3**/**3E** and diastereomers **3**/**4**: (a) CD spectra of enantiomers **3**/**3E** showing the impartation of a chiral sense on the perylene core by the proximal amino acid residues; (b) UV-vis spectra of **3** (**3E**) showing spectral profiles indicative of solvent-dependent changes in the modes aggregation; (c) CD spectra of diastereomers **3**/**4** indicating a chiral chromophore assembly and displaying pseudo-enantiomeric behavior; (d) UV-vis spectra of **4** showing a similar solvent-dependent aggregation response to that of PDIs **3**/**3E**. (Figure adapted from Eakins et al.[177] with permission from Taylor and Francis.)

Since the chiral templation originates from the amino acid residues proximal to the perylene core, the selective inversion of the stereocenters in just the alanine residues

allows PDI **4** to influence the chirality of the supramolecular self-assembly much the same as does **3E**. PDI **4**, therefore, acts as a pseudo-enantiomer to PDI **3**.

For PDIs **3**, **3E**, and **4**, the UV-vis spectra (Figure 4.2b,d) were mutually similar consistent with the solvent-dependent changes to the mode of aggregation previously described; however, for **3**, **3E**, and **4**, the placement of proximal chiral centers translated into chiral architectures associated with the aggregate behavior. With the chiral architectures formed, a solvent-dependent response was also seen in the CD spectra. Slight differences were seen in the CD spectral profiles between the aqueous and acetonitrile solutions (Figure 4.2a,c) consistent with the different solvent-dependent modes of aggregation indicated by UV-vis spectroscopy. Solutions in DMSO were seen to express a weak, but non-zero CD response near the baseline, suggesting the absence of a PDI assembly comprised of a majority population of PDI units with a dominant, extended chiral order. This result was consistent with a solution having a majority population of well-solvated, monomeric (unassembled) PDI units as indicated by the spectral signature observed in the UV-vis spectra of the DMSO solutions.

4.2.4.1 Effect of Side-Chain Changes

Modification of the central structural region of the peptides to incorporate amino acid residues with side-chains of higher steric demand (PDIs **7**, **8**, and **6**) yielded compounds with similar spectral behavior to that observed for PDIs **3**/**3E** and **4**, as illustrated in Figure 4.3. The increase in side-chain size, therefore, was not found to prevent the impartation of chirality onto the aggregate assembly. Side-chain steric demand was observed, however, to impact the absolute intensity of Δε. In a sequential progression from PDI **3** to **7** to **6**, the absolute intensity of Δε was seen to decrease with increasing steric demand. An explanation of this trend can be inferred from a simplified model of two identical, parallel, perpendicularly-separated, and exciton-coupled chromophores, for which the derived relationship describing Δε is expressed by Equation 4.1, where μ_a and μ_b are the electronic transition dipoles of the two chromophores, R_{ab} is their center-to-center transition, θ

is the angle between the transition dipoles, and λ is the associated wavelength of the transition.[119]

$$\Delta\varepsilon \approx \pm(\pi/4\lambda)\mu_a\mu_b R_{ab}^{-2}\sin(2\theta) \qquad (4.1)$$

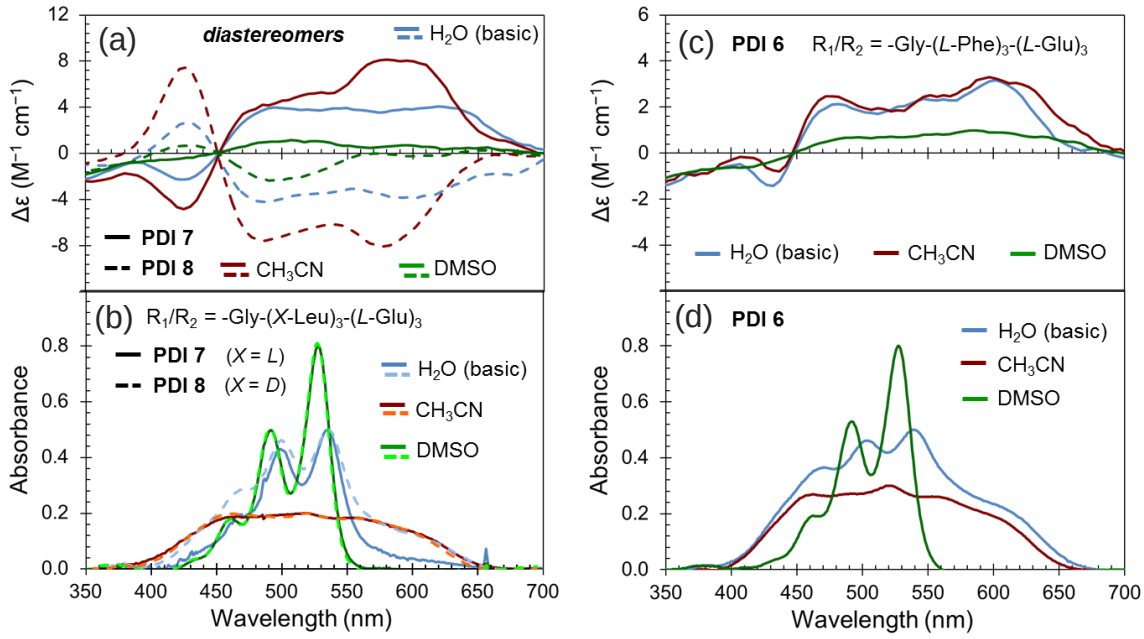

Figure 4.3 CD and UV-vis spectra of diastereomers **7**/**8** and PDI **6**: (a) CD spectra of diastereomers **7**/**8** indicating chiral perylene self-assembly and displaying pseudo-enantiomeric behavior; (b) UV-vis spectra of diastereomers **7**/**8** showing mutually similar spectral profiles indicative of solvent-dependent changes in the modes aggregation; (c) CD spectra of PDI **6** indicating a weak chiral chromophore assembly with a solvent-dependent response; (d) UV-vis spectra of **6** showing solvent-dependent aggregation response. (Figure adapted from Eakins et al.[177] with permission from Taylor and Francis.)

In the simplified model, the intensity of Δε is inversely proportional to the square of the separation distance between the chromophores. As a result, the trend of decreasing Δε (from 15 to 8 to 4 $M^{-1}cm^{-1}$) in the progression from PDI **3** to **7** to **6**, respectively, indicates that the increasing steric demand of the amino acid side-chains in the progression imposed a larger separation distance and/or a larger torsional angle between the dipoles of the PDI units in the chiral assemblies, thus diminishing the exciton coupling and intensity of the Cotton Effect across the series.

Another notable and distinct aspect seen in the CD spectra of Figure 4.3 is the emergence of a broad peak or band-like feature centered near 580 nm. While the peaks near 425 and 475 nm which comprise the Cotton Effect (centered near 450 nm) are due to the in-phase and out-of-phase dipolar interactions associated with exciton coupling,[112,178] the additional, lower energy feature centered near 580 nm appears to emerge from other interactions associated with the longer-wavelength edge of the band-like π-aggregate profiles seen in the UV-vis absorption spectra. Although a scattering artifact cannot be completely ruled out with regard to these features, since the HT data do show some scattering in this range, the size and shape of these features may suggest something real. It is proposed here that this CD feature centered near 580 nm is the result of an interchain excimer within highly ordered, π-stacked species. Delocalization within the π-stacked perylene aggregates would prompt such a feature to occur at lower energy (longer wavelengths) within the spectra. The sign of Δε for the feature would arise from the coincident interaction of the precise helical form of the perylene aggregate and the specific helicity of the circularly polarized light absorbed. As illustrated in Figure 4.4, both left-handed circularly polarized light (E_L) and an M-helix made of perylene chromophores have dipoles which rotate counter-clockwise around the helical axis when moving along the direction of propagation. Similarly, right-handed circularly polarized light (E_R) and a P-helix have a clockwise configuration along the direction of propagation. Absorption of E_L by an M-helix would, therefore, induce a favorable, coincident interaction not present between E_L and a P-helix. (A similar case would exist between E_R and a P-helix versus an M-helix.) An excimer transition dipole which is delocalized along the length of a helix through the same π-stacked, chiral environment would experience the same helical interactions with the circularly polarized light. Therefore, the sign of Δε for the low energy lobe of a Cotton Effect associated with a given perylene helix configuration should be the same expressed by the interchain excimer.

By way of example, in Figure 4.3a, PDI **8** shows a negative Cotton Effect (Δε of the exciton couplet lobes switches from positive to negative with increasing wavelength), indicating that the perylene chromophores are arranged in a left-handed M-helix with a counter-clockwise rotation (Figure 4.4). Since the lower

energy lobe of the Cotton Effect of PDI **8** (near 530 nm) has a negative Δε, a negative Δε should also be expected for the interchain excimer (but at a longer wavelength). This is indeed seen in the spectra near 580 nm. In fact, for all cases in the CD spectra of Figures 4.2 and 4.3, the sign of Δε for the low energy lobe of the Cotton Effect is matched at longer wavelengths by the expressed excimeric feature. Overall across the CD spectra, with an increasing central amino acid side-chain length, a decreasing exciton coupling was seen along with a greater propensity toward the expression of this excimeric coupling.

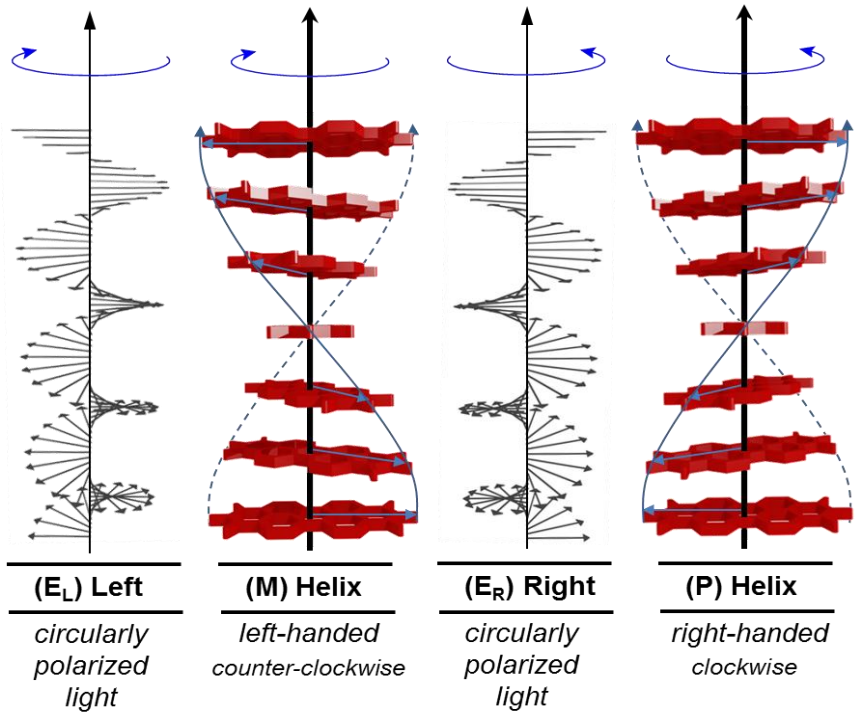

Figure 4.4 Illustrations of M and P perylene imide helices compared to the helical configurations of left and right circularly polarized light. Clockwise and counter-clockwise conventions around the helical axes are specified moving along the direction of helix propagation. (Figure shown from Eakins et al.[177] with permission from Taylor and Francis.)

4.2.4.2 Effect of a Hexyl Chain Replacement

An additional structural variation investigated in this study was that of replacing one of the imide peptide substituents with an alkyl hexyl chain to generate a

strongly amphiphilic, unsymmetrical structure for self-assembly. Although enantiomers **3H** and **3HE** were synthesized along with the corresponding diastereomer **4H**, these compounds produced a weak CD response near the baseline, as shown by the diastereomer pair plots in Figure 4.5. This minimal, but non-zero CD response indicated the absence of a singular, dominant, extended chiral architecture, suggesting the highly amphiphilic nature of these structures is less conducive to extended chiral self-assembly.

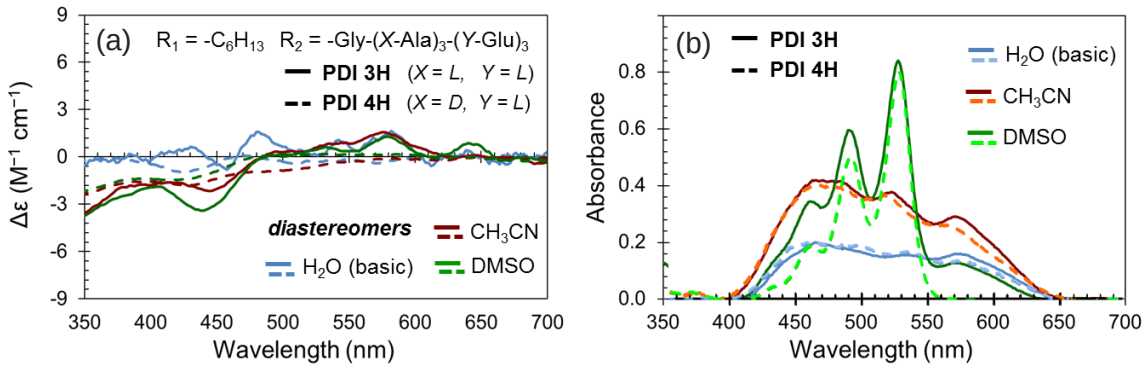

Figure 4.5 CD and UV-vis spectra of unsymmetrical, highly amphiphilic diastereomers **3H**/**4H**: (a) CD spectra showing a weak, non-zero response; (b) UV-vis spectra of diastereomers **3H**/**4H** showing mutually similar spectral profiles indicative of solvent-dependent changes in the modes aggregation. (Figure adapted from Eakins et al.[177] with permission from Taylor and Francis.)

4.2.4.3 Effect of a Modified Perylene Core

One final structural variation investigated in this study was that of modifying the perylene core itself to yield perylene imide bis(*n*-butyl)ester (PIBE) **Q3**. Although this core structure is typically just an intermediate used in the synthesis of unsymmetrical perylene imide derivatives such as **3H**, **3HE**, **3M**, or **4H** (as it was in this study), investigation of **Q3** yielded, interesting results. As shown in Figure 4.6a, a strong solvent-dependent CD response with clear Cotton Effects was observed. While the DMSO solution of **Q3** was CD silent, indicating a well-solvated, monomeric solution, solutions in both water and acetonitrile expressed strong signs of exciton coupling and chiral self-assembly. The CD spectrum for the acetonitrile

solution also expressed an apparent dual peak, which may represent the overlap of the positive lobe of the Cotton Effect with an interchain excimer feature or an axially chiral arrangement. Unlike the other compounds in this study, PIBE **Q3** displayed an inversion of the CD couplet when changing from an acetonitrile solution to an aqueous solution. These distinctly different CD features along with the Cotton Effect inversion suggest that the PIBE core is more configurationally responsive to a changing solvent environment than are the PDI compounds, in spite of minimal differences between the aggregate UV-vis spectral profiles for acetonitrile and water shown in Figure 4.6b. In addition to these spectral characteristics, however, PIBE **Q3** was also found by atomic force microscopy (AFM) to form very diffusive networks of long fibers as seen in Figure 4.6c. These results suggest that the PIBE structures more generally are worthy of consideration for further study in self-assembly applications as alternative perylene moieties having greater solubility and solvent responsiveness.

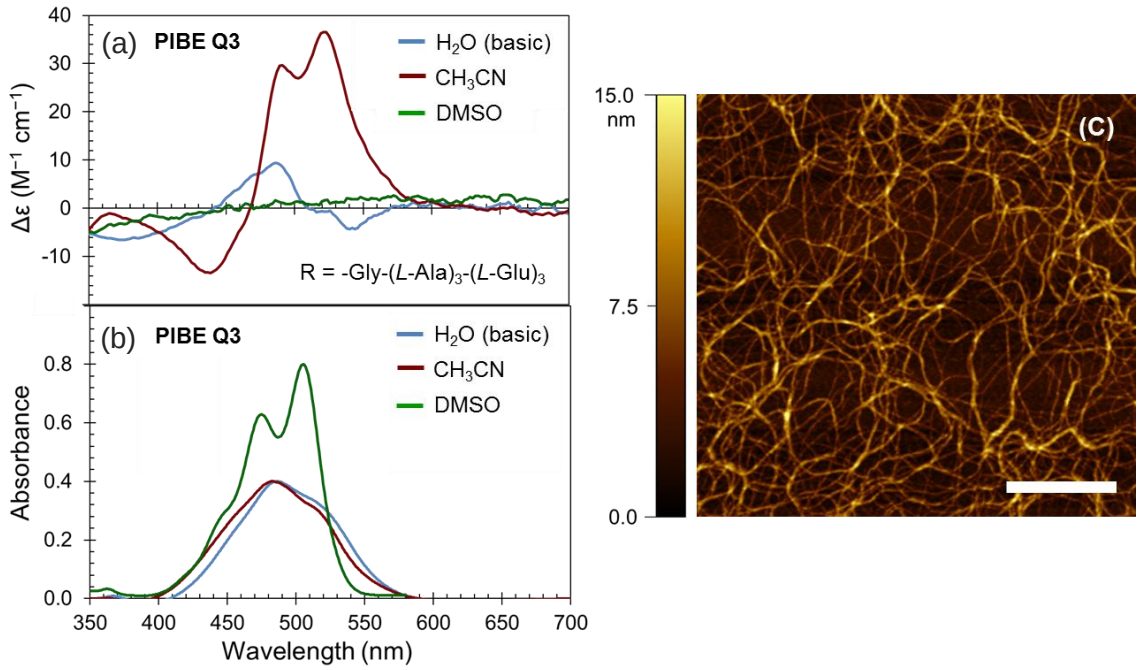

Figure 4.6 CD and UV-vis spectra of perylene imide bisester **Q3**: (a) CD spectra of PIBE **Q3** indicating solvent-responsive, chiral self-assembly behavior; (b) UV-vis spectra of PIBE **Q3** showing solvent-dependent changes in the modes aggregation; (c) AFM image of nanofibers formed by the self-assembly of PIBE **Q3** (scale bar = 1 μm). (Figure adapted from ref. 177 with permission from Taylor and Francis.)

4.3 Conclusions

A series of chiral peptide-functionalized perylene imide molecules were designed and synthesized to examine the effect of peptide chirality on the self-assembly of nanofibers. An investigation was undertaken to evaluate peptide stereogenic positions, stereochemical configurations, and amphiphilic substitution along with perylene core modification as structural features impacting chiral influence. It was found that stereocenters in peptide residue positions proximal to the perylene core (1-5 units) were effective to impart helical chirality to the perylene core, while stereocenters in more distal residue positions were not seen to exert a chiral influence. Accordingly, it was observed that diastereomers involving an inverted stereocenter configuration within the proximal residues manifested spectroscopically as pseudo-enantiomers. The use of amino acids with increased side-chain steric demand in the proximal positions exhibited similar chiral behavior, but the increased steric demand was seen to diminish the intensity of the observed bisignate Cotton Effects likely due to an increased monomer separation distance or a larger torsional angle (or both) within the assembled aggregates. Amphiphilic substitution of a peptide with an alkyl chain was seen to disrupt self-assembly (as evidenced by the absence of Cotton Effects) possibly due to the formation of axial or micelle-like assemblies. On the other hand, an amphiphilic structure achieved through the modification of the perylene imide core to incorporate a bisester moiety was seen to achieve strongly exciton-coupled, solvent-responsive self-assembly into long, chiral nanofilaments observed by AFM, advancing such bisester moieties as good candidates for future self-assembly studies. Among the compounds studied, band-like features seen at longer wavelengths in the CD spectra were found to correlate with the helical configuration of the self-assembled fiber, and are proposed as interchain excimers delocalized through the helical stack which interact with circularly polarized light to produce a dichroism with a sign matching that produced by the configuration of the helical fiber. These structural and spectroscopic observations highlight the importance of stereogenic positions and the nature of the amphiphilic structural design within self-assembling peptide-substituted perylene imides.

Chapter 5

Functional Organic Semiconductors Assembled via Natural Aggregating Peptides

5.1 Introduction

The emergence of complex molecular assemblies in natural biological systems highlights the potential of using proteins and peptides to rationally encode the assembly of functional synthetic structures in water.[179–181] For example, while the peroxiredoxin (Prx) family of proteins principally exist as obligate homodimers that further self-assemble into toroidal oligomers,[182] some Prx proteins can be induced to form other supramolecular assemblies[183] such as toroidal stacks,[184,185] tubes,[182,186] clusters,[187] and cages.[188] Identifying the native binding interfaces opens the possibility of exploiting them as building blocks in hybrid materials. Such materials may then be used in devices with entirely different functionalities from their parent proteins. Here, we advance this idea by augmenting organic semiconductor materials with peptides identified from Prx proteins to create organic semiconductor assemblies and transistor devices.

Central to the Prx architectures is the antiparallel β-continuous interface that enables the non-covalent dimerization of two protein units via the same β-strand of

each. Isolation of the β-strand peptides (typically a 7-8 amino acid sequence) out of such interfaces from a variety of protein types has been shown to yield sequences which show liquid crystallinity and which intrinsically self-assemble into nano-architectures while also retaining some properties of their parent protein interfaces.[18] Thus, peptides collected from these types of naturally optimized protein interfaces[129,131] are excellent candidates as tectons for synthetic self-assembly.[18]

While natural peptide interfaces have yet to be exploited in electronic devices, a number of related studies using natural materials highlight the potential of this approach to create new properties and applications.[189] For example, peptides,[190] natural proteins,[191] and DNA-based biopolymers derived from meat processing waste[192] have been used as insulating gate dielectric layers in field-effect transistors. Peptides, proteins, and DNA have also been explored as the active layer components of transistor devices;[193–196] however, this approach is hindered by the wide bandgap and low conductivity of the naturally available electroactive units. Coupling peptides to synthetic organic semiconductors offers a more promising avenue to exploit peptide assembly in the conductive components of electronic devices.[15,70,74] Non-natural peptides have been used to control the assembly of synthetic molecular semiconductors[22,27,79,88] and have been shown to enhance change mobilities in organic photovoltaic and field-effect transistor devices.[197]

Herein, is presented a new family of bioelectronic materials featuring the semiconducting molecule perylene diimide coupled to derivatives of the natural self-assembling peptide identified in the bovine Prx3 protein. The β-continuous interface is retained in the hybrid material upon triggered aggregation of nanofibers. The electronic coupling between neighboring perylene diimides is profoundly affected by the peptide tecton, as revealed by optical spectroscopy. These new properties are exploited through fabricating a water-processed bioorganic field-effect transistor (biOFET) based on a native β-interface.

5.2 Results and Discussion

5.2.1 Material Design

Scheme 5.1a illustrates the natural self-assembly of the Prx3 protein via a β-continuous interface with the IKHLSVN sequence. Before attempting to synthesize this sequence and couple it to perylene diimides (Scheme 1b), the synthetic route must be carefully considered. Standard solid-phase peptide synthesis (SPPS) protocols is used to access the 7-mer peptide[88,198] and after cleaving from the resin, the peptide amine groups are condensed with perylene anhydride precursors in molten imidazole.[86,88] Accordingly, the native IKHLSVN sequence presented the possibility of amine condensation reactions at both the peptide amino terminus as well as on the lysine side-chain.

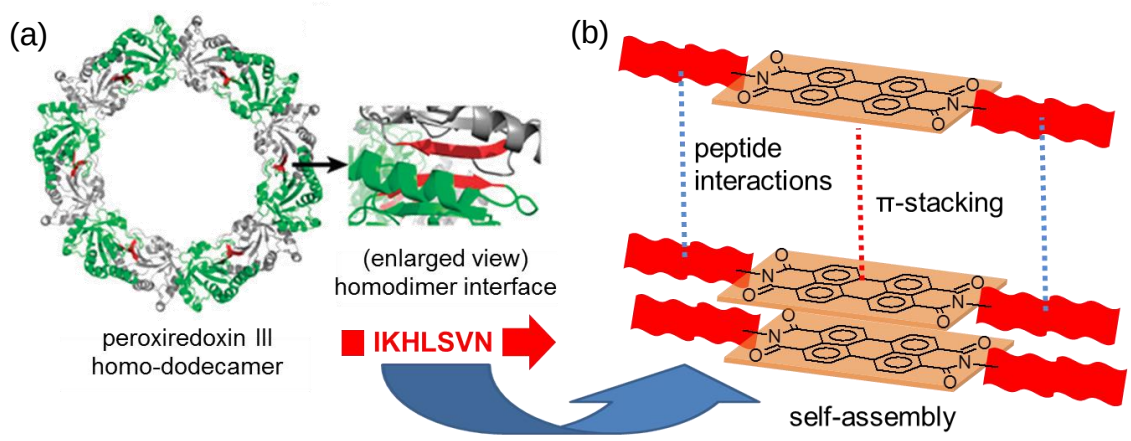

Scheme 5.1 (a) Protein homo-oligomer (pdb crystal structure for peroxiredoxin III (Prx3) homo-dodecamer (1ZYE) with enlarged view into the homodimer IKHLSVN peptide interface (interface contacts shown in red, as determined by PISA software). (b) Incorporation of the modified IKHLSVN interface peptide into a perylene diimide, yielding organic semiconductor nanofiber self-assembly from perylene core π-stacking directed by interface peptide β-sheet formation. (Scheme adapted from Eakins et al.[199] with permission from Wiley-VCH.)

While perylene imides formed exclusively with the lysine side-chain were initially synthesized as test compounds **12** and **12H**, coupling through the peptide amine

terminus was of primary interest since it would not disrupt the β-interface. This issue was addressed via two alternate strategies. The lysine residue of the original IKHLSVN sequence could either be protected until after forming the imide, or it could be replaced with arginine to permit the terminal coupling mode depicted in Scheme 1b (i.e., IRHLSVN).

Based on residue substitution matrices, which assess the probability of a given amino acid substitution in natural systems,[200,201] arginine was expected to be a favorable natural mutation and synthetically advantageous. While acting as a favorable natural replacement preserving the charged character of the lysine position in the peptide sequence, arginine also afforded the advantage of being inert toward the amine condensation reaction.

The primary aggregating IRHLSVN sequence was further augmented at either end with groups to control its hybridization with perylene and to manipulate the hybrid material, as shown in Scheme 5.2a. The opposite end to where the perylene imide core is to be coupled featured three glutamic acid residues. These ionizable residues assisted with solubility of the final peptide-perylene imide product and also provided a means to invoke pH-triggered self-assembly in the compounds.[22,23,79,88,97] At the other end, a two-carbon linking unit with a reactive amino moiety was added to provide a low steric demand spacer unit between the perylene core and the central binding region of the peptide.

Using this three-region strategy, two versions of the peptide moiety were synthesized in order to permit two modes of attachment to the perylene imide core and investigate how the peptide assembly influenced the electronic properties of the core. In the "forward-attached" case, the peptide was attached via the amino terminus using a glycine linker such that peptide backbone extends away from the core with an N to C orientation. In the "reverse-attached" case, the peptide was attached via the carboxyl terminus using an ethylamino linker, allowing reversal of the peptide backbone orientation to C to N extending away from the core. This did not simply represent the reversal of residue sequence order relative to the core (which would conserve the N to C peptide backbone orientation relative to the perylene imide core); rather, as shown Scheme 5.2, this design produced compound

pairs in which the same central binding sequence is attached in each compound within the pair by opposite ends of its backbone with the -Glu-Glu-Glu region always positioned distal to the perylene imide core.

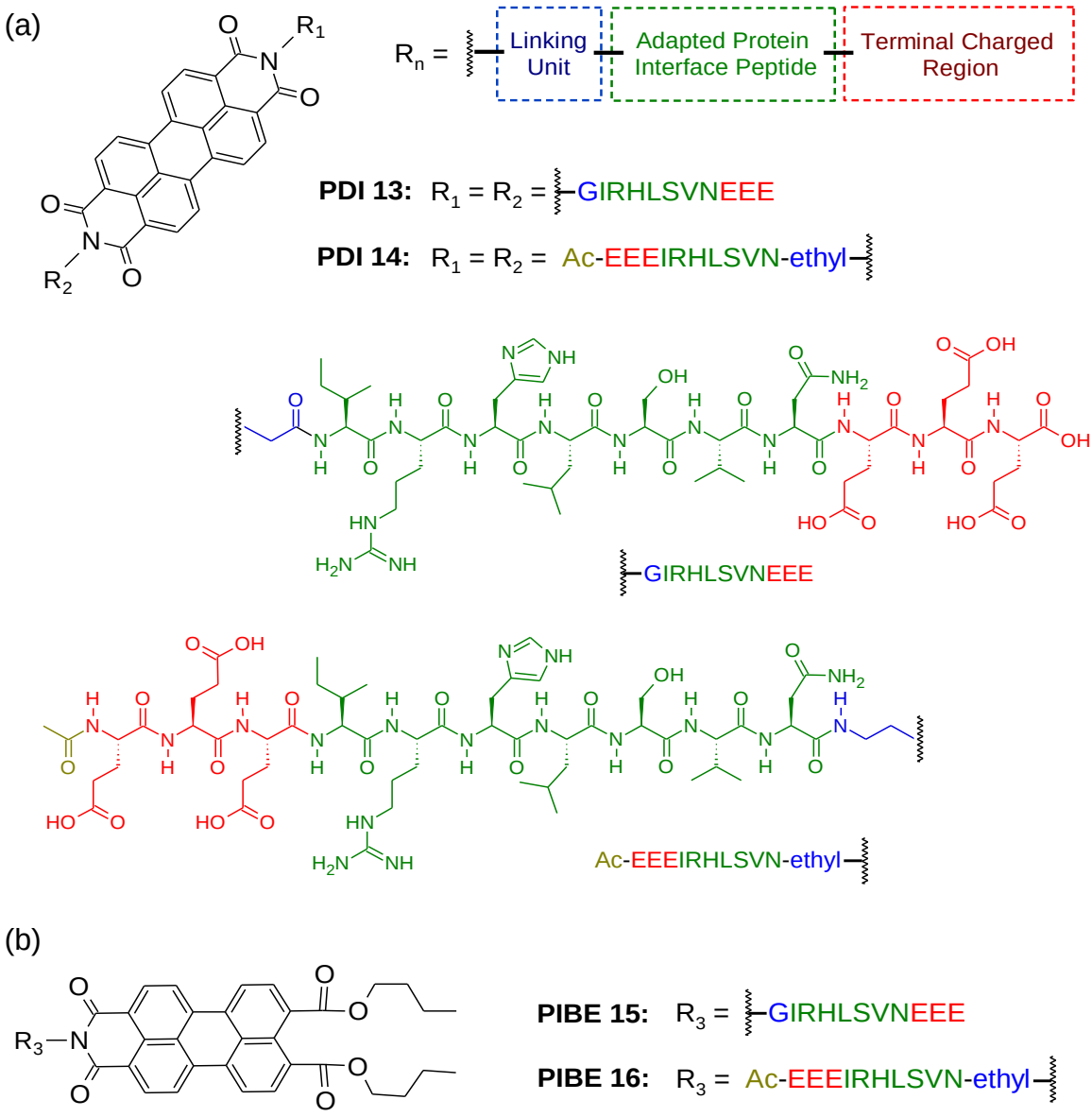

Scheme 5.2 Structures of the compounds investigated in this study, employing adaptations of the Prx3 homo-dodecamer protein interface peptide: (a) Dipeptide-PDIs **13**, **14**, and (b) Peptide-PIBEs **15**, **16**. (Scheme adapted from Eakins et al.[199] with permission from Wiley-VCH.)

Additionally, for the forward- and reverse-attached peptide modes, two different perylene imide core variations were examined for self-assembly using the adapted

Prx3 interface. Compounds **13** and **14** represented a complementary pair of symmetrically disubstituted perylene diimides (PDIs), while compounds **15** and **16** provided an analogous pair of perylene imide bisesters (PIBEs) each substituted with a single peptide substituent.

5.2.2 Solution Preparation and Self-Assembly Process

Solutions of compounds used for spectroscopy were prepared using the same methods and self-assembly processes as those described in Chapters 3-4 by diluting small aliquots of compound stock solutions into water or DMSO. The solvent used for the stock solutions, however, was changed to accommodate the needs of the analyses undertaken. Stock solutions to be used for UV-vis spectroscopy were prepared in TFA (for the PDIs) and HFIP (for the more acid-labile PIBEs), yielding aqueous solutions with residual acid upon dilution. Stock solutions to be used for CD spectroscopy in the visible range were prepared in 2% aqueous pyridine, while stock solutions to be used for CD spectroscopy in the UV range were prepared in 0.01 M NaOH (to avoid UV interference from pyridine) and then promptly analyzed (to prevent potential degradation from prolonged exposure to NaOH).

5.2.3 CD Spectroscopy Methodology

CD spectra were collected in both the UV and the visible ranges of the spectrum to assess compound self-assembly. Here it is noted that the CD spectra in Chapters 3-4 did not examine the UV region of the CD spectrum due to the strong interference from the residual pyridine present in the desired solutions for those studies. Here, however, the UV region of the spectrum is examined to address important considerations about the peptide substituent behavior during chromophore self-assembly. Solution analysis in the UV was enabled through careful preparation of stock solutions of the compounds in dilute NaOH as outlined in Section 5.2.2.

For all CD spectra presented in this chapter, HT voltages were maintained below 600 V with most spectra exhibiting HT profiles below 500 V. Sloping of the HT

data baseline (indicative of scattering) was moderately observed at longer wavelengths (in the visible spectra) and at the shorter wavelengths (in the UV spectra), but the impact of the scattering was determined not to compromise the spectral data acquired.

5.2.4 Aggregation in Peptide-Perylene Imide Conjugates

Since the peptide sequences to be coupled with perylene imides were adaptations of the original Prx3 peptide, synthetic peptides lacking the perylene imide were first compared with the original peptide. Several complementary experiments confirmed that the adapted peptides retained the strong β-sheet forming behavior of the original sequence after the modifications. Spectral features indicative of β-sheets are characterized in the UV range of CD spectra via a spectral profile with a positive band maximum near 190-200 nm followed by a single, often broad, and trailing negative band with a minimum near 215-220 nm.[115] Consistent with this profile, Figure 5.1a shows that each of the peptide mutants retains the same CD spectral shape that characterizes β-sheets (Figure 5.1b) in the native sequence. The formation of β-sheets was further verified via a thioflavin-T fluorescence assay of the peptide mutations (Figure 5.1c). When this fluorophore binds to β-sheets, its excitation and emission maxima shift from 385 and 445 nm to 450 and 485 nm, enabling simple quantification of the extent of β-sheet assembly,[202,203] which is what was observed when thioflavin-T was blended with the native and mutant peptide sequences investigated here. Affirmation was further seen in a turbidity assay of the same samples (Figure 5.1d). These observations were found to be in agreement with analysis of the amide I band of the IR spectra[98–101] for the targeted GIRHLSVNEEE and Ac-EEEIRHLSVN-ethylamine sequences (Appendix C, Figures C.26, C.27), which displayed a band near 1630 cm^{-1} indicative of β-sheet structures. The β-sheet interactions expressed by the native peptide variants, were ultimately found to produce ordered peptide nanostructures as observed via transmission electron microscopy (Figure 5.1e-h). The results in Figure 5.1 confirmed that each of our modifications to the native sequence were innocent with respect to self-assembly; the lysine residue can be replaced with arginine, short linking units can be added, likewise for solubilizing glutamic acid residues.

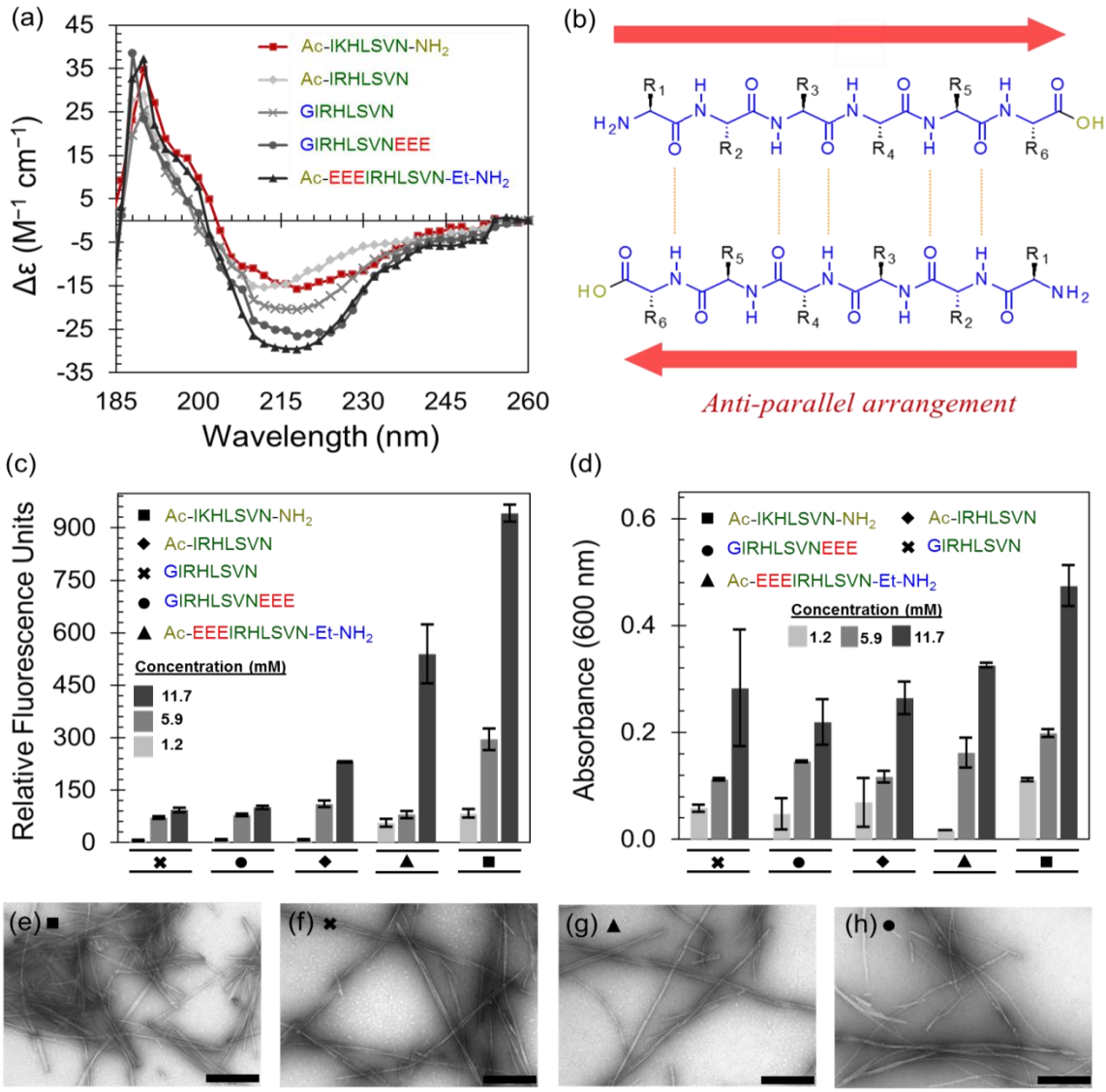

Figure 5.1 (a) CD spectra of the native peptides for five relevant sequence variations (aqueous buffer solution, 0.1 mg/mL peptide concentration). (b) Illustration of an anti-parallel β-sheet structure. (c) Results of a thioflavin-T assay of the native peptides (24 hour duration, at three peptide concentrations). (d) Results of a turbidity assay of the same solutions measured in the ThT assay. Selected TEM images of the self-assembled native peptide nanofibers are shown for: (e) Ac-IKHLSVN-NH_2, (f) GIRHLSVN, (g) Ac-EEEIRHLSVN-ethyl-NH_2, and (h) GIRHLSVNEEE (all scale bars = 200 nm). Peptide sequence Ac-IRHLSVN did not form large-scale nanofibers under the range of conditions tested. (Figure adapted from Eakins et al.[199] with permission from Wiley-VCH.)

The CD signature of peptide β-sheet formation was also retained in the peptide-perylene imide conjugates. Seen in Figure 5.2, PDIs **12**, **12H**, **13**, **14** and PIBEs **15**,

16 all displayed CD spectral profiles in the UV range consistent with that of β-sheet secondary structures. These spectra importantly show that the peptide substituents themselves are actively involved in the self-assembly of secondary structures for the overall peptide-perylene imide conjugates and are not just unnecessarily complex substituents exerting simple steric effects on the perylene core.

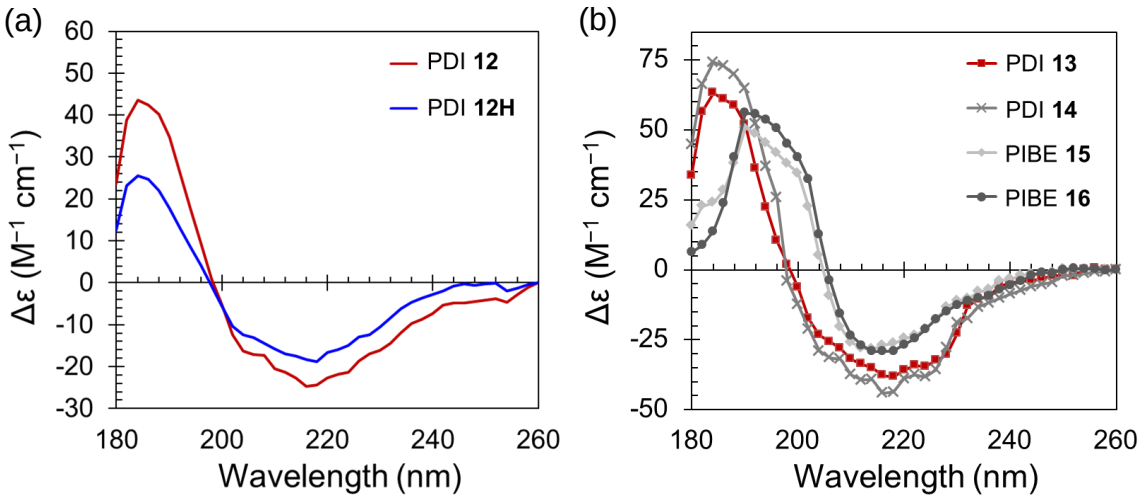

Figure 5.2 CD spectra along the 180-260 nm ultraviolet range, showing peptide substituent β-sheet formation in 0.01 mg/mL aqueous solutions of: (a) self-assembled test compounds **12**, **12H** and (b) self-assembled PDIs **13**, **14** and PIBEs **15**, **16**. (Figure adapted from Eakins et al.[199] with permission from Wiley-VCH.)

Overlapping absorption and fluorescence from the perylene chromophore meant that the thioflavin-T assay could not be applied to these hybrid materials; however, the amide I bands of the IR spectra[98–101] for the PDIs and PIBEs (Appendix C, Figures C.28-C.31), also exhibited a band near 1630 cm^{-1} consistent with β-sheet structure formation.

5.2.5 Optical Spectroscopy of the Aggregates

Assembly of perylene moieties results in significant changes to visible optical absorption spectra. Since imide substituents do not directly affect the frontier molecular orbitals responsible for the visible electronic transition,[39] spectral changes can be used to understand how the substituents affect the relative orientations and

electronic coupling between neighboring perylene monomers.[126,204] The UV-visible absorption spectra shown in Figure 5.3 show that solutions of each of the peptide-substituted perylene imides exhibited clear signatures of aggregation and reveal important distinctions between each.

Solutions of PDIs **13**, **14** in DMSO (Figure 5.3a) both displayed a monomeric spectral profile with minimal differences between each other. Their monomeric nature was indicated by a band with a distinctive three-peak vibronic progression with ~1400 cm^{-1} splitting (indicative of vibrational coupling to the C=C stretching mode) and diminishing intensity for higher energy transitions. However, in aqueous solution, spectra of compounds **13** and **14** were dramatically different, indicating very different modes of monomer self-assembly. In water, PDI **13** displayed a very broad spectral profile, echoing traits of spectra reported for ordered liquid crystalline phases of PDI derivatives.[152–156] The suppression of vibronic structure, along with the enhanced low energy absorption beyond 600 nm, suggest strong coupling between delocalized π-orbitals, which is a highly desirable property for electronic devices. Moreover, a Cotton effect observed in the visible region of the CD spectrum (inset, Figure 5.3a) indicated that the peptide directs assembly of the perylene monomers into ordered, chiral aggregates.[80,119]

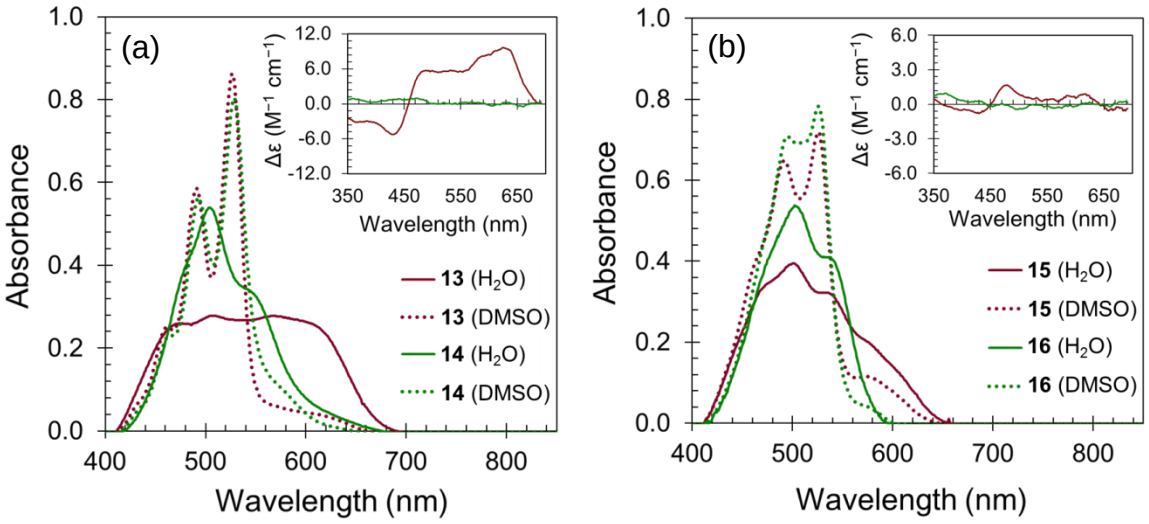

Figure 5.3 UV-vis spectra in DMSO and water with visible CD spectra of 6 μM aqueous solutions (insets) for (a) PDIs **13**, **14** and (b) PIBEs **15**, **16**. (Figure adapted from Eakins et al.[199] with permission from Wiley-VCH.)

PDI **14** – in which the peptide backbone orientation is reversed – gave a very different spectral profile than PDI **13** in water, in spite of their similar composition. The absorption spectrum of PDI **14** does not show the broadening to low energy found for PDI **13**, yet it still differs considerably from the monomer spectrum. In PDI **14**, the intensity of the 0-0 vibronic transition near 540 nm is diminished relative to the 0-1 transition near 500 nm. This intensity pattern is a signature of an H-aggregated system in which co-facially stacked perylene units are rotational displaced with minimal lateral displacement.[55] For strongly exciton-coupled H-aggregates, the 0-0 transition is dipole forbidden, while higher vibronic transitions gain intensity via symmetry breaking vibrational modes. Observing a weaker 0-0 transition relative to the 0-1 transition, as in this case, is expected in a weaker coupling regime and when there is a rotational offset between chromophores.[109] The aggregates formed by PDI **14**, however, did not show a Cotton effect in the visible region of the CD spectrum (inset, Figure 5.3a), indicating that the assembly of the perylene units did not produce a chirally ordered arrangement. The contrasting absorption spectra of PDIs **13** and **14** for the aqueous solutions show that coupling between neighboring electronic units can be impacted by the backbone orientation of the naturally derived β-sheet forming peptide.

In contrast to PDIs **13** and **14**, the spectral profiles of PIBEs **15** and **16** (Figure 5.3b) were mutually very similar. In DMSO, PIBEs **15**, **16** both exhibited vibronically structured spectral profiles consistent with predominantly monomeric species; however, the vibronic peak ratio and the presence of a feature near 580 nm suggested some extent of aggregation. Regardless, a distinctive transition to a more highly aggregated state was evident in the aqueous solutions of PIBEs **15**, **16**. Similar to PDI **14** (above), the spectra of PIBEs **15** and **16** in water both displayed traits consistent with H-aggregate formation, and Cotton effects were absent in the visible CD spectra (inset, Figure 5.3b). The band observed for PIBE **15**, however, expressed a shoulder feature between 580-660 nm, suggesting additional contributions from some other aggregate species with a band-like character similar to that seen for PDI **13**. The absorption spectrum of PIBE **16** was slightly red-shifted compared to PIBE **15**, and with a slightly different vibronic ratio; however, these differences were minimal relative to the comparison of PDIs **13** and **14**. Since the same peptides are compared in both pairs of hybrids, the spectral similarity of

PIBEs **15** and **16** may be explained by greater orientational freedom of the perylene moieties with aggregating peptides on only one side. Conversely, the peptide β-sheets in the symmetrical structures of PDIs **13** and **14** appear to constrain the perylene moiety in a specific configuration, which is strongly π-stacked in the case of PDI **13**.

The reversed peptide backbones of PDIs **13** versus **14** suggested the possibility of blending the two materials to assemble them via anti-parallel β-sheets that more closely mimic the natural protein system. Such an arrangement could be supported in alternating stacks of PDIs **13** and **14**, and may result in modified electronic properties for the central PDI core. However, equimolar binary mixtures of PDIs **13** and **14** were not found to produce any synergistic spectroscopic effects, rather the spectra could be explained by a statistical mixture of **13** and **14** (Figure 5.4).

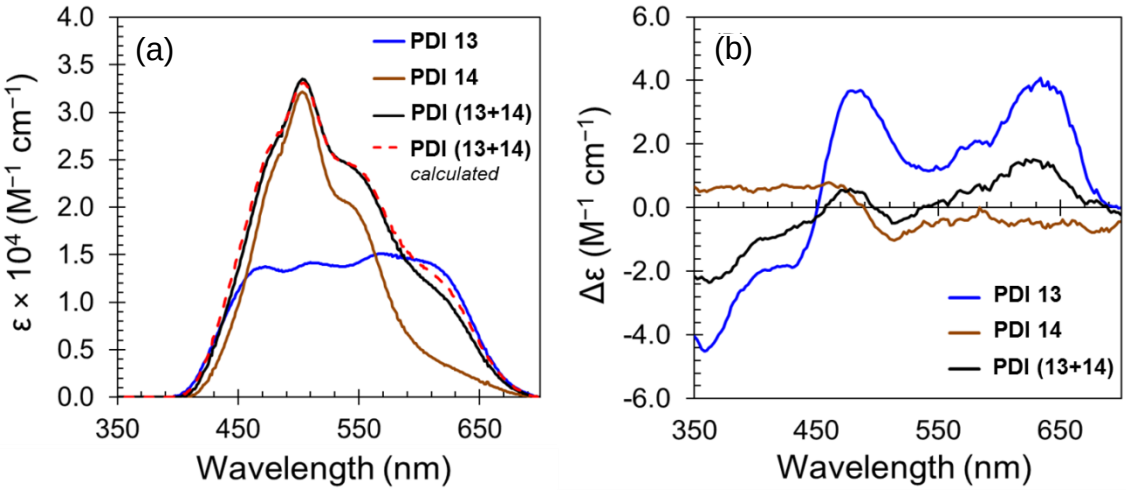

Figure 5.4 Spectroscopic evaluation of 5 μM aqueous solutions of PDIs **13** and **14** made by injecting small volumes of monomeric TFA stock solutions into water to induce aggregation. (a) UV-vis spectral profiles for solutions of PDIs **13** and **14** alone as well as a 1:1 molar mixture of **13**+**14** (mixed concentrated equimolar stock volumes in TFA prior to injection into water). The spectral profile of the mixture matches that of a calculated linear combination of **13** and **14**, showing no synergistic self-assembly in the mixture. (b) CD spectral profiles for 5 μM solutions of PDIs **13** and **14** alone as well as a 1:1 molar mixture **13**+**14** (mixed concentrated equimolar stock volumes in TFA prior to injection into water). (Figure adapted from Eakins et al.[199] with permission from Wiley-VCH.)

These results do not exclude the possibility of realizing an anti-parallel self-assembly motif, but they suggest that the assembly conditions may need to be optimized and the linker groups refined (length, conformational flexibility, etc.) in order to achieve the desired registry between neighboring molecules.

5.2.6 Nanostructure Formation

The aggregate species spectroscopically characterized in solution were confirmed, in most cases, to result from ordered nanofiber assemblies that were visualized by atomic force microscopy (AFM) and transmission electron microscopy (TEM). As shown in Figure 5.5a-c, PDIs **13**, **14**, and PIBE **15** assembled into diffusive interlaced networks of narrow fibers. The notable exception was compound PIBE **16** (Figure 5.5d), which appeared to form only amorphous, plate-like accretions under the conditions tested.

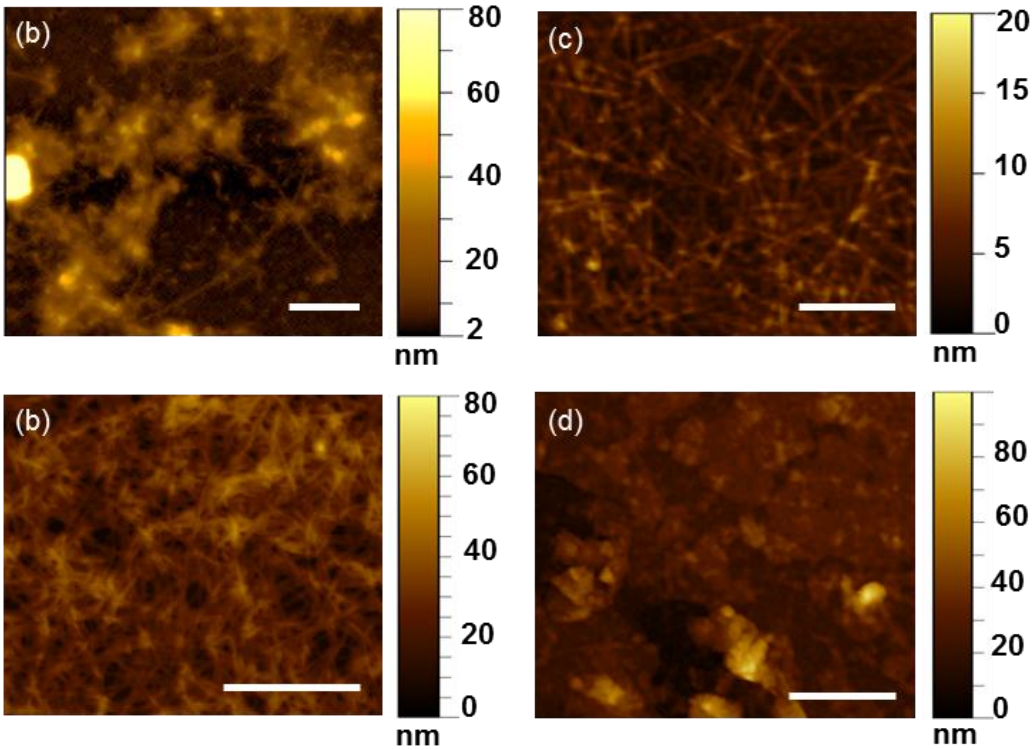

Figure 5.5 AFM images of dry nanofibers deposited on mica of (a) PDI **13** (scale bar = 500 nm), (b) PDI **14** (scale bar = 500 nm), (c) PIBE **15** (scale bar = 25 nm), and (d) PIBE **16** (scale bar = 500 nm). (Figure adapted from Eakins et al.[199] with permission from Wiley-VCH.)

Extensive fibrillar formation was also seen for PDIs **13**, **14** via TEM, as shown in Figure 5.6. Out of the fiber-forming compounds, PDI **13** appeared to have a slight morphological distinction, presenting clusters of fiber networks with greater fiber density, length, and width. By AFM, the fiber segments formed by PDI **14** and PIBE **15** appeared to be roughly 100-200 nm in length; whereas the fibers formed by PDI **13** were longer, being roughly 200-300 nm long within the fiber clusters and exceeding a micron for isolated strands visible between the clusters. By both TEM and AFM, PDI **13** was clearly seen to form fibers of greater size than PDI **14**, with PDI **13** forming more ribbon-like structures in comparison to the thread-like assemblies of PDI **14** (Figure 5.6).

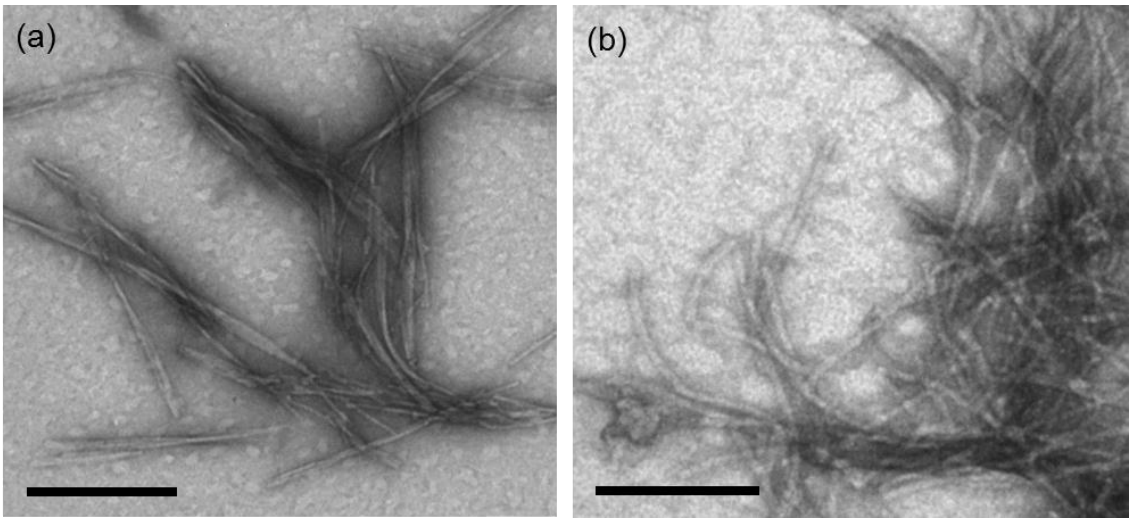

Figure 5.6 TEM images of self-assembled nanofibers of (a) PDI **13** (scale bar = 200 nm) and (b) PDI **14** (scale bar = 100 nm). (Figure adapted from Eakins et al.[199] with permission from Wiley-VCH.)

The morphological differences between compound pairs **13**, **14** and **15**, **16** (along with the spectroscopic distinctions noted previously) highlight the relevance of the mode of peptide sequence attachment toward self-assembly outcomes. Comparison of the morphologies observed via microscopy informed by the spectroscopic indications from solution suggested that PDI **13** provided larger, longer range nanostructures which were the most promising for field-effect device applications out of the four compounds studied.

5.2.7 OFET Fabrication and Performance

After examining the peptide-driven aggregation of each compound, bio-organic field-effect transistor (biOFET) devices were fabricated using them as the active semiconductor layer. As shown in Figure 5.7a,b the devices were fabricated on highly doped silicon substrates (serving as the back gate) using a bottom-contact gold electrode channel configuration, with a spin coated layer of polydimethylsiloxane PDMS acting as dielectric layer. Flakes of the perylene imide active material were grown via slow solvent evaporation in small vials (from a 1:4 pyridine/water solution heated overnight to 75-80 °C) and transferred to span across an electrode channel on substrates with pre-patterned electrodes applied onto a PDMS dielectric layer.

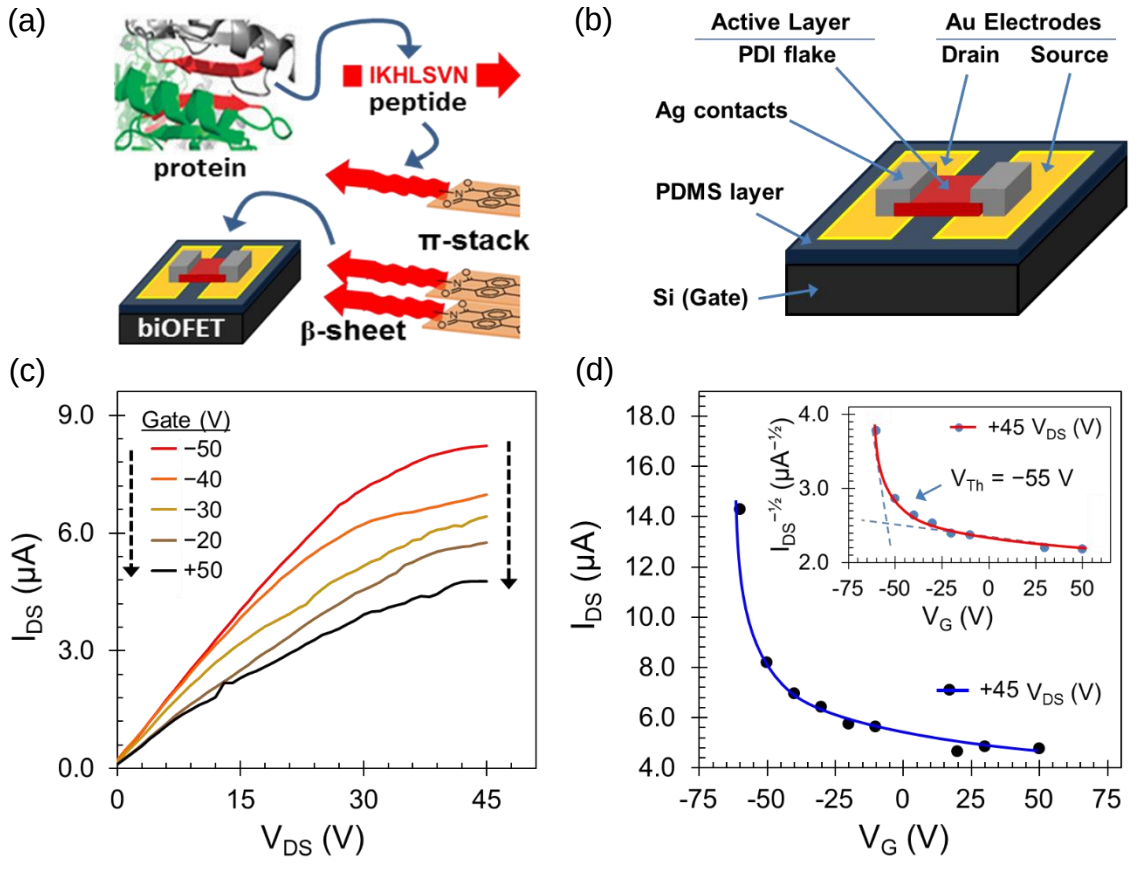

Figure 5.7 Device performance measurements of an organic field-effect transistor fabricated utilizing PDI **13** across a 40 μm channel: (a) Protein to device development pathway; (b) Device fabrication schematic; (c) Output characteristics; (d) Transfer characteristics with threshold voltage evaluation (inset). (Figure adapted from Eakins et al.[199] with permission from Wiley-VCH.)

Contact between the flakes and the gold electrodes were enhanced by the conductive silver paste. This approach was taken because the films were too brittle to survive mechanical contact with the shadow mask required for thermal evaporation of contacts. The PDMS layer also acted as an adhesive for the flakes on the device substrate. The brittle nature of the active material samples also made it very easy to break the devices by mechanical actions post deposition onto the PDMS films.

Of the materials examined in this study, only PDI **1** yielded functioning devices, giving output and transfer characteristics as shown in Figure 5.7b,c. Although n-type semiconducting behavior was anticipated as being most probable for PDI **1** because of the high electron affinity of the perylene core and numerous examples of n-type behavior reported for perylene imide materials in literature,[205] the output characteristics of PDI **13** (Figure 5.7c) are consistent with weak p-type behavior, yielding a decreasing current with increasing positive gate bias. Ongoing investigations of this unexpected behavior may reveal the role of the peptide and associated ions in modulating charge injection and transport in this material. Using these output curves to extract the ratio between the magnitude of the drain current (I_{DS}) at the highest and lowest gate voltage (I_{DS} taken at V_{DS} = 45 when $V_G = \pm 50$, the on/off ratio (I_{on}/I_{off}) for the device was evaluated to be 1.7. From the transfer plot in Figure 5.7c, the threshold voltage for the device was evaluated to occur near −55 V. The poorly defined channel dimensions in this contact configuration prevented deeper analysis of the device response. It should also be noted that the PDMS layer is on the order of 10 μm thick and therefore the field dependent nature of the PDI **13** may be more apparent if a thinner dielectric or a material with a higher dielectric constant is used. The field dependency was observed on several samples and the example shown in Figure 5.7c,d is representative of the behavior and was observed, irrespective of the doping polarity of underlying Si back gate.

The p-type (hole-conducting) behavior observed for the device performance in Figure 5.7 is notably rare for devices made from perylene diimide materials. PDI materials almost invariably exhibit n-type (electron-conducting) properties in reported OFETs, as exemplified by a recent review of such PDI devices.[205] Nevertheless, a few p-type examples of PDI OFETs have been reported by Pron

and coworkers.[206] Due to its rarity, therefore, the p-type PDI biOFET behavior observed here merits further discussion.

Theoretically, all organic semiconductors should be capable of conveying either electron vacancies (holes) or electrons as charge carriers (depending upon which is most efficiently relayed through the material); however, material factors usually preferentially select one or the other.[207] Such factors include the internal molecular reorganization energy of the organic compound and the work function of the device electrode relative to the HOMO and LUMO of the organic semiconductor.[207–210] Despite the theoretical possibilities, in practice, the intrinsic instability of most organic anions in air and water[145,211] and complications from oxygen-trapping within the organic materials[212,213] cause p-type behavior to be most common in organic semiconductors, generally.[214] On these points, PDIs are distinctive, having high electron affinity and good n-type characteristics, arising (in part) from the ability to form highly stable radical anion, dianion, and oxidized species[215–217] as well as from the ability to associate in closely packed π-planes which may inhibit the ingress of oxygen and promote greater n-type OFET stability in air.[205,218] Exceptions to n-type behavior by PDI materials in OFETs are accordingly rare. Instances of p-type PDI OFET behavior, therefore, are worth some consideration.

Pron and coworkers have reported both a *N*,*N*′-bis(triphenylamino)naphthalene diimide and a *N*,*N*′-bis(triphenylamino)perylene diimide OFET each exhibiting unexpected p-type characteristics.[206] The p-type behavior in these cases was proposed to have resulted from the amorphous nature of the thin diimide semiconducting layers applied, such that the amorphous film distribution not significantly perturb the transport pathways of holes via triphenylamine segments but strongly impeded the transport of electrons through diimide core segments.[206] A similar explanation seems less certain for the biOFET reported here in Figure 5.7. In the OFETs reported by Pron et al., the triphenylamino *N*-substituent used is also a known p-type organic semiconductor, and morphologically influenced charge carrier pathways to p-type outcomes are plausible. Yet for the biOFET in Figure 5.7, the peptide substituent seems unlikely to function as a p-type semiconductor. Although cyclic peptides have been utilized to modulate charge transfer between appended chromophores[219] and self-assembled cyclic peptide nanotubes alone have

been shown to be minimally conductive (with current only in the nanoamp range),[194] in OFETs, peptides normally behave as insulating dielectric materials.[190] Even a highly ordered peptide β-sheet domain within the peptide-PDI material of the biOFET in Figure 5.7 seems unlikely to serve as a p-type semiconductor suitable to convey current in the microamp range observed. Nevertheless, the non-redox protein apoferritin has been successfully utilized as the semiconducting active layer in a reported biOFET with operating output in the microamp range.[193]

Another aspect to consider is that of charge injection into the peptide-PDI semiconductor active layer. In an OFET device, charge is usually injected into the organic semiconductor via metal electrodes (as is the case with the biOFET reported here). At this interface, an important property is the work function of the metal (defined as the energy needed to move an electron to the vacuum level[209]). For charge carriers (electron or holes) to be efficiently injected into the organic semiconductor from the metal electrode, a metal should be chosen with a work function that matches either the HOMO or the LUMO of the organic semiconductor within a few tenths of an electron volt.[208,220] Although larger differences may be operable, significant energetic misalignment will increase in the contact resistance of the device.[209] Selecting an appropriate metal for the electrode contact depends upon the energy levels of the organic semiconductor to be used as well as the nature of the device to be fabricated. For p-type OFETs, the metal used for the electrodes should have a work function near that of the organic semiconductor HOMO energy level; conversely, for n-type OFETs, the electrode metal work function should be near that of the LUMO energy level.[209] As shown in Figure 5.7b and Figure 5.8a, the biOFET reported in this chapter employs a dual metallic contact; the first is the primary gold electrode fabricated with the silicon device substrate, whereas the other is an amorphous silver contact (from the silver paste used to affix the organic semiconductor flake on top of the gold electrodes). Using the electrochemically determined reduction and oxidation potentials versus the ferrocene/ferrocenium redox couple (−1.0 V and 1.1 V, respectively) reported for a typical PDI with an unsubstituted rylene core,[221] HOMO and LUMO levels were calculated according to previously reported methods[222] and compared to the values of the gold and silver metal work functions (Φ)[210] as illustrated in Figure 5.8b.

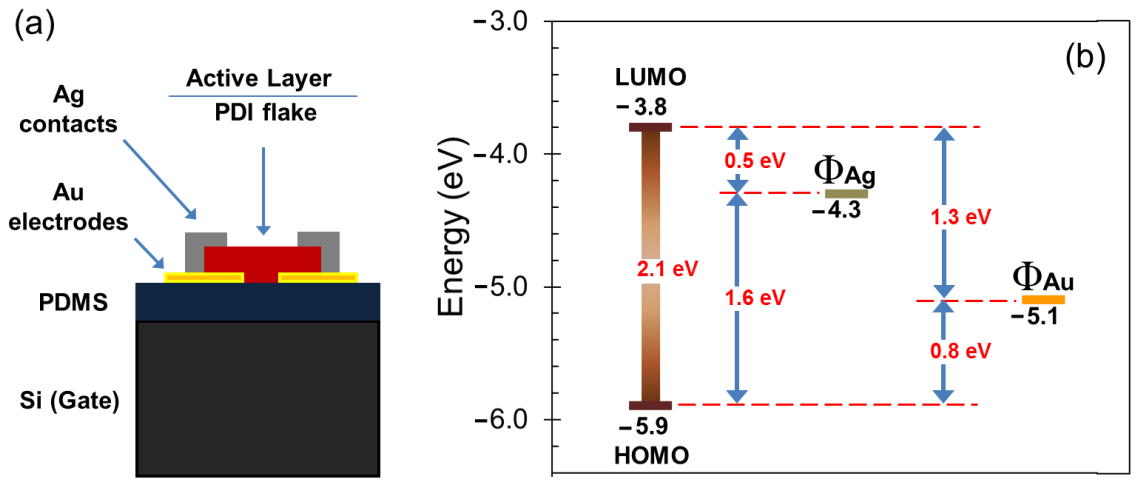

Figure 5.8 Evaluation of a device with a dual metallic electrode contact: (a) Device fabrication schematic; (b) A comparison of the HOMO and LUMO energy levels for a typical PDI with an unsubstituted rylene core with to work functions of gold and silver. Energy values are reported with respect to vacuum level (0.0 eV).

Although many metals have a lower work function than gold and should, in principle, work better for n-type device electrodes due to better energy level alignment with typical organic semiconductor LUMOs, in practice these metals often degrade or form oxides which make them unsuitable. The stability and lack of reactivity by gold, therefore, make it desirable, and it has been shown to make excellent contacts for n-type materials in spite of the added contact resistance.[214,223] In fact, the vast majority of reported PDI OFETs use gold for the device contact electrodes. In light of this background, the biOFET presented in this chapter would still be expected to exhibit n-type performance despite its work function being closer to the HOMO level. Moreover, the proximity of the silver work function to the LUMO (see Figure 5.8b) might be expected to enhance such an outcome. The observed p-type behavior, therefore suggest that a combination of morphological factors (such as those proposed by Pron et al.[206]) and the proximity of the gold work function to the HOMO level (Figure 5.8b) together promoted the atypical injection of holes as charge carriers through the PDI material.

5.3 Conclusion

We have created a new class of hybrid materials featuring organic semiconductors augmented with aggregating β-sheet peptide interfaces derived from natural peroxiredoxin proteins. We confirmed that the peptides retain their β-sheet forming propensity when additional amino acids and linker units were added to manipulate their solubility and coupling with perylene imides. A series of perylene imides substituted with the same core peptide sequence (IRHLSVN) were synthesized to compare the effect of the number of peptide substituents and the directionality of their connectivity. Optical absorption and circular dichroism spectroscopy revealed distinct differences in the electronic coupling between neighboring perylene units imparted by the peptides, which was also manifest in different fiber morphologies. The bis-substituted material where the peptides were oriented in the N-to-C direction (away from the perylene diimide) resulted in strong π-stacking and long-range order. These properties were exploited in the realization of a biOFET device with unexpected p-type behavior. The approach outlined highlights the opportunity to create hybrid functional materials with new properties by repurposing natural peptide sequences to encode their self-assembly.

Chapter 6

Conclusions

Throughout the course of this study, the self-assembly and photophysical properties of several perylene imides have been explored to better understand the behavior and application of these materials. These endeavors had been roughly followed three avenues of inquiry: (1) The evaluation of structure-property relationships from a thermodynamic perspective, (2) The examination of peptide chiral effects upon properties and self-assembly, and (3) An application of the understanding gained from the rationally designed systems to effectively utilize naturally optimized peptides in bio-organic electronics. The major conclusions and outcomes from these lines of inquiry are summarized here followed by a wider view forward.

To investigate structure-property relationships from a thermodynamic perspective, a series of peptide-functionalized PDI molecules were synthesized which were designed to establish design rules for peptide-driven aggregation through incremental variations in peptide hydrophobicity, length, charge density, as well as stereocenter inversion and amphiphilic substitution. Having observed the formation of nanostructures in solution, a spectroscopic investigation of the thermodynamics and nature of aggregation for the series of peptides was implemented. It was found that non-specific effects like peptide hydrophobicity and nonsymmetrical substitution with a hexyl chain had the greatest impact on binding thermodynamics. However, more specific variations like diastereomeric substitution were also shown to have a significant impact, particularly on the dominance of H- versus π-aggregates, highlighting how peptide packing modulates coupling between PDI

units. Solvent dependent spectroscopy also highlighted the range of peptide- and PDI-based interactions responsible for aggregation in these materials.

To examine the effect of peptide chirality on the self-assembly of the perylene imide core into nanofibers, a series of chiral peptide-functionalized perylene imide molecules was synthesized. CD spectroscopy of the series evaluated peptide stereogenic positions, stereochemical configurations, and amphiphilic substitution along with perylene core modification as structural features impacting chiral influence, and the results revealed that stereocenters in peptide residue positions proximal to the perylene core (1-5 units) were principally responsible for imparting helical chirality to the perylene core, while stereocenters in more distal residue positions were not seen to exert a chiral influence. Accordingly, diastereomers involving an inverted stereocenter configuration within the proximal residues were found to behave spectroscopically as pseudo-enantiomers. The use of amino acids with increased side-chain steric demand in the proximal positions exhibited similar chiral behavior, but the increased steric demand was seen to diminish the intensity of the observed bisignate Cotton Effects, which was likely due to increased monomer separation distance or a larger torsional angle (or both) between the assembled aggregate monomers. Amphiphilic substitution of a peptide with an alkyl chain was seen to disrupt self-assembly (as evidenced by the absence of Cotton Effects) possibly due to the formation of axial or micelle-like assemblies; however, amphiphilic structures achieved through the modification of the perylene imide core to incorporate a bisester moiety were seen to achieve strongly exciton-coupled, chiral, solvent-responsive self-assembly into long nanofilaments (as observed by AFM). Among the compounds studied, band-like features seen at longer wavelengths in the CD spectra were found to correlate with the helical configuration of the self-assembled fiber, and are proposed as interchain excimers delocalized through the helical stack which interact with circularly polarized light to produce a dichroism with a sign matching that produced by the configuration of the helical fiber. These structural and spectroscopic observations highlight the importance of stereogenic positions and the nature of the amphiphilic structural design within self-assembling peptide-substituted perylene imides.

To apply the understanding gained in this study, a new class of hybrid materials featuring organic semiconductors augmented with aggregating β-sheet peptide interfaces derived from natural peroxiredoxin proteins was produced to demonstrate an important proof-of-concept. The results reported confirmed that the peptides utilized retained their β-sheet forming propensity when additional amino acids and linker units were added to manipulate their solubility and coupling with perylene imides. The synthesized series of perylene imides substituted with the same core peptide sequence (IRHLSVN) gave valuable insight for the effect of the number of peptide substituents and the directionality of their connectivity, which has not been as widely explored in the literature. Optical absorption and circular dichroism spectroscopy revealed distinct differences in the electronic coupling between neighboring perylene units imparted by the peptides, which was also manifest in different fiber morphologies. The bis-substituted material where the peptides were oriented in the N-to-C direction (away from the perylene diimide) resulted in strong π-stacking and long-range order. These properties were exploited in the realization of a biOFET device with unexpected p-type behavior. This protein-to-device approach outlined highlights the opportunity to create hybrid functional materials with new properties by repurposing natural peptide sequences to encode their self-assembly.

Across these investigations, the results from the bisester compounds suggest that bisester moieties may be good candidates for future self-assembly studies as a perylene derivative with similar photophysical properties to PDIs, but greater solubility and solvent-responsiveness. The bisesters also highlight a very important point, which is that all of the insights gained in this study regarding the use of peptides as an agent of self-assembly may be more widely applied with other molecular systems. While perylene compounds have been the emphasis of this study, other intriguing molecules for self-assembly and bio-organic electronics abound. One such example will be discussed in the next section which looks ahead to propose future work with peptide-substituted, self-assembling systems.

Chapter 7

Future Work

7.1 Introduction

Designing systems which invoke and control the self-assembly of perylene imide chromophores is an important step toward utilizing these materials in beneficial applications such as electronic devices and sensors. While numerous, previously unknown aspects of the self-assembly and function of peptide-perylene imide systems have been revealed during this study, these discoveries yet highlight many additional questions and intriguing possibilities. These opportunities broadly reside in three categories: (1) new structural designs, (2) new applications, and (3) new materials for peptide-guided self-assembly.

First, with regard to new structural designs, the most obvious next step would be the further exploration of new peptide sequences. Through both rational design and the utilization of the multitude of promising peptides found in nature, a vast range of sequences are possible. Sequence change alone, however, may be insufficient to invoke dramatically new or advantageous modes of self-assembly. While measurable, sequence-dependent aggregate tuning was observed and quantified during this study (Chapter 3), the differences seen were small. Invoking changes of greater distinction and magnitude during tuning may require the alteration of the self-assembly design in order to capitalize on additional aspects afforded by peptide structures. To this end, residue-specific traits may be useful. For example, residues such as histidine and lysine which are capable of forming metal complexes could be

strategically used within the peptide as units to aid, alter, or tune self-assembly through the addition of metal ions. Similarly, the redox sensitivity of cysteine towards the formation of disulfide links could be employed to achieve or switch modes of self-assembly. Beyond sequence changes or residue-specific influences, the design of the underlying peptide-chromophore unit being self-assembled could also be altered. Employing two or more chromophores linked by a single peptide scaffold would bring enforced intramolecular chromophore associations in addition to intermolecular self-assembly interactions between the peptide-chromophore dimer (or oligomer) units. The imposed constraints within the unit structure would translate into further constraints for the overall mode of self-assembly of the units.

Second, with regard to applications for peptide-perylene imide compounds, applying these materials in electronic devices remains highly desirable. However, achieving suitable conductive thin film morphologies for devices during this study was unsuccessful, and the devices fabricated involved semi-crystalline flakes (Chapter 5). Developing processing methods to remedy this limitation remains an area needing further research. Structural modifications to enhance solubility may be further helpful in this effort.

Although this study focused primarily on the application of self-assembled perylene imides as semiconductors for electronic devices (Chapter 5), sensors could also be possible perylene imide applications. For example, structures involving amino acid residues capable of metal complex formation might be applied as colorimetric or fluorometric metal ion sensors provided that compounds could be designed to self-assemble in ways which exhibit discriminating photophysical responses upon complexation with different metal ions. Alternatively, the presently untapped ability of peptides to impart a chiral sense on the supramolecular chromophore architectures formed (Chapter 4) could potentially be a feature applied in chiro-optical sensors for the detection biomolecules with particular chiral configurations provided that suitable, selective target interactions could be encoded into the self-assembly design. Beyond this, a more radical sensing design might be applied using aspects of aptasensing, wherein an aptamer (perhaps a shorter aptamer) with a selective affinity to a desired target molecule could be conjugated to a peptide-perylene imide moiety. If conformational changes by the aptamer (upon target

acquisition) could be harnessed to induce spectroscopically detectible changes in the perylene imide electronic environment, sensing might be accomplished using the structural composite.

Finally, the principles described in this study for the use of peptides to aid in the self-assembly of perylene imides may more broadly be applied to other molecules of interest. Since many other moieties in addition to perylene imides also possess desirable properties for organic electronics or for sensing, applying peptides for self-assembly with these systems would continue as a wide area open for investigation.

With the preceding discussion in mind, the remaining sections of this chapter present two specific avenues for future exploration directly inspired and informed by this study.

7.2 New Structural Designs Using Lysine

The use of lysine residues in peptide sequences would offer unique structural possibilities due to the presence of its side-chain amino group. If suitable protecting group strategies were applied to guard against unwanted side-reactions during synthetic steps, the side-chain amino group could be employed as a useful peptide scaffold component enabling new structural opportunities. The side-chain amino group could be used to bond to new chromophore moieties, or it could be left available in the final synthetic product produced to act as a moiety to apply in pH triggered self-assembly, to assist in solubility of the final product, or to be available to form metal complexes. For purposes of bonding the peptide to a chromophore as was done in this study, lysine could, thus, act as a branching moiety for the attachment of more than one chromophore onto a peptide scaffold. The structural differences this could provide in a molecular unit designed for self-assembly strategies could be important.

As a demonstration and a proof of concept for future work, this section briefly describes some comparisons of some synthesized test structures involving lysine.

Highlighted in this section are some key differences achieved with the test structures in comparison to the compounds analyzed in this study.

In comparison to **PDI 3**, which is disubstituted with peptide -Gly-$(Ala)_3$-$(Glu)_3$, replacement of the glutamic acid residues with lysine to form test compound **PDI 9** generated a differing aggregate spectral profile and an inverse pH behavior to that seen for **PDI 3** (Figure 7.1b).

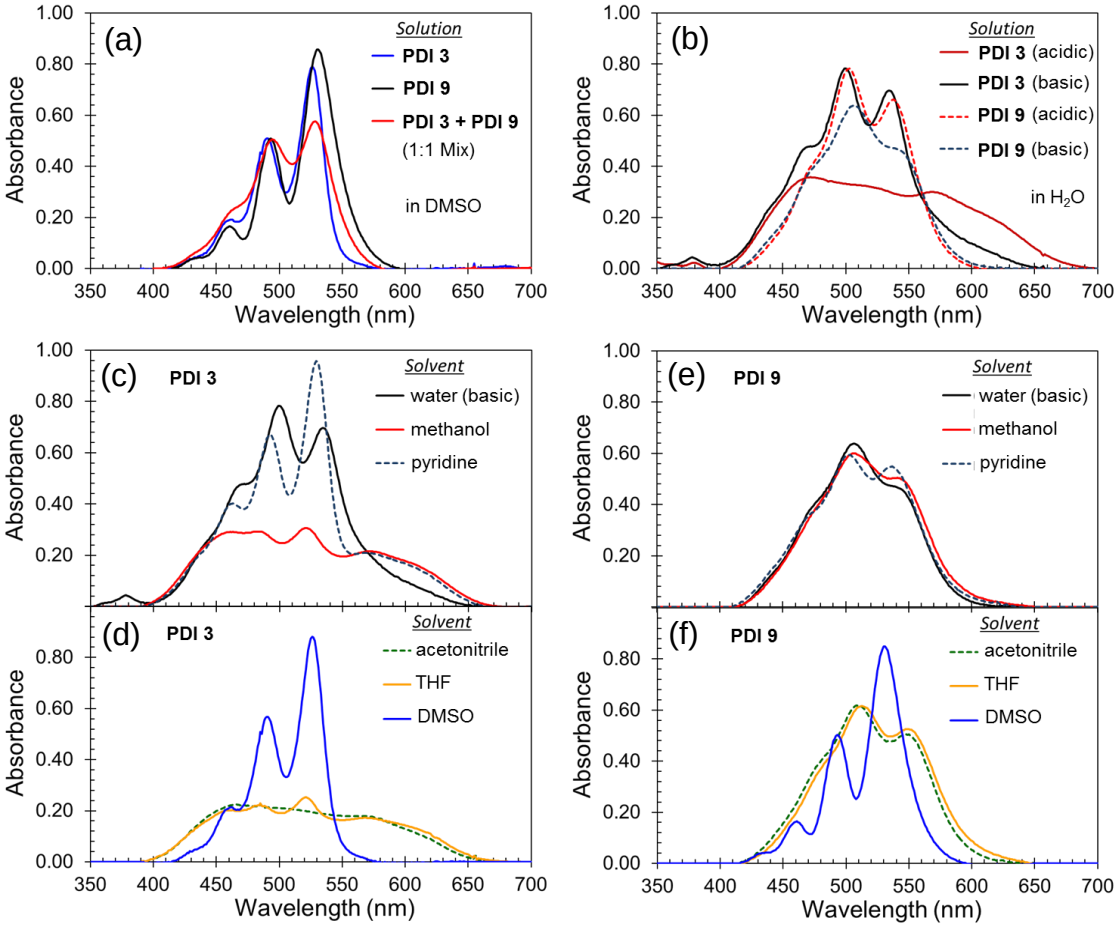

Figure 7.1 Spectroscopic comparisons of **PDIs 3** and **9** in various solvents: (a) Spectra of each compound alone and a 1:1 molar mixture of each in DMSO; (b) pH response of each compound in aqueous solution; (c,d) Spectra of **PDI 3** in selected solvents; (e,f) Spectra of **PDI 9** in selected solvents.

Consistent with the compounds from this study, both PDI **3** and **9** exhibited monomeric behavior in DMSO, but the complimentary acid-base natures of the two compounds nevertheless induced some extent of aggregation — even in DMSO

— upon mixing the two compounds in a 1:1 molar ratio (Figure 7.1a). Comparatively, **PDI 3** exhibited greater responsiveness to a change in solvent environment than did **PDI 9** (Figure 7.1c,d vs. Figure 7.1e,f) which may be due to greater hydrogen-bonding behavior in **PDI 9**. From this result, the use of lysine as a peptide scaffold branch appears to hold greater promise in achieving new self-assembly architectures.

As a modification of the glycine linker used in this study, lysine could instead be applied as a bifurcated linker. Using this approach permitted the successful synthesis of test PDIs **10** and **11**. These perylene imide "dimers" linked by the same peptide displayed spectral profiles different to similar non-bifurcated structural designs, as seen in Figures 7.2 and 7.3. The associated structural constraints arising from the peptide linkage configuration enforced a particular geometric configuration between the chromophores which would not otherwise be obtained. In the case of PDI **10**, this produced an intense H-aggregated response, not seen in PDI **3H**.

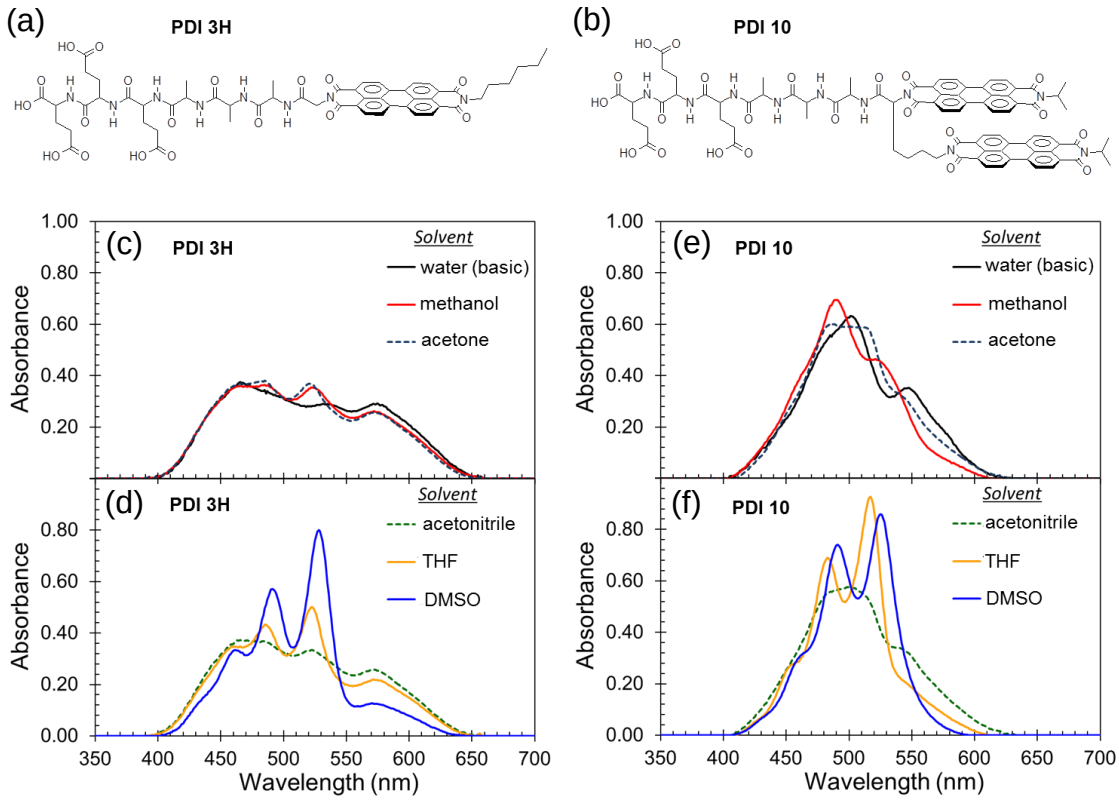

Figure 7.2 Spectral comparisons of (a) PDI **3H** with (b) PDI **10** in various solvents, giving spectral profiles for **3H** (c,d) contrasted with the profiles of **10** (e,f).

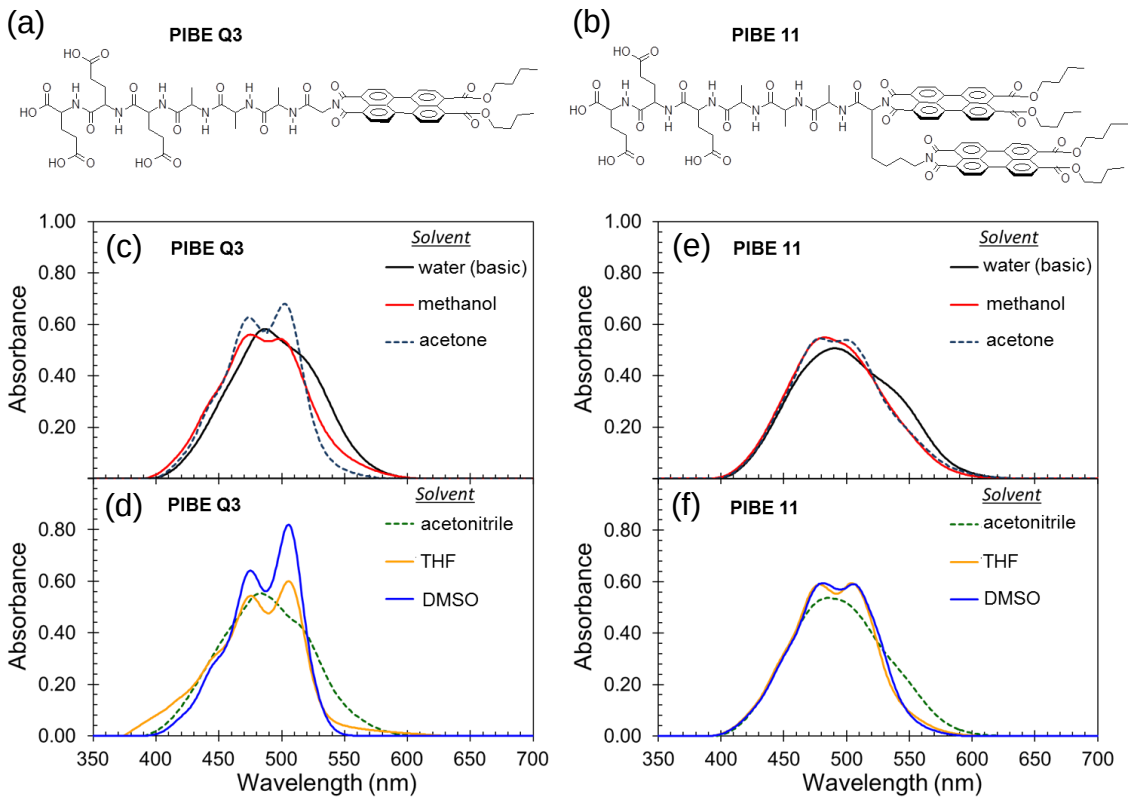

Figure 7.3 Spectral comparisons of (a) PIBE **Q3** with (b) PIBE **11** in various solvents, giving spectral profiles for **Q3** (c,d) contrasted with the profiles of **11** (e,f).

While a less pronounced spectral difference was seen between an analogous test compound bisester dimer (**11**) and the structurally related compound **Q3**, the important development was that of again achieving a spectral difference from the bifurcated design. Based on these results, the strategy could be further developed by examining tuning from differently sized side-chain lengths (via synthetic amino acid analogs of lysine). Additionally, lysine (or similar linkers) could be applied to position chromophores along the length of a peptide at specific residue positions.

Beyond simply facilitating changes in the number or position of chromophores along a peptide scaffold, lysine may allow the construction of responsive dimer assemblies which close more tightly upon hydrogen-bonding or metal cation addition. While test compounds **10** and **11** incorporate simple alkyl imide substituents in the unsymmetrical structures, other moieties with strong hydrogen-bonding affinity or those with a strong ability to form metal complexes could instead be incorporated into the structures in place of the simple alkyl groups. Invoking hydrogen-bonding or complex-formation would engage an added self-

assembly dimension in the fundamental units undergoing π-stacking and would prompt an altered photophysical response as the chromophores mutually reorient configurationally. A generalized schematic of this strategy is depicted in Figure 7.4. A multitude of other similar strategies using modified designs (even cyclic motifs) would doubtlessly be possible.

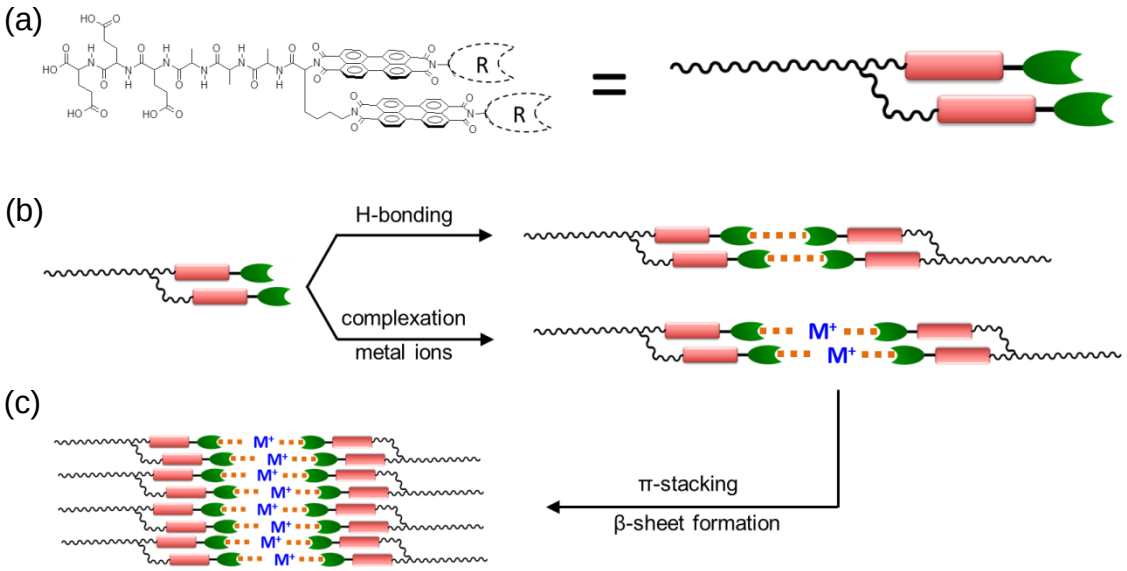

Figure 7.4 A general schematic showing the self-assembly of a peptide linked chromophore dimer enhanced by hydrogen-bonding or metal complex forming substituents (R groups). Action by the R-group moieties drives a responsive reorientation of the perylene units.

7.3 New Molecules to Assemble

Informed by the work with peptide-substituted perylene imides from this study, natural and rationally-designed peptides may be advantageously applied for the self-assembly of other organic semiconductors of interest. While numerous molecular candidates could be considered, this section will examine possible future work with indigo and the related compound Tyrian purple, which both have distinctive appeal. A synthetic union of these natural indigoids with natural peptides found in protein interfaces would generate a "natural" ensemble for self-assembly and form a structural partnership of natural components which could be

applied within organic electronics. As will be discussed, these indigoid compounds also possess structures which could lend well to synthetic methods employing peptides.

Although indigo and Tyrian purple are natural dyes which have been known for more than 4000 years, the semiconducting properties of these compounds was only discovered in recent years.[224–226] From an electronic perspective, these indigoids have many desirable properties. These compounds are noted to have good resistance toward degradation by heat or chemical redox processes, and the structures also show a strong tendency toward long range order via their strong, intrinsic, extensive, intermolecular (and intramolecular) hydrogen-bonding behavior.[189] Along with the low bandgaps of indigo (1.7 eV) and Tyrian purple (1.8 eV), both compounds possess a reversible two-electron reduction and oxidation and give high, almost perfectly balanced electron and hole charge transport in OFET devices.[189] Due to these factors, these indigoids have been shown to perform very well among small molecule semiconductors, with the reported field effect mobility of Tyrian purple falling within one order of magnitude of the highest reported value from molecules in its class.[189,227] The high device performance of these indigoids in spite of their Spartan intramolecular conjugation appears to be due to highly ordered self-assembly driven by hydrogen-bonding. Given the importance of hydrogen-bonding for the performance and behavior of these compounds, the primary question if applying peptides for self-assembly of these indigoids is whether or not the introduction of the peptide moiety into the indigoid structures will enhance self-assembly or disrupt it.

An initial investigation of these compounds could begin with the commercially available, lower cost indigo. An immediate avenue for investigation would be a possible synthetic route for peptide attachment. Since the structure of indigo contains two secondary, heterocyclic amines, and since peptide chemistry makes extensive use of amines, these moieties would be of initial interest. As shown in Scheme 7.1, one immediately essential reaction to explore would be to see if an amide link could be formed between the cyclic amines and a low steric demand amino acid (such as glycine). Due to the inherent steric hindrance present in the indigo structure, and the strong intermolecular hydrogen-bonding between the

cyclic amines and the neighboring carbonyl, a successful amide linkage here would not be guaranteed. Even if requiring extended reaction times or strong conditions, if the amide linkage could be achieved, a significant synthetic avenue would thus be open for peptide inclusion. In such a case, indigoid precursors could be formed as outlined in Scheme 7.1, using either an excess of Fmoc-protected amino acid to achieve an indigoid with two amino acid linkers, or using an excess of indigoid to achieve a product having a single linker. The excess reagent would drive the amide formation equilibrium toward completion, and the chosen reagent of excess would select the product obtained. Purification could likely be performed using extraction (with water) followed by column chromatography.

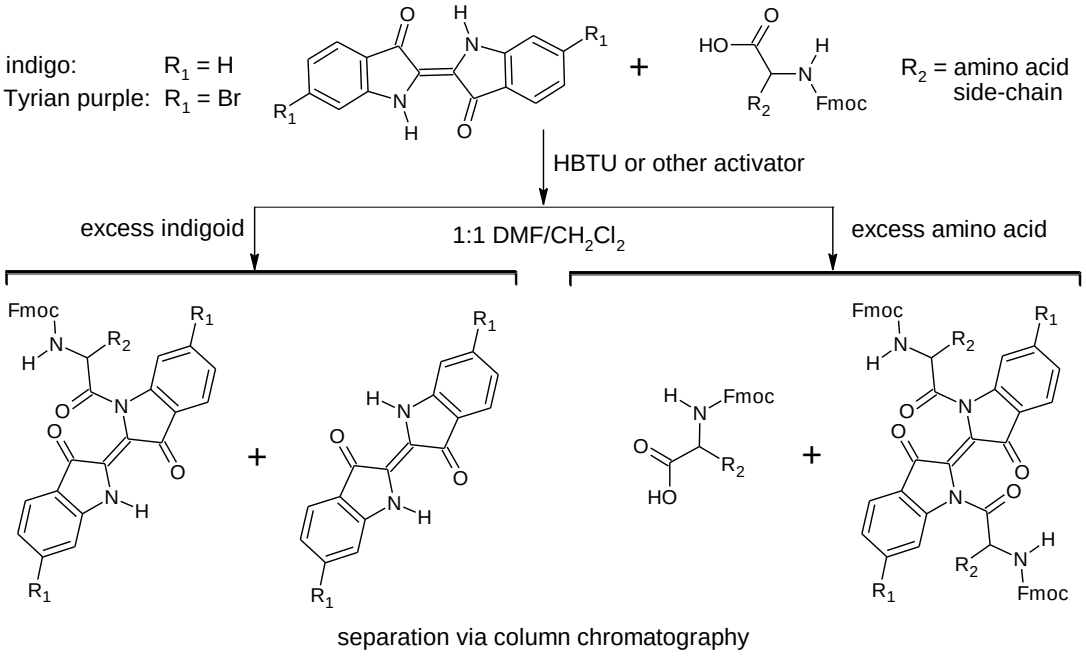

Scheme 7.1 A proposed reaction for the formation of amino acid indigoid conjugates to be used as precursors in peptide-indigoid synthesis.

If the reaction in Scheme 7.1 were successful, the chosen linker applied could also play a role in tuning the indigoid bandgap. Strong intramolecular hydrogen bonding between the heterocyclic N-H and the neighboring carbonyl have been shown to influence the indigoid bandgap by influencing conjugation and molecular alignment,[189] and structural changes which add a linker at this N-H position may be accordingly relevant. If the reaction in Scheme 7.1 were found to be unworkable, alternative functional group strategies could be considered such as a metal-

catalyzed coupling through the bromine functionality of Tyrian purple, or the synthesis of functionalized indigoids via substituted precursors (analogous to Scheme 7.2).[228]

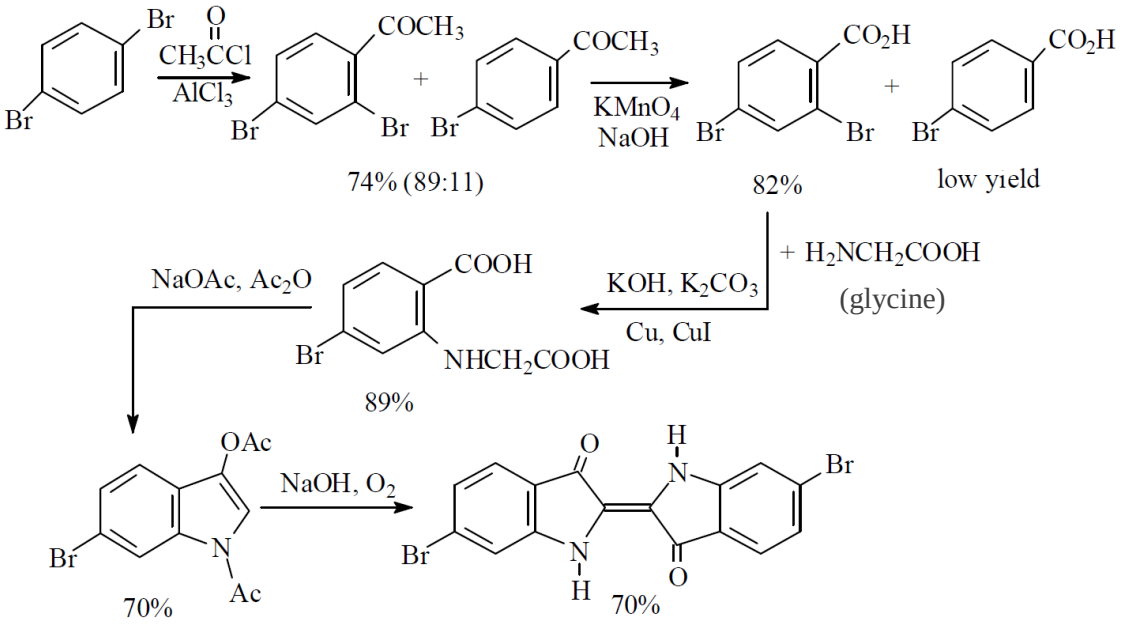

Scheme 7.2 Synthetic pathway for the synthesis of Tyrian purple. (Scheme adapted for review from Wolk and Frimer[228] with permission from MDPI.)

While the commercially available indigo would be attractive for synthesis on larger scales, synthetic pathways such as that outlined in Scheme 7.2 could provide access to other derivatives. In fact, if suitable naphthalene building blocks could be obtained, such precursors might be similarly applied to produce indigoids with additional fused rings and extended conjugation. Once the appropriate indigoids were obtained or synthesized, if the solubility of the compounds was compatible with the conditions of solid-phase peptide synthesis (SPPS), a potentially facile, solid-phase route to produce peptide-substituted indigoids could be envisioned.

Following from these ideas discussed in this section, a proposed solid-phase reaction protocol is presented here in Scheme 7.3. While the peptide sequence presented in Scheme 7.3 is that of an oligo-alanine (for illustrative simplicity), it could be easily replaced by a natural peptide sequence of interest. For this protocol, a solvent combination such as a 1:1 mixture of DMF and dichloromethane would

be anticipated to satisfy the solubility demands of both the SPPS reagents as well as the indigoids. SPPS would initially proceed as usual to produce the first oligo-alanine strand. Following this, the first of two aspartic acid linkers with an allyl ester would be appended. This represents a key feature of this protocol. The aspartic acid provides two carboxylic acid moieties for synthesis (through the terminus and side-chain), and the allyl ester strategy would make them selectively available without disrupting the Fmoc group or other protecting groups used in the synthesis. The allyl ester (OAll) could be removed when needed via the use of $Pd(PPh_3)_4$. During amino acid coupling reactions, these aspartic acid linkers would also allow a selective "switch" that could change the on-chain receptive site of the peptide from an amino group to a carboxyl group (or vice versa).

The use of the Fmoc-protected aspartic acid linking units with the allyl esters would effectively give a means to "reverse" the direction of the oligo-amide backbone of the peptide attached to the indigoid by linking through the aspartic acid side-chain. Two versions of the aspartic acid would be applied; one would have the allyl ester on the side-chain carboxyl group, while the other would have a carboxyl terminus allyl ester. These would be applied on the opposite sides of the indigoid moiety during synthesis. While the synthesis of a unsymmetrical product is shown in Scheme 7.3 (with the peptides each attached by a different end), a symmetrical product could be obtained by altering the aspartic acid switching decisions and coupling the resin-bound chain with an Fmoc-protected oligoalanine peptide. Alternatively, additional nonsymmetrical products with a single appended peptide strand could be obtained by stopping the reaction after the coupling of the indigoid.

The reactions with the indigoid shown in Scheme 7.3 assume sufficient reactivity of the cyclic indigoid amines to permit the reaction to occur. Even though two amino groups are free on the indigoid, protecting groups should be unnecessary for preventing crosslinking between resin-bound peptide strands by the indigoid — provided that a high excess of the indigoid is used during the coupling reaction. Otherwise, an unsymmetrical derivative like that shown in Scheme 7.1 might be necessary. If steric constraints were to forbid the coupling reaction from occurring as shown in Scheme 7.3, and if indigoid precursors with linkers already attached were necessary, Scheme 7.3 could still be applied with slight modifications.

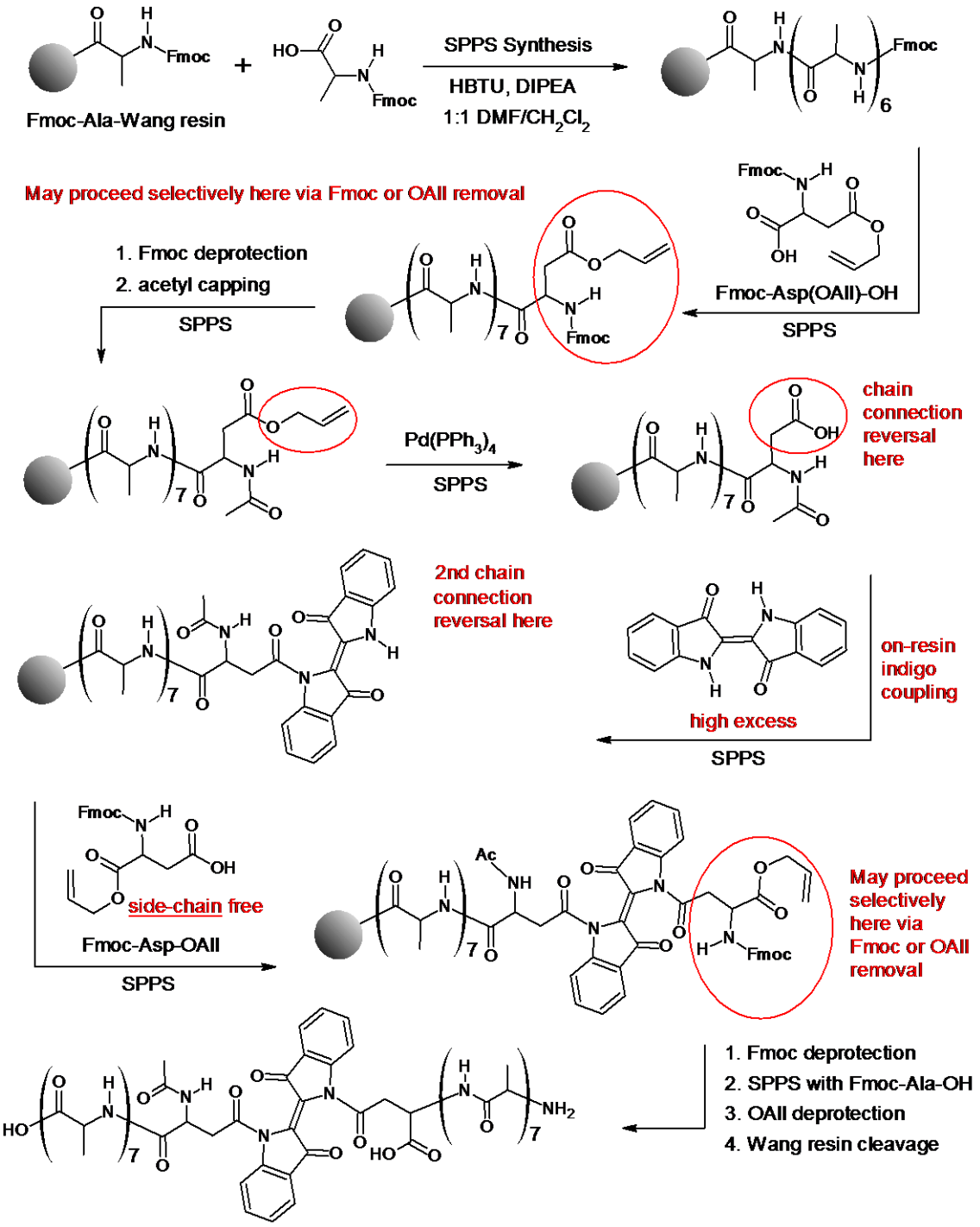

Scheme 7.3 A proposed SPPS protocol to produce a peptide-substituted indigoid.

7.4 Summary

Informed by the work with peptide-substituted perylene imides from this study, residue-specific traits for lysine and other amino acids remain rich areas for the

exploration of self-assembly. A multitude of peptide sequences (from both natural protein interfaces and rational design) hold further opportunities for guiding self-assembly. Applying this potential of peptides to enhance self-assembly may be advantageous in a variety of semiconductor moieties aside from perylene imides. Among those worth consideration are natural dyes such as indigo and Tyrian purple, which could form the basis for self-assembling natural moiety ensembles.

Chapter 8

Experimental

8.1 Materials

The termini end-capped (acetylated and amidated) Ac-IKHLSVN-NH_2 peptide was purchased from Mimotopes (R.P. 617113, Melbourne, Australia) with a purity >95% (as an acetate salt). All other peptides were synthesized via standard Fmoc solid-phase peptide synthesis (SPPS) protocols as outlined in Chapter 2.

Non-symmetric perylene precursors **Q1**, **Q2**, **Q3**, and **Q4** were received from the lab of Dr. Pall Thordarson (University of New South Wales, Sydney, Australia) and were synthesized according to previously published methods as indicated in Section 8.15. Synthesis of all peptide-perylene imide conjugates was accomplished via condensation of the terminal peptide amines (or amine linkers) with the desired perylene anhydride moiety as discussed generally in Chapter 2.

For the syntheses described, all amino acid derivatives, synthetic resins, chemical reagents, and solvents were purchased in high purity from various commercial suppliers and used as received. Specific synthetic and characterization details are discussed in this chapter along with a presentation of compound characterization data. NMR spectra, MALDI mass spectra, and IR spectra for all compounds are shown as supporting information in the appendices.

8.2 NMR Spectroscopy

NMR data were collected on a Varian Unity Inova operating at 500 MHz (^{1}H) or 125 MHz (^{13}C), or on a Varian Direct-Drive spectrometer equipped with a HCN cold probe operating at 600 MHz (^{1}H) or 150 MHz (^{13}C). All NMR spectra were referenced internally to residual solvent peaks.[229] PDI compound spectra were collected from solutions with concentrations matching the solubility limit of each compound. ^{1}H NMR peak assignments were based on two-dimensional nuclear magnetic resonance (2D NMR) correlation spectroscopy (COSY) assessments evaluated from the free peptide solutions in DMSO-d_6. Residue assignment labels are numbered sequentially along the N- to C-terminal directionality.

8.3 High Resolution (ESI) Mass Spectrometry

High resolution mass spectrometry analyses for the synthesized peptides were performed on an Agilent 6530 Q-TOF system equipped with an electrospray ion (ESI) source operated in positive ion mode. All mass spectra were obtained using a system mixture of water:acetonitrile (5:95) with 5 mM ammonium formate added.

8.4 Matrix-Assisted Laser Desorption Ionization (MALDI-TOF) Mass Spectrometry

Spectra were collected on an AB Sciex TOF/TOF 5800 mass spectrometer. Samples were analyzed in a matrix consisting of 2,5-dihydroxybenzoic acid (10 mg/mL) dissolved in an aqueous solution of 50% acetonitrile and 0.1% (v/v) trifluoroacetic acid. Small portions (1 μL) of dilute (10^{-4} to 10^{-6} M) solutions of each compound in 0.2% (v/v) pyridine/water were added with 20-40 μL of the matrix. One microliter volumes of the PDI/matrix mixtures were deposited on a sample plate and air-dried prior to analysis.

8.5 Fourier Transform Infrared Spectroscopy

Conversion of the anhydride functional group to the imide structure was verified using Fourier-transform infrared (FT-IR) spectroscopy. The FT-IR spectra were collected on a Perkin Elmer Spectrum One spectrometer using freshly prepared potassium bromide pellets and recorded in the range of 4000-450 cm^{-1} and averaged over 16 scans. FT-IR analysis of the amide I and II peptide bands was accomplished based on methods reported in literature.[98–101] Briefly, spectra were collected in solid-state (KBr) and averaged over 50 scans. The spectra were then baseline-corrected and smoothed using the Savitzky-Golay method with a polynomial order of 3 (via Matlab software) prior to numerically evaluating the second derivative of each spectrum. Using the minima of the second derivative to determine the number and positions of the Gaussian peaks to be applied, the measured IR spectra were then computationally fit as a sum of Gaussian peaks. The peak parameters were computationally, iteratively adjusted to minimize the fit residual. For the fitting process, peak positions were constrained to ±5 cm^{-1} from the initial values set on the basis of the second derivative minima.

8.6 UV-vis Spectroscopy

UV-vis absorption spectra were collected on an Agilent 8463 UV-vis spectrometer using a 1.0 cm quartz cell. All spectra were baseline corrected to remove effects attributed to scattering from aggregated particles. *General solution preparation*: Concentrated stock solutions were prepared in either an aqueous base or in an organic acid by dissolving 1.3-1.8 mg samples of the perylene imide compounds into 1 mL of the chosen stock solvent, thus producing 800 μM perylene imide stock solutions. Aqueous bases used as stock solvents were aqueous pyridine (200 μL pyridine in 10 mL of water) or 0.01 M NaOH. Organic acids used as stock solvents were TFA or HFIP. (Stock solvents were selected according to the compound characteristics and the demands of the analysis to be performed.) Subsequently, solutions for spectroscopic analyses were prepared by diluting (injecting) small volumes (20-40 μL) of the previously prepared perylene imide stock solutions into 5

mL of the solvents of interest, thus triggering self-assembly and producing 3-6 μM solutions for spectroscopic analysis. Specific solution preparations for a given study are given in their respective chapters.

8.7 Circular Dichroism Spectroscopy

Circular dichroism (CD) spectra were recorded at room temperature using a 1.0 cm quartz cell. Far UV circular dichroism (CD) spectra were collected with a Jasco J-815 spectrometer, and visible CD spectra were recorded on an Applied Photophysics Chirascan CD spectrometer. Solutions for analysis were prepared using the methods outlined for UV-vis spectroscopy (Section 8.6). (CD spectra in the far UV were collected by collaborators at Canterbury University – Christchurch, New Zealand.)

8.8 Thioflavin-T Fluorescence Binding Assays

Peptide samples were dissolved in an aqueous solution of Thioflavin-T (ThT), such that the final concentrations in each sample were 25 μM ThT and 1-10 mg/mL of peptide. The peptide solutions analyzed were prepared by diluting from aqueous stock solutions with concentrations of 20-30 mg/mL. Upon dilution, the resulting solutions to be analyzed were left to equilibrate at 4°C for 24 h before recording fluorescence intensity. Fluorescence intensity was measured from 100 μL aliquots placed into sample well plates using a Molecular Devices SpectraMax M5 fluorimeter equipped with a plate reader. Samples were excited at 440 nm, and fluorescence intensity was recorded at 482 nm, using a 25 μM ThT solution in water as a blank. The fluorescence intensity values reported resulted from the average of 3 recordings for each sample. For the samples analyzed, an additional turbidity assay was also performed as supporting evidence for the aggregation of the peptide sequences, showing the absorbance of the peptide solutions recorded at 600 nm. (ThT assays were performed by collaborators at Canterbury University – Christchurch, New Zealand.)

8.9 Transmission Electron Microscopy (TEM)

TEM imaging for Chapter 3 was performed using a Tecnai T12 transmission electron microscope operated at 120 kV. *Sample Preparation:* 8 μL of each sample was applied to 300-mesh copper grid coated with carbon (on nitrocellulose support) and was left to air dry for 10 minutes; the remaining solvent was blotted from the back side of the grid. (TEM imaging was performed by collaborators at the Weizmann Institute of Science – Rehovot, Israel.)

TEM imaging for Chapter 5 was performed using a FEI Morgagni 268D transmission electron microscope operating at 80 kV, with magnifications up to 180k. Micrographs were captured using a SIS/Olympus Megapixel III digital camera mounted above the phosphor screen. *Sample Preparation:* The peptide samples were pelleted by centrifuging at 10k rpm for 10 minutes. The pellet was then re-suspended in 2.5% gluteraldehyde solution and stored overnight at 4 ˚C. Following overnight incubation, the peptide sample was re-pelleted and further suspended in water prior to grid preparation. (Note: The volume of water added was the same as that of the decanted supernatant to maintain the concentration.) Carbon-coated Formvar 200-mesh copper grids (ProSciTech, Australia) were deposited successively for one minute each onto 15 μL drops of (i) aqueous peptide solutions, (ii) water (3 times) and (iii) a 2% w/w uranyl acetate solution in water (as a negative stain). Filter paper was used to remove the excess liquid from the grids, which were then left to dry for a few hours before electron microscopy observations. (TEM imaging was performed by collaborators at Canterbury University – Christchurch, New Zealand.)

Cryogenic TEM (cryo-TEM) imaging was performed using a Tecnai F20 transmission electron microscope operating at 200 kV, using a Gatan 626 cooling holder, and a transfer station with a Gatan US4000 CCD digital camera, or a Tecnai T12 transmission electron microscope operating at 120 kV, using a Gatan 626 cooling holder and transfer station, with a TVIPS F244HD CCD digital camera. *Sample Preparation:* 8 μL of each sample was applied to a 300-mesh copper grid coated with holey carbon (Pacific Grid-Tech supplies). The samples were blotted at 25 °C and 95% relative humidity, and plunged into liquid ethane using a Leica EM-

GP Automatic Grid Plunger. Specimens were equilibrated at −178 °C in the microscope prior to the imaging process. (TEM imaging was performed by collaborators at the Weizmann Institute of Science – Rehovot, Israel.)

8.10 Atomic Force Microscopy (AFM)

AFM images were acquired using a Bruker MultiMode® 8 with Nanoscope J controller. Samples were scanned in ScanAsyst mode using a ScanAsyst-Air tip (Silicon Nitride, 2-12 nm tip radius, k = 0.4 N/m). The sample environment was a Bruker stainless steel cantilever holder (MFMA), and all samples were imaged in air. Images were processed using Gwyddion 2.28 software.

Sample Preparation (Chapter 3): PDI samples were sonicated into an aqueous sodium hydroxide (0.01 M) yielding a red solution (0.5 mM). An aliquot (2 μL) of this solution was dropped into aqueous hydrochloric acid (0.1 M, 20 μL) or into water, yielding a cloudy dark red solution (0.05 mM). This solution was left for 72 hours to allow fiber formation, and was then pipetted onto a freshly cleaved muscovite mica surface, and incubated in the dark until dried (≈ 1 h). Solution concentrations and solution aging times were adjusted where required to investigate concentration and kinetic effects.

Sample Preparation (Chapter 4): Samples were prepared at a concentration of 4 mg/mL in DMSO and a drop of this solution (≈ 50 μL) added to 500 μL of water. A drop of this mixture was then spin coated onto a freshly cleaved mica substrate for three minutes at 3000 rpm. After spin coating, these samples were left to dry in air overnight.

Sample Preparation (Chapter 5): In a typical experiment, 1 mg of sample was briefly sonicated and gently heated into a pyridine/water mixture (9:1) yielding a red solution. An equimolar equivalent of glacial acetic was then added to neutralize the residual pyridine in solution. An aliquot (50 μL) of this solution was then spread onto a freshly cleaved mica substrate and left to dry for 24 hours before imaging. (AFM imaging was performed by collaborators at the University of New South Wales – Sydney, Australia.)

8.11 OFET Device Fabrication

Bioorganic field-effect transistor (biOFET) devices were fabricated by integrating flakes of the hybrid peptide material as the active channel in a bottom contact, back gate device structure. Initially the device substrates were prepared by taking highly doped n-type silicon substrates (Silicon Quest International) and depositing a gold electrode onto the silicon to act as the back gate. P-type silicon substrates were also tested for a comparison. The top surfaces were then spin-coated with polydimethylsiloxane (PDMS) (sylgard 184) at 6000 rpm for 60 s on highly doped (0.01-0.02 Ω·cm) n-type silicon substrates to provide the dual purpose of a gate dielectric, as well as being a soft and adhesive site for the peptide flakes. Gold electrodes (70 nm) with channel widths of 40 μm channel spacing were deposited via a precision Osilla OFET shadow mask using the Angstrom Engineering Nexdep evaporator. Flakes of the active materials grown in vials via slow solvent evaporation from a 1:4 pyridine/water solution (heated to 75-80 °C) were then mounted across the gold electrode channels using conductive silver paste (ethyl acetate paste solvent). All device measurements were conducted in air at room temperature. (The biOFET devices were fabricated jointly by the author and the Plank Research Group – Victoria University of Wellington.)

8.12 General Solid-Phase Peptide Synthesis (SPPS)

Synthesis employed standard Fmoc-based solid-phase peptide synthesis (SPPS) protocols,[198] which are discussed in detail Chapter 2. Following below is a brief detailed summary of the general SPPS protocols used as the basis for the synthesis of the peptides presented in this work.

A sample of Fmoc-Glu(OtBu)-Wang resin (0.50 g, loading 0.33-0.56 mmol/g) was prepared by swelling the resin in dichloromethane (DCM) (7 mL) for 30 minutes and then washing the resin with dimethylformamide (DMF) (7 mL). Sequentially alternating Fmoc-deprotection and amino acid coupling reactions with the desired Fmoc-protected amino acids afford the desired peptide sequence. Fmoc-

deprotection reactions were performed using 30% (v/v) piperidine/DMF (7 mL) with gentle shaking for 30 minutes followed by thorough washes of the resin with DMF. Amino acid coupling reactions were performed using a mixture of the desired amino acid (4 molar equivalents), *O*-benzotriazole-*N*,*N*,*N*′,*N*′-tetramethyluronium hexafluorophosphate (HBTU) (3.95 molar equivalents), and *N*,*N*-diisopropylethylamine (DIPEA) (6 molar equivalents) in molar excess relative to the loading of the Wang resin. The coupling reaction mixtures were gently shaken for 30 minutes followed by a thorough wash of the resin. A Kaiser test was conducted after each coupling reaction to confirm completion. Upon removal of the terminal Fmoc protecting group from the completed peptide sequence, the resin was washed thoroughly with DMF followed by several washes with DCM. Cleavage of the completed peptide sequence from the Wang resin was achieved by gently shaking the resin for 3 hours in a mixture of trifluoroacetic acid (TFA) and DCM (7 mL, 3:4 TFA/DCM) or an alternative TFA cleavage mixture with added scavenger compounds (such as triisopropylsilane and phenol). The cleavage solution was collected, the resin was washed with DCM (5 mL), and the wash was added with the collected cleavage solution. Cold diethyl ether (40 mL, 0-5 °C) was added to the cleavage solution and chilled for 30 minutes to precipitate the peptide product. The precipitate was collected by filtration, washed with cold diethyl ether, and dried under vacuum to yield the peptide product. Residual traces of scavengers or other compounds detected in the peptide product were removed via additional washes with acetonitrile or ethyl acetate.

Where applicable, modifications to the resin used, to the cleavage solution applied (including the use of scavengers), or to the washing steps performed during specific syntheses are noted within the details for the relevant compound within the compound-specific information listed in section 8.15.

8.13 General Perylene Imide Synthesis Procedures

Synthesis of the peptide-substituted perylene imides was based on amine condensation with an anhydride moiety following methods for the synthesis of perylene imide derivatives as reported in literature.[86]

For the *N*,*N*′-dipeptide perylene diimides, a mixture of the desired peptide and perylene 3,4,9,10-tetracarboxylic acid dianhydride (PTCDA) were combined in a 2:1 molar ratio (with a slight peptide excess) in imidazole (0.80-1.0 g) and stirred at 124-135 °C for 12-24 hours under nitrogen.

Synthesis of *N*-hexyl-*N*′-peptide perylene diimides was performed by analogous procedures used for the dipeptide diimides using a mixture of the desired peptide and perylene-3,4-anhydride-9,10-hexylimide in a 1:1 molar ratio with a slight peptide excess.

Synthesis of *N*-peptide perylene imide bis(n-butyl)esters (peptide-PIBEs) was performed by condensation reaction of the desired peptide with a perylene-3,4-monoanhydride-9,10-bis(n-butyl)ester[87] precursor by heated stirring in DMF or by stirring in imidazole in a 1:1 molar ratio with a slight peptide excess.

Following the condensation reaction, the mixture was allowed to cool to room temperature with continued stirring followed by the addition of 3 mL of water to the mixture upon reaching 90 °C. Upon cooling, the solution was loaded onto an HP20ss column with the addition of small amounts of water. Once fully loaded onto the resin, the mixture was eluted and cyclically loaded through the column using dilute aqueous acetic acid with an increasing acid gradient until all dark red/purple components were retained within the resin and the eluted solvent became yellow to colorless. The dark solids retained in the resin were then thoroughly washed with 5-7% (v/v) acetic acid (700-1200 mL) until the eluted wash changed from yellow to nearly colorless. A subsequent wash with acetone (150-300 mL) was made to remove traces of any reddish impurity. Removal of the desired product from the resin following the washes was accomplished using 20-50% (v/v) pyridine in water. Removal of the solvent under reduced pressure afforded the dark colored peptide-substituted perylene imides.

Where applicable, modifications to these protocols are noted within the specified details for the relevant compound within the compound-specific information listed in section 8.15.

8.14 Purification of the Compounds

The purification protocol reported here capitalized on the low solubility and pH-triggered aggregation of the desired final products to accomplish separation. The reverse-phase HP20ss resin allowed charged species to pass through the column while retaining uncharged species. The use of the acetic acid washes easily protonated species such as the imidazole and free peptide, rendering them as charged ionic components not retained by the resin, while simultaneously triggering the aggregation and retention of the desired perylene imide product within the resin. Removal of the remaining imidazole and other impurities was accomplished via the use of polar acetone washes. The product was then easily removed by flushing with basic washes to ionize the glutamic acid units.

During the synthesis of dipeptide-perylene diimides, the formation of monopeptide-perylene species was expected to be minimal since the reactions were conducted with a slight excess of the peptides; however, any monopeptide-perylene imide species formed would have greater solubility than the desired products. As such, these monopeptide species would release from the HP20ss resin more readily than the desired dipeptide products during the successive acetic acid/acetone flushes during the purification protocol.

While the strongly aggregating products obtained in this study were not amenable to quantification by HPLC, on the basis of cross-checking the combined characterization data collected, the compound purity was estimated to be >95% (exclusive of residual solvents). Persistent residual solvents (from synthetic or washing steps) were not rigorously removed since the free peptides primarily served as synthetic intermediates for the formation of the peptide-perylene imide conjugates (which were subsequently purified by reverse-phase chromatography) A summary of residual solvent impurities detected in some NMR spectra of the compounds are given in Table 8.1.

Table 8.1. NMR Chemical Shifts of Residual Solvent Impurities

NMR Solvent	Impurity [a]	^{1}H Resonances (ppm)		^{13}C Resonances (ppm)	
DMSO-d_6	DMSO residual [b]	2.50	s	39.52	hept.
	water [b]	3.33	br. s	—	
	diethyl ether [c]	3.38	t	15.12	
		1.09	q	62.05	
	TFA [c]	11.5	br. s	158.68	q [g]
				117.02	q [g,h]
	acetone [d]	2.09	s	206.31	
	acetonitrile [d]	2.07	s	117.91	
	ethyl acetate [d]	1.99	s	20.68	
		4.03	q	59.74	
		1.17	t	14.40	
		—	-	170.31	
$CDCl_3$	$CHCl_3$ residual [b]	7.27	s	77.16	t
	TFA [b]	11.5	br. s	162.77	q [g]
		6.60	3 (s) [f]	114.66	q [g,i]
	acetic acid [e]	2.10	s	20.81	
		—	-	175.99	
	dichloromethane [b]	5.30	s	53.52	

[a] Persistent solvent residuals present with the peptide samples

[b] Traces present in the NMR solvent used

[c] Persistent traces introduced during peptide synthesis

[d] Introduced from peptide washing, filtration, and drying steps

[e] Present along with partially fluorine-substituted acetic acid variants within the TFA used

[f] TFA/$CDCl_3$ interaction gives a weak, triplet-like formation (peaks at 6.69, 6.60, 6.50)

[g] Mutual splitting between ^{13}C and ^{19}F, produces two quartet-type formations

[h] Large coupling constant. Resembles four well-separated peaks: 120.5, 118.1, 115.8, 113.4

[i] Large coupling constant. Resembles four well-separated peaks: 117.5, 115.6, 113.7, 111.8

The most commonly observed solvent impurities in the peptide ^{1}H NMR spectra were diethyl ether and TFA, since the final synthetic step for peptide collection involved a mixture of these solvents. Diethyl ether was seen to be remarkably persistent despite lengthy drying under vacuum, and TFA residuals were expected since the peptide initially precipitates as a trifluoroacetate salt upon addition of diethyl ether into the TFA cleavage mixture. It should be noted here that the presence of TFA in the samples exhibits distinctive resonance groups within the ^{13}C NMR spectra due to mutual splitting by the ^{13}C and ^{19}F nuclei. This produces two quartet-like signals centered at 158.7 and 117.0 ppm (in DMSO-d_6). A large coupling constant is observed for the signal at lower chemical shift, making the formation appear somewhat like four distinct, well-separated peaks in the aromatic region of the spectrum. These TFA resonances are seen to occur with aromatic compound resonances such as those from phenylalanine or histidine, but the TFA signal can be distinguished by identifying the regularly-spaced splitting intervals.

In cases where persistent scavengers (introduced from the peptide cleavage solution) were present, the peptide solids were washed in solvents such as acetonitrile and ethyl acetate to draw out adsorbed scavenger materials. Traces of these solvents were sometimes observed in the NMR spectrum; however, these solvents (and the others previously noted) were inert to subsequent reactions using the peptides and were not rigorously removed from the samples.

8.15 Compound Synthesis and Characterization

NH_2 – Gly – $(Gly)_3$ – $(Glu)_3$ – OH (P1)

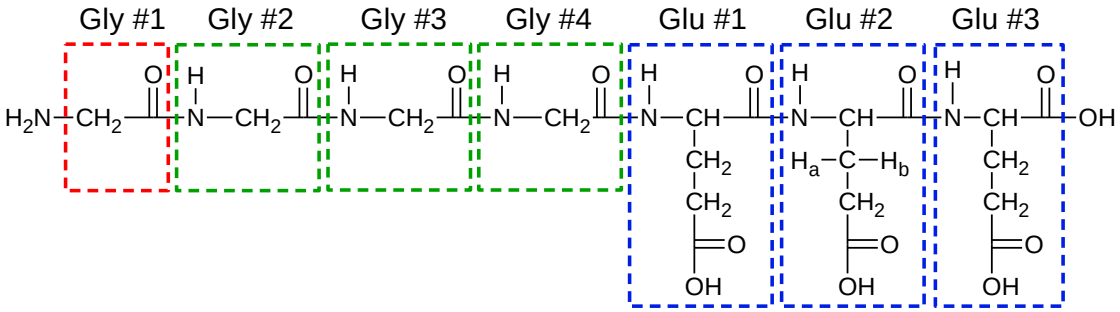

Figure 8.1 Chemical structure of peptide **P1**

Synthesis was performed according to the general SPPS procedure with a sample of Fmoc-Glu(OtBu)-Wang resin (0.50 g, loading 0.52 mmol/g, 0.26 mmol) affording *title compound* **P1** as a pale, off-white solid (0.15 g, 88%). ^{1}H NMR (500 MHz, DMSO-d_6): δ = 8.62 (1H, t, *J* = 5.5 Hz, NH Gly #2), 8.30 (1H, t, *J* = 5.7 Hz, NH Gly #3), 8.17 (1H, d, *J* = 7.6 Hz, NH Glu #3), 8.13 (1H, t, *J* = 5.6 Hz, NH Gly #4), 8.02 (4H, m, NH_2 Gly #1, NH Glu #1-2), 4.29 (1H, m, αCH Glu #1), 4.24 (1H, m, αCH Glu #2), 4.17 (1H, m, αCH Glu #3), 3.85 (2H, d, *J* = 5.4 Hz, CH_2 Gly #2), 3.75 (4H, d, *J* = 5.9 Hz, CH_2 Gly #3-4), 3.61 (2H, br s, CH_2 Gly #1), 2.26 (6H, m, γCH_2 Glu #1-3), 1.92 (3H, m, βCH_2 Glu #3, βCH_b Glu #2), 1.75 (3H, m, βCH_a Glu #2, βCH_2 Glu #1); ^{13}C NMR (125 MHz, DMSO-d_6): δ = 174.1, 174.0, 173.8, 173.1, 171.2, 171.0, 169.1, 168.8, 168.7, 166.3, 51.8, 51.5, 51.3, 45.3, 42.0, 41.9, 40.2, 30.7, 30.1, 30.0, 27.5, 27.3, 26.2; HRMS (ESI$^+$) *m/z*: Calculated for $C_{23}H_{36}N_7O_{14}$ $[M+H]^+$ 634.2315, found 634.2297; Calculated for $C_{23}H_{35}N_7NaO_{14}$ $[M+Na]^+$ 656.2129, found 656.2115.

***N,N′*-di[– Gly – $(Gly)_3$ – $(Glu)_3$ – OH]perylene-3,4,9,10-tetracarboxylic acid diimide (1).** Condensation of PTCDA (0.052 g, 0.13 mmol) and peptide **P1** (0.15 g, 0.23 mmol) performed according to the general perylene imide synthesis procedures afforded *title compound* **1** as dark purple solid (0.15 g, 70%). ^{1}H NMR (600 MHz, $CDCl_3$/CF_3COOH, 2:1): δ = 8.84 (m, Ar-H), 8.15-7.38 (NH proton exchange traces), 5.22 (m, CH_2 Gly #1), 4.47-4.12 (m, αCH Gly #2-4, αCH Glu #1-3), 2.85-

2.11 (m, γCH_2 Glu #1-3), 1.77-1.23 (m, βCH_2 Glu #1-3); MS (MALDI) *m/z*: Calculated for $C_{70}H_{74}N_{14}NaO_{32}$ $[M+Na]^+$ 1645.45, found 1645.42; IR (KBr): *v* = 3436, 2926, 2855, 1692, 1659, 1594, 1439, 1401, 1366, 1341, 1277, 1249, 1175, 1125, 1033, 1010, 862, 810, 755, 698, 656 cm^{-1}.

Perylene-3,4-anhydride-9,10-hexylimide (Q1). Synthesis and purification were accomplished as previously reported.[88] Characterization data matched that reported in the literature.

***N*-hexyl-*N′*-[– Gly – $(Gly)_3$ – $(Glu)_3$ – OH]perylene-3,4,9,10-tetracarboxylic acid diimide (1H).** Condensation of perylene-3,4-anhydride-9,10-hexylimide **Q1** (0.015 g, 0.032 mmol) and peptide **P1** (0.023 g, 0.036 mmol) performed according to the general perylene imide synthesis procedures afforded *title compound* **1H** as dark purple solid (0.021 g, 61%). ^{1}H NMR (600 MHz, $CDCl_3/CF_3COOH$, 2:1): δ = 8.83 (m, Ar-H), 8.73-7.41 (NH proton exchange traces), 5.23 (s, CH_2 Gly #1), 5.20 (s, CH_2 Gly #2), 4.47 (m, αCH Glu #1-3), 4.33 (s, CH_2 Gly #3), 4.32 (s, CH_2 Gly #4), 4.28 (t, *J* = 6.5 Hz, hexyl NCH_2), 2.46 (m, γCH_2 Glu #1-3), 2.23 (m, βCH_2 Glu #1-3), 1.80 (quin. *J* = 6.5 Hz, hexyl βCH_2), 1.71-1.24 (m, hexyl CH_2), 0.92 (t, *J* = 6.0 Hz, hexyl CH_3); MS (MALDI) *m/z*: Calculated for $C_{53}H_{54}N_8NaO_{18}$ $[M+Na]^+$ 1113.34, found 1113.38; IR (KBr): *v* = 3413, 3150, 3070, 2925, 2853, 1696, 1656, 1593, 1438, 1403, 1374, 1343, 1248, 1174, 1087, 1022, 997, 855, 809, 794, 749, 628 cm^{-1}.

NH_2 – Gly – $(Ala)_3$ – Glu – OH (P2)

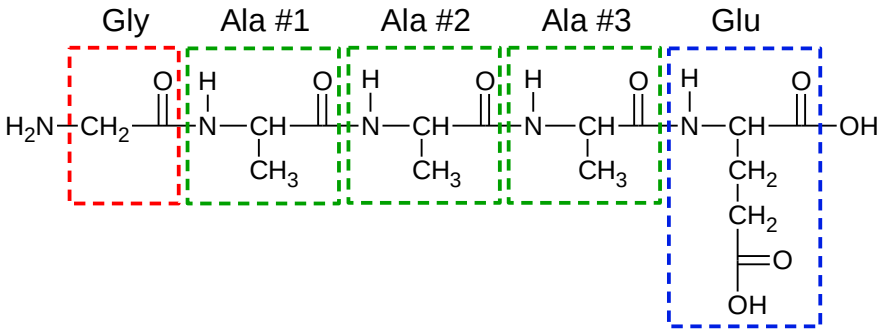

Figure 8.2 Chemical structure of peptide **P2**

Synthesis was performed according to the general SPPS procedure with a sample of Fmoc-Glu(OtBu)-Wang resin (0.50 g, loading 0.56 mmol/g, 0.28 mmol) affording *title compound* **P2** as a pale, off-white solid (0.10 g, 89%). ^{1}H NMR (500 MHz, DMSO-d_6): δ = 8.55 (1H, d, *J*= 7.3 Hz, NH Ala #1), 8.23 (1H, d, *J* = 7.6 Hz, NH Ala #2), 8.10 (1H, d, *J* = 7.8 Hz, NH Glu), 7.99 (2H, br s, NH_2 Gly), 7.90 (1H, d, *J* = 7.3 Hz, NH Ala #3), 4.39 (1H, quin, *J* = 7.0 Hz, αCH Ala #1), 4.27 (2H, quin, *J* = 6.7 Hz, αCH Ala #2-3), 4.19 (1H, td, *J* = 8.4 Hz, *J* = 5.2 Hz, αCH Glu), 3.56 (2H, br s, CH_2 Gly), 2.27 (2H, t, *J* = 7.9 Hz, γCH_2 Glu), 1.96 (1H, td, *J* = 13.4 Hz, *J* = 7.6 Hz, βCH_b Glu), 1.76 (1H, m, βCH_a Glu), 1.21 (9H, m, CH_3 Ala #1-3); ^{13}C NMR (125 MHz, DMSO-d_6): δ = 173.8, 173.1, 172.2, 171.6, 171.5, 165.5, 51.1, 48.2, 48.0, 47.9, 30.7, 30.0, 26.4, 18.5, 18.2, 18.1; HRMS (ESI$^+$) *m/z*: Calculated for $C_{16}H_{27}N_5NaO_8$ $[M+Na]^+$ 440.1752, found 440.1736, Calculated for $C_{16}H_{28}N_5O_8$ $[M+H]^+$ 418.1932, found 418.1917.

***N,N'*-di[– Gly – $(Ala)_3$ – Glu – OH]perylene-3,4,9,10-tetracarboxylic acid diimide (2).** Condensation of PTCDA (0.047 g, 0.12 mmol) and peptide **P2** (0.10 g, 0.24 mmol) performed according to the general perylene imide synthesis procedures afforded *title compound* **2** as a dark purple solid (0.11 g, 74%). ^{1}H NMR (600 MHz, $CDCl_3$/CF_3COOH, 2:1): δ = 8.84 (m, Ar-H), 8.15-7.32 (NH proton exchange traces), 5.22 (m, CH_a Gly), 5.12 (m, CH_b Gly), 4.90-4.51 (m,

NCH_2), 2.62 (m, γCH_2 Glu), 2.42 (m, βCH_a Glu), 2.14 (m, βCH_b Glu), 1.80 (quin. J = 6.5 Hz, hexyl βCH_2), 1.65-1.23 (m, CH_3 Ala #1-3, hexyl CH_2), 0.90 (t, J = 6.0 Hz, hexyl CH_3); MS (MALDI) m/z: Calculated for $C_{46}H_{46}N_6NaO_{12}$ $[M+Na]^+$ 897.31, found 897.72; IR (KBr): ν = 3396, 3302, 3080, 2929, 2856, 1697, 1657, 1594, 1541, 1439, 1403, 1343, 1279, 1248, 1174, 1128, 1089, 1029, 997, 853, 810, 742, 625 cm^{-1}.

NH_2 – Gly – $(Ala)_3$ – $(Glu)_3$ – OH (P3)

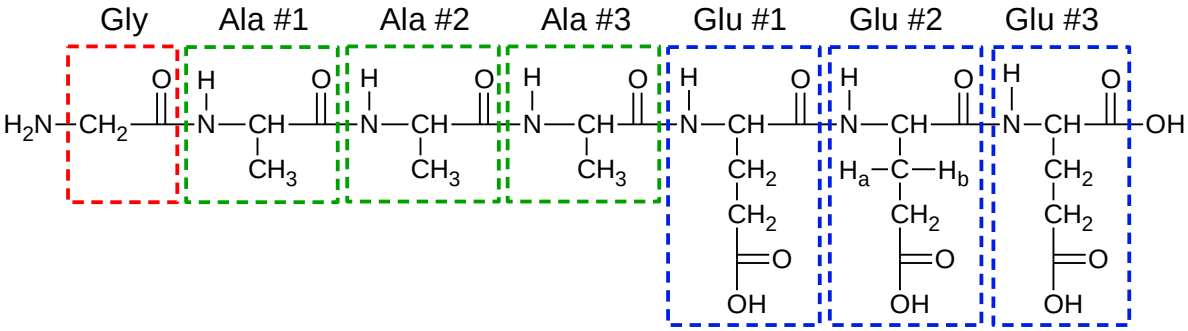

Figure 8.3 Chemical structure of peptide **P3**

Synthesis was performed according to the general SPPS procedure with a sample of Fmoc-Glu(OtBu)-Wang resin (0.50 g, loading 0.52 mmol/g, 0.26 mmol) affording *title compound* **P3** as a pale, off-white solid (0.16 g, 91%). ^{1}H NMR (500 MHz, DMSO-d_6): δ = 8.55 (1H, d, J= 7.3 Hz, NH Ala #1), 8.22 (1H, d, J = 7.3 Hz, NH Ala #2), 8.19 (1H, d, J = 7.6 Hz, NH Glu #3), 7.97 (4H, m, NH Ala #3, NH Glu #2, NH_2 Gly), 7.91 (1H, d, J = 7.8 Hz, NH Glu #1), 4.39 (1H, quin, J = 7.1 Hz, αCH Ala #1), 4.25 (4H, m, αCH Ala #2-3, αCH Glu #1-2), 4.17 (1H, m, αCH Glu #3), 3.56 (2H, br s, CH_2 Gly), 2.29 (6H, m, γCH_2 Glu #1-3), 1.93 (3H, m, βCH_2 Glu #3, βCH_a Glu #2), 1.75 (3H, m, βCH_2 Glu #1, βCH_b Glu #2), 1.20 (9H, m, CH_3 Ala #1-3); ^{13}C NMR (125 MHz, DMSO-d_6): δ = 174.0, 173.8, 173.1, 172.4, 172.1, 171.8, 171.5, 171.1, 170.8, 165.5, 51.7, 51.6, 51.3, 48.21, 48.16, 48.1, 40.2, 30.7, 30.1, 29.9, 27.5, 27.4, 26.2, 18.5, 18.1, 18.0; HRMS (ESI^+) m/z: Calculated for $C_{26}H_{42}N_7O_{14}$ $[M+H]^+$ 676.2784, found 676.2764.

***N,N′*-di[– Gly – $(Ala)_3$ – $(Glu)_3$ – OH]perylene-3,4,9,10-tetracarboxylic acid diimide (3).** Condensation of PTCDA (0.060 g, 0.15 mmol) and peptide **P3** (0.19 g, 0.28 mmol) performed according to the general perylene imide synthesis procedures

afforded *title compound* **3** as a dark purple solid (0.20 g, 84%). ^{1}H NMR (600 MHz, $CDCl_3/CF_3COOH$, 2:1): δ = 8.84 (m, Ar-H), 5.20 (m, CH_a Gly), 5.08 (m, CH_b Gly), 4.88-4.45 (m, αCH Ala #1-3, αCH Glu #1-3), 2.63 (m, γCH_2 Glu #1-3), 2.50-1.98 (m, βCH_2 Glu #1-3), 1.67-1.19 (m, CH_3 Ala #1-3); MS (MALDI) *m/z*: Calculated for $C_{76}H_{86}N_{14}NaO_{32}$ $[M+Na]^+$ 1729.54, found 1729.56, Calculated for $C_{76}H_{86}N_{14}Na_2O_{32}$ $[M+2Na]^+$ 1752.53, found 1752.55; IR (KBr): *v* = 3416, 3283, 3061, 2979, 2929, 2855, 1696, 1662, 1594, 1546, 1438, 1401, 1364, 1339, 1277, 1245, 1174, 1038, 1003, 861, 810, 737, 699, 660, 626 cm^{-1}.

***N*-hexyl-*N′*-[– Gly – (Ala)$_3$ – (Glu)$_3$ – OH]perylene-3,4,9,10-tetracarboxylic acid diimide (3H).** Condensation of perylene-3,4-anhydride-9,10-hexylimide **Q1** (0.020 g, 0.042 mmol) and peptide **P3** (0.029 g, 0.044 mmol) performed according to the general perylene imide synthesis procedures afforded *title compound* **3H** as a dark purple solid (0.038 g, 79%). ^{1}H NMR (600 MHz, $CDCl_3/CF_3COOH$, 2:1): δ = 8.82 (m, Ar-H), 8.13-7.29 (NH proton exchange traces), 5.22 (m, CH_a Gly), 5.04 (m, CH_b Gly), 4.83-4.49 (m, αCH Ala #1-3, αCH Glu #1-3), 4.27 (t, *J* = 7.7 Hz, hexyl NCH_2), 2.60 (m, γCH_2 Glu #1-3), 2.43 (m, βCH_2 Glu #3), 2.29-2.00 (m, βCH_2 Glu #1-2), 1.79 (quin. *J* = 7.6 Hz, hexyl βCH_2), 1.66-1.19 (m, CH_3 Ala #1-3, hexyl CH_2), 0.90 (t, *J* = 6.8 Hz, hexyl CH_3); MS (MALDI) *m/z*: Calculated for $C_{56}H_{60}N_8NaO_{18}$ $[M+Na]^+$ 1155.39, found 1155.36; IR (KBr): *v* = 3385, 3304, 3150, 2952, 2927, 2855, 1693, 1656, 1594, 1439, 1402, 1342, 1279, 1248, 1173, 1088, 1033, 997, 843, 810, 794, 742, 655, 625 cm^{-1}.

NH_2 – Gly – (*D*-Ala)$_3$ – (*D*-Glu)$_3$ – OH (P3E)

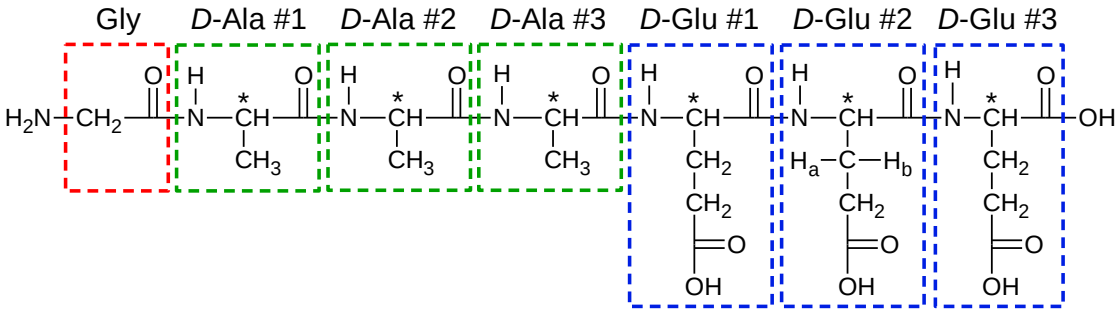

Figure 8.4 Chemical structure of peptide **P3E**

Synthesis was performed according to the general SPPS procedure with a sample of Fmoc-*D*-Glu(OtBu)-Wang resin (0.50 g, loading 0.52 mmol/g, 0.27 mmol) affording *title compound* **P3E** as a pale, off-white solid (0.11 g, 60%). ^{1}H NMR (500 MHz, DMSO-d_6): δ = 8.54 (1H, d, *J*= 7.3 Hz, NH *D*-Ala #1), 8.23 (1H, d, *J* = 7.5 Hz, NH *D*-Ala #2), 8.20 (1H, d, *J* = 7.5 Hz, NH *D*-Glu #3), 7.97 (4H, m, NH *D*-Ala #3, NH *D*-Glu #2, NH_2 Gly), 7.91 (1H, d, *J* = 7.8 Hz, NH *D*-Glu #1), 4.40 (1H, quin, *J* = 7.1 Hz, αCH *D*-Ala #1), 4.26 (4H, m, αCH *D*-Ala #2, αCH *D*-Ala #3, αCH Glu #1, αCH *D*-Glu #2), 4.17 (1H, m, αCH *D*-Glu #3), 3.57 (2H, dd, *J* = 4.4 Hz, *J* = 2.0 Hz, CH_2 Gly), 2.26 (6H, m, γCH_2 *D*-Glu #2, γCH_2 *D*-Glu #3, γCH_2 *D*-Glu #1), 1.95 (3H, m, βCH_2 *D*-Glu #3, βCH_a *D*-Glu #2), 1.75 (3H, m, βCH_2 *D*-Glu #1, βCH_b *D*-Glu #2), 1.21 (9H, m, CH_3 *D*-Ala #1-3); ^{13}C NMR (125 MHz, DMSO-d_6): *δ* = 174.1, 173.9, 173.2, 172.3, 172.0, 171.9, 171.7, 171.2, 170.9, 165.6, 51.9, 51.7, 51.4, 48.30, 48.27, 48.2, 40.2, 30.2, 30.1, 30.0, 27.6, 27.4, 26.3, 18.5, 18.2, 18.0; HRMS (ESI$^+$) *m/z*: Calculated for $C_{26}H_{42}N_7O_{14}$ $[M+H]^+$ 676.2784, found 676.2808.

***N,N′*-di[– Gly – (*D*-Ala)$_3$ – (*D*-Glu)$_3$ – OH]perylene-3,4,9,10-tetracarboxylic acid diimide (3E).** Condensation of PTCDA (0.014 g, 0.036 mmol) and peptide **P3E** (0.050 g, 0.074 mmol) performed according to the general perylene imide synthesis procedures afforded *title compound* **3E** as a dark purple solid (0.040 g, 66%). ^{1}H NMR (500 MHz, $CDCl_3$/CF_3COOH, 2:1): δ = 8.84 (m, Ar-H), 8.13-7.30 (NH proton exchange traces), 5.24 (m, CH_a Gly), 5.06 (m, CH_b Gly), 4.88-4.45 (m, αCH Ala #1-3, αCH Glu #1-3), 2.63 (m, γCH_2 Glu #1-3), 2.50-1.98 (m, βCH_2 Glu #1-3), 1.70-1.26 (m, CH_3 Ala #1-3); MS (MALDI) *m/z*: Calculated for $C_{76}H_{86}N_{14}NaO_{32}$ $[M+Na]^+$ 1729.54, found 1729.67; IR (KBr): *ν* = 3281, 3069, 2982, 1703, 1652, 1594, 1542, 1439, 1402, 1366, 1338, 1310, 1246, 1174, 1039, 1002, 963, 853, 811, 794, 743, 627 cm^{-1}.

***N*-hexyl-*N′*-[– Gly – (*D*-Ala)$_3$ – (*D*-Glu)$_3$ – OH]perylene-3,4,9,10-tetracarboxylic acid diimide (3HE).** Condensation of perylene-3,4-anhydride-9,10-hexylimide **Q1** (0.020 g, 0.042 mmol) and peptide **P3E** (0.030 g, 0.044 mmol) performed according to the general perylene imide synthesis procedures afforded *title compound* **3HE** as dark purple solid (0.040 g, 77%).^{1}H NMR (500 MHz, $CDCl_3$/CF_3COOH, 2:1): δ = 8.86 (m, Ar-H), 8.16-7.30 (NH proton exchange traces), 5.27 (m, CH_a Gly), 5.12 (m,

CH_b Gly), 4.91-4.56 (m, αCH Ala #1-3, αCH Glu #1-3), 4.32 (t, J = 7.7 Hz, hexyl NCH_2), 2.67 (m, γCH_2 Glu #1-3), 2.47 (m, βCH_2 Glu #3), 2.35-2.00 (m, βCH_2 Glu #1-2), 1.83 (quin. J = 7.5 Hz, hexyl βCH_2), 1.54 (m, CH_3 Ala #1-2, hexyl CH_2CH_2), 1.40 (m, CH_3 Ala #3, hexyl CH_2), 0.93 (t, J = 6.8 Hz, hexyl CH_3); MS (MALDI) *m/z*: Calculated for $C_{56}H_{60}N_8NaO_{18}$ $[M+Na]^+$ 1155.39, found 1155.54; IR (KBr): ν = 3289, 2953, 2930, 2855, 1695, 1654, 1594, 1577, 1541, 1440, 1403, 1374, 1343, 1250, 1174, 1088, 1029, 997, 853, 810, 794, 748, 627 cm^{-1}.

Perylene-3,4-monoanhydride-9,10-bis(n-butyl) ester (Q2). Synthesis and purification were accomplished as previously described.[87] Characterization matched that reported in the literature.

***N*-[-Gly-(Ala)$_3$-(Glu)$_3$]perylene-3,4-imide-9,10-bis(n-butyl) ester (Q3).** Peptide **P3** (0.060 g, 0.089 mmol) was combined with perylene-3,4-monoanhydride-9,10-bis(n-butyl ester) **Q2** (0.090 g, 0.17 mmol) in DMF (2.5 mL) and DMSO (2.5 mL) with diisopropylethylamine (0.10 mL) and stirred overnight at room temperature. The reaction was then precipitated with addition of hydrochloric acid solution (2 M, 0.5 mL). The precipitate was collected via filtration and washed sequentially with hydrochloric acid (2 M, aq., 3 x 10 mL), methanol (3 x 10 mL), and dichloromethane (2 x 10 mL). Drying of the washed precipitate yielded peptide-perylene bisester **Q3** as a fuzzy red solid (0.069 g, 66%). ^{1}H NMR (300 MHz, DMSO-d_6): δ = 8.72 (4H, d, J = 8.4 Hz, Ar-H), 8.55 (1H, d, J = 6.9 Hz, NH Ala #1), 8.46 (2H, d, J = 7.8 Hz, NH Ala #2-3), 8.05 (4H, m, Ar-H), 7.90 (3H, m, NH Glu #1-3), 4.74 (2H, m, αCH_2 Gly), 4.40-4.10 (10H, m, αCH Ala #1-3, αCH Glu #1-3, OCH_2 esters), 2.24 (6H, m, γCH_2 Glu #1-3), 1.91 (3H, m, βCH_2 Glu #3, βCH_a Glu #2), 1.73 (6H, m, βCH_b Glu #2, βCH_2 Glu #1, CH_3 Ala #1), 1.44 (4H, hex, J = 7.5 Hz, βCH_2 esters), 1.24 (6H, dd, J = 7.1 Hz, J = 1.5 Hz, CH_3 Ala #2-3), 1.14 (4H, d, J = 7.2 Hz, γCH_2 esters), 0.95 (6H, t, J = 7.8 Hz, CH_3 esters).

***N*-[– Gly – (*D*-Ala)$_3$ – (*D*-Glu)$_3$ – OH]-*N*′-[– Gly – (*L*-Ala)$_3$ – (*L*-Glu)$_3$ – OH]perylene-3,4,9,10-tetracarboxylic acid diimide (3M).** *N*-[-Gly-(Ala)$_3$-(Glu)$_3$]perylene-3,4-imide-9,10-bis(n-butyl) ester **Q3** (0.053 g, 0.045 mmol) and p-toluenesulfonic acid (0.050 g) were suspended in toluene and heated to 90 °C for 6 hours. The reaction mixture was then cooled to room temperature and the resulting

dark red solid collected via filtration. This dark red solid was washed with toluene (3 x 25 mL) and methanol (3 x 25 mL), collected and dried under high vacuum overnight. Condensation of a portion of the resulting dried peptide-substituted perylene imide anhydride (0.020 g, 0.019 mmol) with peptide **P3E** (0.020 g, 0.030 mmol) performed according to the general perylene imide synthesis procedures afforded *title compound* **3M** as a dark purple solid (0.026 g, 82%). ^{1}H NMR (500 MHz, $CDCl_3/CF_3COOH$, 2:1): δ = 8.88 (m, Ar-H), 8.05-7.29 (NH proton exchange traces), 5.24 (m, CH_a Gly), 5.10 (m, CH_b Gly), 4.88-4.51 (m, αCH Ala #1-3, αCH Glu #1-3), 2.64 (m, γCH_2 Glu #1-3), 2.53-2.03 (m, βCH_2 Glu #1-3), 1.72-1.22 (m, CH_3 Ala #1-3); MS (MALDI) *m/z*: Calculated for $C_{76}H_{86}N_{14}NaO_{32}$ $[M+Na]^+$ 1729.54, found 1729.26; IR (KBr): *v* = 3297, 3060, 2965, 2928, 2855, 1694, 1658, 1595, 1578, 1541, 1439, 1401, 1365, 1337, 1277, 1245, 1174, 1102, 1002, 964, 852, 811, 794, 748, 698, 656, 627, 582 cm^{-1}.

NH_2 – Gly – (*D*-Ala)$_3$ – (Glu)$_3$ – OH (P4)

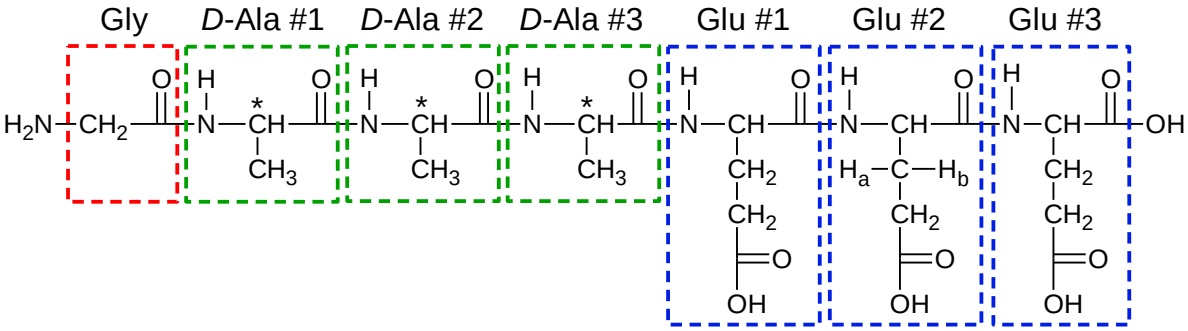

Figure 8.5 Chemical structure of peptide **P4**

Synthesis was performed according to the general SPPS procedure with a sample of Fmoc-Glu(OtBu)-Wang resin (0.51 g, loading 0.52 mmol/g, 0.27 mmol) affording *title compound* **P4** as a pale, off-white solid (0.16 g, 88%). ^{1}H NMR (500 MHz, DMSO-d_6): δ = 8.55 (1H, d, *J*= 7.6 Hz, NH *D*-Ala #1), 8.22 (1H, d, *J* = 7.1 Hz, NH *D*-Ala #2), 8.17 (1H, d, *J* = 7.6 Hz, NH Glu #3), 8.02 (4H, m, NH *D*-Ala #3, NH Glu #2, NH_2 Gly), 7.96 (1H, d, *J* = 6.8 Hz, NH Glu #1), 4.39 (1H, quin, *J* = 7.0 Hz, αCH *D*-Ala #1), 4.25 (4H, m, αCH *D*-Ala #2, αCH *D*-Ala #3, αCH Glu #1, αCH Glu #2), 4.16 (1H, m, αCH Glu #3), 3.56 (2H, d, *J* = 5.1 Hz, CH_2 Gly), 2.27 (4H, q, *J* = 8.6 Hz, γCH_2 Glu #2, γCH_2 Glu #3), 2.20 (2H, t, *J* = 7.9 Hz, γCH_2 Glu

#1), 1.94 (3H, m, βCH$_2$ Glu #3, βCH$_a$ Glu #2), 1.74 (3H, m, βCH$_2$ Glu #1, βCH$_b$ Glu #2), 1.21 (9H, m, CH$_3$ *D*-Ala #1-3); ^{13}C NMR (125 MHz, DMSO-d$_6$): δ = 174.1, 174.0, 173.8, 173.2, 172.2, 171.8, 171.6, 171.2, 170.9, 165.6, 51.8, 51.6, 51.3, 48.5, 48.2, 48.1, 40.2, 30.1, 30.07, 30.06, 27.5, 27.4, 26.2, 18.5, 18.4, 18.0; HRMS (ESI$^+$) *m/z*: Calculated for $C_{26}H_{42}N_7O_{14}$ $[M+H]^+$ 676.2784, found 676.2796, Calculated for $C_{26}H_{41}N_7NaO_{14}$ $[M+Na]^+$ 698.2604, found 698.2598; HRMS (ESI$^-$) *m/z*: Calculated for $C_{26}H_{40}N_7O_{14}$ $[M-H]^-$ 674.2639, found 674.2647.

***N,N′*-di[– Gly – (*D*-Ala)$_3$ – (Glu)$_3$ – OH]perylene-3,4,9,10-tetracarboxylic acid diimide (4).** Condensation of PTCDA (0.022 g, 0.056 mmol) and peptide **P4** (0.076 g, 0.11 mmol) performed according to the general perylene imide synthesis procedures afforded *title compound* **4** as a dark purple solid (0.086 g, 90%). ^{1}H NMR (600 MHz, CDCl$_3$/CF$_3$COOH, 2:1): δ = 8.83 (m, Ar-H), 8.15-6.90 (NH proton exchange traces), 5.19 (m, CH$_a$ Gly), 5.05 (m, CH$_b$ Gly), 4.85-4.41 (m, αCH *D*-Ala #1-3, αCH Glu #1-3), 2.61 (m, γCH$_2$ Glu #1-3), 2.50-1.77 (m, βCH$_2$ Glu #1-3), 1.70-1.19 (m, CH$_3$ *D*-Ala #1-3); MS (MALDI) *m/z*: Calculated for $C_{76}H_{86}N_{14}NaO_{32}$ $[M+Na]^+$ 1729.54, found 1729.58; IR (KBr): *v* = 3435, 2971, 2929, 1697, 1664, 1632, 1595, 1545, 1440, 1403, 1384, 1368, 1247, 1204, 1175, 1129, 1044, 810, 699, 600 cm^{-1}.

***N*-hexyl-*N′*-[– Gly – (*D*-Ala)$_3$ – (Glu)$_3$ – OH]perylene-3,4,9,10-tetracarboxylic acid diimide (4H).** Condensation of perylene-3,4-anhydride-9,10-hexylimide **Q1** (0.015 g, 0.032 mmol) and peptide **P4** (0.028 g, 0.041 mmol) performed according to the general perylene imide synthesis procedures afforded *title compound* **4H** as dark purple solid (0.025 g, 89%). ^{1}H NMR (600 MHz, CDCl$_3$/CF$_3$COOH, 2:1): δ = 8.83 (m, Ar-H), 8.15-7.33 (NH proton exchange traces), 5.24 (m, CH$_a$ Gly), 5.05 (m, CH$_b$ Gly), 4.85-4.46 (m, αCH Ala #1-3, αCH Glu #1-3), 4.29 (t, *J* = 6.5 Hz, hexyl NCH$_2$), 2.63 (m, γCH$_2$ Glu #1-3), 2.50-2.04 (m, βCH$_2$ Glu #1-3), 1.80 (quin. *J* = 7.7 Hz, hexyl βCH$_2$), 1.66-1.24 (m, CH$_3$ Ala #1-3, hexyl CH$_2$), 0.92 (t, *J* = 6.0 Hz, hexyl CH$_3$); MS (MALDI) *m/z*: Calculated for $C_{56}H_{60}N_8NaO_{18}$ $[M+Na]^+$ 1155.39, found 1155.09; IR (KBr): *v* = 3430, 2929, 2857, 1697, 1655, 1594, 1540, 1440, 1403, 1375, 1344, 1281, 1249, 1174, 1129, 1089, 1033, 997, 853, 810, 748, 628 cm^{-1}.

NH_2 – Gly – $(Glu)_3$ – OH (P5)

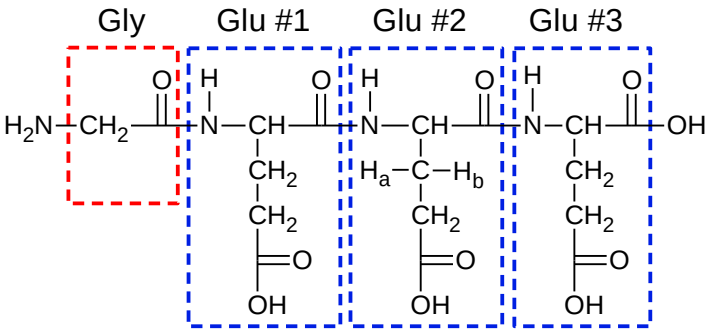

Figure 8.6 Chemical structure of peptide **P5**

Synthesis was performed according to the general SPPS procedure with a sample of Fmoc-Glu(OtBu)-Wang resin (0.50 g, loading 0.56 mmol/g, 0.28 mmol) affording *title compound* **P5** as an hygroscopic, off-white solid (0.13 g, 98%). ^{1}H NMR (500 MHz, DMSO-d_6): δ = 8.54 (1H, d, *J* = 7.8 Hz, NH Glu #1), 8.22 (2H, m, NH Glu #2-3), 8.01 (2H, br s, NH_2 Gly), 4.40 (1H, m, αCH Glu #1), 4.25 (1H, m, αCH Glu #2), 4.18 (1H, m, αCH Glu #3), 3.59 (2H, d, *J* = 6.8 Hz, CH_2 Gly), 2.28 (6H, m, γCH_2 Glu #1-3), 1.92 (3H, m, βCH_2 Glu#1, βCH_a Glu#2), 1.75 (3H, m, βCH_b Glu#3); ^{13}C NMR (125 MHz, DMSO-d_6): δ = 174.1, 174.0, 173.8, 173.1, 171.1, 170.6, 165.8, 54.8, 51.8, 51.3, 40.2, 30.8, 30.09, 30.07, 27.9, 27.4, 26.2, 24.7; HRMS (ESI$^+$) *m/z*: Calculated for $C_{17}H_{27}N_4O_{11}$ $[M+H]^+$ 463.1671, found 463.1666; Calculated for $C_{17}H_{26}N_4NaO_{11}$ $[M+Na]^+$ 485.1490, found 485.1481.

***N,N′*-di[– Gly – $(Glu)_3$ – OH]perylene-3,4,9,10-tetracarboxylic acid diimide (5).** Condensation of PTCDA (0.021 g, 0.053 mmol) and peptide **P5** (0.049 g, 0.11 mmol) performed according to the general perylene imide synthesis procedures afforded *title compound* **5** as dark purple solid (0.038 g, 55%). ^{1}H NMR (600 MHz, $CDCl_3$/CF_3COOH, 2:1): δ = 8.89 (m, Ar-H), 8.43-7.35 (NH proton exchange traces), 5.24 (m, CH_2 Gly), 5.00-4.76 (m, αCH Glu #1-3), 2.72 (m, γCH_2 Glu #1-3), 2.58-2.13 (m, βCH_2 Glu #1-3); MS (MALDI) *m/z*: Calculated for $C_{58}H_{56}N_8NaO_{26}$ $[M+Na]^+$ 1303.32, found 1303.16; IR (KBr): *ν* = 3428, 3060, 1692, 1658, 1593, 1577, 1437, 1401, 1364, 1339, 1274, 1245, 1173, 1132, 1002, 862, 810, 794, 752, 655, 625 cm^{-1}.

***N*-hexyl-*N'*-[– Gly – $(Glu)_3$ – OH]perylene-3,4,9,10-tetracarboxylic acid diimide (5H).** Condensation of perylene-3,4-anhydride-9,10-hexylimide **Q1** (0.015 g, 0.032 mmol) and peptide **P5** (0.027 g, 0.058 mmol) performed according to the general perylene imide synthesis procedures afforded *title compound* **5H** as dark purple solid (0.020 g, 67%). ^{1}H NMR (600 MHz, $CDCl_3/CF_3COOH$, 2:1): δ = 8.84 (m, Ar-H), 8.15-7.33 (NH proton exchange traces), 5.20 (m, CH_2 Gly), 4.28 (t, *J* = 6.5 Hz, hexyl NCH_2), 3.26 (q, *J* = 6.0, αCH Glu #1-3), 2.80-2.58 (m, γCH_2 Glu #1-3), 2.51-2.09 (m, βCH_2 Glu #1-3), 1.79 (quin. *J* = 6.5 Hz, hexyl βCH_2), 1.68-1.21 (m, hexyl CH_2), 0.92 (t, *J* = 6.0 Hz, hexyl CH_3); MS (MALDI) *m/z*: Calculated for $C_{47}H_{45}N_5NaO_{15}$ $[M+Na]^+$ 942.28, found 942.28; IR (KBr): *v* = 3409, 2954, 2925, 2854, 1696, 1658, 1593, 1507, 1438, 1403, 1372, 1343, 1248, 1174, 1087, 1032, 997, 855, 809, 793, 748, 698, 628 cm^{-1}.

NH_2 – Gly – $(Phe)_3$ – $(Glu)_3$ – OH (P6)

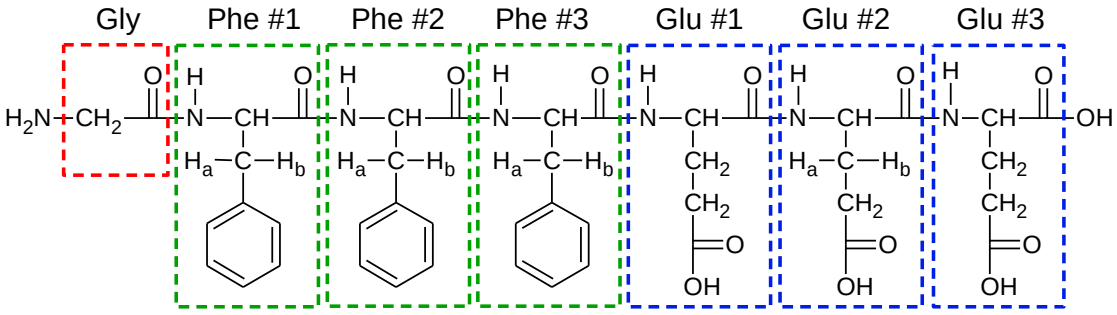

Figure 8.7 Chemical structure of peptide **P6**

Synthesis was performed according to the general SPPS procedure except that reaction times for the coupling reactions of the phenylalanine amino acids were increased to 4 hours. A sample of Fmoc-Glu(OtBu)-Wang resin (0.51 g, loading 0.52 mmol/g, 0.27 mmol) was used for the reaction sequence. Precipitation, filtration, and drying of the product from the Wang resin cleavage solution afforded *title compound* **P6** as a pale off-white solid (0.19 g, 80%). ^{1}H NMR (500 MHz, DMSO-d_6): δ = 8.50 (1H, d, *J* = 8.5 Hz, NH Phe #1), 8.34 (1H, d, *J* = 8.5 Hz, NH Phe #2), 8.23 (3H, d, *J* = 7.5 Hz, NH Phe #3, NH Glu #2, NH Glu #3), 8.04 (1H, d, *J* = 8.0 Hz, NH Glu #1), 7.93 (2H, br s, NH_2), 7.12-7.31 (15H, m, Ph-H), 4.56 (3H, m, αCH Phe #1, αCH Phe #2, αCH Phe #3), 4.31 (2H, m, αCH Glu #1, αCH

Glu #3), 4.18 (1H, m, αCH Glu #2), 3.47 (2H, d, J = 14.0 Hz, CH_2 Gly), 3.02 (2H, td, J = 13.9 Hz, J = 3.9 Hz, βCH_a Phe #2, βCH_a Phe #3), 2.94 (1H, dd, J = 13.9 Hz, J = 3.4 Hz, βCH_a Phe #1), 2.84 (1H, dd, J = 13.9 Hz, J = 9.3 Hz, βCH_b Phe #3), 2.76 (1H, dd, J = 13.9 Hz, J = 9.5 Hz, βCH_b Phe #2), 2.63 (1H, dd, J = 13.9 Hz, J = 9.8 Hz, βCH_b Phe #1), 2.27 (6H, m, γCH_2 Glu #1, γCH_2 Glu #2, γCH_2 Glu #3), 1.95 (3H, m, βCH_2 Glu #3, βCH_a Glu #2), 1.77 (3H, m, βCH_2 Glu #1, βCH_b Glu #2); ^{13}C NMR (125 MHz, DMSO-d_6): δ = 177.3, 174.2, 174.1, 173.8, 173.2, 171.2, 171.0, 170.9, 170.5, 165.5, 137.8, 137.7, 137.5, 129.4, 129.3, 128.2, 128.1, 126.4, 126.3, 56.4, 54.0, 53.9, 53.8, 51.9, 51.7, 51.4, 38.0, 37.6, 37.4, 30.3, 30.2, 30.1, 27.7, 27.6, 26.3; HRMS (ESI$^+$) *m/z*: Calculated for $C_{44}H_{54}N_7O_{14}$ $[M+H]^+$ 904.3723, found 904.3703, Calculated for $C_{44}H_{53}N_7NaO_{14}$ $[M+Na]^+$ 926.3543, found 926.3547.

***N,N′*-di[– Gly – (Phe)$_3$ – (Glu)$_3$ – OH]perylene-3,4,9,10-tetracarboxylic acid diimide (6).** Synthesis was performed according to the general perylene imide synthesis procedures with the exception that the acetone wash was omitted since **6** was found to elute from the HP20ss with acetone. Condensation of PTCDA (0.022 g, 0.057 mmol) and peptide **P6** (0.10 g, 0.11 mmol) afforded *title compound* **6** as dark purple solid (0.11 g, 90%). ^{1}H NMR (600 MHz, $CDCl_3$/CF_3COOH, 2:1): δ = 8.83 (m, Ar-H), 8.39-7.49 (NH proton exchange traces), 7.43-6.95 (m, Ph-H), 5.13 (m, CH_a Gly), 5.03 (m, CH_b Gly), 4.97-4.55 (m, αCH Phe #1-3, αCH Glu #1-3), 3.25-2.70 (m, βCH_2 Phe #1-3), 2.70-1.85 (m, γCH_2 Glu #1-3), 1.78-1.16 (m, βCH_2 Glu #1-3); MS (MALDI) *m/z*: Calculated for $C_{112}H_{110}N_{14}NaO_{32}$ $[M+Na]^+$ 2185.73, found 2185.76; IR (KBr): ν = 3430, 3276, 3061, 3025, 2921, 2852, 1701, 1667, 1638, 1594, 1539, 1492, 1452, 1403, 1365, 1339, 1273, 1248, 1174, 1122, 1068, 1028, 1013, 971, 942, 906, 810, 747, 698, 534 cm^{-1}.

NH_2 – Gly – $(Leu)_3$ – $(Glu)_3$ – OH (P7)

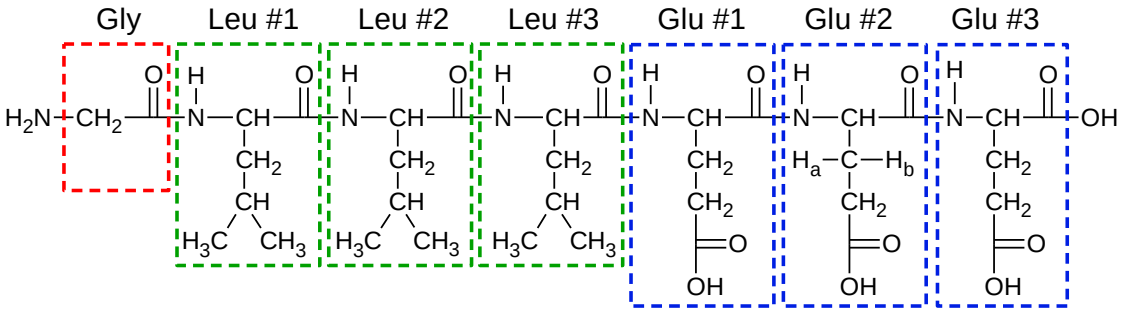

Figure 8.8 Chemical structure of peptide **P7**

Synthesis was performed according to the general SPPS procedure with a sample of Fmoc-Glu(OtBu)-Wang resin (0.50 g, loading 0.52 mmol/g, 0.26 mmol) affording *title compound* **P7** as a pale, off-white solid (0.20 g, 95%). ^{1}H NMR (600 MHz, DMSO-d_6): δ = 8.47 (1H, d, *J* = 8.5 Hz, NH Leu #1), 8.24 (1H, d, *J* = 8.2 Hz, NH Leu #2), 8.22 (1H, d, *J* = 7.6 Hz, NH Glu #3), 7.95 (5H, m, NH_2 Gly, NH Glu #1-2, NH Leu #3), 4.44 (1H, m, 1H, αCH Leu #1), 4.28 (3H, m, αCH Leu #2-3, αCH Glu #2), 4.17 (2H, m, αCH Glu #1,3), 3.56 (2H, q, *J* = 5.6 Hz, CH_2 Gly), 2.24 (6H, m, γCH_2 Glu #1-3), 1.81 (6H, m, βCH_2 Glu #1-3), 1.57 (3H, m, γCH Leu #1-3), 1.42 (6H, m, βCH_2 Leu #1-3), 0.85 (18H, m, CH_3 Leu #1-3); ^{13}C NMR (150 MHz, DMSO-d_6): δ = 174.5, 174.4, 174.1, 173.5, 172.0, 171.8, 171.5, 171.1, 170.9, 165.9, 51.7, 51.2, 51.2, 41.9, 40.8, 40.5, 30.5, 30.4, 30.0, 28.0, 27.8, 26.6, 24.6, 24.5, 24.5, 23.6, 23.4, 22.2, 22.1, 21.9, 21.7, 21.5; HRMS (ESI$^+$) *m/z*: Calculated for $C_{35}H_{60}N_7O_{14}$ $[M+H]^+$ 802.4193, found 802.4177.

***N,N′*-di[– Gly – $(Leu)_3$ – $(Glu)_3$ – OH]perylene-3,4,9,10-tetracarboxylic acid diimide (7).** Condensation of PTCDA (0.035 g, 0.09 mmol) and peptide **P7** (0.14 g, 0.18 mmol) performed according to the general perylene imide synthesis procedures afforded *title compound* **7** as a dark purple solid (0.12 g, 71%). ^{1}H NMR (500 MHz, DMSO-d_6): δ = 8.85 (m, Ar-H), 8.20-7.30 (NH proton exchange traces), 5.22 (m, CH_a Gly), 5.12 (m, CH_b Gly), 4.87-4.48 (m, αCH Leu #1-3, αCH Glu #1-3), 2.64 (m, γCH_2 Glu #1-3), 2.52-2.03 (m, βCH_2 Glu #1-3), 1.84-1.47 (m, βCH_2 Leu #1-3), 1.08-0.78 (m, γCH Leu #1-3, CH_3 Leu #1-3); MS (MALDI) *m/z*: Calculated for $C_{94}H_{122}N_{14}NaO_{32}$ $[M+Na]^+$ 1981.82, found 1982.09; Calculated for $C_{94}H_{122}N_{14}Na_2O_{32}$ $[M+2Na]^+$ 2004.81, found 2005.11; IR (KBr): *ν* = 3426, 3291,

3074, 2959, 2931, 2872, 1703, 1663, 1642, 1595, 1542, 1438, 1402, 1369, 1341, 1248, 1174, 1130, 1038, 1002, 811 cm^{-1}.

NH_2 – Gly – (*D*-Leu)$_3$ – (Glu)$_3$ – OH (P8)

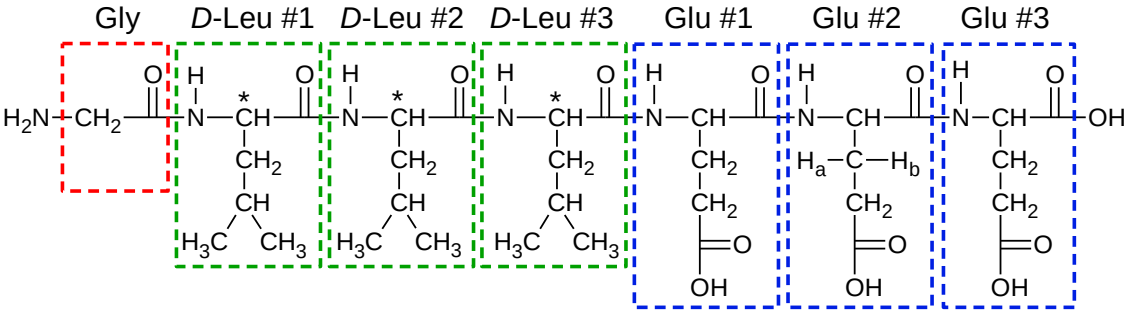

Figure 8.9 Chemical structure of peptide **P8**

Synthesis was performed according to the general SPPS procedure with a sample of Fmoc-Glu(OtBu)-Wang resin (0.50 g, loading 0.52 mmol/g, 0.26 mmol) affording *title compound* **P8** as a pale, off-white solid (0.19 g, 92%). ^{1}H NMR (500 MHz, DMSO-d_6): δ = 8.50 (1H, d, *J*= 8.1 Hz, NH *D*-Leu #1), 8.28 (1H, d, *J* = 8.1 Hz, NH *D*-Leu #2), 8.19 (1H, d, *J* = 7.3 Hz, NH Glu #3), 8.02 (4H, m, NH *D*-Leu #3, NH Glu #2, NH_2 Gly), 7.93 (1H, d, *J* = 8.1 Hz, NH Glu #1), 4.44 (1H, q, *J* = 7.6 Hz, αCH *D*-Leu #1), 4.27 (4H, m, αCH *D*-Leu #2, αCH *D*-Leu #3, αCH Glu #1, αCH Glu #2), 4.18 (1H, q, *J* = 7.0 Hz, αCH Glu #3), 3.58 (2H, q, *J* = 5.4 Hz, CH_2 Gly), 2.28 (4H, m, γCH_2 Glu #2, γCH_2 Glu #3), 2.21 (2H, t, *J* = 8.0 Hz, γCH_2 Glu #1), 1.94 (3H, m, βCH_2 Glu #3, βCH_a Glu #2), 1.76 (3H, m, βCH_2 Glu #1, βCH_b Glu #2), 1.57 (3H, m, γCH *D*-Leu #1, γCH *D*-Leu #2, γCH *D*-Leu #3), 1.44 (6H, m, βCH_2 *D*-Leu #1, βCH_2 *D*-Leu #2, βCH_2 Glu #3), 0.85 (24H, m, CH_3 *D*-Leu #1, CH_3 *D*-Leu #2, CH_3 *D*-Leu #3, γCH_2 Glu #1, γCH_2 Glu #2, γCH_2 Glu #3); ^{13}C NMR (125 MHz, DMSO-d_6): δ = 174.1, 174.0, 173.8, 173.1, 172.1, 171.6, 171.5, 171.2, 170.9, 165.6, 51.6, 51.4, 50.9, 41.5, 41.0, 40.2, 30.8, 30.11, 30.0, 27.5, 27.4, 26.3, 24.3, 24.14, 24.11, 23.2, 23.1, 22.9, 21.9, 21.7, 21.5; HRMS (ESI$^+$) *m/z*: Calculated for $C_{35}H_{60}N_7O_{14}$ $[M+H]^+$ 802.4193, found 802.4204, Calculated for $C_{35}H_{59}N_7NaO_{14}$ $[M+Na]^+$ 824.4012, found 824.4009.

***N,N'*-di[– Gly – (*D*-Leu)$_3$ – (Glu)$_3$ – OH]perylene-3,4,9,10-tetracarboxylic acid diimide (8).** Condensation of PTCDA (0.024 g, 0.061 mmol) and peptide **P8** (0.097 g, 0.12 mmol) performed according to the general perylene imide synthesis procedures afforded *title compound* **8** as dark purple solid (0.076 g, 64%). ^{1}H NMR (500 MHz, DMSO-d$_6$): δ = 8.88 (m, Ar-H), 8.15-7.36 (NH proton exchange traces), 5.22 (m, CH$_a$ Gly), 5.14 (m, CH$_b$ Gly), 4.88-4.53 (m, αCH Leu #1-3, αCH Glu #1-3), 2.67 (m, γCH$_2$ Glu #1-3), 2.54-2.06 (m, βCH$_2$ Glu #1-3), 1.90-1.52 (m, βCH$_2$ Leu #1-3), 1.12-0.80 (m, γCH Leu #1-3, CH$_3$ Leu #1-3); MS (MALDI) *m/z*: Calculated for $C_{94}H_{122}N_{14}NaO_{32}$ $[M+Na]^+$ 1981.82, found 1981.88, Calculated for $C_{94}H_{122}N_{14}Na_2O_{32}$ $[M+2Na]^+$ 2004.81, found 2005.90; IR (KBr): *ν* = 3430, 3284, 3066, 2958, 2872, 1703, 1665, 1641, 1594, 1540, 1437, 1401, 1364, 1339, 1277, 1245, 1172, 1123, 1032, 1012, 859, 810, 738, 659, 626 cm^{-1}.

NH$_2$ – Gly – (Ala)$_3$ – [Lys(Boc)]$_3$ – OH (P9)

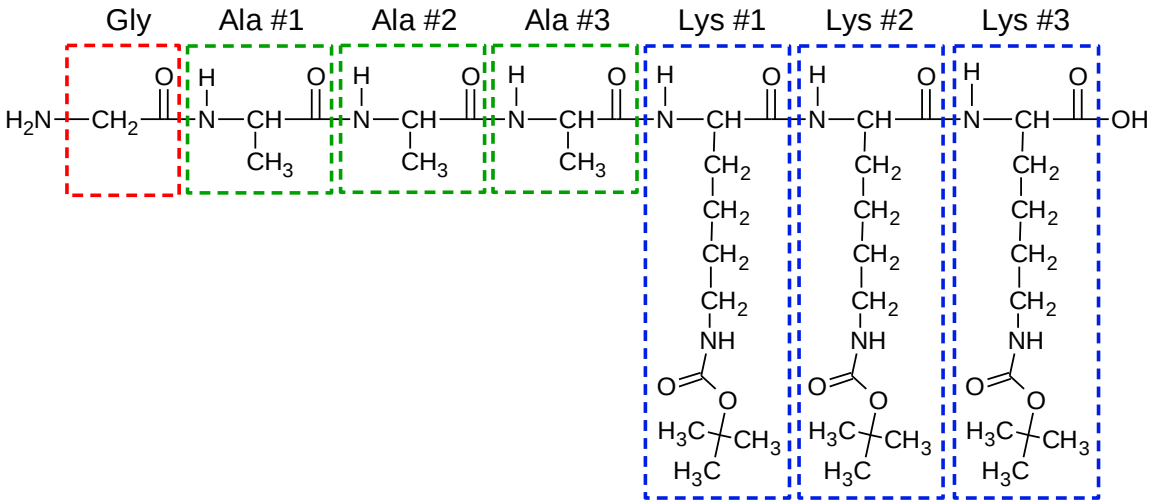

Figure 8.10 Chemical structure of peptide **P9**

Synthesis was performed according to the general SPPS procedure using a sample of H-Lys(Boc)-2-Cl-Trt resin (0.65 g, loading 0.33 mmol/g, 0.21 mmol). Resin cleavage was accomplished by shaking the resin in a 1:4 HFIP/CH_2Cl_2 solution[83] with 5% (v/v) TIPS for a duration of 1 h, 15 min. Removal of the HFIP under reduced pressure afforded *title compound* **P9** as a pale, off-white solid (0.13 g, 63%). ^{1}H NMR (500 MHz, DMSO-d$_6$): δ = 8.41 (1H, m, NH Ala #1), 8.32 (1H, d, *J* = 7.3 Hz, NH Ala #2), 8.00 (1H, d, *J* = 6.6 Hz, NH Lys #3), 7.93 (1H, d, *J* = 7.8 Hz, NH

Lys #2), 7.87 (1H, d, J = 6.8 Hz, NH Ala #3), 7.64 (1H, d, J = 5.9 Hz, NH Lys #1), 6.75 (3H, m, NH-Boc Lys #1-3), 4.32 (1H, m, αCH Ala #1), 4.24 (1H, m, αCH Ala #2), 4.15 (2H, m, αCH Lys #2-3), 4.02 (1H, m, αCH Ala #3), 3.92 (1H, m, αCH Lys #1), 3.32 (2H, br s, CH_2 Gly), 2.85 (6H, m, εCH_2 Lys #1-3), 1.64 (3H, m, βCH_2 Lys #3, βCH_a Lys #2), 1.49 (3H, m, βCH_b Lys #2, βCH_2 Lys #1), 1.35 (27H, m, CH_3 Lys-Boc #1-3), 1.20 (9H, m, CH_3 Ala #1-3), 0.97 (12H, m, γCH_2 Lys #1-3, δCH_2 Lys #1-3); HRMS (ESI^+) *m/z*: Calculated for $C_{44}H_{81}N_{10}O_{14}$ $[M+H]^+$ 973.5928, found 973.5947, Calculated for $C_{44}H_{80}N_{10}NaO_{14}$ $[M+Na]^+$ 995.5748, found 995.5761; MS (MALDI) *m/z*: Calculated for $C_{44}H_{80}N_{10}NaO_{14}$ $[M+Na]^+$ 995.57, found 995.63, Calculated for $C_{44}H_{80}N_{10}KO_{14}$ $[M+K]^+$ 1011.55, found 1011.57.

***N,N′*-di[– Gly – $(Ala)_3$ – $(Lys)_3$ – OH]perylene-3,4,9,10-tetracarboxylic acid diimide (9).** PTCDA (0.020 g, 0.050 mmol) and peptide **P9** (0.10 g, 0.11 mmol) were stirred under N_2 in imidazole (1.0 g) at 130-135 °C for 27 hours, producing a dark purple mixture. The mixture was then cooled to 95 °C and diluted with 3 mL of water to prevent solidification. After cooling to room temperature, the mixture was diluted with 40 mL of water and acidified by the dropwise addition of glacial acetic acid (1.2 mL). The resulting precipitate was collected via filtration and washed with water. The collected solid was added to a deprotection solution consisting of TFA (6 mL), CH_2Cl_2 (8 mL), water (1 mL), and TIPS (0.70 mL) and stirred vigorously for 3 hours under N_2. Ice cold diethyl ether (40 mL) was then added to the solution to induce precipitation and the mixture was chilled (4 °C) and allowed to settle. Collection of the resulting precipitate via filtration followed by washes with cold diethyl ether (40 mL) and drying of the solids afforded the TFA salt of the *title compound* **9** as granular purple solid (0.11 g, 95%). ^1H NMR (600 MHz, CF_3COOD): δ = 8.92 (8H, m, Ar-H), 5.38 (2H, m, CH_a Gly), 5.25 (2H, m, CH_b Gly), 4.75 (12H, m, αCH Ala #1-3, αCH Lys #1-3), 3.34 (12H, m, εCH_2 Lys #1-3), 2.44 (6H, m, βCH_2 Lys #3, βCH_a Lys #2), 1.96 (24H, m, βCH_b Lys #2, βCH_2 Lys #1, CH_3 Ala #1-3), 1.67 (24H, m, γCH_2 Lys #1-3, δCH_2 Lys #1-3); MS (MALDI) *m/z*: Calculated for $C_{82}H_{116}N_{20}NaO_{20}$ $[M+Na]^+$ 1723.86, found 1723.81; IR (KBr): ν = 3448, 3293, 3181, 3008, 1699, 1662, 1643, 1574, 1426, 1410, 1335, 1249, 1172, 1019, 925, 877, 809, 748, 667, 643, 520 cm^{-1}.

NH_2 – Lys – $(Ala)_3$ – $(Glu)_3$ – OH (P10)

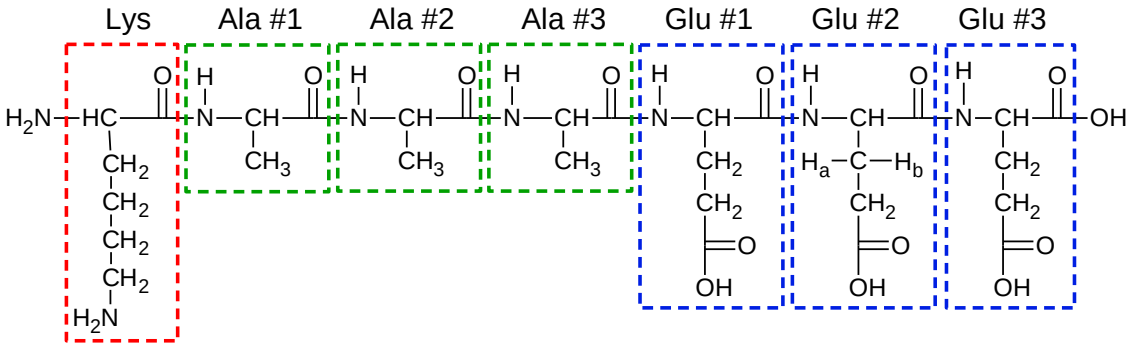

Figure 8.11 Chemical structure of peptide **P10**

Synthesis was performed according to the general SPPS procedure with a sample of Fmoc-Glu(OtBu)-Wang resin (0.50 g, loading 0.48 mmol/g, 0.24 mmol) affording *title compound* **P10** as a pale, off-white solid (0.16 g, 91%). ^{1}H NMR (500 MHz, DMSO-d_6): δ = 8.61 (1H, d, *J* = 7.1 Hz, NH Ala #1), 8.20 (1H, d, *J* = 7.3 Hz, NH Ala #2), 8.17 (1H, d, *J* = 7.3 Hz, NH Ala #3), 7.98 (2H, t, *J* = 6.8 Hz, NH Glu #3, NH Glu #2), 7.93 (1H, d, *J* = 7.6 Hz, NH Glu #1), 7.89 (4H, br. s, αNH_2, εNH_2, Lys), 4.36 (1H, quin, *J* = 7.1 Hz, αCH Ala #1), 4.25 (4H, m, αCH Ala #2, αCH Glu #1-3), 4.16 (1H, m, αCH Ala #3), 3.77 (1H, t, *J* = 6.3 Hz, αCH Lys), 2.75 (2H, m, εCH_2 Lys), 2.26 (6H, m, γCH_2 Glu #1-3), 1.92 (3H, m, βCH_2 Glu #3, βCH_a Glu #2), 1.74 (5H, m, βCH_2 Glu #1, βCH_b Glu #2, βCH_2 Lys), 1.53 (2H, quin, *J* = 7.5 Hz, γCH_2 Lys), 1.36 (2H, m, δCH_2 Lys), 1.24 (3H, d, *J* = 7.1 Hz, CH_3 Ala #1), 1.20 (6H, m, CH_3 Ala #2-3); ^{13}C NMR (125 MHz, DMSO-d_6): δ = 174.02, 174.00 173.7, 173.1, 172.1, 171.8, 171.5, 171.1, 170.8, 168.1, 51.8, 51.7, 51.6, 51.3, 48.2, 48.0, 38.5, 30.5, 30.1, 29.9, 27.5, 27.4, 26.5, 26.2, 21.0, 18.13, 18.08; HRMS (ESI$^+$) *m/z*: Calculated for $C_{30}H_{51}N_8O_{14}$ $[M+H]^+$ 747.3519, found 747.3501, Calculated for $C_{30}H_{52}N_8O_{14}$ $[M+2H]^{+2}$ 374.1796, found 374.1797, Calculated for $C_{30}H_{50}N_8NaO_{14}$ $[M+Na]^+$ 769.3339, found 769.3301.

Perylene-3,4-anhydride-9,10-isopropylimide (Q4). Synthesis and purification were accomplished by analogous procedure for perylene-3,4-anhydride-9,10-hexylimide **Q1** as previously reported.[88]

***N*-yl-*N'*-isopropyl-perylene-3,4,9,10-diimide) – Lys(*N*-yl-*N'*-isopropyl-perylene-3,4,9,10-diimide) – $(Ala)_3$ – $(Glu)_3$ – OH (10)**

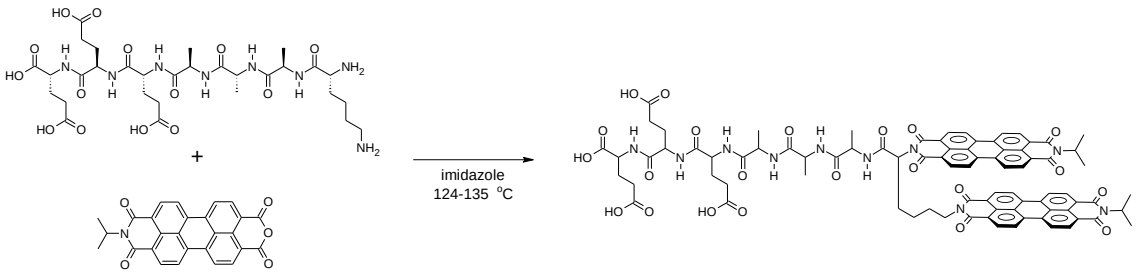

Figure 8.12 Reaction to form compound **10**

Condensation of perylene-3,4-anhydride-9,10-isopropylimide **Q4** (0.022 g, 0.051 mmol) and peptide **P10** (0.017 g, 0.023 mmol) performed according to the general perylene imide synthesis procedures afforded *title compound* **10** as dark purple solid (0.037 g, 67%). ^{1}H NMR (500 MHz, $CDCl_3/CF_3COOH$, 2:1): δ = 8.86 (8H, m, Ar-H #1), 8.75 (8H, m, Ar-H #2), 8.39-7.33 (NH exchange traces), 6.15 (1H, m, αCH Lys), 6.02 (2H, m, NCH isopropyl #1,2), 5.52 (2H, m, NCH_2 Lys), 4.70 (3H, m, Ala #1-3), 4.30 (3H, m, Glu #1-3), 2.77-2.21 (6H, m, γCH_2 Glu #1-3), 1.94 (6H, m, βCH_2 Glu #1-3), 1.83-1.31 (27H, m, CH_3 Ala#1-3, CH_3 isopropyl, βCH_2 Lys, γCH_2 Lys, δCH_2 Lys); MS (MALDI) *m/z*: Calculated for $C_{84}H_{76}N_{10}NaO_{22}$ $[M+Na]^+$ 1599.50, found 1599.37; IR (KBr): *v* = 3427, 2982, 1700, 1653, 1593, 1507, 1440, 1404, 1340, 1317, 1254, 1146, 1122, 1084, 1017, 856, 809, 738, 626 cm^{-1}.

[*N*-yl-perylene-3,4-imide-9,10-bis(n-butyl) ester] – Lys[*N*-yl-perylene-3,4-imide-9,10-bis(n-butyl) ester] – $(Ala)_3$ – $(Glu)_3$ – OH (11)

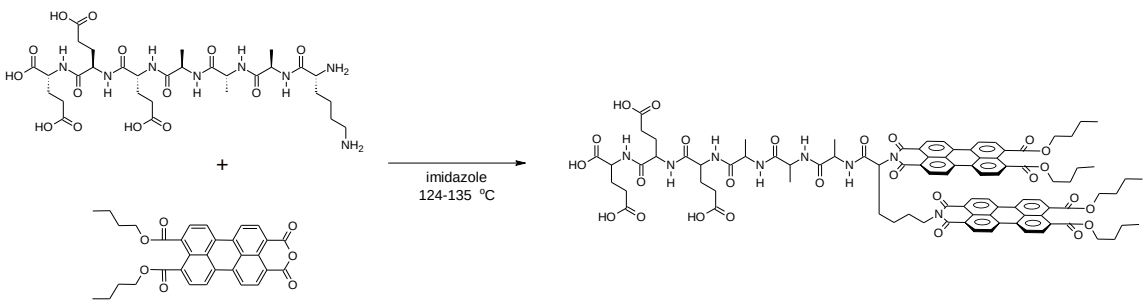

Figure 8.13 Reaction to form compound **11**

Condensation of perylene-3,4-monoanhydride-9,10-bis(n-butyl ester) **Q2** (0.13 g, 0.25 mmol) and peptide **P10** (0.090 g, 0.12 mmol) performed according to the general perylene imide synthesis procedures afforded *title compound* **11** as dark purple solid (0.070 g, 77%). ^{1}H NMR: Data unavailable due to poor compound solubility and the presence of the acid-labile ester groups preventing the use of TFA; MS (MALDI) *m/z*: Calculated for $C_{94}H_{98}N_8NaO_{26}$ $[M+Na]^+$ 1777.65, found 1777.60; IR (KBr): ν = 3324, 3070, 2960, 2936, 2873, 1770, 1699, 1653, 1594, 1531, 1450, 1416, 1404, 1360, 1298, 1261, 1214, 1202, 1170, 1102, 1078, 1025, 956, 853, 827, 808, 748, 652 cm^{-1}.

N,N'-di[Ac-Ile-Lys(-yl)-His-Leu-Ser-Val-Asn-NH_2]perylene-3,4,9,10-tetracarboxylic acid diimide (12)

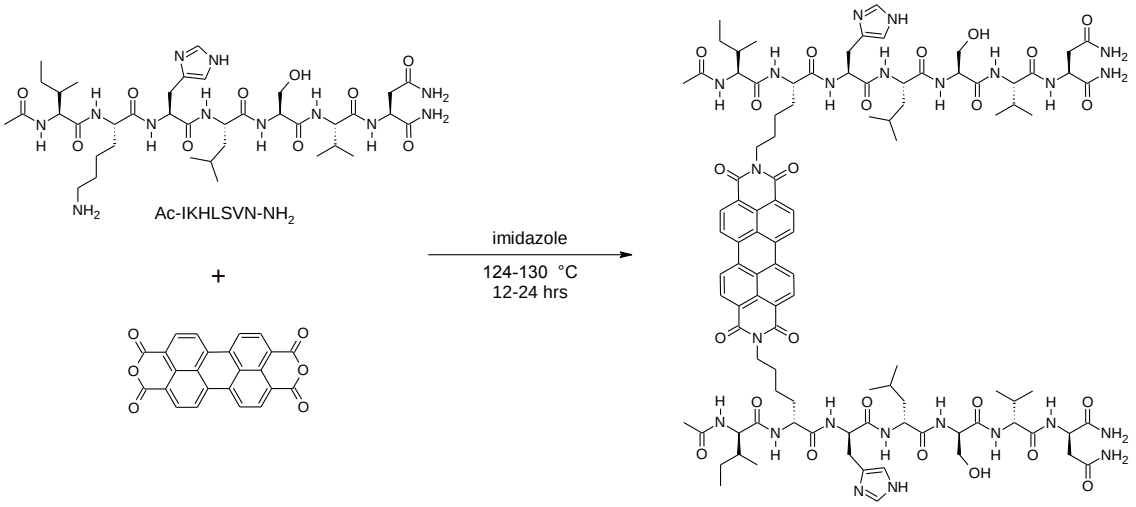

Figure 8.14 Reaction to form compound **12**

Condensation of PTCDA (0.015 g, 0.038 mmol) and terminal-protected peptide Ac-IKHLSVN-NH_2 (Mimotops) (0.061 g, 0.072 mmol) performed according to the general perylene imide synthesis procedures afforded *title compound* **12** as dark purple solid (0.051 g, 66%). ^{1}H NMR (500 MHz, CF_3COOD): δ = 8.99 (8H, m, Ar-H), 8.83 (2H, s, CH=N His), 8.80-7.55 (NH exchange traces), 7.57 (4H, s, NH_2 Asn-terminus), 7.52 (4H, s, NH_2 Asn side-chain), 7.33 (2H, s, CH=C His), 5.21 (2H, m, αCH Asn), 4.84 (2H, m, αCH His), 4.61 (6H, m, αCH Ser, αCH Leu, αCH Lys), 4.44 (4H, m, NCH_2 Lys), 4.29 (2H, m, αCH Val), 4.21 (2H, m, αCH Ile), 3.58 (4H,

m, βCH$_2$ Ser), 3.43 (4H, m, βCH$_2$ His), 3.18 (4H, m, βCH$_2$ Asn), 2.36 (8H, m, CH$_3$ Ac-Ile, βCH Val), 2.03 (6H, m, βCH$_2$ Lys, βCH Ile), 1.75 (10H, m, βCH$_2$ Leu, δCH$_2$ Lys, γCH Leu), 1.40 (8H, m, γCH$_2$ Lys, γCH$_2$ Ile), 1.04 (36H, m, γCH$_3$ Val, γCH$_3$ Ile, δCH$_3$ Ile, δCH$_3$ Leu); MS (MALDI) *m/z*: Calculated for $C_{104}H_{145}N_{24}O_{24}$ $[M+H]^+$ 2114.09, found 2114.10, Calculated for $C_{104}H_{144}N_{24}NaO_{24}$ $[M+Na]^+$ 2136.07, found 2136.08; IR (KBr): ν = 3433, 2966, 2876, 1695, 1635, 1595, 1540, 1440, 1402, 1384, 1346, 1279, 1203, 1166, 1080, 1066, 850, 810, 794, 748, 700, 624 cm^{-1}.

Ac-Ile-Lys(*N*-yl-*N'*-hexyl-perylene-3,4,9,10-tetracarboxylic acid diimide)-His-Leu-Ser-Val-Asn-NH$_2$ (12H)

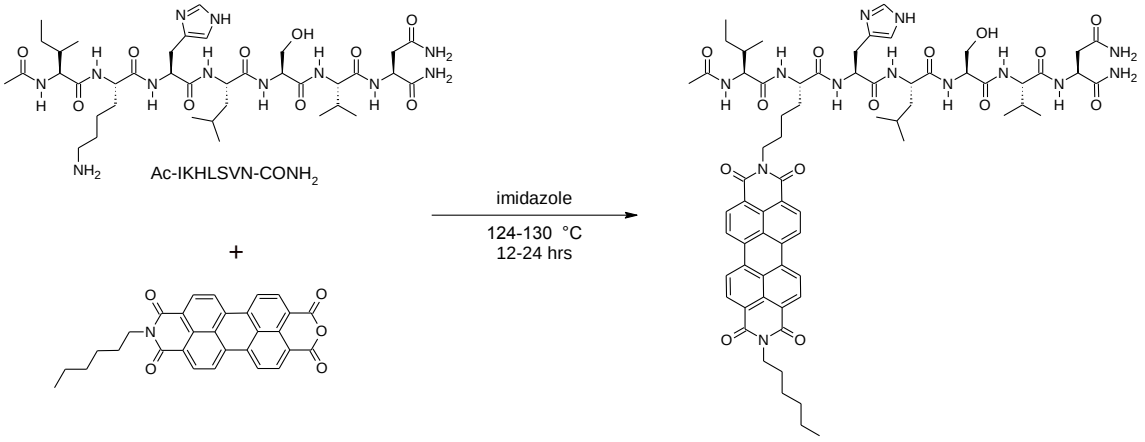

Figure 8.15 Reaction to form compound **12H**

Condensation of perylene-3,4-anhydride-9,10-hexylimide **Q1** (0.014 g, 0.029 mmol) and terminal-protected peptide Ac-IKHLSVN-NH$_2$ (Mimotops) (0.026 g, 0.030 mmol) performed according to the general perylene imide synthesis procedures afforded *title compound* **12H** as dark purple solid (0.031 g, 80%).^{1}H NMR (500 MHz, CF_3COOD): δ = 8.97 (8H, m, Ar-H), 8.72 (1H, s, CH=N His), 8.66-7.57 (NH exchange traces), 7.59 (2H, m, NH$_2$ Asn-terminus), 7.52 (2H, s, NH$_2$ Asn side-chain), 7.32 (1H, s, CH=C His), 5.23 (1H, m, αCH Asn), 4.85 (1H, m, αCH His), 4.68 (1H, m, αCH Ser), 4.59 (2H, m, αCH Leu, αCH Lys), 4.43 (4H, m, NCH$_2$ Lys, NCH$_2$ hexyl), 4.31 (1H, m, αCH Val), 4.22 (1H, m, αCH Ile), 3.59 (2H, m, βCH$_2$ Ser), 3.44 (2H, m, βCH$_2$ His), 3.20 (2H, m, βCH$_2$ Asn), 2.38 (4H, m, CH$_3$ Ac-Ile, βCH Val), 2.05 (4H, m, βCH$_2$ Lys, βCH$_2$ Leu), 1.94 (3H, m, βCH Ile, δCH$_2$ Lys),

1.78 (2H, m, βCH$_2$ hexyl), 1.71 (2H, m, γCH$_2$ Lys), 1.62 (3H, m, γCH Leu, γCH$_2$ hexyl), 1.49 (4H, m, δCH$_2$, εCH$_2$ hexyl), 1.40 (2H, m, γCH$_2$ Ile), 1.07 (21H, m, δCH$_3$ Leu, γCH$_3$ Ile, γCH$_3$ Val, CH$_3$ hexyl, δCH$_3$ Ile); MS (MALDI) *m/z*: Calculated for $C_{70}H_{89}N_{13}NaO_{14}$ $[M+Na]^+$ 1358.65, found 1358.67, Calculated for $C_{70}H_{89}N_{13}KO_{14}$ $[M+K]^+$ 1374.63, found 1374.65, Calculated for $C_{70}H_{89}N_{13}Na_2O_{14}$ $[M+2Na]^+$ 1381.64, found 1381.64; IR (KBr): ν = 3433, 3061, 2957, 2869, 1694, 1648, 1635, 1595, 1540, 1440, 1403, 1374, 1344, 1279, 1249, 1169, 1122, 1088, 853, 810, 794, 747, 655, 623 cm^{-1}.

NH_2 – Gly – Ile – Arg – His – Leu – Ser – Val – Asn – Glu – Glu – Glu – OH (P13)

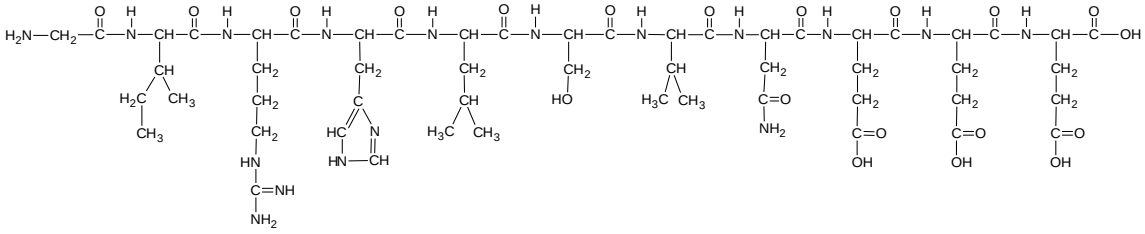

Figure 8.16 Chemical structure of peptide **P13**

Synthesis was performed using Fmoc-Glu(OtBu)-Wang resin (0.50 g, loading 0.48 mmol/g, 0.24 mmol) according to the general SPPS procedure with a modified resin cleavage solution consisting of TFA (8.8 mL), water (0.5 mL), toluene (0.5 mL), and triisopropylsilane (0.2 mL). The dried peptide was successively soaked in acetonitrile and toluene and decanted to remove trace scavengers. Final drying of the soaked peptide afforded the *title compound* **P13** as a pale, off-white solid (0.29 g, 95%). ^{1}H NMR (500 MHz, DMSO-d$_6$): δ = 8.91 (1H, m, CH=N His), 8.44 (1H, d, *J* = 7.8 Hz, NH Arg), 8.34 (1H, d, *J* = 6.3 Hz, NH Ile), 8.19 (3H, m, NH Ser, NH His, NH Asn), 8.06 (2H, m, NH Glu #1, NH Leu), 7.97 (3H, m, NH$_2$ Gly, NH Glu #2), 7.74 (1H, m, NH Glu #3), 7.68 (1H, d, *J* = 8.3 Hz, NH Val), 7.42 (2H, br. s, NH$_2$ Asn), 7.34 (1H, m, NH His ring), 7.30 (1H, m, NH Arg guanidine), 7.06 (2H, br. s, C=NH, NH$_2$ Arg guanidine), 6.93 (1H, br. s, CH=C His), 4.55 (2H, m, αCH Asn, αCH His), 4.36 (2H, m, αCH Ser, αCH Glu #1), 4.21 (6H, m, αCH Glu #2-3, αCH Leu, αCH Arg, αCH Val, αCH Ile), 3.61 (4H, m, CH$_2$ Gly, βCH$_2$ Ser), 3.02 (2H, m, βCH$_a$ His, δCH$_2$ Arg), 2.94 (1H, m, βCH$_b$ His), 2.56 (1H, dd, *J* = 15.3 Hz, *J* = 6.2 Hz, βCH$_a$ Asn), 2.39 (1H, dd, *J* = 15.5 Hz, *J* = 7.2 Hz, βCH$_b$ Asn), 2.24

(6H, m, γCH_2 Glu #1-3), 1.95 (4H, m, βCH_2 Glu #1, βCH_2 Glu #2), 1.79 (3H, m, βCH Val, βCH_2 Arg), 1.70 (1H, m, βCH Ile), 1.61 (2H, m, βCH_2 Glu #3), 1.43 (5H, m, βCH_2 Leu, γCH_2 Arg, γCH Leu), 1.07 (2H, m, γCH_2 Ile), 0.82 (18H, m, δCH_3 Leu, γCH_3 Ile, γCH_3 Val, δCH_3 Ile); ^{13}C NMR (125 MHz, DMSO-d_6): δ = 174.0, 173.8, 173.1, 172.5, 172.1, 171.7, 171.6, 171.2, 171.0, 170.8, 170.7, 170.6, 169.9, 169.6, 165.8, 156.8, 133.8, 129.0, 117.0, 65.0, 61.4, 57.2, 56.8, 55.0, 52.6, 51.8, 51.4, 51.3, 49.7, 40.9, 40.5, 40.2, 37.0, 36.9, 30.9, 30.1, 30.0, 28.7, 27.3, 27.2, 26.2, 25.1, 24.3, 24.2, 23.1, 21.4, 19.2, 17.8, 17.7, 15.2, 11.0; HRMS (ESI$^+$) *m/z*: Calculated for $C_{53}H_{88}N_{17}O_{20}$ $[M+H]^+$ 1282.6386, found 1282.6367, Calculated for $C_{53}H_{89}N_{17}O_{20}$ $[M+2H]^{+2}$ 641.8229, found 641.8244, Calculated for $C_{53}H_{87}N_{17}Na_2O_{20}$ $[M+2Na]^{+2}$ 663.8049, found 663.8058.

***N,N′*-di[-Gly-Ile-Arg-His-Leu-Ser-Val-Asn-Glu-Glu-Glu-OH]perylene-3,4,9,10-tetracarboxylic acid diimide (13).** Condensation of PTCDA (0.020 g, 0.051 mmol) and peptide **P13** (0.13 g, 0.10 mmol) in imidazole (1.0 g) at 130-135 °C under N_2 produced a solidifying dark black mixture after 20 minutes. The mixture was then cooled to 95 °C and dissolved in 3 mL of water prior to fully hardening. After cooling to room temperature, purification on HP20ss resin as outlined in the general perylene imide synthesis procedures afforded *title compound* **13** as dark purple solid (0.13 g, 84%). ^{1}H NMR (600 MHz, CF_3COOD): δ = 8.94 (8H, m, Ar-H), 8.69 (2H, m, CH=N His), 7.51 (2H, m, CH=C His), 5.34 (4H, m, CH_2 Gly), 5.18 (4H, m, αCH Asn, αCH His), 4.94 (6H, m, αCH Ser, αCH Glu #1-2), 4.80 (6H, m, αCH Glu #3, αCH Leu, αCH Arg), 4.57 (4H, m, αCH Val, αCH Ile), 3.53 (2H, m, βCH_a His), 3.39 (6H, m, βCH_b His, βCH_2 Ser), 3.19 (4H, m, δCH_2 Arg), 2.76 (12H, m, γCH_2 Glu #1-3), 2.57 (2H, m, Asn βCH_a), 2.42 (2H, m, Asn βCH_b), 2.26 (8H, m, βCH_2 Glu #1, βCH_2 Glu #2), 2.01 (8H, m, βCH Val, βCH_2 Arg, βCH Ile), 1.81 (12H, m, βCH_2 Glu #3, βCH_2 Leu, γCH_2 Arg), 1.37 (6H, m, γCH Leu, γCH_2 Ile), 1.05 (36H, m, δCH_3 Leu, γCH_3 Ile, γCH_3 Val, δCH_3 Ile); MS (MALDI) *m/z*: Calculated for $C_{130}H_{179}N_{34}O_{44}$ $[M+H]^+$ 2920.28, found 2920.22, Calculated for $C_{130}H_{178}N_{34}NaO_{44}$ $[M+Na]^+$ 2942.26, found 2942.24; IR (KBr): *ν* = 3424, 3280, 3073, 2963, 2931, 2870, 1658, 1634, 1594, 1543, 1437, 1399, 1363, 1337, 1302, 1276, 1237, 1174, 1025, 859, 810, 794, 733, 657, 630 cm^{-1}.

Ac – $(Glu)_3$ – Ile – Arg – His – Leu – Ser – Val – Asn – NH – CH_2CH_2 – NH_2 (P14)

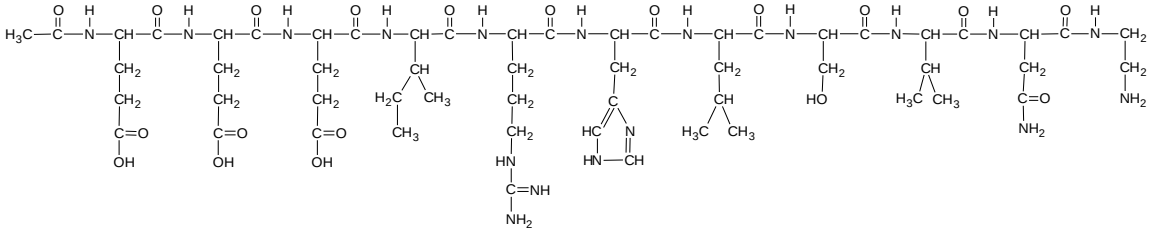

Figure 8.17 Chemical structure of peptide **P14**

Synthesis was performed according to the general SPPS procedure with a sample of 1,2-diaminoethane-trityl resin (0.31 g, loading 0.96 mmol/g, 0.30 mmol) according to the general SPPS procedure with a modified resin cleavage solution consisting of TFA (8.8 mL), water (0.5 mL), toluene (0.5 mL), and triisopropylsilane (0.2 mL), affording *title compound* **P14** as a pale, off-white solid (0.35 g, 92%). ^{1}H NMR (500 MHz, DMSO-d_6): δ = 8.95 (1H, m, CH=N His), 8.26 (1H, d, *J* = 7.3 Hz, NH Arg), 8.11 (5H, m, NH Ile, NH Ser, NH His, NH Asn, NH Glu #1), 7.97 (2H, m, NH Glu #2-3) 7.78 (3H, m, NH_2 ethyl, NH ethyl), 7.72 (1H, d, *J* = 8.13 Hz, NH Leu), 7.63 (1H, m, NH Val), 7.49 (2H, br. s, NH_2 Asn), 7.34 (1H, m, NH His ring), 7.31-7.05 (NH Arg guanidine exchange traces), 7.01 (1H, br. s, CH=C His), 4.60 (1H, m, αCH Asn), 4.45 (1H, m, αCH His), 4.36 (2H, m, αCH Ser, αCH Glu #3), 4.22 (3H, m, αCH Glu #1-2, αCH Leu), 4.14 (2H, m, αCH Arg, αCH Ile), 4.01 (1H, m, αCH Val), 3.60 (2H, m, βCH_2 Ser), 3.37 (2H, m, αCH_2 Asn-ethyl), 3.23 (2H, m, βCH_2 Asn-ethyl), 3.06 (3H, m, βCH_a His, βCH_2 Arg), 2.95 (1H, m, βCH_b His), 2.55 (1H, dd, *J* = 15.3 Hz, *J* = 6.5 Hz, βCH_a Asn), 2.44 (1H, dd, *J* = 15.3 Hz, *J* = 7.0 Hz, βCH_b Asn), 2.23 (6H, m, γCH_2 Glu #1-3), 1.97 (1H, m, βCH Val), 1.85 (7H, m, βCH_2 Glu #2-3, CH_3 Ac-Glu #1), 1.67 (5H, m, βCH Ile, βCH_2 Arg, βCH_2 Glu #1), 1.45 (5H, m, βCH_2 Leu, γCH_2 Arg, γCH Leu), 1.07 (2H, m, γCH_2 Ile), 0.80 (18H, m, δCH_3 Leu, γCH_3 Ile, γCH_3 Val, δCH_3 Ile); ^{13}C NMR (125 MHz, DMSO-d_6): δ = 174.1, 174.02, 173.96, 172.4, 171.8, 171.7, 171.5, 171.3, 171.1, 170.7, 170.5, 170.2, 169.9, 169.7, 169.6, 156.8, 133.8, 129.0, 117.0, 65.0, 61.4, 57.7, 56.8, 54.9, 52.4, 52.0, 51.4, 51.1, 50.0, 40.8, 40.4, 38.7, 37.0, 36.5, 36.4, 30.5, 30.4, 30.2, 30.1, 28.7, 27.1, 25.0, 24.3, 24.2, 23.1, 22.5, 21.4, 19.1, 19.0, 17.9, 17.8, 15.2, 10.9; HRMS (ESI^+) *m/z*: Calculated for $C_{55}H_{93}N_{18}O_{19}$ $[M+H]^+$ 1309.6859, found 1309.6825, Calculated for $C_{55}H_{94}N_{18}O_{19}$ $[M+2H]^{+2}$ 655.8480, found 655.8490, Calculated for

$C_{55}H_{95}N_{18}O_{19}$ $[M+3H]^{+3}$ 437.2335, found 437.2349, Calculated for $C_{55}H_{92}N_{18}NaO_{19}$ $[M+Na]^{+}$ 1331.6678, found 1331.6699.

***N,N′*-di[Ac-Glu-Glu-Glu-Ile-Arg-His-Leu-Ser-Val-Asn-NH-CH_2CH_2-]perylene-3,4,9,10-tetra-carboxylic acid diimide (14).** Condensation of PTCDA (0.020 g, 0.051 mmol) and peptide **P14** (0.14 g, 0.11 mmol) performed according to the general perylene imide synthesis procedures afforded *title compound* **14** as dark purple solid (0.11 g, 71%). ^{1}H NMR (600 MHz, CF_3COOD): δ = 8.89 (8H, m, Ar-H), 8.62 (2H, m, CH=N His), 7.50 (2H, m, CH=C His), 5.13 (4H, m, αCH Asn, αCH His), 5.00 (2H, m, αCH Ser), 4.86 (4H, m, αCH Glu #3, αCH Glu #2), 4.72 (10H, m, αCH Glu #1, αCH Leu, αCH Arg, αCH Ile, αCH Val), 4.47 (4H, m, CH_2 ethylimide), 4.25 (4H, m, CH_2 Asn-ethylamide), 3.86 (4H, m, βCH_2 Ser), 3.53 (2H, m, βCH_a His), 3.36 (6H, m, βCH_b His, βCH_2 Arg), 3.11 (4H, m, Asn βCH_2), 2.76 (12H, m, γCH_2 Glu #1-3), 2.33 (6H, m, Val βCH, Glu #1 βCH_2), 2.23 (10H, m, βCH_2 Glu #2-3, CH_3 Ac-Glu #1), 1.95 (8H, m, βCH_2 Glu #1, βCH_2 Arg), 1.72 (10H, m, βCH Ile, βCH_2 Leu, γCH_2 Arg), 1.31 (6H, m, γCH Leu, γCH_2 Ile), 1.01 (36H, m, δCH_3 Leu, γCH_3 Ile, γCH_3 Val, δCH_3 Ile); IR (KBr): ν = 3478, 3308, 3060, 2961, 2928, 2870, 1692, 1658, 1594, 1539, 1442, 1402, 1363, 1344, 1247, 1180, 1104, 1026, 852, 810, 747, 697 cm^{-1}.

***N*-[-Gly-Ile-Arg-His-Leu-Ser-Val-Asn-Glu-Glu-Glu-OH]perylene-3,4-imide-9,10-bis(n-butyl)ester (15).** Condensation of perylene-3,4-monoanhydride-9,10-bis(n-butyl ester) **Q2** (0.020 g, 0.038 mmol) and peptide **P13** (0.061 g, 0.048 mmol) was performed according to the general perylene imide synthesis procedures. The reaction mixture was cooled to 95 °C, diluted with 3 mL of water, and cooled to room temperature. The reaction mixture was then loaded onto HP20ss resin and the resin was successively flushed with ten 100 mL aqueous acetone solutions, forming a gradient series beginning at 10% (v/v) acetone/water increasing by 10% acetone with each 100 mL. Removal of the desired product using pyridine followed by 20% (v/v) pyridine/water followed by removal of the solvent under reduced pressure afforded *title compound* **15** as small dark purple needles (0.037 g, 76%). ^{1}H NMR (500 MHz, D_2O/pyridine-d_5, 4:1): δ = 7.55 (8H, br. m, Ar-H), 6.76 (2H, m, CH=N His, CH=C His), 4.08 (3H, m, αCH Asn, αCH His, αCH Ser), 3.89 (4H, m, OCH_2 esters), 3.49 (1H, m, αCH_a Gly), 3.29 (1H, m, αCH_b Gly), 2.77 (3H, m, αCH

Arg, αCH Leu, αCH Glu #1), 2.59 (2H, m, αCH Glu #2-3), 2.48 (2H, m, αCH Val, αCH Ile), 2.32 (2H, m, βCH_2 Ser), 1.99 (6H, m, βCH_2 His, βCH_2 Asn, δCH_2 Arg), 1.85 (4H, m, βCH_2 esters), 1.67 (6H, m, βCH_2 Glu #1-3), 1.24 (8H, m, γCH_2 esters, βCH Ile, βCH Val, γCH_2 Glu #1), 0.98 (9H, m, γCH_2 Glu #2-3, βCH_2 Arg, βCH_2 Leu, γCH Leu), 0.48 (28H, m, γCH_2 Arg, δCH_3 esters, γCH_2 Ile, γCH_3 Val, γCH_3 Ile, δCH_3 Leu, δCH_3 Ile); MS (MALDI) *m/z*: Calculated for $C_{85}H_{112}N_{17}O_{26}$ $[M+H]^+$ 1786.80, found 1786.72; IR (KBr): ν = 3357, 3056, 2956, 2930, 2860, 1690, 1658, 1594, 1577, 1545, 1438, 1400, 1363, 1346, 1275, 1243, 1174, 1084, 987, 852, 810, 795, 743, 700, 656, 628 cm^{-1}.

***N*-[Ac-Glu-Glu-Glu-Ile-Arg-His-Leu-Ser-Val-Asn-NH-CH_2CH_2-]perylene-3,4-imide-9,10-bis(n-butyl)ester (16).** Condensation of perylene-3,4-monoanhydride-9,10-bis(n-butyl ester) **Q2** (0.020 g, 0.038 mmol) and peptide **P14** (0.061 g, 0.046 mmol) was performed according to the general perylene imide synthesis procedures. The reaction mixture was cooled to 95 °C, diluted with 3 mL of water, and cooled to room temperature. The reaction mixture was then loaded onto HP20ss resin and the resin was successively flushed with ten 100 mL aqueous acetone solutions, forming a gradient series beginning at 10% (v/v) acetone/water increasing by 10% acetone with each 100 mL. Removal of the desired product using pyridine followed by 20% (v/v) pyridine/water followed by removal of the solvent under reduced pressure afforded *title compound* **16** as a dark purple solid (0.031 g, 64%). ^{1}H NMR (500 MHz, D_2O/pyridine-d_5, 4:1): δ = 7.51 (8H, br. m, Ar-H), 6.77 (2H, m, CH=N His, CH=C His), 3.92 (7H, m, αCH Asn, αCH His, αCH Ser, OCH_2 esters), 3.25 (2H, m, CH_2 ethylimide), 2.95 (2H, m, CH_2 ethylamide), 2.72 (3H, m, αCH Arg, αCH Leu, αCH Glu #1), 2.39 (6H, m, αCH Glu #2-3, αCH Val, αCH Ile, βCH_2 Ser), 1.99 (6H, m, βCH_2 His, βCH_2 Asn, δCH_2 Arg), 1.76 (7H, m, CH_3 Ac-Glu #1, βCH_2 esters), 1.61 (6H, m, βCH_2 Glu #1-3), 1.08 (12H, m, γCH_2 esters, βCH Ile, βCH Val, γCH_2 Glu #1-3), 0.90 (5H, m, βCH_2 Arg, βCH_2 Leu, γCH Leu), 0.44 (28H, m, γCH_2 Arg, δCH_3 esters, γCH_2 Ile, γCH_3 Val, γCH_3 Ile, δCH_3 Leu, δCH_3 Ile); MS (MALDI) *m/z*: Calculated for $C_{87}H_{110}N_{18}Na_2O_{22}$ $[M+2Na\ -3H_2O]^+$ 1804.75, found 1804.39; IR (KBr): ν = 3420, 3163, 2957, 2870, 1699, 1657, 1594, 1539, 1509, 1437, 1400, 1362, 1344, 1294, 1262, 1241, 1165, 1099, 1079, 1017, 953, 849, 809, 748, 652, 624 cm^{-1}.

NH_2 – Gly – Ile – Arg – His – Leu – Ser – Val – Asn – OH (P15)

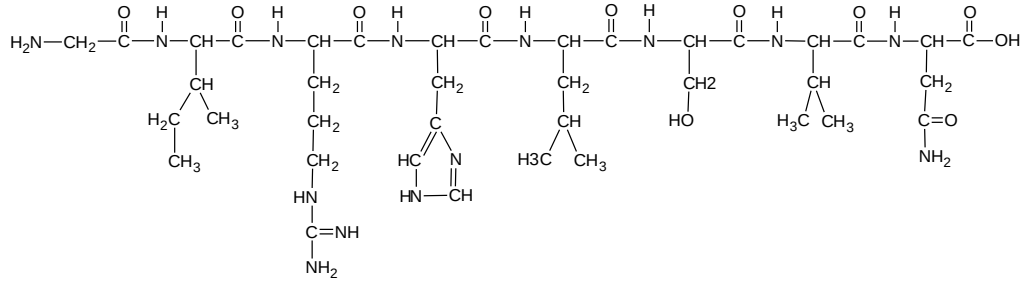

Figure 8.18 Chemical structure of peptide **P15**

Synthesis was performed using Fmoc-Asn(Trt)-Wang resin (0.50 g, loading 0.51 mmol/g, 0.26 mmol) according to the general SPPS procedure with a modified resin cleavage solution consisting of TFA (8.8 mL), water (0.5 mL), phenol (0.5 g), and triisopropylsilane (0.2 mL). The dried peptide was successively soaked in acetonitrile and toluene (followed by centrifugation and decanting the solvent) to remove trace scavengers. Drying of the rinsed peptide afforded the *title compound* **P15** as a pale, off-white solid (0.21 g, 92%). ^{1}H NMR (500 MHz, DMSO-d_6): δ = 8.96 (1H, s, CH=N His), 8.42 (1H, d, J = 8.5 Hz, NH Arg), 8.31 (2H, m, NH Ile, NH Ser), 8.23 (1H, d, J = 7.6 Hz, NH His), 8.19 (1H, d, J = 7.8 Hz, NH Asn), 8.12 (1H, d, J = 7.8 Hz, NH Leu), 8.01 (2H, br s, NH_2 Gly), 7.71 (1H, s, NH Arg guanidine), 7.58 (1H, d, J = 9.0 Hz, NH Val), 7.39 (1H, s, NH His ring), 7.36 (2H, s, NH_2 Asn), 7.29-6.98 (2H, NH_2 exchange traces, Arg guanidine), 6.92 (1H, br. s, CH=C His), 4.61 (1H, m, αCH Asn), 4.50 (1H, m, αCH His), 4.36 (2H, m, αCH Ser, αCH Leu), 4.24 (3H, m, αCH Arg, αCH Val, αCH Ile), 3.60 (4H, m, CH_2 Gly, βCH_2 Ser), 3.06 (3H, m, βCH_2 His, δCH_a Arg), 2.95 (1H, m, δCH_b Arg), 2.55 (1H, dd, J = 15.6 Hz, J = 5.6 Hz, βCH_a Asn), 2.43 (1H, dd, J = 15.6 Hz, J = 7.3 Hz, βCH_b Asn), 1.99 (1H, dq, J = 12.9 Hz, J = 6.7 Hz, βCH Val), 1.64 (3H, m, βCH_2 Arg, βCH Ile), 1.44 (5H, m, βCH_2 Leu, γCH_2 Arg, γCH Leu), 1.06 (2H, m, γCH_2 Ile), 0.83 (18H, m, CH_3 Leu, γCH_3 Ile, CH_3 Val, δCH_3 Ile); ^{13}C NMR (125 MHz, DMSO-d_6): δ = 172.8, 172.6, 171.2, 170.9, 170.5, 169.7, 169.6, 165.9, 156.9, 144.5, 117.8, 117.1, 115.3, 61.4, 57.0, 56.9, 55.1, 52.6, 51.4, 51.2, 48.8, 40.9, 40.5, 40.2, 37.0, 36.6, 31.0, 28.8, 25.1, 24.2, 23.1, 21.5, 19.2, 17.5, 15.3, 11.0; HRMS (ESI^+) *m/z*: Calculated for $C_{38}H_{66}N_{14}O_{11}$ $[M+2H]^{+2}$ 448.2591, found 448.2588; Calculated for $C_{38}H_{66}N_{14}O_{11}$ $[M+H]^+$ 895.5108, found 895.5089.

Ac – Ile – Arg – His – Leu – Ser – Val – Asn – OH (P16)

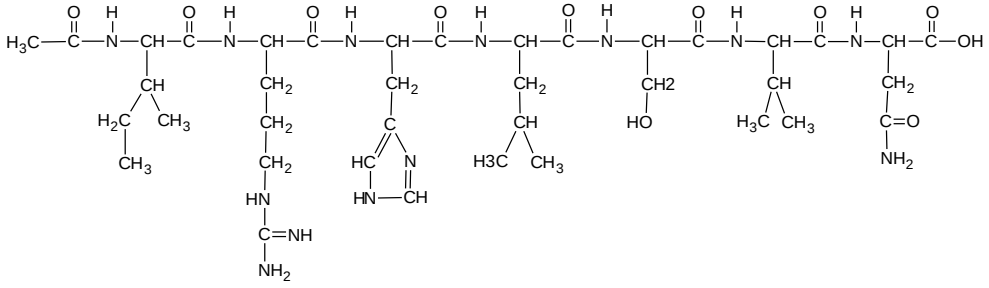

Figure 8.19 Chemical structure of peptide **P16**

Synthesis was performed using Fmoc-Asn(Trt)-Wang resin Fmoc-Asn(Trt)-Wang resin (0.51 g, loading 0.51 mmol/g, 0.26 mmol) according to the general SPPS procedure with a modified resin cleavage solution consisting of TFA (8.8 mL), water (0.5 mL), phenol (0.5 g), and triisopropylsilane (0.2 mL). The dried peptide was successively soaked in acetonitrile and toluene and decanted to remove trace scavengers. Final drying of the soaked peptide afforded the *title compound* **P16** as a pale, off-white solid (0.19 g, 85%). ^{1}H NMR (500 MHz, DMSO-d_6): δ = 8.83 (1H, br s, CH=N His), 8.57 (1H, m, AcNH Ile), 8.28 (1H, d, J = 7.3 Hz, NH Arg), 8.21 (1H, m, NH Ile), 8.15 (1H, m, NH Ser), 8.10 (2H, m, NH His, NH Asn), 7.96 (1H, d, J = 8.2 Hz, NH Leu), 7.62 (1H, br s, NH Arg guanidine), 7.58 (1H, d, J = 8.8 Hz, NH Val), 7.39 (2H, s, NH_2 Asn), 7.30 (1H, s, NH His ring), 7.29-6.98 (2H, NH_2 exchange traces, Arg guanidine), 6.92 (1H, br. s, CH=C His), 4.58 (1H, m, αCH Asn), 4.49 (1H, m, αCH His), 4.35 (2H, m, αCH Ser, αCH Leu), 4.22 (2H, m, αCH Arg, αCH Val), 4.10 (1H, t, J = 7.9 Hz, αCH Ile), 3.59 (2H, m, βCH_2 Ser), 3.07 (3H, m, βCH_a His, δCH_2 Arg), 2.96 (1H, dd, J = 15.1 Hz, J = 7.5 Hz, βCH_b His), 2.54 (1H, dd, J = 15.6 Hz, J = 5.9 Hz, βCH_a Asn), 2.43 (1H, dd, J = 15.7 Hz, J = 7.2 Hz, βCH_b Asn), 1.99 (1H, dd, J = 12.9 Hz, J = 6.5 Hz, βCH Val), 1.86 (3H, s, CH_3 Ile acetamide), 1.62 (3H, m, βCH_2 Arg, βCH Ile), 1.45 (5H, m, βCH_2 Leu, γCH_2 Arg, γCH Leu), 1.08 (2H, m, γCH_2 Ile), 0.81 (18H, m, δCH_3 Leu, γCH_3 Ile, γCH_3 Val, δCH_3 Ile); ^{13}C NMR (150 MHz, DMSO-d_6): δ = 172.7, 172.5, 171.7, 171.3, 171.2, 170.5, 169.7, 169.6, 156.8, 149.5, 133.8, 124.1, 117.1, 61.4, 57.2, 57.0, 55.1, 52.4, 51.2, 48.8, 40.8, 40.5, 36.6, 36.2, 31.0, 28.6, 25.1, 24.6, 24.2, 23.1, 22.5, 21.4, 19.1, 17.5, 15.4, 11.0; HRMS (ESI$^+$) *m/z*: Calculated for $C_{38}H_{65}N_{13}O_{11}$ $[M+2H]^{+2}$ 441.2550, found 441.2559.

Appendix - A

NMR Spectra of Synthesized Compounds

A.1 ^{1}H and ^{13}C NMR Spectra of Synthesized Peptides

A.2 ^{1}H NMR Spectra of Synthesized PDIs (with Peptide ^{1}H NMR Spectral Comparisons)

A.1 ^{1}H and ^{13}C NMR Spectra of Synthesized Peptides

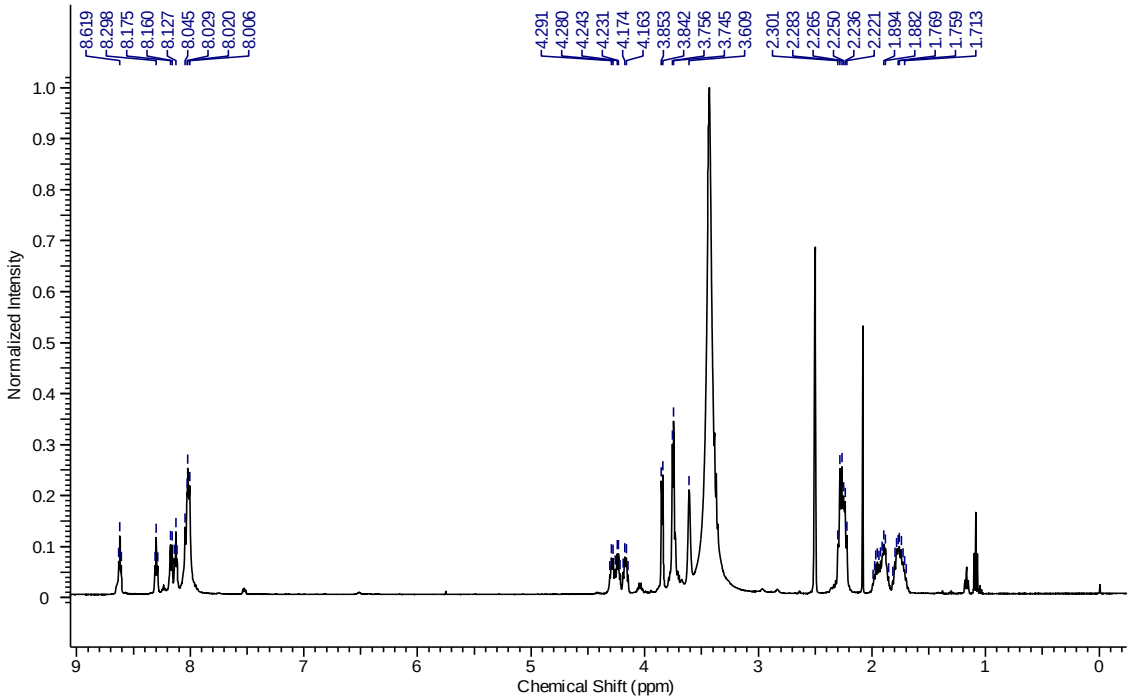

Figure A.1 ^{1}H NMR spectrum of **P1**, NH_2-Gly-$(Gly)_3$-$(Glu)_3$, in DMSO-d_6.

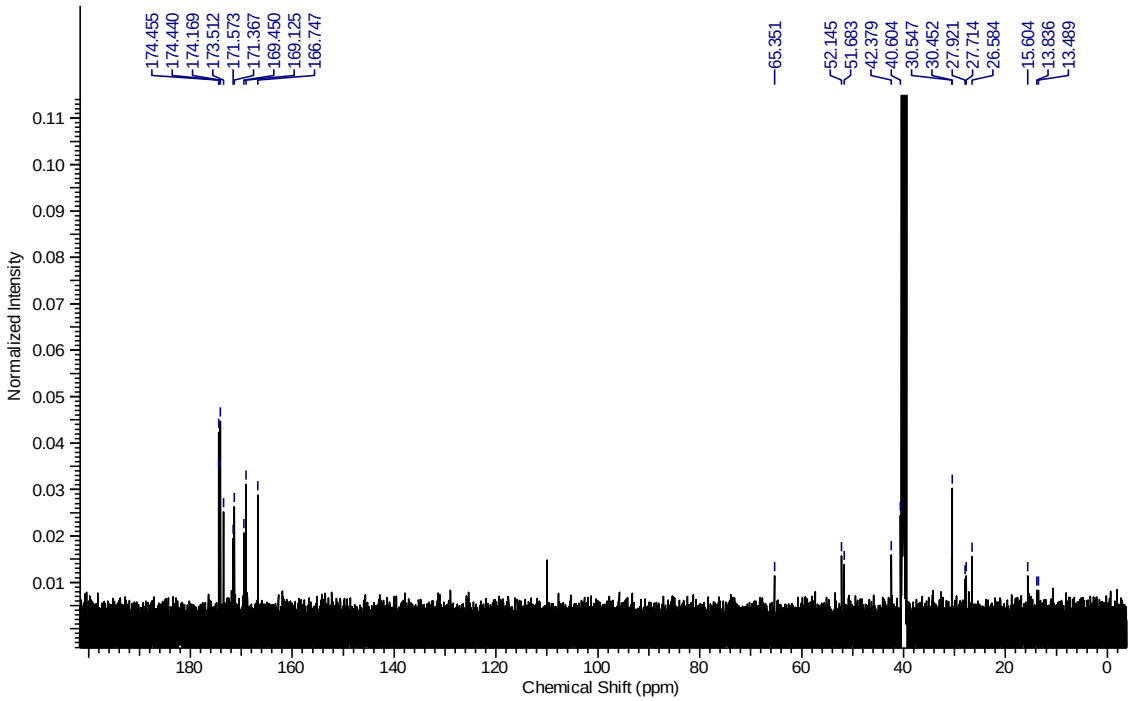

Figure A.2 ^{13}C NMR spectrum of **P1**, NH_2-Gly-$(Gly)_3$-$(Glu)_3$, in DMSO-d_6.

A.1 ^{1}H and ^{13}C NMR Spectra of Synthesized Peptides

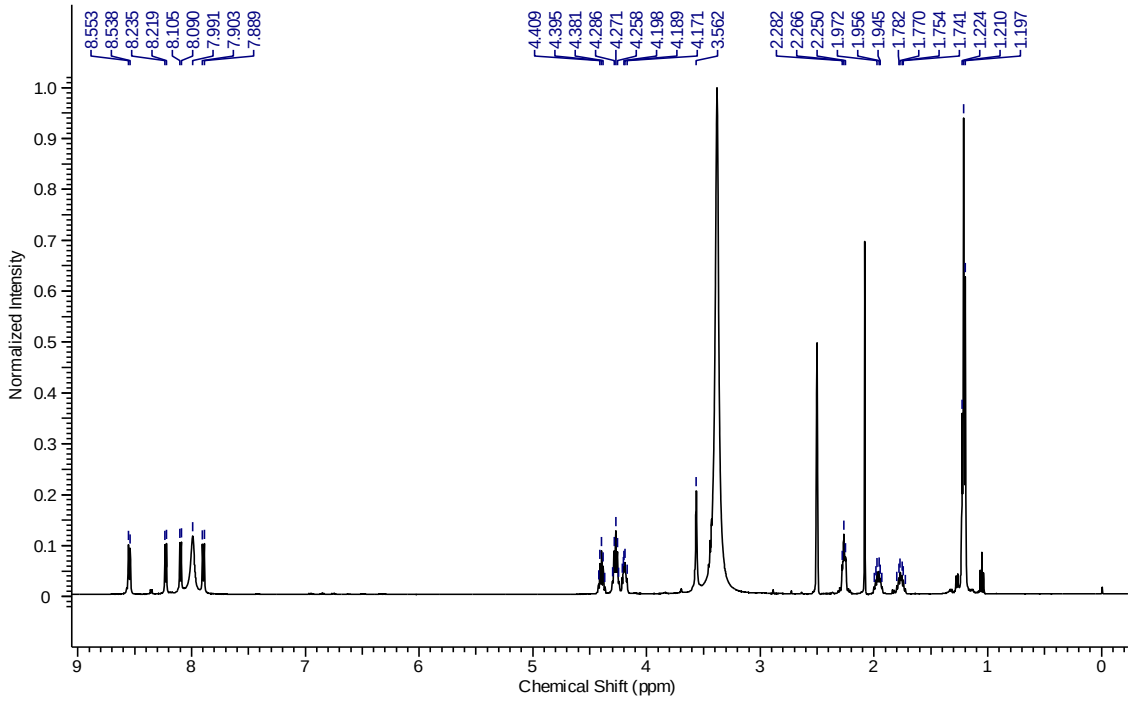

Figure A.3 ^{1}H NMR spectrum of **P2**, NH_2-Gly-$(Ala)_3$-Glu, in DMSO-d_6.

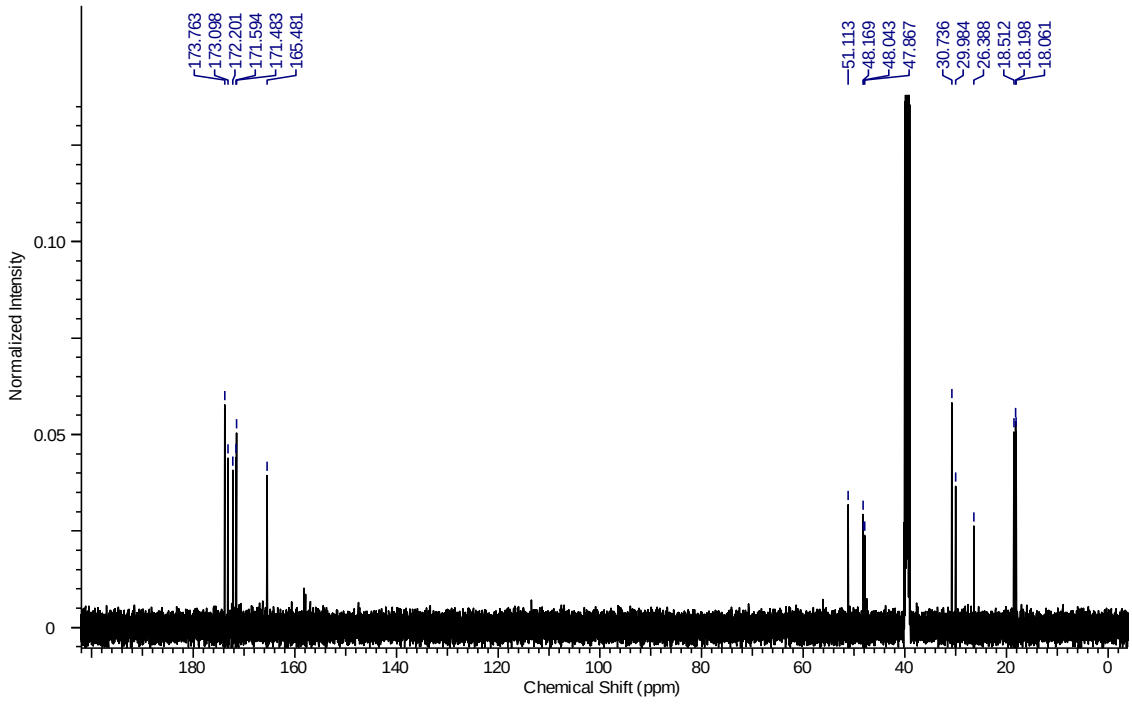

Figure A.4 ^{13}C NMR spectrum of **P2**, NH_2-Gly-$(Ala)_3$-Glu, in DMSO-d_6.

A.1 ^{1}H and ^{13}C NMR Spectra of Synthesized Peptides

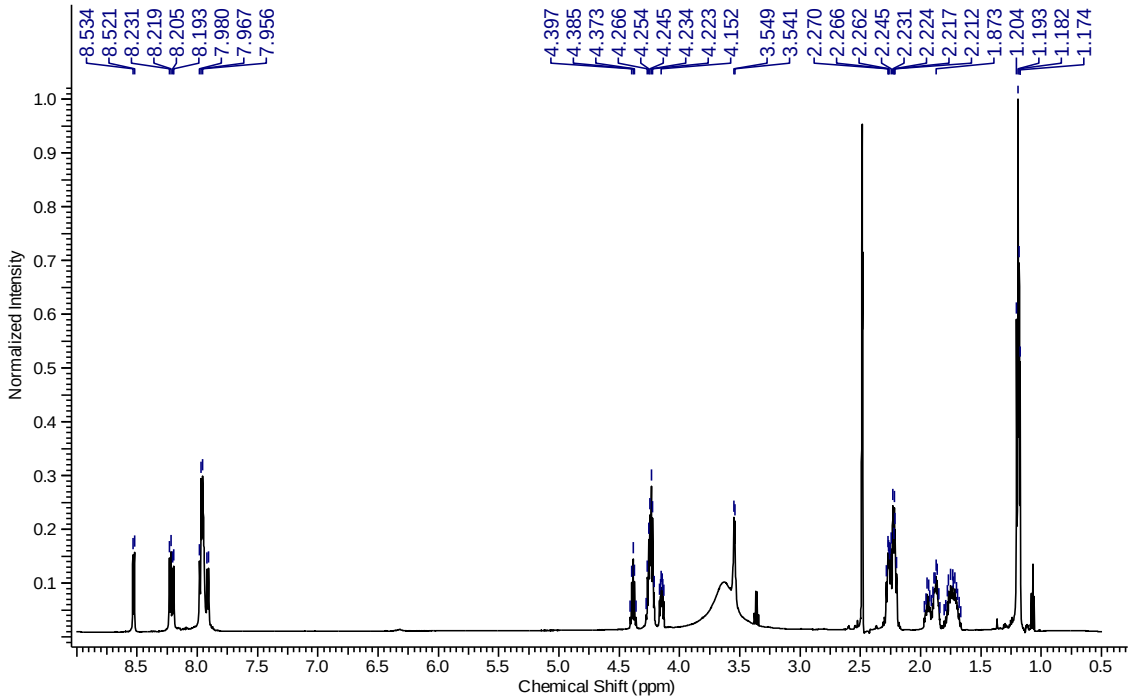

Figure A.5 ^{1}H NMR spectrum of **P3**, NH_2-Gly-$(Ala)_3$-$(Glu)_3$, in DMSO-d_6.

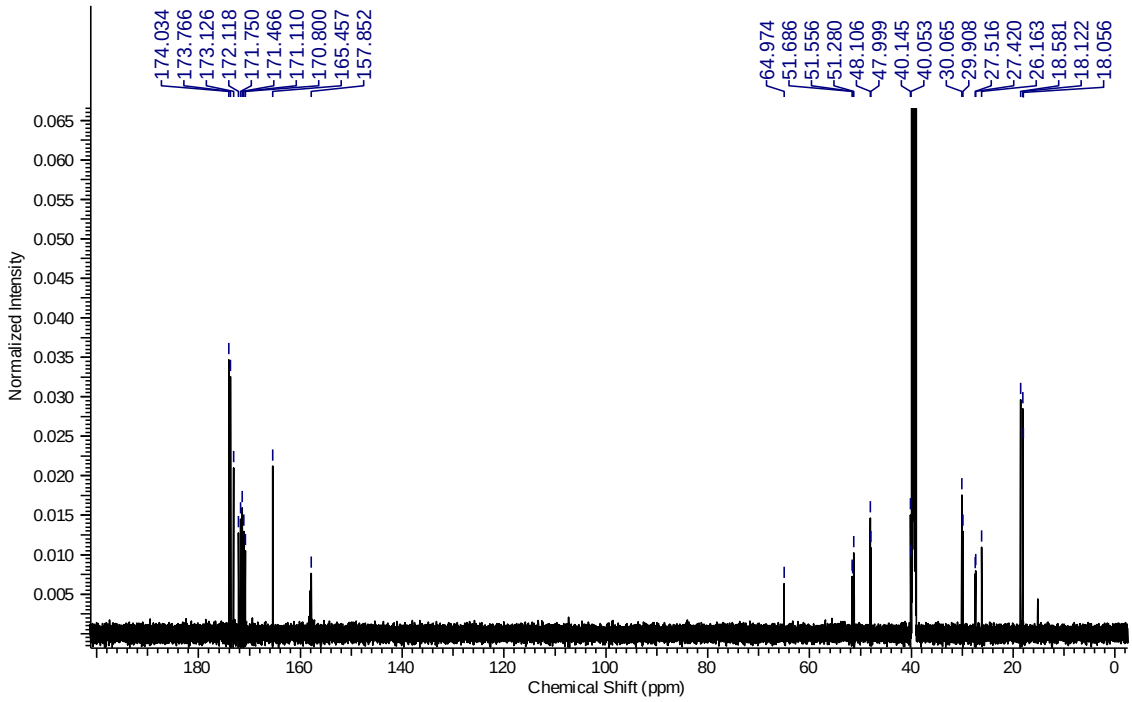

Figure A.6 ^{13}C NMR spectrum of **P3**, NH_2-Gly-$(Ala)_3$-$(Glu)_3$, in DMSO-d_6.

A.1 ^{1}H and ^{13}C NMR Spectra of Synthesized Peptides

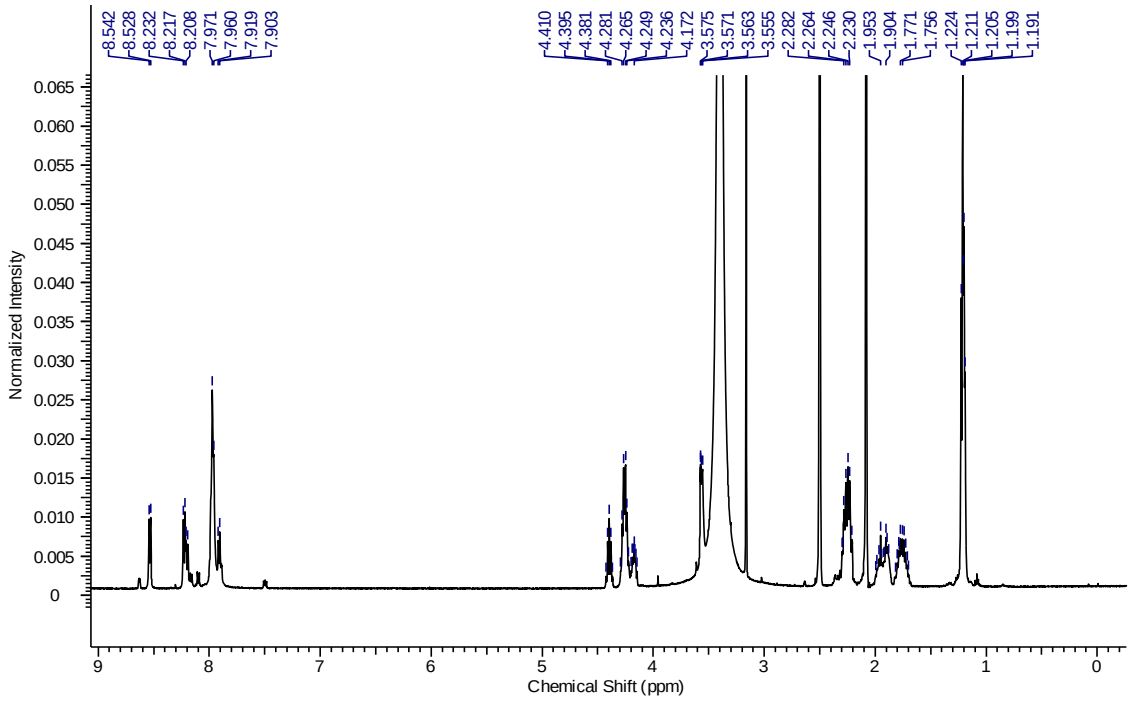

Figure A.7 ^{1}H NMR spectrum of **P3E**, NH_2-Gly-(*D*-Ala)$_3$-(*D*-Glu)$_3$, in DMSO-d$_6$.

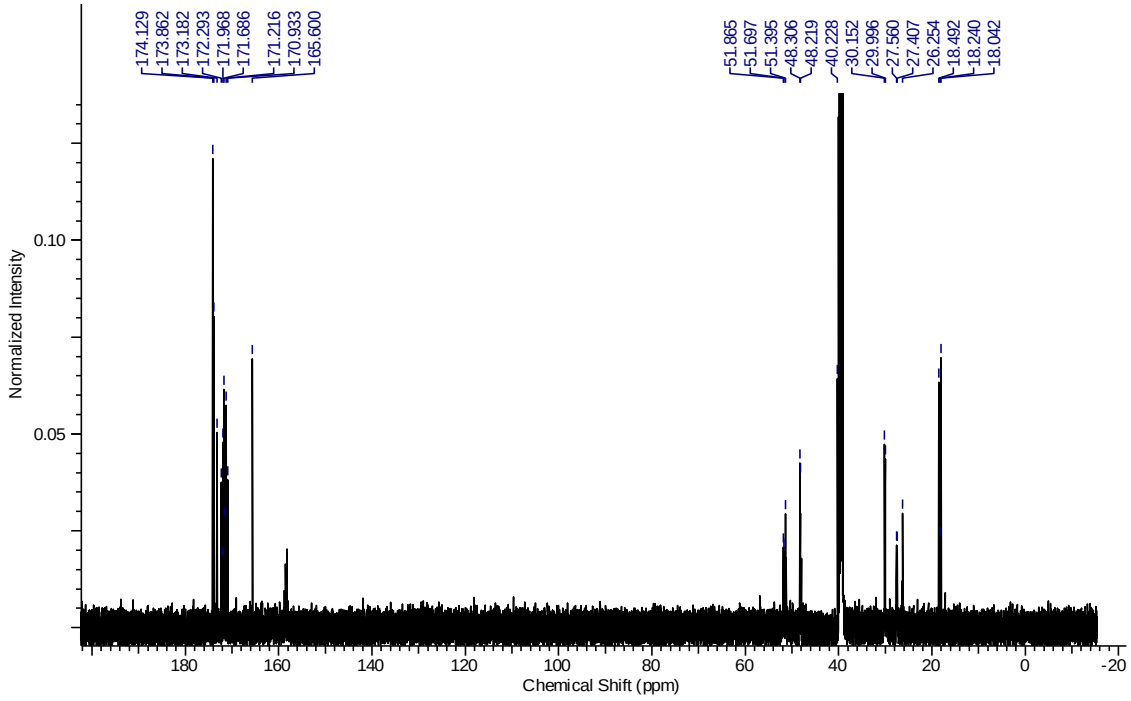

Figure A.8 ^{13}C NMR spectrum of **P3E**, NH_2-Gly-(*D*-Ala)$_3$-(*D*-Glu)$_3$, in DMSO-d$_6$.

A.1 ^{1}H and ^{13}C NMR Spectra of Synthesized Peptides

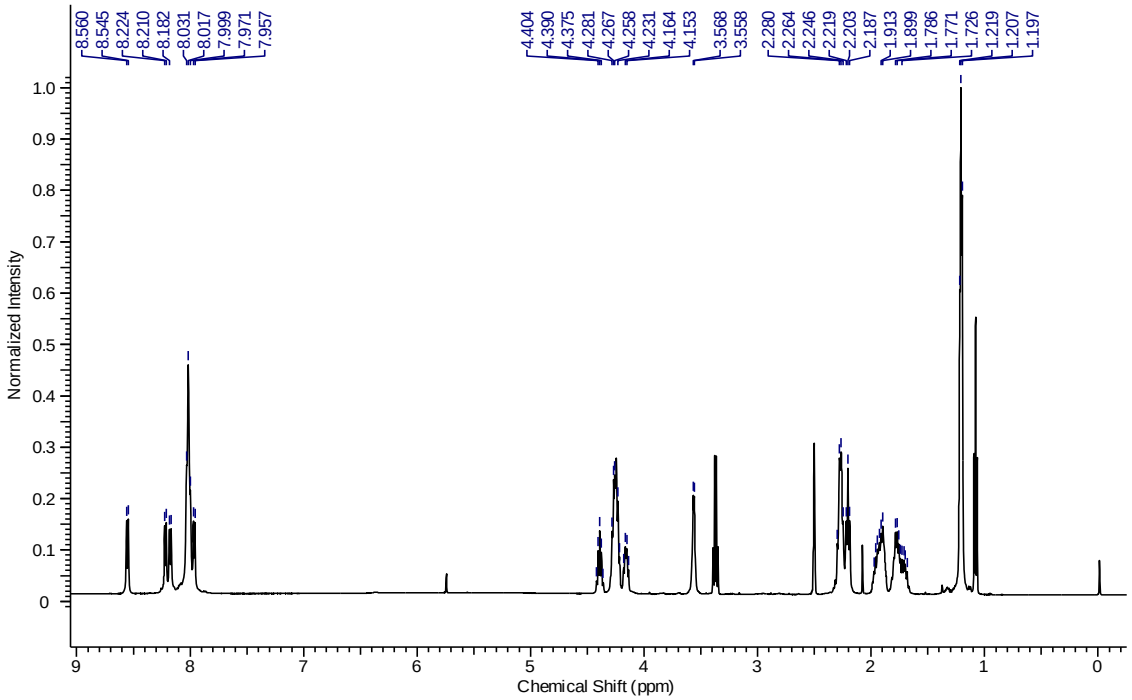

Figure A.9 ^{1}H NMR spectrum of **P4**, NH_2-Gly-(*D*-Ala)$_3$-(Glu)$_3$, in DMSO-d$_6$.

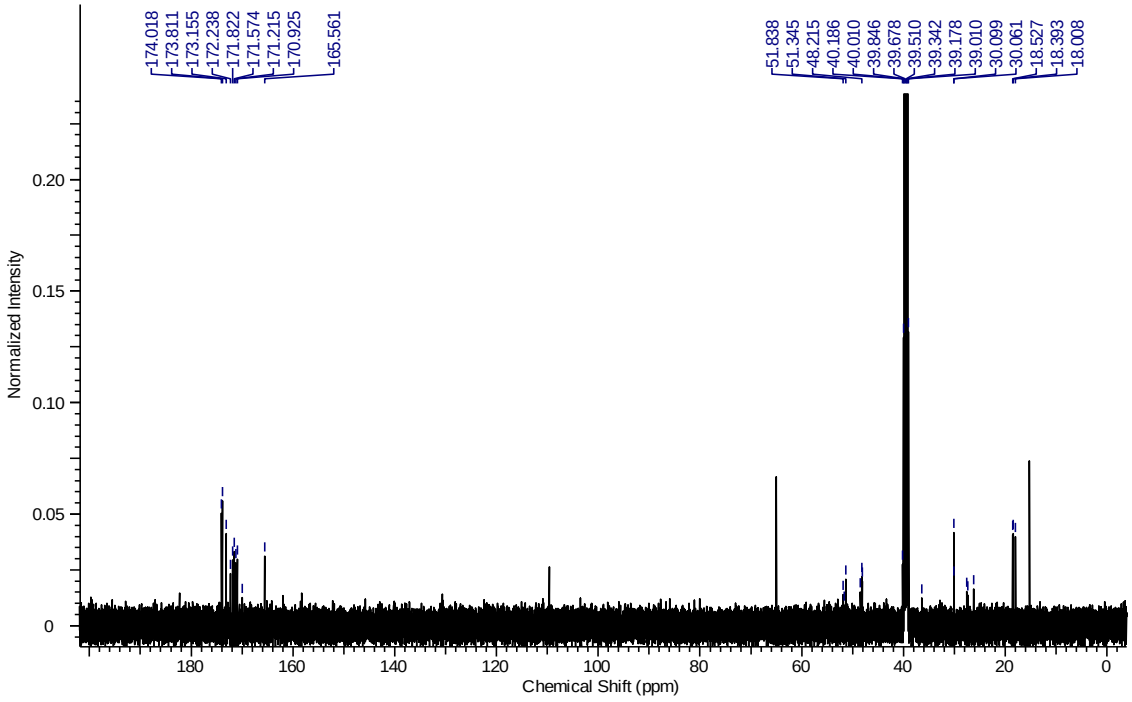

Figure A.10 ^{13}C NMR spectrum of **P4**, NH_2-Gly-(*D*-Ala)$_3$-(Glu)$_3$, in DMSO-d$_6$.

A.1 ^{1}H and ^{13}C NMR Spectra of Synthesized Peptides

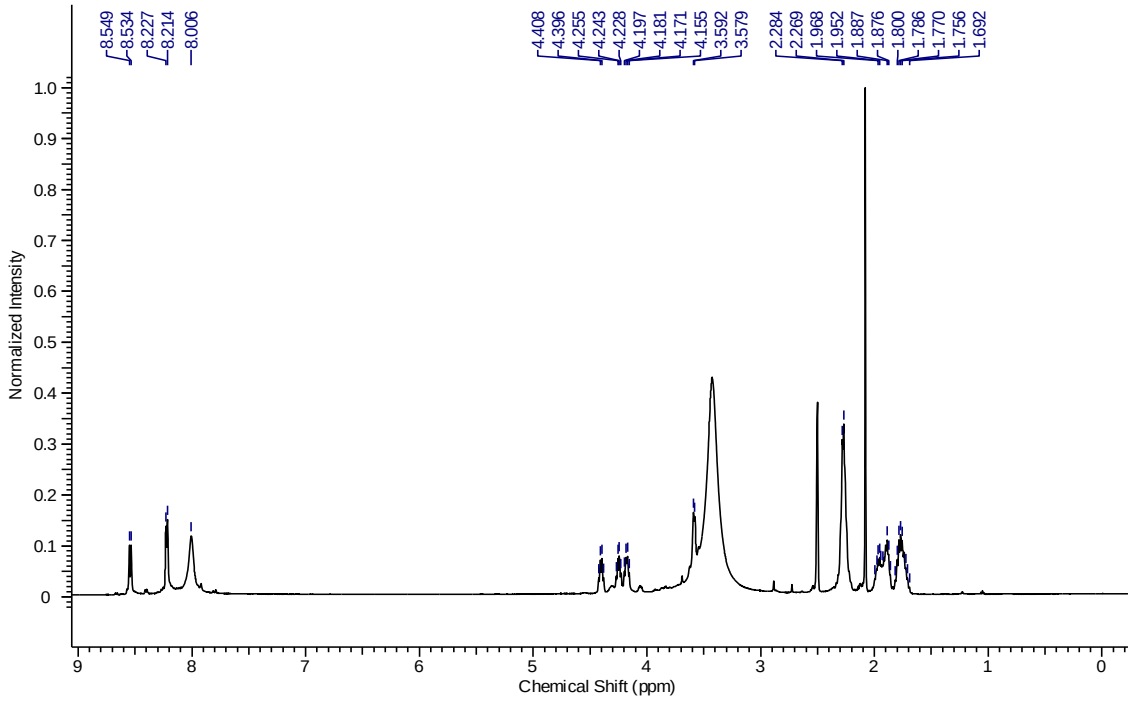

Figure A.11 ^{1}H NMR spectrum of **P5**, NH_2-Gly-$(Glu)_3$, in DMSO-d_6.

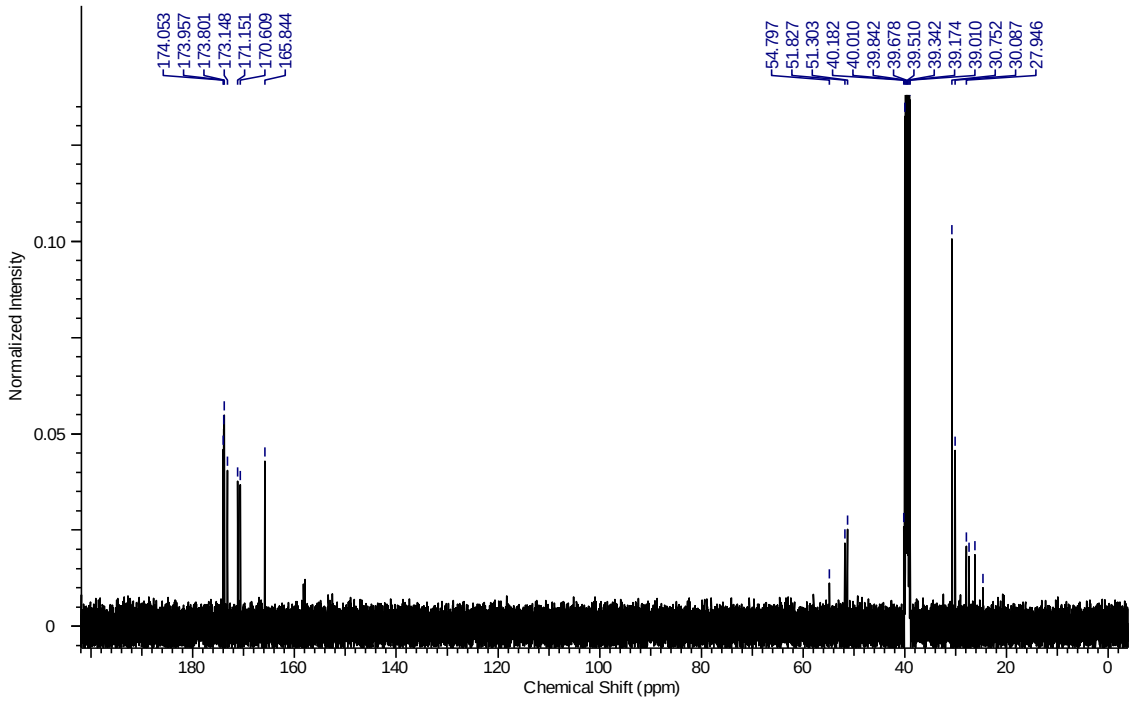

Figure A.12 ^{13}C NMR spectrum of **P5**, NH_2-Gly-$(Glu)_3$, in DMSO-d_6.

A.1 ^{1}H and ^{13}C NMR Spectra of Synthesized Peptides

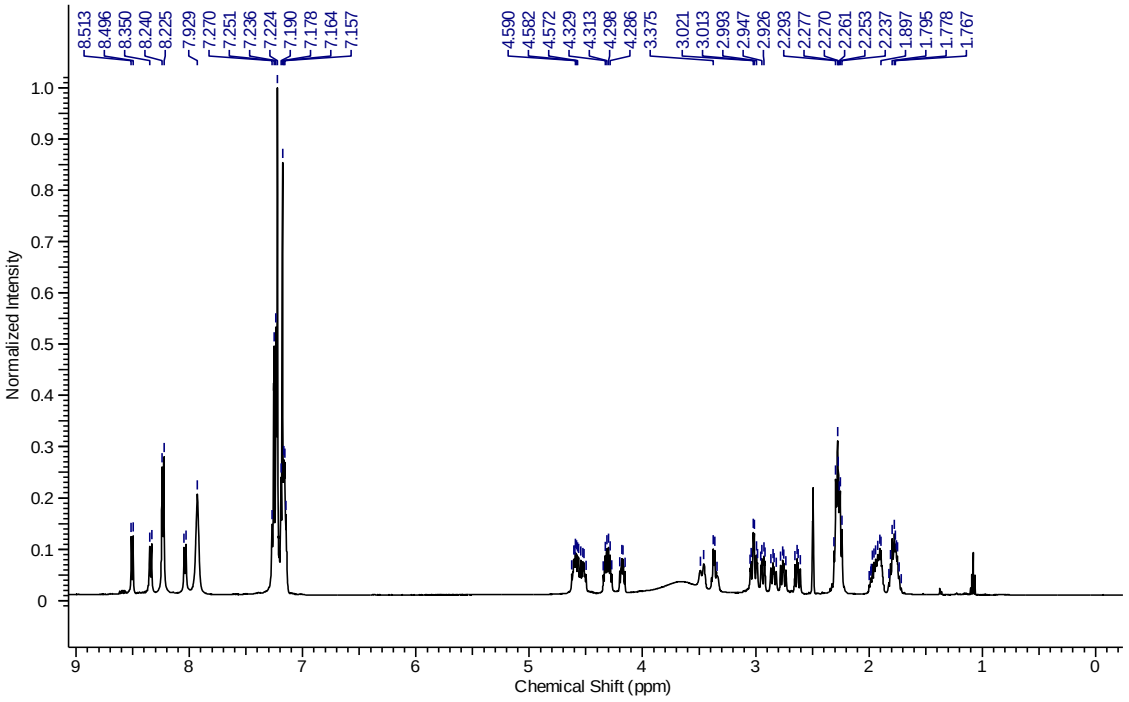

Figure A.13 ^{1}H NMR spectrum of **P6**, NH_2-Gly-$(Phe)_3$-$(Glu)_3$, in DMSO-d_6.

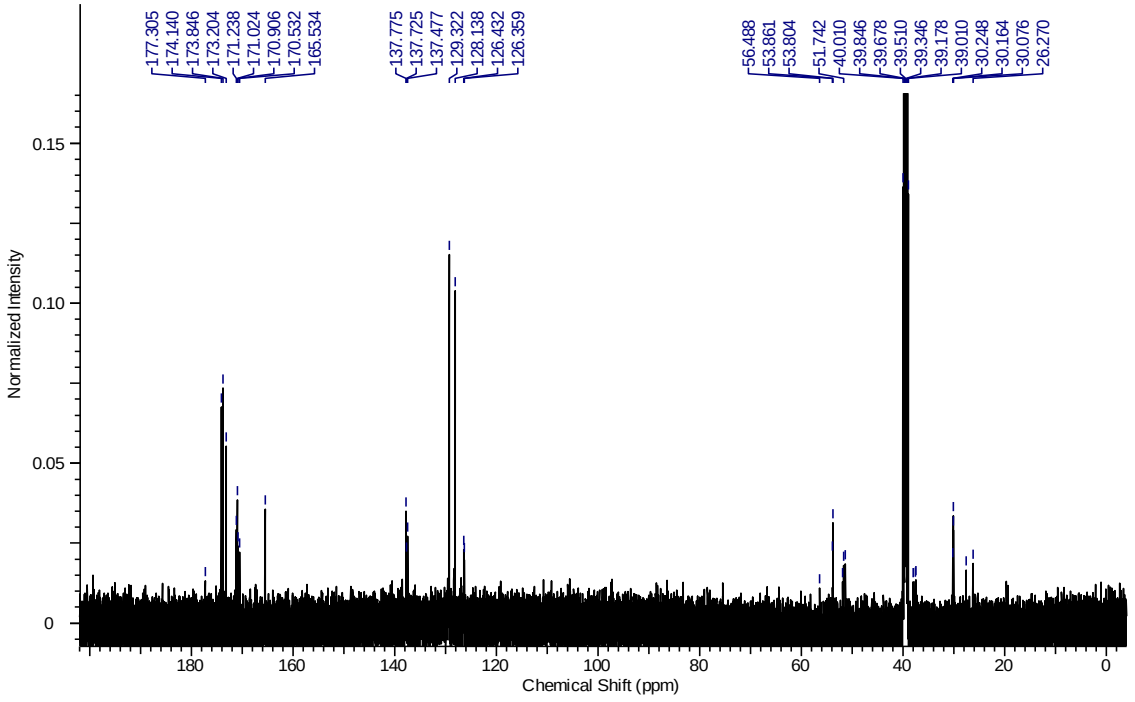

Figure A.14 ^{13}C NMR spectrum of **P6**, NH_2-Gly-$(Phe)_3$-$(Glu)_3$, in DMSO-d_6.

A.1 ^{1}H and ^{13}C NMR Spectra of Synthesized Peptides

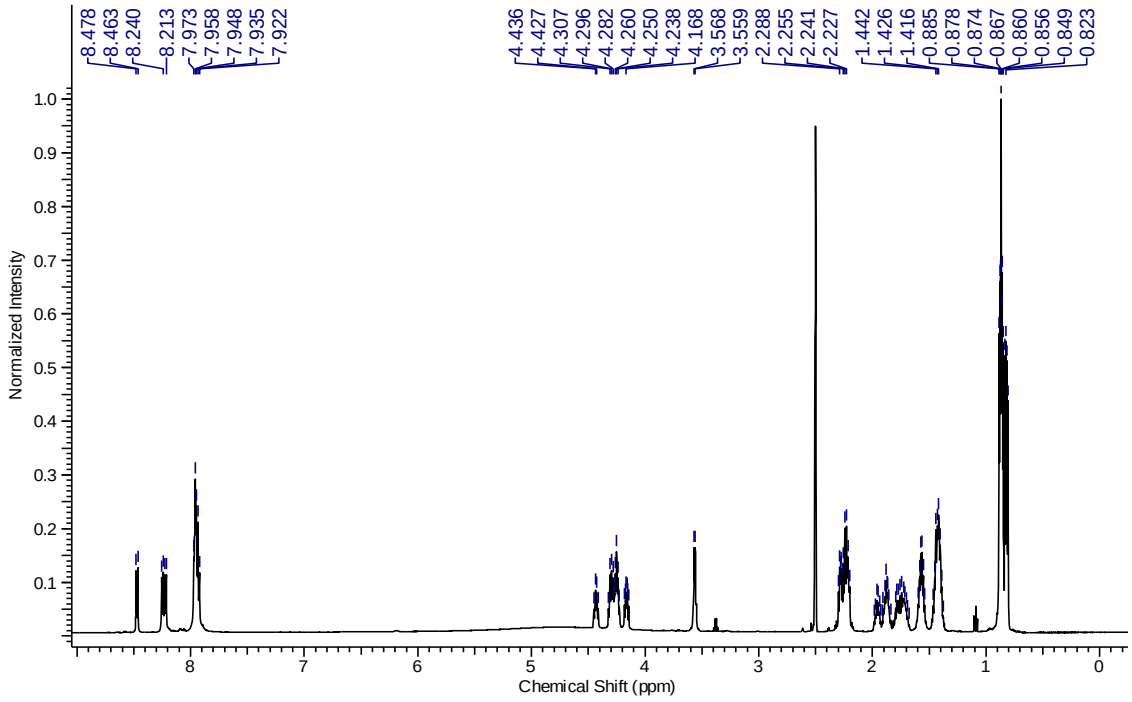

Figure A.15 ^{1}H NMR spectrum of **P7**, NH_2-Gly-$(Leu)_3$-$(Glu)_3$, in DMSO-d_6.

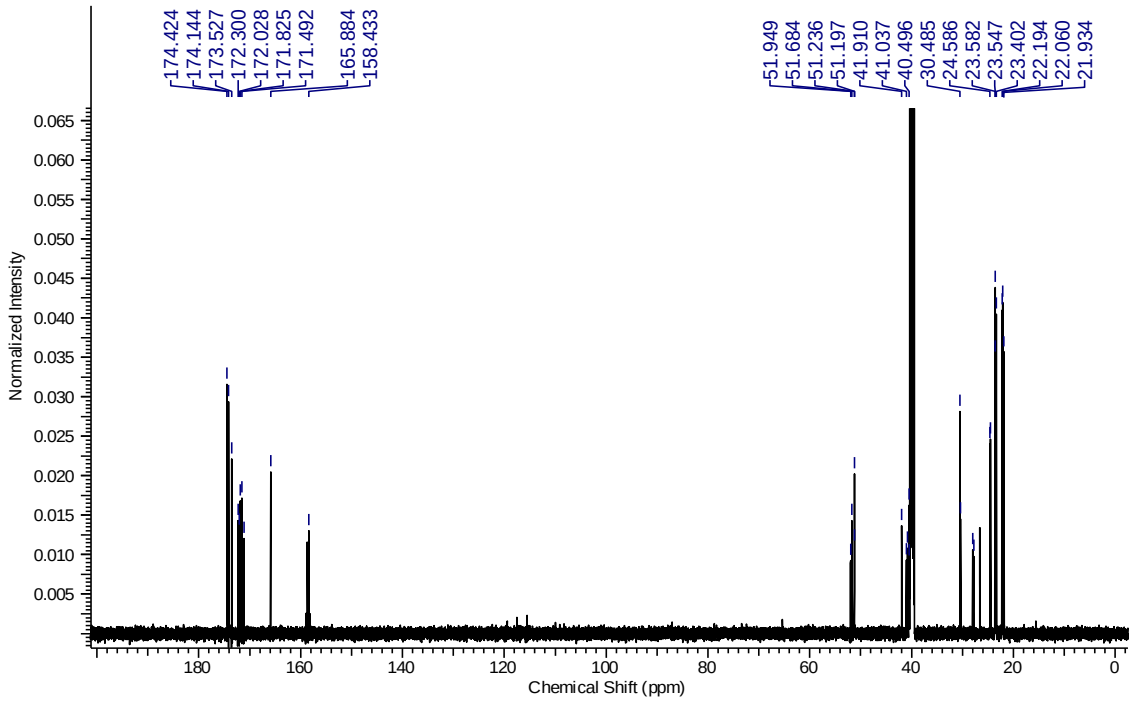

Figure A.16 ^{13}C NMR spectrum of **P7**, NH_2-Gly-$(Leu)_3$-$(Glu)_3$, in DMSO-d_6.

A.1 ^{1}H and ^{13}C NMR Spectra of Synthesized Peptides

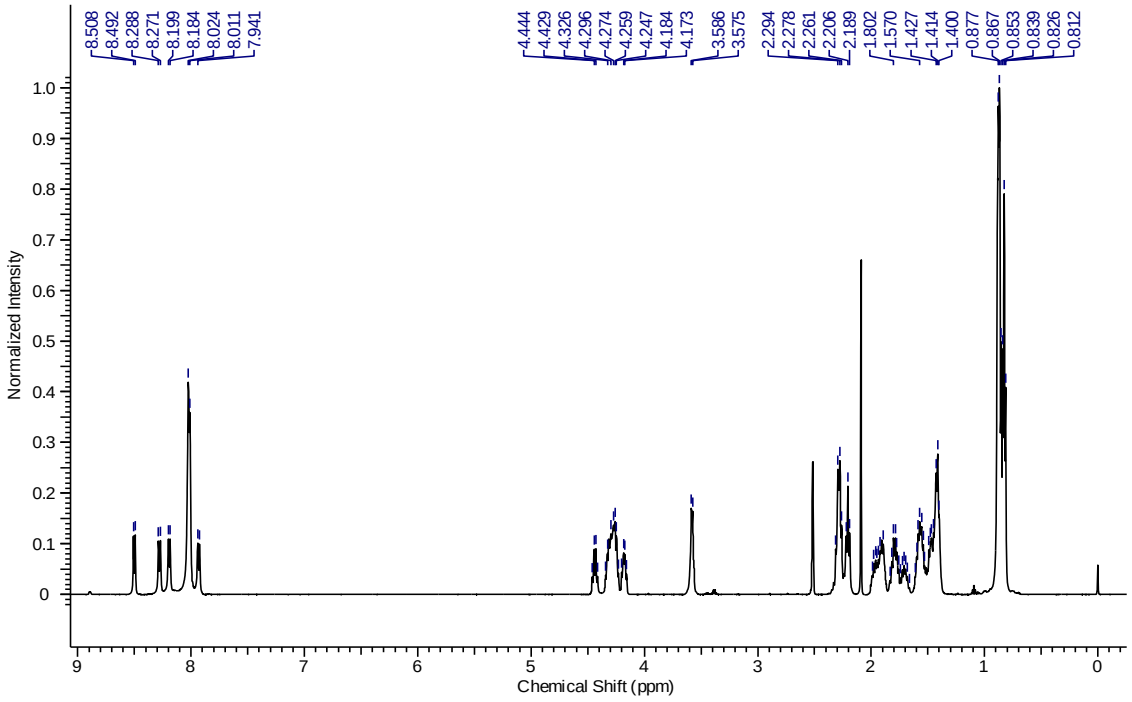

Figure A.17 ^{1}H NMR spectrum of **P8**, NH_2-Gly-(*D*-Leu)$_3$-(Glu)$_3$, in DMSO-d$_6$.

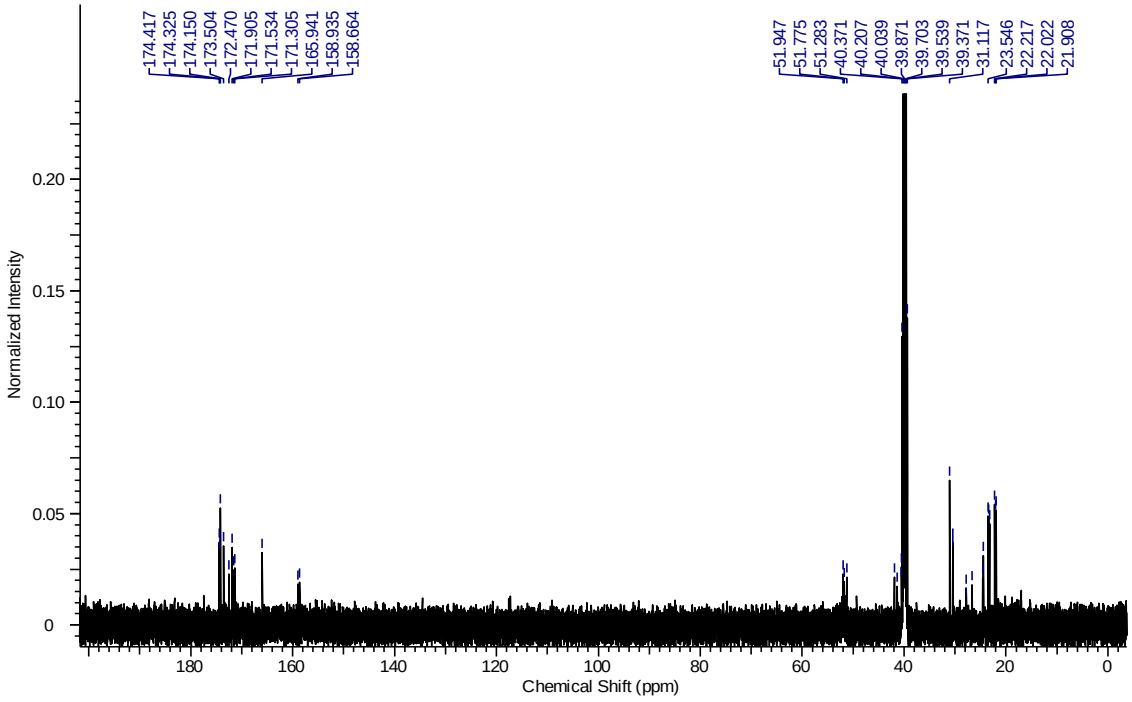

Figure A.18 ^{13}C NMR spectrum of **P8**, NH_2-Gly-(*D*-Leu)$_3$-(Glu)$_3$, in DMSO-d$_6$.

A.1 ^{1}H and ^{13}C NMR Spectra of Synthesized Peptides

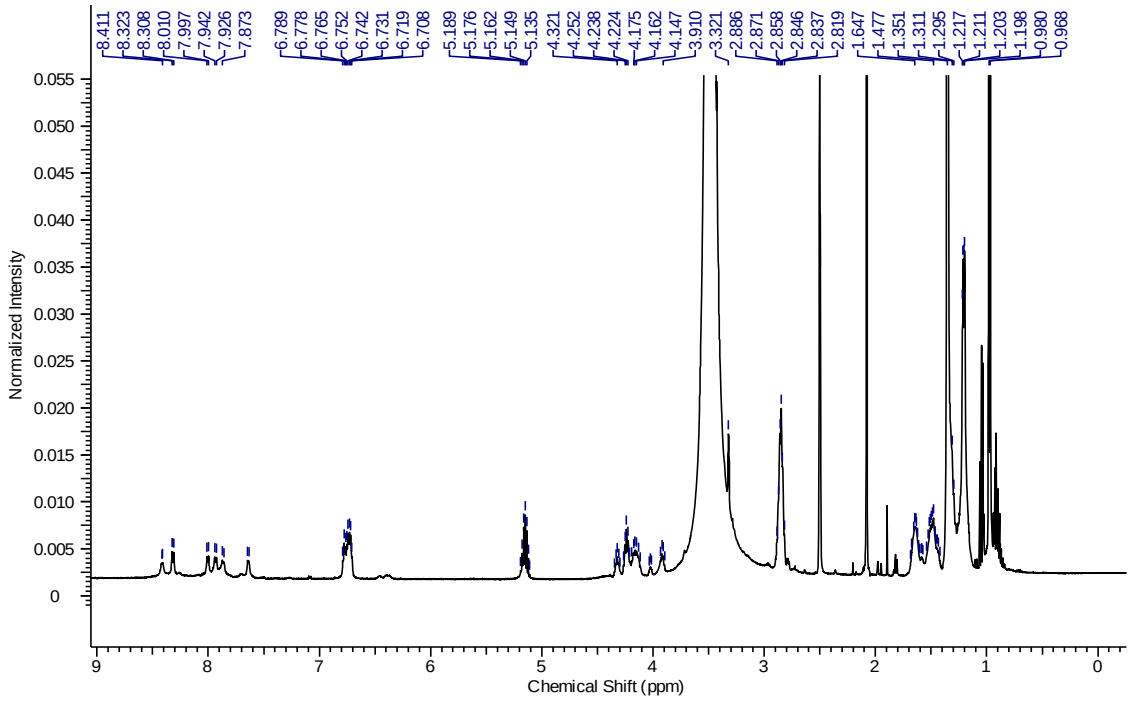

Figure A.19 ^{1}H NMR spectrum of **P9**, NH_2-Gly-$(Ala)_3$-$[Lys(Boc)]_3$, in DMSO-d_6.

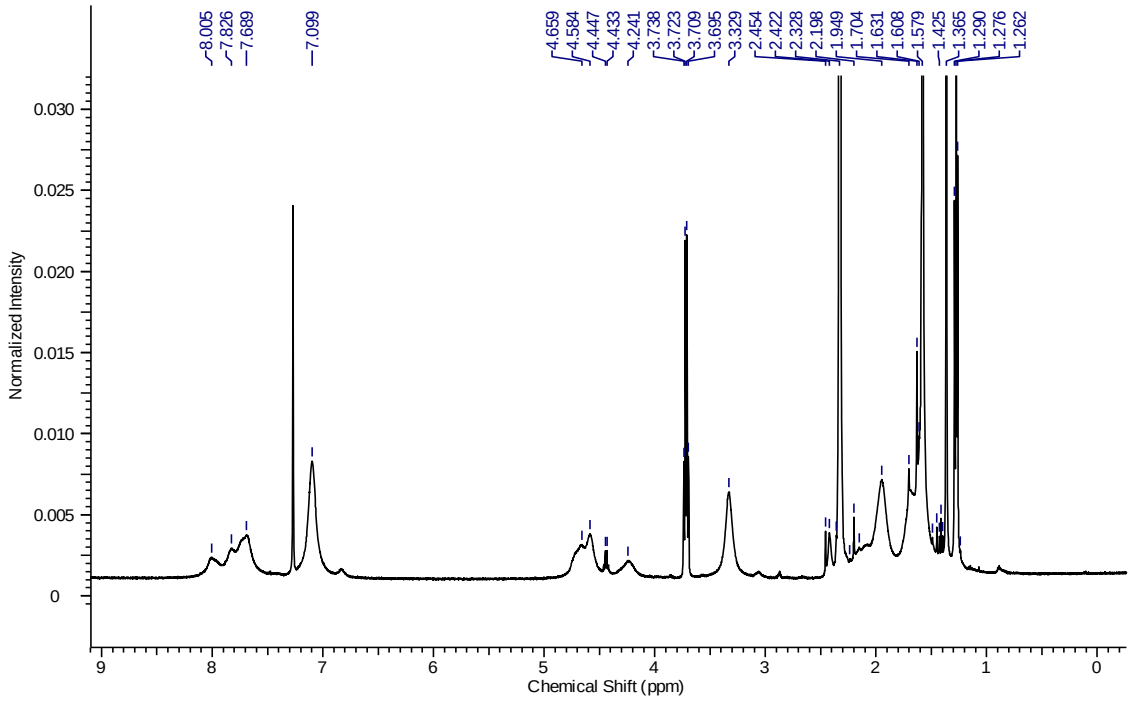

Figure A.20 ^{1}H NMR spectrum of **P9**, NH_2-Gly-$(Ala)_3$-$[Lys(Boc)]_3$, in $CDCl_3$.

A.1 ^{1}H and ^{13}C NMR Spectra of Synthesized Peptides

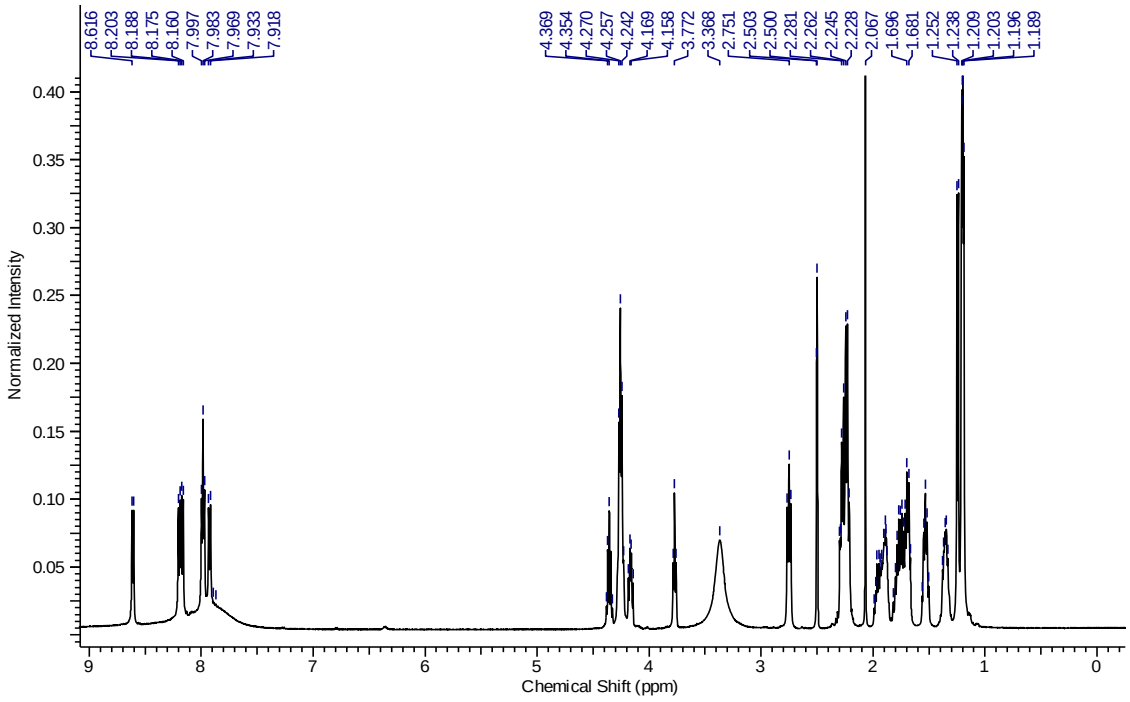

Figure A.21 ^{1}H NMR spectrum of **P10**, NH_2-Lys-$(Ala)_3$-$(Glu)_3$, in DMSO-d_6.

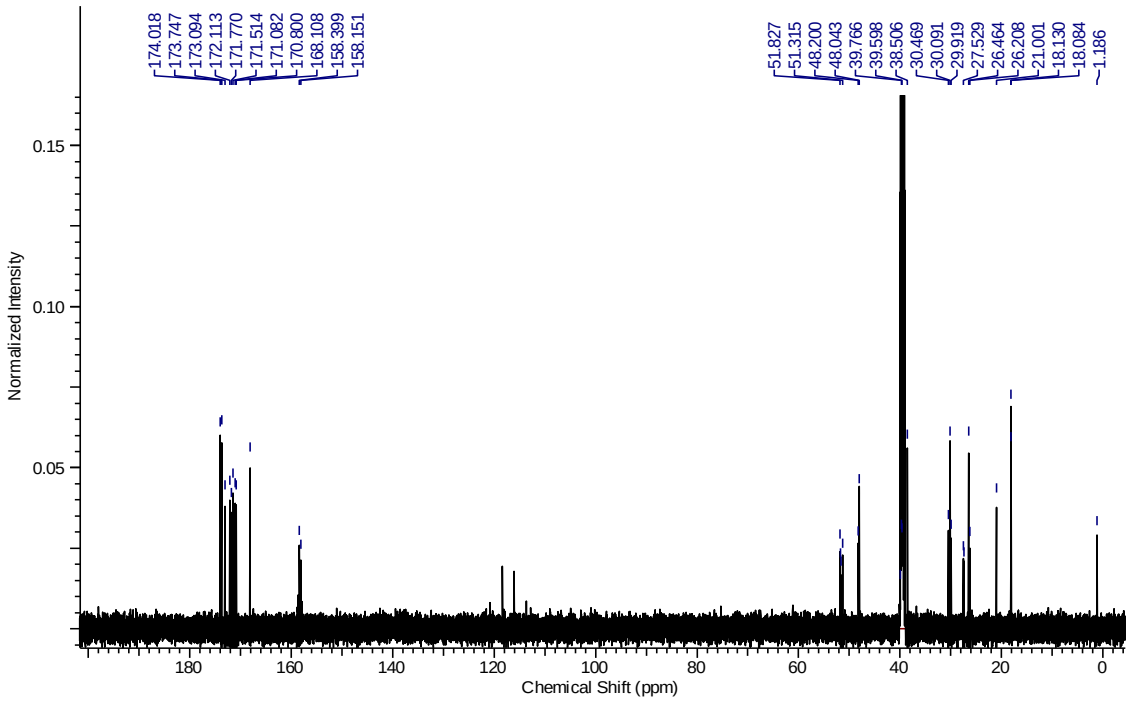

Figure A.22 ^{13}C NMR spectrum of **P10**, NH_2-Lys-$(Ala)_3$-$(Glu)_3$, in DMSO-d_6.

A.1 ^{1}H and ^{13}C NMR Spectra of Synthesized Peptides

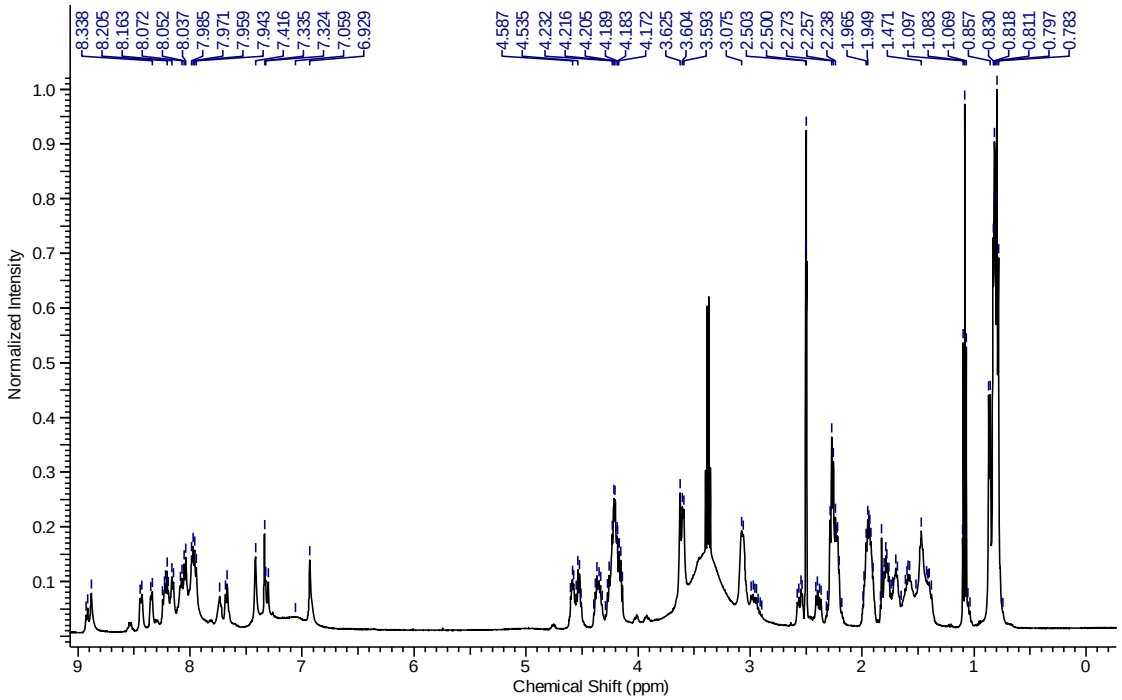

Figure A.23 ^{1}H NMR spectrum of **P13**, NH_2-Gly-Ile-Arg-His-Leu-Ser-Val-Asn-Glu-Glu-Glu-OH, in DMSO-d_6.

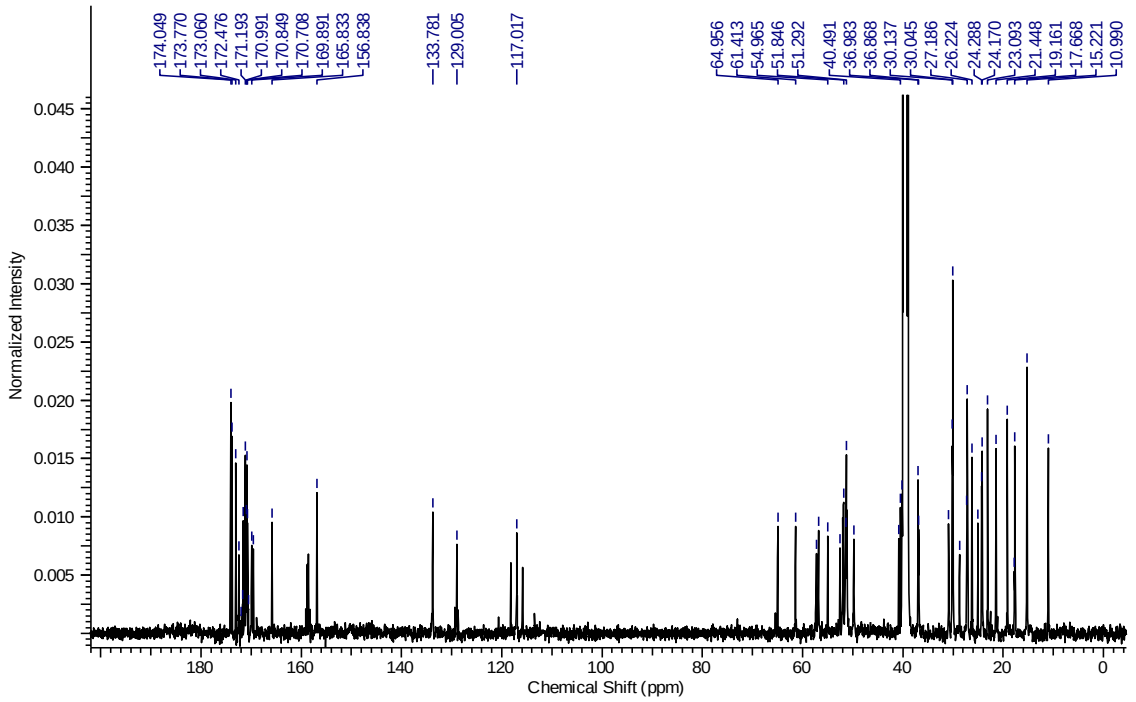

Figure A.24 ^{13}C NMR spectrum of **P13**, NH_2-Gly-Ile-Arg-His-Leu-Ser-Val-Asn-Glu-Glu-Glu-OH, in DMSO-d_6.

A.1 ^{1}H and ^{13}C NMR Spectra of Synthesized Peptides

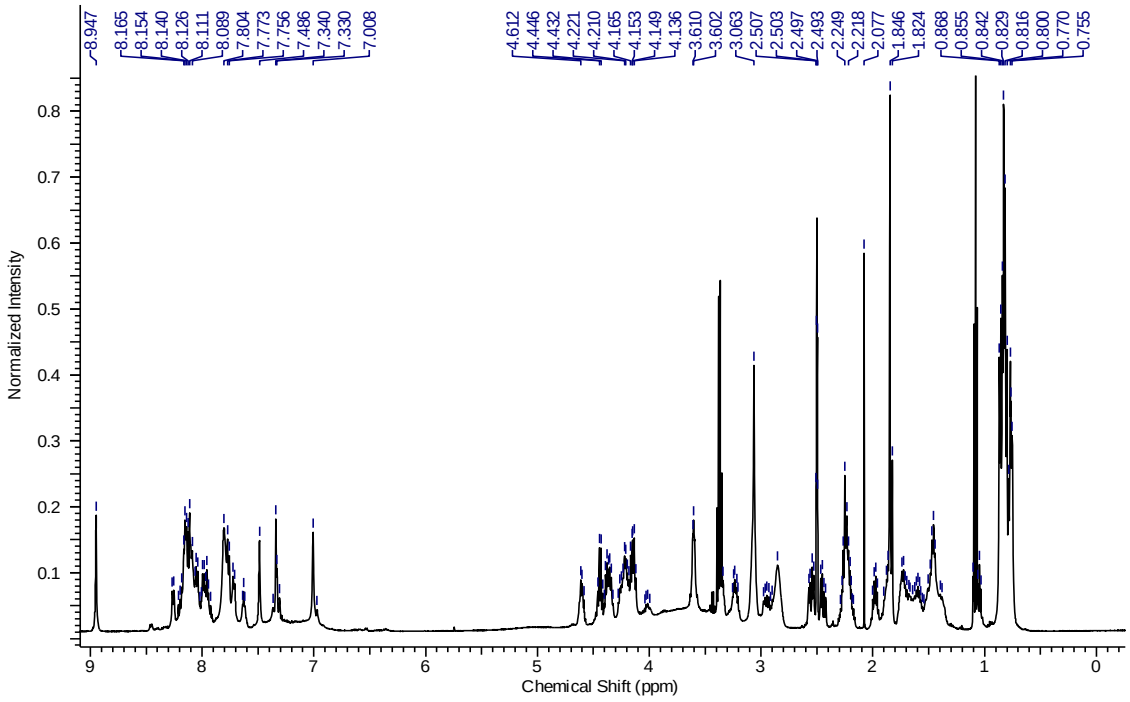

Figure A.25 ^{1}H NMR spectrum of **P14**, Ac-Glu-Glu-Glu-Ile-Arg-His-Leu-Ser-Val-Asn-NH-CH_2CH_2-NH_2, in DMSO-d_6.

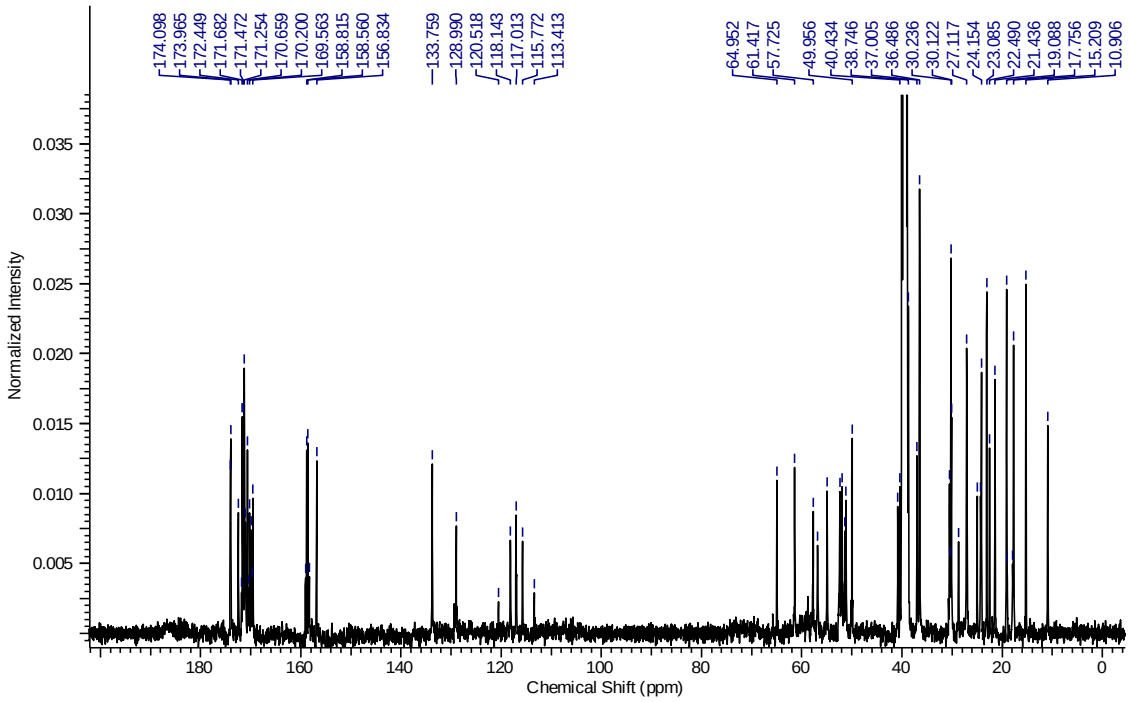

Figure A.26 ^{13}C NMR spectrum of **P14**, Ac-Glu-Glu-Glu-Ile-Arg-His-Leu-Ser-Val-Asn-NH-CH_2CH_2-NH_2, in DMSO-d_6.

A.2 ^{1}H NMR Spectra of Synthesized PDIs (with Peptide ^{1}H NMR Spectral Comparisons)

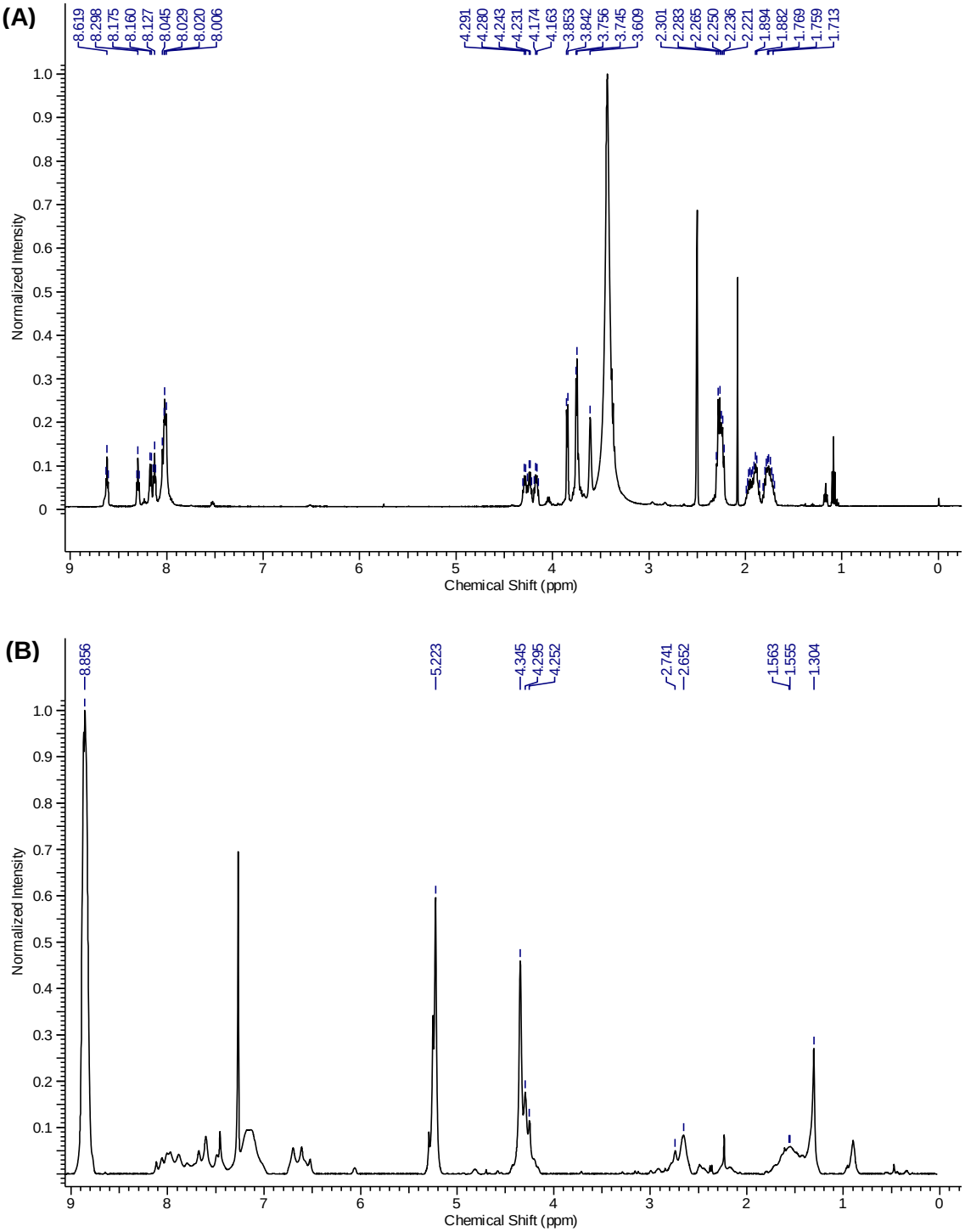

Figure A.27 ^{1}H NMR spectral comparison of: (A) NH_2-Gly-$(Gly)_3$-$(Glu)_3$ peptide (**P1**) in DMSO-d_6 and (B) *N*,*N*′-di[-Gly-$(Gly)_3$-$(Glu)_3$]perylene-3,4,9,10-tetracarboxylic acid diimide (**1**) in 2:1 $CDCl_3$/TFA.

A.2 ^{1}H NMR Spectra of Synthesized PDIs (with Peptide ^{1}H NMR Spectral Comparisons)

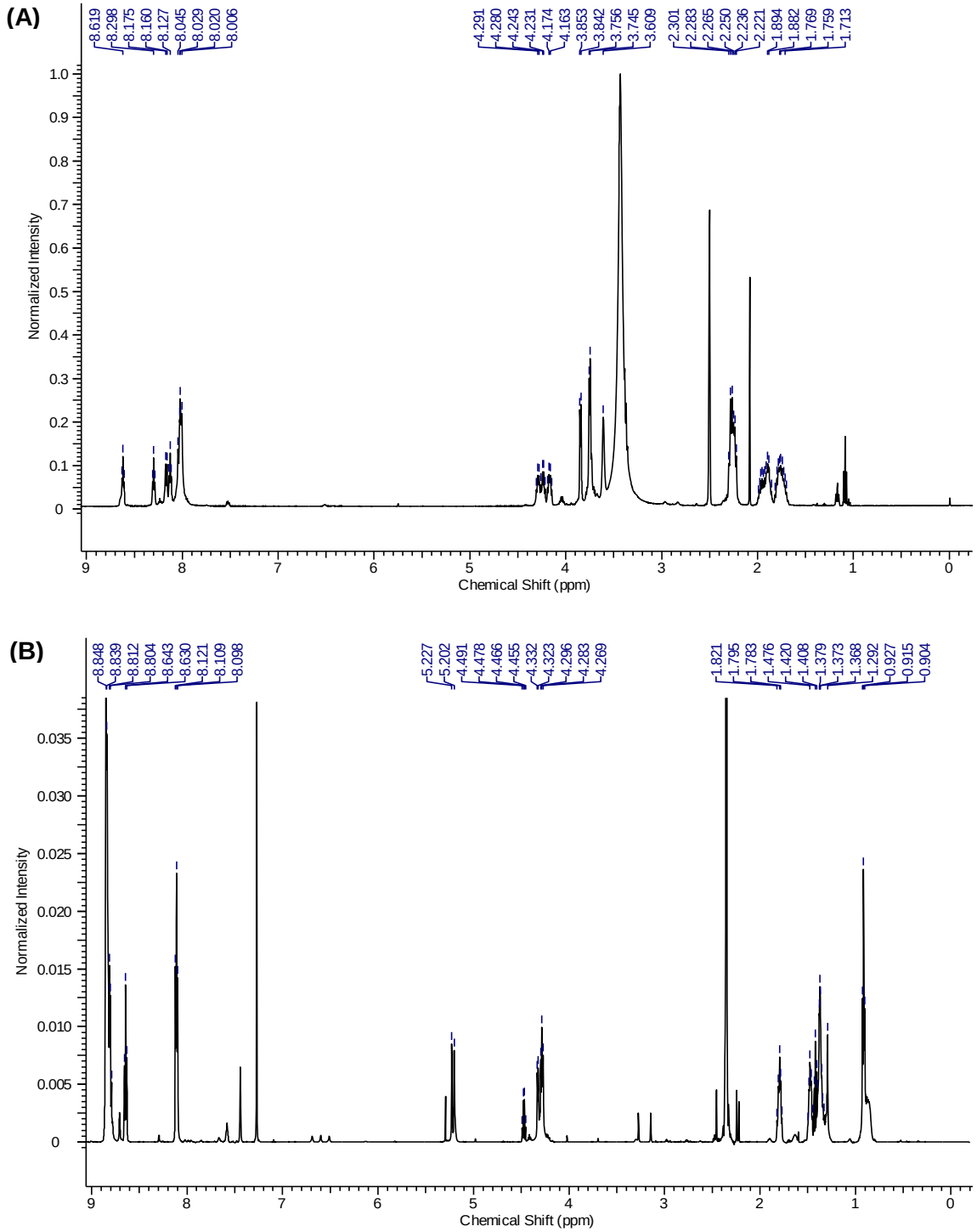

Figure A.28 ^{1}H NMR spectral comparison of: (A) NH_2-Gly-$(Gly)_3$-$(Glu)_3$ peptide (**P1**) in DMSO-d_6 and (B) *N*-hexyl-*N*′-[-Gly-$(Gly)_3$-$(Glu)_3$]perylene-3,4,9,10-tetracarboxylic acid diimide (**1H**) in 2:1 $CDCl_3$/TFA.

A.2 ^{1}H NMR Spectra of Synthesized PDIs (with Peptide ^{1}H NMR Spectral Comparisons)

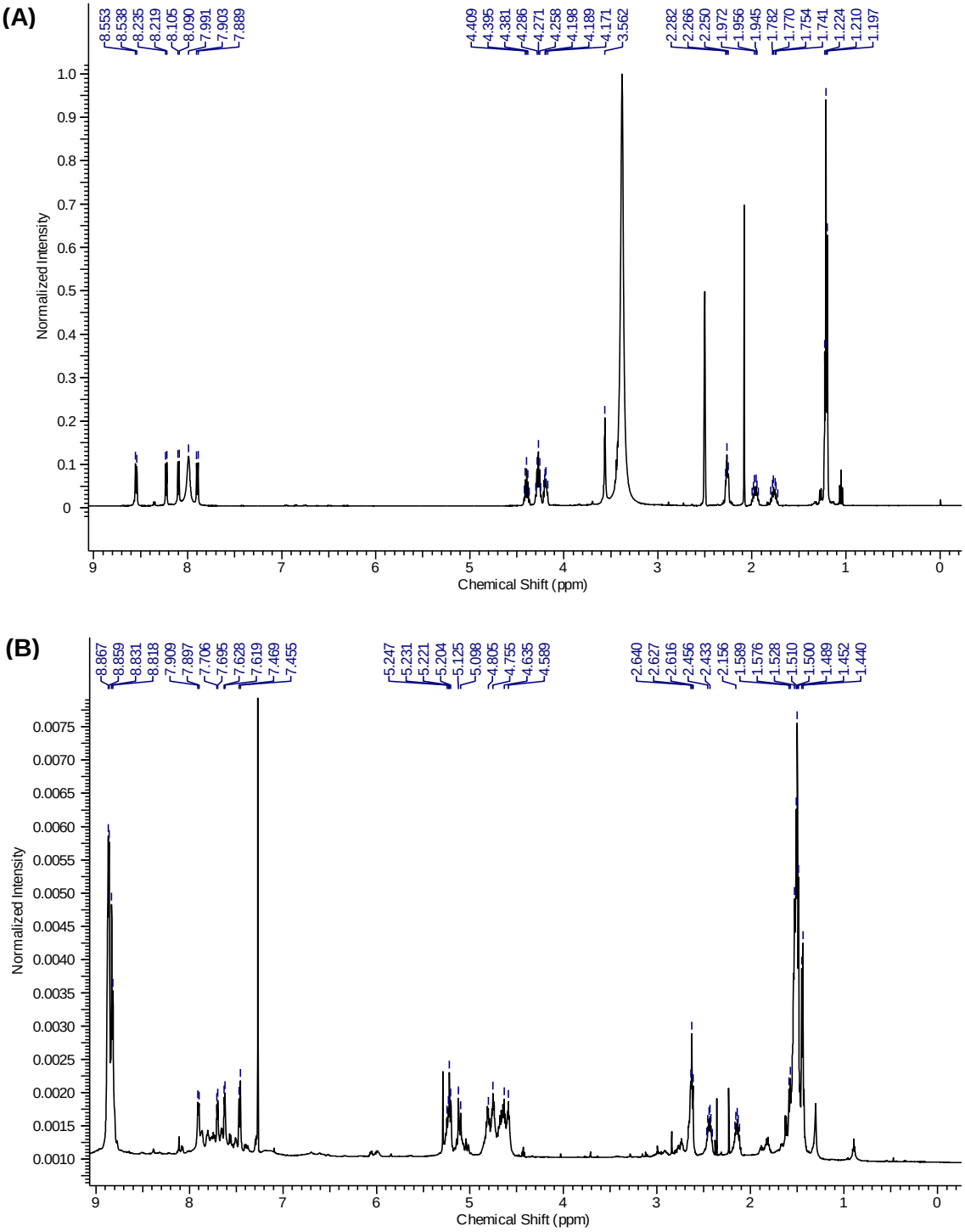

Figure A.29 ^{1}H NMR spectral comparison of: (A) NH_2-Gly-$(Ala)_3$-Glu peptide (**P2**) in DMSO-d_6 and (B) *N*,*N*′-di[-Gly-$(Ala)_3$-Glu]perylene-3,4,9,10-tetracarboxylic acid diimide (**2**) in 2:1 $CDCl_3$/TFA.

A.2 ^{1}H NMR Spectra of Synthesized PDIs (with Peptide ^{1}H NMR Spectral Comparisons)

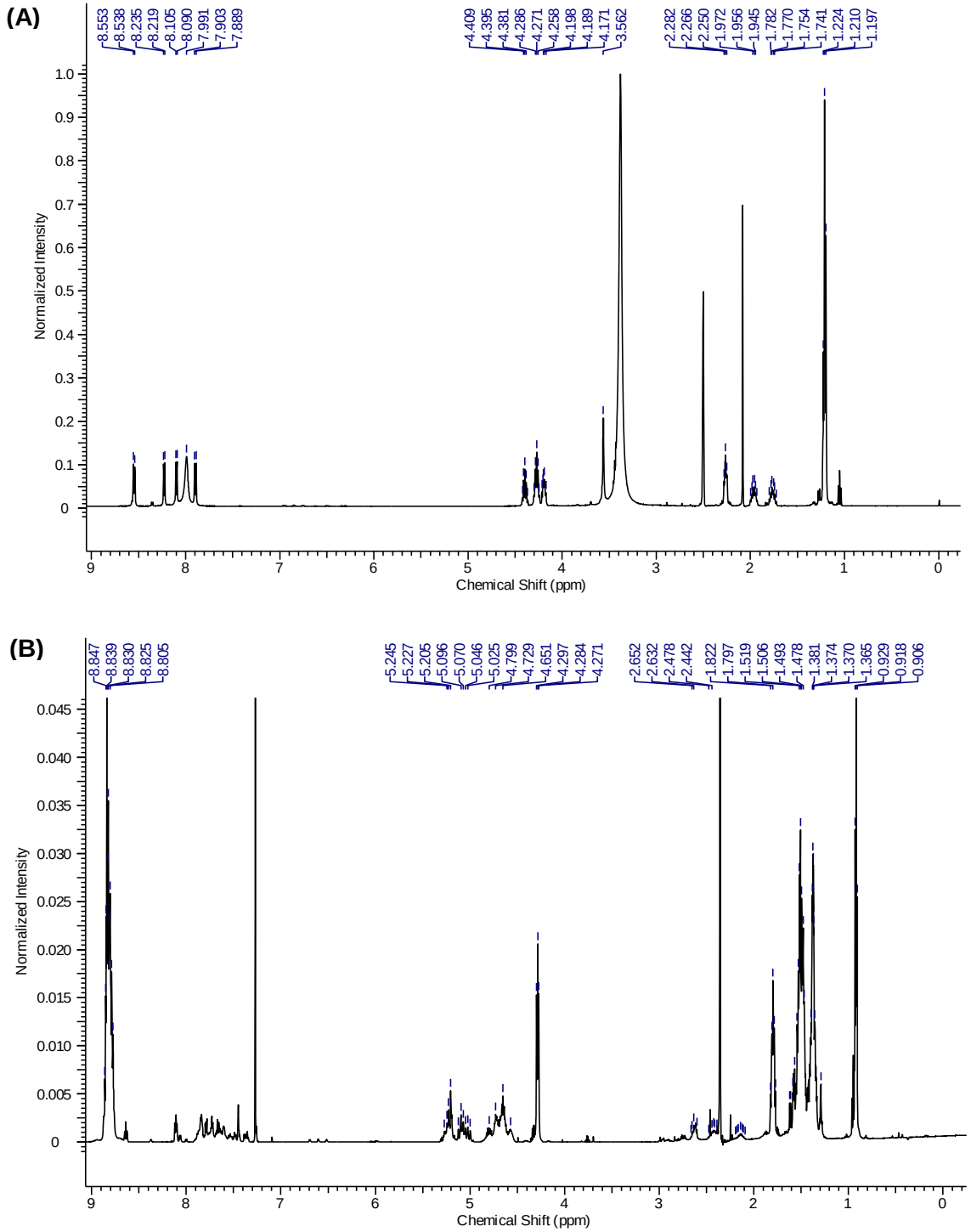

Figure A.30 ^{1}H NMR spectral comparison of: (A) NH_2-Gly-$(Ala)_3$-Glu peptide (**P2**) in DMSO-d_6 and (B) *N*-hexyl-*N′*-[-Gly-$(Ala)_3$-Glu]perylene-3,4,9,10-tetracarboxylic acid diimide (**2H**) in 2:1 $CDCl_3$/TFA.

A.2 ^{1}H NMR Spectra of Synthesized PDIs (with Peptide ^{1}H NMR Spectral Comparisons)

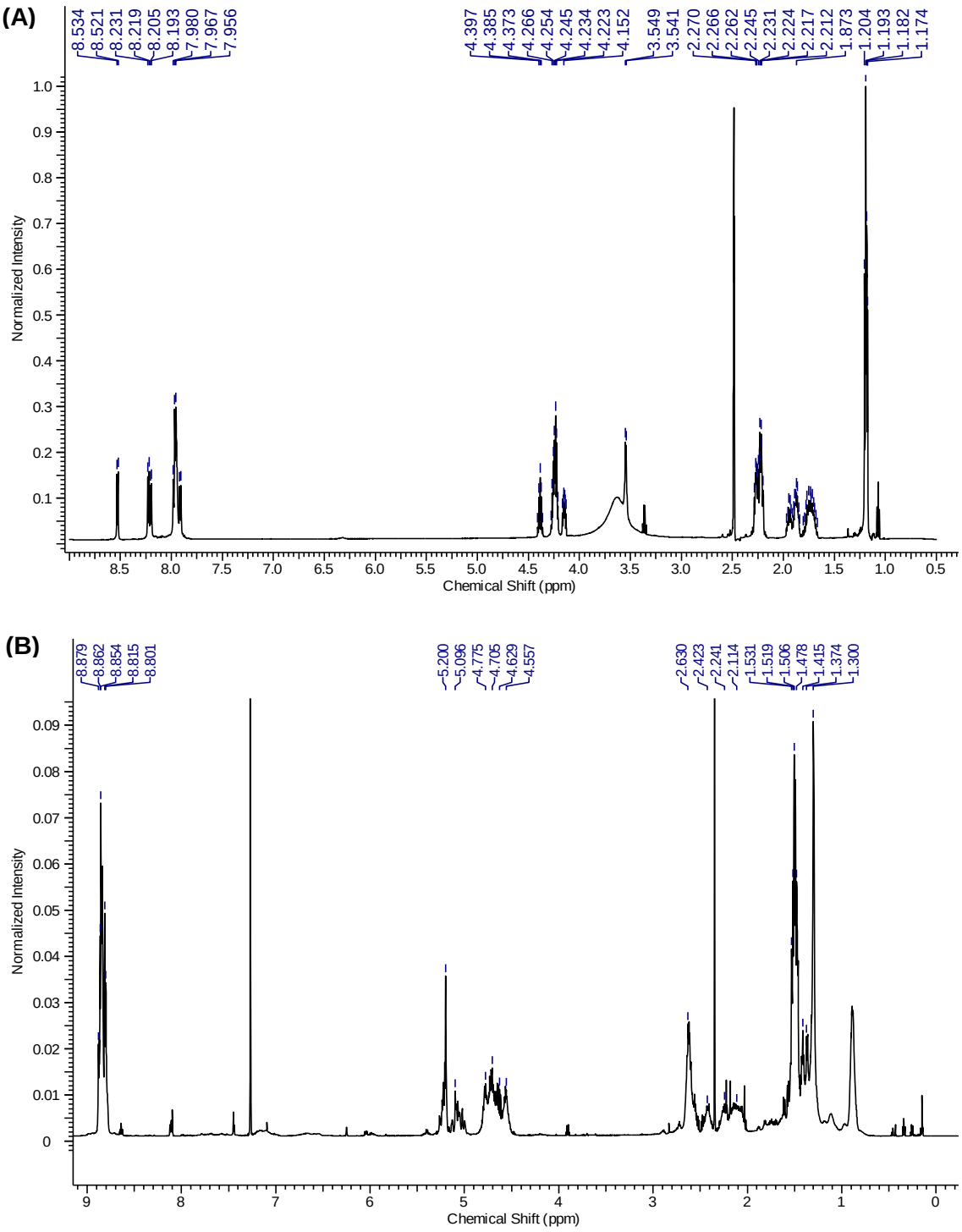

Figure A.31 ^{1}H NMR spectral comparison of: (A) NH_2-Gly-$(Ala)_3$-$(Glu)_3$ peptide (**P3**) in DMSO-d_6 and (B) *N*,*N*′-di[-Gly-$(Ala)_3$-$(Glu)_3$]perylene-3,4,9,10-tetracarboxylic acid diimide (**3**) in 2:1 $CDCl_3$/TFA.

A.2 ^{1}H NMR Spectra of Synthesized PDIs (with Peptide ^{1}H NMR Spectral Comparisons)

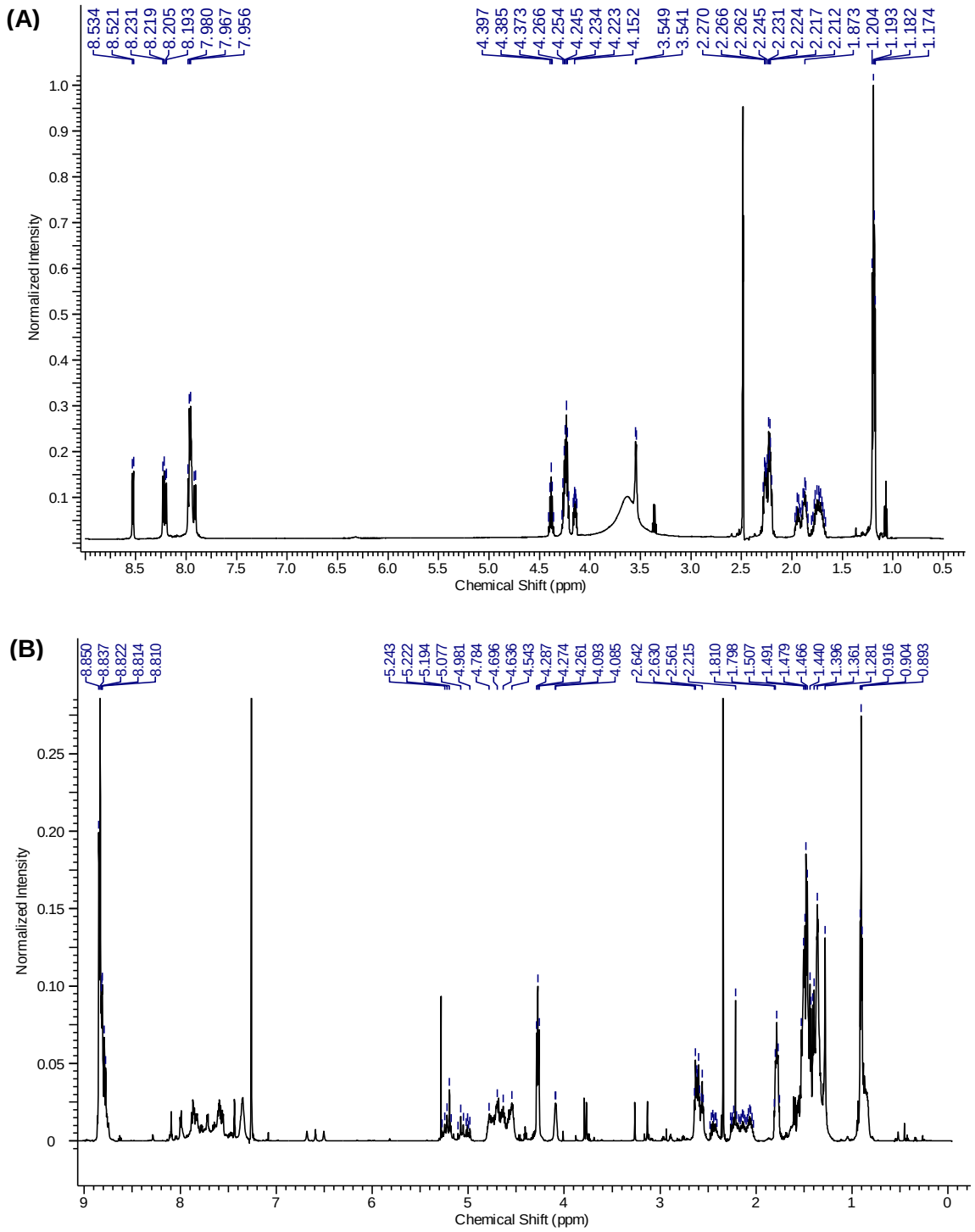

Figure A.32 ^{1}H NMR spectral comparison of: (A) NH_2-Gly-$(Ala)_3$-$(Glu)_3$ peptide (**P3**) in DMSO-d_6 and (B) *N*-hexyl-*N*′-[-Gly-$(Ala)_3$-$(Glu)_3$]perylene-3,4,9,10-tetracarboxylic acid diimide (**3H**) in 2:1 $CDCl_3$/TFA.

A.2 ^{1}H NMR Spectra of Synthesized PDIs (with Peptide ^{1}H NMR Spectral Comparisons)

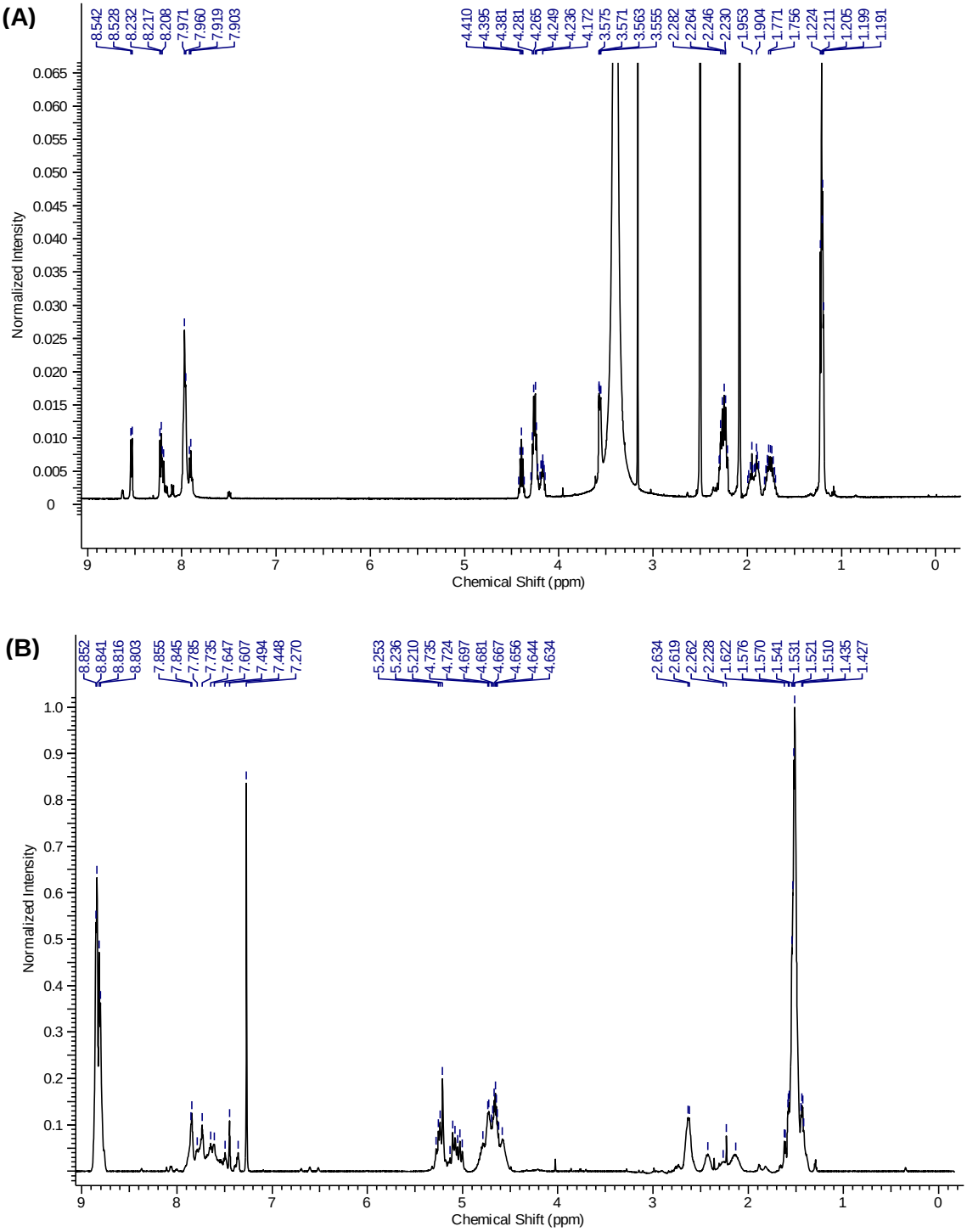

Figure A.33 ^{1}H NMR spectral comparison of: (A) NH_2-Gly-(*D*-Ala)$_3$-(*D*-Glu)$_3$ peptide (**P3E**) in DMSO-d_6 and (B) *N*,*N*′-di[-Gly-(*D*-Ala)$_3$-(*D*-Glu)$_3$]perylene-3,4,9,10- tetracarboxylic acid diimide (**3E**) in 2:1 $CDCl_3$/TFA.

A.2 ^{1}H NMR Spectra of Synthesized PDIs (with Peptide ^{1}H NMR Spectral Comparisons)

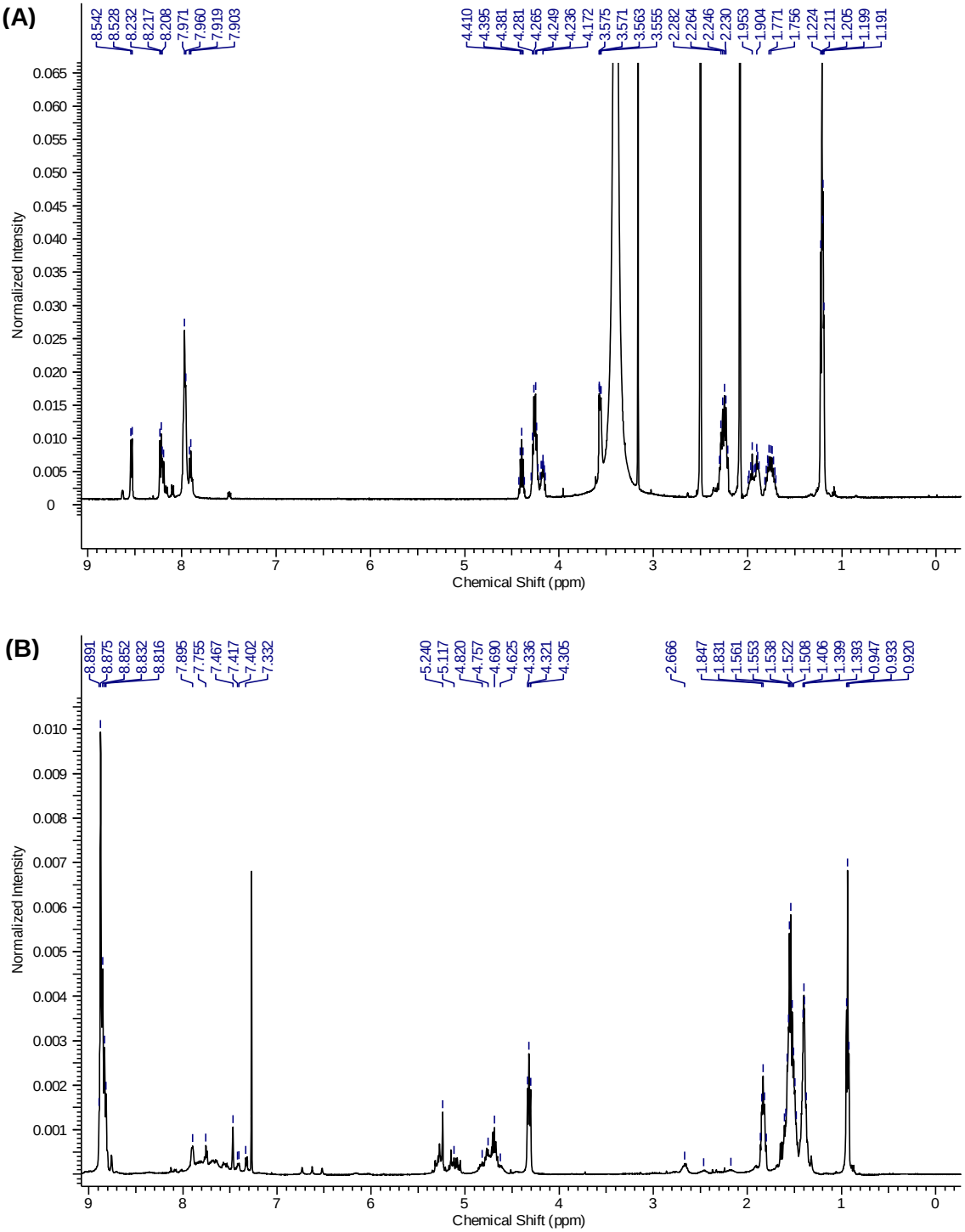

Figure A.34 ^{1}H NMR spectral comparison of: (A) NH_2-Gly-(*D*-Ala)$_3$-(*D*-Glu)$_3$ peptide (**P3E**) in DMSO-d$_6$ and (B) *N*-hexyl-*N'*-[-Gly-(*D*-Ala)$_3$-(*D*-Glu)$_3$]perylene-3,4,9,10- tetracarboxylic acid diimide (**3HE**) in 2:1 $CDCl_3$/TFA.

A.2 ^{1}H NMR Spectra of Synthesized PDIs (with Peptide ^{1}H NMR Spectral Comparisons)

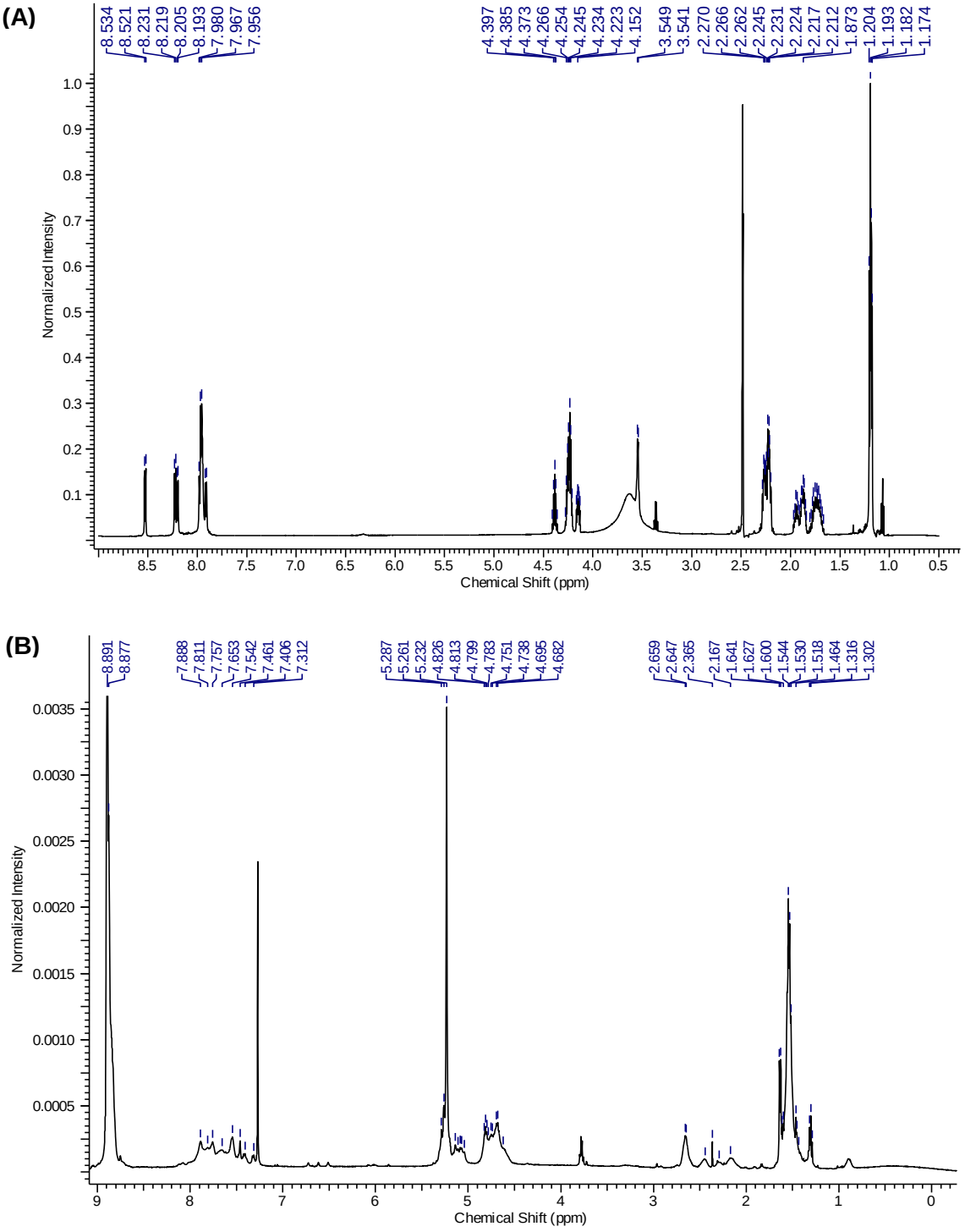

Figure A.35 ^{1}H NMR spectral comparison of: (A) NH_2-Gly-$(Ala)_3$-$(Glu)_3$ peptide (**P3**) in DMSO-d_6 and (B) *N*-[-Gly-(*L*-Ala)$_3$-(*L*-Glu)$_3$]-*N'*-[-Gly-(*D*-Ala)$_3$-(*D*-Glu)$_3$]-perylene-3,4,9,10- tetracarboxylic acid diimide (**3M**) in 2:1 $CDCl_3$/TFA.

A.2 ^{1}H NMR Spectra of Synthesized PDIs (with Peptide ^{1}H NMR Spectral Comparisons)

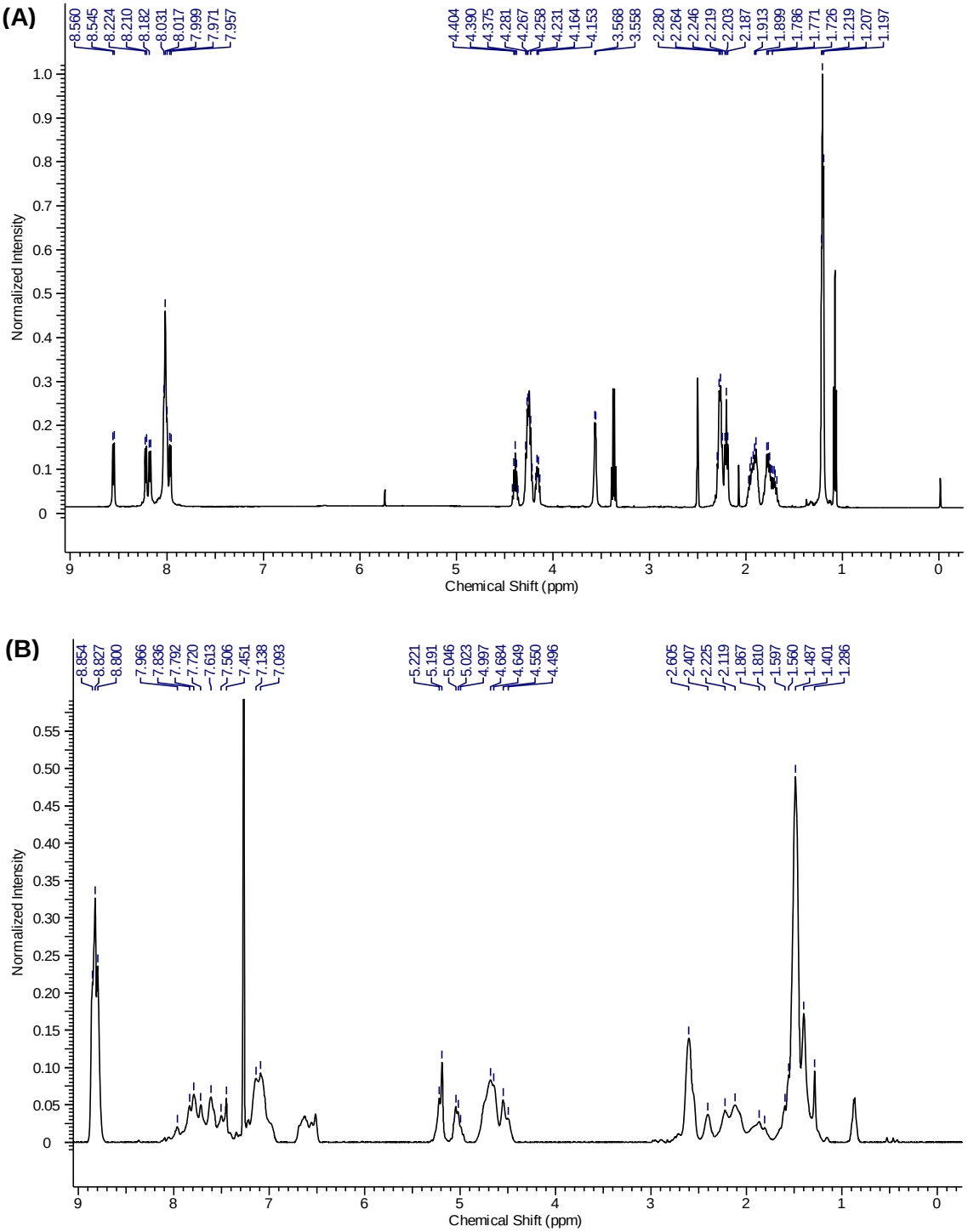

Figure A.36 ^{1}H NMR spectral comparison of: (A) NH_2-Gly-(*D*-Ala)$_3$-(Glu)$_3$ peptide (**P4**) in DMSO-d_6 and (B) *N*,*N*′-di[-Gly-(*D*-Ala)$_3$-(Glu)$_3$]perylene-3,4,9,10-tetracarboxylic acid diimide (**4**) in 2:1 $CDCl_3$/TFA.

A.2 ^{1}H NMR Spectra of Synthesized PDIs (with Peptide ^{1}H NMR Spectral Comparisons)

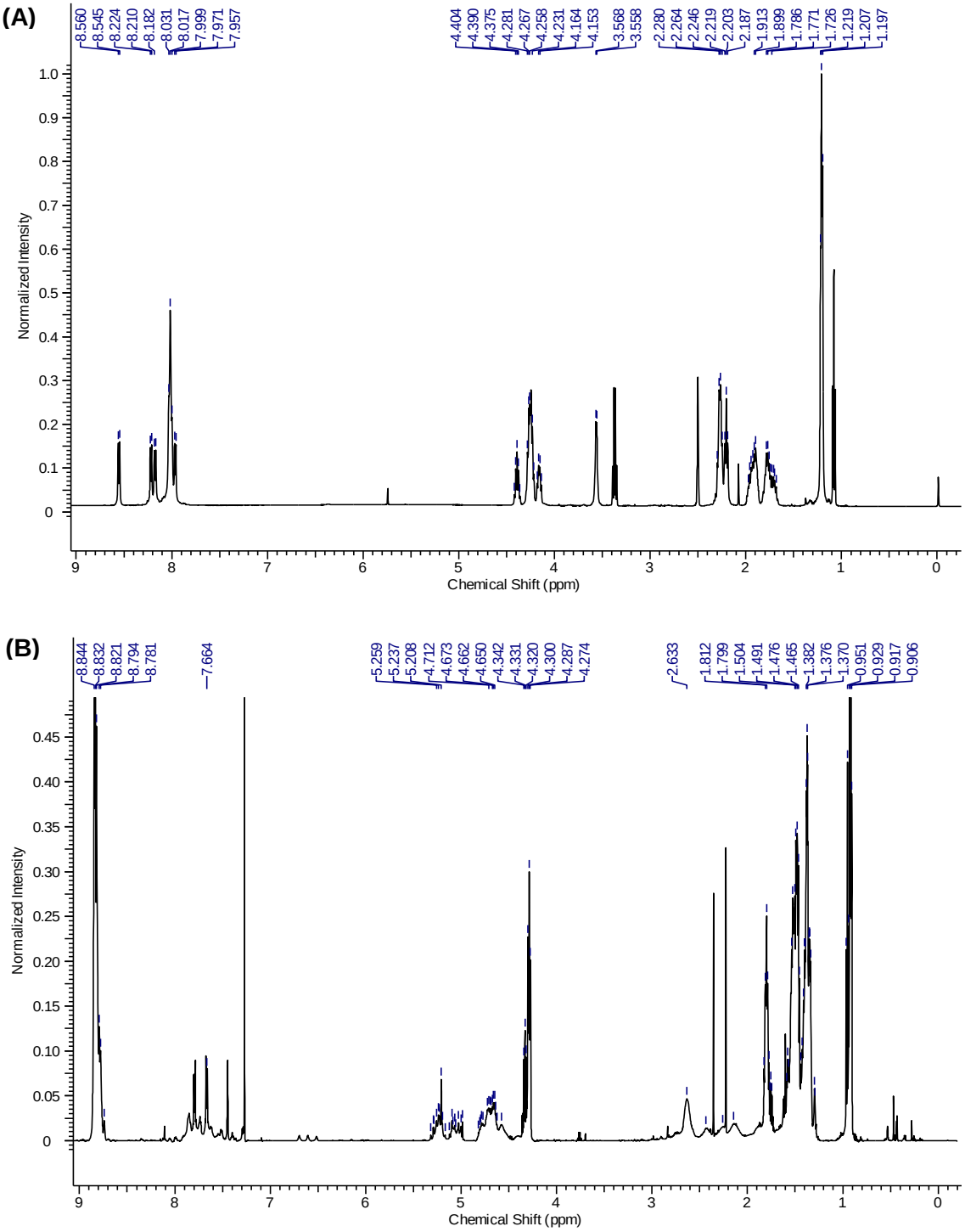

Figure A.37 ^{1}H NMR spectral comparison of: (A) NH_2-Gly-(*D*-Ala)$_3$-(Glu)$_3$ peptide (**P4**) in DMSO-d_6 and (B) *N*-hexyl-*N*′-[-Gly-(*D*-Ala)$_3$-(Glu)$_3$]perylene-3,4,9,10- tetracarboxylic acid diimide (**4H**) in 2:1 $CDCl_3$/TFA.

A.2 ^{1}H NMR Spectra of Synthesized PDIs (with Peptide ^{1}H NMR Spectral Comparisons)

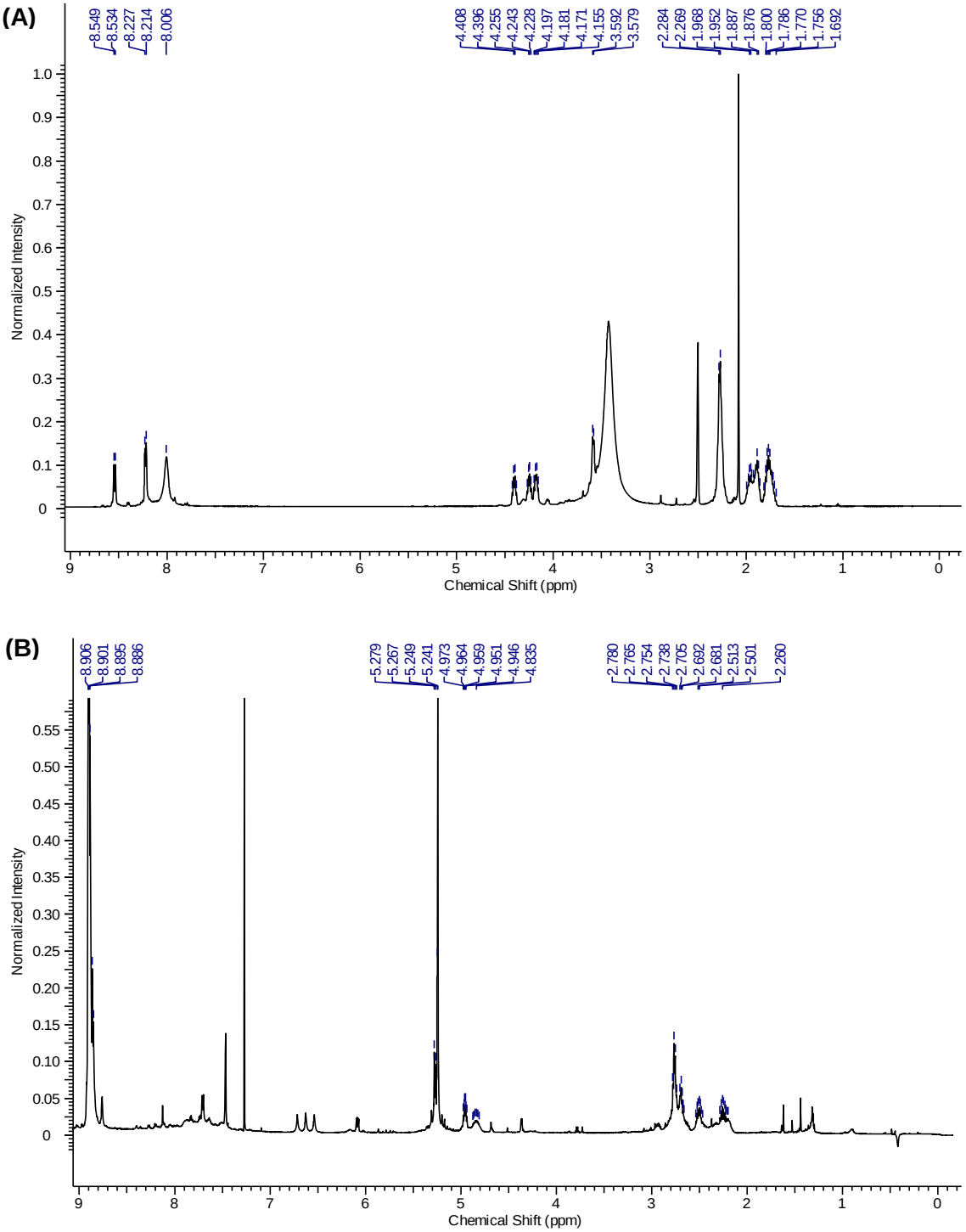

Figure A.38 ^{1}H NMR spectral comparison of: (A) NH_2-Gly-$(Glu)_3$ peptide (**P5**) in DMSO-d_6 and (B) *N*,*N*′-di[-Gly-$(Glu)_3$]perylene-3,4,9,10- tetracarboxylic acid diimide (**5**) in 2:1 $CDCl_3$/TFA.

A.2 ^{1}H NMR Spectra of Synthesized PDIs (with Peptide ^{1}H NMR Spectral Comparisons)

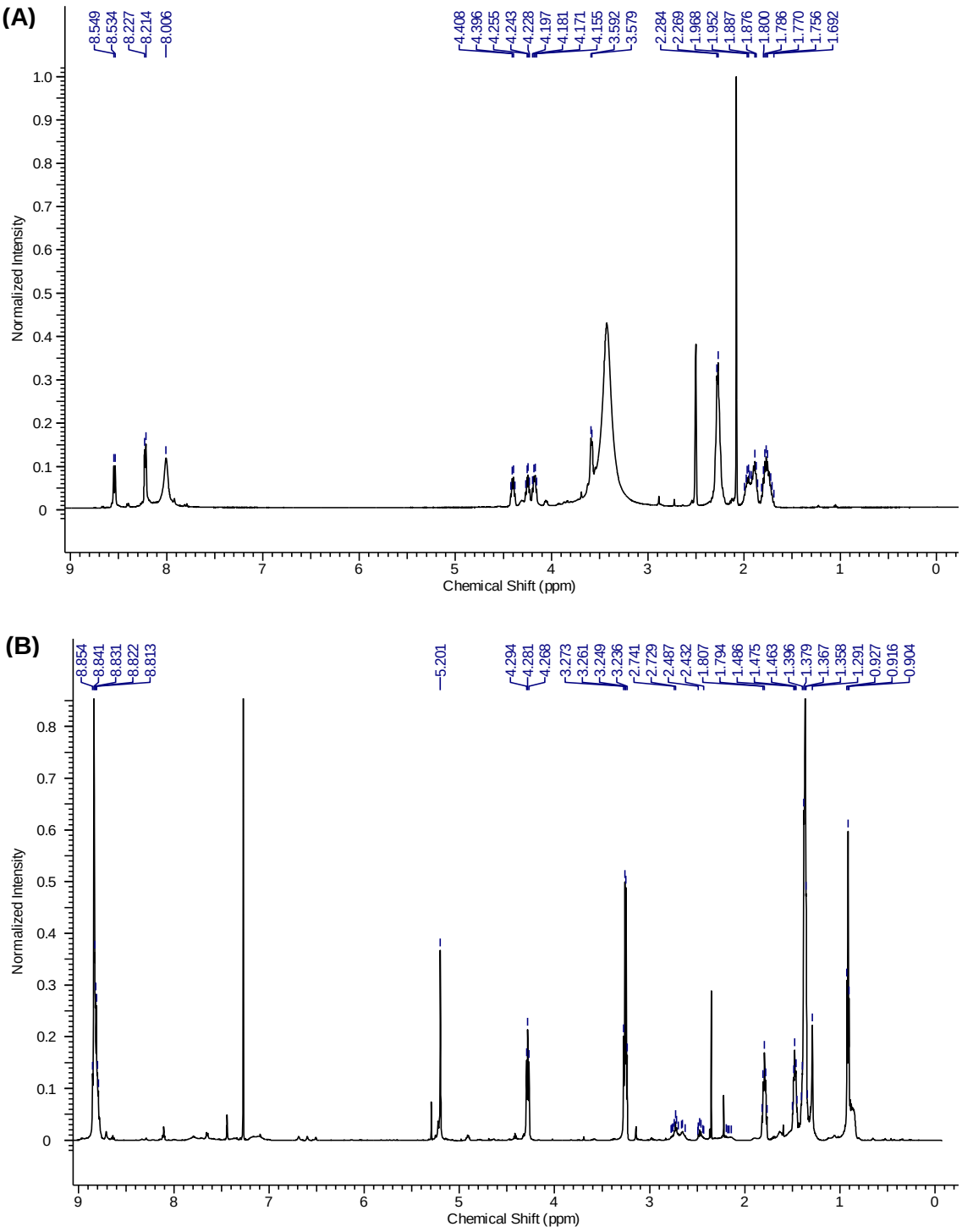

Figure A.39 ^{1}H NMR spectral comparison of: (A) NH_2-Gly-$(Glu)_3$ peptide (**P5**) in DMSO-d_6 and (B) *N*-hexyl-*N'*-[-Gly-$(Glu)_3$]perylene-3,4,9,10- tetracarboxylic acid diimide (**5H**) in 2:1 $CDCl_3$/TFA.

A.2 ^{1}H NMR Spectra of Synthesized PDIs (with Peptide ^{1}H NMR Spectral Comparisons)

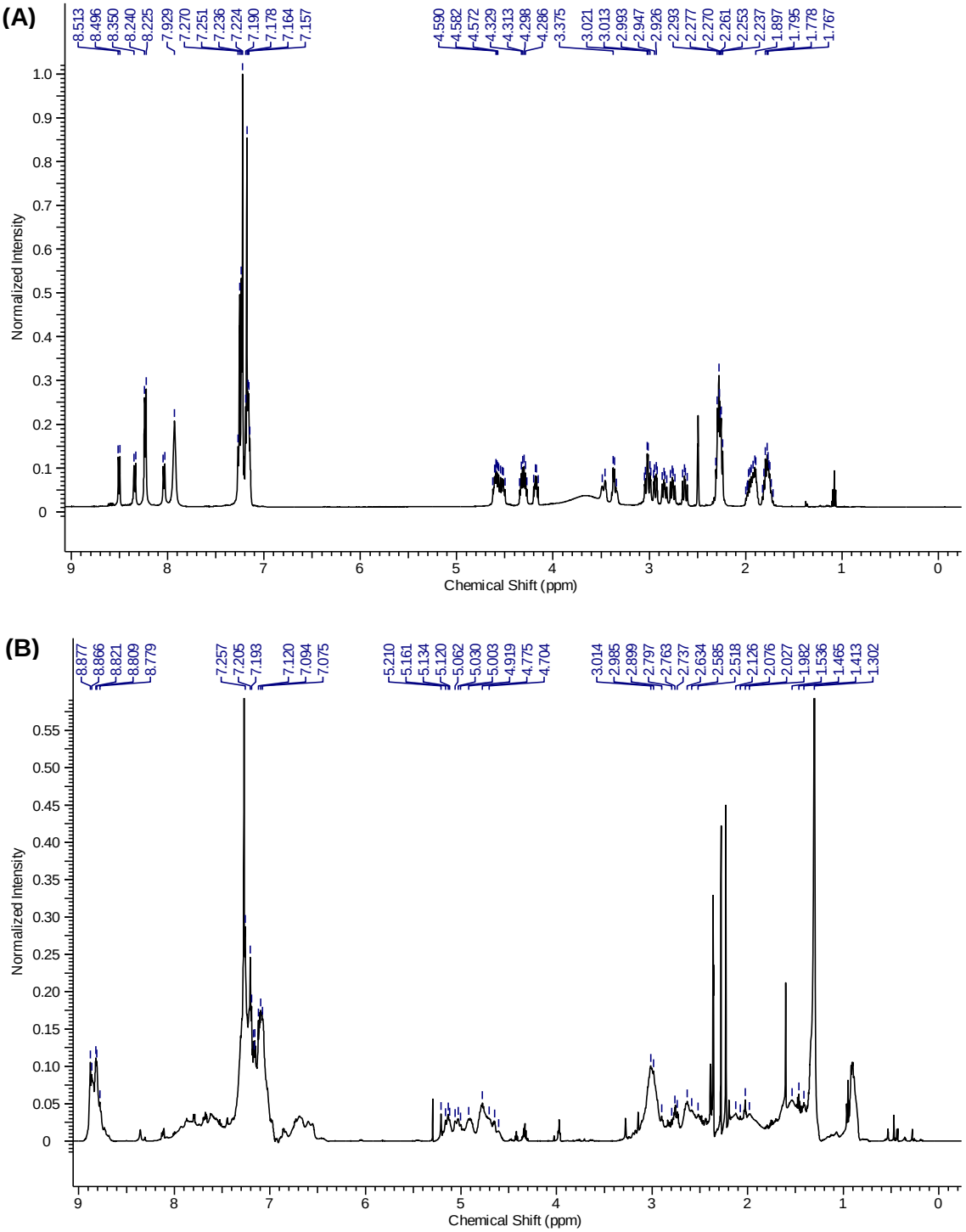

Figure A.40 ^{1}H NMR spectral comparison of: (A) NH_2-Gly-$(Phe)_3$-$(Glu)_3$ peptide (**P6**) in DMSO-d_6 and (B) *N,N′*-di[-Gly-$(Phe)_3$-$(Glu)_3$]perylene-3,4,9,10-tetracarboxylic acid diimide (**6**) in 2:1 $CDCl_3$/TFA.

A.2 ^{1}H NMR Spectra of Synthesized PDIs (with Peptide ^{1}H NMR Spectral Comparisons)

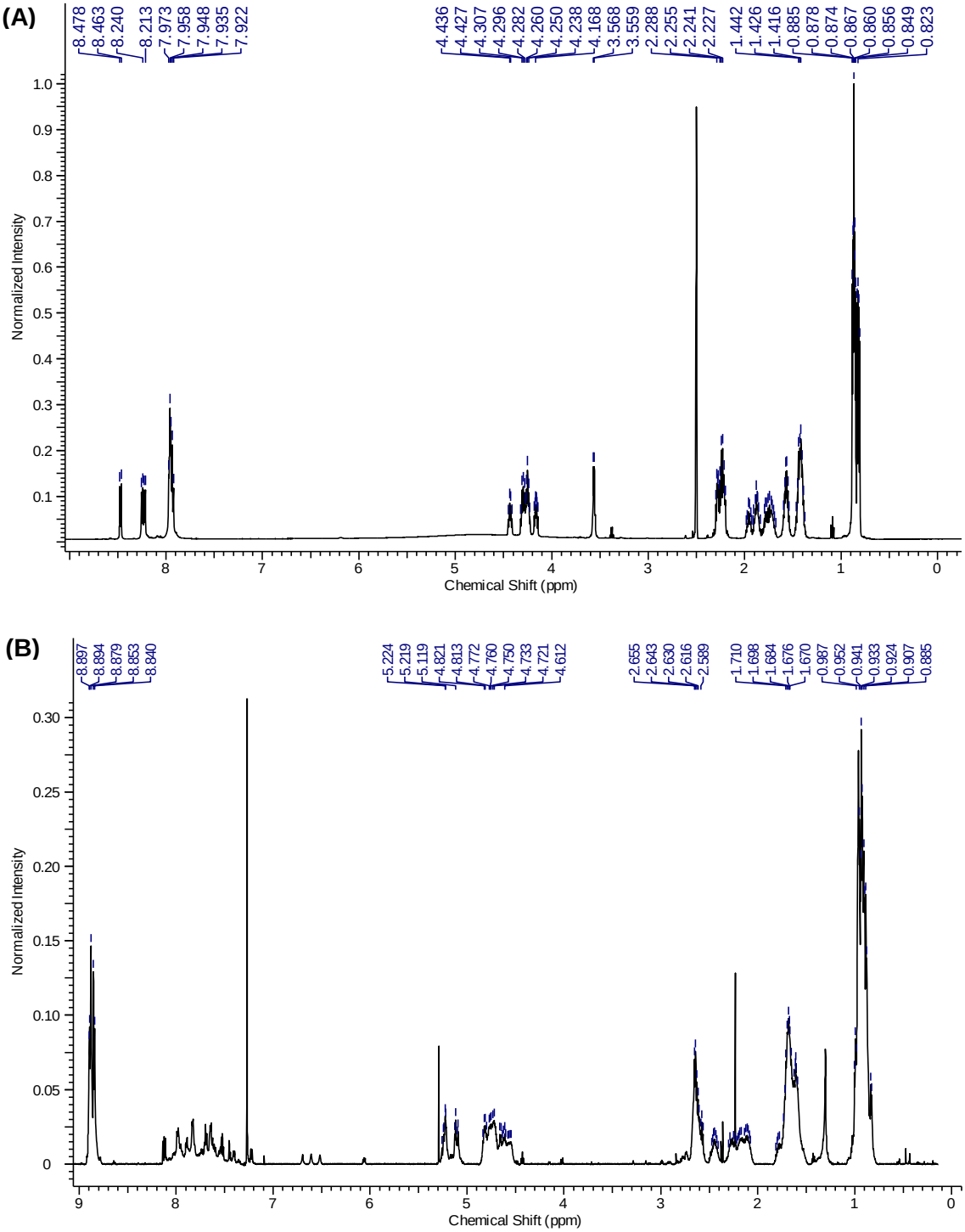

Figure A.41 ^{1}H NMR spectral comparison of: (A) NH_2-Gly-$(Leu)_3$-$(Glu)_3$ peptide (**P7**) in DMSO-d_6 and (B) *N*,*N*′-di[-Gly-$(Leu)_3$-$(Glu)_3$]perylene-3,4,9,10-tetracarboxylic acid diimide (**7**) in 2:1 $CDCl_3$/TFA.

A.2 ^{1}H NMR Spectra of Synthesized PDIs (with Peptide ^{1}H NMR Spectral Comparisons)

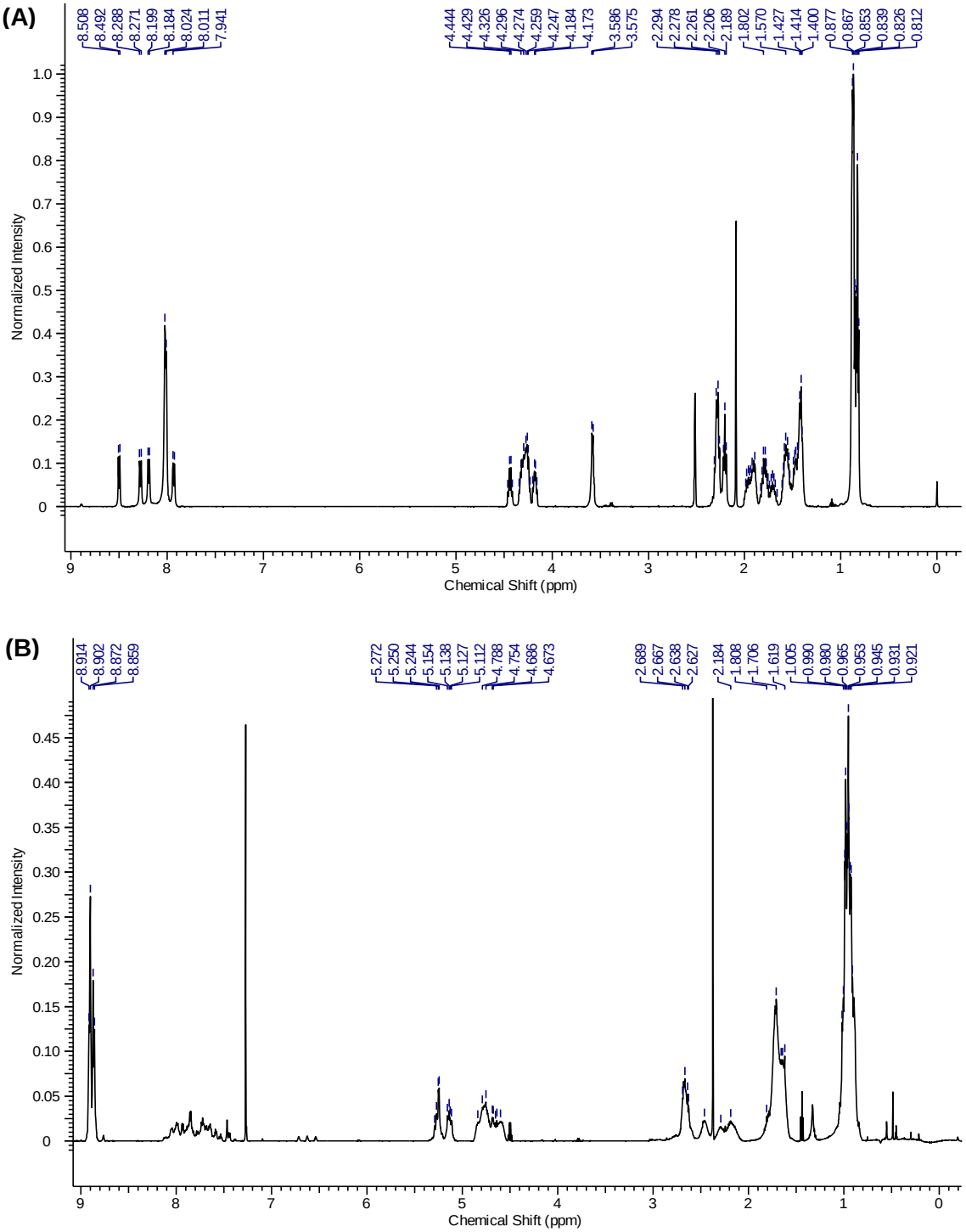

Figure A.42 ^{1}H NMR spectral comparison of: (A) NH_2-Gly-(*D*-Leu)$_3$-(Glu)$_3$ peptide (**P8**) in DMSO-d_6 and (B) *N*,*N*′-di[-Gly-(*D*-Leu)$_3$-(Glu)$_3$]perylene-3,4,9,10-tetracarboxylic acid diimide (**8**) in 2:1 $CDCl_3$/TFA.

A.2 ^{1}H NMR Spectra of Synthesized PDIs (with Peptide ^{1}H NMR Spectral Comparisons)

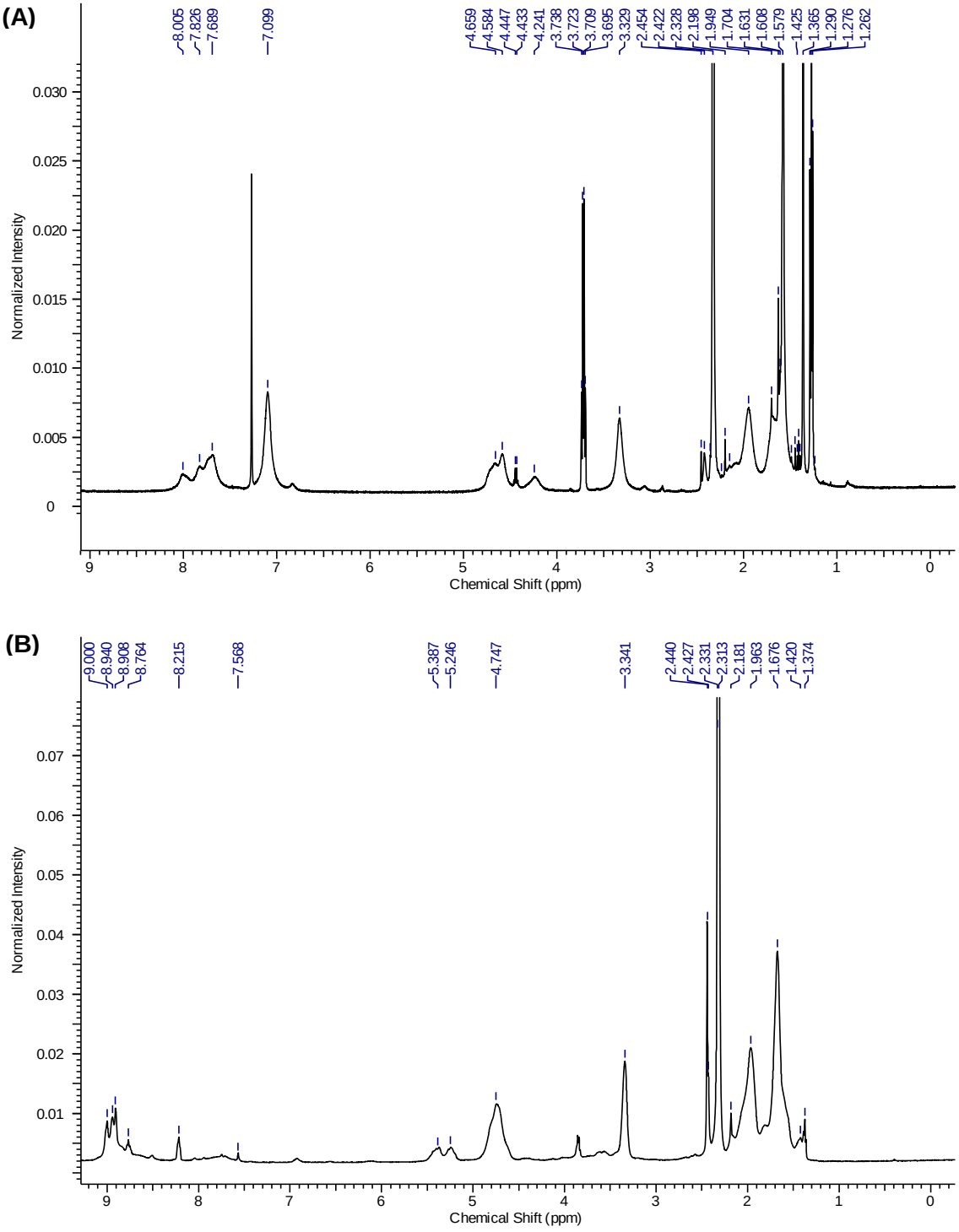

Figure A.43 ^{1}H NMR spectral comparison of: (A) NH_2-Gly-$(Ala)_3$-$[Lys(Boc)]_3$ peptide (**P9**) in $CDCl_3$ and (B) *N*,*N*′-di[-Gly-$(Ala)_3$-$(Lys)_3$]perylene-3,4,9,10-tetracarboxylic acid diimide (**9**) in CF_3COOD.

A.2 ^{1}H NMR Spectra of Synthesized PDIs (with Peptide ^{1}H NMR Spectral Comparisons)

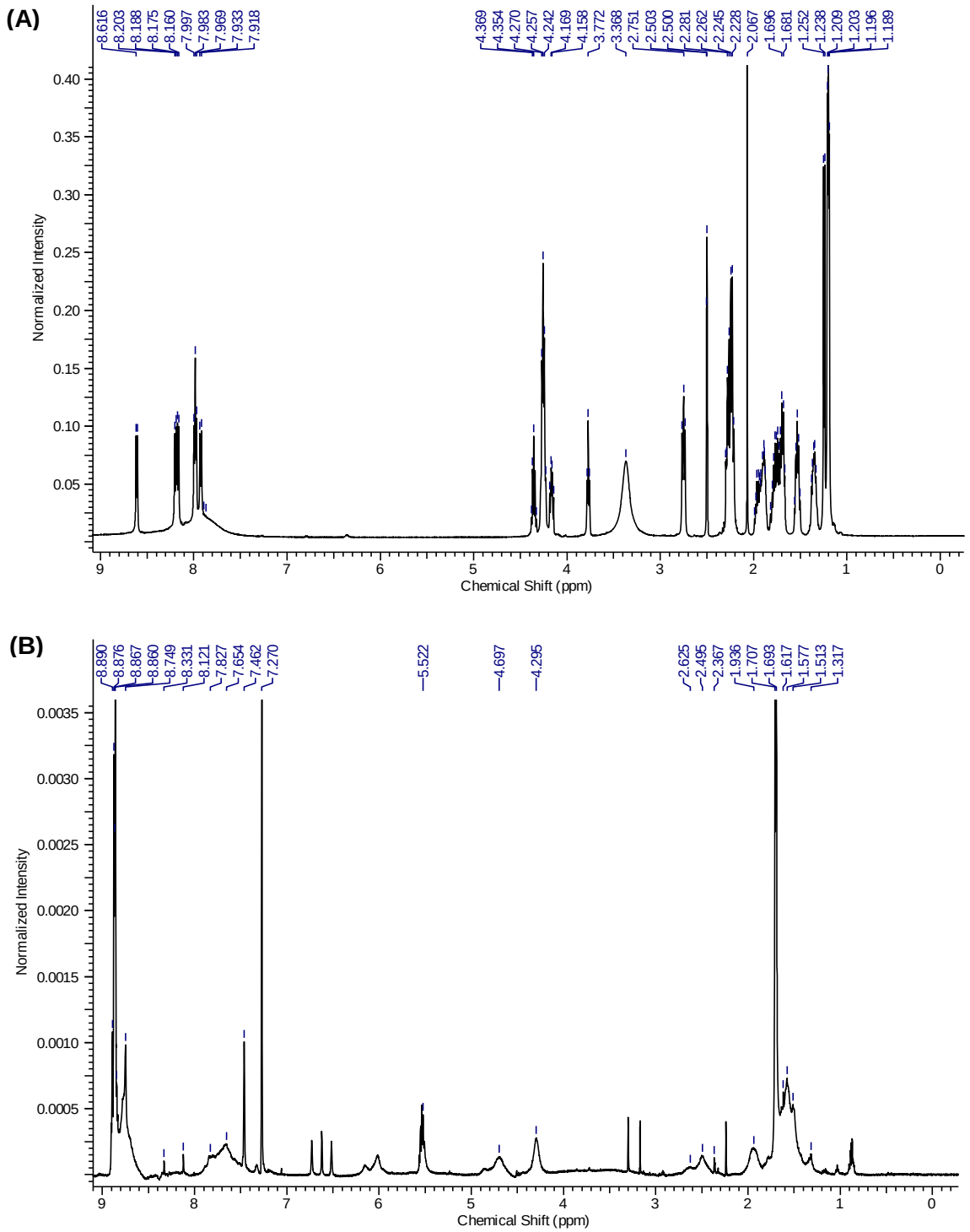

Figure A.44 ^{1}H NMR spectral comparison of: (A) NH_2-Lys-$(Ala)_3$-$(Glu)_3$ peptide (**P10**) in DMSO-d_6 and (B) (*N*-yl-*N'*-isopropyl-perylene-3,4,9,10-diimide)$_2$-Lys-$(Ala)_3$-$(Glu)_3$-OH (**10**) in 2:1 $CDCl_3$/TFA.

A.2 ^{1}H NMR Spectra of Synthesized PDIs (with Peptide ^{1}H NMR Spectral Comparisons)

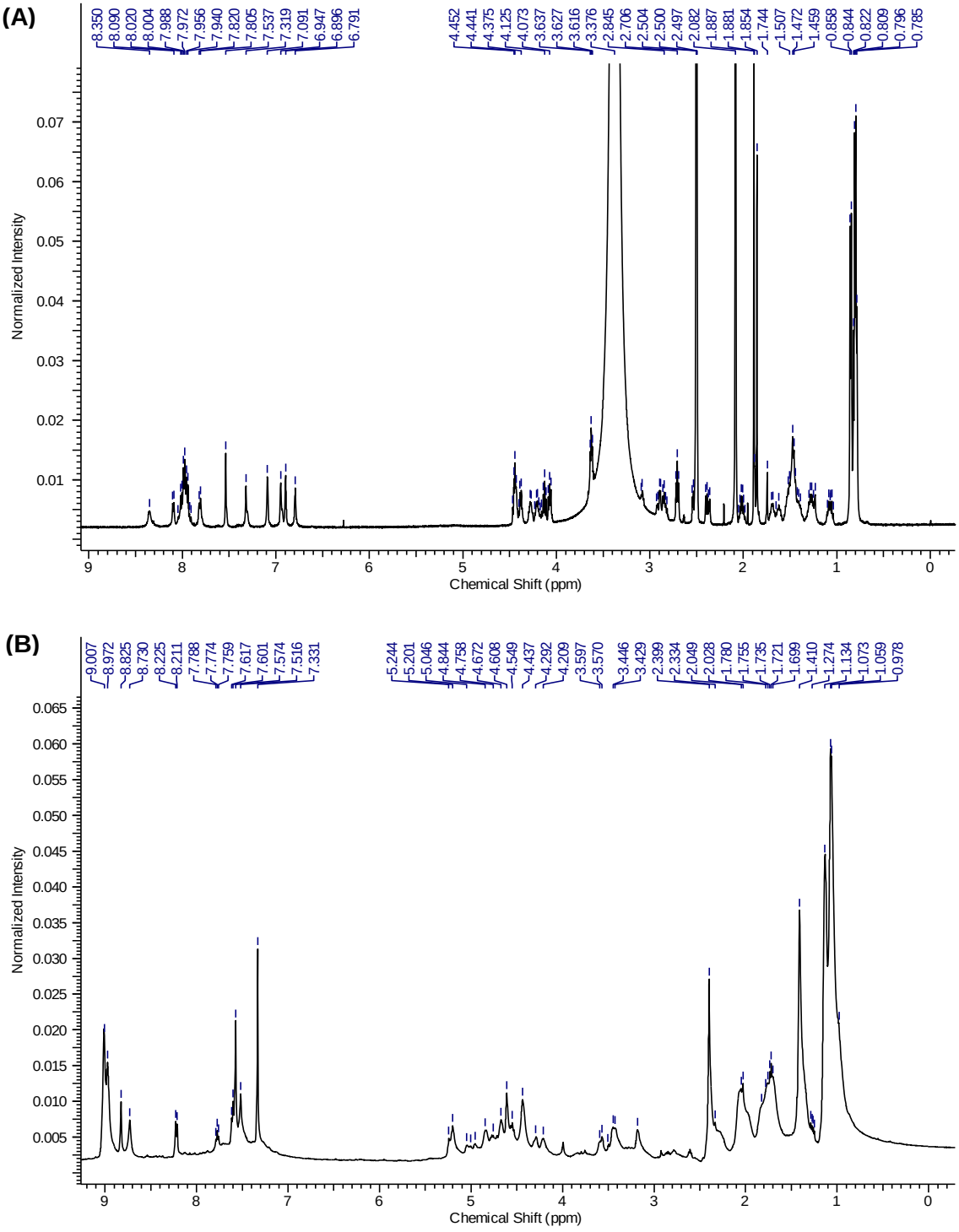

Figure A.45 ^{1}H NMR spectral comparison of: (A) Ac-Ile-Lys-His-Leu-Ser-Val-Asn-NH_2 peptide in DMSO-d_6 and (B) *N*,*N*′-di[Ac-Ile-Lys(-yl)-His-Leu-Ser-Val-Asn-NH_2]perylene-3,4,9,10-tetracarboxylic acid diimide (**12**) in CF_3COOD.

A.2 ^{1}H NMR Spectra of Synthesized PDIs (with Peptide ^{1}H NMR Spectral Comparisons)

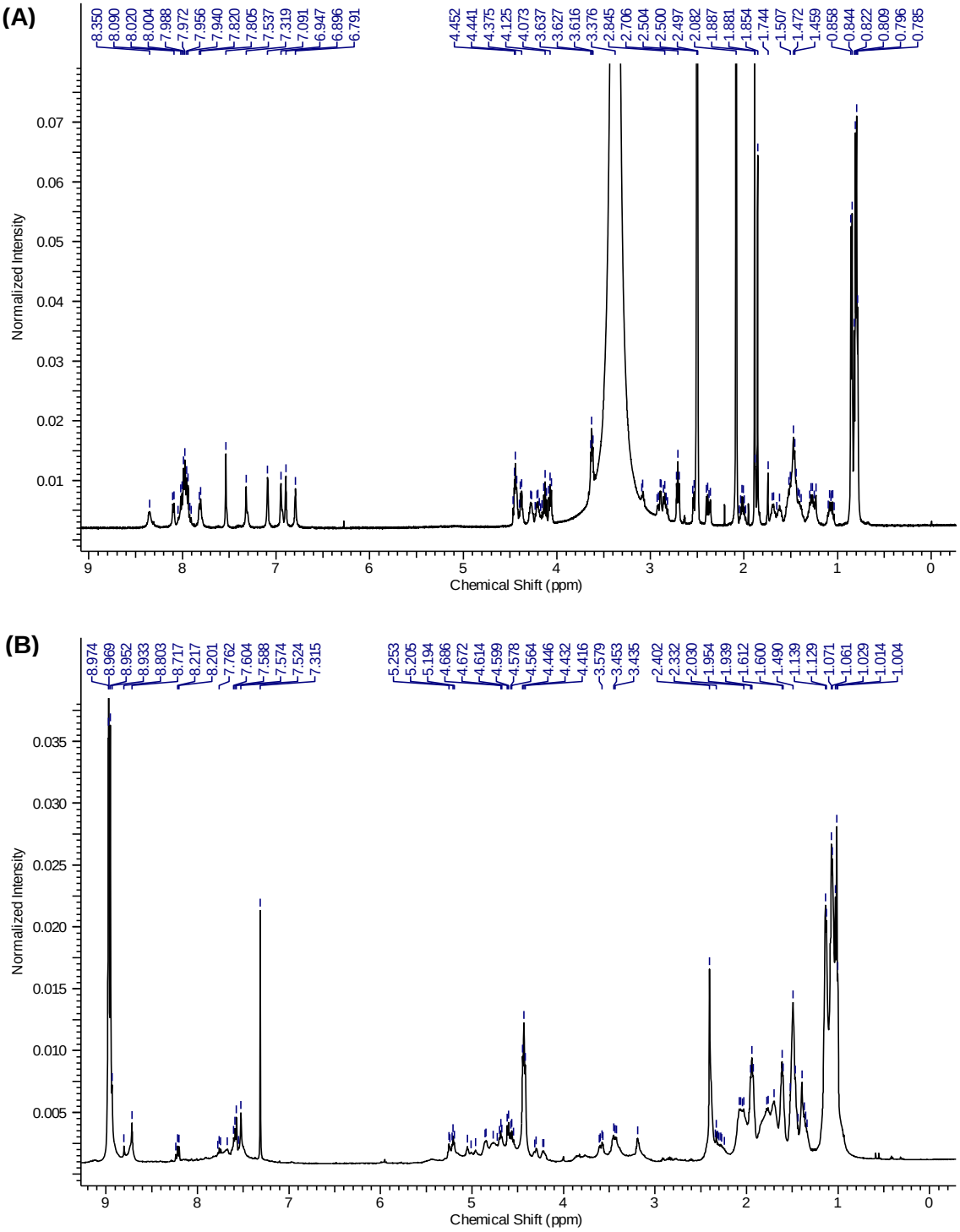

Figure A.46 ^{1}H NMR spectral comparison of: (A) Ac-Ile-Lys-His-Leu-Ser-Val-Asn-NH_2 peptide in DMSO-d_6 and (B) *N*-hexyl-*N*′-[Ac-Ile-Lys(-yl)-His-Leu-Ser-Val-Asn-NH_2]perylene-3,4,9,10-tetracarboxylic acid diimide (**12H**) in CF_3COOD.

A.2 ^{1}H NMR Spectra of Synthesized PDIs (with Peptide ^{1}H NMR Spectral Comparisons)

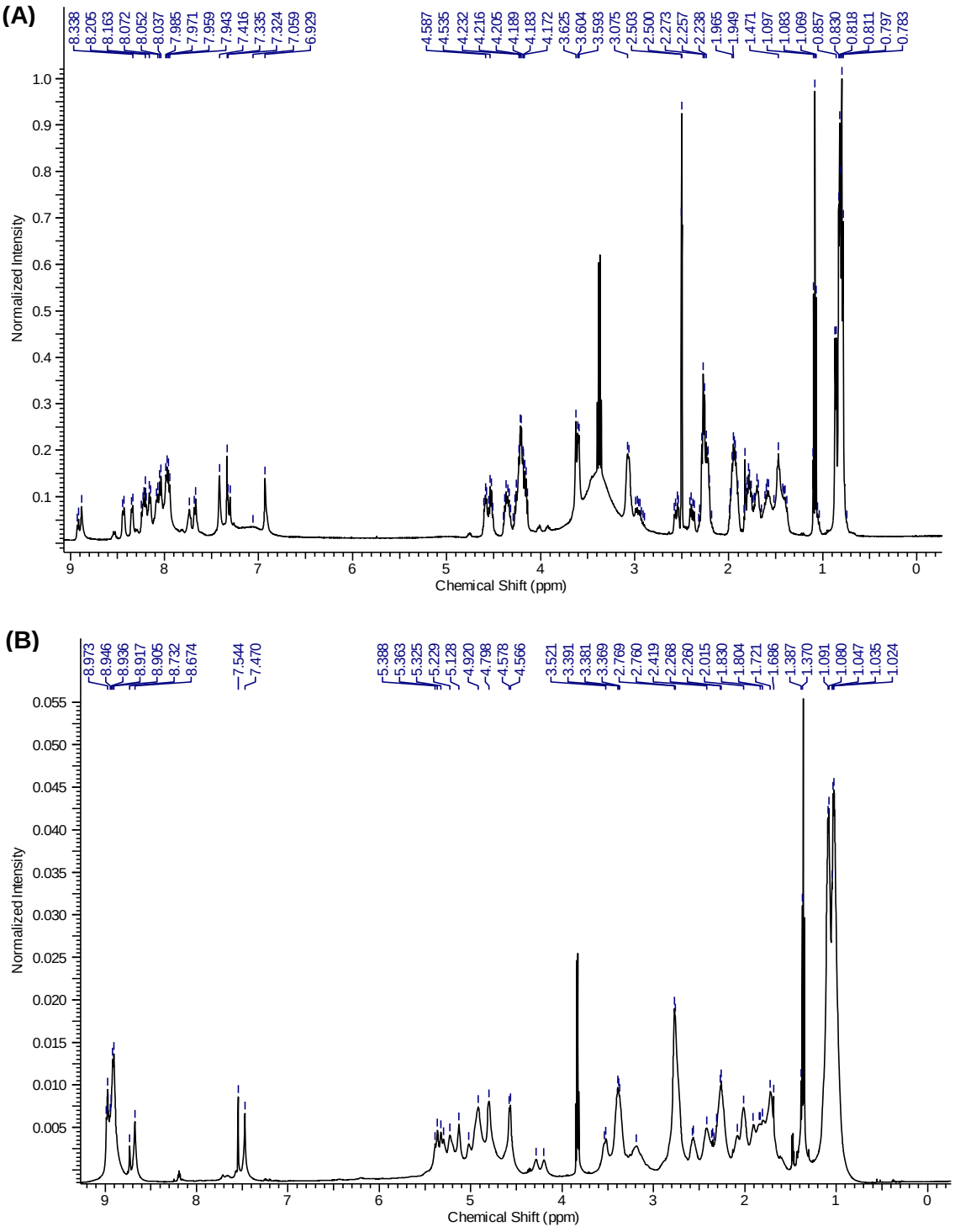

Figure A.47 ^{1}H NMR spectral comparison of: (A) GIRHLSVNEEE peptide (**P13**) in DMSO-d_6 and (B) *N*,*N*′-di[-GIRHLSVNEEE]perylene-3,4,9,10-tetracarboxylic acid diimide (**13**) in CF_3COOD.

A.2 ^{1}H NMR Spectra of Synthesized PDIs (with Peptide ^{1}H NMR Spectral Comparisons)

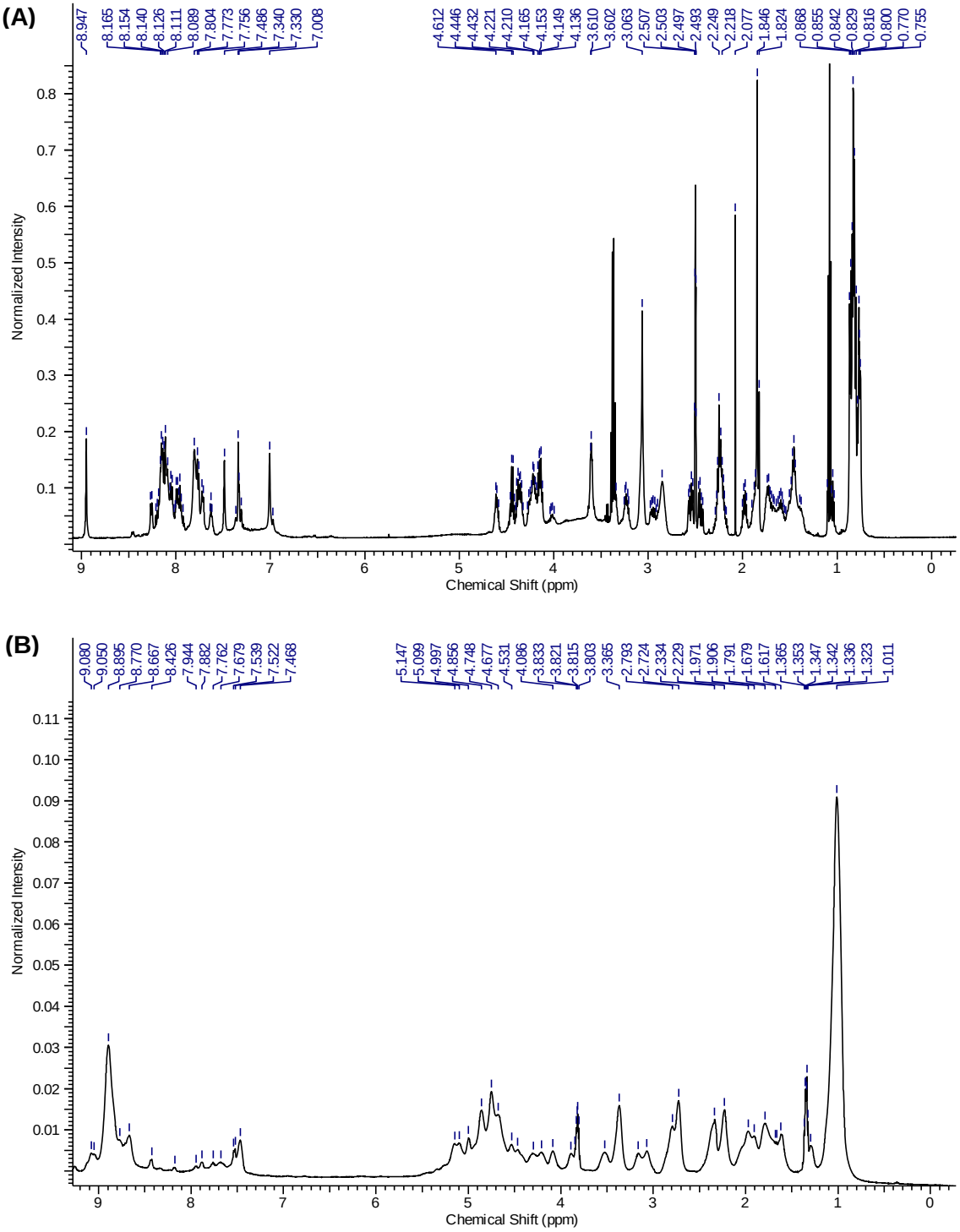

Figure A.48 ^{1}H NMR spectral comparison of: (A) Ac-EEEIRHLSVN-amidoethylamine peptide (**P14**) in DMSO-d_6 and (B) *N*,*N*′-di[Ac-EEEIRHLSVN-amidoethyl]perylene-3,4,9,10-tetracarboxylic acid diimide (**14**) in CF_3COOD.

A.2 ^{1}H NMR Spectra of Synthesized PDIs (with Peptide ^{1}H NMR Spectral Comparisons)

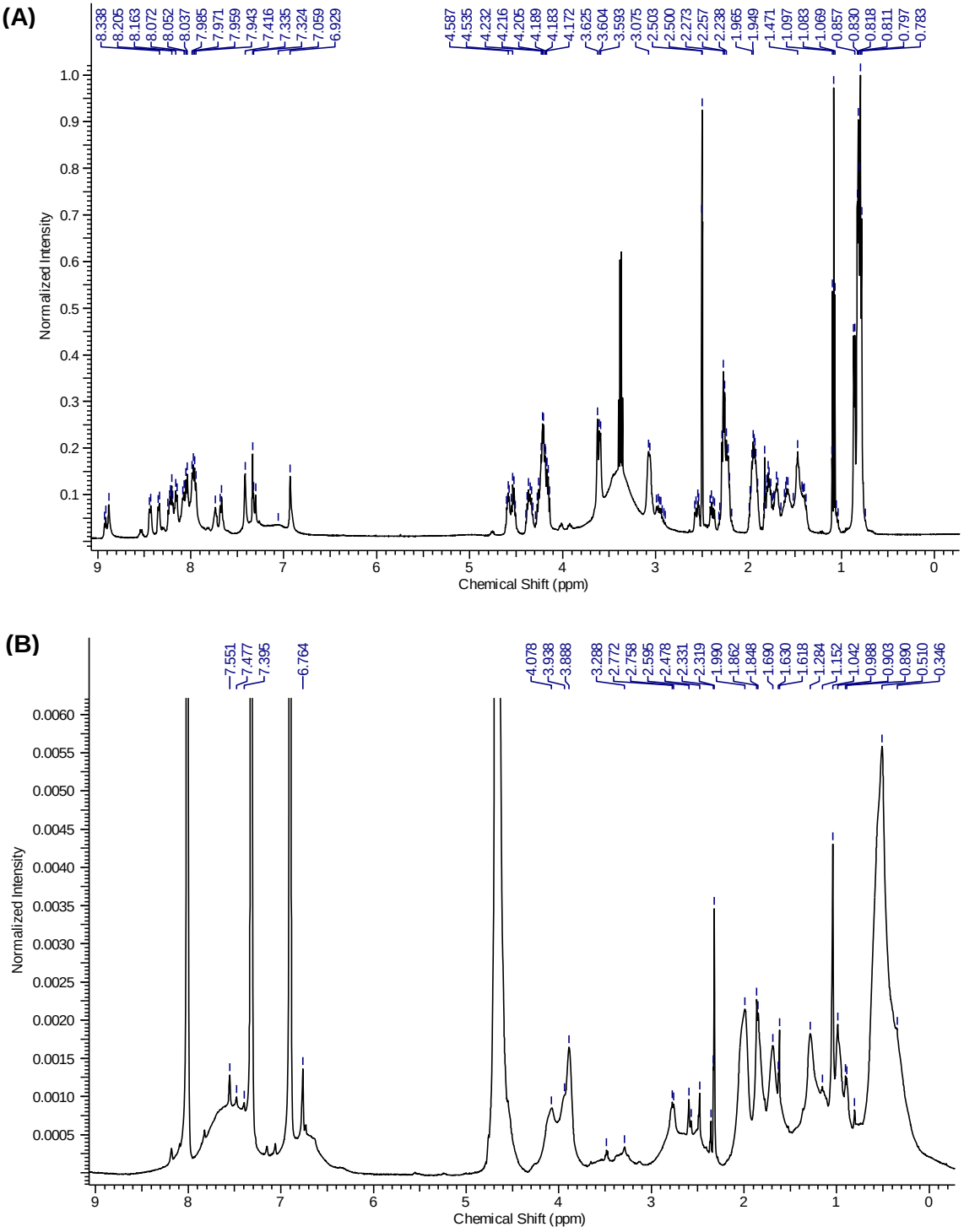

Figure A.49 ^{1}H NMR spectral comparison of: (A) GIRHLSVNEEE peptide (**P13**) in DMSO-d_6 and (B) *N*-[-GIRHLSVNEEE]perylene-3,4-imide-9,10-bis(n-butyl) ester (**15**) in 4:1 D_2O/pyridine-d_5.

A.2 ^{1}H NMR Spectra of Synthesized PDIs (with Peptide ^{1}H NMR Spectral Comparisons)

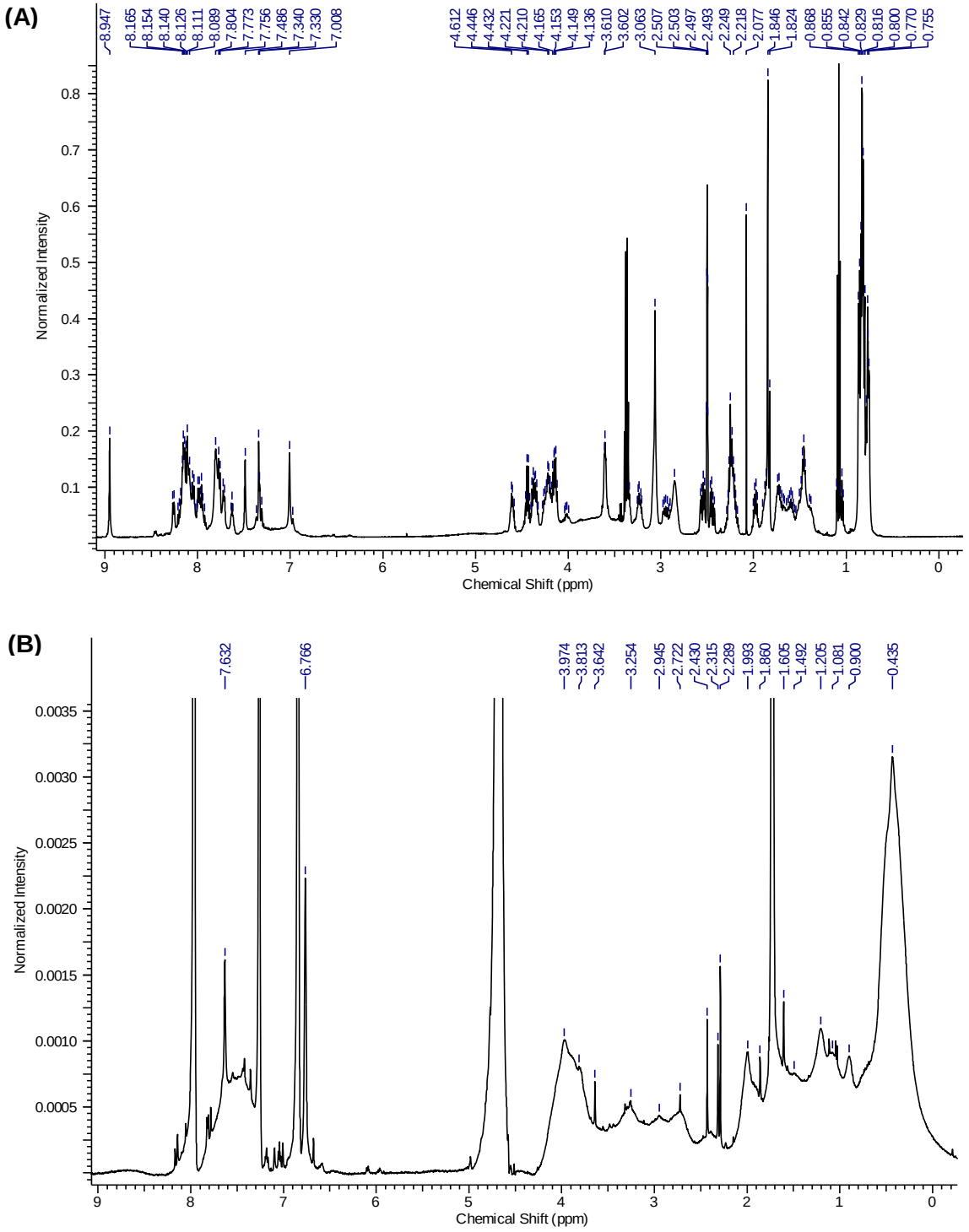

Figure A.50 ^{1}H NMR spectral comparison of: (A) Ac-EEEIRHLSVN-amidoethylamine peptide (**P14**) in DMSO-d_6 and (B) *N*-[Ac-EEEIRHLSVN-amidoethyl]perylene-3,4-imide-9,10-bis(n-butyl) ester (**16**) in 4:1 D_2O/pyridine-d_5.

Appendix - B

MALDI Mass Spectra of Synthesized Perylene Imides

B.1 Primary Ion Spectra with Selected Ion Fragmentation Spectra

B.1 MALDI Mass Spectra

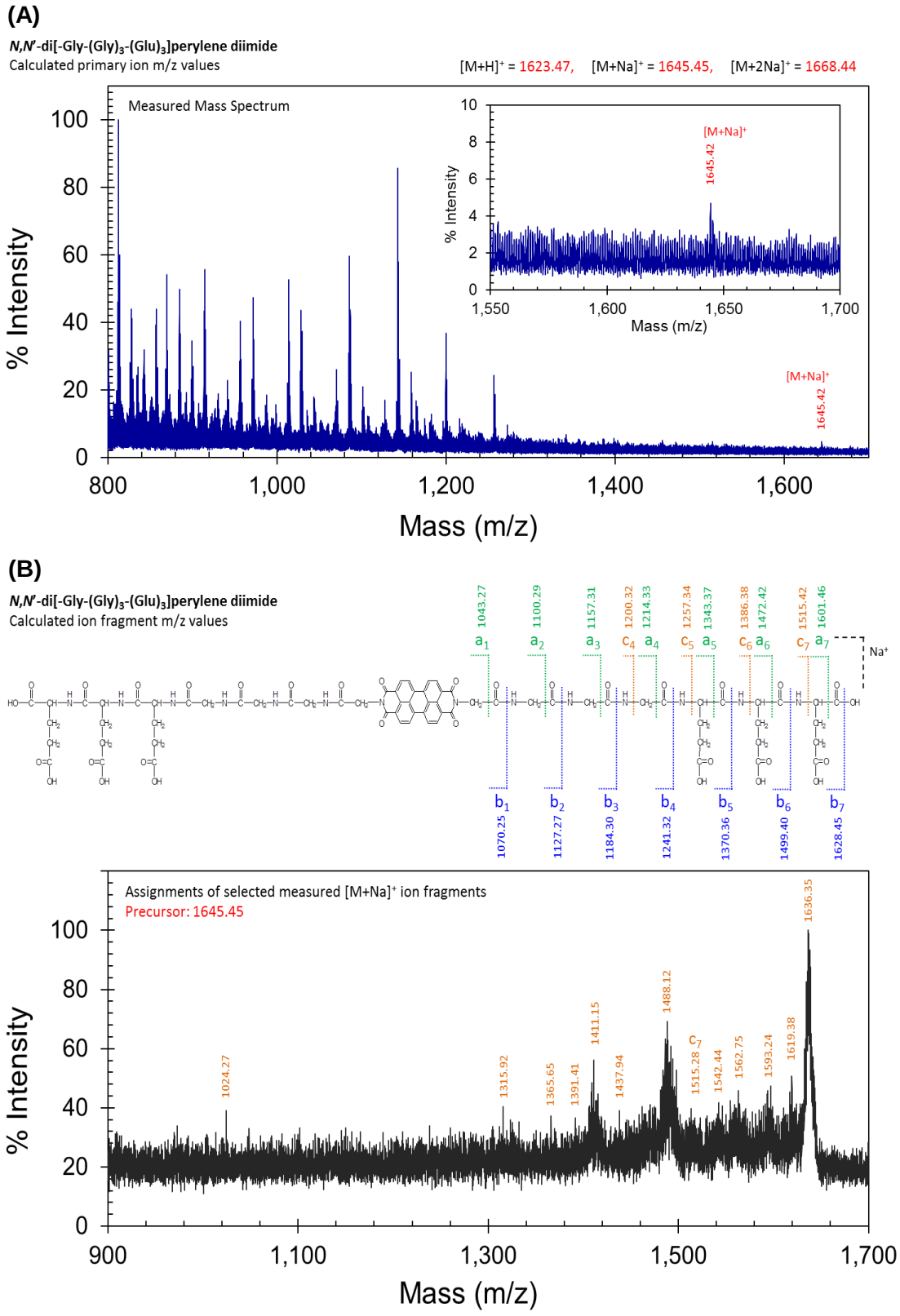

Figure B.1 MALDI mass spectra of PDI **1**: (A) Primary ion spectrum; (B) $[M+Na]^+$ ion fragmentation spectrum.

B.1 MALDI Mass Spectra

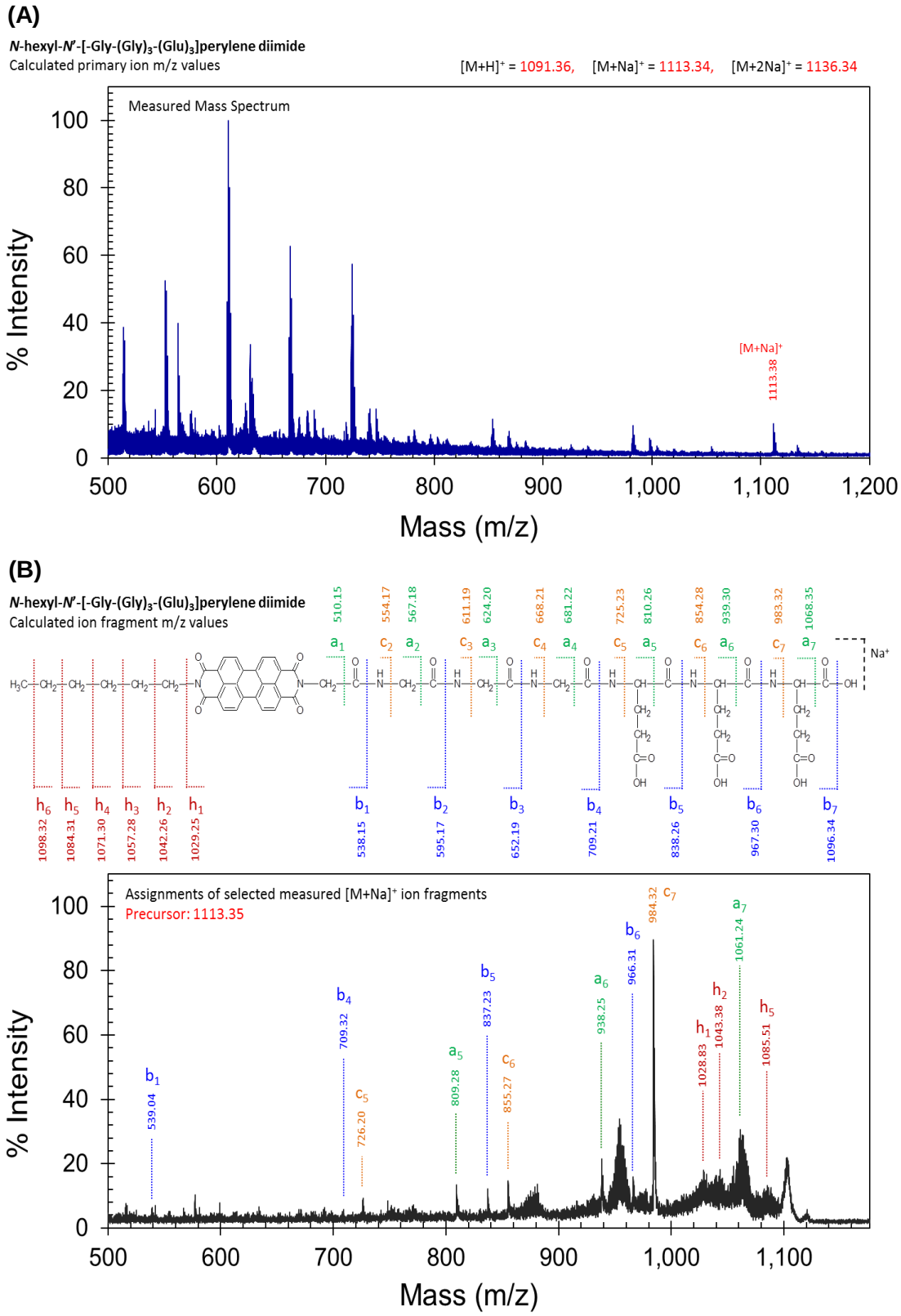

Figure B.2 MALDI mass spectra of PDI **1H**: (A) Primary ion spectrum; (B) $[M+Na]^+$ ion fragmentation spectrum with assigned ion fragments.

B.1 MALDI Mass Spectra

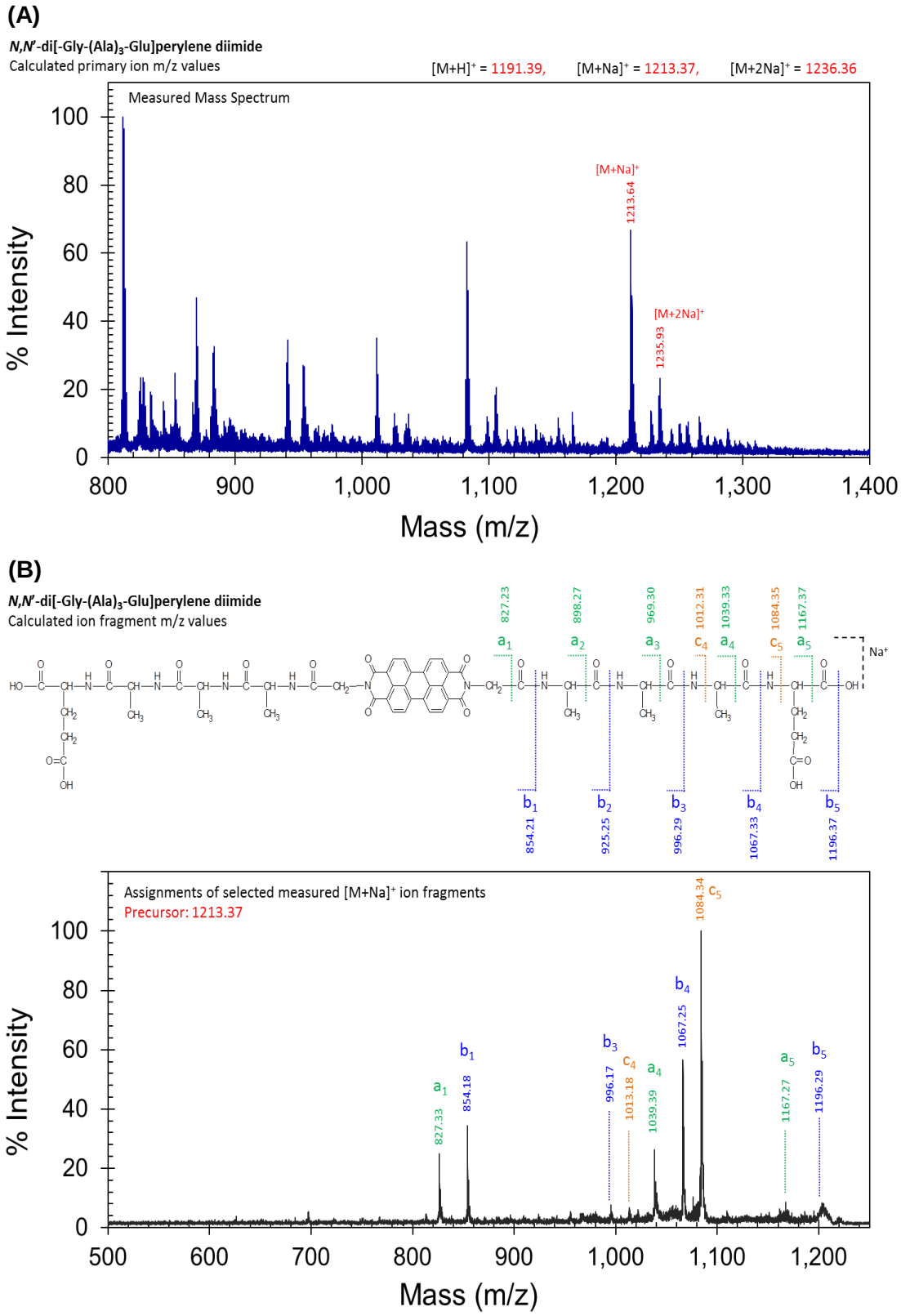

Figure B.3 MALDI mass spectra of PDI **2**: (A) Primary ion spectrum; (B) $[M+Na]^+$ ion fragmentation spectrum with assigned ion fragments.

B.1 MALDI Mass Spectra

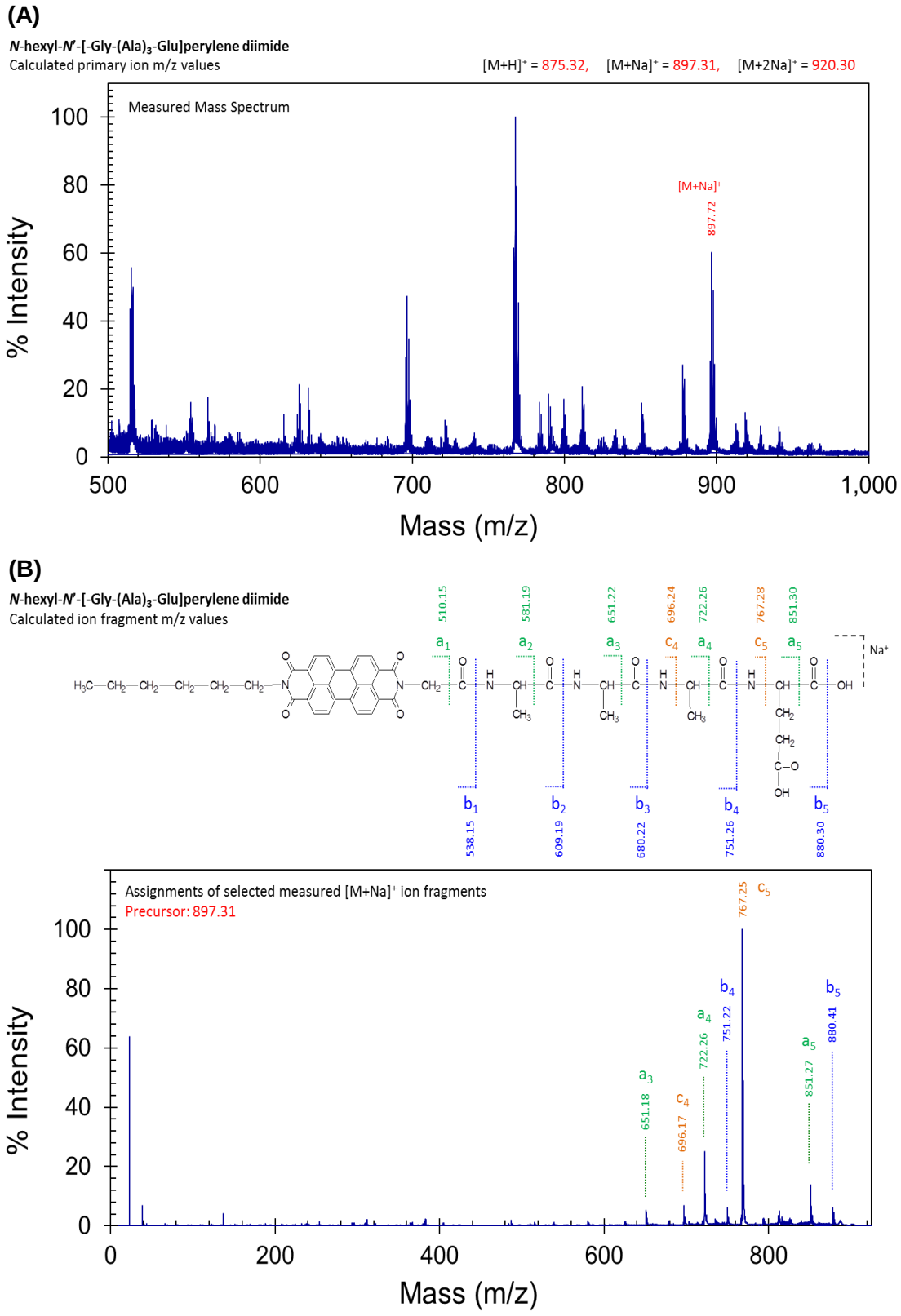

Figure B.4 MALDI mass spectra of PDI **2H**: (A) Primary ion spectrum; (B) $[M+Na]^+$ ion fragmentation spectrum with assigned ion fragments.

B.1 MALDI Mass Spectra

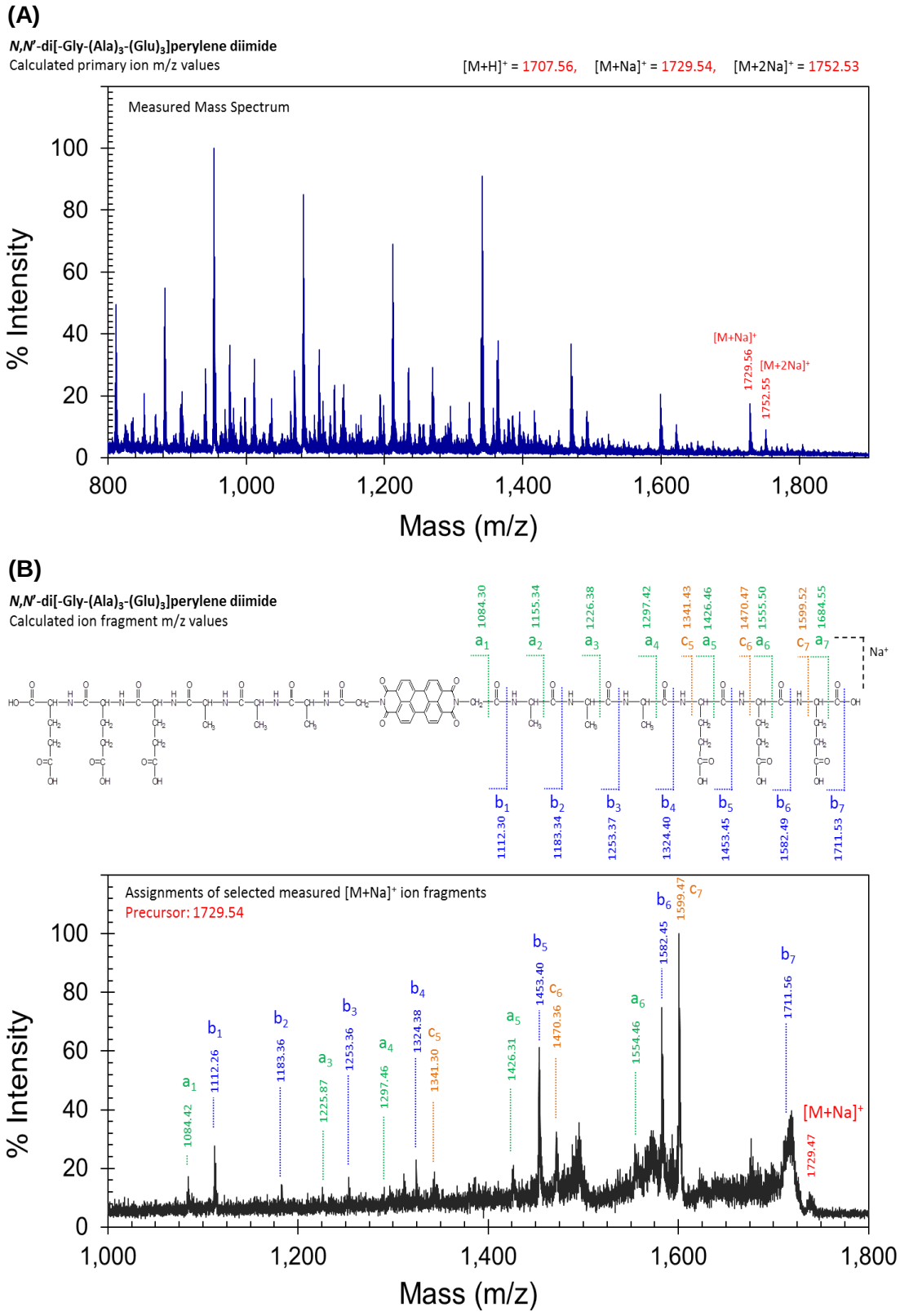

Figure B.5 MALDI mass spectra of PDI **3**: (A) Primary ion spectrum; (B) $[M+Na]^+$ ion fragmentation spectrum with assigned ion fragments.

B.1 MALDI Mass Spectra

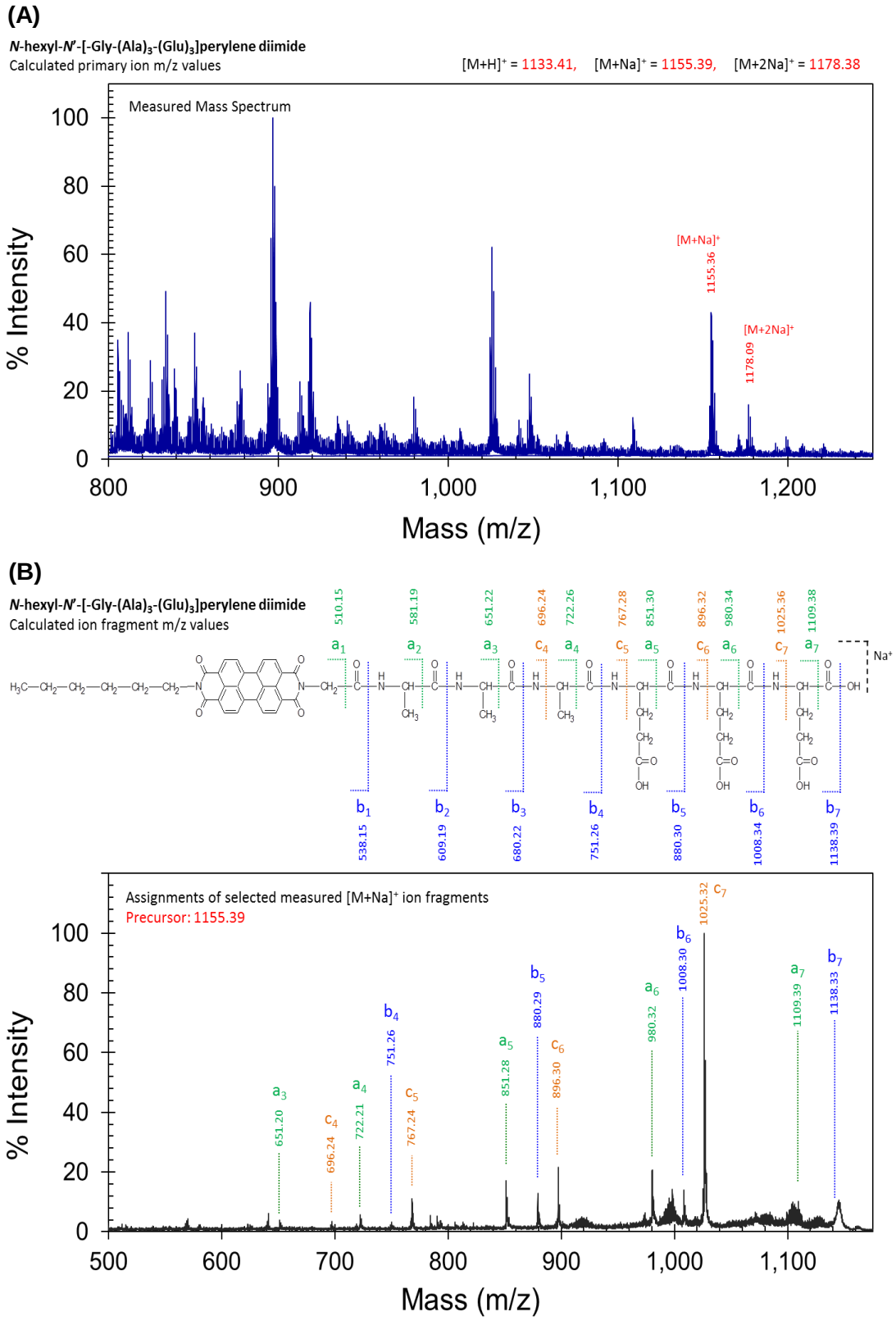

Figure B.6 MALDI mass spectra of PDI **3H**: (A) Primary ion spectrum; (B) $[M+Na]^+$ ion fragmentation spectrum with assigned ion fragments.

B.1 MALDI Mass Spectra

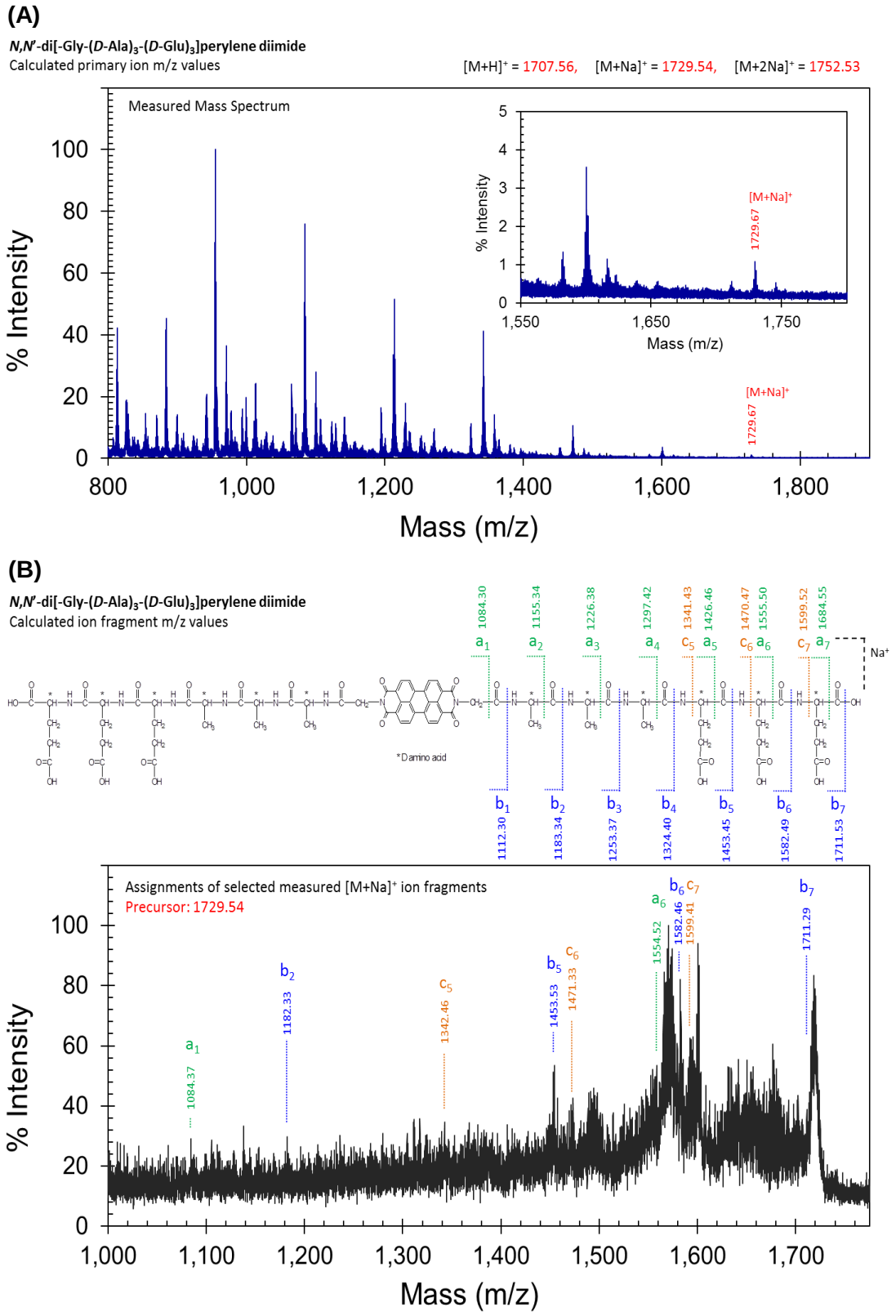

Figure B.7 MALDI mass spectra of PDI **3E**: (A) Primary ion spectrum; (B) $[M+Na]^+$ ion fragmentation spectrum.

B.1 MALDI Mass Spectra

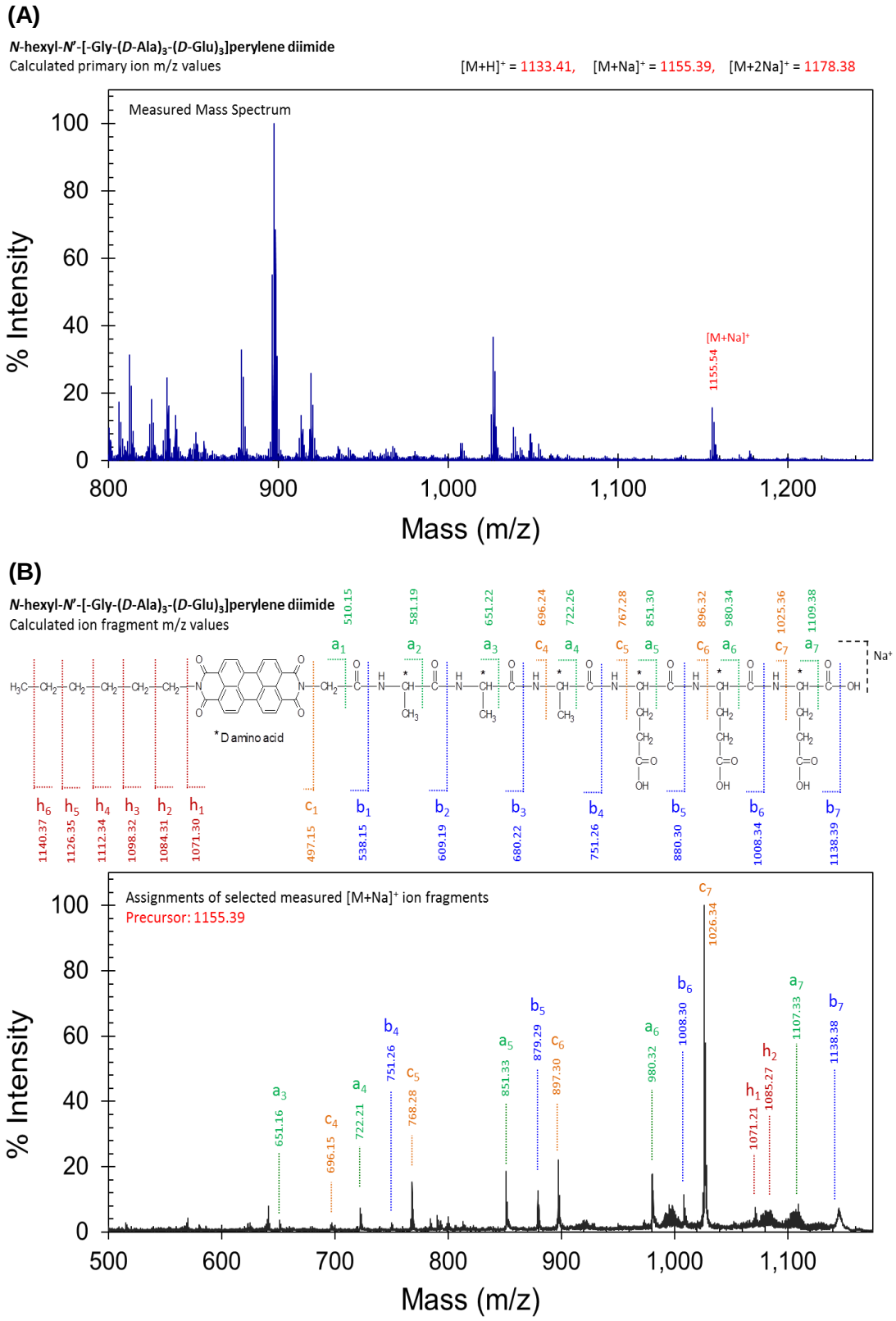

Figure B.8 MALDI mass spectra of PDI **3HE**: (A) Primary ion spectrum; (B) $[M+Na]^+$ ion fragmentation spectrum with assigned ion fragments.

B.1 MALDI Mass Spectra

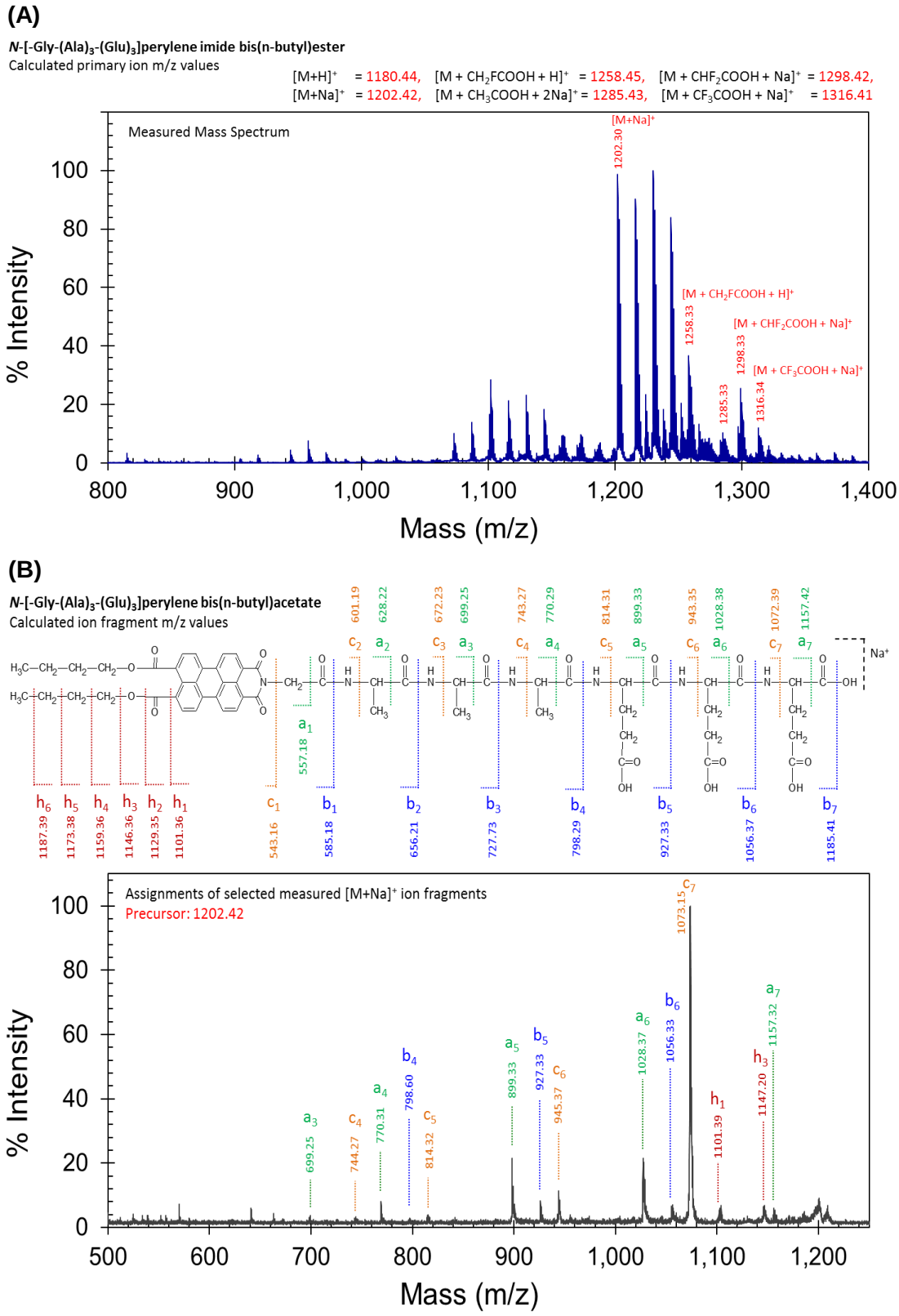

Figure B.9 MALDI mass spectra of perylene imide bisester **Q2**: (A) Primary ion spectrum; (B) $[M+Na]^+$ ion fragmentation spectrum with assigned ion fragments.

B.1 MALDI Mass Spectra

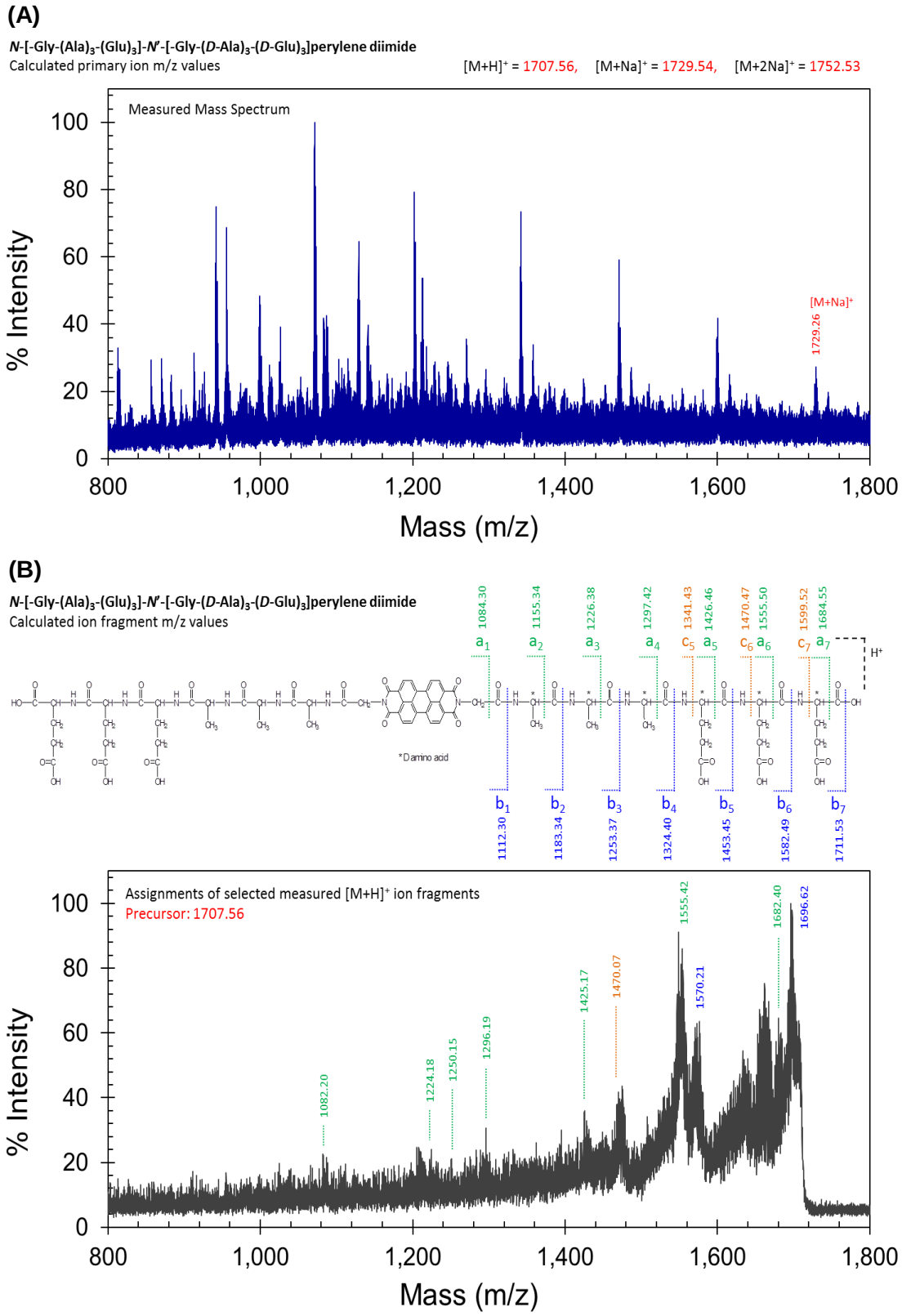

Figure B.10 MALDI mass spectra of PDI **3M**: (A) Primary ion spectrum; (B) $[M+H]^+$ ion fragmentation spectrum.

B.1 MALDI Mass Spectra

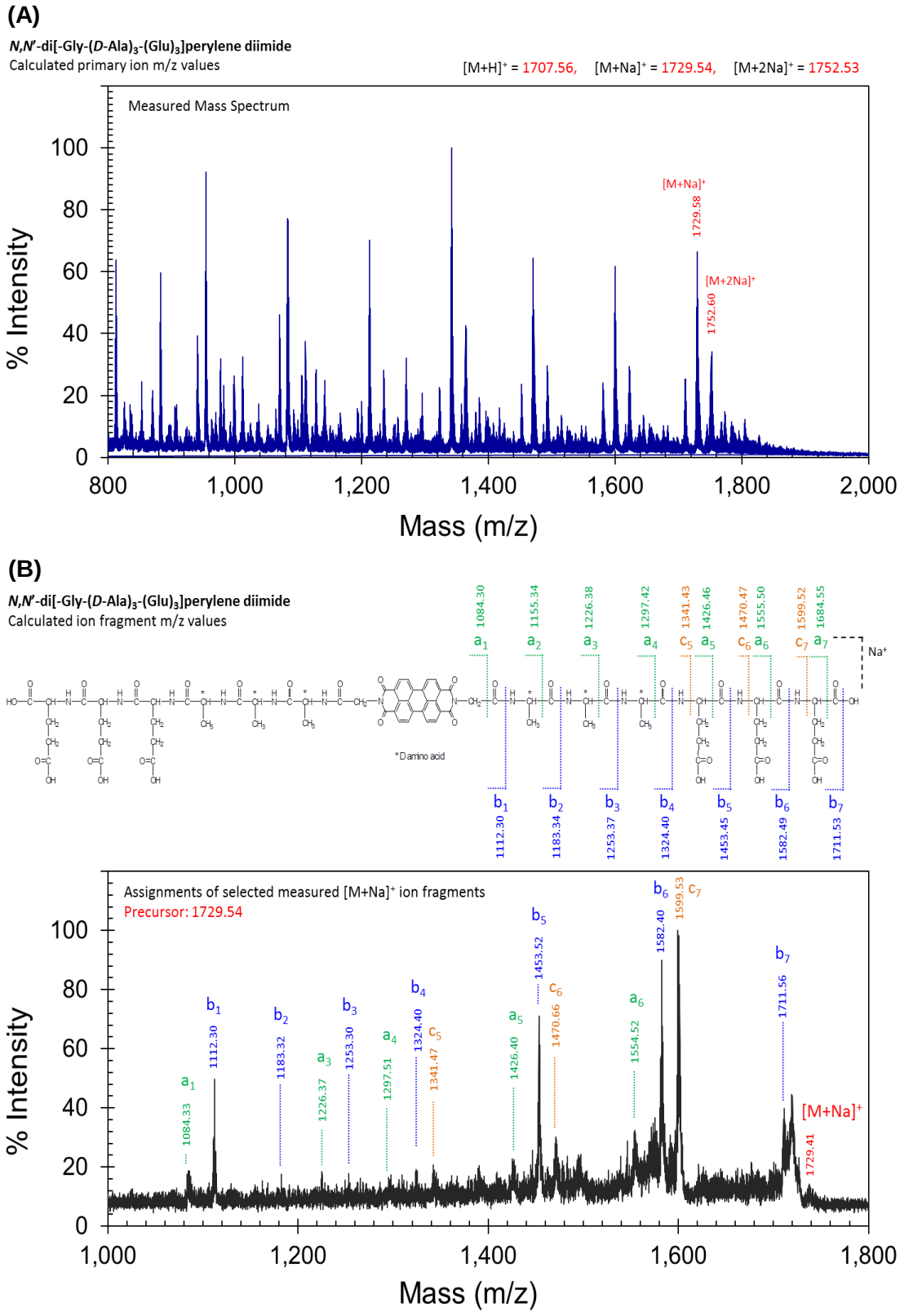

Figure B.11 MALDI mass spectra of PDI **4**: (A) Primary ion spectrum; (B) $[M+Na]^+$ ion fragmentation spectrum with assigned ion fragments.

B.1 MALDI Mass Spectra

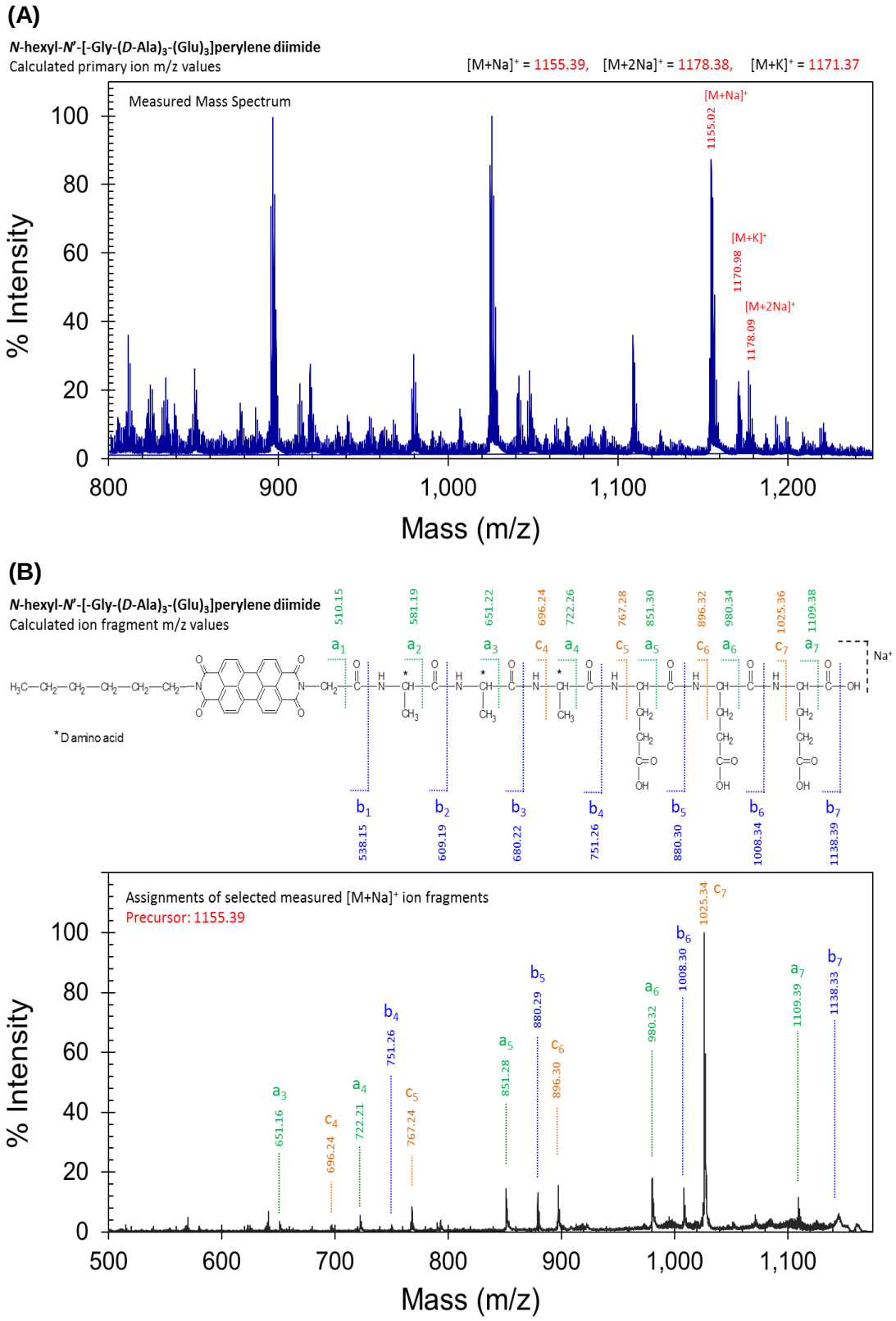

Figure B.12 MALDI mass spectra of PDI **4H**: (A) Primary ion spectrum; (B) $[M+Na]^+$ ion fragmentation spectrum with assigned ion fragments.

B.1 MALDI Mass Spectra

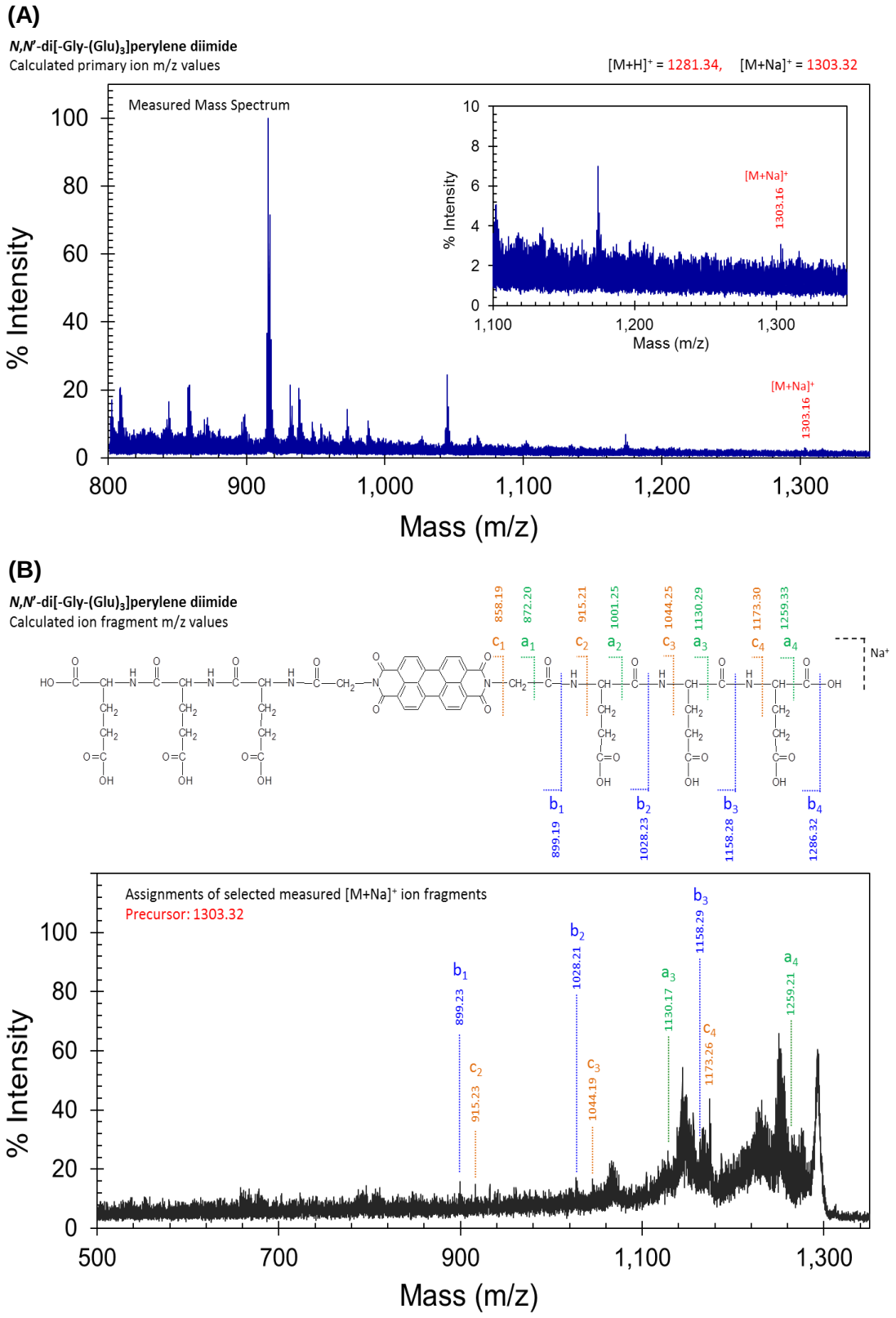

Figure B.13 MALDI mass spectra of PDI **5**: (A) Primary ion spectrum; (B) $[M+Na]^+$ ion fragmentation spectrum with assigned ion fragments.

B.1 MALDI Mass Spectra

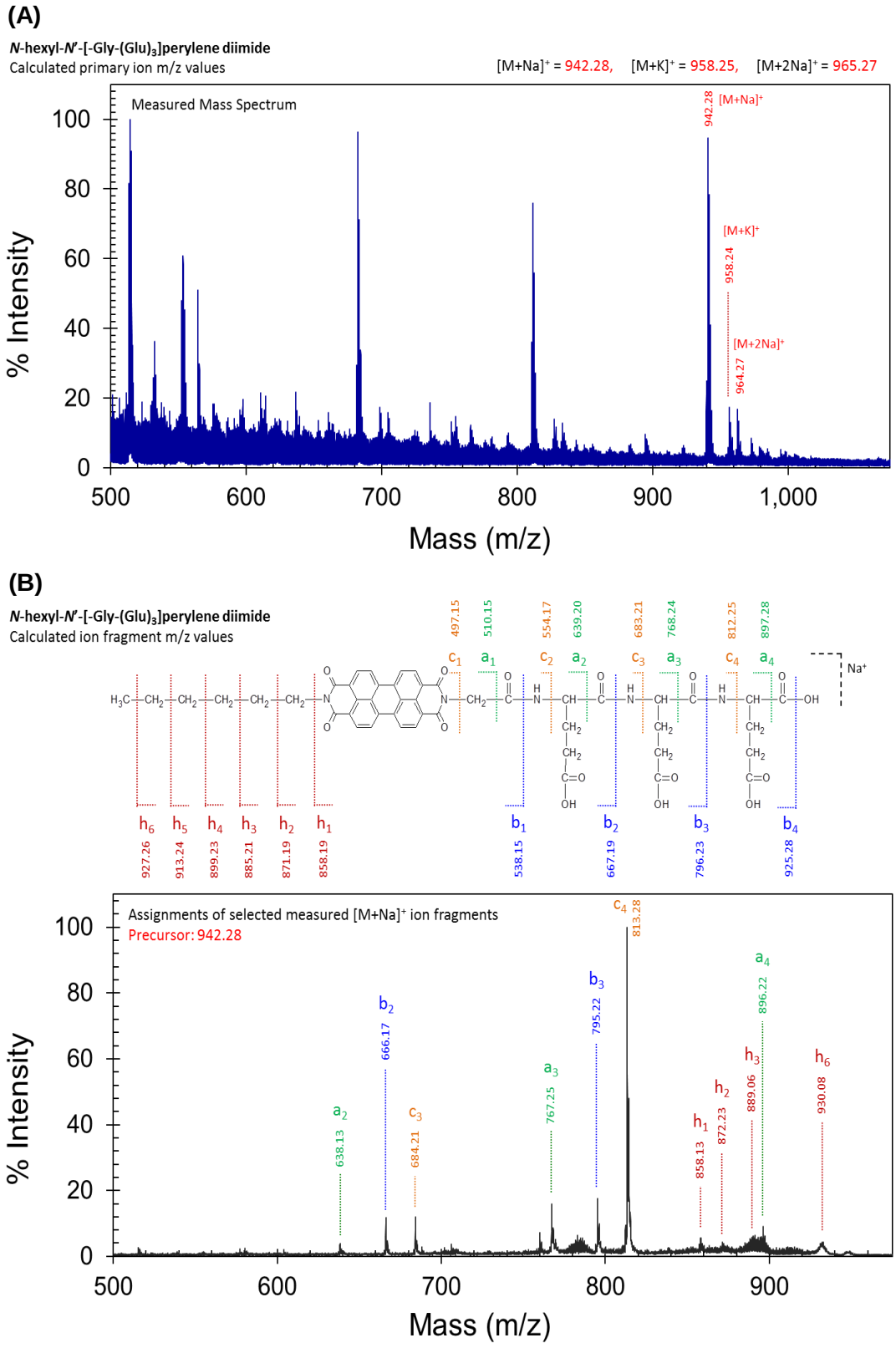

Figure B.14 MALDI mass spectra of PDI **5H**: (A) Primary ion spectrum; (B) $[M+Na]^+$ ion fragmentation spectrum with assigned ion fragments.

B.1 MALDI Mass Spectra

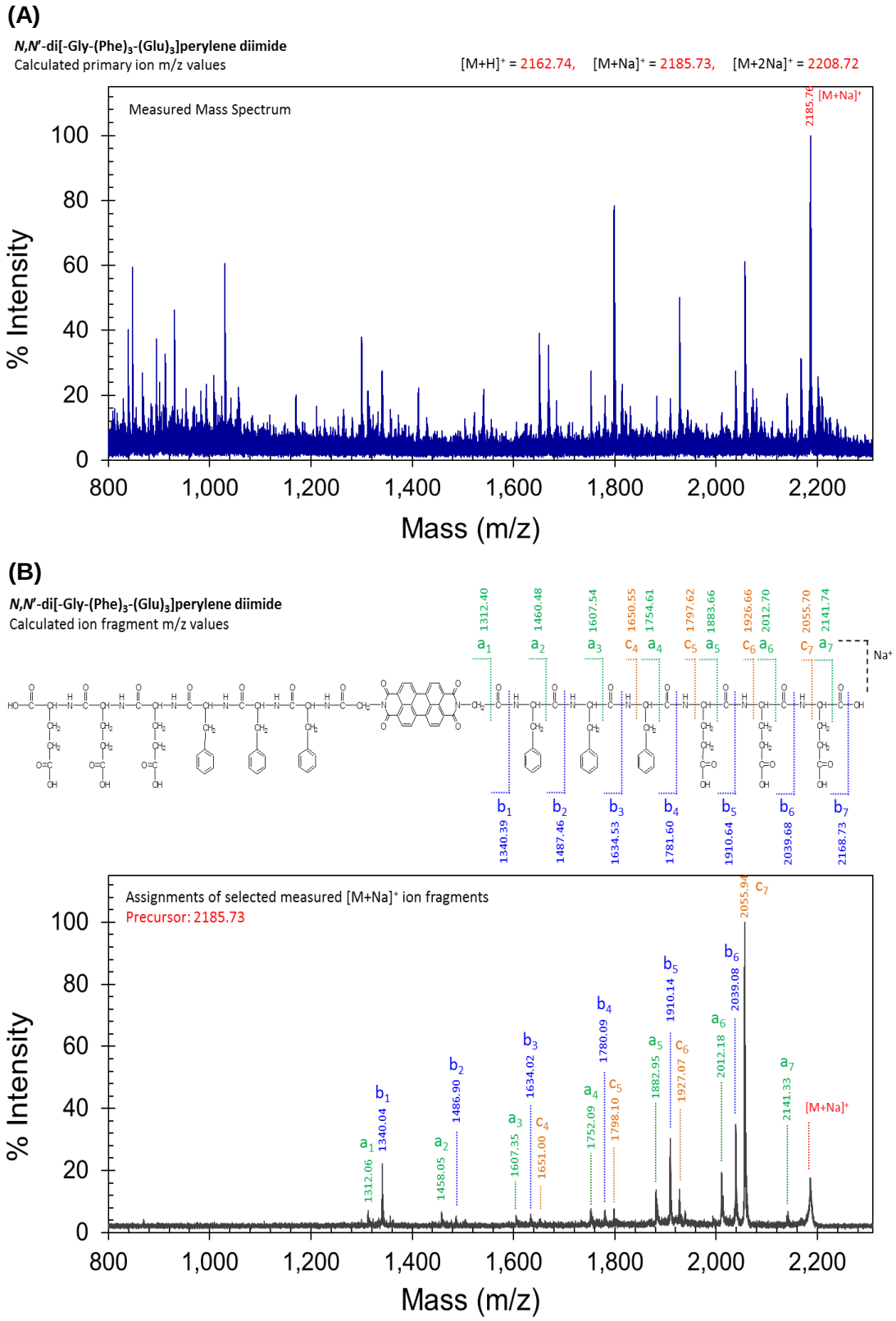

Figure B.15 MALDI mass spectra of PDI **6**: (A) Primary ion spectrum; (B) $[M+Na]^+$ ion fragmentation spectrum with assigned ion fragments.

B.1 MALDI Mass Spectra

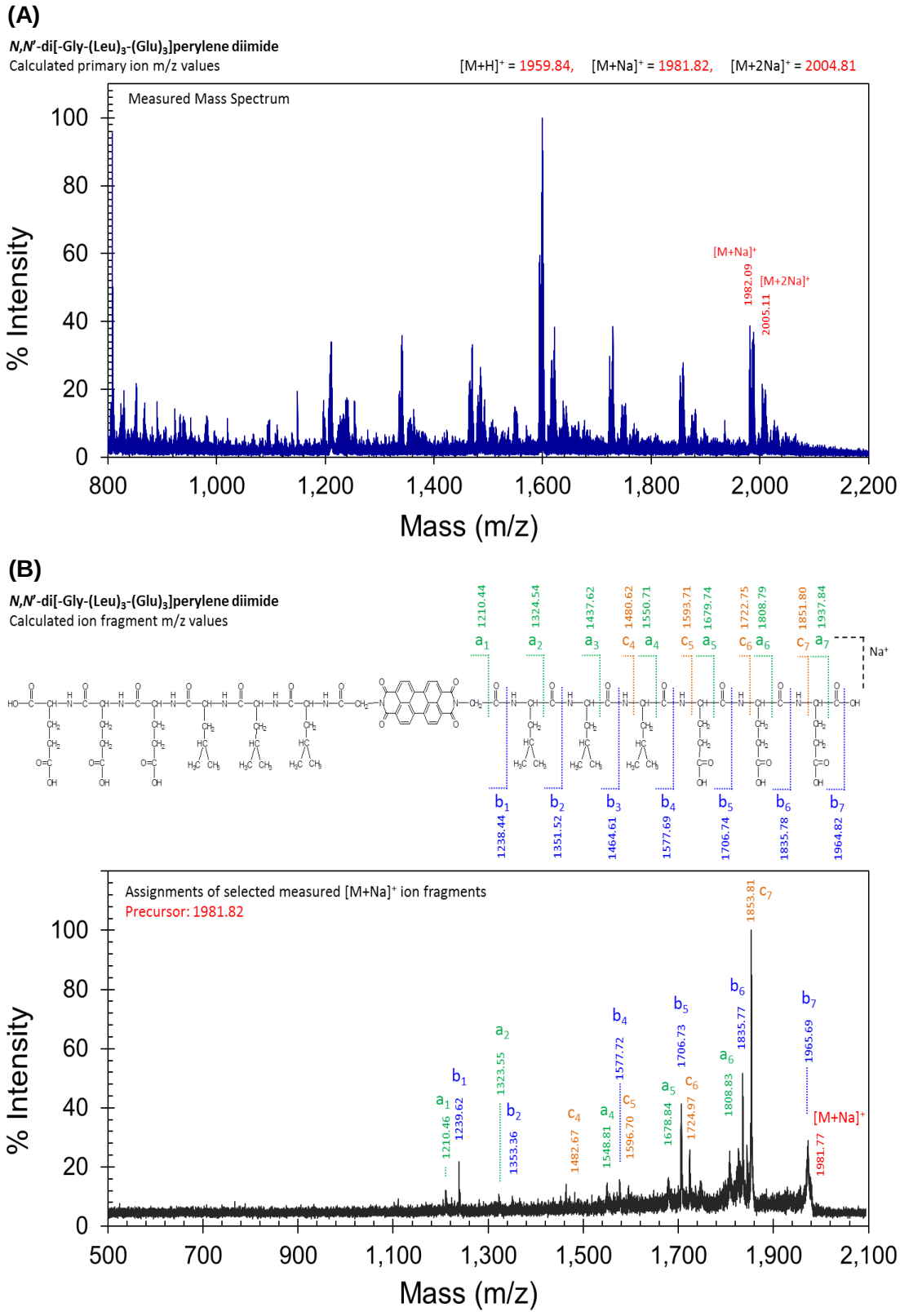

Figure B.16 MALDI mass spectra of PDI **7**: (A) Primary ion spectrum; (B) $[M+Na]^+$ ion fragmentation spectrum with assigned ion fragments.

B.1 MALDI Mass Spectra

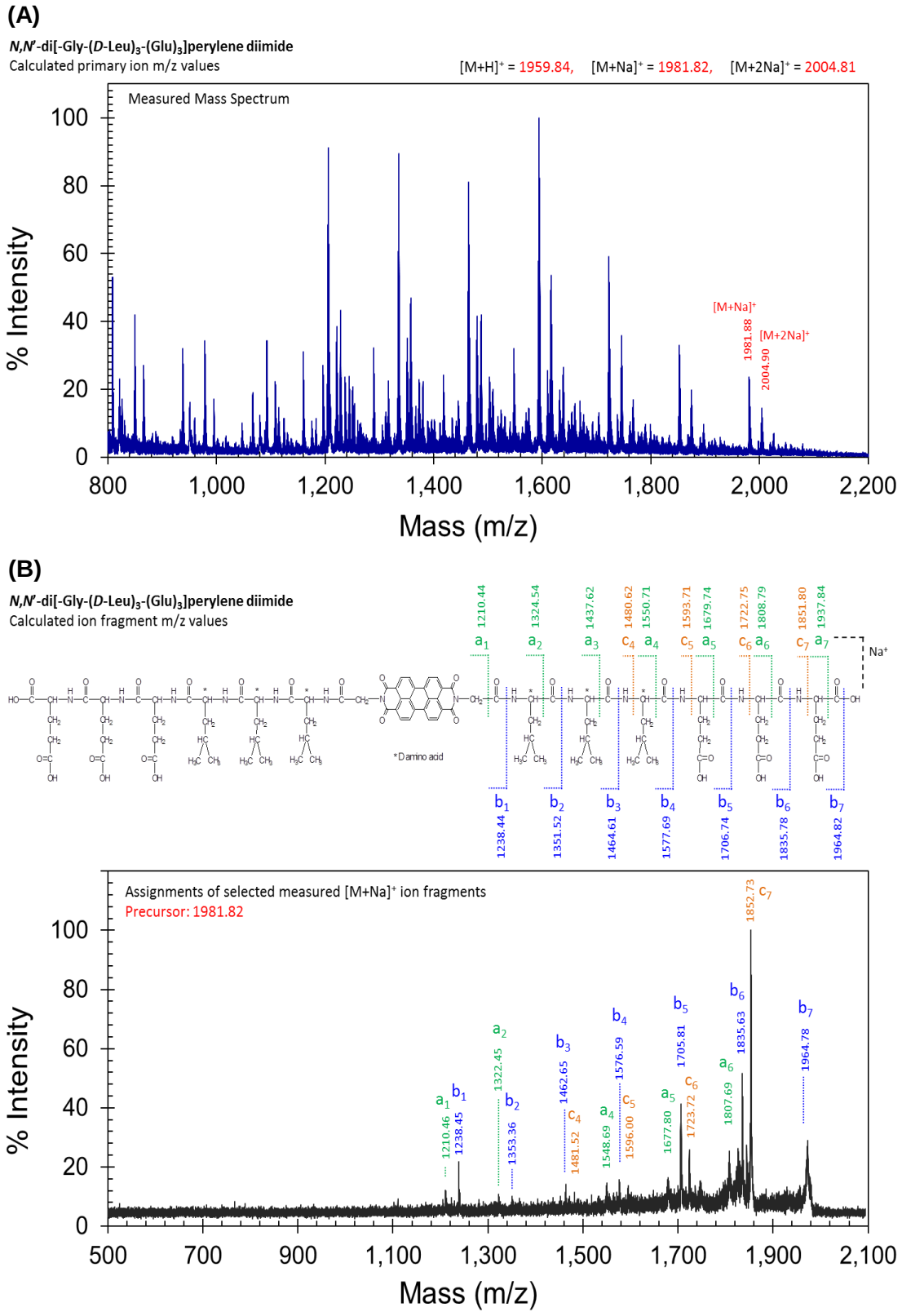

Figure B.17 MALDI mass spectra of PDI **8**: (A) Primary ion spectrum; (B) $[M+Na]^+$ ion fragmentation spectrum with assigned ion fragments.

B.1 MALDI Mass Spectra

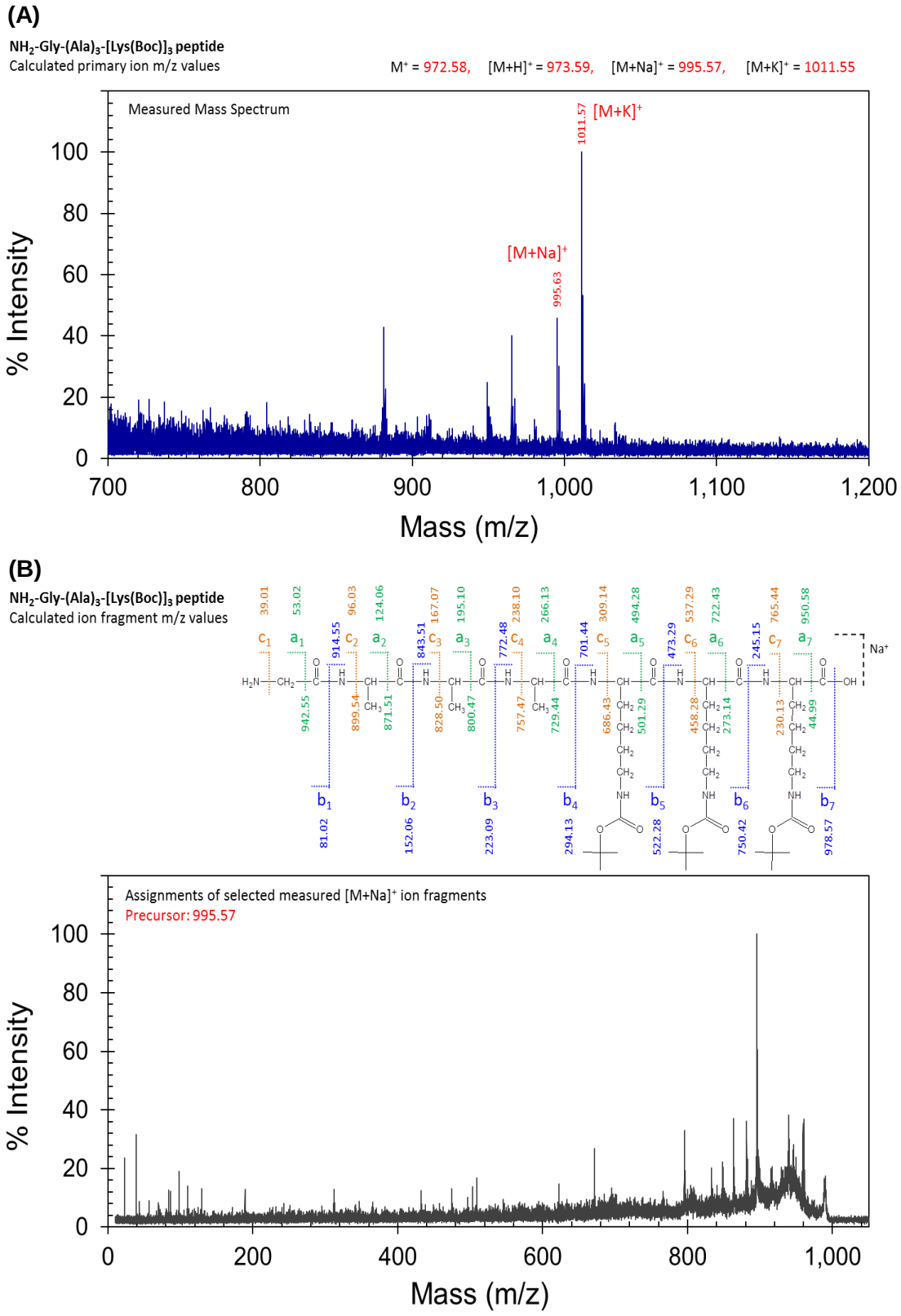

Figure B.18 MALDI mass spectra of NH_2-Gly-$(Ala)_3$-$[Lys(Boc)]_3$ peptide **P9**: (A) Primary ion spectrum; (B) $[M+Na]^+$ ion fragmentation spectrum.

B.1 MALDI Mass Spectra

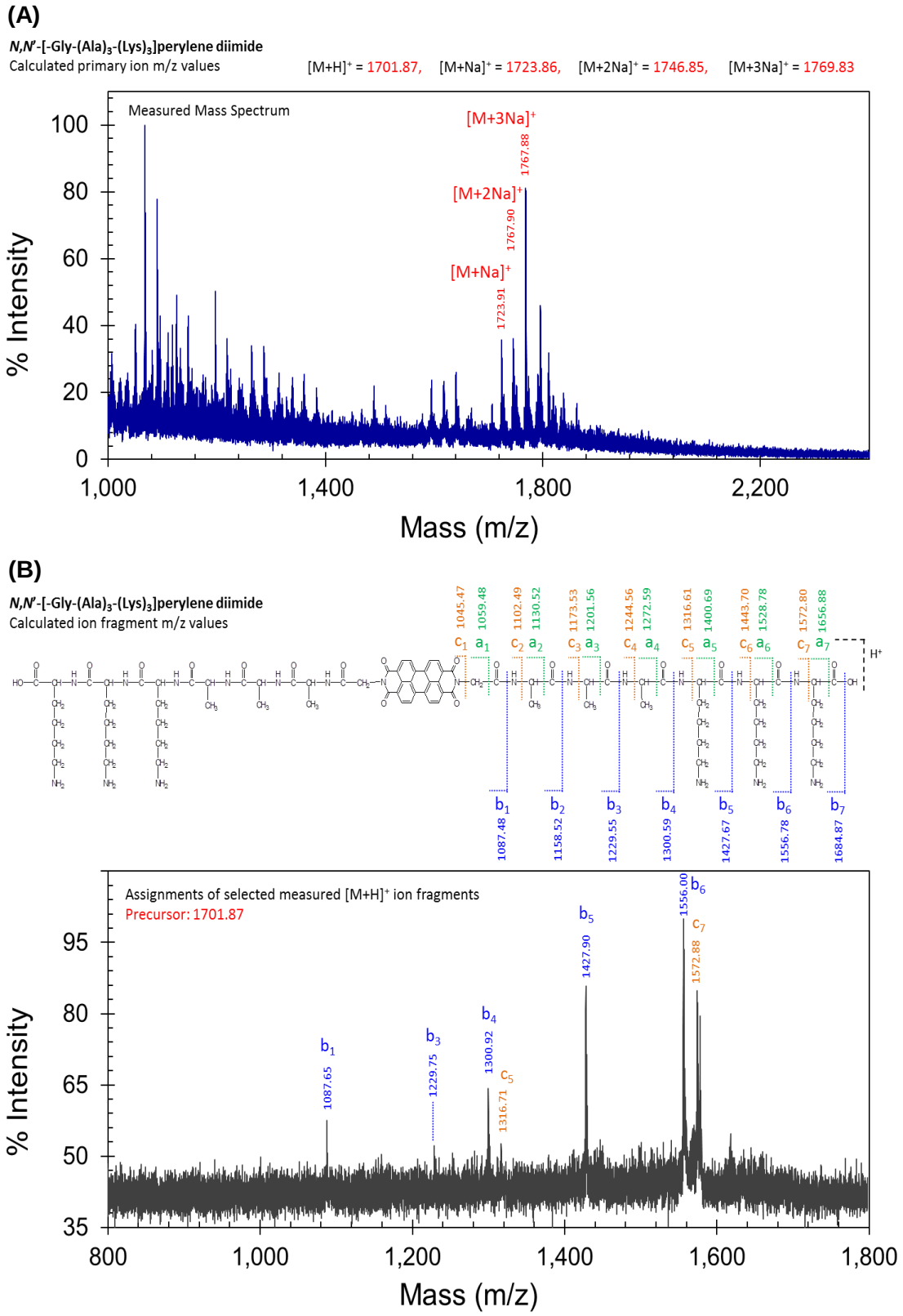

Figure B.19 MALDI mass spectra of PDI **9**: (A) Primary ion spectrum; (B) $[M+H]^+$ ion fragmentation spectrum with assigned ion fragments.

B.1 MALDI Mass Spectra

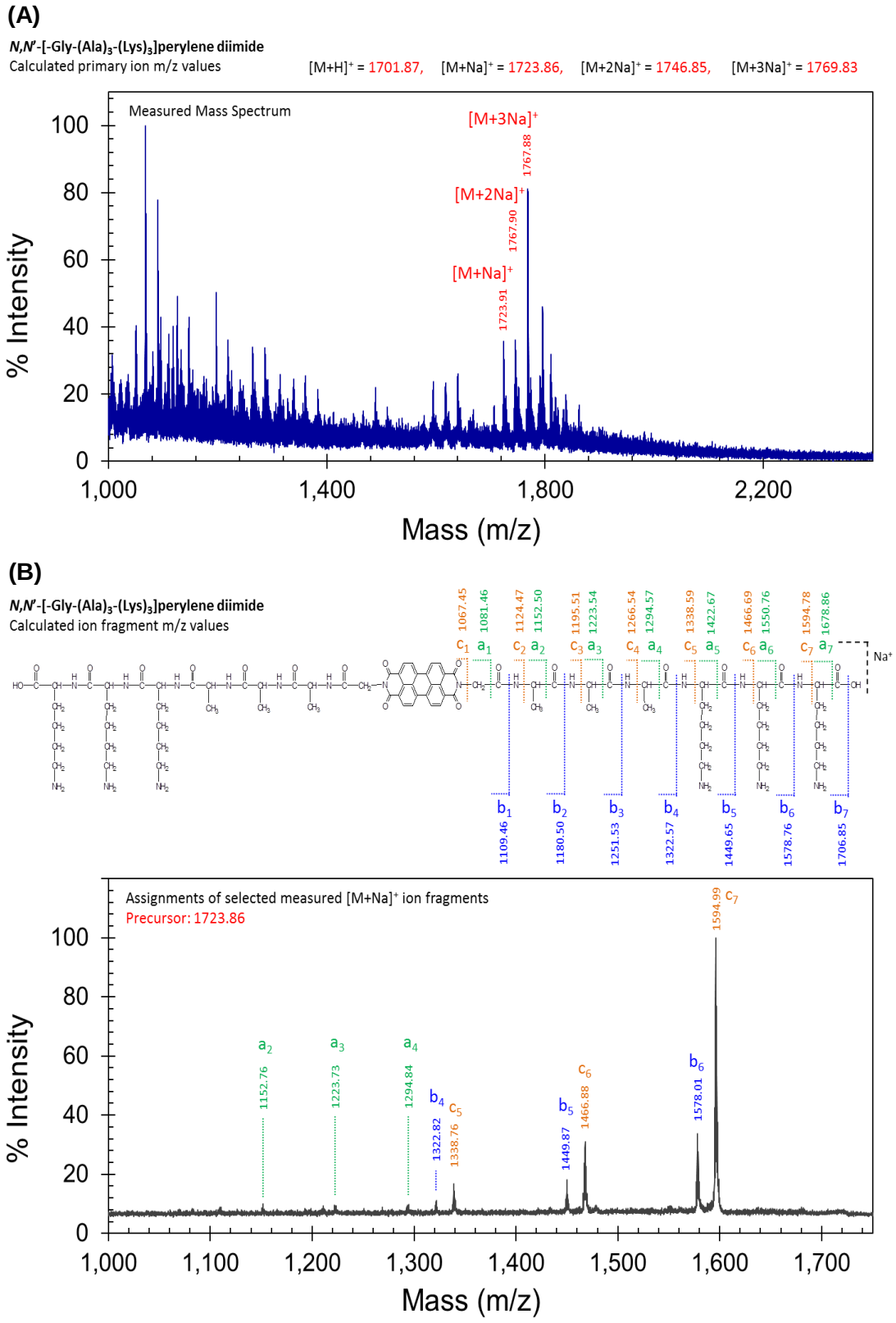

Figure B.20 MALDI mass spectra of PDI **9**: (A) Primary ion spectrum; (B) $[M+Na]^+$ ion fragmentation spectrum with assigned ion fragments.

B.1 MALDI Mass Spectra

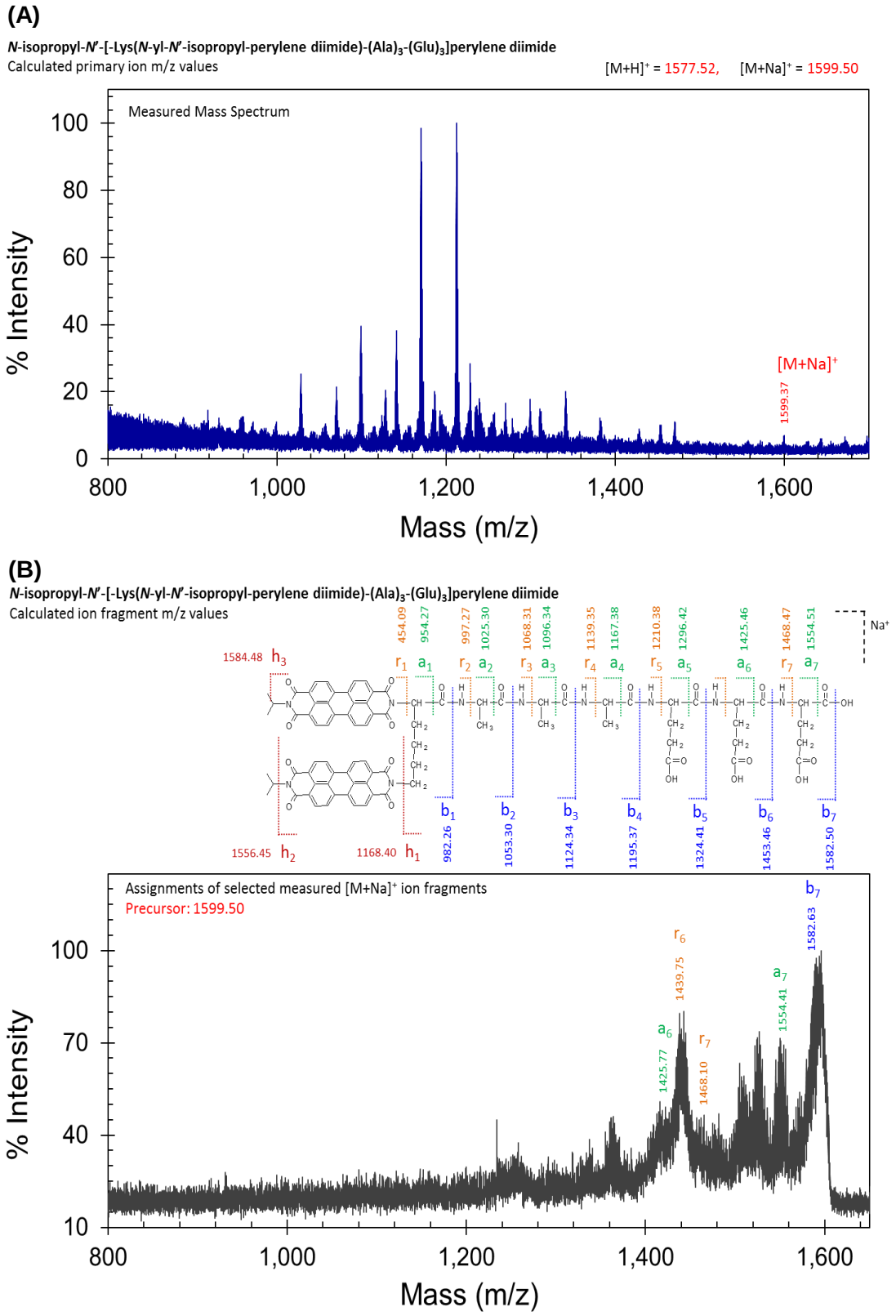

Figure B.21 MALDI mass spectra of compound **10**: (A) Primary ion spectrum; (B) $[M+Na]^+$ ion fragmentation spectrum.

B.1 MALDI Mass Spectra

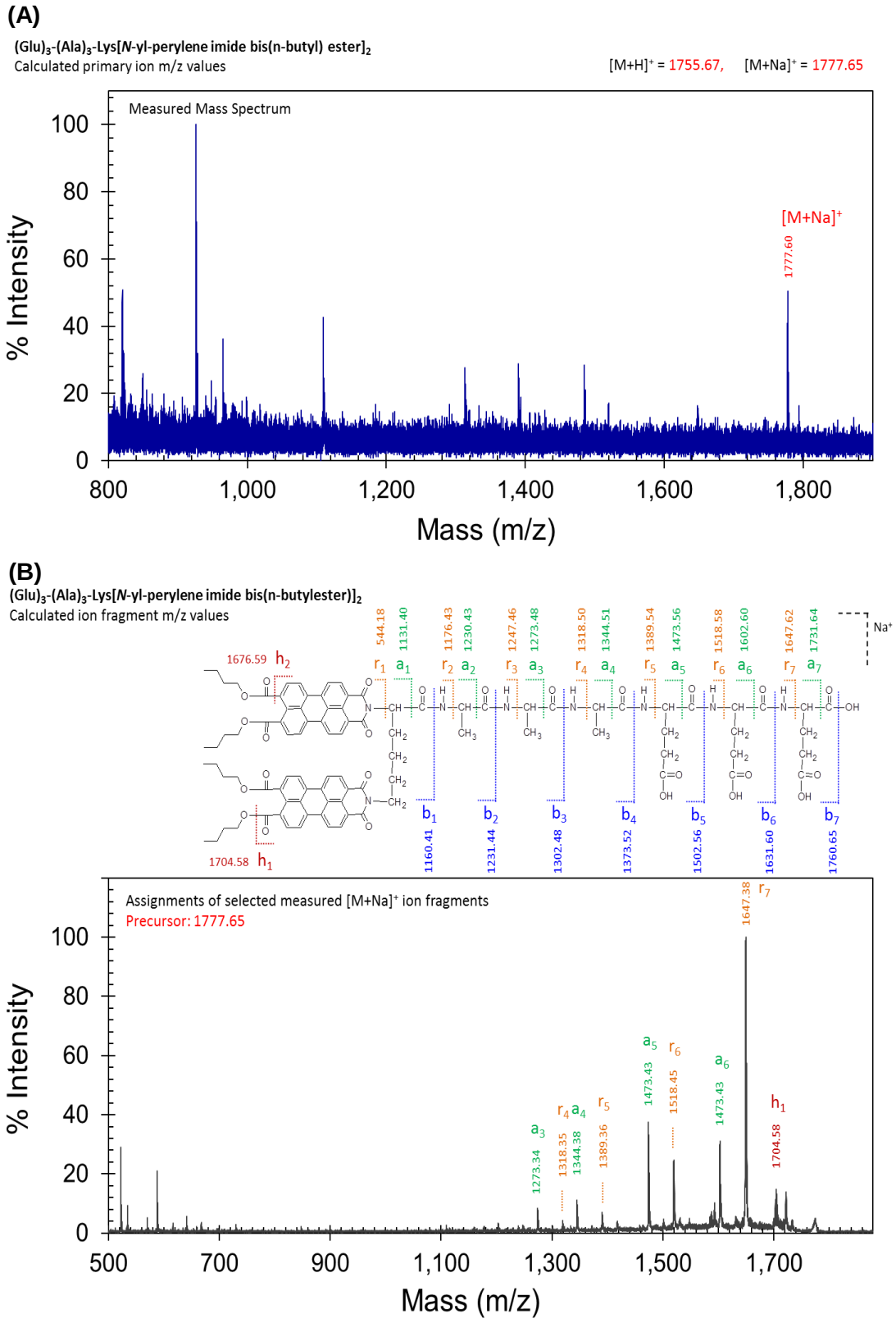

Figure B.22 MALDI mass spectra of compound **11**: (A) Primary ion spectrum; (B) $[M+Na]^+$ ion fragmentation spectrum with assigned ion fragments.

B.1 MALDI Mass Spectra

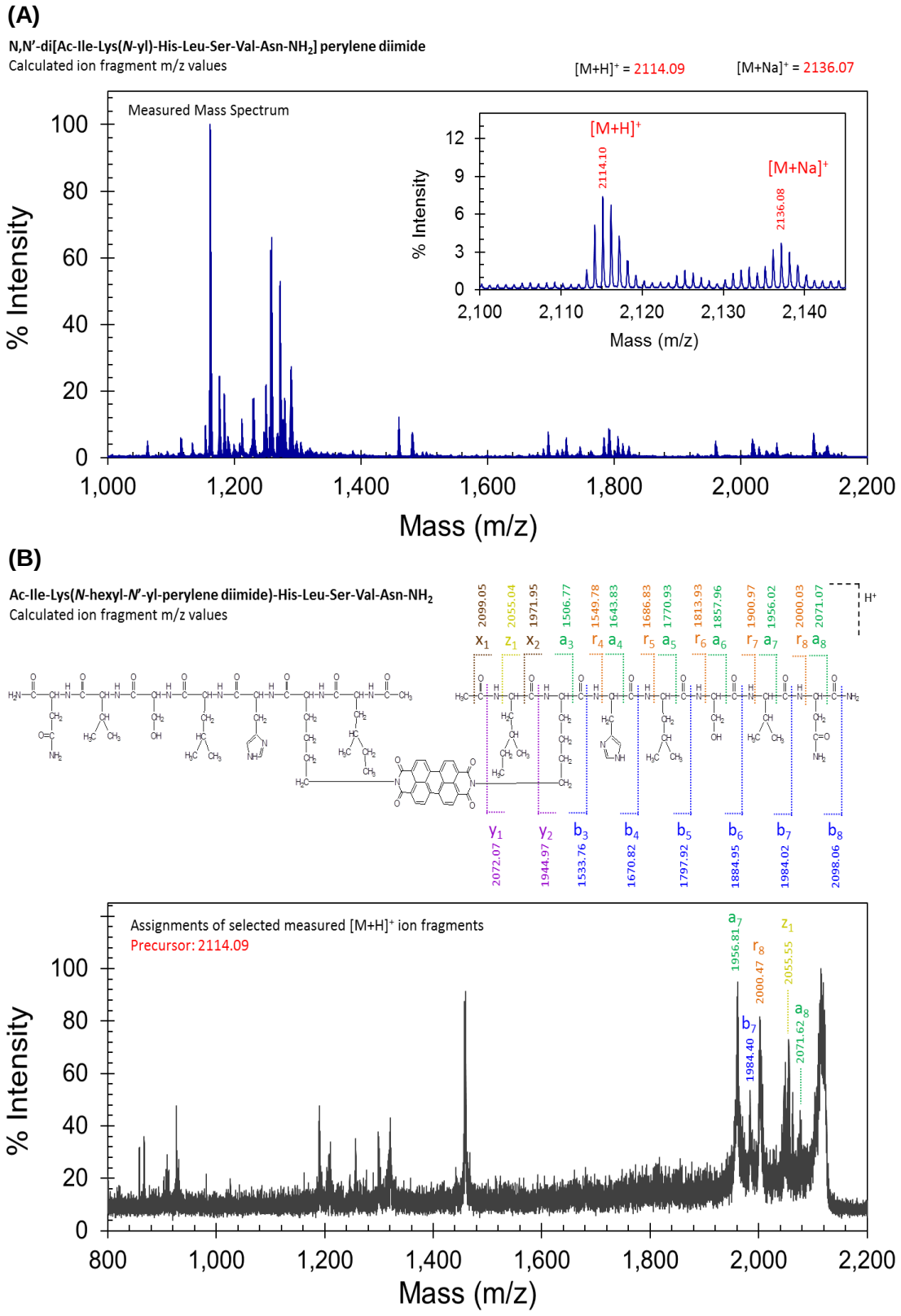

Figure B.23 MALDI mass spectra of PDI **12**: (A) Primary ion spectrum; (B) $[M+H]^+$ ion fragmentation spectrum.

B.1 MALDI Mass Spectra

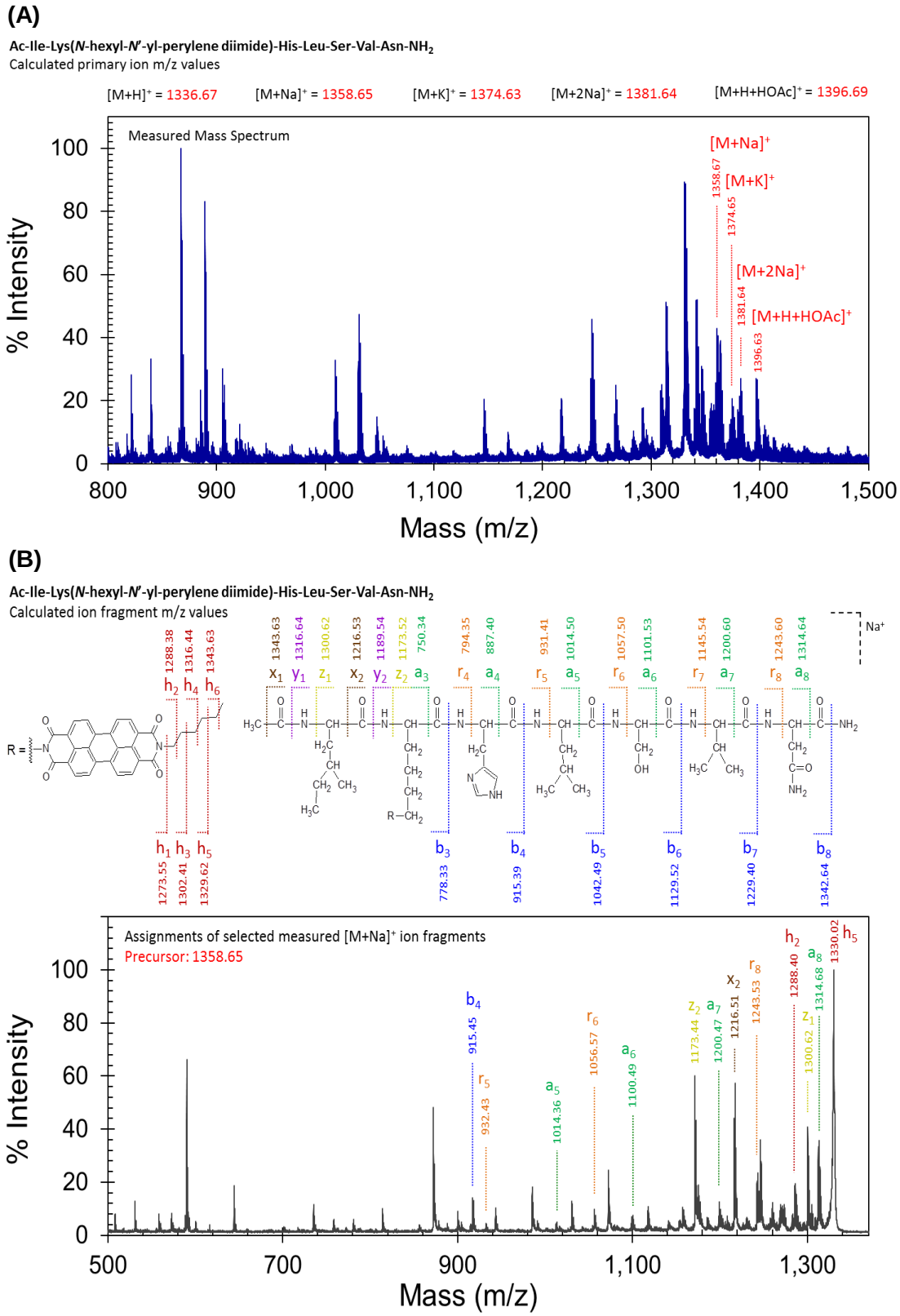

Figure B.24 MALDI mass spectra of PDI **12H**: (A) Primary ion spectrum; (B) $[M+Na]^+$ ion fragmentation spectrum with assigned ion fragments.

B.1 MALDI Mass Spectra

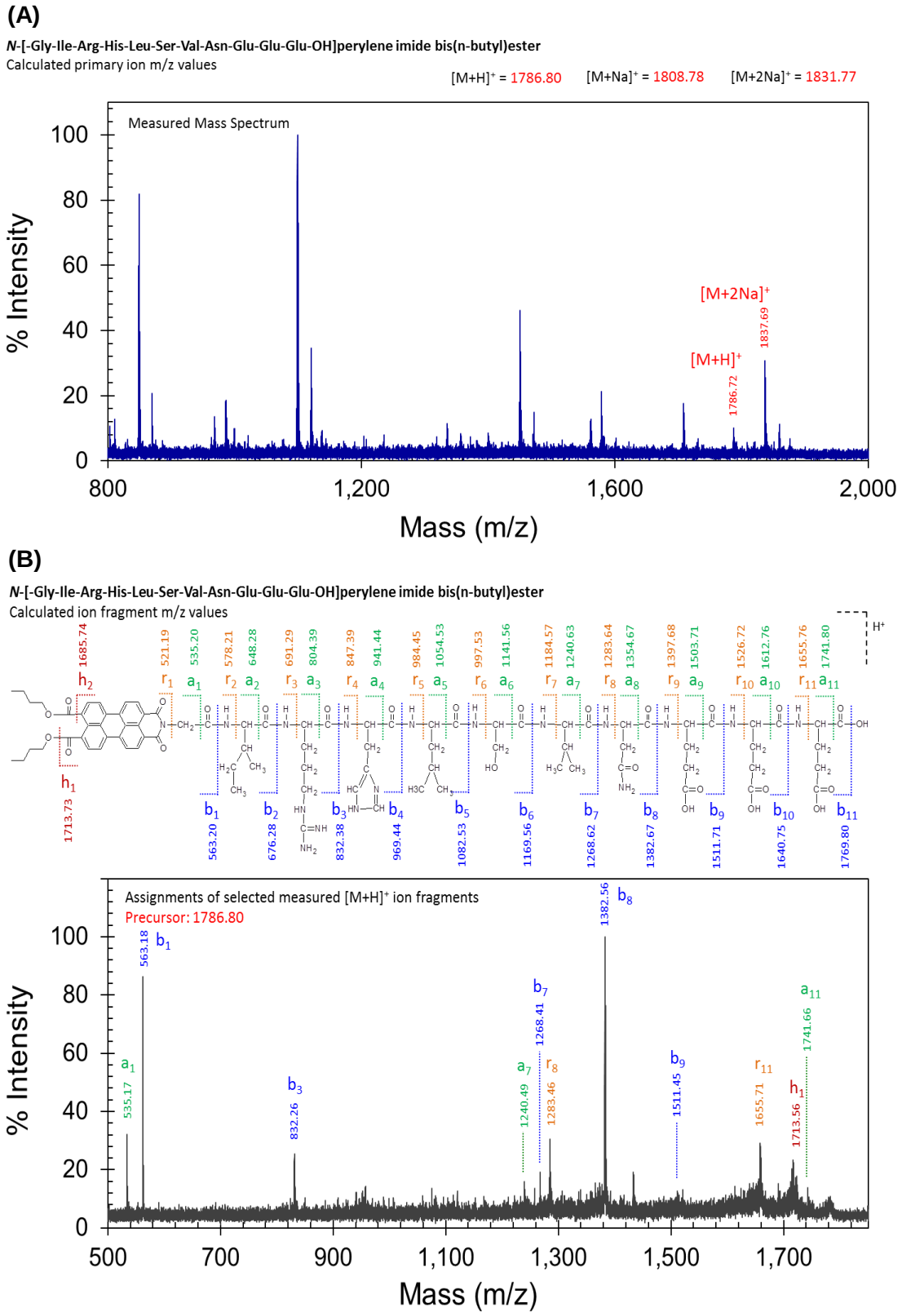

Figure B.25 MALDI mass spectra of compound **15**: (A) Primary ion spectrum; (B) $[M+H]^+$ ion fragmentation spectrum with assigned ion fragments.

B.1 MALDI Mass Spectra

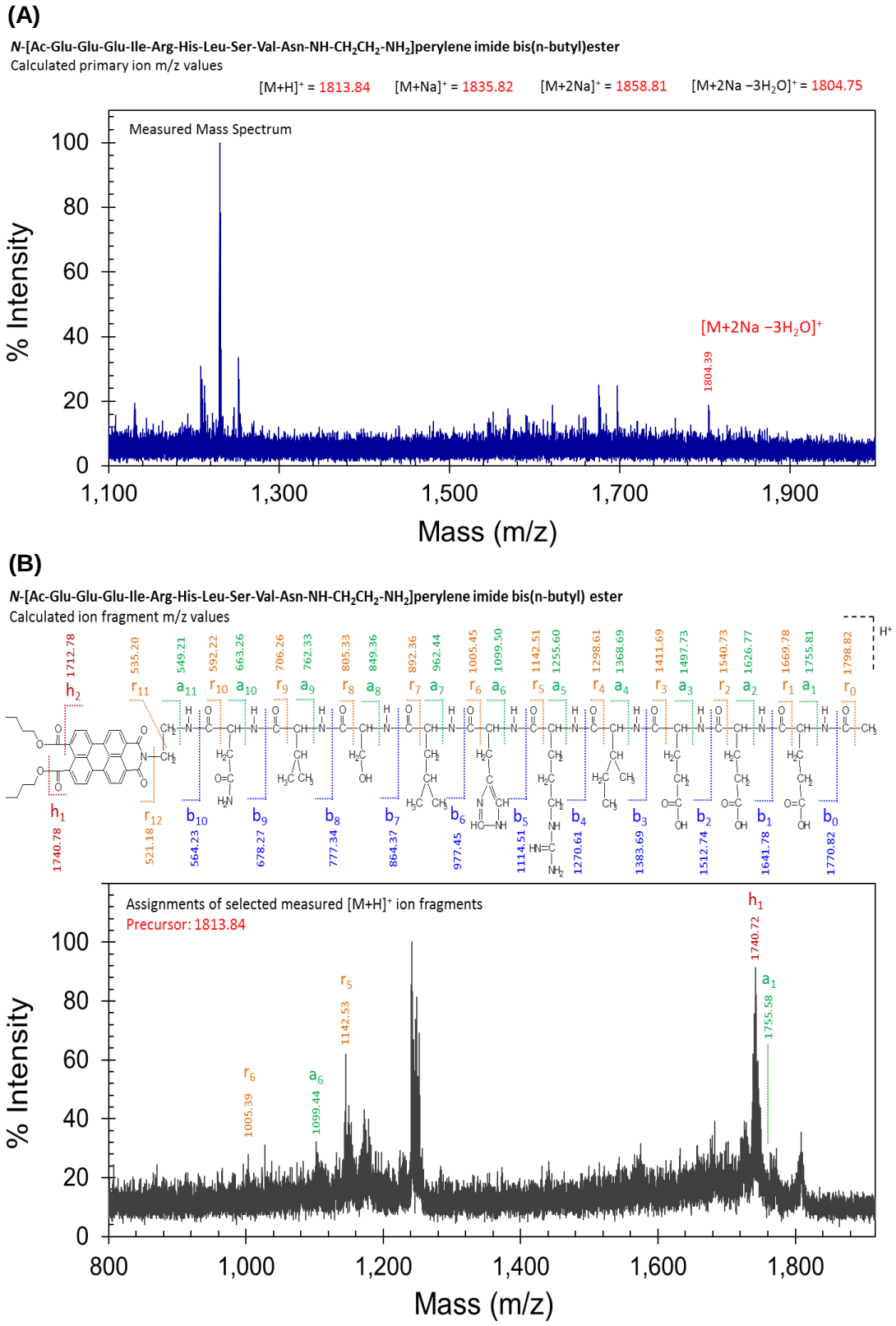

Figure B.26 MALDI mass spectra of compound **16**: (A) Primary ion spectrum; (B) $[M+H]^+$ ion fragmentation spectrum.

B.1 MALDI Mass Spectra

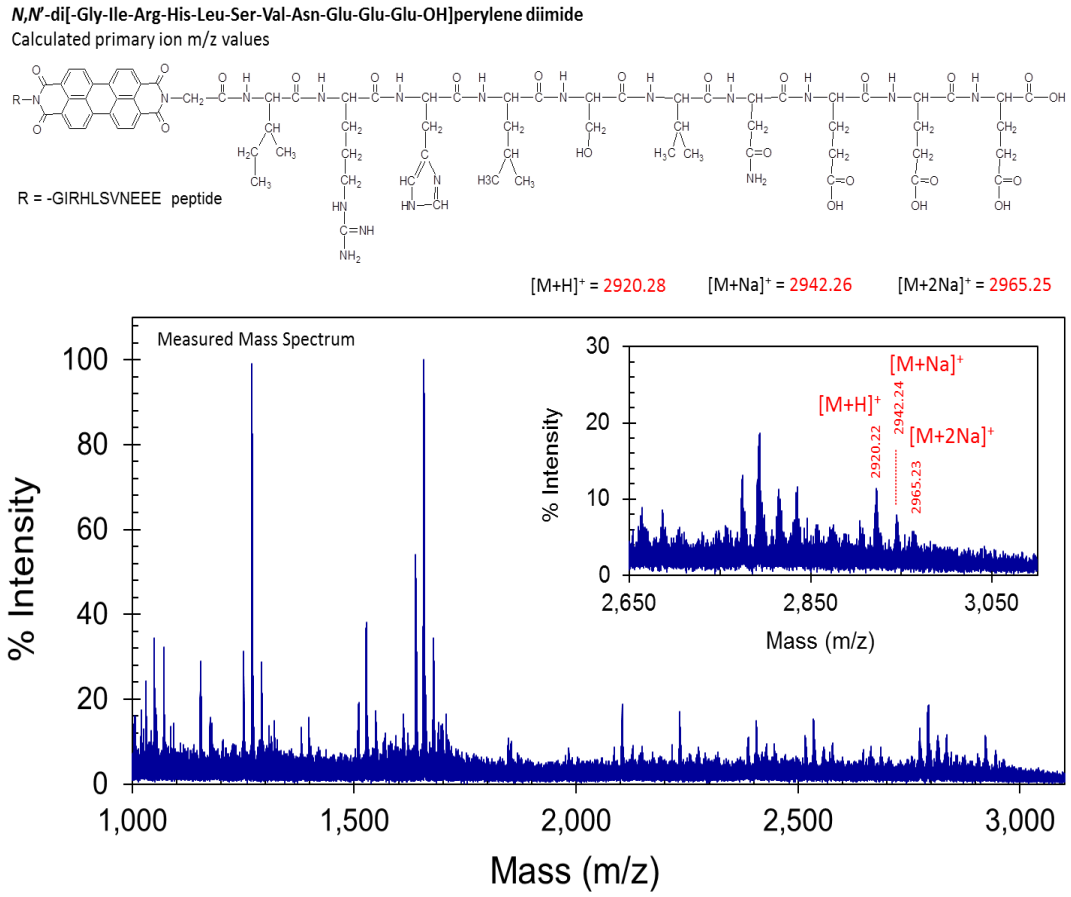

Figure B.27 Primary ion MALDI mass spectrum of compound **13**.

Appendix - C

FT-IR Spectra of Synthesized Perylene Imides

C.1 FT-IR Spectra with Fingerprint Region Spectral Comparisons

C.2 Amide I and II Band Analysis

C.1 FT-IR Spectra of Synthesized Perylene Imides

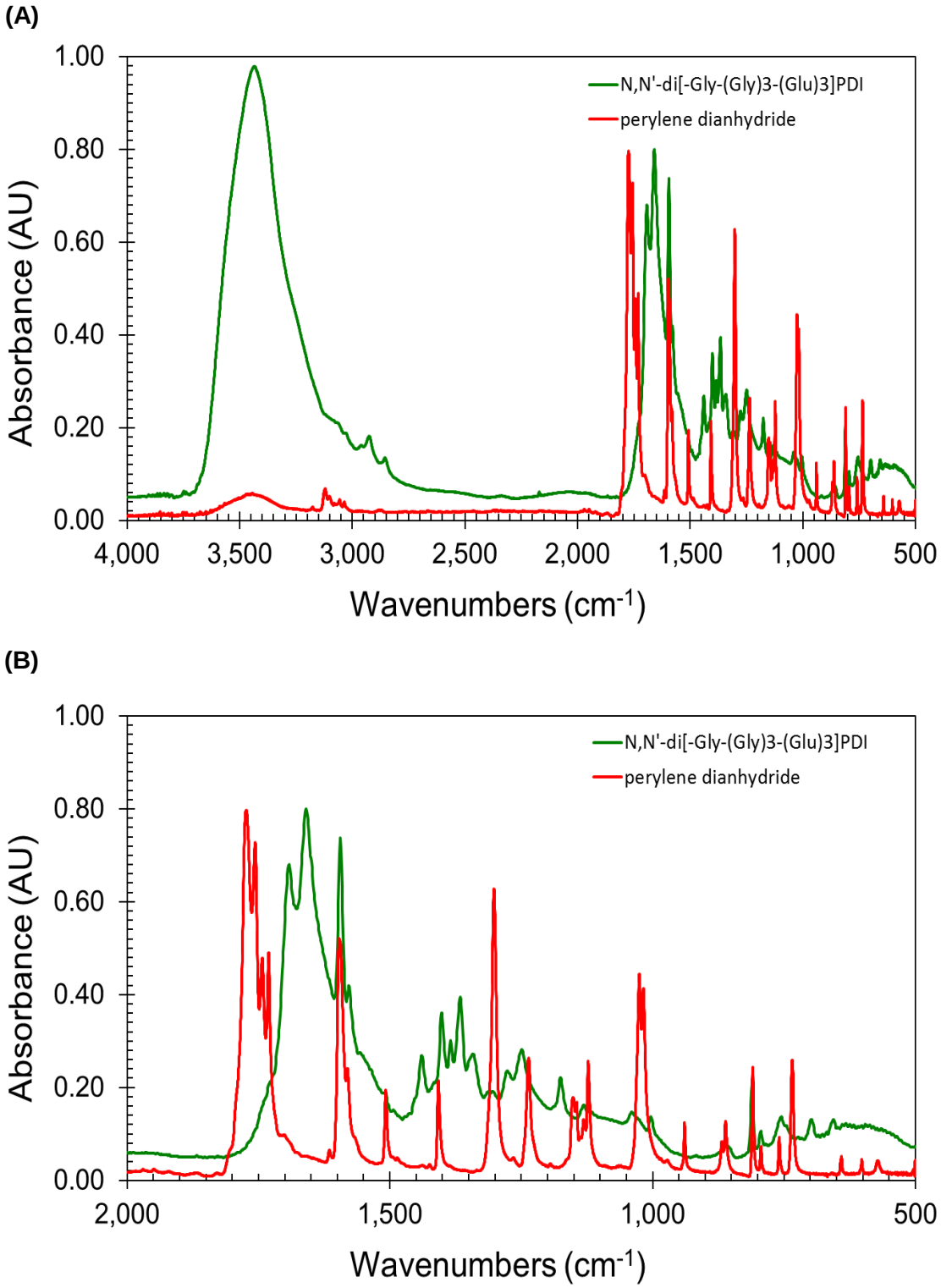

Figure C.1 FT-IR spectra of compound **1**: (A) Spectral range 4000-500 cm^{-1}; (B) Fingerprint region spectral comparison showing anhydride to imide conversion.

C.1 FT-IR Spectra of Synthesized Perylene Imides

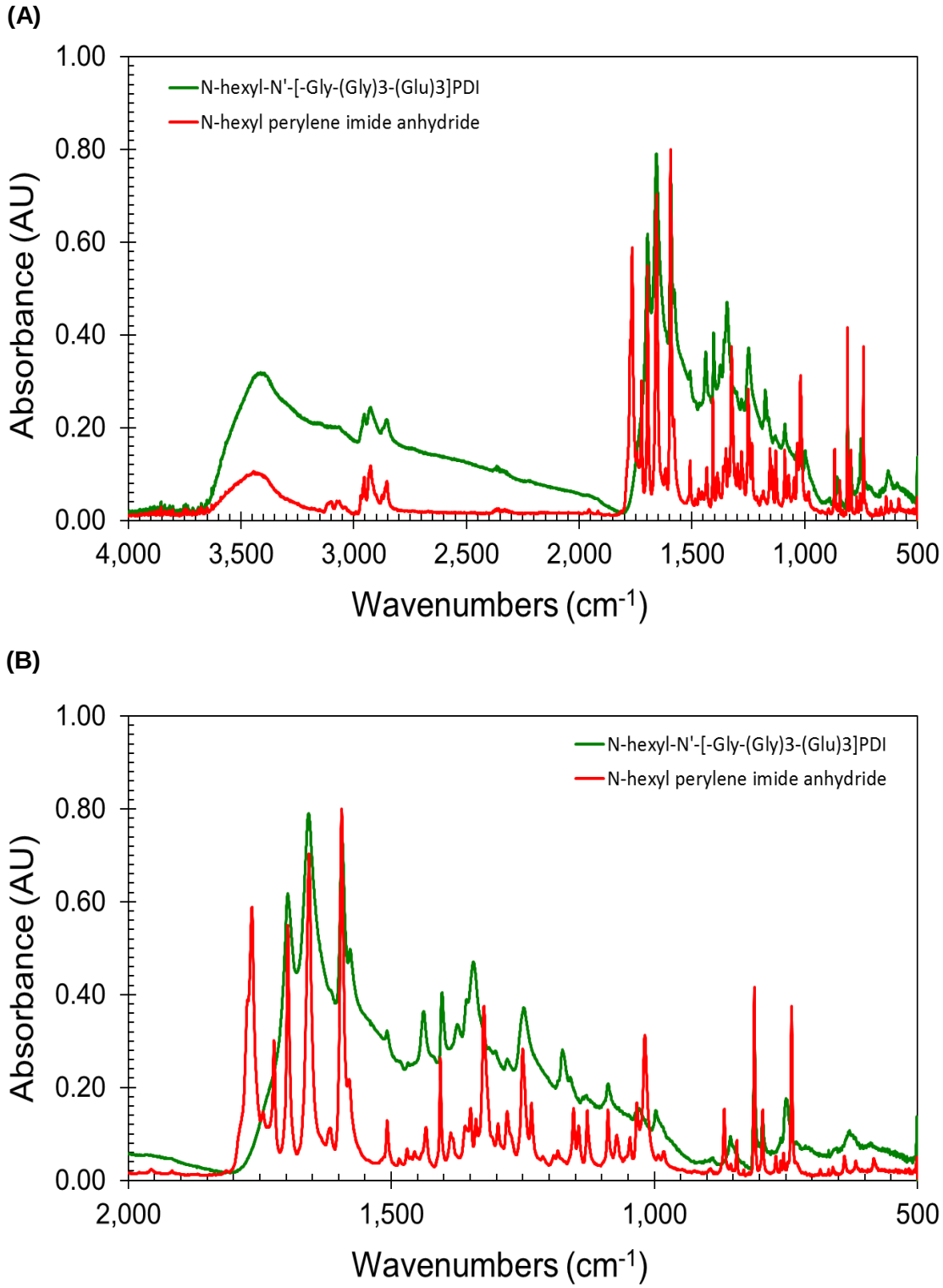

Figure C.2 FT-IR spectra of compound **1H**: (A) Spectral range 4000-500 cm^{-1}; (B) Fingerprint region spectral comparison showing anhydride to imide conversion.

C.1 FT-IR Spectra of Synthesized Perylene Imides

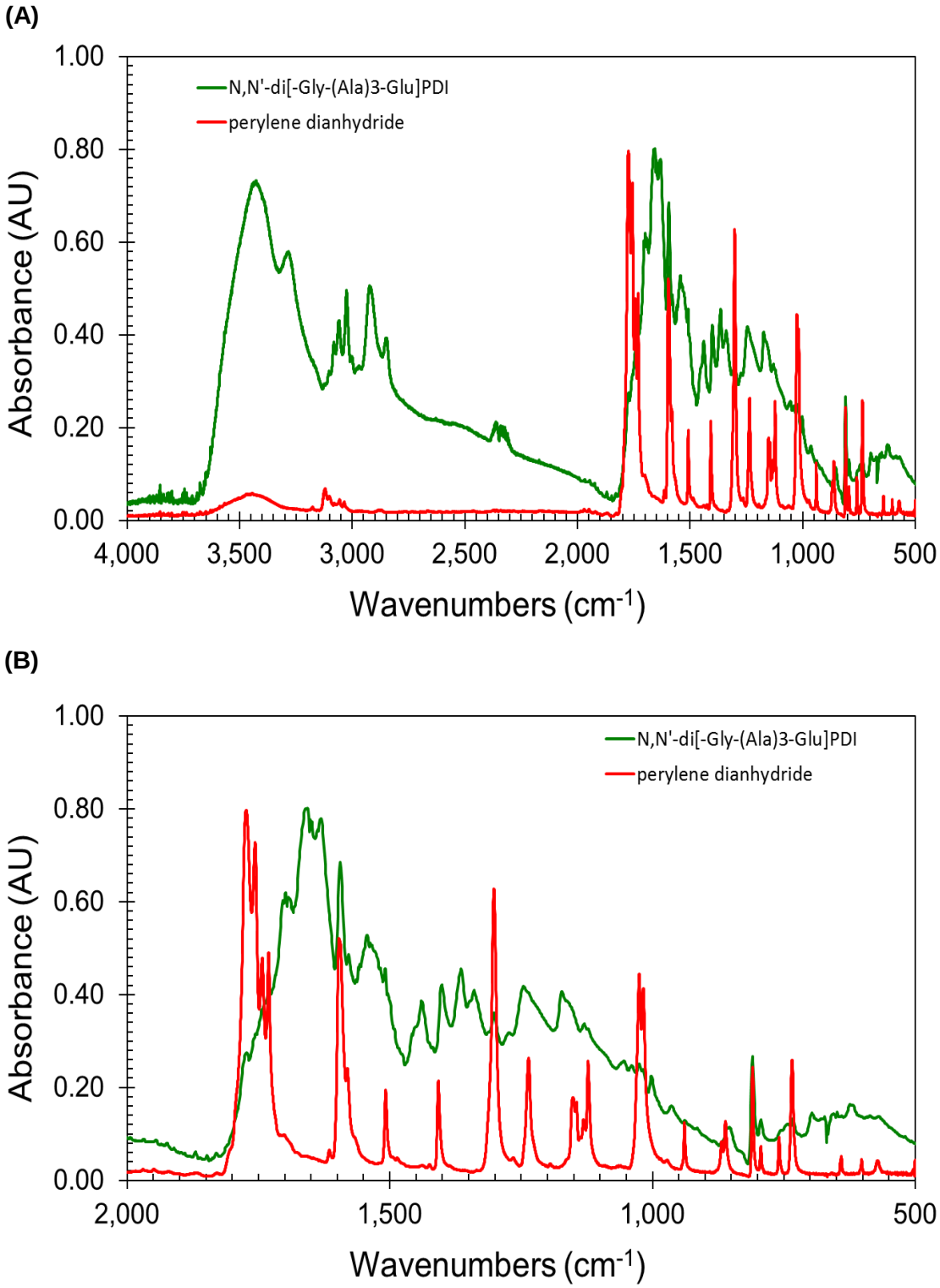

Figure C.3 FT-IR spectra of compound **2**: (A) Spectral range 4000-500 cm^{-1}; (B) Fingerprint region spectral comparison showing anhydride to imide conversion.

C.1 FT-IR Spectra of Synthesized Perylene Imides

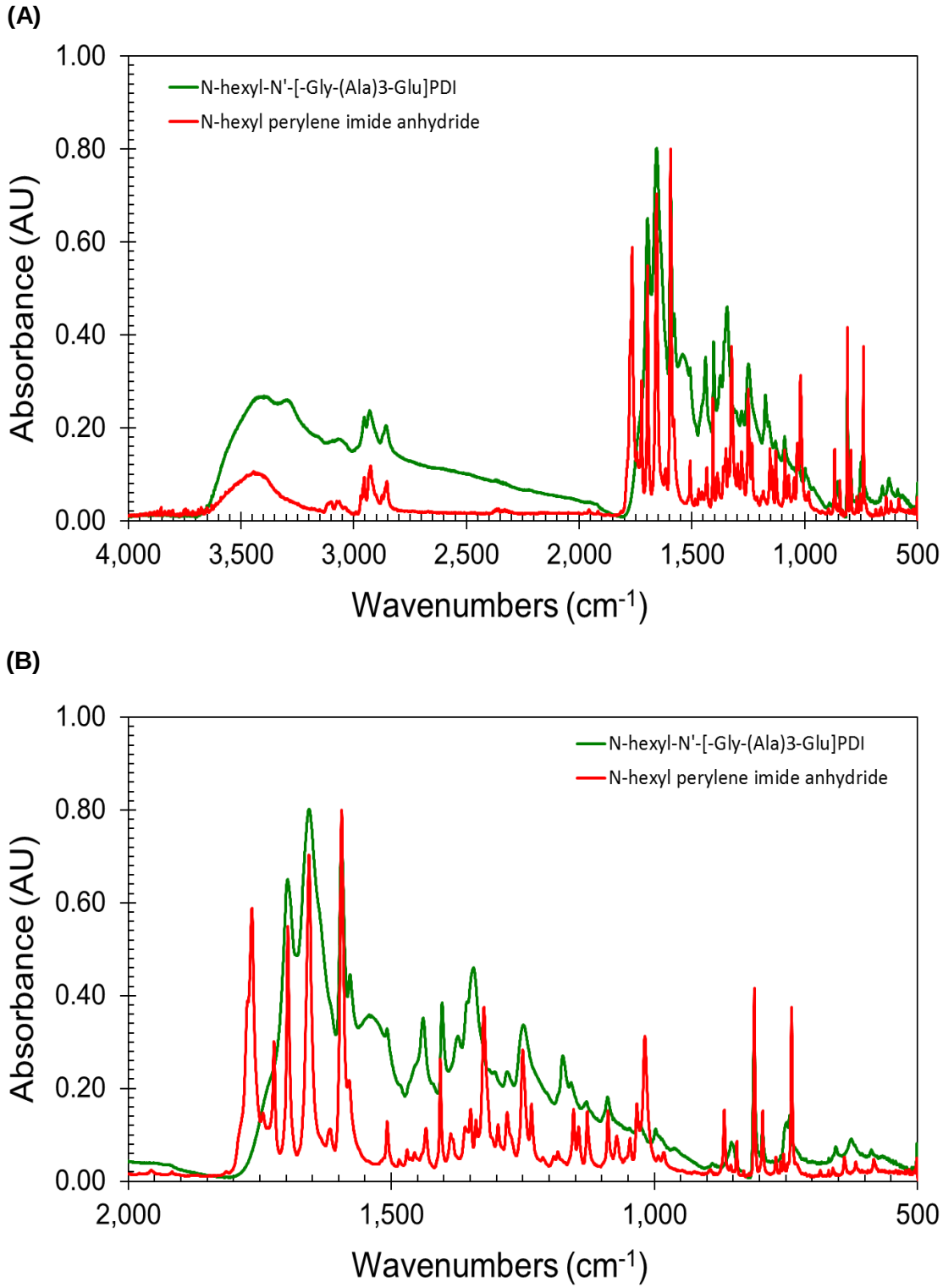

Figure C.4 FT-IR spectra of compound **2H**: (A) Spectral range 4000-500 cm^{-1}; (B) Fingerprint region spectral comparison showing anhydride to imide conversion.

C.1 FT-IR Spectra of Synthesized Perylene Imides

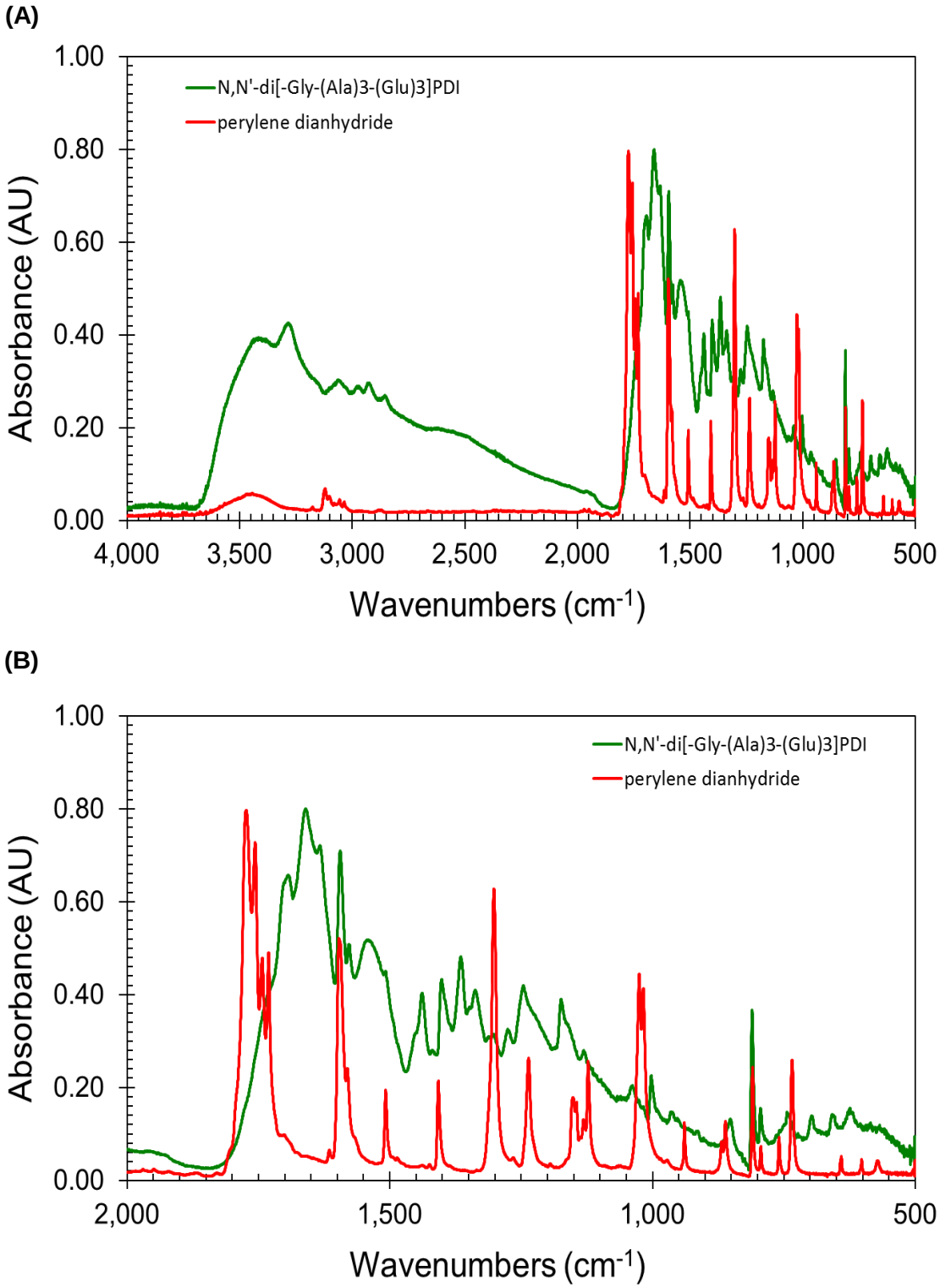

Figure C.5 FT-IR spectra of compound **3**: (A) Spectral range 4000-500 cm^{-1}; (B) Fingerprint region spectral comparison showing anhydride to imide conversion.

C.1 FT-IR Spectra of Synthesized Perylene Imides

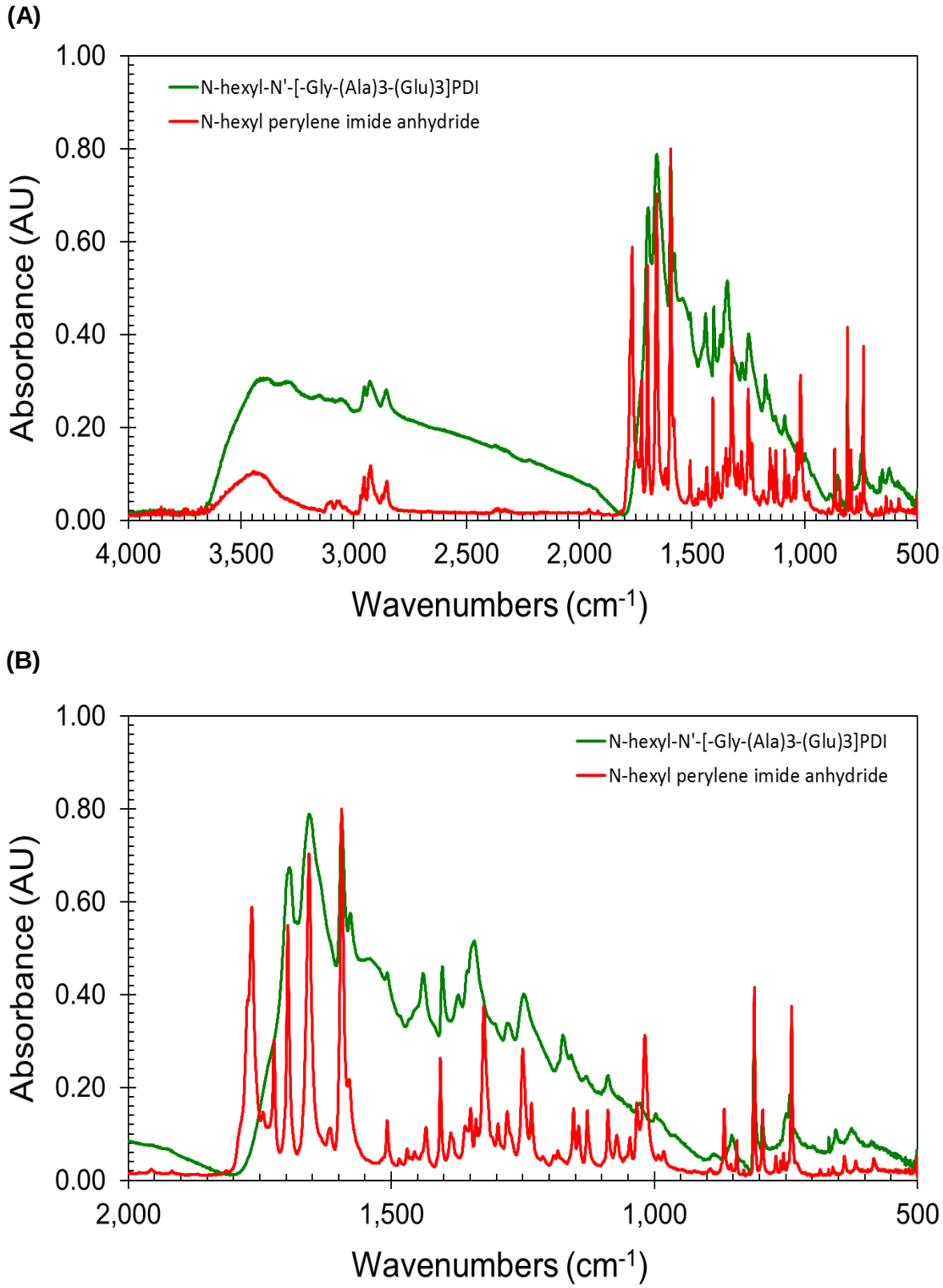

Figure C.6 FT-IR spectra of compound **3H**: (A) Spectral range 4000-500 cm^{-1}; (B) Fingerprint region spectral comparison showing anhydride to imide conversion.

C.1 FT-IR Spectra of Synthesized Perylene Imides

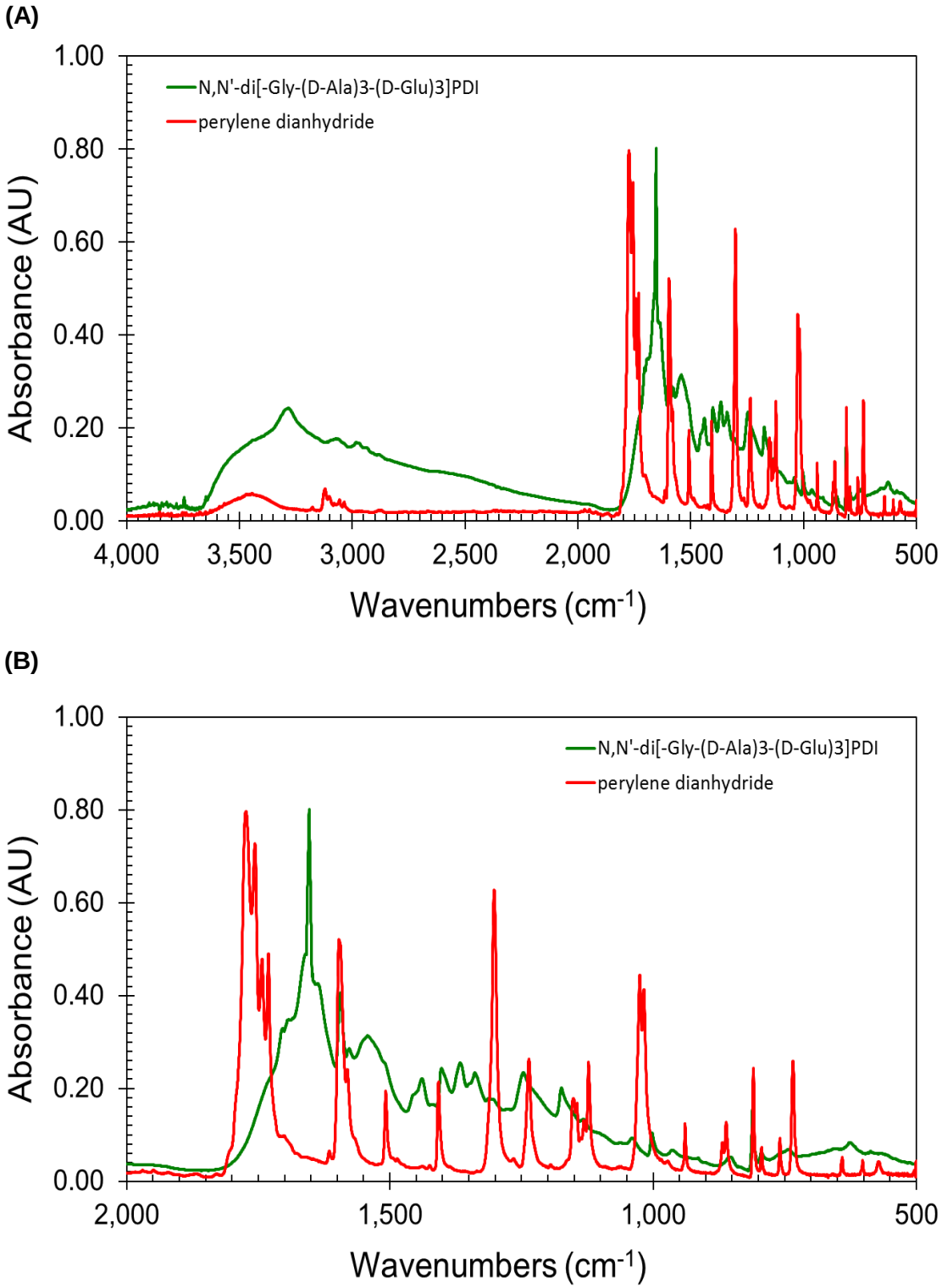

Figure C.7 FT-IR spectra of compound **3E**: (A) Spectral range 4000-500 cm^{-1}; (B) Fingerprint region spectral comparison showing anhydride to imide conversion.

C.1 FT-IR Spectra of Synthesized Perylene Imides

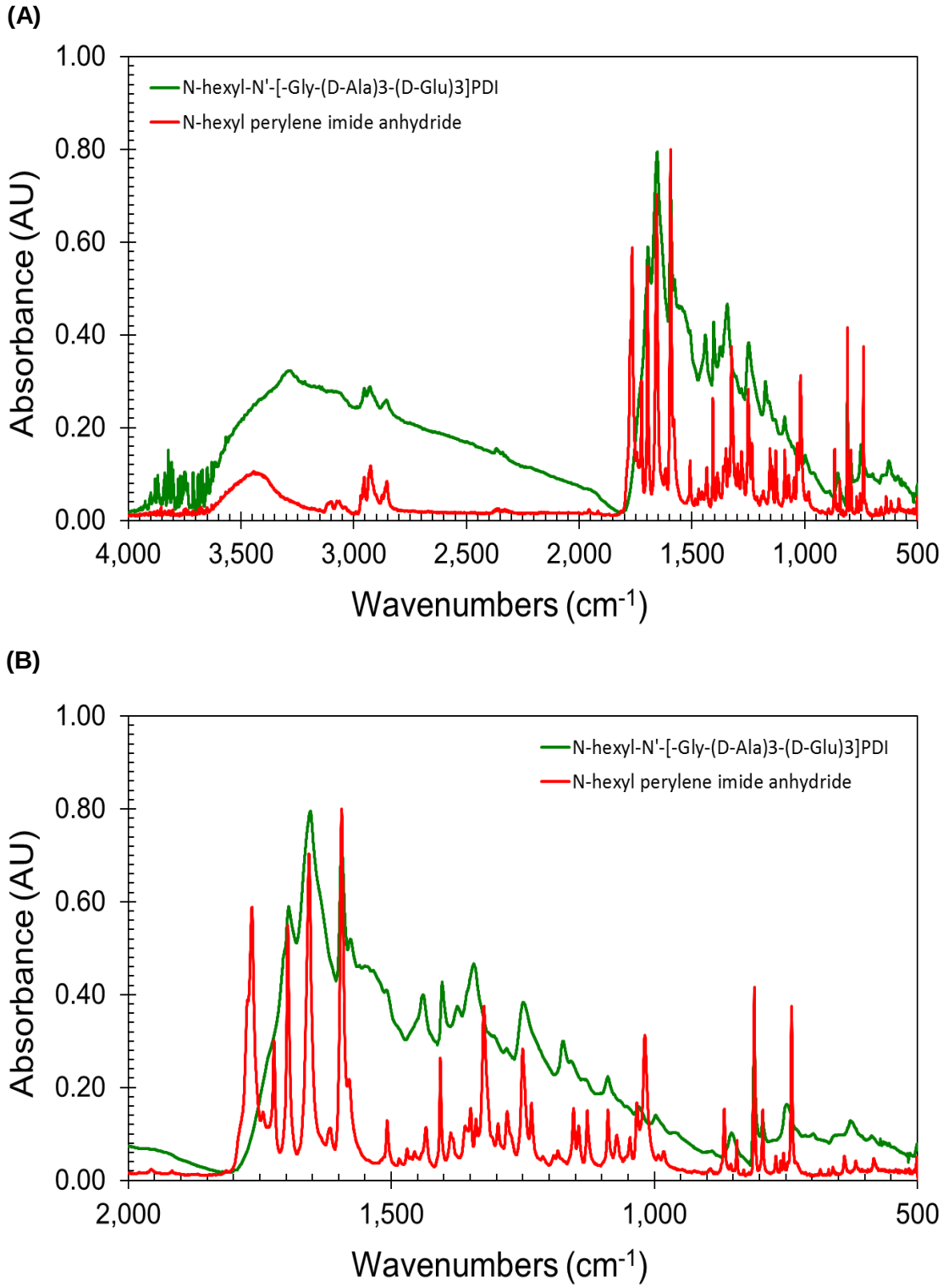

Figure C.8 FT-IR spectra of compound **3HE**: (A) Spectral range 4000-500 cm^{-1}; (B) Fingerprint region spectral comparison showing anhydride to imide conversion.

C.1 FT-IR Spectra of Synthesized Perylene Imides

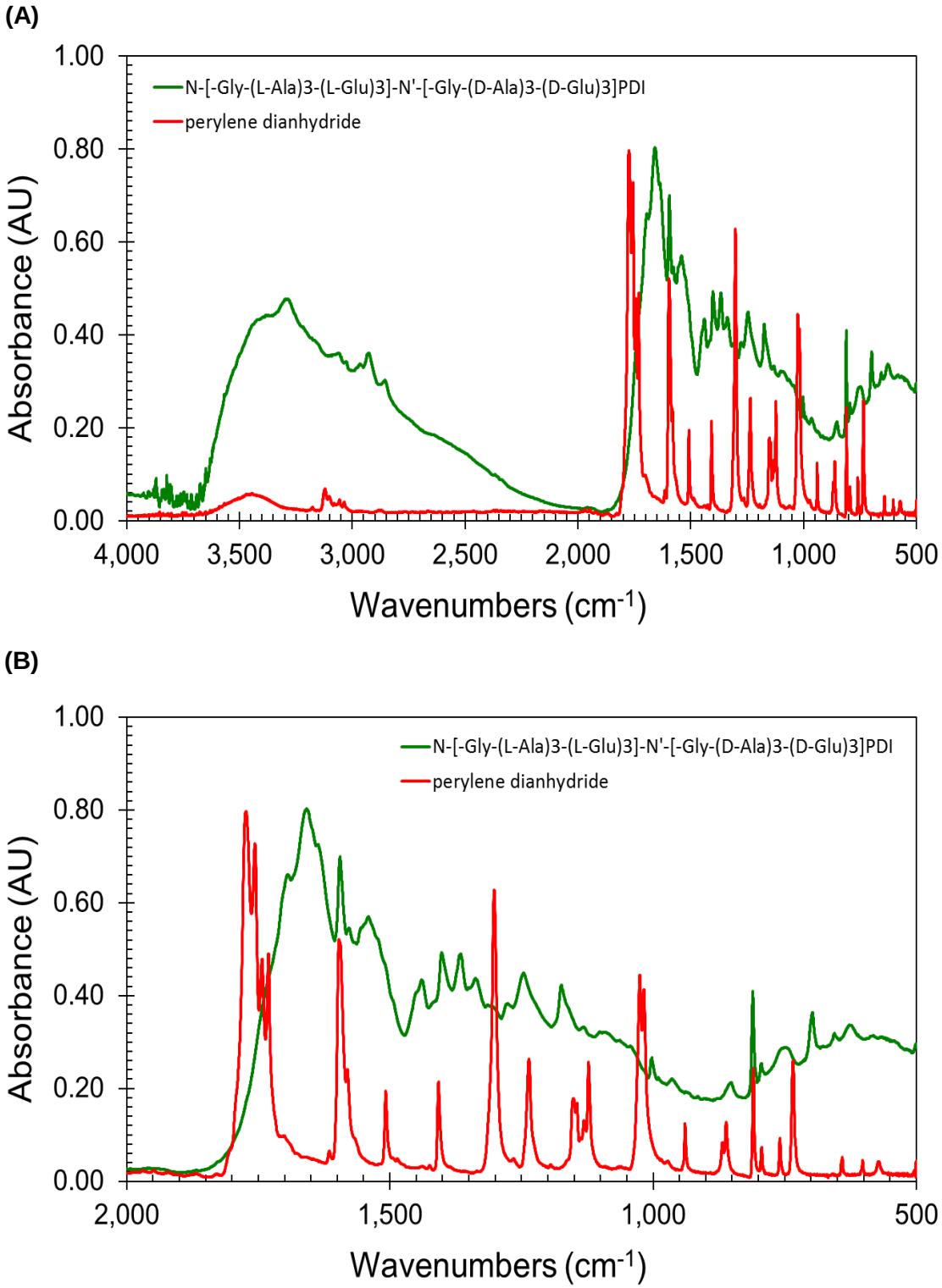

Figure C.9 FT-IR spectra of compound **3M**: (A) Spectral range 4000-500 cm^{-1}; (B) Fingerprint region spectral comparison showing anhydride to imide conversion.

C.1 FT-IR Spectra of Synthesized Perylene Imides

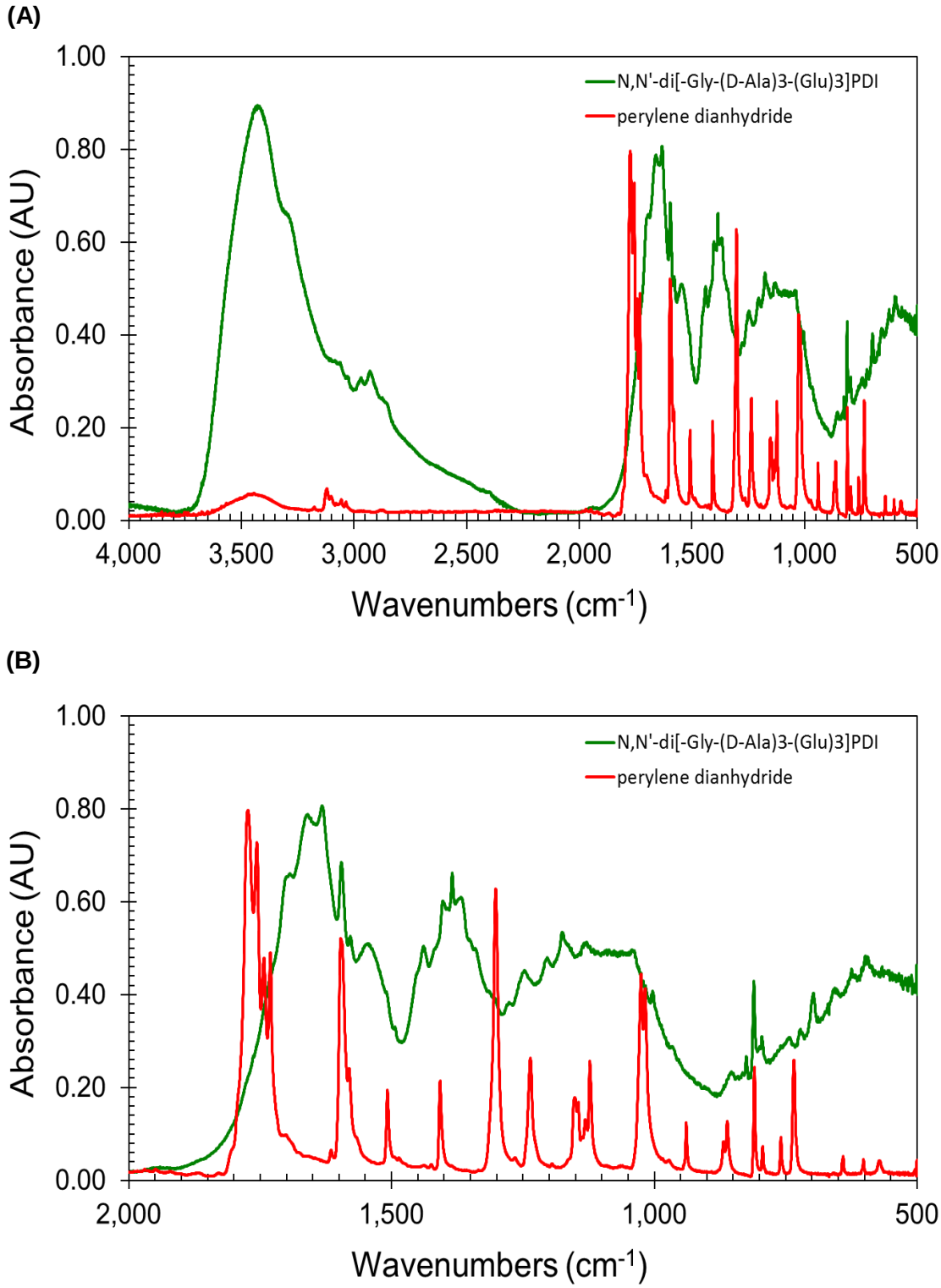

Figure C.10 FT-IR spectra of compound **4**: (A) Spectral range 4000-500 cm^{-1}; (B) Fingerprint region spectral comparison showing anhydride to imide conversion.

C.1 FT-IR Spectra of Synthesized Perylene Imides

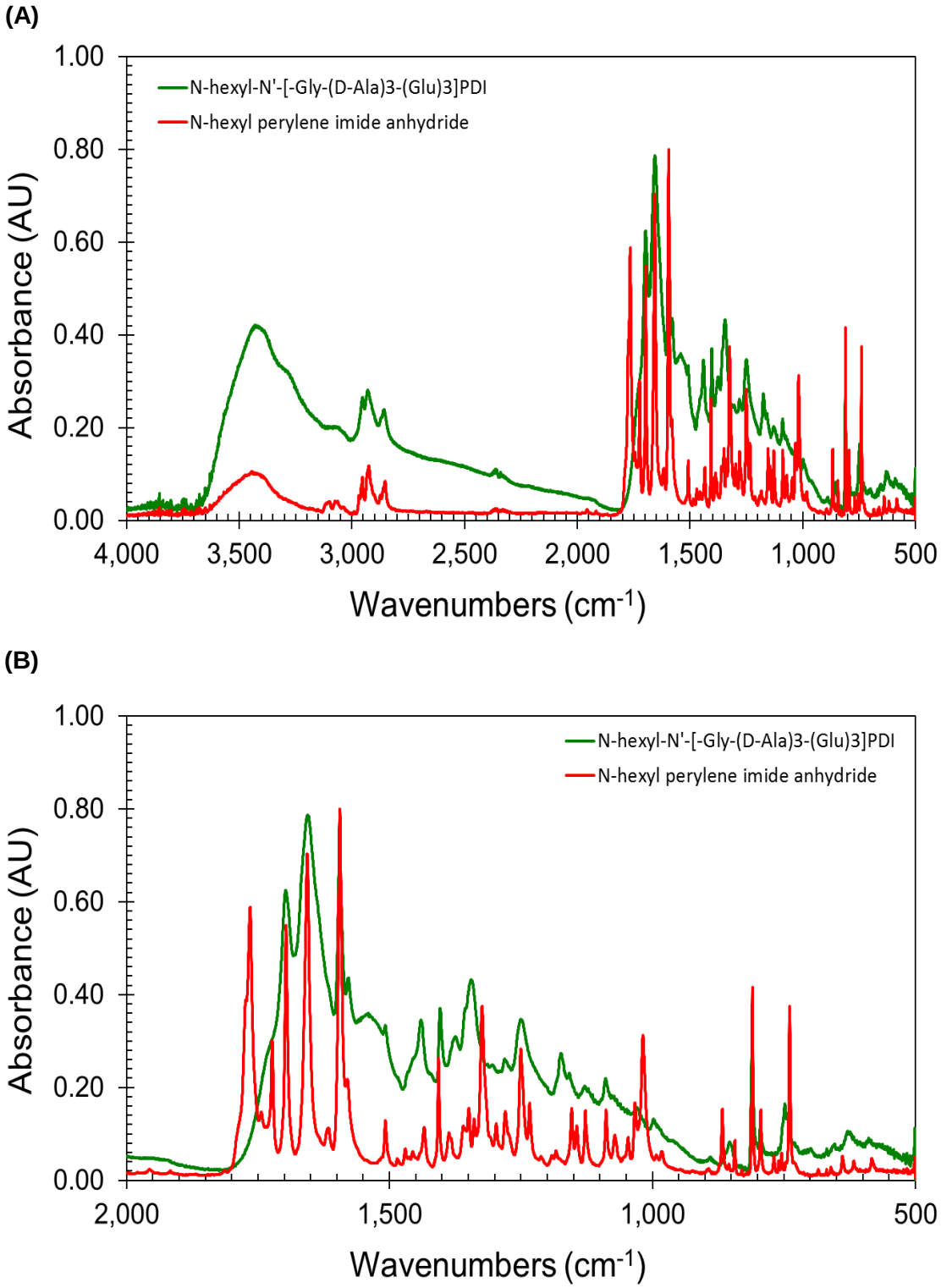

Figure C.11 FT-IR spectra of compound **4H**: (A) Spectral range 4000-500 cm^{-1}; (B) Fingerprint region spectral comparison showing anhydride to imide conversion.

C.1 FT-IR Spectra of Synthesized Perylene Imides

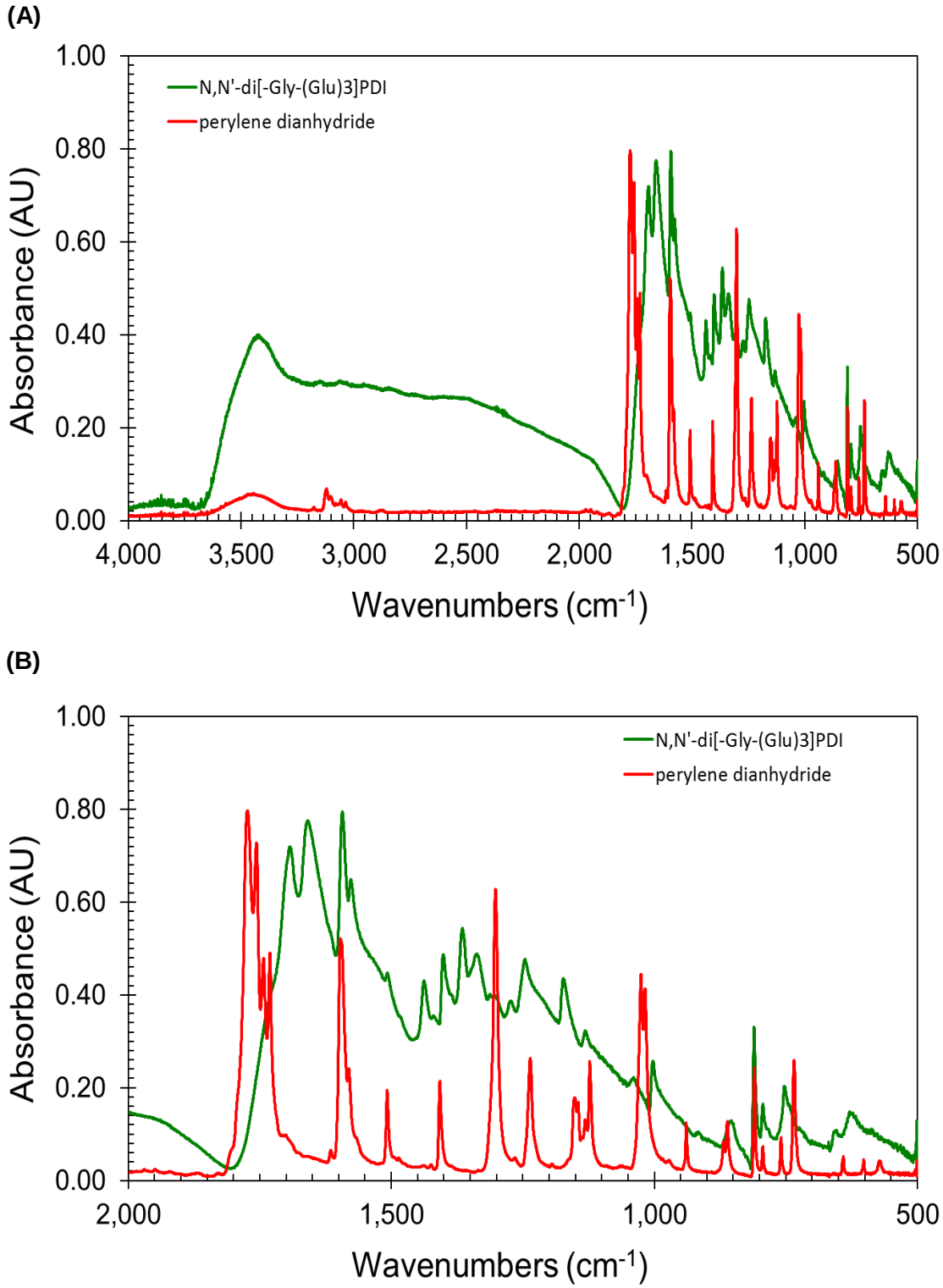

Figure C.12 FT-IR spectra of compound **5**: (A) Spectral range 4000-500 cm^{-1}; (B) Fingerprint region spectral comparison showing anhydride to imide conversion.

C.1 FT-IR Spectra of Synthesized Perylene Imides

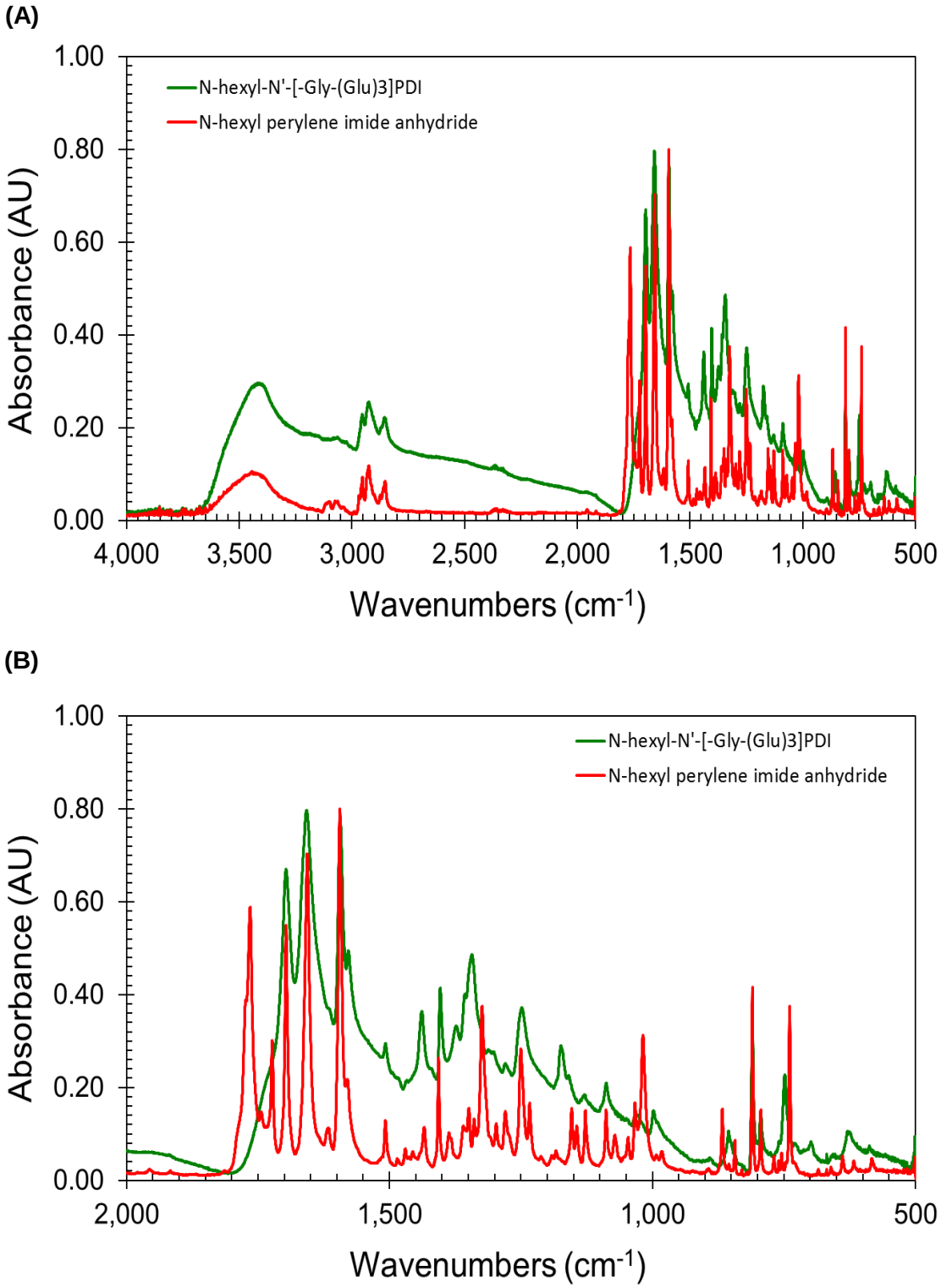

Figure C.13 FT-IR spectra of compound **5H**: (A) Spectral range 4000-500 cm^{-1}; (B) Fingerprint region spectral comparison showing anhydride to imide conversion.

C.1 FT-IR Spectra of Synthesized Perylene Imides

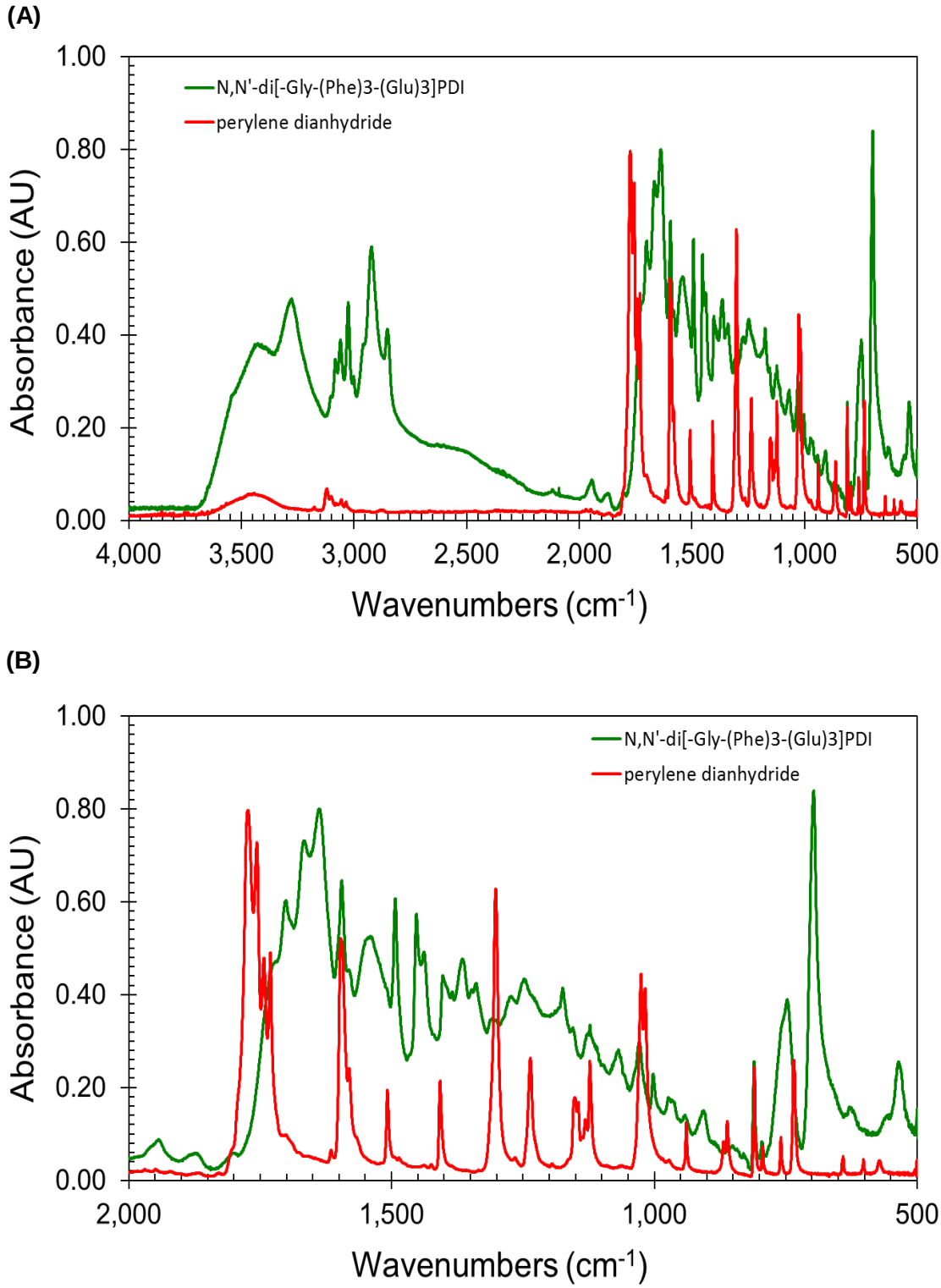

Figure C.14 FT-IR spectra of compound **6**: (A) Spectral range 4000-500 cm^{-1}; (B) Fingerprint region spectral comparison showing anhydride to imide conversion.

C.1 FT-IR Spectra of Synthesized Perylene Imides

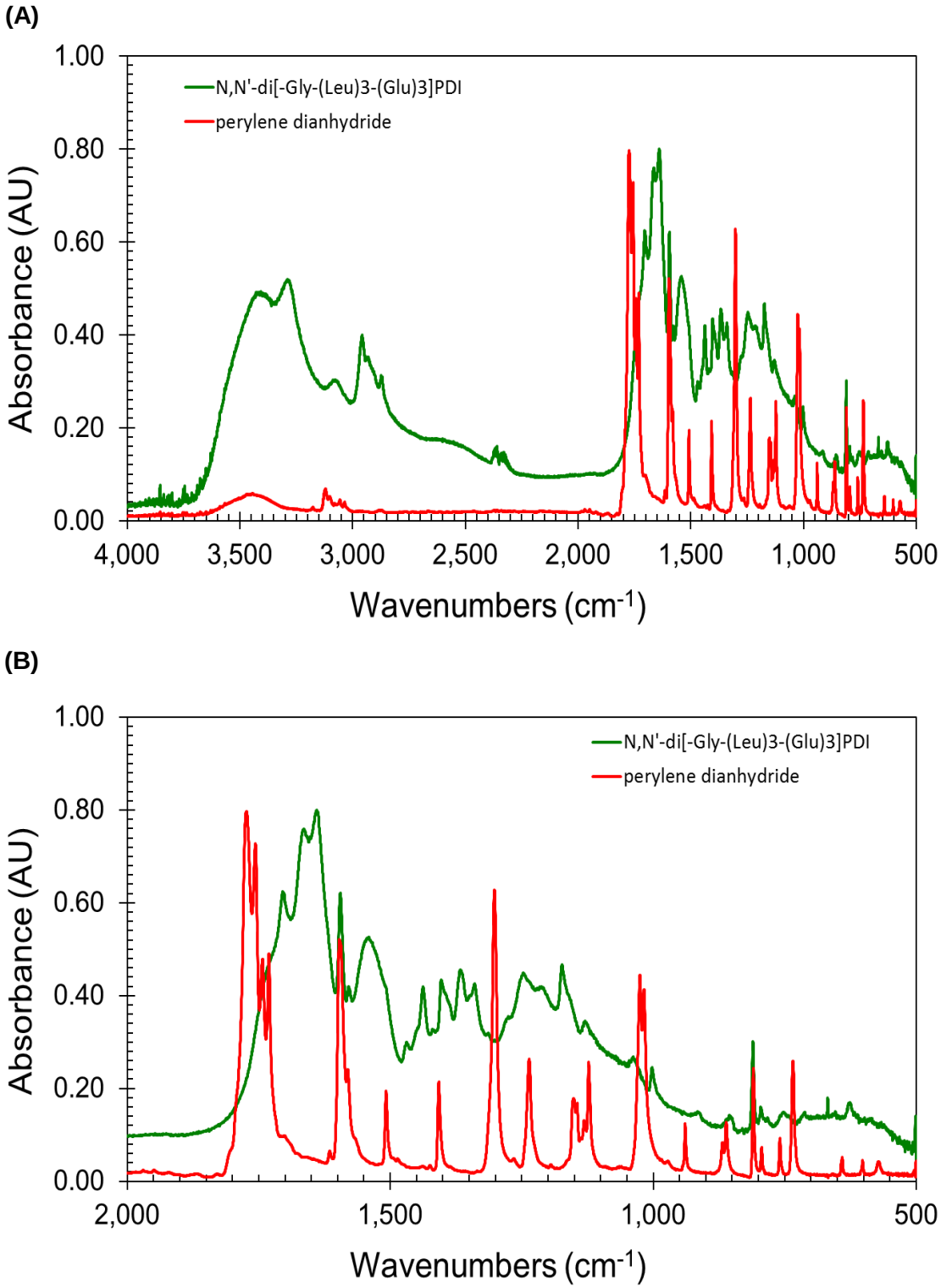

Figure C.15 FT-IR spectra of compound **7**: (A) Spectral range 4000-500 cm^{-1}; (B) Fingerprint region spectral comparison showing anhydride to imide conversion.

C.1 FT-IR Spectra of Synthesized Perylene Imides

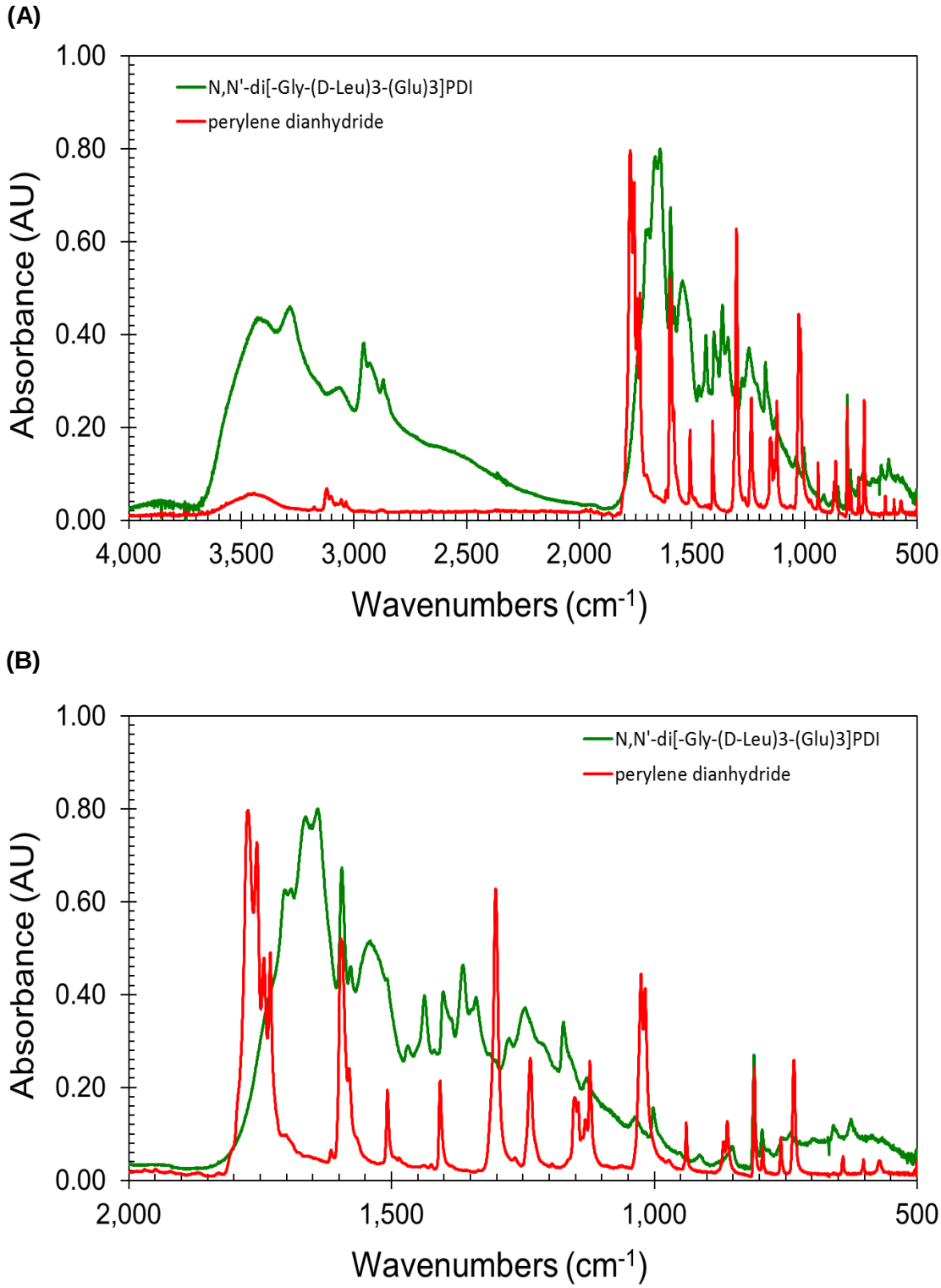

Figure C.16 FT-IR spectra of compound **8**: (A) Spectral range 4000-500 cm^{-1}; (B) Fingerprint region spectral comparison showing anhydride to imide conversion.

C.1 FT-IR Spectra of Synthesized Perylene Imides

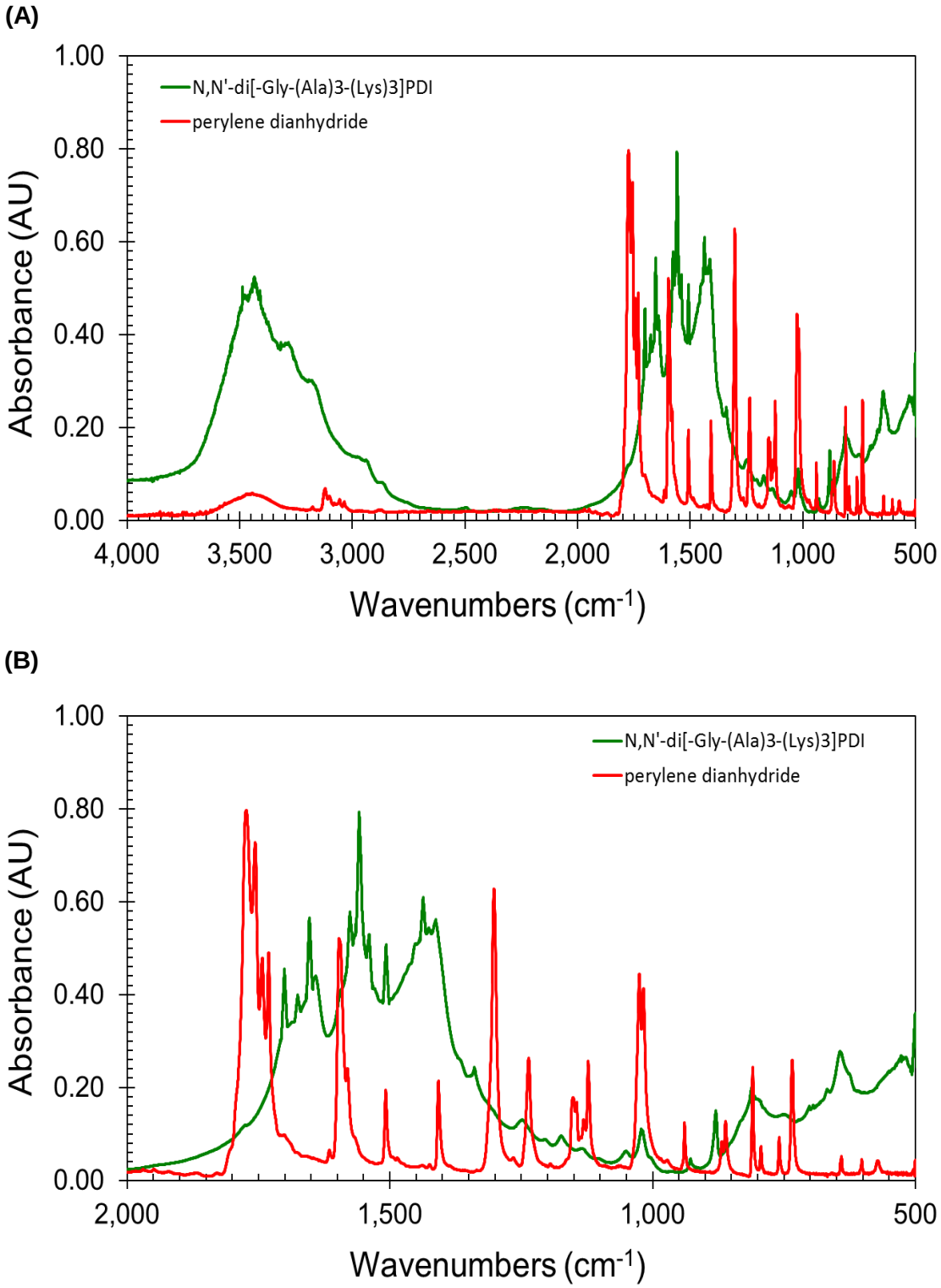

Figure C.17 FT-IR spectra of compound **9**: (A) Spectral range 4000-500 cm^{-1}; (B) Fingerprint region spectral comparison showing anhydride to imide conversion.

C.1 FT-IR Spectra of Synthesized Perylene Imides

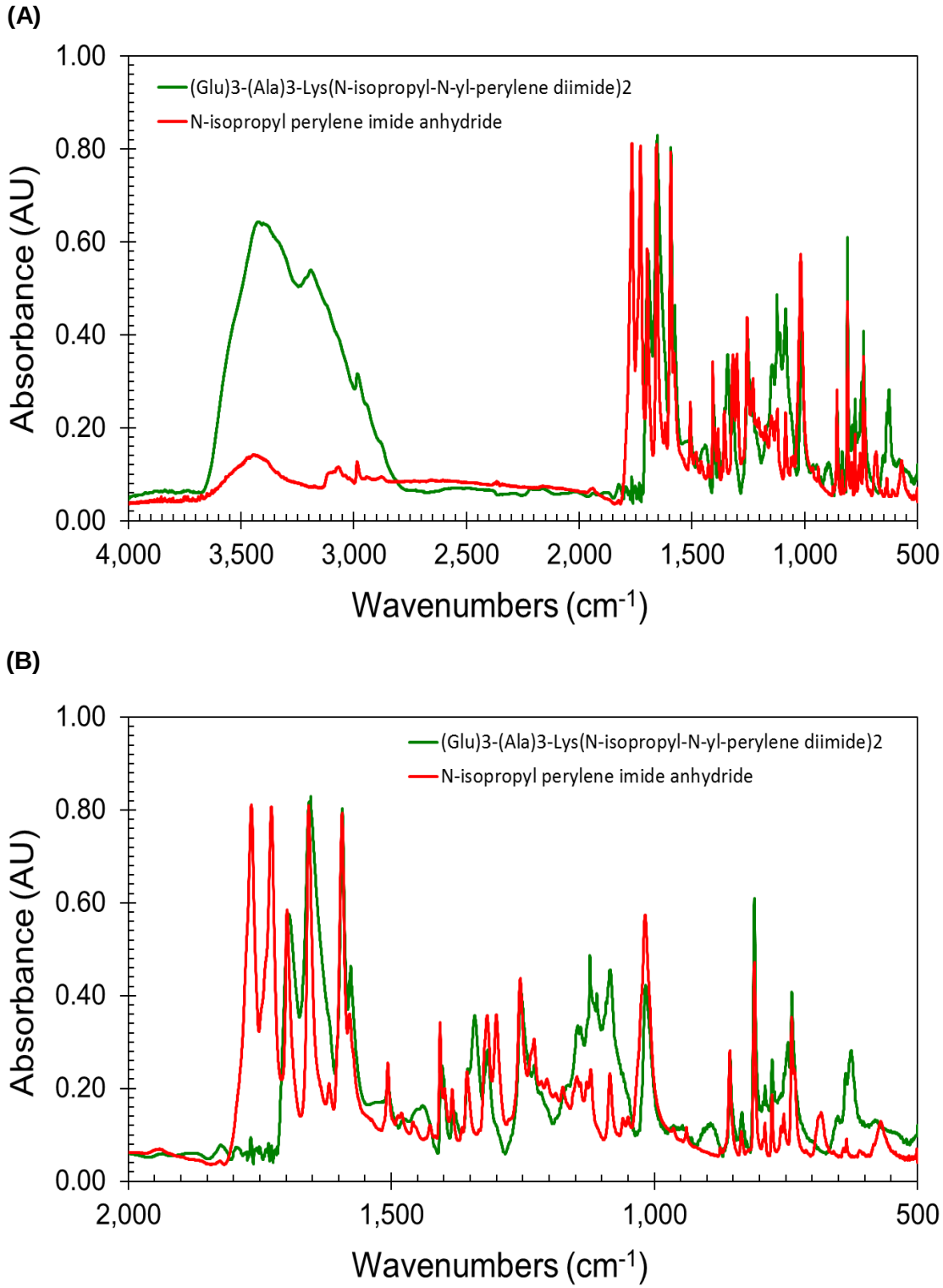

Figure C.18 FT-IR spectra of compound **10**: (A) Spectral range 4000-500 cm^{-1}; (B) Fingerprint region spectral comparison showing anhydride to imide conversion.

C.1 FT-IR Spectra of Synthesized Perylene Imides

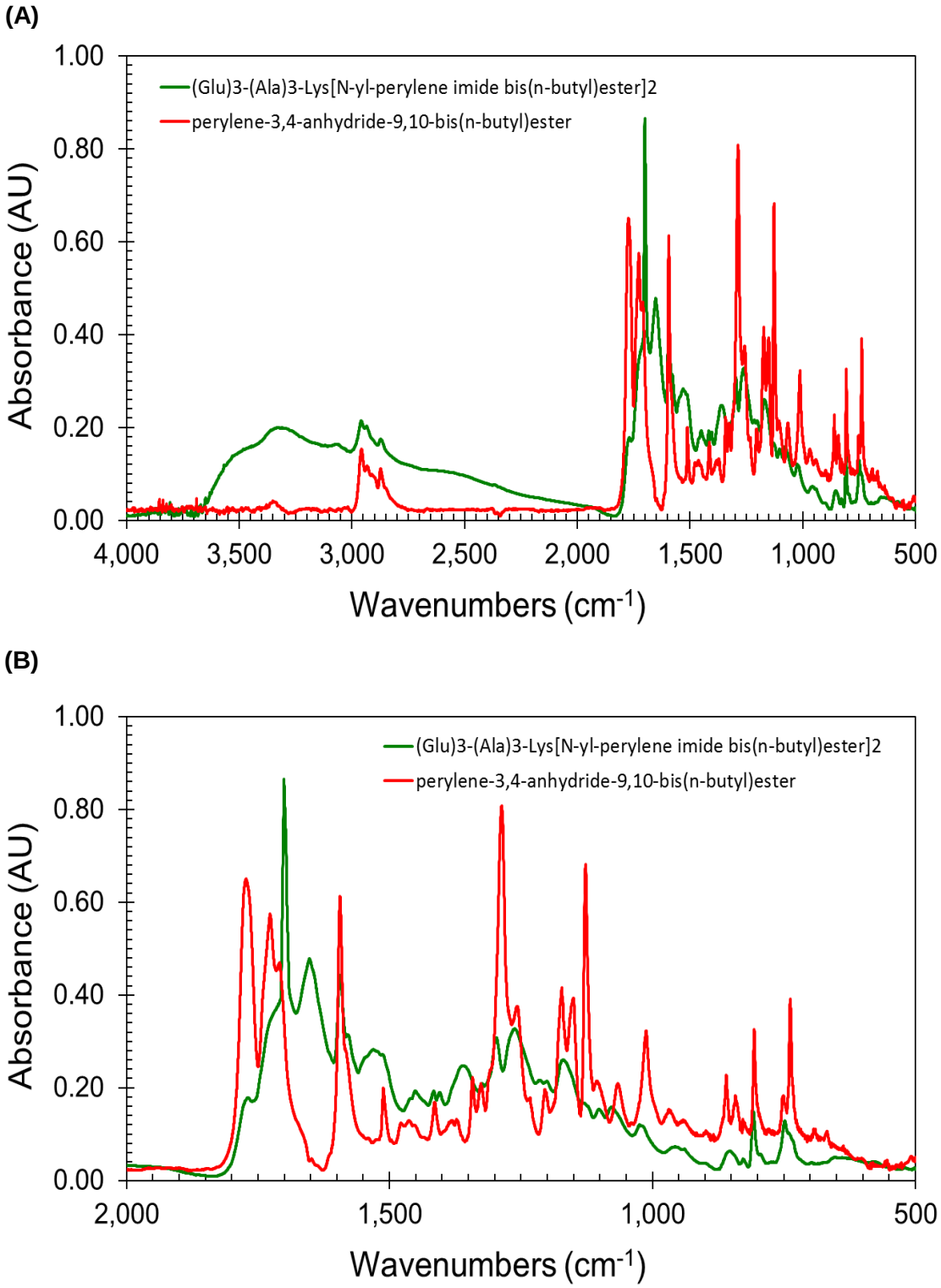

Figure C.19 FT-IR spectra of compound **11**: (A) Spectral range 4000-500 cm^{-1}; (B) Fingerprint region spectral comparison showing anhydride to imide conversion.

C.1 FT-IR Spectra of Synthesized Perylene Imides

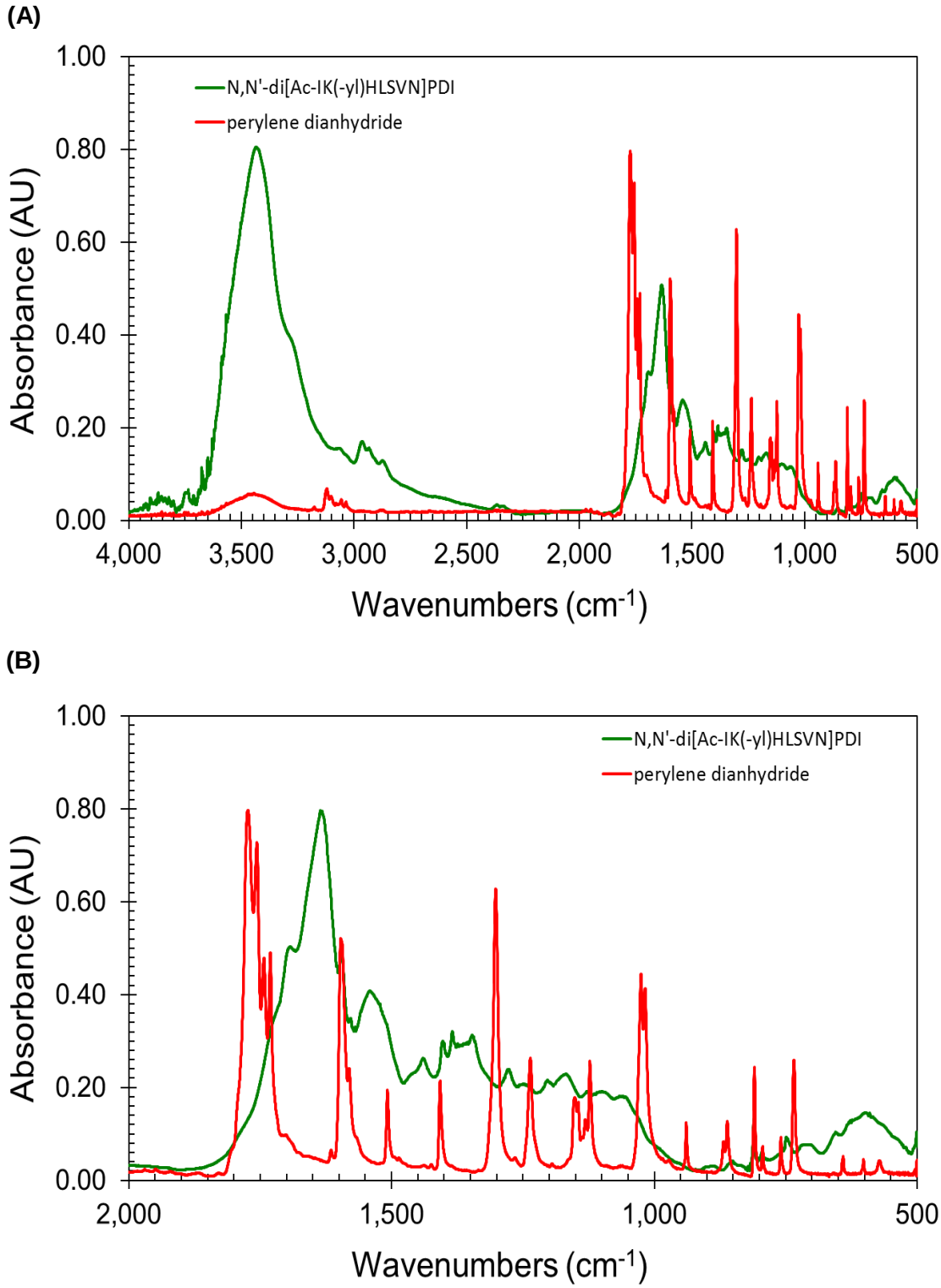

Figure C.20 FT-IR spectra of compound **12**: (A) Spectral range 4000-500 cm^{-1}; (B) Fingerprint region spectral comparison showing anhydride to imide conversion.

C.1 FT-IR Spectra of Synthesized Perylene Imides

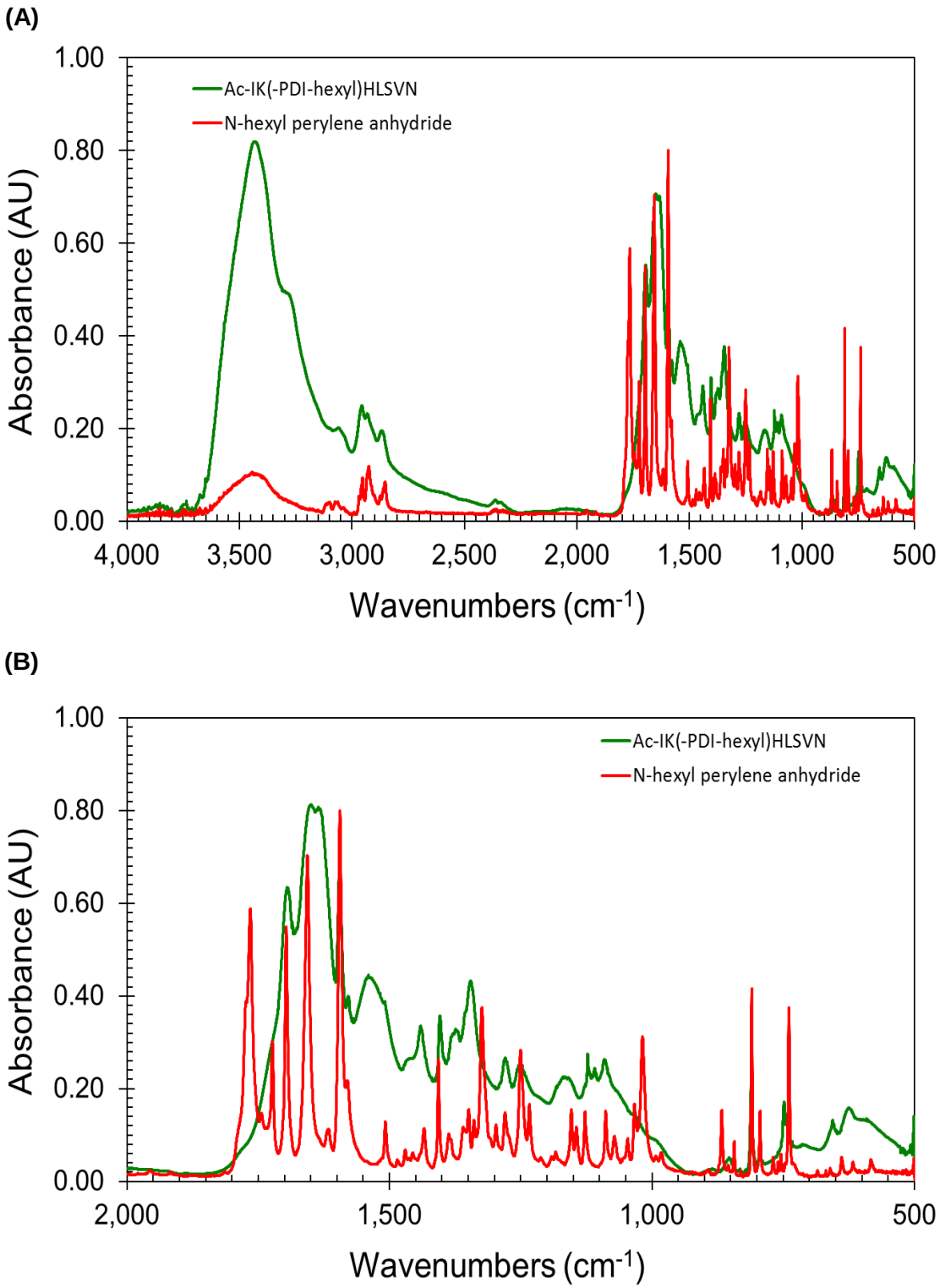

Figure C.21 FT-IR spectra of compound **12H**: (A) Spectral range 4000-500 cm^{-1}; (B) Fingerprint region spectral comparison showing anhydride to imide conversion.

C.1 FT-IR Spectra of Synthesized Perylene Imides

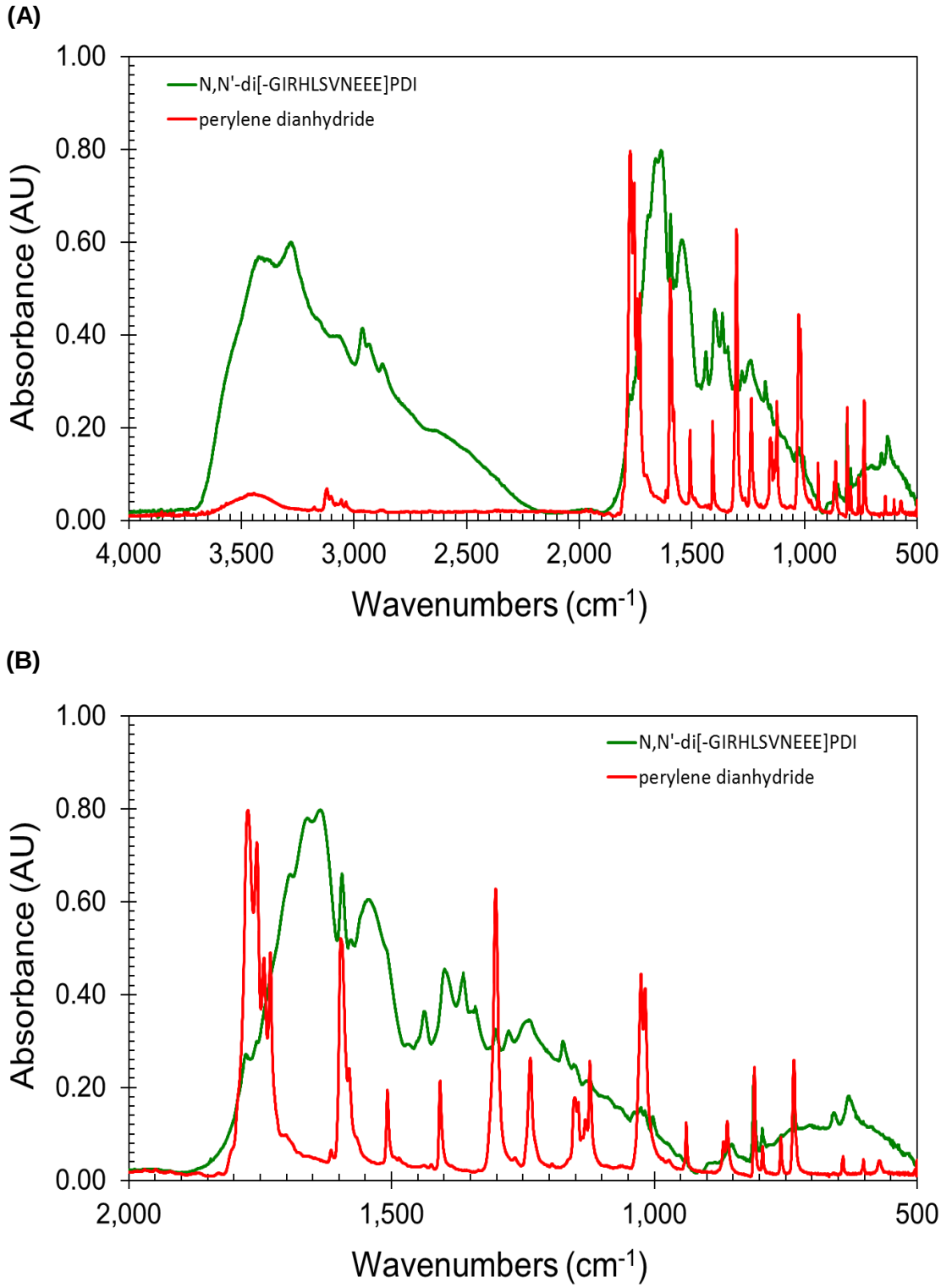

Figure C.22 FT-IR spectra of compound **13**: (A) Spectral range 4000-500 cm^{-1}; (B) Fingerprint region spectral comparison showing anhydride to imide conversion.

C.1 FT-IR Spectra of Synthesized Perylene Imides

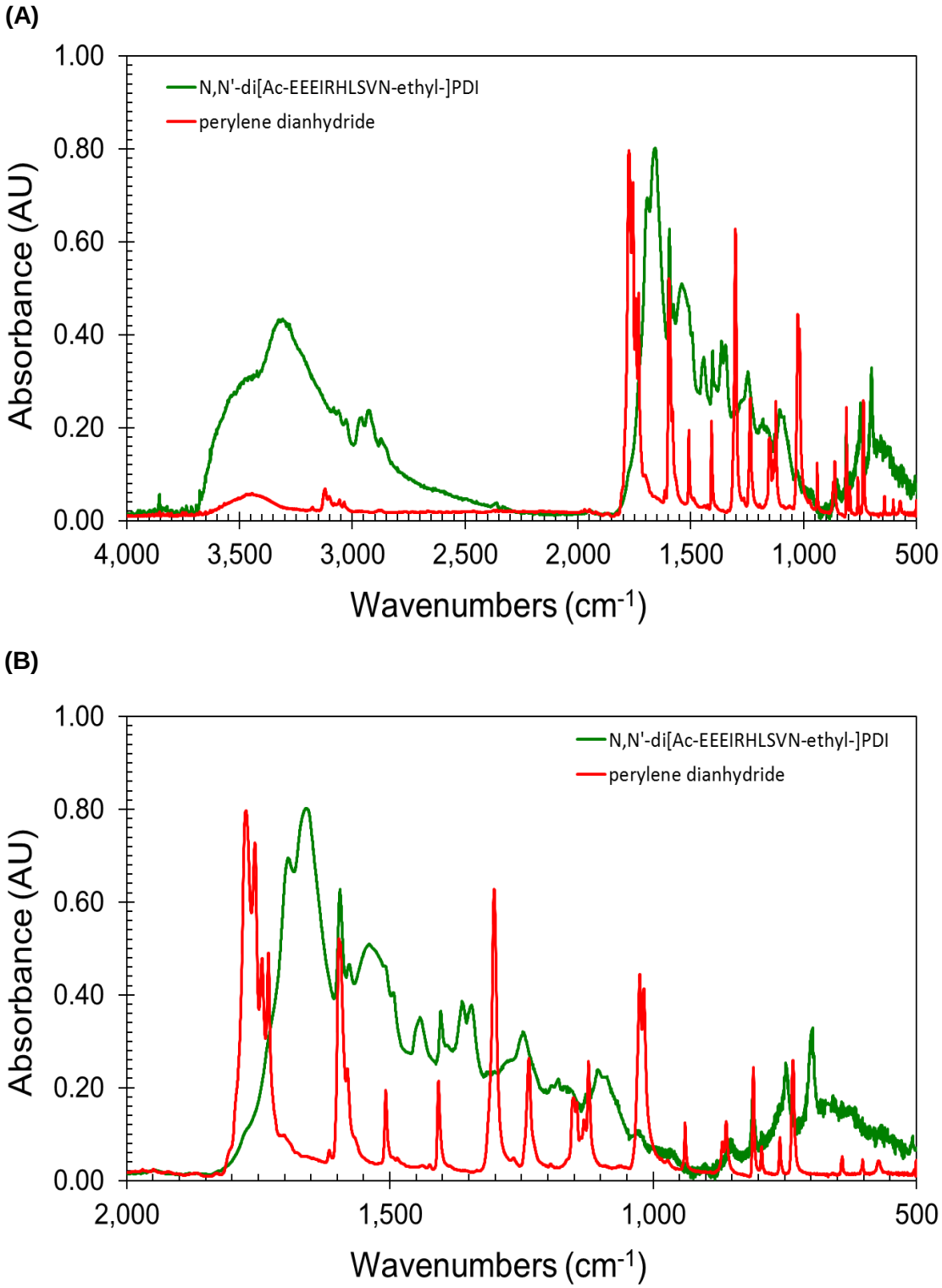

Figure C.23 FT-IR spectra of compound **14**: (A) Spectral range 4000-500 cm^{-1}; (B) Fingerprint region spectral comparison showing anhydride to imide conversion.

C.1 FT-IR Spectra of Synthesized Perylene Imides

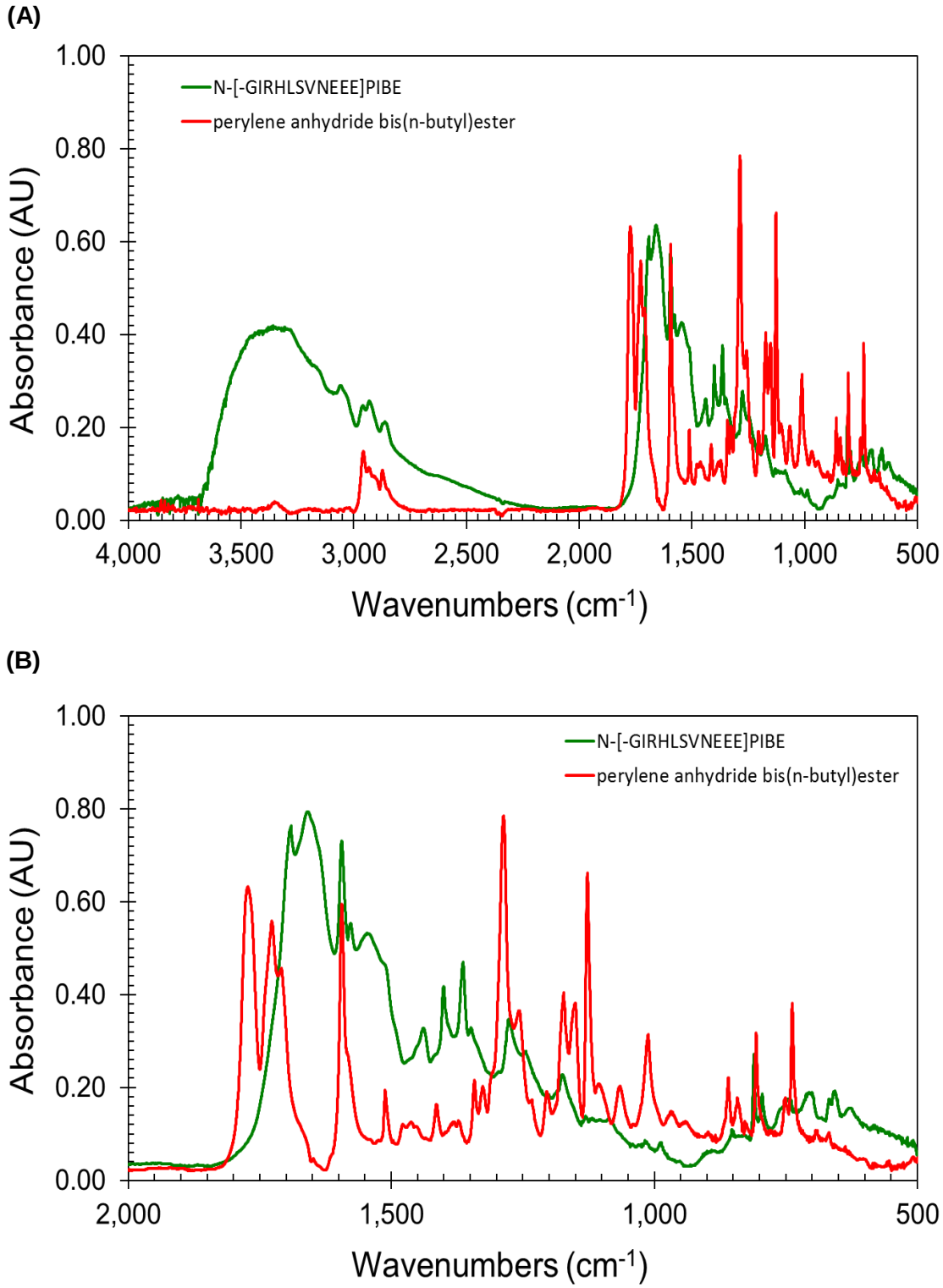

Figure C.24 FT-IR spectra of compound **15**: (A) Spectral range 4000-500 cm^{-1}; (B) Fingerprint region spectral comparison showing anhydride to imide conversion.

C.1 FT-IR Spectra of Synthesized Perylene Imides

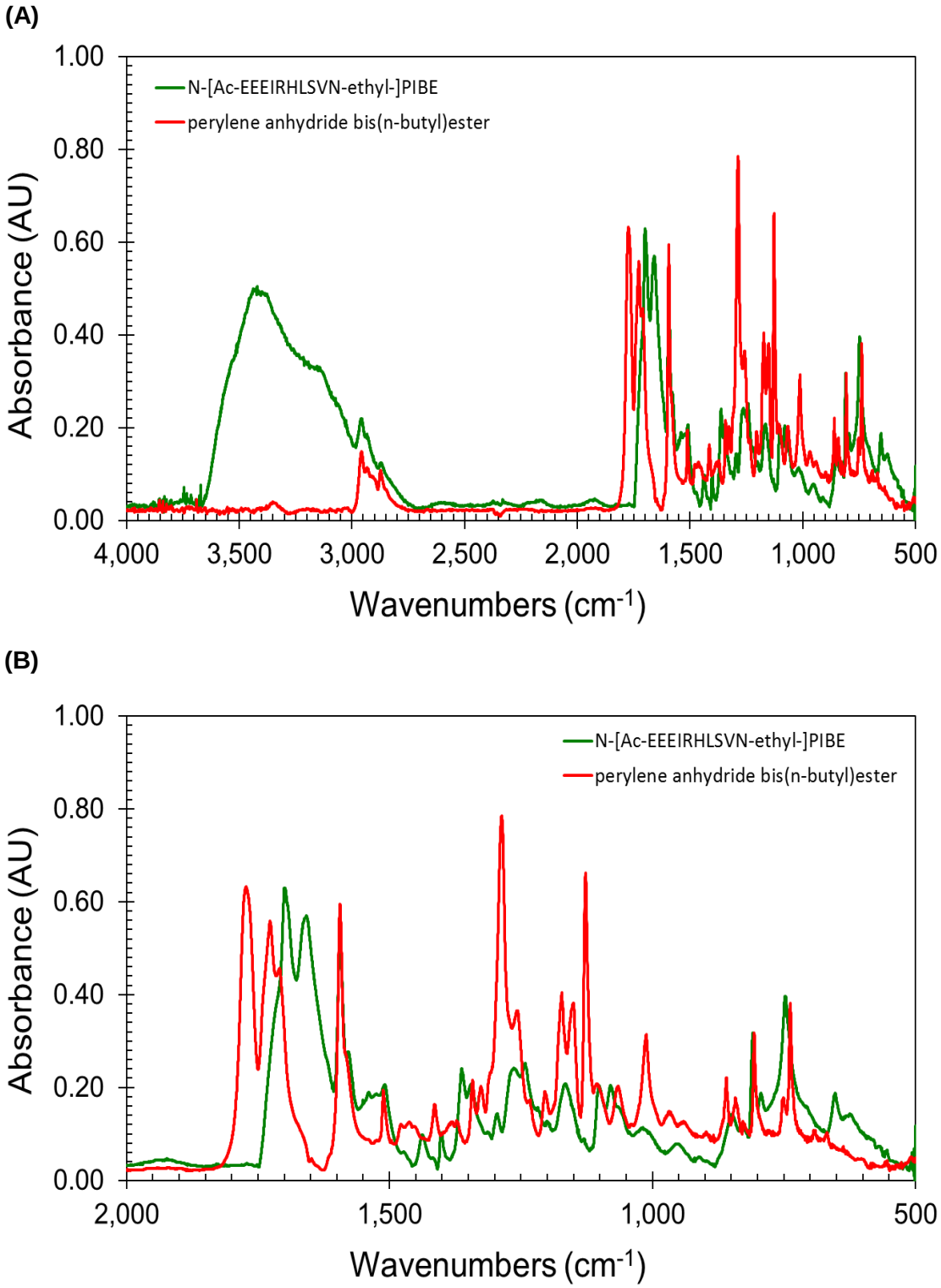

Figure C.25 FT-IR spectra of compound **16**: (A) Spectral range 4000-500 cm^{-1}; (B) Fingerprint region spectral comparison showing anhydride to imide conversion.

C.2 Amide I and II Band Analysis

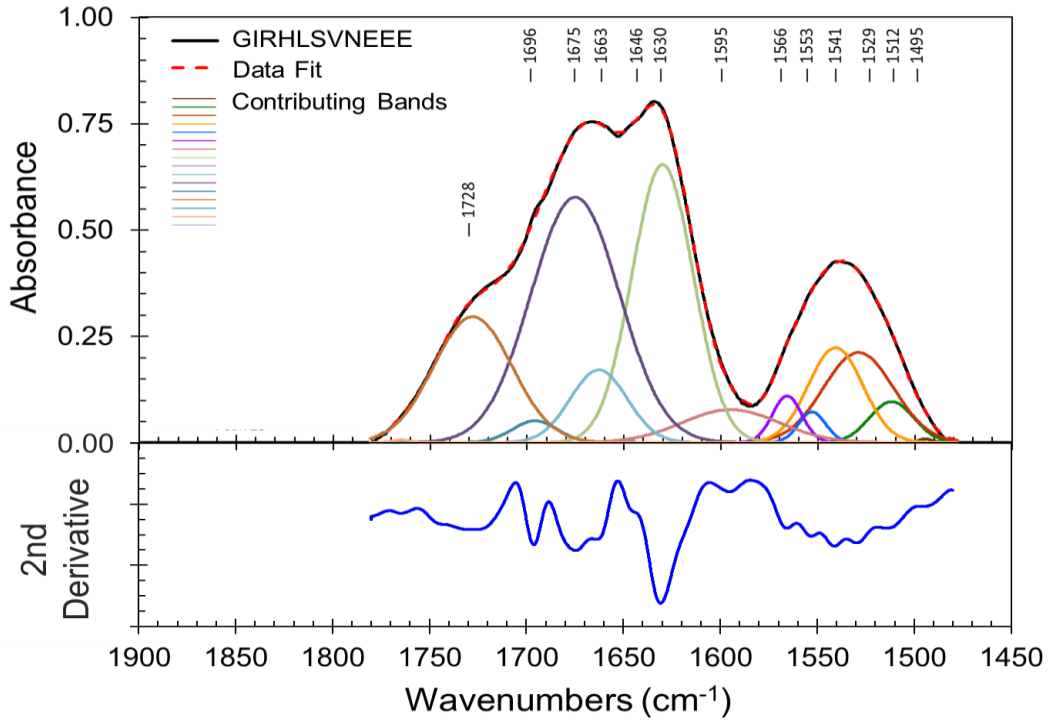

Figure C.26 FT-IR spectral analysis of the amide I and II bands of peptide **P13**.

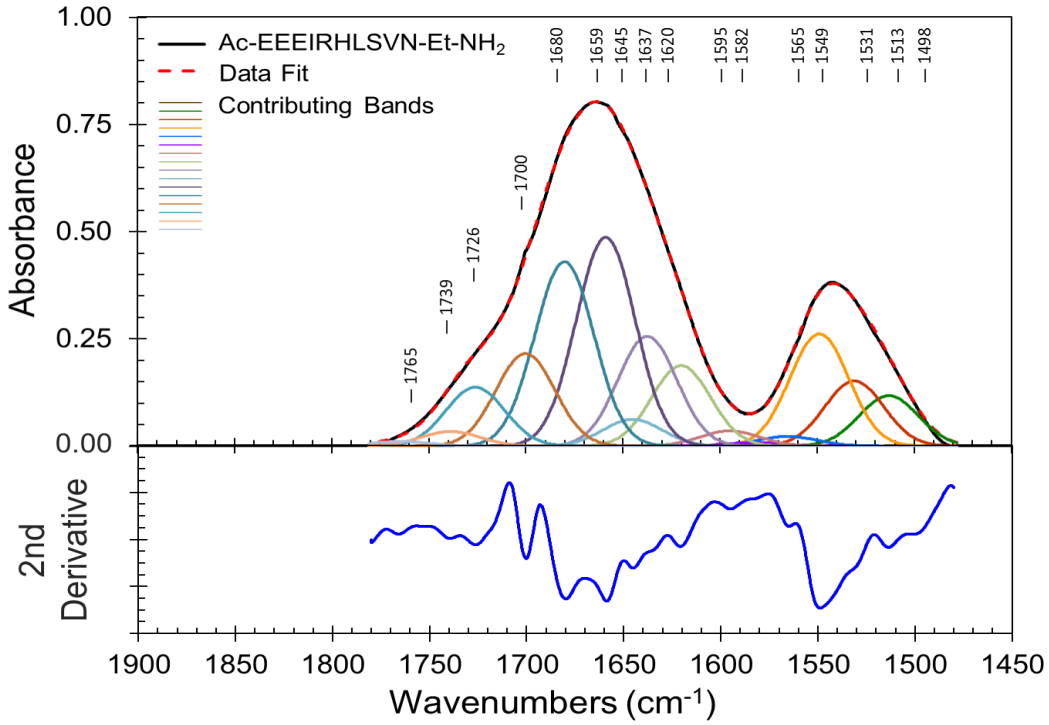

Figure C.27 FT-IR spectral analysis of the amide I and II bands of peptide **P14**.

C.2 Amide I and II Band Analysis

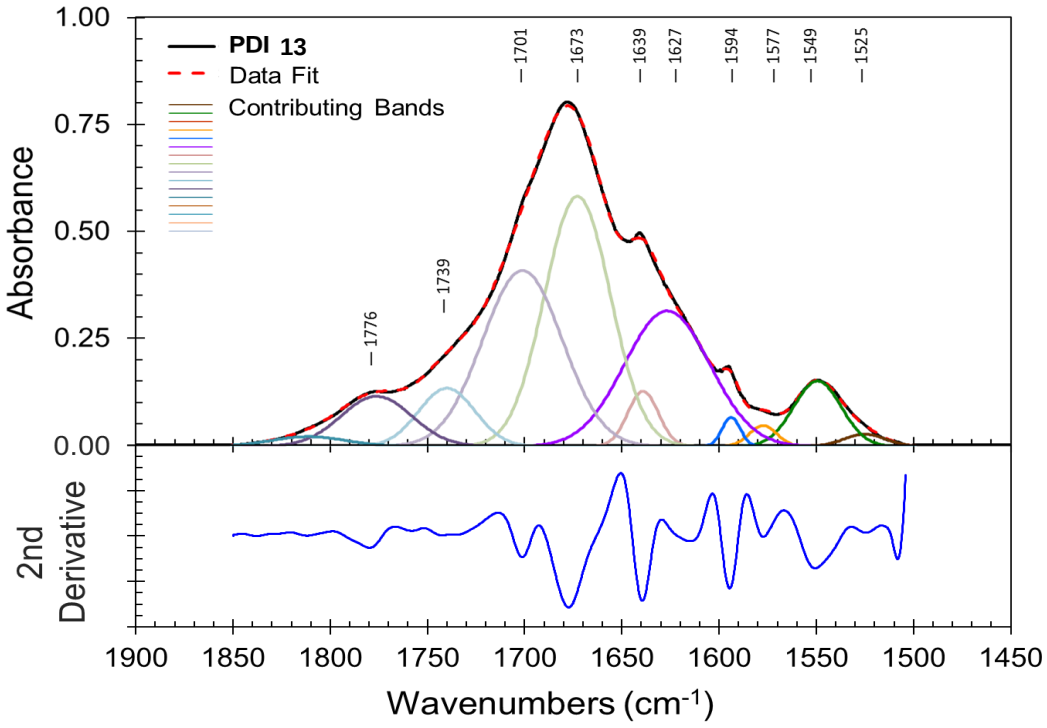

Figure C.28 FT-IR spectral analysis of the amide I and II bands of compound **13**.

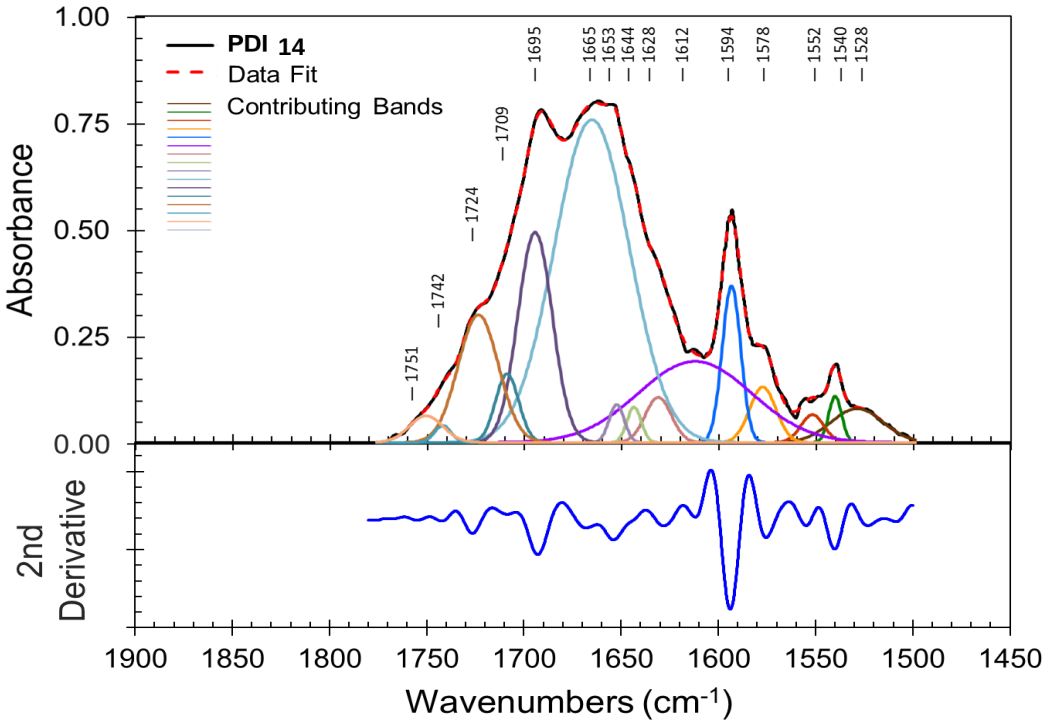

Figure C.29 FT-IR spectral analysis of the amide I and II bands of compound **14**.

C.2 Amide I and II Band Analysis

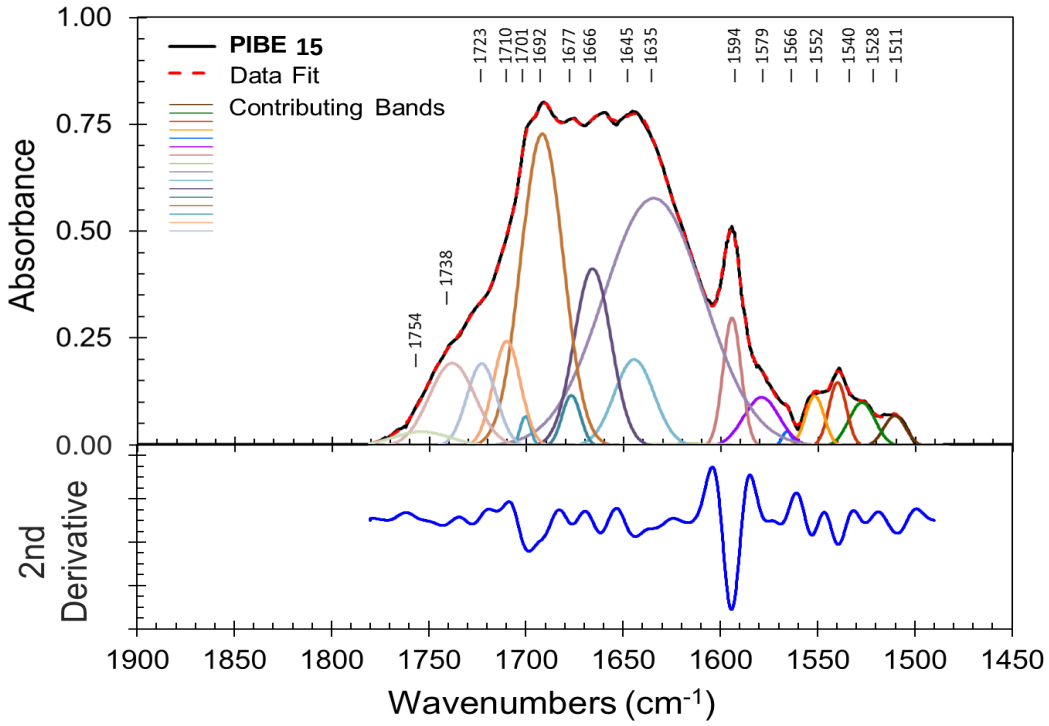

Figure C.30 FT-IR spectral analysis of the amide I and II bands of compound **15**.

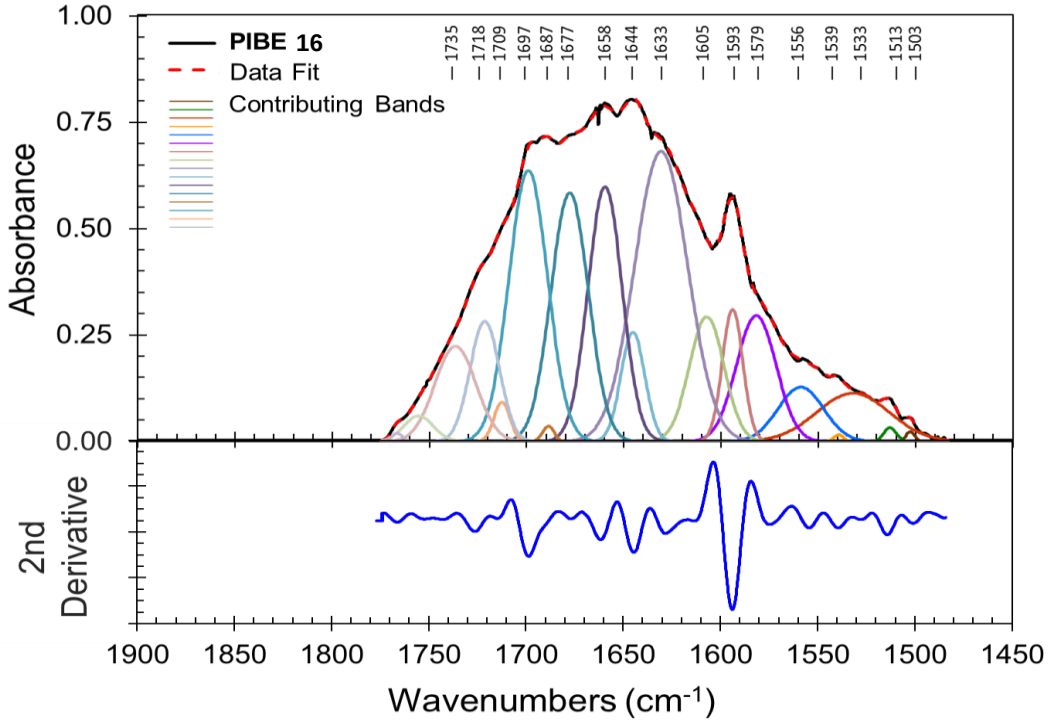

Figure C.31 FT-IR spectral analysis of the amide I and II bands of compound **16**.

Appendix - D

Temperature-Dependent Spectral Fitting

D.1 Temperature-Dependent Spectra of Aqueous PDI Solutions

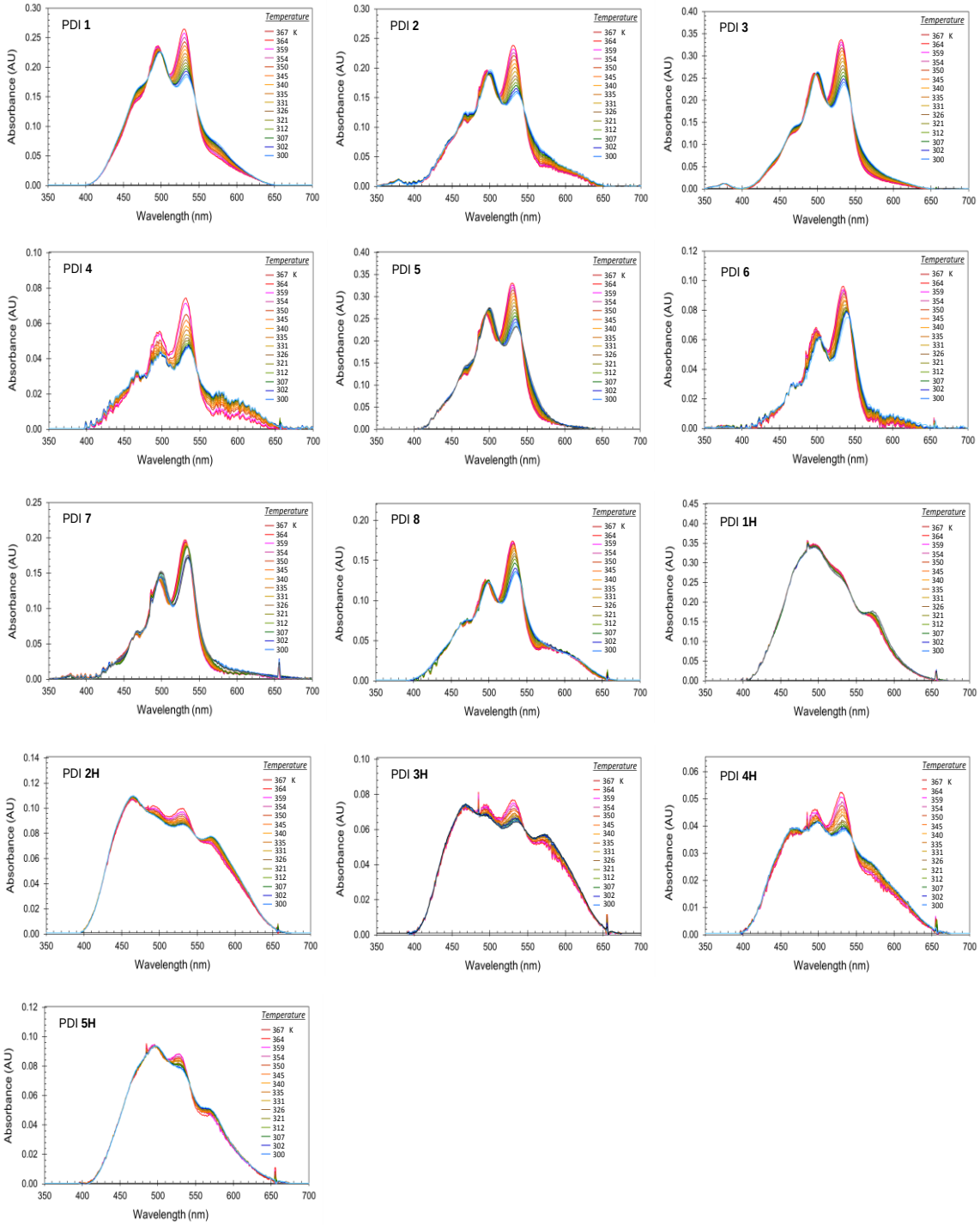

Figure D.1 Temperature-dependent spectra of aqueous solutions of PDIs **1**-**8** and **1H**-**5H** from the thermodynamic study discussed in Chapter 3.

D.2 Spectral Data Fitting of Aqueous PDI Solutions

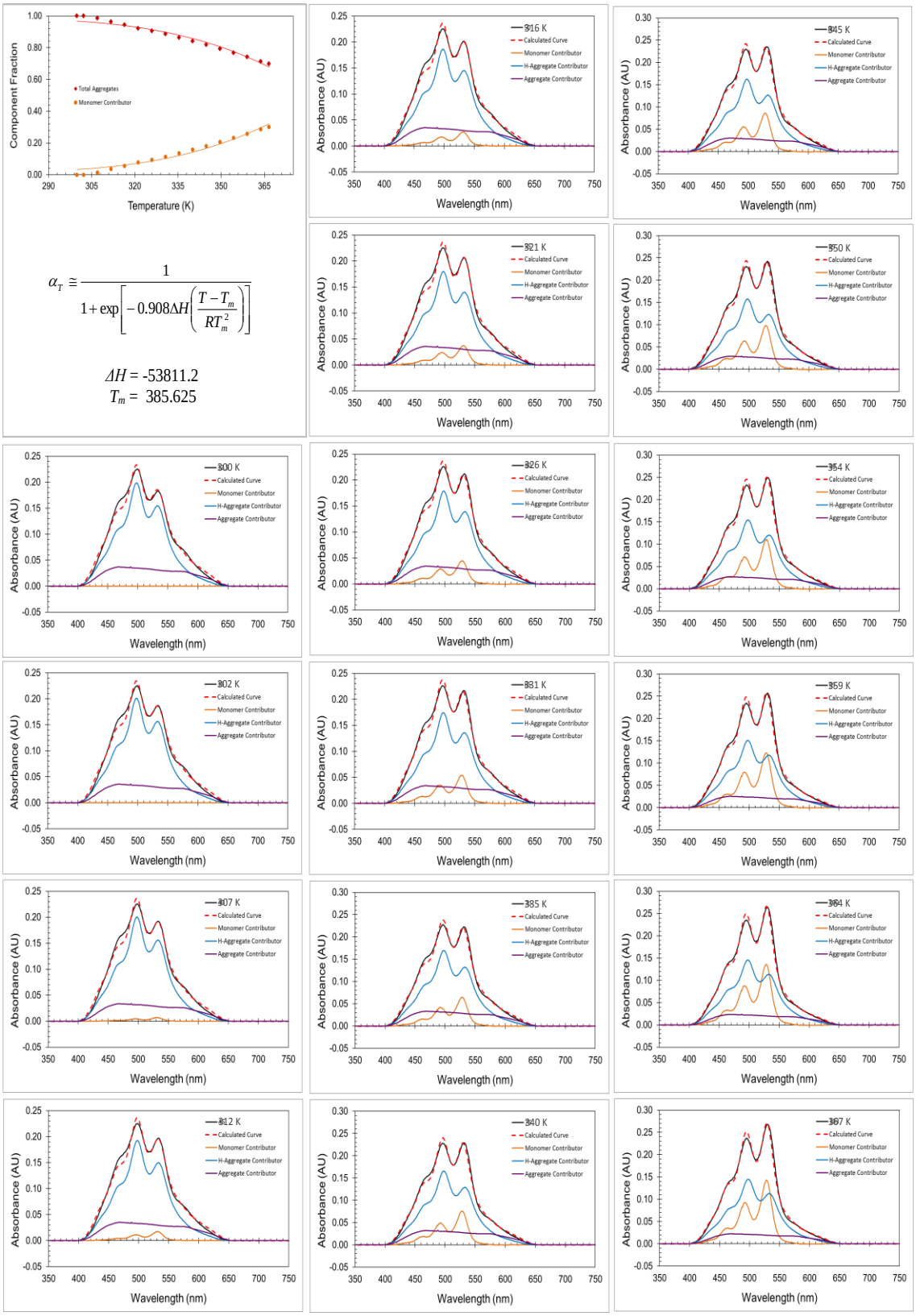

Figure D.2 Spectral data fitting for PDI **1** in water with increasing temperature.

D.2 Spectral Data Fitting of Aqueous PDI Solutions

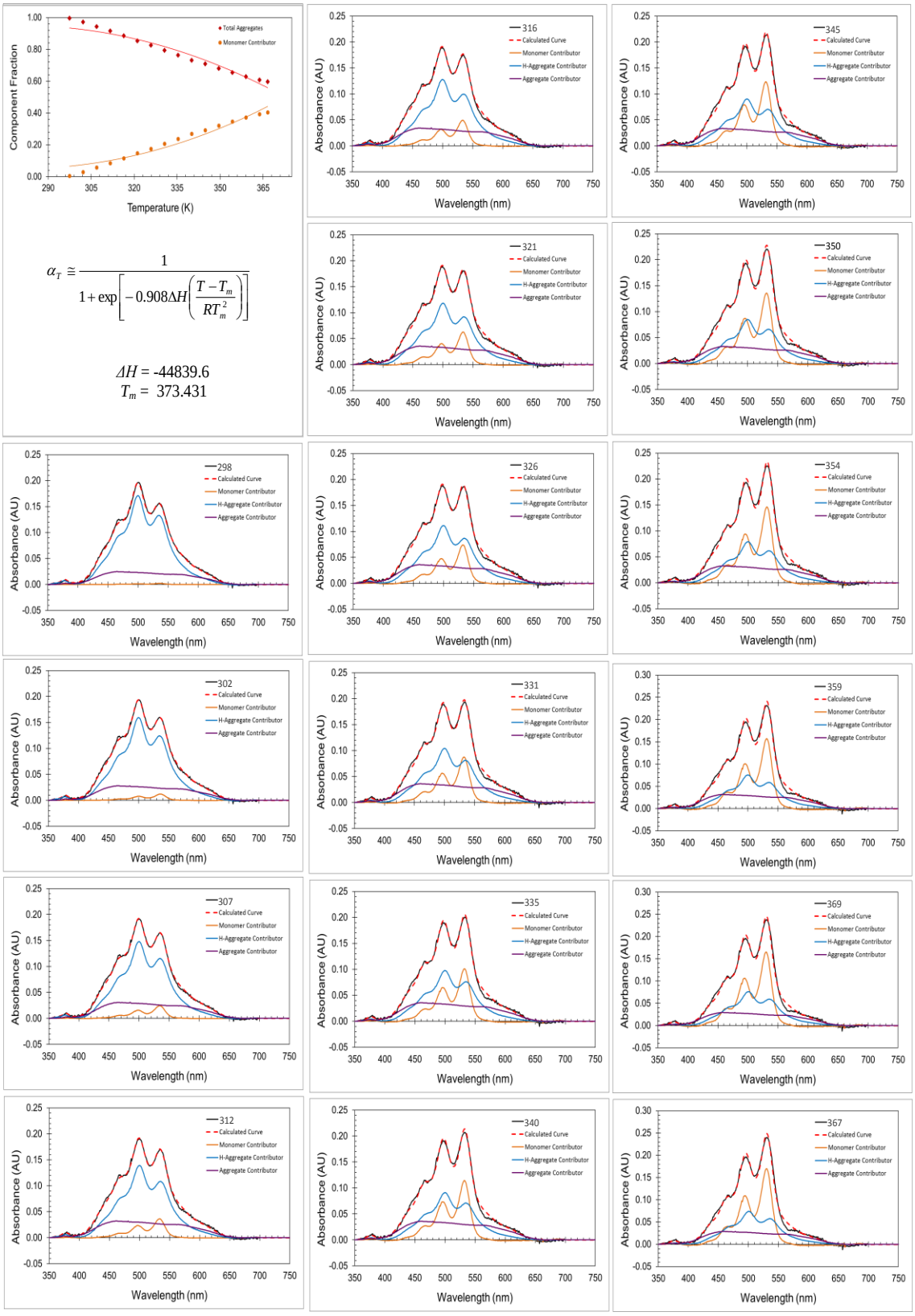

Figure D.3 Spectral data fitting for PDI **2** in water with increasing temperature.

D.2 Spectral Data Fitting of Aqueous PDI Solutions

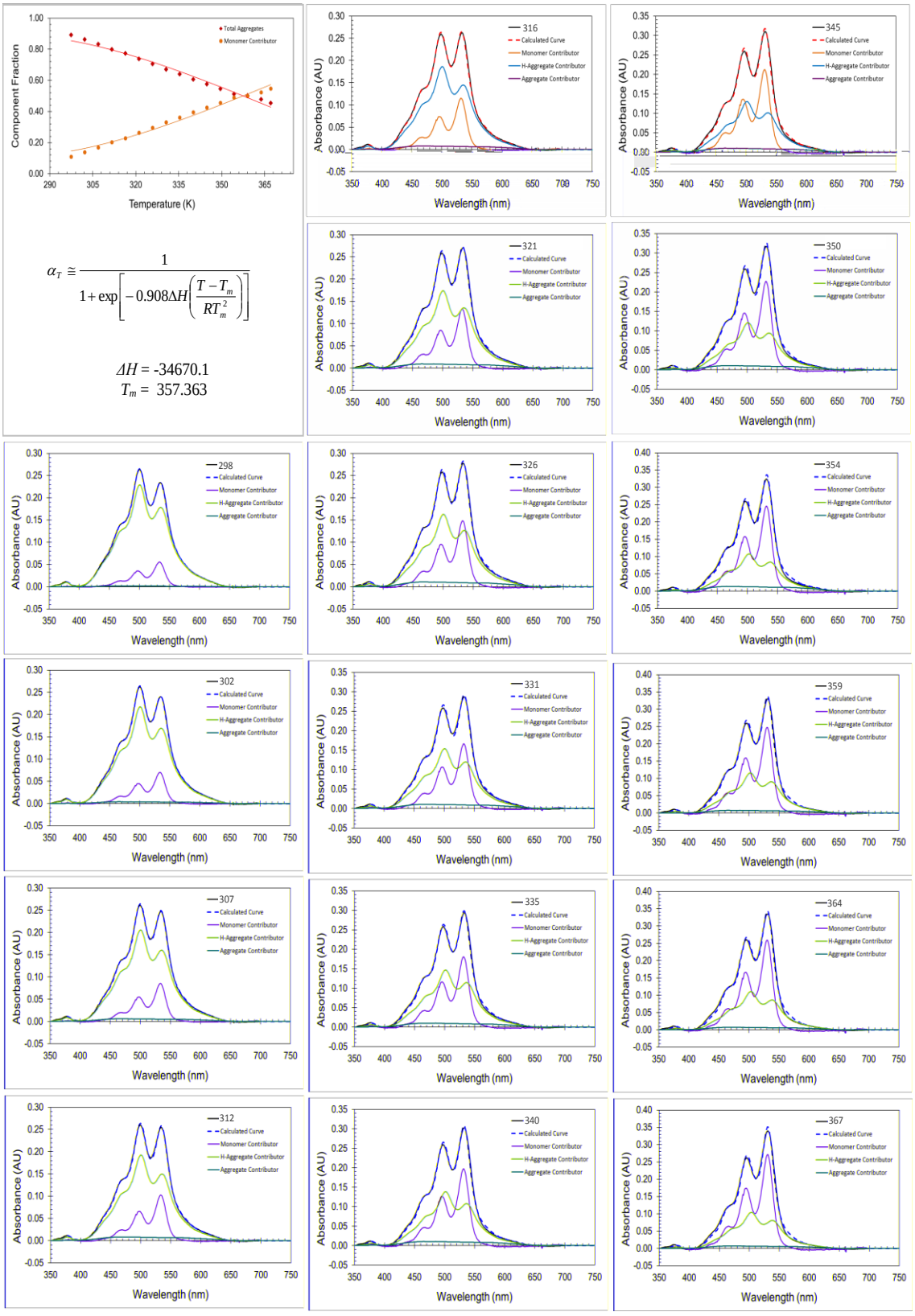

Figure D.4 Spectral data fitting for PDI **3** in water with increasing temperature.

D.2 Spectral Data Fitting of Aqueous PDI Solutions

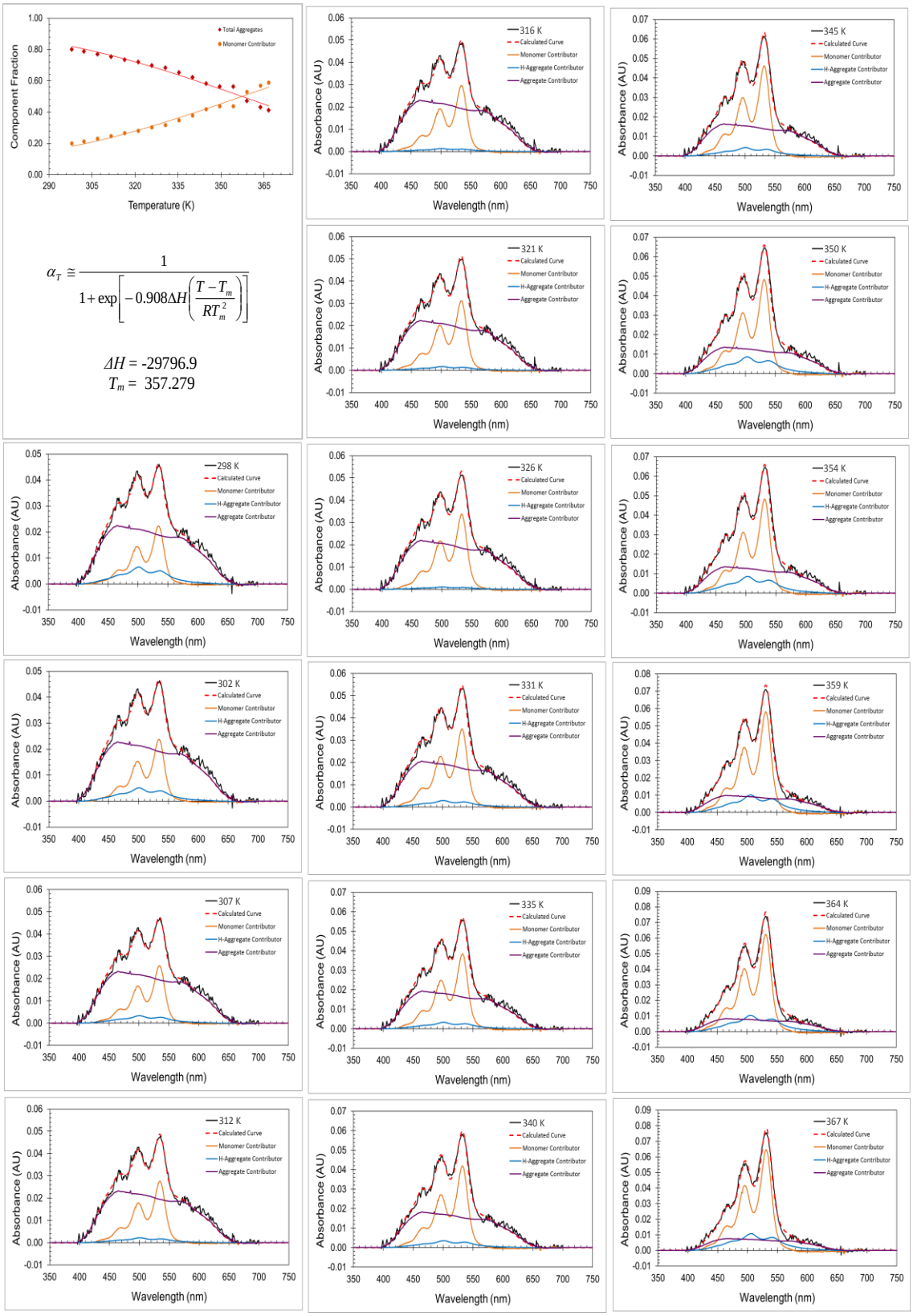

Figure D.5 Spectral data fitting for PDI **4** in water with increasing temperature.

D.2 Spectral Data Fitting of Aqueous PDI Solutions

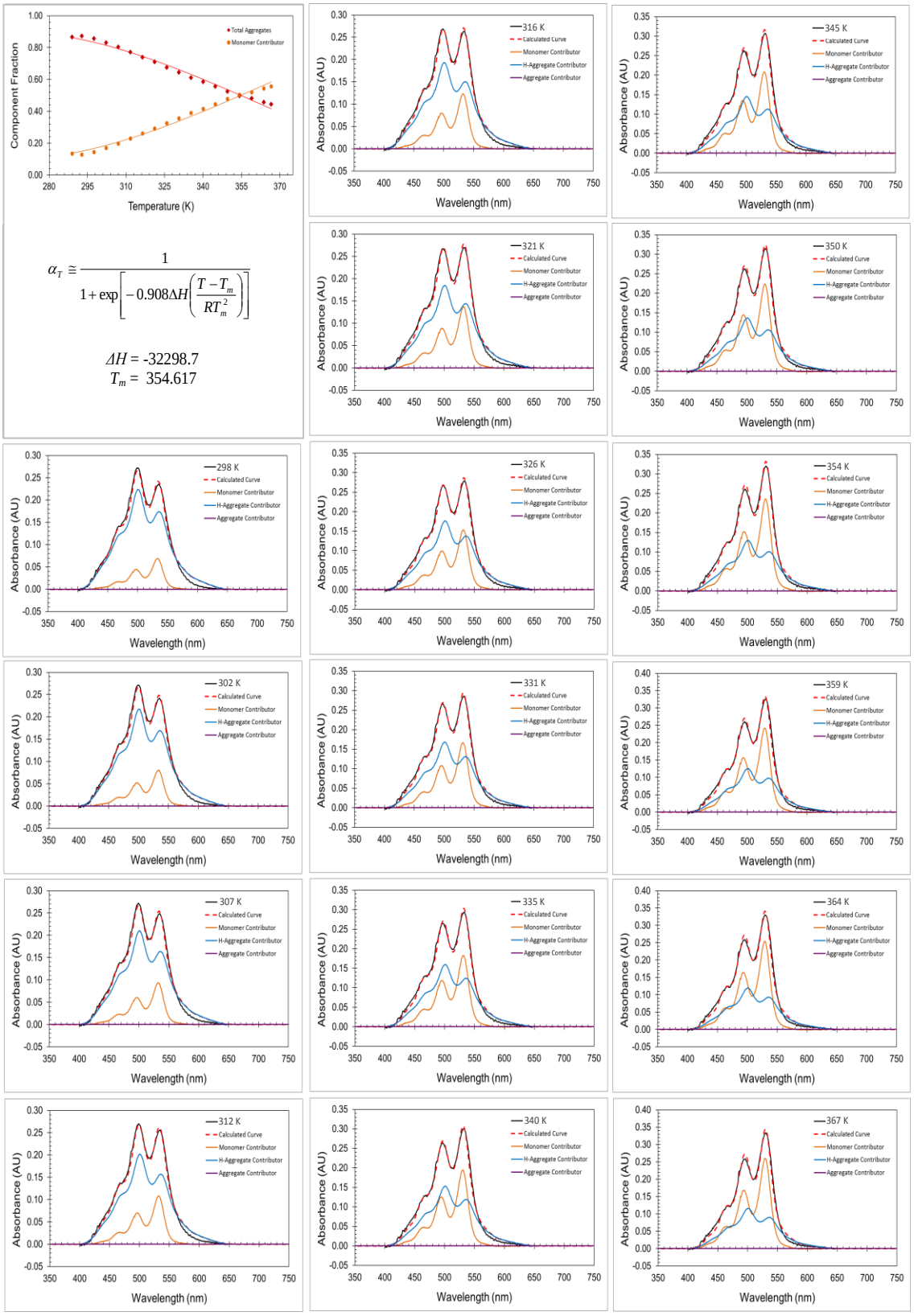

Figure D.6 Spectral data fitting for PDI **5** in water with increasing temperature.

D.2 Spectral Data Fitting of Aqueous PDI Solutions

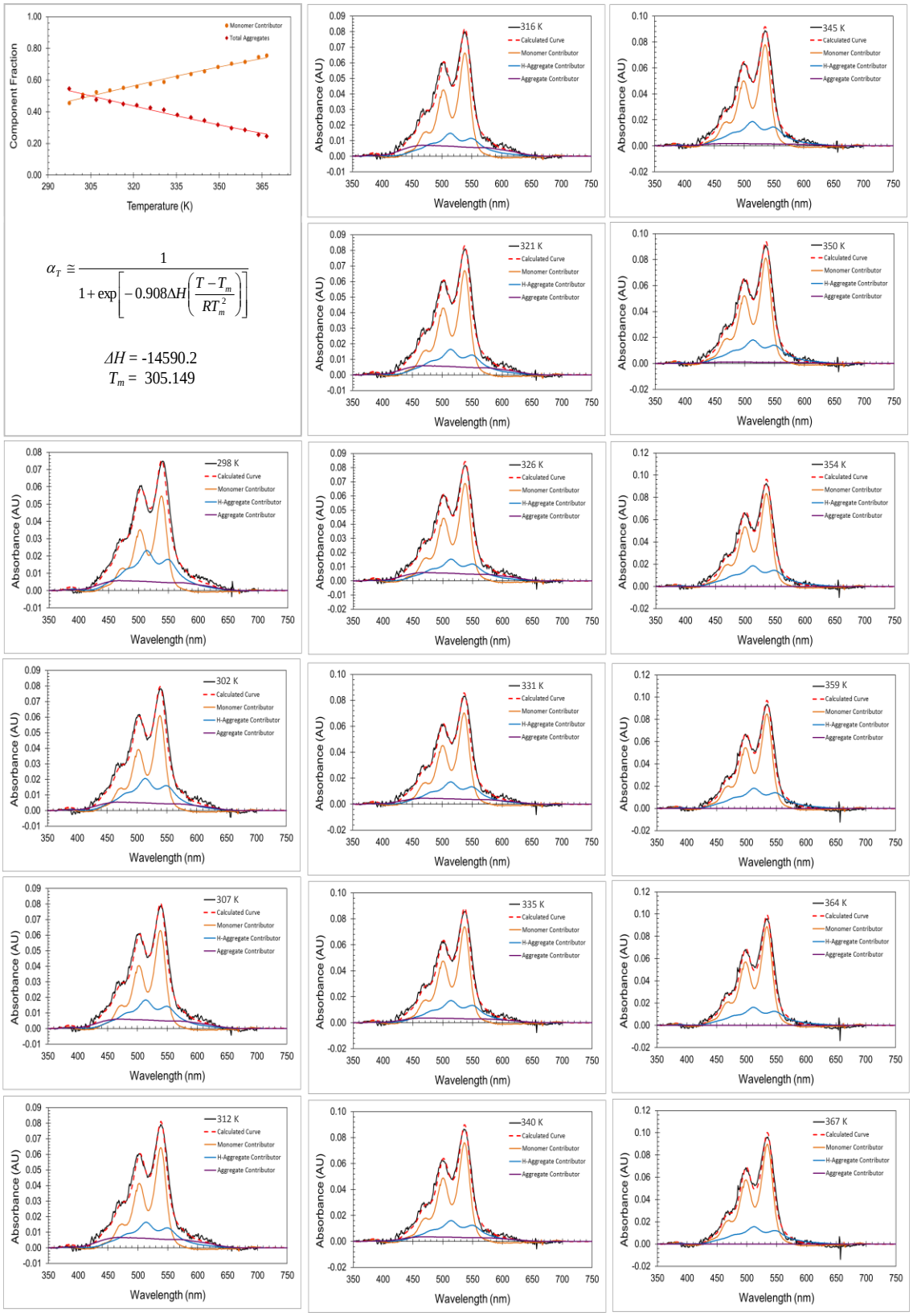

Figure D.7 Spectral data fitting for PDI **6** in water with increasing temperature.

D.2 Spectral Data Fitting of Aqueous PDI Solutions

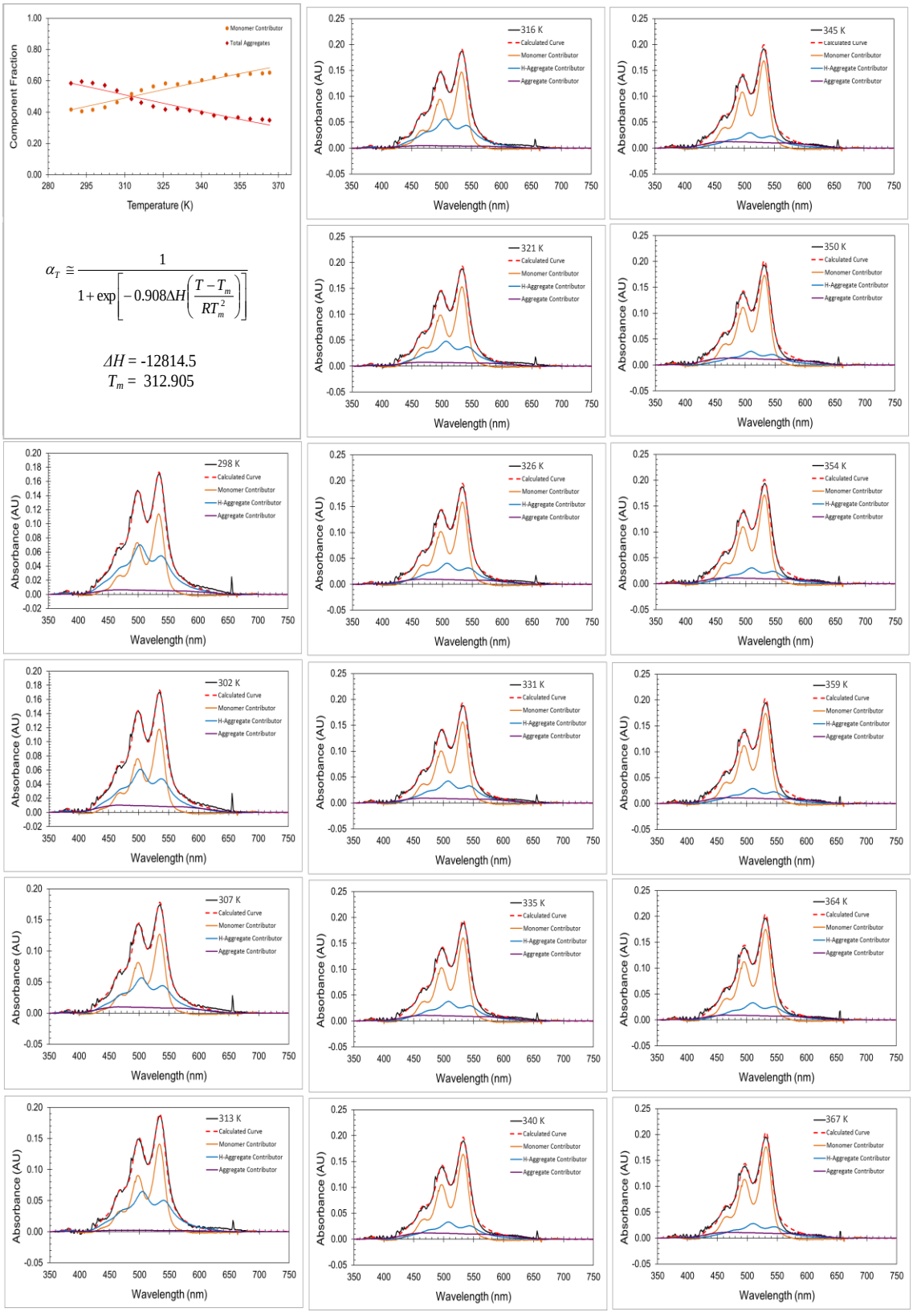

Figure D.8 Spectral data fitting for PDI **7** in water with increasing temperature.

D.2 Spectral Data Fitting of Aqueous PDI Solutions

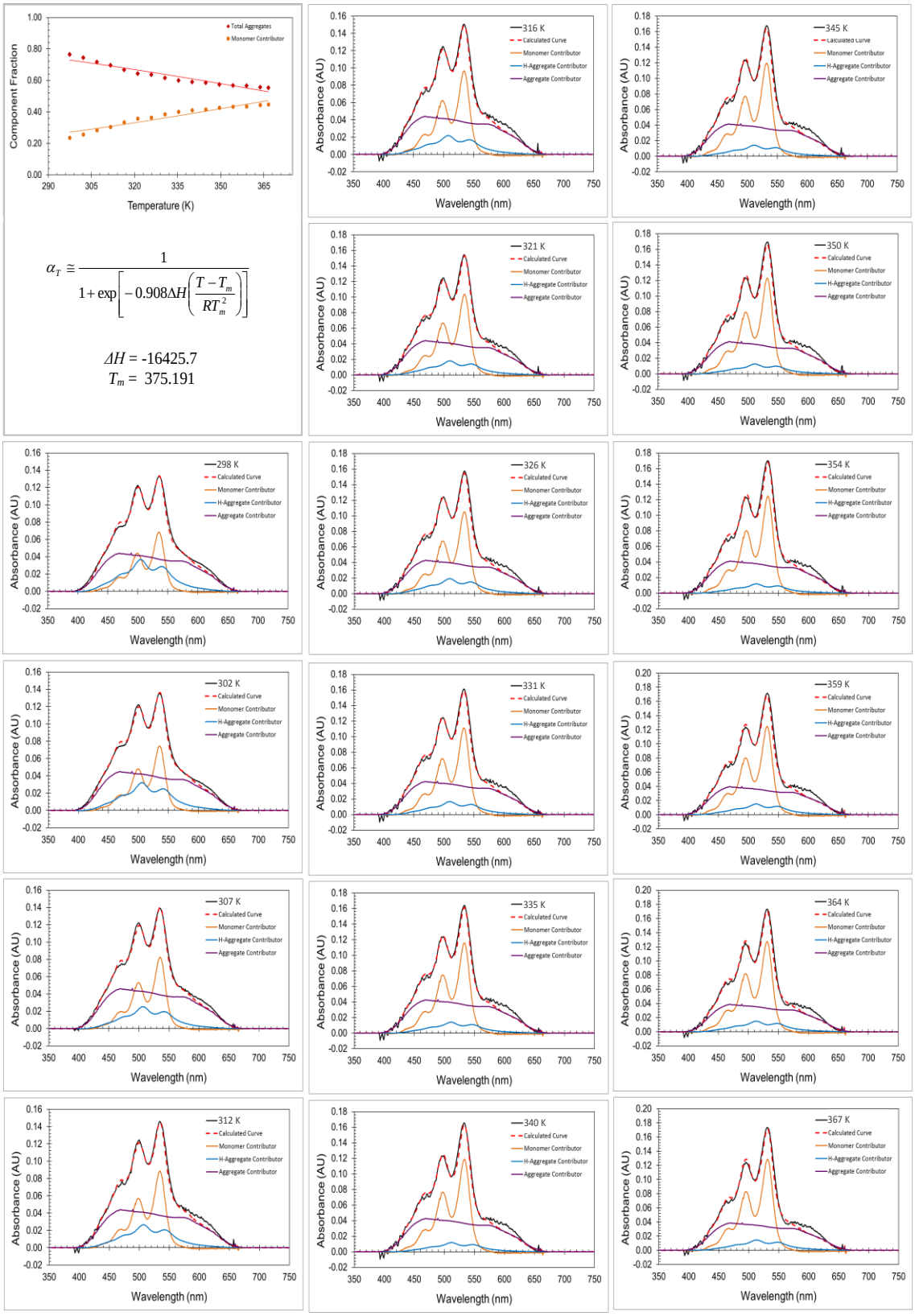

Figure D.9 Spectral data fitting for PDI **8** in water with increasing temperature.

D.2 Spectral Data Fitting of Aqueous PDI Solutions

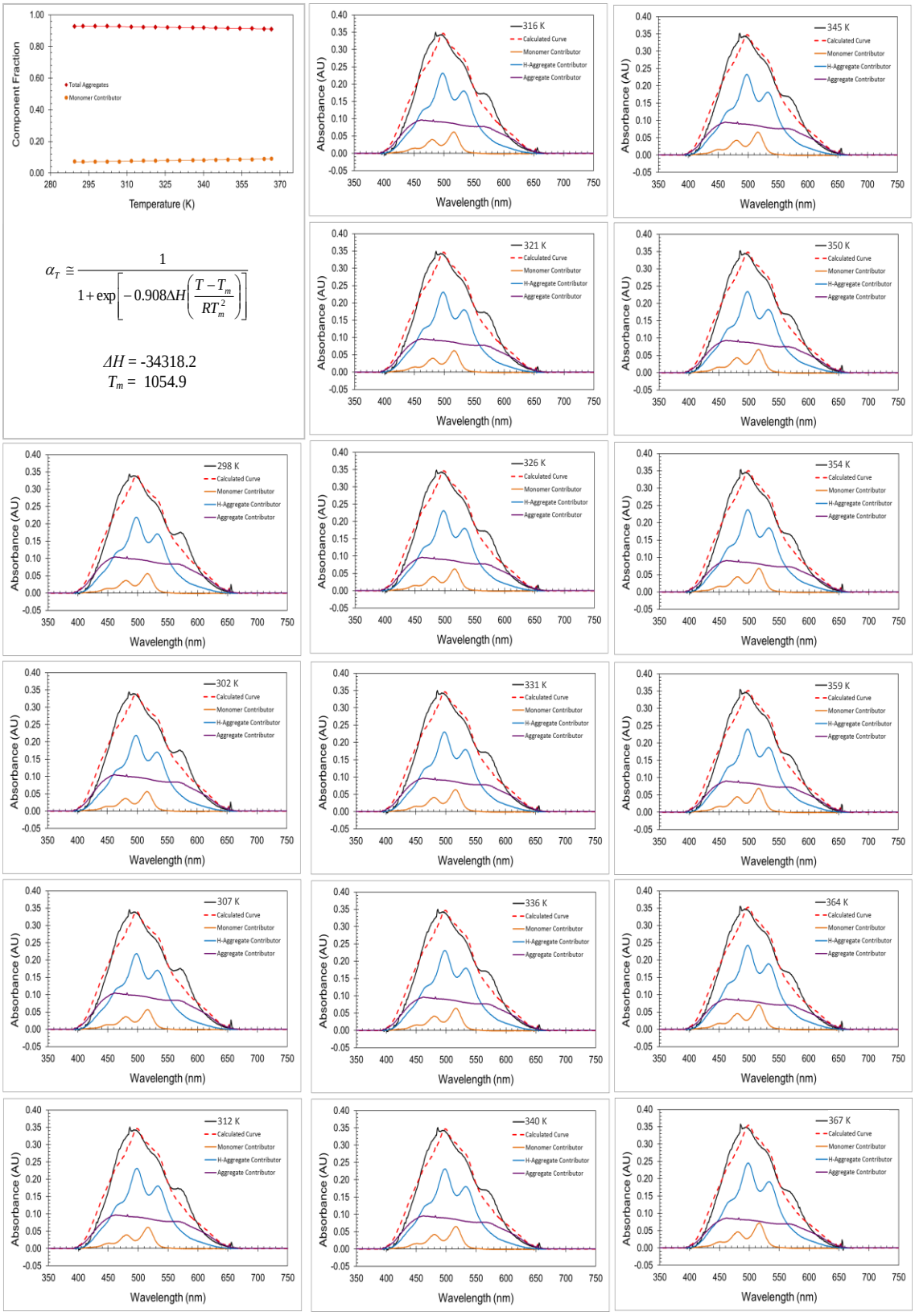

Figure D.10 Spectral data fitting for PDI **1H** in water with increasing temperature.

D.2 Spectral Data Fitting of Aqueous PDI Solutions

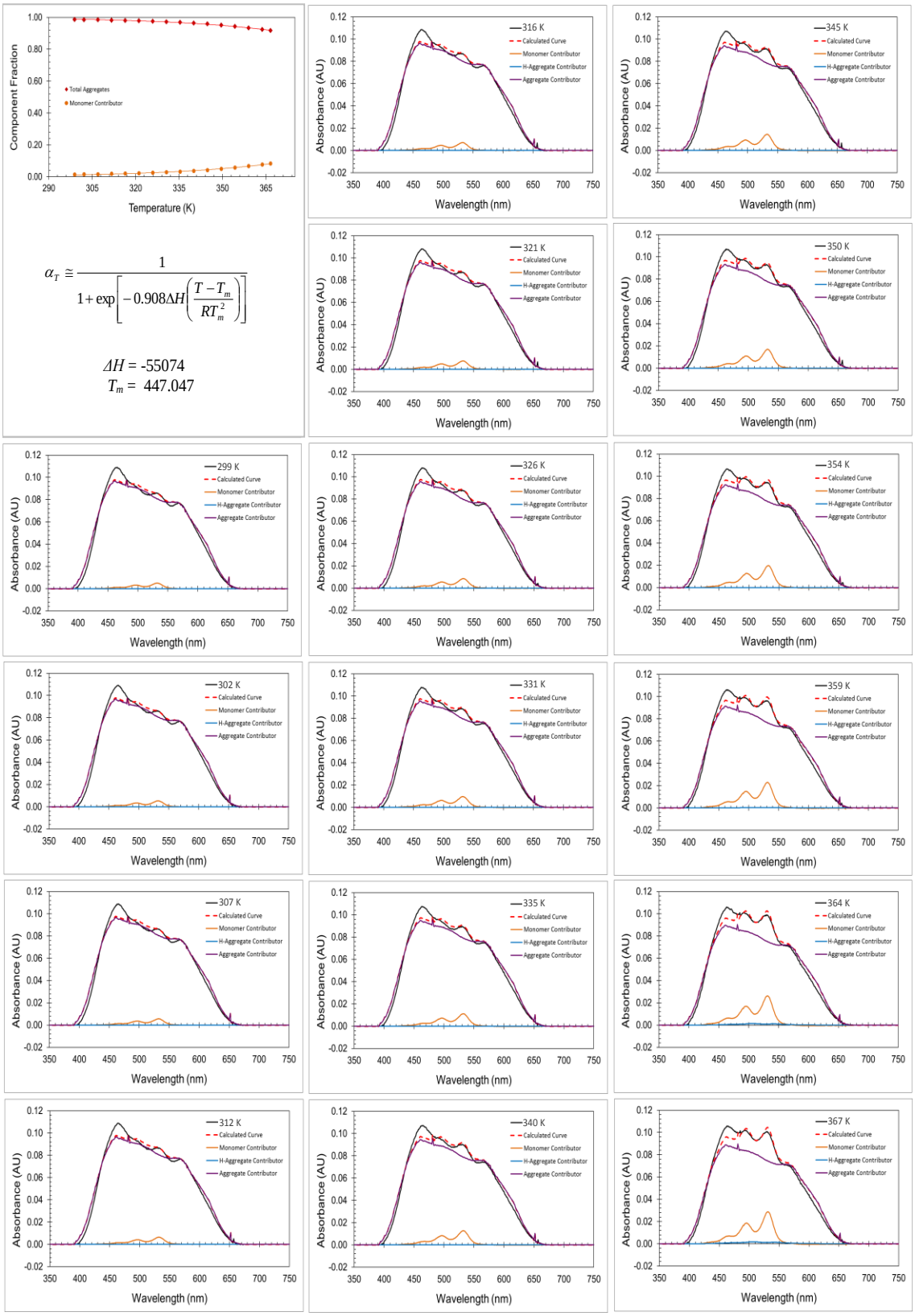

Figure D.11 Spectral data fitting for PDI **2H** in water with increasing temperature.

D.2 Spectral Data Fitting of Aqueous PDI Solutions

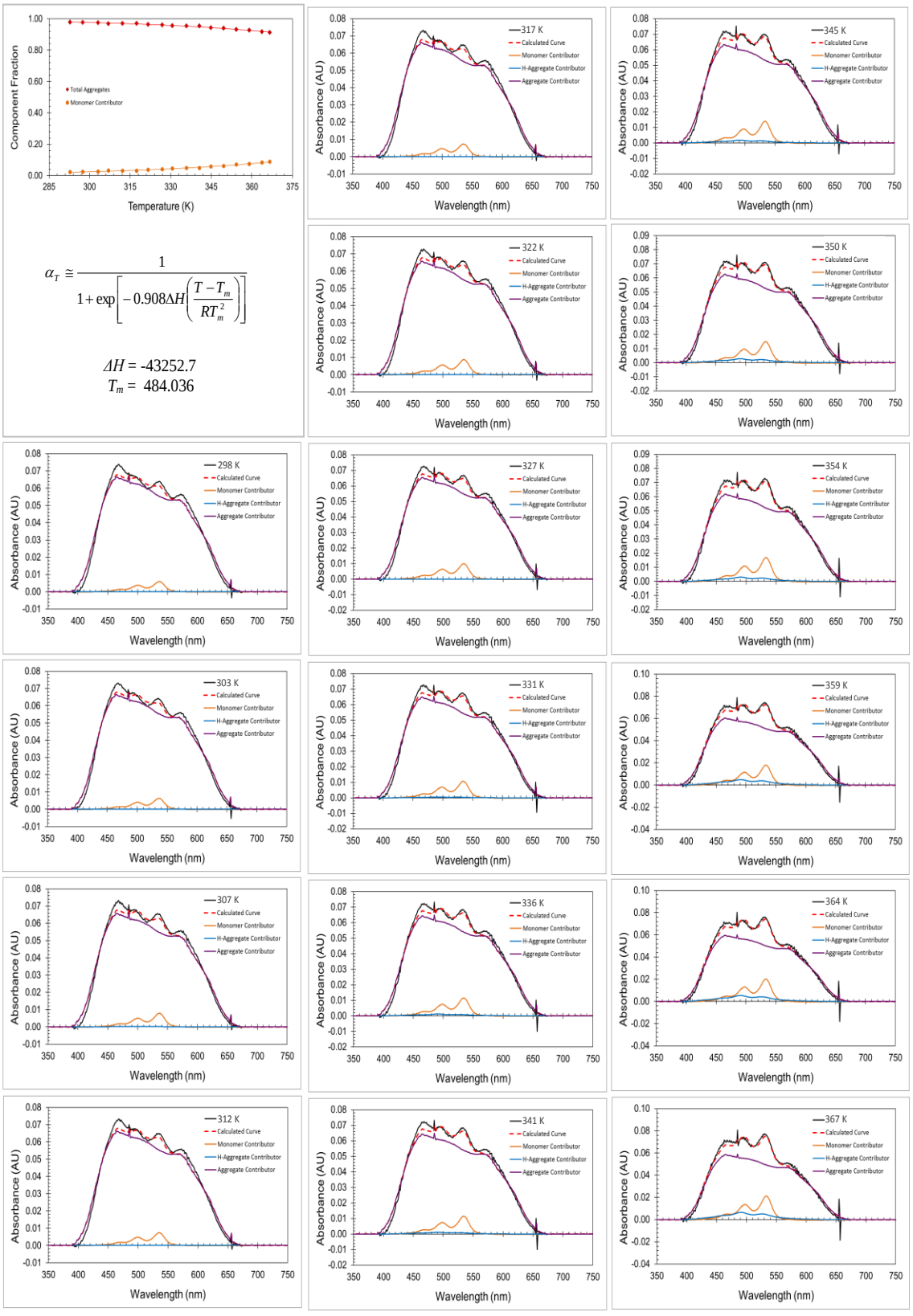

Figure D.12 Spectral data fitting for PDI **3H** in water with increasing temperature.

D.2 Spectral Data Fitting of Aqueous PDI Solutions

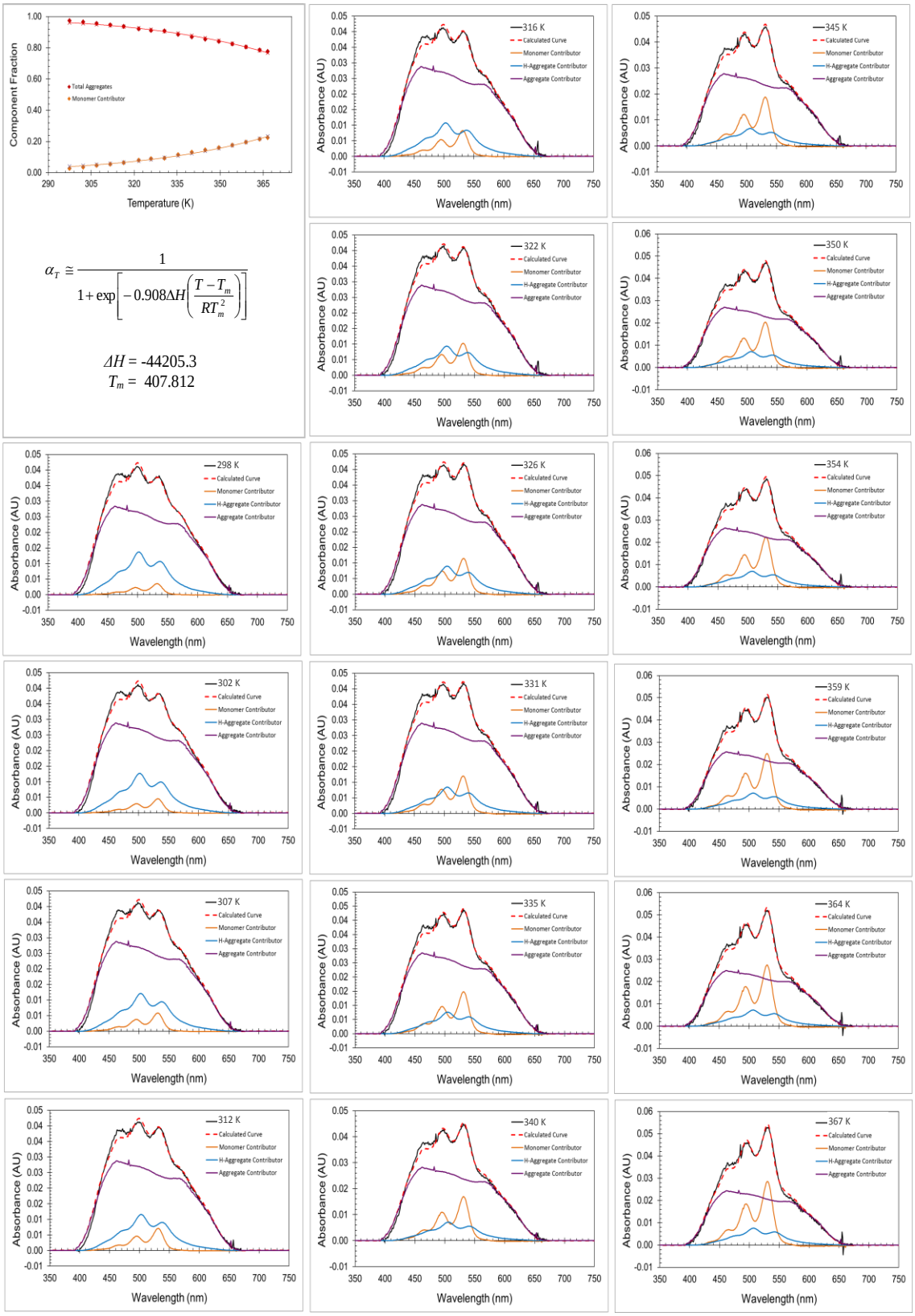

Figure D.13 Spectral data fitting for PDI **4H** in water with increasing temperature.

D.2 Spectral Data Fitting of Aqueous PDI Solutions

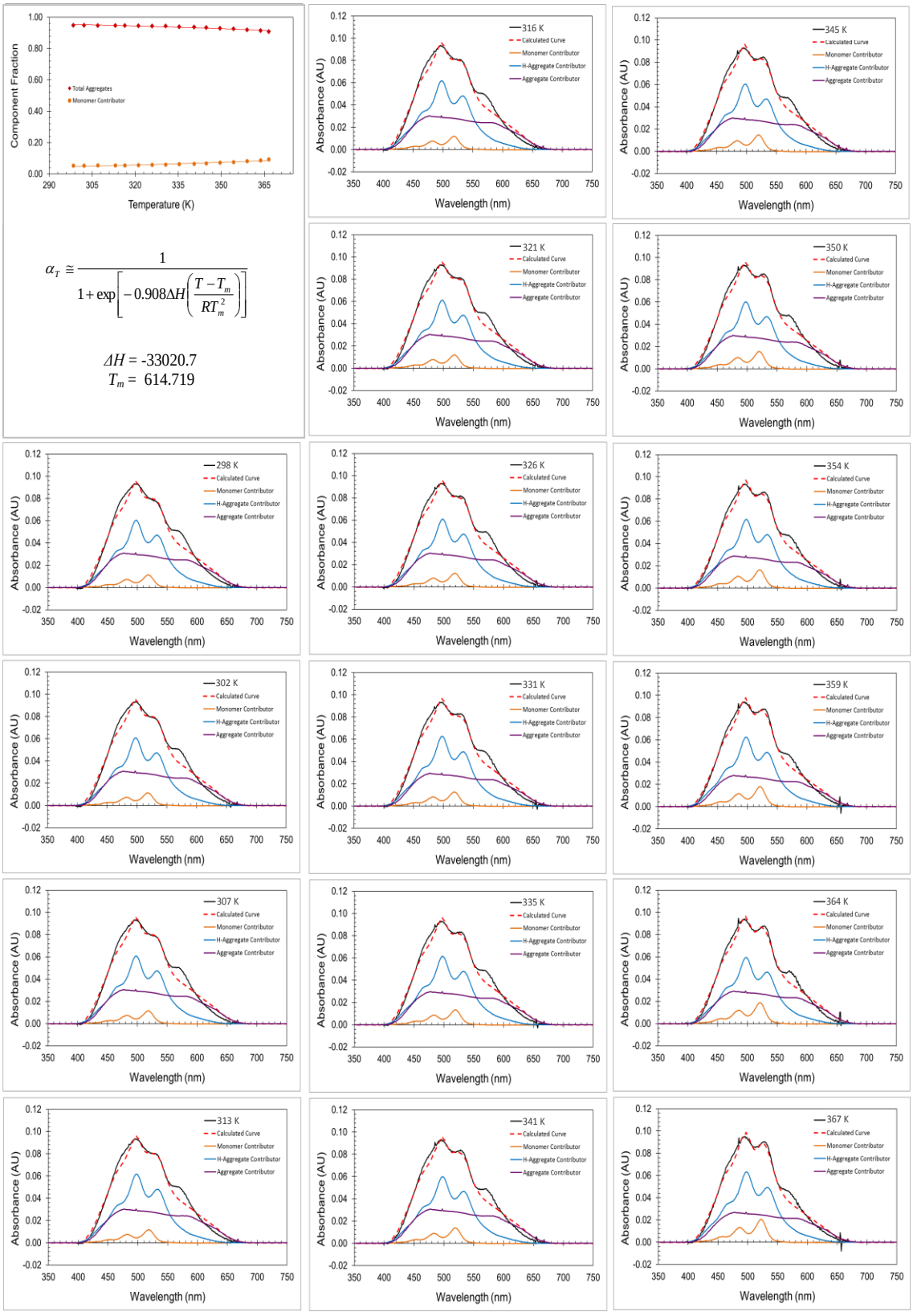

Figure D.14 Spectral data fitting for PDI **5H** in water with increasing temperature.

D.3 Spectral Data Fitting of Selected Organic PDI Solutions

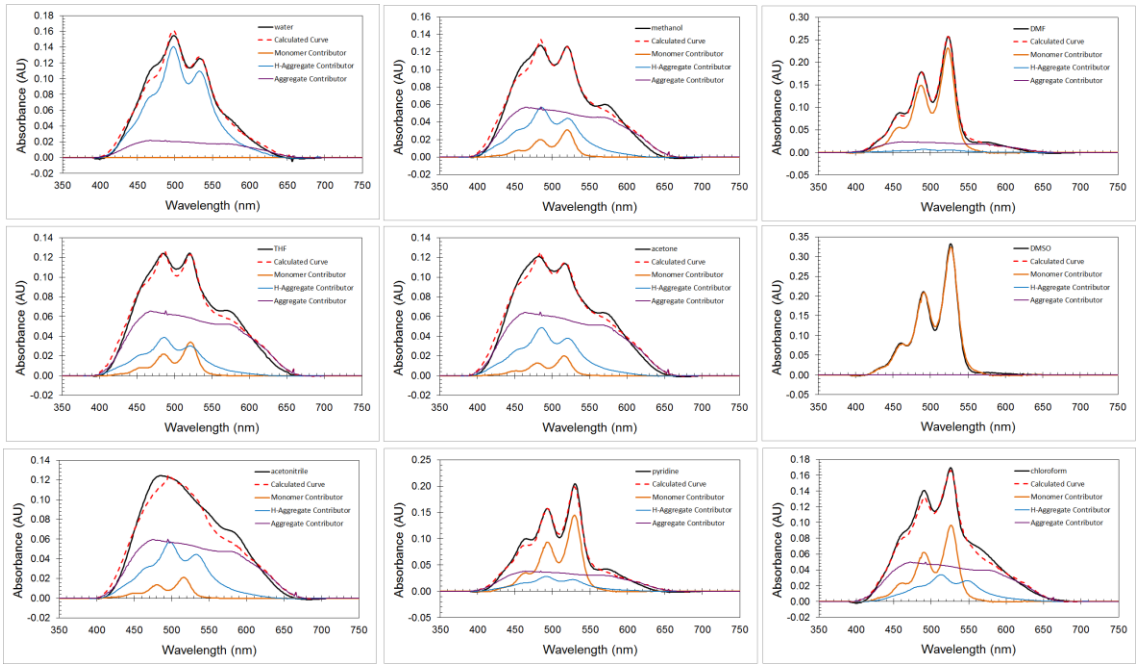

Figure D.15 Spectral data fitting for PDI **1** in selected organic solvents (water comparison included).

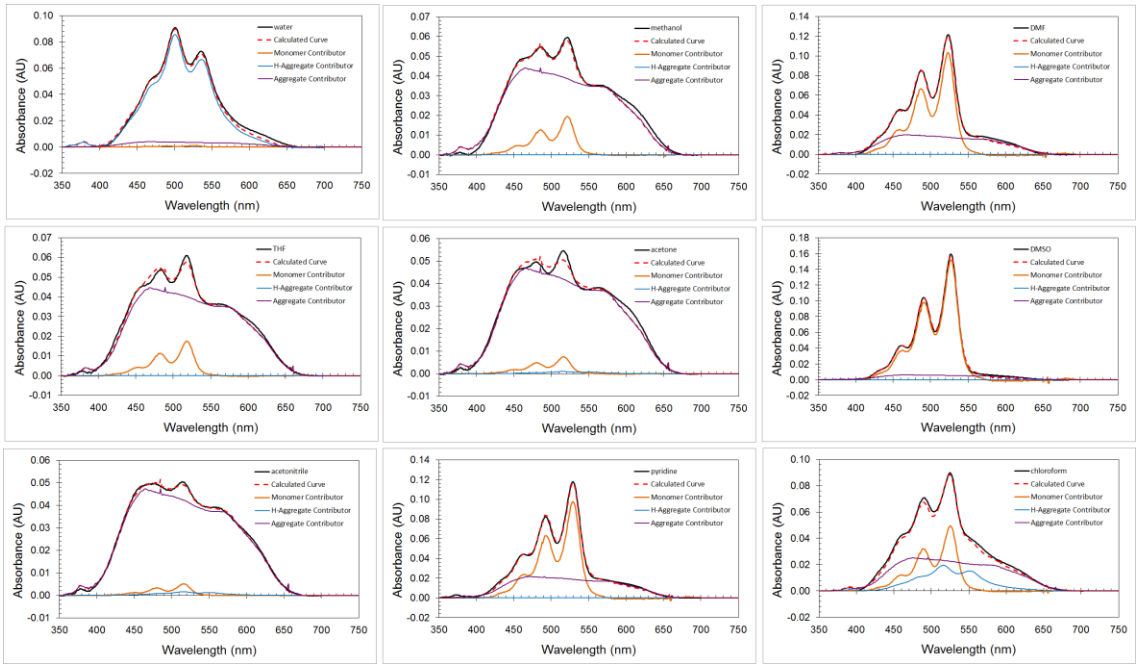

Figure D.16 Spectral data fitting for PDI **2** in selected organic solvents (water comparison included).

D.3 Spectral Data Fitting of Selected Organic PDI Solutions

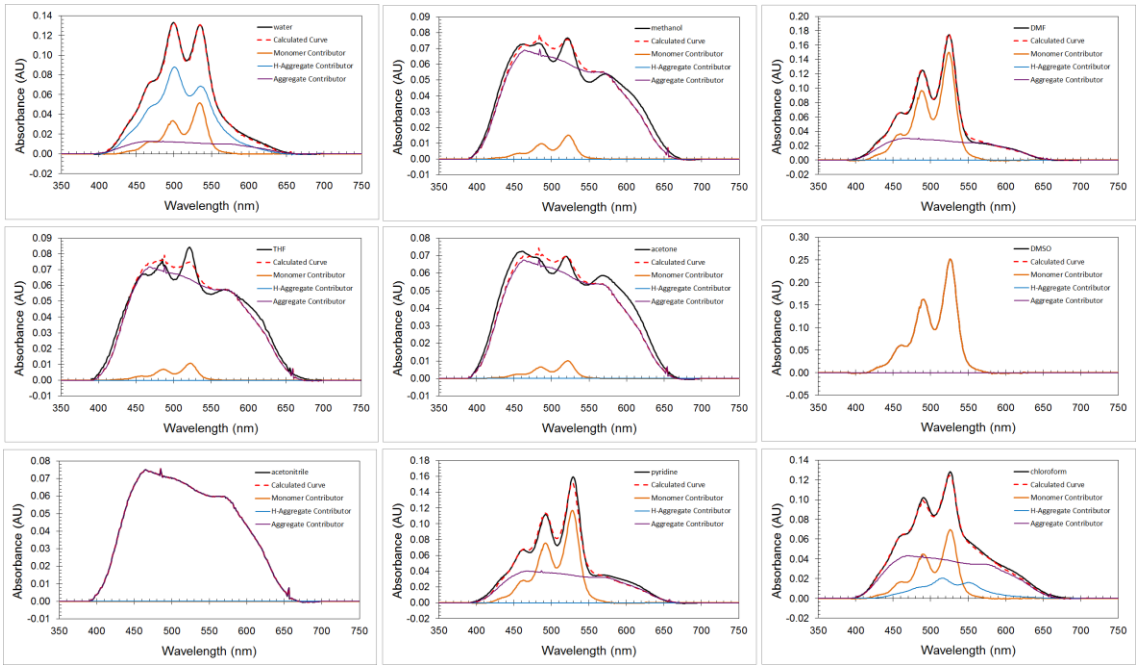

Figure D.17 Spectral data fitting for PDI **3** in selected organic solvents (water comparison included).

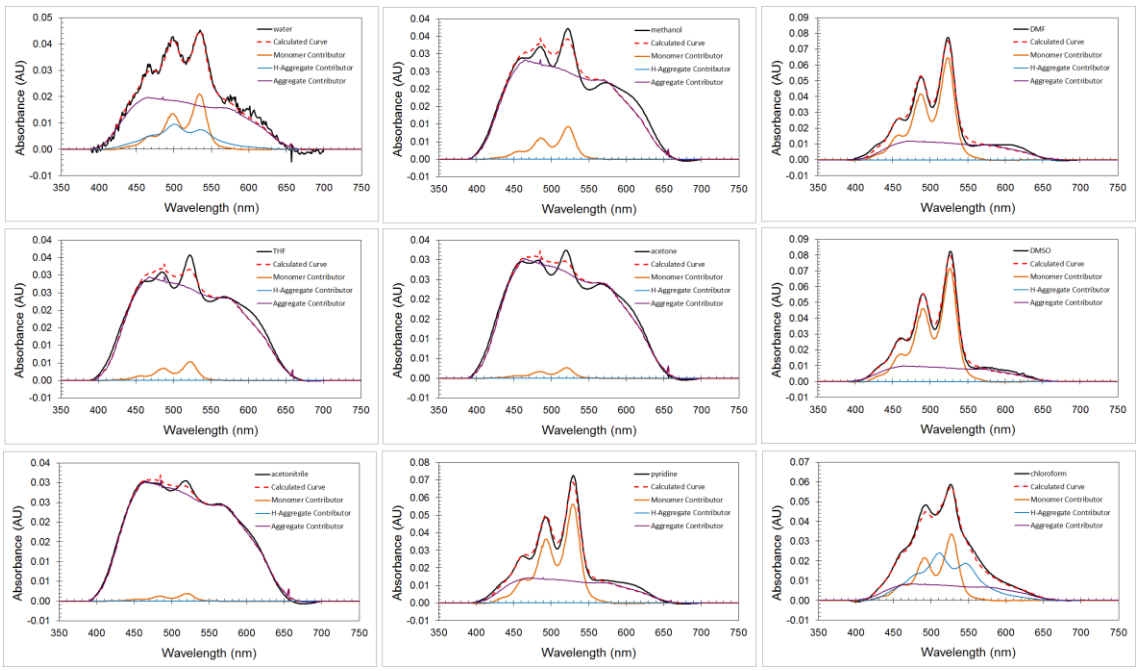

Figure D.18 Spectral data fitting for PDI **4** in selected organic solvents (water comparison included).

D.3 Spectral Data Fitting of Selected Organic PDI Solutions

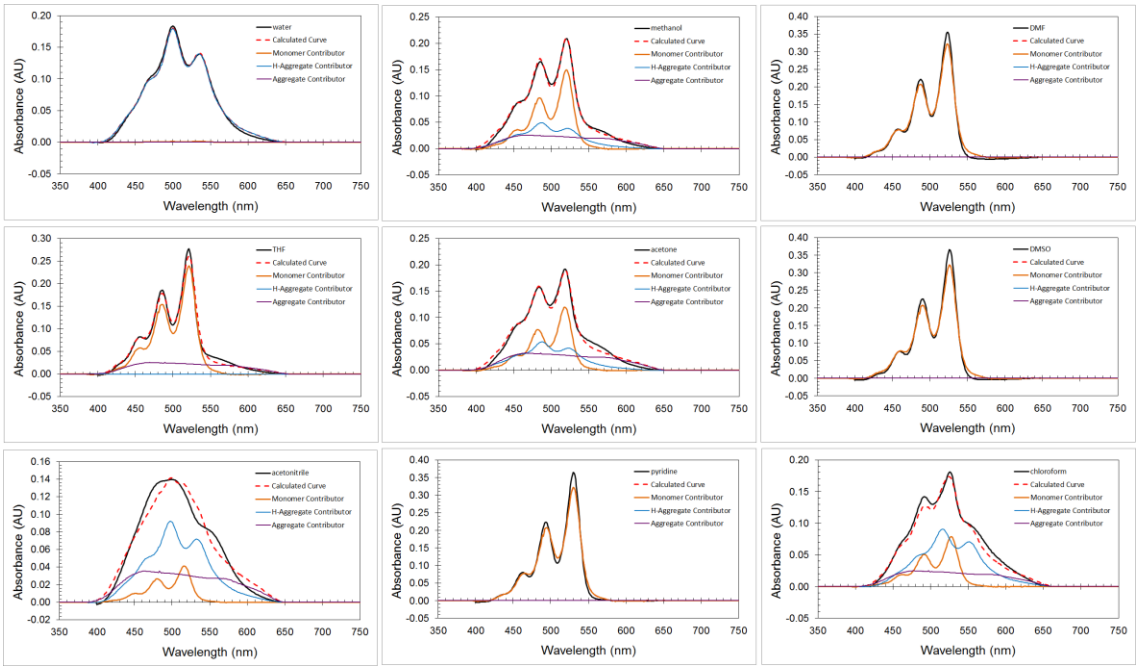

Figure D.19 Spectral data fitting for PDI **5** in selected organic solvents (water comparison included).

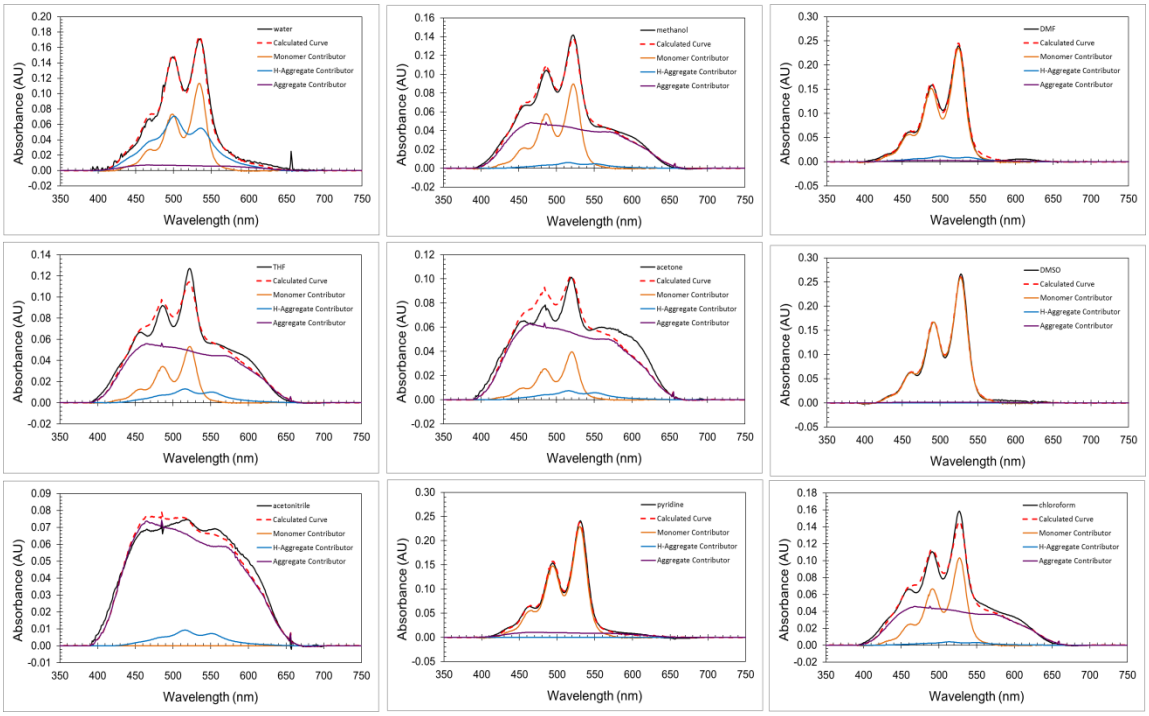

Figure D.20 Spectral data fitting for PDI **7** in selected organic solvents (water comparison included).

D.3 Spectral Data Fitting of Selected Organic PDI Solutions

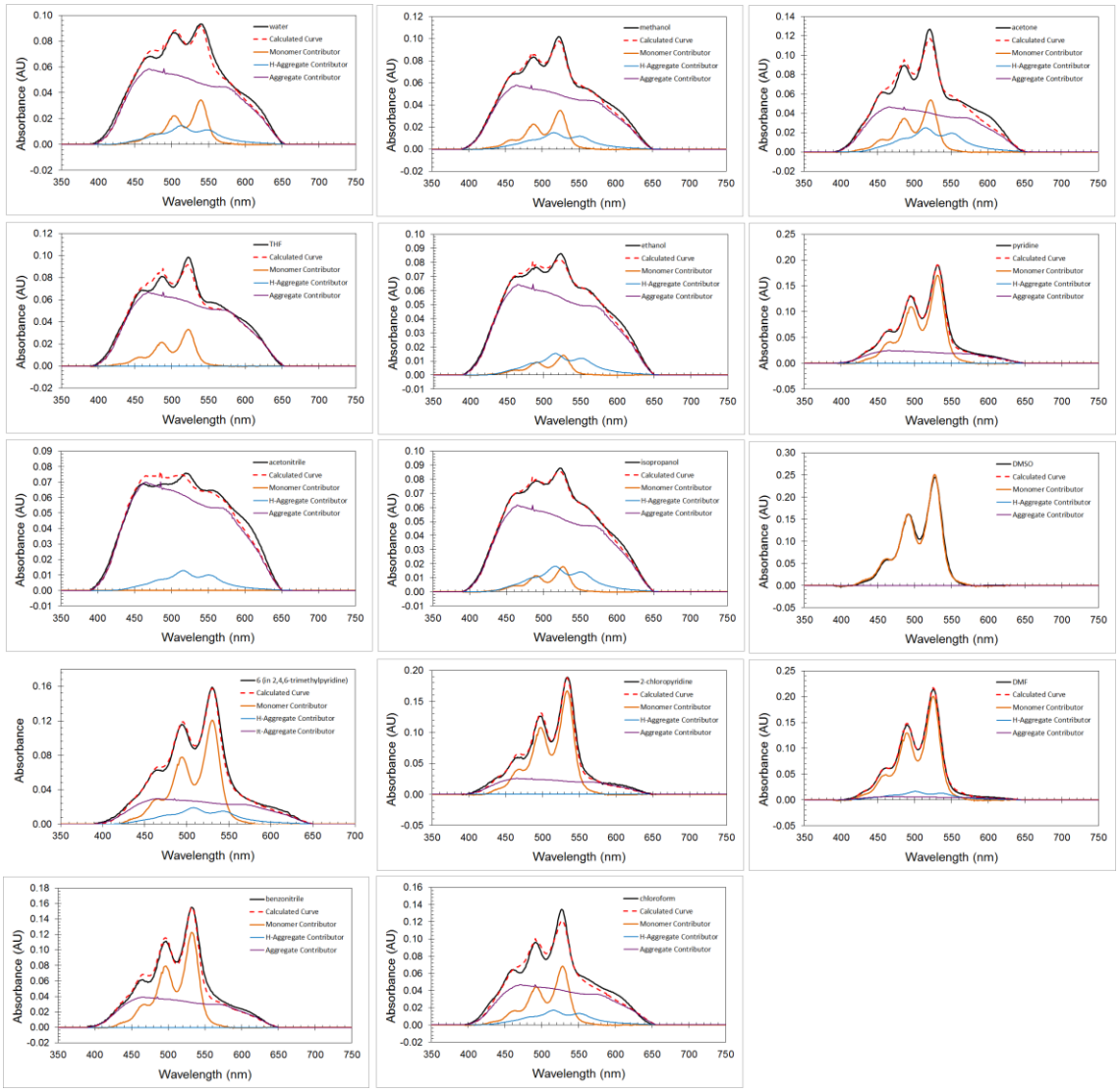

Figure D.21 Spectral data fitting for PDI **6** in selected organic solvents (water comparison included).

D.3 Spectral Data Fitting of Selected Organic PDI Solutions

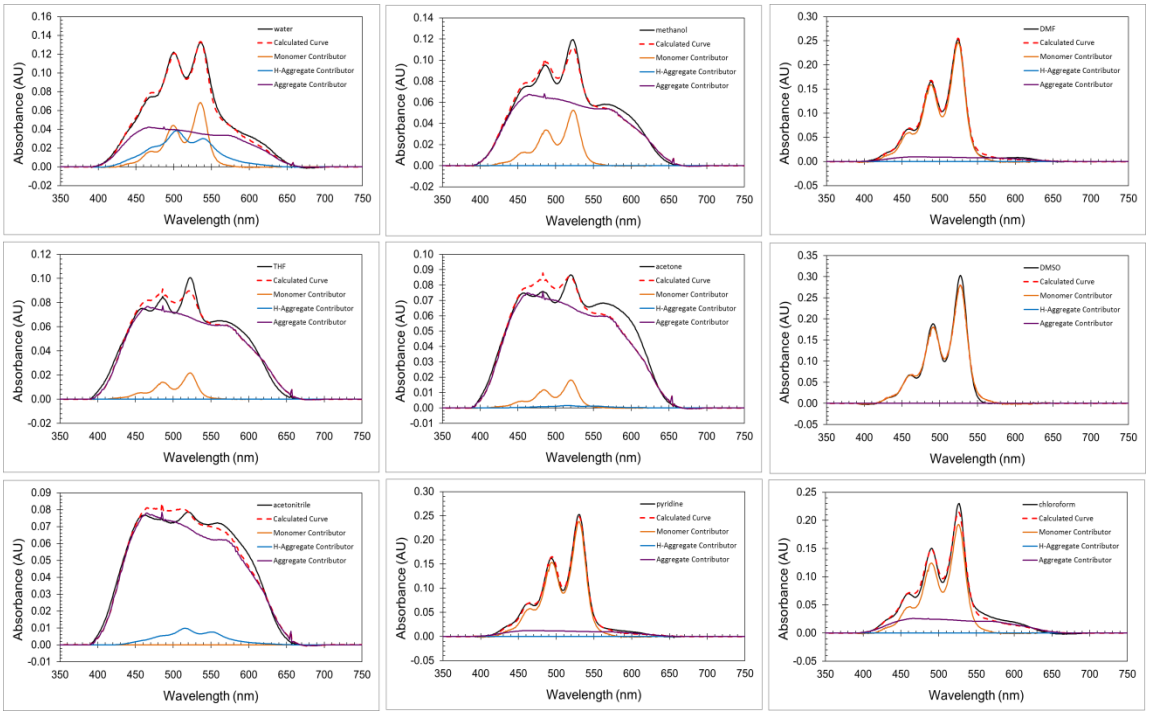

Figure D.22 Spectral data fitting for PDI **8** in selected organic solvents (water comparison included).

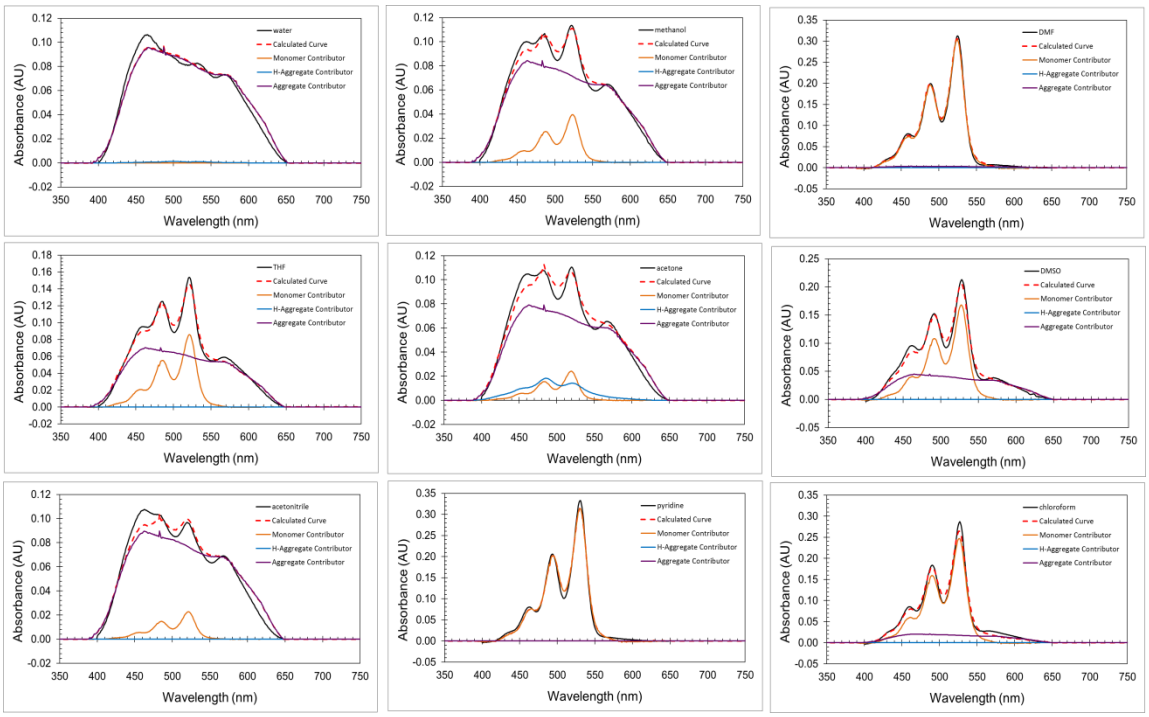

Figure D.23 Spectral data fitting for PDI **2H** in selected organic solvents (water comparison included).

D.3 Spectral Data Fitting of Selected Organic PDI Solutions

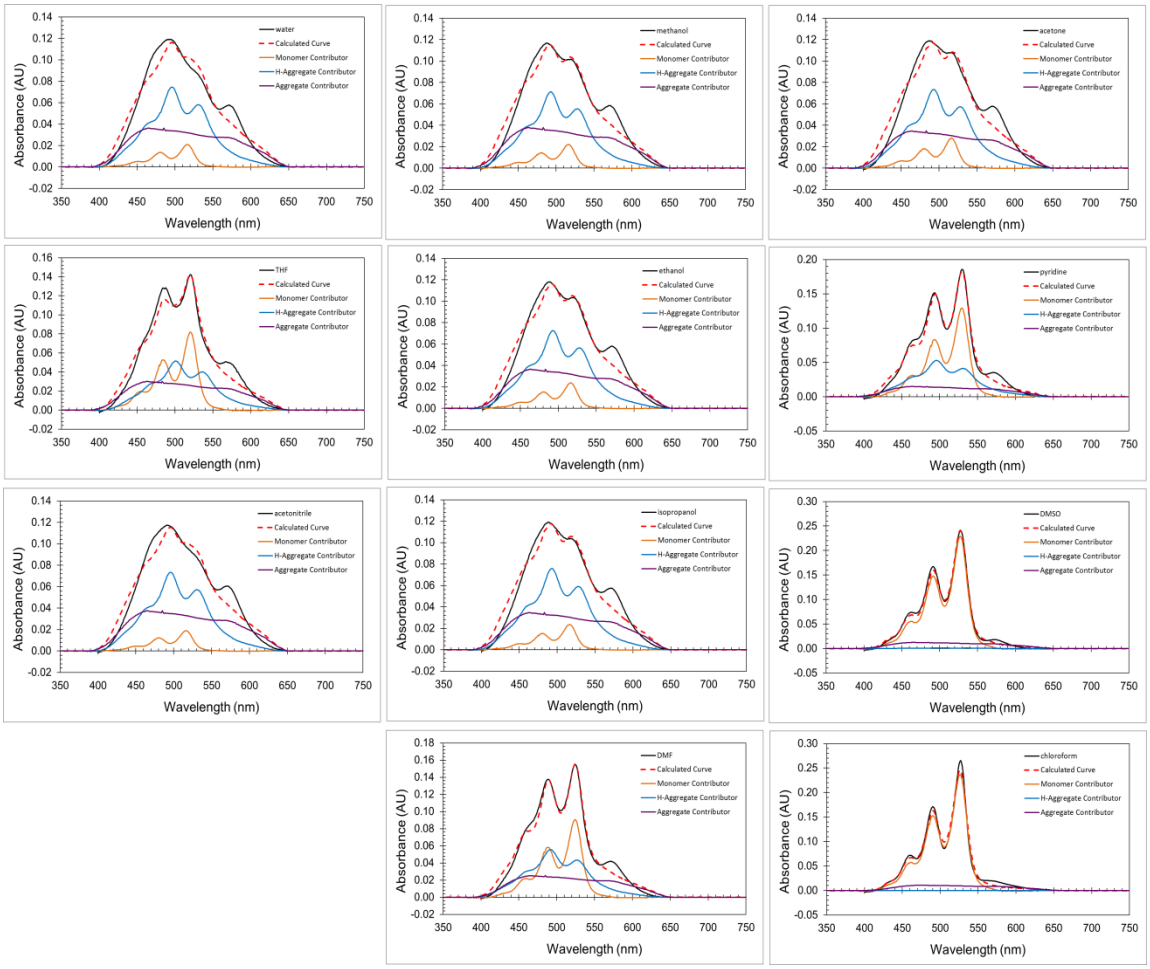

Figure D.24 Spectral data fitting for PDI **1H** in selected organic solvents (water comparison included).

D.3 Spectral Data Fitting of Selected Organic PDI Solutions

Figure D.25 Spectral data fitting for PDI **3H** in selected organic solvents (water comparison included).

D.3 Spectral Data Fitting of Selected Organic PDI Solutions

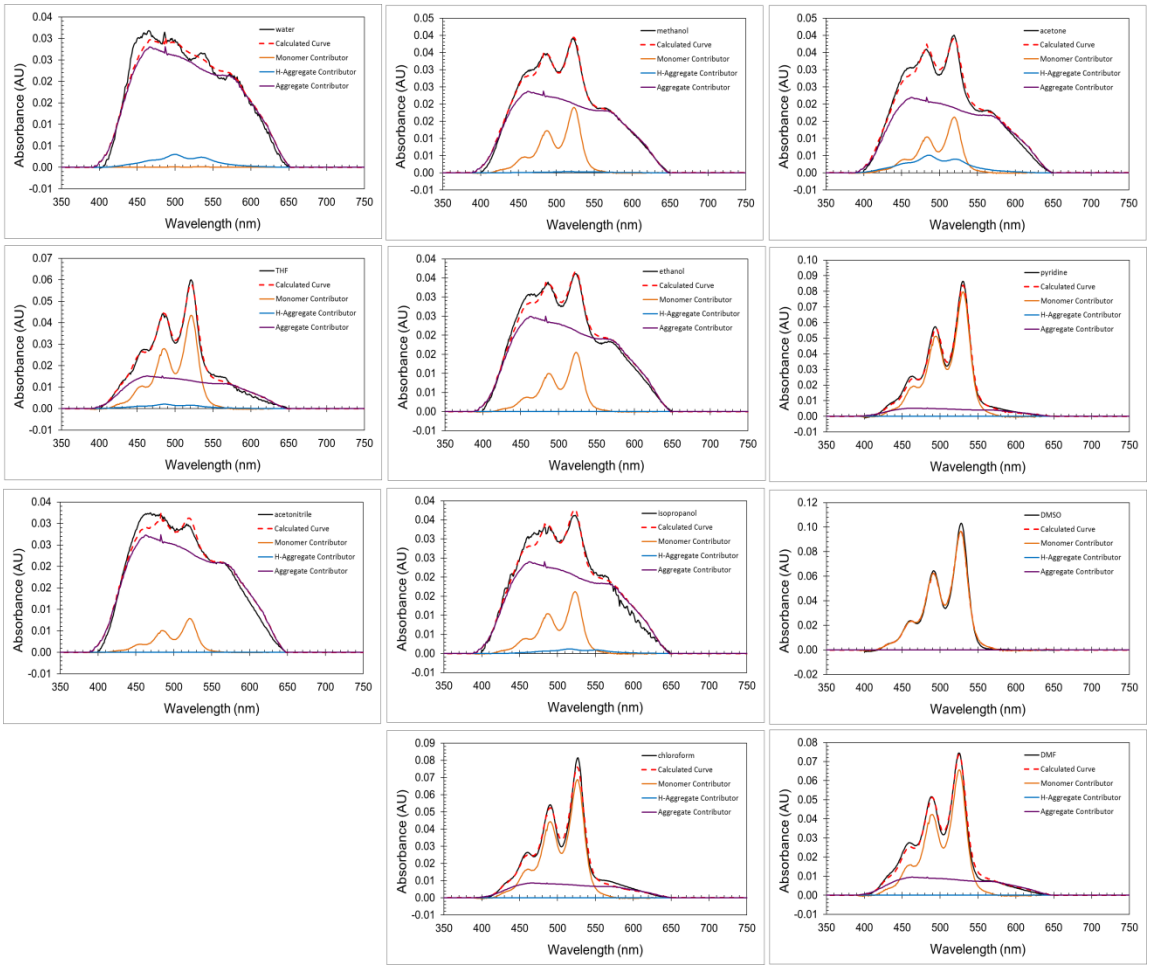

Figure D.26 Spectral data fitting for PDI **4H** in selected organic solvents (water comparison included).

D.3 Spectral Data Fitting of Selected Organic PDI Solutions

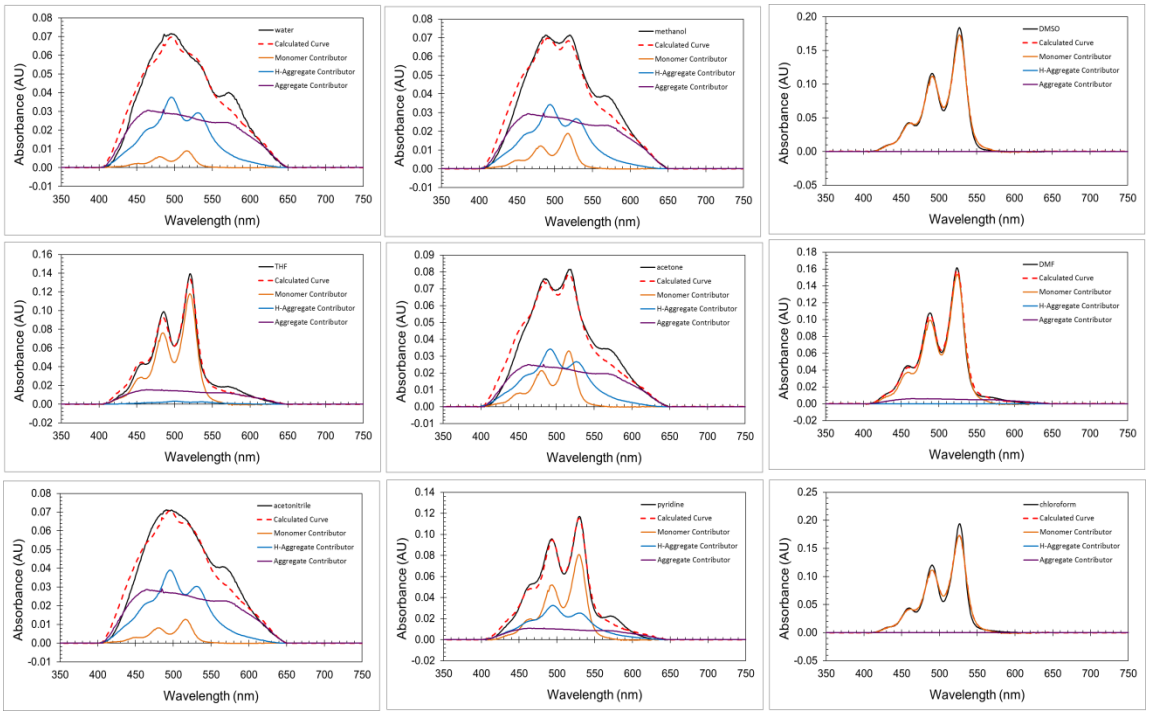

Figure D.27 Spectral data fitting for PDI **5H** in selected organic solvents (water comparison included).

References

(1) Whitesides, G. M.; Boncheva, M. *Proc. Natl. Acad. Sci. U. S. A.* **2002**, *99* (8), 4769–4774.

(2) Zhou, C.; Cheng, X.; Zhao, Q.; Yan, Y.; Wang, J.; Huang, J. *Sci. Rep.* **2014**, *4* (7533), 1–6.

(3) Shaw, J. M.; Seidler, P. F. *IBM J. Res. Dev.* **2001**, *45* (1), 3–9.

(4) Müllen, K.; Scherf, U. *Organic Light-Emitting Devices: Synthesis, Properties, and Applications*; Wiley-VCH Verlag GMbH & Co. KGaA: Weinheim, 2006.

(5) Wang, C.; Batsanov, A. S.; Bryce, M. R. *Faraday Discuss.* **2006**, *131*, 221–234.

(6) Levin, A.; Mason, T. O.; Adler-Abramovich, L.; Buell, A. K.; Meisl, G.; Galvagnion, C.; Bram, Y.; Stratford, S. A.; Dobson, C. M.; Knowles, T. P. J.; Gazit, E. *Nat. Commun.* **2014**, *5*, 1–8.

(7) Hoeben, F. J. M.; Jonkheijm, P.; Meijer, E. W.; Schenning, A. P. H. J. *Chem. Rev.* **2005**, *105* (4), 1491–1546.

(8) Lin, Y.; Mao, C. *Front. Mater. Sci.* **2011**, *5* (3), 247–265.

(9) Hoeben, F. J. M.; Herz, L. M.; Daniel, C.; Jonkheijm, P.; Schenning, A. P. H. J.; Silva, C.; Meskers, S. C. J.; Beljonne, D.; Phillips, R. T.; Friend, R. H.; Meijer, E. W. *Angew. Chemie Int. Ed.* **2004**, *43* (15), 1976–1979.

(10) Krieg, E.; Rybtchinski, B. *Chem. - Eur. J.* **2011**, *17* (33), 9016–9026.

(11) Yoo, Y.-S.; Choi, J.-H.; Song, J.-H.; Oh, N.-K.; Zin, W.-C.; Park, S.; Chang, T.; Lee, M. *J. Am. Chem. Soc.* **2004**, *126*, 6294–6300.

(12) Thünemann, A. F.; Kubowicz, S.; Burger, C.; Watson, M. D.; Tchebotareva, N.; Müllen, K. *J. Am. Chem. Soc.* **2003**, *125*, 352–356.

(13) Haris, P. I.; Chapman, D. *Biopolymers* **1995**, *37* (4), 251–263.

(14) Greenfield, N. *Nat Protoc.* **2006**, *1* (6), 2876–2890.

(15) Shao, H.; Parquette, J. R. *Chem. Commun.* **2010**, *46* (24), 4285–4287.

(16) Hamley, I. W.; Dehsorkhi, A.; Castelletto, V. *Chem. Commun. (Camb).* **2013**, *49* (18), 1850–1852.

(17) Hartgerink, J. D.; Beniash, E.; Stupp, S. I. *Science* **2001**, *294* (5547), 1684–1688.

(18) Valéry, C.; Pandey, R.; Gerrard, J. A. *Chem. Commun.* **2013**, *49* (27), 2825–2827.

(19) Toksoz, S.; Mammadov, R.; Tekinay, A. B.; Guler, M. O. *J. Colloid Interface Sci.* **2011**, *356* (1), 131–137.

(20) Paramonov, S. E.; Jun, H. W.; Hartgerink, J. D. *J. Am. Chem. Soc.* **2006**, *128* (22), 7291–7298.

(21) White, S. H.; Wimley, W. C. *Biochim. Biophys. Acta* **1998**, *1376* (3), 339–352.

(22) Guler, M. O.; Claussen, R. C.; Stupp, S. I. *J. Mater. Chem.* **2005**, *15* (42), 4507–4512.

(23) Hartgerink, J. D.; Beniash, E.; Stupp, S. I. *Proc. Natl. Acad. Sci. U. S. A.* **2002**, *99* (8), 5133–5138.

(24) Channon, K. J.; Devlin, G. L.; Magennis, S. W.; Finlayson, C. E.; Tickler, A. K.; Silva, C.; MacPhee, C. E. *J. Am. Chem. Soc.* **2008**, *130* (16), 5487–5491.

(25) Adler-Abramovich, L.; Gazit, E. *Chem. Soc. Rev.* **2014**, *43* (20), 6881–6893.

(26) Rathore, O.; Sogah, D. Y. *J. Am. Chem. Soc.* **2001**, *123* (22), 5231–5239.

(27) Matmour, R.; De Cat, I.; George, S. J.; Adriaens, W.; Leclère, P.; Bomans, P. H. H.; Sommerdijk, N. A. J. M.; Gielen, J. C.; Christianen, P. C. M.; Heldens, J. T.; van Hest, J. C. M.; Löwik, D. W. P. M.; De Feyter, S.; Meijer, E. W.; Schenning, A. P. H. J. *J. Am. Chem. Soc.* **2008**, *130* (44), 14576–14583.

(28) Croisier, E.; Liang, S.; Schweizer, T.; Balog, S.; Mionić, M.; Snellings, R.; Cugnoni, J.; Michaud, V.; Frauenrath, H. *Nat. Commun.* **2014**, *5* (4728), 1–10.

(29) Simmons, A. H.; Michal, C. A.; Jelinski, L. W. *Science (80-.).* **1996**, *271*, 84–87.

(30) O'Brien, J. P.; Fahnestock, S. R.; Termonia, Y.; Gardner, K. H. *Adv. Mater.* **1998**, *10*, 1185–1195.

(31) Porter, D.; Vollrath, F. *Adv. Mater.* **2009**, *21*, 487–492.

(32) Du, N.; Yang, Z.; Liu, X. Y.; Li, Y.; Xu, H. Y. *Adv. Funct. Mater.* **2011**, *21*, 772–778.

(33) Keten, S.; Xu, Z. P.; Ihle, B.; Buehler, M. J. *Nat. Mater.* **2010**, *9*, 359–367.

(34) Jelinski, L. W. *Curr. Opin. Solid State Mater. Sci.* **1998**, *3*, 237–245.

(35) Pesavento, P. V.; Chesterfield, R. J.; Newman, C. R.; Frisbie, C. D. *J. Appl. Phys.* **2004**, *96*, 7312–7324.

(36) Guo, X.; Whalley, A.; Klare, J. E.; Huang, L.; O'Brien, S.; Steigerwald, M.; Nuckolls, C. *Nano Lett.* **2007**, *7*, 1119–1122.

(37) Struijk, C. W.; Sieval, A. B.; Dakhorst, J. E. J.; Dijk, M. V.; Kimkes, P.; Koehorst, R. B. M.; Donker, H. .; Schaafsma, T. J.; Picken, S. J.; Van De Craats, A. M.; Warman, J. M.; Zuilhof, H.; Sudhlter, E. J. R. *J. Am. Chem. Soc.* **2000**, *122*, 11057–11066.

(38) Lee, S. K.; Zu, Y.; Herrmann, A.; Geerts, Y.; Müllen, K.; Bard, A. J. *J. Am. Chem. Soc.* **1999**, *121*, 3513–3520.

(39) Würthner, F. *Chem. Commun.* **2004**, 1564–1579.

(40) Mais, S.; Tittel, J.; Basché, T. .; Bräuchle, C.; Göhde, W.; Fuchs, H.; Müller, G.; Müllen, K. *J. Phys. Chem. A* **1997**, *101*, 8435–8440.

(41) Langhals, H.; Jaschke, H.; Ring, U.; Unold, P. V. *Angew. Chem., Int. Ed.* **1999**, *38*, 201–203.

(42) Yagai, S.; Seki, T.; Murayama, H.; Wakikawa, Y.; Ikoma, T.; Kikkawa, Y.; Karatsu, T.; Kitamura, A.; Honsho, Y.; Seki, S. *Small* **2010**, *6* (23), 2731–2740.

(43) Yan, P.; Chowdhury, A.; Holman, M. W.; Adams, D. M. *J. Phys. Chem. B* **2005**, *109* (2), 724–730.

(44) Baram, J.; Shirman, E.; Ben-Shitrit, N.; Ustinov, A.; Weissman, H.; Pinkas, I.; Wolf, S. G.; Rybtchinski, B. *J. Am. Chem. Soc.* **2008**, *130* (45), 14966–14967.

(45) De Witte, P. A. J.; Hernando, J.; Neuteboom, E. E.; Van Dijk, E. M. H. P.; Meskers, S. C. J.; Janssen, R. A. J.; Van Hulst, N. F.; Nolte, R. J. M.; García-Parajó, M. F.; Rowan, A. E. *J. Phys. Chem. B* **2006**, *110* (15), 7803–7812.

(46) Dehm, V.; Chen, Z.; Baumeister, U.; Prins, P.; Siebbeles, L. D. A.; Würthner, F. *Org. Lett.* **2007**, *9* (6), 1085–1088.

(47) Seki, T.; Asano, A.; Seki, S.; Kikkawa, Y.; Murayama, H.; Karatsu, T.; Kitamura, A.; Yagai, S. *Chem. - Eur. J.* **2011**, *17* (13), 3599–3608.

(48) Shahar, C.; Baram, J.; Tidhar, Y.; Weissman, H.; Cohen, S. R.; Pinkas, I.; Rybtchinski, B. *ACS Nano* **2013**, *7* (4), 3547–3556.

(49) Lu, X.; Guo, Z.; Sun, C.; Tian, H.; Zhu, W. *J. Phys. Chem. B* **2011**, *115* (37), 10871–10876.

(50) Wang, K.-R.; An, H.-W.; Wu, L.; Zhang, J.-C.; Li, X.-L. *Chem. Commun.* **2012**, *48* (45), 5644.

(51) Würthner, F.; Thalacker, C.; Diele, S.; Tschierske, C. *Chem. Eur. J.* **2001**, *7* (10), 2245–2253.

(52) Lewis, F. D. *Pure Appl. Chem.* **2006**, *78* (12), 2287–2295.

(53) Wang, W.; Li, L. S.; Helms, G.; Zhou, H. H.; Li, A. D. Q. *J. Am. Chem. Soc.* **2003**, *125* (5), 1120–1121.

(54) Wang, W.; Wan, W.; Zhou, H. H.; Niu, S.; Li, A. D. Q. *J. Am. Chem. Soc.* **2003**, *125* (18), 5248–5249.

(55) Chen, Z.; Stepanenko, V.; Dehm, V.; Prins, P.; Siebbeles, L. D. A.; Seibt, J.; Marquetand, P.; Engel, V.; Wuerthner, F. *Chem. - Eur. J.* **2007**, *13* (2), 436–449.

(56) Refiker, H.; Icil, H. *Turkish J. Chem.* **2011**, *35*, 847–859.

(57) Georgiev, N. I.; Sakr, A. R.; Bojinov, V. B. *Dye. Pigment.* **2011**, *91* (3), 332–339.

(58) Spenst, P.; Würthner, F. *Angew. Chem., Int. Ed.* **2015**, *54*, 10165–10168.

(59) Li, X.-Q.; Stepanenko, V.; Chen, Z.; Prins, P.; Siebbeles, L. D. A.; Würthner, F. *Chem. Commun.* **2006**, 3871–3873.

(60) Foster, S.; Finlayson, C. E.; Keivanidis, P. E.; Huang, Y.-S.; Hwang, I.; Friend, R. H.; Otten, M. B. J.; Lu, L.-P.; Schwartz, E.; Nolte, R. J. M.; Rowan, A. E. *Macromolecules* **2009**, *42* (6), 2023–2030.

(61) Finlayson, C. E.; Friend, R. H.; Otten, M. B. J.; Schwartz, E.; Cornelissen, J. J. L. M.; Nolte, R. J. M.; Rowan, A. E.; Samorì, P.; Palermo, V.; Liscio, A.; Peneva, K.; Müllen, K.; Trapani, S.; Beljonne, D. *Adv. Funct. Mater.* **2008**, *18* (24), 3947–3955.

(62) Schwartz, E.; Palermo, V.; Finlayson, C. E.; Huang, Y.-S.; Otten, M. B. J.; Liscio, A.; Trapani, S.; González-Valls, I.; Brocorens, P.; Cornelissen, J. J. L. M.; Peneva, K.; Müllen, K.; Spano, F. C.; Yartsev, A.; Westenhoff, S.; Friend, R. H.; Beljonne, D.; Nolte, R. J. M.; Samorì, P.; Rowan, A. E. *Chem. - Eur. J.* **2009**, *15* (11), 2536–2547.

(63) Palermo, V.; Otten, M. B. J.; Liscio, A.; Schwartz, E.; de Witte, P. A. J.; Castriciano, M. A.; Wienk, M. M.; Nolde, F.; De Luca, G.; Cornelissen, J. J. L. M.; Janssen, R. A. J.; Müllen, K.; Rowan, A. E.; Nolte, R. J. M.; Samorì, P. *J. Am. Chem. Soc.* **2008**, *130* (44), 14605–14614.

(64) Wicklein, A.; Ghosh, S.; Sommer, M.; Würthner, F.; Thelakkat, M. *ACS Nano* **2009**, *3* (5), 1107–1114.

(65) Briseno, A. L.; Mannsfeld, S. C. B.; Reese, C.; Hancock, J. M.; Xiong, Y.; Jenekhe, S. A.; Bao, Z.; Xia, Y. *Nano Lett.* **2007**, *7* (9), 2847–2853.

(66) Krieg, E.; Shirman, E.; Weissman, H.; Shimoni, E.; Wolf, S. G.; Pinkas, I.; Rybtchinski, B. *J. Am. Chem. Soc.* **2009**, *131* (40), 14365–14373.

(67) Chen, Z.; Fimmel, B.; Würthner, F. *Org. Biomol. Chem.* **2012**, *10* (30), 5845–5855.

(68) Zhang, Z.; Zhan, C.; Zhang, X.; Zhang, S.; Huang, J.; Li, A. D. Q.; Yao, J. *Chem. - Eur. J.* **2012**, *18* (39), 12305–12313.

(69) Avinash, M. B.; Govindaraju, T. *Adv. Mater.* **2012**, *24* (29), 3905–3922.

(70) Avinash, M. B.; Govindaraju, T. *Nanoscale* **2011**, *3* (6), 2536–2543.

(71) Avinash, M. B.; Govindaraju, T. *Adv. Funct. Mater.* **2011**, *21*, 3875–3882.

(72) Tomasulo, M.; Naistat, D. M.; White, A. J. P.; Williams, D. J.; Raymo, F. M. *Tetrahedron Lett.* **2005**, *46*, 5695–5698.

(73) Hu, Z.; Pantos, G. D.; Kuganathan, N.; Arrowsmith, R. L.; Jacobs, R. M. J.; Kociok-Köhn, G.; O'Byrne, J.; Jurkschat, K.; Burgos, P.; Tyrrell, R. M.; Botchway, S. W.; Sanders, J. K. M.; Pascu, S. I. *Adv. Funct. Mater.* **2012**, *22*, 503–518.

(74) Sun, Y.; He, C.; Sun, K.; Li, Y.; Dong, H.; Wang, Z.; Li, Z. *Langmuir* **2011**, *27* (18), 11364–11371.

(75) Draper, E. R.; Walsh, J. J.; McDonald, T. O.; Zwijnenburg, M. a.; Cameron, P. J.; Cowan, A. J.; Adams, D. J. *J. Mater. Chem. C* **2014**, *2* (28), 5570–5575.

(76) Roy, S.; Kumar Maiti, D.; Panigrahi, S.; Basak, D.; Banerjee, A. *RSC Adv.* **2012**, *2* (29), 11053–11060.

(77) Roy, S.; Maiti, D. K.; Panigrahi, S.; Basak, D.; Banerjee, A. *Phys. Chem. Chem. Phys.* **2014**, *16* (13), 6041–6049.

(78) Bai, S.; Debnath, S.; Javid, N.; Frederix, P. W. J. M.; Fleming, S.; Pappas, C.; Ulijn, R. V. *Langmuir* **2014**, *30* (25), 7576–7584.

(79) Gallaher, J. K.; Aitken, E. J.; Keyzers, R. A.; Hodgkiss, J. M. *Chem. Commun.* **2012**, *48* (64), 7961.

(80) Marty, R.; Szilluweit, R.; Sánchez-Ferrer, A.; Bolisetty, S.; Adamcik, J.; Mezzenga, R.; Spitzner, E.-C.; Feifer, M.; Steinmann, S. N.; Corminboeuf, C.; Frauenrath, H. *ACS Nano* **2013**, *7* (10), 8498–8508.

(81) Merrifield, R. B. *J. Am. Chem. Soc.* **1963**, *85*, 2149–2154.

(82) Amblard, M.; Fehrentz, J.-A.; Martinez, J.; Subra, G. *Mol. Biotechnol.* **2006**, *33*, 239–254.

(83) Bollhagen, R.; Schmiedberger, M.; Barlos, K.; Grell, E. *J. Chem. Soc., Chem. Commun.* **1994**, 2259–2260.

(84) Isidro-llobet, A.; Mercedes, A. *Chem. Rev.* **2009**, *109*, 2455–2504.

(85) Kaiser, E.; Colescott, R. L.; Bossiriger, C. D.; Cook, P. *Anal. Biochem.* **1970**, *34*, 595–598.

(86) Wicklein, A.; Lang, A.; Muth, M.; Thelakkat, M. *J. Am. Chem. Soc.* **2009**, *131* (40), 14442–14453.

(87) Wang, R.; Shi, Z.; Zhang, C.; Zhang, A.; Chen, J.; Guo, W.; Sun, Z. *Dye. Pigment.* **2013**, *98* (3), 450–458.

(88) Eakins, G. L.; Gallaher, J. K.; Keyzers, R. A.; Falber, A.; Webb, J. E. A.; Laos, A.; Tidhar, Y.; Weissman, H.; Rybtchinski, B.; Thordarson, P.; Hodgkiss, J. M. *J. Phys. Chem. B* **2014**, *118* (29), 8642–8651.

(89) Ananiichuk, N. A.; Tret'yakov, Y. P.; Kut'ina, L. V; Oleinik, V. G.; Kozhura, M. T.; Gritsenko, L. P. *Fibre Chem.* **1980**, *11* (6), 444–446.

(90) Claussen, R. C.; Rabatic, B. M.; Stupp, S. I. *J. Am. Chem. Soc.* **2003**, *125* (42), 12680–12681.

(91) Niece, K. L.; Hartgerink, J. D.; Donners; Stupp, S. I. *J. Am. Chem. Soc.* **2003**, *125*, 7146–7147.

(92) Behanna, H. A.; Donners, J.; Gordon, A. C.; Stupp, S. I. *J. Am. Chem. Soc.* **2005**, *127*, 1193–1200.

(93) Tovar, J. D.; Claussen, R. C.; Stupp, S. I. *J. Am. Chem. Soc.* **2005**, *127*, 7337–7345.

(94) Cui, H.; Muraoka, T.; Cheetham, A. G.; Stupp, S. I. *Nano Lett.* **2009**, *9*, 945–951.

(95) Pashuck, E. T.; Stupp, S. I. *J. Am. Chem. Soc.* **2010**, *132*, 8819–8821.

(96) Cui, H.; Webber, M. J.; Stupp, S. I. *Biopolymers* **2010**, *94*, 1–18.

(97) Dehsorkhi, A.; Castelletto, V.; Hamley, I. W. *J. Pept. Sci.* **2014**, *20* (7), 453–467.

(98) Arrondo, J. L.; Goñi, F. M. *Prog. Biophys. Mol. Biol.* **1999**, *72* (4), 367–405.

(99) Byler, D. M.; Susi, H. *Biopolymers* **1986**, *25* (3), 469–487.

(100) Bloemendal, M.; Johnson, W. C. *Pharm. Biotechnol.* **1995**, *7*, 65–100.

(101) Surewicz, W. K.; Mantsch, H. H.; Stahl, G. L.; Epand, R. M. *Proc. Natl. Acad. Sci. U. S. A.* **1987**, *84* (20), 7028–7030.

(102) Thordarson, P.; Atkin, D. R.; Kalle, W. H. J.; Warr, G. G.; Braet, F. *Aust. J. Chem.* **2006**, *59* (6), 359–375.

(103) Won, Y.-Y. *Korean J. Chem. Eng.* **2004**, *21* (1), 296–302.

(104) Zugenmaier, P.; Duff, J.; Bluhm, T. L. *Cryst. Res. Technol.* **2000**, *35*, 1095–1115.

(105) Gosztola, D.; Niemczyk, M. P.; Svec, W.; Lukas, A. S.; Wasielewski, M. R. *J. Phys. Chem. A* **2000**, *104* (28), 6545–6551.

(106) Camerman, A.; Trotter, J. *Proc. R. Soc. London A* **1964**, *279*, 129.

(107) Liaoning Liangang Pigment and Dyestuff Chemicals Co., L. No Title http://www.chemnet.com/Suppliers/13683/ (accessed Apr 15, 2015).

(108) Huang, C.; Barlow, S.; Marder, S. R. *J. Org. Chem.* **2011**, *76* (8), 2386–2407.

(109) Spano, F. C. *Acc. Chem. Res.* **2010**, *43* (3), 429–439.

(110) Giaimo, J. M.; Lockard, J. V.; Sinks, L. E.; Scott, A. M.; Wilson, T. M.; Wasielewski, M. R. *J. Phys. Chem. A* **2008**, *112* (11), 2322–2330.

(111) Kistler, K. A.; Pochas, C. M.; Yamagata, H.; Matsika, S.; Spano, F. C. *J. Phys. Chem. B* **2012**, *116* (1), 77–86.

(112) Telfer, S. G.; McLean, T. M.; Waterland, M. R. *Dalton Trans.* **2011**, *40* (13), 3097–3108.

(113) Schellman, J. A. *Acc. Chem. Res.* **1968**, *1*, 144–151.

(114) Berova, N.; Di Bari, L.; Pescitelli, G. *Chem. Soc. Rev.* **2007**, *36* (6), 914–931.

(115) Kelly, S. M.; Jess, T. J.; Price, N. C. *Biochim. Biophys. Acta* **2005**, *1751* (2), 119–139.

(116) Trifonov, A.; Buchvarov, I.; Lohr, A.; Würthner, F.; Fiebig, T. *Rev. Sci. Instrum.* **2010**, *81* (043014), 1–6.

(117) Whitmore, L.; Wallace, B. A. *Biopolymers* **2008**, *89* (5), 392–400.

(118) Juban, M.; Javadpour, M.; Barkley, M. In *Antibacterial Peptide Protocols SE - 6*; Shafer, W., Ed.; Methods In Molecular Biology; Humana Press, 1997; Vol. 78, pp 73–78.

(119) Franke, D.; Vos, M.; Antonietti, M.; Sommerdijk, N. A. J. M.; Faul, C. F. J. *Chem. Mater.* **2006**, *18* (7), 1839–1847.

(120) Thalacker, C.; Würthner, F. *Adv. Funct. Mater.* **2002**, *12* (3), 209–218.

(121) Würthner, F.; Chen, Z.; Hoeben, F. J. M.; Osswald, P.; You, C. C.; Jonkheijm, P.; Herrikhuyzen, J. V.; Schenning, A. P. H. J.; Van Der Schoot, P. P. A. M.; Meijer, E. W.; Beckers, E. H. A.; Meskers, S. C. J.; Janssen, R. A. J. *J. Am. Chem. Soc.* **2004**, *126* (34), 10611–10618.

(122) Schmidt, C. D.; Bòttcher, C.; Hirsch, A. *European J. Org. Chem.* **2009**, No. 31, 5337–5349.

(123) Superchi, S.; Giorgio, E.; Rosini, C. *Chirality* **2004**, *16* (7), 422–451.

(124) Langeveld-Voss, B. M. W.; Beljonne, D.; Shuai, Z.; Janssen, R. a J.; Meskers, S. C. J.; Meijer, E. W.; Brédas, J.-L. *Adv. Mater.* **1998**, *10* (16), 1343–1348.

(125) Richardson, F. S.; Hilmes, G.; Jenkins, J. J. *Theor. Chim. Acta* **1975**, *39* (1), 75–91.

(126) Seibt, J.; Marquetand, P.; Engel, V.; Chen, Z.; Dehm, V.; Würthner, F. *Chem. Phys.* **2006**, *328* (1-3), 354–362.

(127) Wang, H.; Kaiser, T. E.; Uemura, S.; Würthner, F. *Chem. Commun.* **2008**, *1* (10), 1181–1183.

(128) Geyer, C. J. In *Handbook of Markov Chain Monte Carlo*; Brooks, S., Gelman, A., Jones, G. L., Meng, X.-L., Eds.; Chapman and Hall/CRC Press: New York, 2011; pp 3–47.

(129) Nooren, I. M. A.; Thornton, J. M. *J. Mol. Biol.* **2003**, *325* (5), 991–1018.

(130) Chothia, C.; Janin, J. *Nature* **1975**, *256*, 705–708.

(131) Dey, S.; Pal, A.; Chakrabarti, P.; Janin, J. *J. Mol. Biol.* **2010**, *398* (1), 146–160.

(132) Zhang, S.; Greenfield, M. A.; Mata, A.; Palmer, L. C.; Bitton, R.; Mantei, J. R.; Aparicio, C.; de la Cruz, M. O.; Stupp, S. I. *Nat. Mater.* **2010**, *9*, 594–600.

(133) Ueda, M.; Makino, A.; Imai, T.; Sugiyama, J.; Kimura, S. *Polym. J.* **2013**, *45*, 509–515.

(134) Gore, T.; Dori, Y.; Talmon, Y.; Tirrell, M.; Bianco-Peled, H. *Langmuir* **2001**, *17*, 5352–5360.

(135) Capito, R. M.; Azevedo, H. S.; Velichko, Y. S.; Mata, A.; Stupp, S. I. *Science* **2008**, *319* (5871), 1812–1816.

(136) Tovar, J. D.; Rabatic, B. M.; Stupp, S. I. *Small* **2007**, *3*, 2024–2028.

(137) Bull, S. R.; Guler, M. O.; Bras, R. E.; Meade, T. J.; Stupp, S. I. *Nano Lett.* **2005**, *5*, 1–4.

(138) Busseron, E.; Ruff, Y.; Moulin, E.; Giuseppone, N. *Nanoscale* **2013**, *5* (16), 7098–7140.

(139) Tidhar, Y.; Weissman, H.; Wolf, S. G.; Gulino, A.; Rybtchinski, B. *Chem. - Eur. J.* **2011**, *17* (22), 6068–6075.

(140) Sun, R.; Xue, C.; Owak, M.; Peetz, R. M.; Jin, S. *Tetrahedron Lett.* **2007**, *48* (38), 6696–6699.

(141) Matmour, R.; De Cat, I.; George, S. J.; Adriaens, W.; Leclère, P.; Bomans, P. H. H.; Sommerdijk, N. A. J. M.; Gielen, J. C.; Christianen, P. C. M.; Heldens, J. T.; van Hest, J. C. M.; Löwik, D. W. P. M.; De Feyter, S.; Meijer, E. W.; Schenning, A. P. H. J. *J. Am. Chem. Soc.* **2008**, *130* (44), 14576–14583.

(142) Wall, B. D.; Zacca, A. E.; Sanders, A. M.; Wilson, W. L.; Ferguson, A. L.; Tovar, J. D. *Langmuir* **2014**, *30* (20), 5946–5956.

(143) Chen, L.; Morris, K.; Laybourn, A.; Elias, D.; Hicks, M. R.; Rodger, A.; Serpell, L.; Adams, D. J. *Langmuir* **2010**, *26*, 5232–5242.

(144) Puniredd, S. R.; Kiersnowski, A.; Battagliarin, G.; Zajączkowski, W.; Wong, W. W. H.; Kirby, N.; Müllen, K.; Pisula, W. *J. Mater. Chem. C* **2013**, *1*, 2433–2440.

(145) Dimitrakopolous, C. D.; Malenfant, P. R. L. *Adv. Mater.* **2002**, *14*, 99–117.

(146) Li, C.; Wonneberger, H. *Adv. Mater.* **2012**, *24*, 613–636.

(147) Kozma, E.; Catellani, M. *Dye. Pigment.* **2013**, *98*, 160–179.

(148) Hains, A. W.; Chen, H.-Y.; Reilly III, T. H.; Gregg, B. A. *ACS Appl. Mater. Interfaces* **2011**, *3*, 4381–4387.

(149) Balakrishnan, K.; Datar, A.; Naddo, T.; Huang, J.; Oitker, R.; Yen, M.; Zhao, J.; Zang, L. *J. Am. Chem. Soc.* **2006**, *128* (22), 7390–7398.

(150) Rybtchinski, B. *ACS Nano* **2011**, *5*, 6791–6818.

(151) Raeburn, J.; Zamith Cardoso, A.; Adams, D. J. *Chem. Soc. Rev.* **2013**, *42* (12), 5143.

(152) Liu, S. G.; Sui, G.; Cormier, R. A.; Leblanc, R. M.; Gregg, B. A. *J. Phys. Chem. B* **2002**, *106* (6), 1307–1315.

(153) Gao, B.; Xia, D.; Zhang, L.; Bai, Q.; Bai, L.; Yang, T.; Ba, X. *J. Mater. Chem.* **2011**, *21* (40), 15975–15980.

(154) Zhang, T.; Sun, D.; Ren, X.; Liu, L.; Wen, G.; Ren, Z.; Li, H.; Yan, S. *Soft Matter* **2013**, *9* (45), 10739–10745.

(155) Mizoshita, N.; Tani, T.; Inagaki, S. *Adv. Funct. Mater.* **2011**, *21* (17), 3291–3296.

(156) Struijk, C. W.; Sieval, A. B.; Dakhorst, J. E. J.; Dijk, M. Van; Koehorst, R. B. M.; Donker, H.; Schaafsma, T. J.; Picken, S. J.; Craats, A. M. Van De; Warman, J. M.; Zuilhof, H.; Sudhlter, E. J. R. *J. Am. Chem. Soc.* **2000**, *122* (45), 11057–11066.

(157) Chen, Z.; Lohr, A.; Saha-Möller, C. R.; Würthner, F. *Chem. Soc. Rev.* **2009**, *38* (2), 564–584.

(158) Smulders, M. M. J.; Nieuwenhuizen, M. M. L.; De Greef, T. F. a; Van Der Schoot, P.; Schenning, A. P. H. J.; Meijer, E. W. *Chem. - Eur. J.* **2010**, *16* (1), 362–367.

(159) Reichardt, C. *Chem. Rev.* **1994**, *94*, 2319–2358.

(160) Rosés, M.; Ortega, J. **1995**, *24* (1), 51–63.

(161) Imae, T.; Hayashi, N.; Matsumoto, T.; Tada, T.; Furusaka, M. *J. Colloid Interface Sci.* **2000**, *225* (2), 285–290.

(162) Boettcher, C.; Schade, B.; Fuhrhop, J.-H. *Langmuir* **2001**, *17* (3), 873–877.

(163) Imae, T.; Takahashi, Y.; Muramatsu, H. *J. Am. Chem. Soc.* **1992**, *114* (9), 3414–3419.

(164) Yoza, K.; Amanokura, N.; Ono, Y.; Akao, T.; Shinmori, H.; Takeuchi, M.; Shinkai, S.; Reinhoudt, D. N. *Chem. - Eur. J.* **1999**, *5* (9), 2722–2729.

(165) Gronwald, O.; Shinkai, S. *Chem. - Eur. J.* **2001**, *7* (20), 4328–4334.

(166) Jung, J. H.; John, G.; Masuda, M.; Yoshida, K.; Shinkai, S.; Shimizu, T. *Langmuir* **2001**, *17* (23), 7229–7232.

(167) Fuhrhop, J. H.; Boettcher, C. *J. Am. Chem. Soc.* **1990**, *112* (5), 1768–1776.

(168) Hafkamp, R. J. H.; Feiters, M. C.; Nolte, R. J. M. *J. Org. Chem.* **1999**, *64* (2), 412–426.

(169) De Loos, M.; van Esch, J.; Kellogg, R. M.; Feringa, B. L. *Angew. Chemie Int. Ed.* **2001**, *40* (3), 613–616.

(170) Estroff, L. A.; Hamilton, A. D. *Angew. Chemie Int. Ed.* **2000**, *39* (19), 3447–3450.

(171) Fuhrhop, J. H.; Demoulin, C.; Boettcher, C.; Koening, J.; Siggel, U. *J. Am. Chem. Soc.* **1992**, *114* (11), 4159–4165.

(172) Babu, P.; Sangeetha, N. M.; Vijaykumar, P.; Maitra, U.; Rissanen, K.; Raju, A. R. *Chem. - Eur. J.* **2003**, *9* (9), 1922–1932.

(173) Mamiya, J.; Kanie, K.; Hiyama, T.; Ikeda, T.; Kato, T. *Chem. Commun.* **2002**, 1870–1871.

(174) Brizard, A.; Oda, R.; Huc, I. *Top. Curr. Chem.* **2005**, *256*, 167–218.

(175) Fuhrhop, J. H.; Schnieder, P.; Boekema, E.; Helfrich, W. *J. Am. Chem. Soc.* **1988**, *110* (9), 2861–2867.

(176) Huang, Y.; Wei, Z. *Chinese Sci. Bull.* **2012**, *57* (33), 4246–4256.

(177) Eakins, G. L.; Wojciechowski, J. P.; Martin, A. D.; Webb, J. E. A.; Thordarson, P.; Hodgkiss, J. M. *Supramol. Chem.* **2015**, doi: 10.1080/10610278.2015.1066011.

(178) Harada, N.; Nakanishi, K. *Acc. Chem. Res.* **1972**, *5* (8), 257–263.

(179) Zhang, S. *Biotechnol. Adv.* **2002**, *20* (5–6), 321–339.

(180) Waterhouse, S. H.; Gerrard, J. A. *Aust. J. Chem.* **2004**, *57* (6), 519–523.

(181) Ellis-Behnke, R. G.; Liang, Y.-X.; You, S.-W.; Tay, D. K. C.; Zhang, S.; So, K.-F.; Schneider, G. E. *Proc. Natl. Acad. Sci. U. S. A.* **2006**, *103* (13), 5054–5059.

(182) Phillips, A. J.; Littlejohn, J.; Yewdall, N. A.; Zhu, T.; Valéry, C.; Pearce, F. G.; Mitra, A. K.; Radjainia, M.; Gerrard, J. A. *Biomacromolecules* **2014**, *15* (5), 1871–1881.

(183) Karplus, P. A.; Hall, A. In *Peroxiredoxin Systems*; Flohé, L., Harris, J. R., Eds.; Springer Science and Business Media Inc.: New York, 2007; pp 41–60.

(184) Angelucci, F.; Saccoccia, F.; Ardini, M.; Boumis, G.; Brunori, M.; Di Leandro, L.; Ippoliti, R.; Miele, A. E.; Natoli, G.; Scotti, S.; Bellelli, A. *J. Mol. Biol.* **2013**, *425* (22), 4556–4568.

(185) Kato, H.; Asanoi, M. .; Nakazawa, T. .; Maruyama, K. . *Zool. Sci.* **1985**, *2*, 485–490.

(186) Harris, J. R.; Schröder, E.; Isupov, M. N.; Scheffler, D.; Kristensen, P.; Littlechild, J. A.; Vagin, A. A.; Meissner, U. *Biochim. Biophys. Acta - Protein Struct. Mol. Enzymol.* **2001**, *1547* (2), 221–234.

(187) Jang, H. H.; Lee, K. O.; Chi, Y. H.; Jung, B. G.; Park, S. K.; Park, J. H.; Lee, J. R.; Lee, S. S.; Moon, J. C.; Yun, J. W.; Choi, Y. O.; Kim, W. Y.; Kang, J. S.; Cheong, G.-W.; Yun, D.-J.; Rhee, S. G.; Cho, M. J.; Lee, S. Y. *Cell* **2015**, *117* (5), 625–635.

(188) Meissner, U.; Schröder, E.; Scheffler, D.; Martin, A. G.; Harris, J. R. *Micron* **2007**, *38* (1), 29–39.

(189) Irimia-Vladu, M. *Chem. Soc. Rev.* **2014**, *43* (2), 588–610.

(190) Cipriano, T.; Knotts, G.; Laudari, A.; Bianchi, R. C.; Alves, W. A.; Guha, S. *ACS Appl. Mater. Interfaces* **2014**, *6* (23), 21408–21415.

(191) Chang, J.-W.; Wang, C.-G.; Huang, C.-Y.; Tsai, T.-D.; Guo, T.-F.; Wen, T.-C. *Adv. Mater.* **2011**, *23*, 4077–4081.

(192) Singh, T.; Sariciftci, N.; Grote, J. In *Organic Electronics*; Grasser, T., Meller, G., Li, L., Eds.; Advances in Polymer Science; Springer: Berlin Heidelberg, 2010; Vol. 223, pp 73–112.

(193) Yau, S. T.; Qian, G. *Appl. Phys. Lett.* **2005**, *86* (10), 1–3.

(194) Mizrahi, M.; Zakrassov, A.; Lerner-Yardeni, J.; Ashkenasy, N. *Nanoscale* **2012**, *4* (2), 518–524.

(195) Liao, C.; Yan, F. *Polym. Rev.* **2013**, *53* (3), 352–406.

(196) Kwon, Y.-W.; Lee, C. H.; Choi, D.-H.; Jin, J.-I. *J. Mater. Chem.* **2009**, *19* (10), 1353–1380.

(197) Kumar, R. J.; MacDonald, J. M.; Singh, T. B.; Waddington, L. J.; Holmes, A. B. *J. Am. Chem. Soc.* **2011**, *133* (22), 8564–8573.

(198) Coin, I.; Beyermann, M.; Bienert, M. *Nat. Protoc.* **2007**, *2* (12), 3247–3256.

(199) Eakins, G. L.; Pandey, R.; Wojciechowski, J. P.; Zheng, H. Y.; Webb, J. E. a.; Valéry, C.; Thordarson, P.; Plank, N. O. V.; Gerrard, J. a.; Hodgkiss, J. M. *Adv. Funct. Mater.* **2015**, *25* (35), 5640–5649.

(200) Henikoff, S.; Henikoff, J. G. *Proc. Natl. Acad. Sci. U. S. A.* **1992**, *89* (22), 10915–10919.

(201) Betts, M. J.; Russell, R. B. In *Bioinformatics for Geneticists: A Bioinformatics Primer for the Analysis of Genetic Data*; Barnes, M. R., Gray, I. C., Eds.; John Wiley & Sons, Ltd.: West Sussex, 2003; pp 289–316.

(202) Biancalana, M.; Koide, S. *Biochim. Biophys. Acta* **2010**, *1804* (7), 1405–1412.

(203) Khurana, R.; Coleman, C.; Ionescu-Zanetti, C.; Carter, S. A.; Krishna, V.; Grover, R. K.; Roy, R.; Singh, S. *J. Struct. Biol.* **2005**, *151* (3), 229–238.

(204) Ghosh, S.; Li, X. Q.; Stepanenko, V.; Würthner, F. *Chem. -Eur. J.* **2008**, *14* (36), 11343–11357.

(205) Zhao, Y.; Guo, Y.; Liu, Y. *Adv. Mater.* **2013**, *25* (38), 5372–5391.

(206) Pron, A.; Reghu, R. R.; Rybakiewicz, R.; Cybulski, H.; Djurado, D.; Grazulevicius, J. V.; Zagorska, M.; Kulszewicz-Bajer, I.; Verilhac, J. M. *J. Phys. Chem. C* **2011**, *115* (30), 15008–15017.

(207) Hutchison, G. R.; Ratner, M. A.; Marks, T. J. *J. Am. Chem. Soc.* **2005**, *127*, 16866–16881.

(208) Fabiano, S.; Braun, S.; Fahlman, M.; Crispin, X.; Berggren, M. *Adv. Funct. Mater.* **2014**, *24* (5), 695–700.

(209) Pfattner, R.; Rovira, C.; Mas-Torrent, M. *Phys. Chem. Chem. Phys.* **2014**, 26545–26552.

(210) Kumatani, A.; Li, Y.; Darmawan, P.; Minari, T.; Tsukagoshi, K. *Sci. Rep.* **2013**, *3*, 3–8.

(211) De Leeuw, D. M.; Simenon, M. M. J.; Brown, A. R.; Einerhand, R. E. F. *Synth. Met.* **1997**, *87* (1), 53–59.

(212) Brown, A. R.; De Leeuw, D. M.; Lous, E. J.; Havinga, E. E. *Synth. Met.* **1994**, *66*, 257–261.

(213) Haddon, R. C.; Perel, A. S.; Morris, R. C.; Palstra, T. T. M.; Hebard, A. F.; Fleming, R. M. *Appl. Phys. Lett.* **1995**, *67*, 121–123.

(214) Murphy, A. R.; Fréchet, J. M. J. *Chem. Rev.* **2007**, *107* (4), 1066–1096.

(215) Salbeck, J.; Kunkely, H.; Langhals, H.; Saalfrank, R. W.; Daub, J. *Chimia (Aarau).* **1989**, *43*, 6–9.

(216) Shirman, E.; Ustinov, A.; Ben-Shitrit, N.; Weissman, H.; Iron, M. A.; Cohen, R.; Rybtchinski, B. *J. Phys. Chem. B* **2008**, *112*, 8855–8858.

(217) Marcon, R. O.; Brochsztain, S. *Langmuir* **2007**, *23*, 11972–11976.

(218) Zhao, Y.; Di, C. A.; Gao, X.; Hu, Y.; Guo, Y.; Zhang, L.; Liu, Y.; Wang, J.; Hu, W.; Zhu, D. *Adv. Mater.* **2011**, *23*, 2448–2453.

(219) Horne, W. S.; Ashkenasy, N.; Ghadiri, M. R. *Chemistry* **2005**, *11* (4), 1137–1144.

(220) Shen, Y. L.; Hosseini, A. R.; Wong, M. H.; Malliaras, G. G. *Chem. Phys. Chem.* **2004**, *5*, 16–25.

(221) Würthner, F.; Saha-Möller, C. R.; Fimmel, B.; Ogi, S.; Leowanawat, P.; Schmidt, D. *Chem. Rev.* **2015**, doi: 10.1021/acs.chemrev.5b00188.

(222) Eakins, G. L.; Cooper, M. W.; Gerasimchuk, N. N.; Phillips, T. J.; Breyfogle, B. E.; Stearman, C. J. *Can. J. Chem.* **2013**, *91* (11), 1059–1071.

(223) Newman, C. R.; Frisbie, C. D.; Silva Filho, D. A.; Bredas, J. L.; Ewbank, P. C.; Mann, K. R. *Chem. Mater.* **2004**, *16*, 4436–4451.

(224) Irimia-Vladu, M.; Gåowacki, E. D.; Troshin, P. A.; Schwabegger, G.; Leonat, L.; Susarova, D. K.; Krystal, O.; Ullah, M.; Kanbur, Y.; Bodea, M. A.; Razumov, V. F.; Sitter, H.; Bauer, S.; Sariciftci, N. S. *Adv. Mater.* **2012**, *24* (3), 375–380.

(225) Kanbur, Y.; Irimia-Vladu, M.; Gåowacki, E. D.; Voss, G.; Baumgartner, M.; Schwabegger, G.; Leonat, L.; Ullah, M.; Sarica, H.; Erten-Ela, S.; Schwödiauer, R.; Sitter, H.; Küükyavuz, Z.; Bauer, S.; Sariciftci, N. S. *Org. Electron.* **2012**, *13* (5), 919–924.

(226) Gowacki, E. D.; Leonat, L.; Voss, G.; Bodea, M. A.; Bozkurt, Z.; Ramil, A. M.; Irimia-Vladu, M.; Bauer, S.; Sariciftci, N. S. *AIP Adv.* **2011**, *1* (4), 6–11.

(227) Mei, J.; Diao, Y.; Appleton, A. L.; Fang, L.; Bao, Z. *J. Am. Chem. Soc.* **2013**, *135*, 6724–6746.

(228) Wolk, J. L.; Frimer, A. A. *Molecules* **2010**, *15* (8), 5561–5580.

(229) Fulmer, G. R.; Miller, A. J. M.; Sherden, N. H.; Gottlieb, H. E.; Nudelman, A.; Stoltz, B. M.; Bercaw, J. E.; Goldberg, K. I. *Organometallics* **2010**, *29*, 2176–2179.